Topics in Current Chemistry 368

Nicolas Ferré
Michael Filatov
Miquel Huix-Rotllant *Editors*

Density-Functional Methods for Excited States

Springer

368
Topics in Current Chemistry

Aims and Scope

The series Topics in Current Chemistry presents critical reviews of the present and future trends in modern chemical research. The scope of coverage includes all areas of chemical science including the interfaces with related disciplines such as biology, medicine and materials science.

The goal of each thematic volume is to give the non-specialist reader, whether at the university or in industry, a comprehensive overview of an area where new insights are emerging that are of interest to larger scientific audience.

Thus each review within the volume critically surveys one aspect of that topic and places it within the context of the volume as a whole. The most significant developments of the last 5 to 10 years should be presented. A description of the laboratory procedures involved is often useful to the reader. The coverage should not be exhaustive in data, but should rather be conceptual, concentrating on the methodological thinking that will allow the non-specialist reader to understand the information presented.

Discussion of possible future research directions in the area is welcome.

Review articles for the individual volumes are invited by the volume editors.

Readership: research chemists at universities or in industry, graduate students.

More information about this series at http://www.springer.com/series/128

Nicolas Ferré • Michael Filatov •
Miquel Huix-Rotllant
Editors

Density-Functional Methods for Excited States

With contributions by

C. Adamo · M. Barbatti · K. Bennett · M.E. Casida ·
R. Crespo-Otero · C. Daniel · M. Filatov · K.J.H. Giesbertz ·
U. De Giovannini · W. Hua · M. Huix-Rotllant · D. Jacquemin ·
M. Krykunov · A.H. Larsen · S. Mukamel · A. Nikiforov ·
Y.C. Park · K. Pernal · A. Rubio · I. Seidu · W. Thiel ·
C.A. Ullrich · Z.-h. Yang · Y. Zhang · T. Ziegler

Springer

Editors
Nicolas Ferré
Institut de Chimie Radicalaire
Université d'Aix-Marseille
Marseille, France

Michael Filatov
Inst. für Physikalische und Theoretische Chemie
Universität Bonn
Bonn, Germany

Miquel Huix-Rotllant
Institut für Physikalische und Theoretische Chemie
Goethe-Universität Frankfurt am Main
Frankfurt, Germany

ISSN 0340-1022 ISSN 1436-5049 (electronic)
Topics in Current Chemistry
ISBN 978-3-319-22080-2 ISBN 978-3-319-22081-9 (eBook)
DOI 10.1007/978-3-319-22081-9

Library of Congress Control Number: 2015947367

Springer Cham Heidelberg New York Dordrecht London

Printed on acid-free paper

Springer International Publishing AG Switzerland is part of Springer Science+Business Media (www.springer.com)

Obituary

It is with great sadness and sorrow that we have learnt about the sudden and untimely death of our colleague, Prof. Dr. Tom Ziegler. Tom was a bright scientist and one of the founders and pioneers of density functional theory. Tom has always supported and encouraged new developments and always took an active part in advancing and promoting them. Tom's recent research on constricted variational density functional theory holds considerable promise for the field of quantum theoretical modeling of excited electronic states, and one of the latest accounts of these developments is published in this book. Tom will be sorely missed by his colleagues and the entire community of quantum theoretical chemists.

Preface

The rapidly expanding use of ultrafast laser spectroscopic methods to study the photodynamics of chemical bonds underlines the importance of accurate theoretical interpretation and modeling of experimental observations. To match this need there was recent progress in the development and application of computational methods based on density functional theory (DFT) designed to describe the excited electronic states and the related potential energy surfaces (PESs). These developments are especially valuable as DFT methods enable one to study the properties of excited states and to obtain on-the-fly the relevant dynamical parameters of large molecular and condensed phase species occurring in natural as well as artificial photoactive systems. As Kohn–Sham DFT is strictly formulated for ground electronic states only [1, 2], excited electronic states are typically accessed through the use of linear response formalism implemented in time-dependent DFT (TD-DFT) methodology [3, 4], which currently enjoys a wide popularity among theoretical photochemists and photophysicists. The widespread use of TD-DFT, however, revealed certain drawbacks and limitations of the methodology, which are being constantly addressed through the development of improved computational protocols, new exchange-correlation density functionals, and conceptually new computational approaches. Besides methodological developments in the domain of linear response TD-DFT, there is growing activity in the field of development of alternative time-independent DFT methods as well as the methods going beyond the paradigm of electronic density and exploring the world of (one-electron) density matrix functionals. Although a number of excellent reviews of TD-DFT formalism can be found in the literature [5–9], the rate of new developments seems to outpace the rate of review publishing. This book attempts to fill the gap by providing a collection of chapters addressing the most recent developments in the realm of DFT methodology for the excited electronic states written by leading experts in the field.

The opening chapter (p. 1) of the book gives a broad perspective on linear response TD-DFT and its formal connection to many-body theory. By exploring the latter, the authors expand on the possibilities to ameliorate some well-known deficiencies of currently available TD-DFT methodology, especially with regard to treatment of double (and, in general, multiple) excitations and proper description of

chemical bond dissociation. The dressed TD-DFT approach and its current and potential capabilities are discussed in detail. An entirely different approach to describing excited states in the context of DFT is taken in the following two chapters, which expand on the use of time-independent methodologies. The constricted-variational DFT method, presented in the second chapter (p. 61), has the potential to outperform the currently available linear response TD-DFT when describing excitations in large conjugated systems or charge transfer excitations, both of which are notoriously difficult for the standard linear response TD-DFT formalism. A practically accessible implementation of ensemble DFT formalism, presented in the next chapter (p. 97), holds great promise for theoretical modeling of non-adiabatic relaxation processes of excited electronic states, relevant to photochemistry and photovoltaics, and provides proper description of real and avoided crossings between the ground and excited electronic states of large molecular species. To complement these new developments, the fourth chapter (p. 125) gives a wide perspective on the general background and practical aspects of a novel quantum theoretical approach to the ground and excited states of electronic systems – density matrix functional theory (DMFT). Although a younger methodology than DFT, DMFT has the potential to overtake its counterpart once practically affordable functionals of the one-body density matrix become available.

Methodological aspects of the theoretical description of excited electronic states in the condensed phase and open quantum systems in the framework of TD-DFT are amply discussed in the fifth and sixth chapters of the book. On p. 185 Ullrich and Yang give a comprehensive survey of currently available exchange-correlation kernels of TD-DFT, analyze their shortcomings, and outline possible remedies for the description of excitonic states in condensed phase systems. A comprehensive and pedagogical review of theoretical approaches, such as complex scaling and open boundary conditions, for the description of time-dependent phenomena in open quantum systems, especially with regard to resonance states photoemission spectroscopy, is given in the chapter by Rubio et al. on p. 219. A contemporary and encyclopedic presentation of various approaches for theoretical modeling of nonlinear core and valence X-ray spectra is presented by Mukamel et al. on p. 273 in the seventh chapter of the book. In this chapter the use of DFT/TD-DFT methods to address the demands of nonlinear X-ray spectroscopy measurements are analyzed in depth and the prospect of their use are outlined.

Practical aspects of using TD-DFT for computational description of molecular electronic spectroscopy are reviewed in the chapter by Jacquemin and Adamo on p. 347. Special emphasis was put on going beyond the vertical excitation approximation in TD-DFT and including vibronic effects for realistic description of 0–0 transition energies in real-life molecular systems. The use of TD-DFT for computational modeling of absorption spectroscopy, emission properties, and ultrafast intersystem crossing processes in transition metal complexes is surveyed by Daniel (p. 377) in Chap. 8, where special attention is paid to the inclusion of spin-orbit and vibronic effects in TD-DFT computations. The ability of the DFT/TD-DFT framework to provide a proper description of dynamical effects on the spectroscopic and photochemical properties of molecular species is analyzed in the chapters by

Barbatti and Crespo-Otero and Huix-Rotllant et al. A comprehensive survey of the use of DFT and TD-DFT methods in the context of quasi-classical surface hopping non-adiabatic molecular dynamics simulations is given in Chap. 10 on p. 415, where the inability of the current linear response TD-DFT in the adiabatic approximation to describe properly the real crossings between the ground and excited electronic sates, the so-called conical intersections, was identified as the major cause of spurious predictions for the photodynamics of excited states. This inability of the standard TD-DFT to describe the conical intersections was analyzed further in the following chapter (p. 445), where approaches represented by the spin-flip TD-DFT and ensemble DFT methodologies were proposed as viable alternative to the conventional TD-DFT calculations.

It is our sincere belief that these chapters, written by renowned experts in quantum molecular and condensed phase theory and computational spectroscopy, present the most contemporary state of affairs in the field of application of density functional theory to the description of excited electronic states and lay down guidelines for future developments, thus assisting the widespread community of computational quantum scientists in extending the range of applicability and improving the quality of predictions of this exciting theoretical methodology.

Nicolas Ferré
Michael Filatov
Miquel Huix-Rotllant

References

1. Hohenberg P, Kohn W (1964) Phys Rev 136:B864
2. Kohn W, Sham LJ (1965) Phys Rev 140:A1133
3. Runge E, Gross EKU (1984) Phys Rev Lett 52:997
4. Casida ME (1995) In: Chong DP (ed) Recent advances in density functional methods, part I. World Scientific, Singapore, pp 155–192
5. Gross EKU, Dobson JF, Petersilka M (1996) In: Nalewajski RF (ed) Density functional theory, Topics in Current Chemistry, vol 181. Springer, Berlin, Heidelberg, pp 81–172
6. Marques MAL, Gross EKU (2004) Annu Rev Phys Chem 55:427
7. Marques MAL, Ullrich CA, Nogueira F, Rubio A, Burke K, Gross EKU (eds) (2006) Time-depended density functional theory, Lecture Notes in Physics, vol 706. Springer, Berlin, Heidelberg
8. Casida ME, Huix-Rotllant M (2012) Annu Rev Phys Chem 63:287
9. Ullrich CA (2012) Time-dependent density-functional theory: concepts and applications. OUP, Oxford

Contents

Top Curr Chem (2016) 368: 1–60
DOI: 10.1007/128_2015_632

Published online: 24 May 2015

Many-Body Perturbation Theory (MBPT) and Time-Dependent Density-Functional Theory (TD-DFT): MBPT Insights About What Is Missing In, and Corrections To, the TD-DFT Adiabatic Approximation

Mark E. Casida and Miquel Huix-Rotllant

Abstract In their famous paper, Kohn and Sham formulated a formally exact density-functional theory (DFT) for the ground-state energy and density of a system of N interacting electrons, albeit limited at the time by certain troubling representability questions. As no practical exact form of the exchange-correlation (xc) energy functional was known, the xc-functional had to be approximated, ideally by a local or semilocal functional. Nowadays, however, the realization that Nature is not always so nearsighted has driven us up Perdew's Jacob's ladder to find increasingly nonlocal density/wavefunction hybrid functionals. Time-dependent (TD-) DFT is a younger development which allows DFT concepts to be used to describe the temporal evolution of the density in the presence of a perturbing field. Linear response (LR) theory then allows spectra and other information about excited states to be extracted from TD-DFT. Once again the exact TD-DFT xc-functional must be approximated in practical calculations and this has historically been done using the TD-DFT adiabatic approximation (AA) which is to TD-DFT very similar to what the local density approximation (LDA) is to conventional ground-state DFT. Although some of the recent advances in TD-DFT focus on what can be done within the AA, others explore ways around the AA. After giving an overview of DFT, TD-DFT, and LR-TD-DFT, this chapter focuses on many-body corrections to LR-TD-DFT as one way to build hybrid density-functional/

M.E. Casida (✉)
Département de Chimie Moléculaire, Institut de Chimie Moléculaire de Grenoble, Université Joseph Fourier (Grenoble I), 301 rue de la Chimie, BP 53, 38041 Grenoble Cedex 9, France
e-mail: mark.casida@ujf-grenoble.fr

M. Huix-Rotllant
Institut für Physikalische und Theoretische Chimie, Universität Frankfurt am Main, Frankfurt, Germany
e-mail: miquel.huix@gmail.com

wavefunction methodology for incorporating aspects of nonlocality in time not present in the AA.

Keywords Electronic excited states · Many-body perturbation theory · Photochemistry · Time-dependent density-functional theory

Contents

1 Introduction

> I have not included chemistry in my list [of the physical sciences] because, though Dynamical Science is continually reclaiming large tracts of good ground from one side of Chemistry, Chemistry is extending with still greater rapidity on the other side, into regions where the dynamics of the present day must put her hand on her mouth. But Chemistry is a Physical Science...
>
> — James Clerk Maxwell, *Encyclopaedia Britannica*, ca. 1873 [1]

Much has changed since Maxwell first defended chemistry as a physical science. The physics applied to chemical systems now involves as much, if not more, quantum mechanics than classical dynamics. However, some things have not changed. Chemistry still seems to extend too rapidly for first principles modeling to keep up. Fortunately, density-functional theory (DFT) has established itself as a computationally simple way to extend ab initio[1] accuracy to larger systems than

[1] The term ab initio is used here as it is typically used in quantum chemistry. That is, ab initio refers to first-principles Hartree–Fock-based theory, excluding DFT. In contrast, the term ab initio used in the solid state physics literature usually encompasses DFT.

where ab initio quantum chemical methods can traditionally be applied. The reluctance to use DFT for describing excited states has even given way as linear response (LR-) time-dependent (TD-) DFT has become an established way to calculate excited-state properties of medium size and large molecules. One of the strengths of TD-DFT is that it is formally an exact theory. However, as in traditional DFT, problems arise in practice because of the need to make approximations. Of course, from the point of view of a developer of new methods, when people are given a little then they immediately want more. As soon as LR-TD-DFT was shown to give reasonably promising results in one context, many people in the modeling community immediately wanted to apply LR-TD-DFT in a whole range of more challenging contexts. It then became urgent to explore the limits of applicability of *approximate* TD-DFT and to improve approximations in order to extend these limits. Much work has been done on this problem and there are many success stories to tell about LR-TD-DFT. Indeed, many of the chapters in this book describe some of these challenging contexts where conventional LR-TD-DFT approximations do work. In this chapter, however, we want to focus on the cutting edge where LR-TD-DFT finds itself seriously challenged and yet progress is being made. In particular, what we have in mind are photochemical applications where interacting excited states of fundamentally different character need to be described with similar accuracy and where bonds may be in the process of breaking or forming. The approach we take is to introduce a hybrid method where many-body perturbation theory (MBPT) corrections are added on top of LR-TD-DFT. We also use the tools we have developed to gain some insight into what needs to be included in the TD-DFT exchange-correlation (xc) functional in order for it to describe photochemical problems better.

Applications of LR-TD-DFT to photochemistry are no longer rare. Perhaps the earliest attempt to apply LR-TD-DFT to photochemistry was the demonstration that avoided crossings between formaldehyde excited-state curves could indeed be described with this method [2]. Further hope for photochemistry from LR-TD-DFT was raised again only a few years later [3, 4], with an example application to the photochemistry of oxirane appearing after another 5 years [5, 6]. Casida et al. [7] provides a recent review of the present state of LR-TD-DFT applied to photochemistry and where some of the difficulties lie.

Let us try to focus on some key problems. Photophenomena are frequently divided into photophysics, when the photoprocess ends with the same molecules with which it started, and photochemistry, when the photoprocess ends with different molecules. This is illustrated by the cartoon in Fig. 1. An example of a typical photophysical process would be beginning at one S_0 minimum, exciting to the singly-excited S_1 state, and reverting to the same S_0 minimum. In contrast, an example of a typical photochemical process would be exciting from one S_0 minimum to an S_1 excited state, followed by moving along the S_1 surface, through avoided crossings, conical intersections, and other photochemical funnels, to end up finally at the other S_0 minimum. State-of-the-art LR-TD-DFT does a reasonable job modeling photophysical processes but has much more difficulty with photochemical processes. The main reason is easily seen in Fig. 1 – namely, that

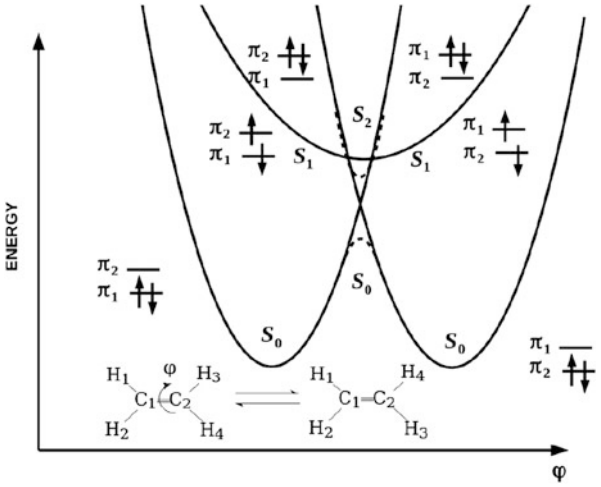

Fig. 1 Typical curves for the singlet photochemical isomerization of ethylene

photochemical processes often require an explicit treatment of doubly excited states and these are beyond the scope of conventional LR-TD-DFT. There are several ways to remedy this problem which have been discussed in a previous review article [8]. In this chapter we concentrate on one way to explore and correct the double excitation problem using a hybrid MBPT/LR-TD-DFT approach.

The rest of this chapter is organized as follows. The next section (Sect. 2) provides a small review of the current state of DFT, TD-DFT, and LR-DFT. Section 3 begins with an introduction to the key notions of MBPT needed to derive corrections to approximate LR-TD-DFT and derives some basic equations. Section 4 shows that these corrections can be used in practical applications through an exploration of dressed LR-TD-DFT. Ideally it would be nice to be able to use these corrections to improve the xc functional of TD-DFT. However, this involves an additional localization step which is examined in Sect. 5. Section 6 sums up with some perspectives.

2 Brief Review

This section reviews a few concepts which in some sense are very old: DFT is about 50 years old, TD-DFT is about 30 years old, and LR-TD-DFT (in the form of the Casida equations) is about 20 years old. Thus many of the basic concepts are now well known. However, this section is necessary to define some notation and because some aspects of these subjects have continued to evolve and so need to be updated.

2.1 Density-Functional Theory (DFT)

Hohenberg and Kohn [9] and Kohn and Sham [10] defined DFT in the mid-1960s when they gave formal rigor to earlier work by Thomas, Fermi, Dirac, Slater, and others. This initial work has been nicely reviewed in well-known texts [11–13] and so we do not dwell on details here but rather concentrate on what is essential in the present context. Hartree atomic units ($\hbar = m_e = e = 1$) are used throughout unless otherwise specified.

Kohn and Sham introduced orthonormal auxiliary functions (Kohn–Sham orbitals) $\psi_i(1)$ and corresponding occupation numbers n_i which allow the density to be expressed as

$$\rho(1) = \sum_i n_i \left|\psi_i(1)\right|^2, \tag{1}$$

and the electronic energy to be expressed as

$$E = \sum_i n_i \left\langle \psi_i \middle| \hat{t}_s + v \middle| \psi_i \right\rangle + E_H[\rho] + E_{\mathrm{xc}}[\rho]. \tag{2}$$

Here we use a notation where $i = (\mathbf{r}_i, \sigma_i)$ stands for the space $\mathbf{r}_i$ and spin σ_i coordinates of electron i, $\hat{t}_s = -(1/2)\nabla^2$ is the noninteracting kinetic energy operator, v is the external potential which represents the attraction of the electron to the nuclei as well as any applied electric fields, $E_H[\rho] = \iint \rho(1)\rho(2)/r_{12}\, d1d2$ is the Hartree (or Coulomb) energy, and $E_{\mathrm{xc}}[\rho]$ is the xc-energy which includes everything not included in the other terms (i.e., exchange, correlation, and the difference between the interacting and noninteracting kinetic energies). Minimizing the energy (2) subject to the constraint of orthonormal orbitals gives the Kohn–Sham orbital equation:

$$\hat{h}_s[\rho]\psi_i = \varepsilon_i \psi_i, \tag{3}$$

where the Kohn–Sham Hamiltonian, $\hat{h}_s[\rho](1)$, is the sum of $\hat{t}_s(1) + v(1)$, the Hartree (or Coulomb) potential $v_H[\rho](1) = \int \rho(2)/r_{12}\, d2$, and the xc-potential $v_{\mathrm{xc}}[\rho](1) = \delta E_{\mathrm{xc}}[\rho]/\delta\rho(1)$.

An important but subtle point is that the Kohn–Sham equation should be solved self-consistently with lower energy orbitals filled before higher energy orbitals (*Aufbau* principle) as befits a system of noninteracting electrons. If this can be done with integer occupancy, then the system is said to be noninteracting v-representable (NVR). Most programs try to enforce NVR, but it now seems likely that NVR fails for many systems, even in exact Kohn–Sham DFT. The alternative is to consider fractional occupation within an ensemble formalism. An important

Table 1 Jacob's ladder for functionals [14] (an updated version is given in [15])

Quantum chemical heaven		
Double-hybrid		$\rho(1)$, $x(1)$, $\tau(1)$, $\psi_i(1)$, $\psi_a(1)$[a]
Hybrid		$\rho(1)$, $x(1)$, $\tau(1)$, $\psi_i(1)$[b]
mGGA[c]		$\rho(1)$, $x(1)$, $\tau(1)$[d], $\nabla^2\rho(1)$[e]
GGA[f]		$\rho(1)$, $x(1)$[g]
LDA[h]		$\rho(1)$
Hartree World		

[a]Unoccupied orbitals
[b]Occupied orbitals
[c]Meta generalized gradient approximation
[d]The local kinetic energy $\tau(1) = \sum_p n_p \psi_p(1) \nabla^2 \psi_p(1)$
[e]There is some indication that the local kinetic energy density $\tau(1)$ and the Laplacian of the charge density $\nabla^2\rho(1)$ contain comparable information [16]
[f]Generalized gradient approximation
[g]The reduced gradient $x(1) = \left|\nabla\rho(1)\right| / \rho^{4/3}(1)$
[h]Local density approximation

theorem then states that only the last occupied degenerate orbitals may be fractionally occupied (see, e.g., [12] pp. 55–56). Suitable algorithms are rare, as maintaining this condition can lead to degenerate orbitals having different occupation numbers which, in turn, may require minimizing the energy with respect to unitary transformations within the space spanned by the degenerate occupied orbitals with different occupation numbers. These points have been previously discussed in somewhat greater detail in [8]. Most programs show at least an effective failure of NVR when using approximate functionals, in particular around regions of strong electron correlation, such as where bonds are being made or broken (e.g., avoided crossing of the S_0 surfaces in Fig. 1) which often shows up as self-consistent field (SCF) convergence failures.

As no practical exact form of E_{xc} is known, it must be approximated in practice. In the original papers, E_{xc} should depend only upon the charge density. However our notation already reflects the modern tendency to allow a spin-dependence in E_{xc} (spin-DFT). This additional degree of freedom makes it easier to develop improved density-functional approximations (DFAs). In recent years, this tendency to add additional functional dependencies into E_{xc} has led to generalized Kohn–Sham theories corresponding to different levels of what Perdew has referred to as Jacob's ladder[2] for functionals (Table 1). The LDA and GGA are pure DFAs. Higher levels no longer fall within the pure DFT formalism [17] and, in particular, are subject to a different interpretation of orbital energies.

[2] "Jacob set out from Beersheba and went on his way towards Harran. He came to a certain place and stopped there for the night, because the sun had set; and, taking one of the stones there, he made it a pillow for his head and lay down to sleep. He dreamt that he saw a ladder, which rested on the ground with its top reaching to heaven, and angels of God were going up and down it." – The Bible, Genesis 28:10–13

Of particular importance to us is the hybrid level which incorporates some Hartree–Fock exchange. Inspired by the adiabatic connection formalism in DFT and seeking functionals with thermodynamic accuracy, Becke suggested a functional of roughly the form [18]

$$E_{\mathrm{xc}}^{\mathrm{hybrid}} = E_{\mathrm{x}}^{\mathrm{GGA}} + a\left(E_{\mathrm{x}}^{\mathrm{HF}} - E_{\mathrm{x}}^{\mathrm{GGA}}\right) + E_{\mathrm{c}}^{\mathrm{GGA}}. \tag{4}$$

The a parameter was initially determined semi-empirically but a choice of $a = 0.25$ was later justified on the basis of MBPT [19]. This is a global hybrid (GH), to distinguish it from yet another type of hybrid, namely the range-separated hybrid (RSH). Initially proposed by Savin [20], RSHs separate the $1/r_{12}$ interelectronic repulsion into a short-range (SR) part to be treated by density-functional theory and a long-range (LR) part to be treated by wavefunction methodology. A convenient choice uses the complementary error function for the short-range part, $(1/r_{12})_{\mathrm{SR}} = \mathrm{erfc}(\gamma r_{12})/r_{12}$, and the error function for the long-range part, $(1/r_{12})_{\mathrm{LR}} = \mathrm{erf}(\gamma r_{12})/r_{12}$. In this case, $\gamma = 0$ corresponds to pure DFT whereas $\gamma = \infty$ corresponds to Hartree–Fock. See [21] for a recent review of one type of RSH.

2.2 Time-Dependent (TD-) DFT

Conventional Hohenberg–Kohn–Sham DFT is limited to the ground stationary state, but chemistry is also concerned with linear and nonlinear optics and molecules in excited states. Time-dependent DFT has been developed to address these issues. This section first reviews formal TD-DFT and then briefly discusses TD-DFAs. There are now a number of review articles on TD-DFT (some of which are cited in this chapter), two summer school multi-author texts [22, 23], and now a single-author textbook [24]. Our review of formal TD-DFT follows [24], which the reader may wish to consult for further details. Our comments about the Frenkel–Dirac variational principle and TD-DFAs come from our own synthesis of the subject.

A great deal of effort has been put into making formal TD-DFT as rigorous as possible and firming up the formal underpinnings of TD-DFT remains an area of active research. At the present time, formal TD-DFT is based upon two theorems, namely the Runge–Gross theorem [25] and the van Leeuwen theorem [26]. They remind one of us (MEC) of some wise words from his thesis director (John E. Harriman) at the time of his (MECs) Ph.D. studies: "Mathematicians always seem to know more than they can prove."[3] The Runge–Gross and van Leeuwen

[3] This is formalized in mathematical logic theory by Gödel's incompleteness theorem which basically says that there are always more things that are true than can be proven to be true.

theorems are true for specific cases where they can be proven, but we believe them to hold more generally and efforts continue to find more general proofs.

2.2.1 Runge–Gross Theorem

This theorem states, with two caveats, that the time-dependent external potential $v(\mathbf{1})$ is determined up to an arbitrary function of time by the initial wavefunction $\Psi_0 = \Psi(t_0)$ at some time t_0 and by the time-dependent charge density $\rho(\mathbf{1})$. Here we have enriched our notation to include time, $\mathbf{i} = (i, t_i) = (\mathbf{r}_i, \sigma_i, t_i)$. The statement that the external potential is only determined up to an arbitrary function of time simply means that the phase of the associated wave function is only determined up to a spatially-constant time-dependent constant. This is because two external potentials differing by an additive function of time $\widetilde{v}(1) = v(1) + c(t_1)$ lead to associated wave functions $\widetilde{\Psi}(t) = e^{-i\alpha(t)}\Psi(t)$ where $d\alpha(t)/dt = c(t)$. A consequence of the Runge–Gross theorem is that expectation values of observables $\hat{A}(t)$ are functionals of the initial wavefunction and of the time-dependent charge density,

$$A[\rho, \Psi_0](t) = \left\langle \Psi[\rho, \Psi_0](t) \middle| \hat{A}\,(t) \middle| \Psi[\rho, \Psi_0](t) \right\rangle. \tag{5}$$

The proof of the theorem assumes (caveat 1) that the external potential is expandable in a Taylor series in time in order to show that the time-dependent current density determines the time-dependent external potential up to an additive function of time. The proof then goes on to make a second assumption (caveat 2) that the external potential goes to zero at large r at least as fast as $1/r$ in order to prove that the time-dependent charge density determines the time-dependent current density.

2.2.2 van Leeuwen Theorem

Given a system with an electron–electron interaction $w(1,2)$, external potential $v(\mathbf{1})$, and initial wavefunction Ψ_0, and another system with the same time-dependent charge density $\rho(\mathbf{1})$, possibly different electron–electron interaction $\widetilde{w}(1,2)$, and initial wavefunction $\widetilde{\Psi}_0$, then the external potential of the second system $\tilde{v}(\mathbf{1})$ is uniquely determined up to an additive function of time. It should be noted that we recover the Runge–Gross theorem when $w(1,2) = \widetilde{w}(1,2)$ and $\Psi_0 = \widetilde{\Psi}_0$. However, the most interesting result is perhaps when $\widetilde{w}(1,2) = 0$ because this corresponds to a Kohn–Sham-like system of noninteracting electrons, showing us that the external potential of such a system is unique and ultimately justifying the time-dependent Kohn–Sham equation

$$\hat{h}\left[\rho, \Psi_0, \widetilde{\Psi}_0\right](\mathbf{1})\psi_i(\mathbf{1}) = i\frac{\partial}{\partial t}\psi_i(\mathbf{1}), \tag{6}$$

where

$$\hat{h}\left[\rho, \Psi_0, \widetilde{\Psi}_0\right](\mathbf{1}) = \hat{t}_s + v(\mathbf{1}) + v_H[\rho](\mathbf{1}) + v^{xc}\left[\rho, \Psi_0, \widetilde{\Psi}_0\right](\mathbf{1}). \tag{7}$$

The proof of the theorem assumes (caveat 1) that the external potential is expandable in a Taylor series in time *and* (caveat 2) that the charge density is expandable in a Taylor series in time. Work on removing these caveats is ongoing [27–30] ([24] provides a brief, but dated, summary).

2.2.3 Frenkel–Dirac Action

This is a powerful and widespread action principle used to derive time-dependent equations within approximate formalisms. Making the action

$$A = \int_{t_0}^{t_1} \left\langle \Psi(t') \middle| i\frac{\partial}{\partial t'} - \hat{H}(t') \middle| \Psi(t') \right\rangle dt', \tag{8}$$

stationary subject to the conditions that $\delta\Psi(t_0) = \delta\Psi(t_1) = 0$ leads to the time-dependent Schrödinger equation $\hat{H}(t)\Psi(t) = i\partial\Psi(t)/\partial t$. Runge and Gross initially suggested that $A = A[\rho, \Psi_0]$ and used this to derive a more explicit formula for the TD-DFT xc-potential as a functional derivative of an xc-action, but this led to causality problems. A simple explanation and way around these contradictions was presented by Vignale [31] who noted that, as the time-dependent Schrödinger equation is a first-order partial differential equation in time, $\Psi(t_1)$ is determined by $\Psi(t_0)$ so that, whereas $\delta\Psi(t_0)$ may be imposed, $\delta\Psi(t_1)$ may not be imposed. The proper Frenkel–Dirac–Vignale action principle is then

$$\delta A = i\left\langle \Psi(t_1) \middle| \delta\Psi(t_1) \right\rangle. \tag{9}$$

In many cases, the original Frenkel–Dirac action principle gives the same results as the more sophisticated Frenkel–Dirac–Vignale action principle. Messud et al. [32] gives one example of where this action principle has been used to derive an xc-potential within a TD-DFA. Other solutions to the Dirac–Frenkel causality problem in TD-DFT may also be found in the literature [33–37].

2.2.4 Time-Dependent Density-Functional Approximations (TD-DFAs)

As the exact TD-DFT xc-functional is unknown, it must be approximated. In most cases we can ignore the initial state dependences because we are treating a system

Table 2 Jacobs ladder for memory functionals [14]

Quantum chemical heaven		
TD-RDMT[a]		$\gamma(1,2,t)$[b], $\theta_i(t)$[c]
TD-OEP[d]		$\psi_i(\mathbf{1})$[e]
L-TD-DFT[f]		Fluid position and deformation tensor
TD-CDFT[g]		$\rho(\mathbf{1})$, $\mathbf{j}(\mathbf{1})$[h]
TD-DFT		$\rho(\mathbf{1})$
Hartree World		

[a]TD reduced-density-matrix theory
[b]TD reduced-density matrix
[c]Natural orbital phases
[d]TD optimized effective potential
[e]TD occupied orbitals
[f]Lagrangian TD-DFT
[g]TD current-density-functional theory
[h]The current density

initially in its ground stationary state exposed to a time-dependent perturbation. This is because if the initial state is the ground stationary state, then, according to the first Hohenberg–Kohn theorem of conventional DFT, $\Psi_0 = \Psi_0[\rho]$ and $\widetilde{\Psi}_0 = \widetilde{\Psi}_0[\rho]$.

The simplest and most successful TD-DFA is the TD-DFT adiabatic approximation (AA) which states that the xc-potential reacts instantaneously and without memory to any temporal change in the time-dependent density,

$$v_{\mathrm{xc}}^{\mathrm{AA}}[\rho](\mathbf{1}) = \frac{\delta E_{\mathrm{xc}}\left[\rho_{t_1}(1)\right]}{\delta \rho_{t_1}(1)}. \tag{10}$$

The notation is a bit subtle here: $\rho_{t_1}(1)$ is $\rho(1) = \rho(1, t_1)$ at a fixed value of time, meaning that $\rho_{t_1}(1)$ is uniquely a function of the space and spin coordinates, albeit at fixed time t_1. The AA approximation has been remarkably successful and effectively defines conventional TD-DFT.

Going beyond the TD-DFT AA is the subject of ongoing work. Defining new Jacob's ladders for TD-DFT may be helpful here. The first attempt to do so was the definition by one of us (MEC) of a "Jacob's jungle gym" consisting of parallel Jacob's ladders for E_{xc}, $v_{\mathrm{xc}}(\mathbf{1})$, $f_{\mathrm{xc}}(\mathbf{1},\mathbf{2}) = \delta v_{\mathrm{xc}}(\mathbf{1})/\delta\rho(\mathbf{2})$, etc. [3]. This permitted the simultaneous use of different functionals on different ladders on the grounds that accurate lower derivatives did not necessarily mean accurate higher derivatives. Of course, being able to use a consistent level of approximation across all ladders could be important for some types of applications (e.g., those involving analytical derivatives). With this in mind, the authors recently suggested a new Jacob's ladder for TD-DFT (Table 2).

2.3 Linear Response (LR-) TD-DFT

As originally formulated, TD-DFT seems ideal for the calculation of nonlinear optical (NLO) properties from the dynamical response of the molecular dipole moment $\mu(t)$ to an applied electric field $\varepsilon(t) = \varepsilon \cos(\omega t)$,

$$\Delta\mu(t) = \int \alpha(t - t')\varepsilon(t')dt' + \text{HOT}, \tag{11}$$

using real-time numerical integration of the TD Kohn–Sham equation, but it may also be used to calculate electronic absorption spectra. This section explains how.

In (11) "HOT" stands for "higher-order terms" and the quantity α is the dynamic dipole polarizability. After Fourier transforming, (11) becomes

$$\Delta\mu(\omega) = \alpha(\omega)\varepsilon(\omega) + \text{HOT}, \tag{12}$$

If the applied field is sufficiently small then we are in the LR regime where we may neglect the HOT and calculate the dipole polarizability as $\alpha_{i,j}(\omega) = \Delta\mu_i(\omega)/\varepsilon_j(\omega)$. Electrical absorption spectra may be calculated from this because of the sum-over-states theorem in optical physics,

$$\alpha(\omega) = \sum_{I \neq 0} \frac{f_I}{\omega_I^2 - \omega^2}, \tag{13}$$

where $\alpha = (1/3)\left(\alpha_{xx} + \alpha_{yy} + \alpha_{zz}\right)$. Here

$$\omega_I = E_I - E_0, \tag{14}$$

is the excitation energy[4] and

$$f_I = \frac{2}{3}\omega_I \left|\langle 0|\mathbf{r}|I\rangle\right|^2, \tag{15}$$

is the corresponding oscillator strength. This sum-over-states theorem makes good physical sense because we expect the response of the charge density and dipole moment to become infinite (i.e., to jump suddenly) when the photon frequency corresponds to an electronic excitation energy. Usually in real-time TD-DFT programs, the spectral function is calculated as

[4] Remember that $\hbar = 1$ in the atomic units used here.

$$S(\omega) = \frac{2\omega}{\pi} \Im\alpha(\omega + i\eta)\,, \tag{16}$$

which generates a Lorentzian broadened spectrum with broadening controlled by the η parameter. The connection with the experimentally observed molar extinction coefficient as a function of $\nu = \omega/(2\pi)$ is

$$\varepsilon(\nu) = \frac{\pi N_A e^2}{m_e c(4\pi\varepsilon_0)\ln(10)} S(2\pi\nu) \tag{17}$$

in SI units.

So far this is fine for calculating spectra but not for assigning and studying individual states. For that, it is better to take another approach using the susceptibility

$$\chi(\mathbf{1},\mathbf{2}) = \frac{\delta\rho(\mathbf{1})}{\delta v_{\text{appl}}(\mathbf{2})}\,, \tag{18}$$

which describes the response of the density to the applied perturbation v_{appl},

$$\delta\rho(\mathbf{1}) = \int \chi(\mathbf{1},\mathbf{2})\delta v_{\text{appl}}(\mathbf{2})\, d\mathbf{2}\,. \tag{19}$$

The response of the density of the Kohn–Sham fictitious system of noninteracting electrons is identical but the potential is now the Kohn–Sham single-particle potential,

$$\delta\rho(\mathbf{1}) = \int \chi_s(\mathbf{1},\mathbf{2})\delta v_s(\mathbf{2})\, d\mathbf{2}\,. \tag{20}$$

In contrast to the interacting susceptibility of (18), the noninteracting susceptibility,

$$\chi_s(\mathbf{1},\mathbf{2}) = \frac{\delta\rho(\mathbf{1})}{\delta v_s(\mathbf{2})}\,, \tag{21}$$

is known exactly from MBPT. Of course the effective potential is the sum of the applied potential and the potential produced by the response of the self-consistent field, v_{Hxc}:

$$\delta v_s(\mathbf{1}) = \delta v_{\text{appl}}(\mathbf{1}) + \int f_{\text{Hxc}}(\mathbf{1},\mathbf{2})\delta\rho(\mathbf{2})\, d\mathbf{2}\,, \tag{22}$$

where $f_{\text{Hxc}}(\mathbf{1},\mathbf{2}) = \delta v_{\text{Hxc}}(\mathbf{1})/\delta\rho(\mathbf{2})$ is the functional derivative of the Hartree plus exchange-correlation self-consistent field. Manipulating these equations is

facilitated by a matrix representation in which the integration is interpreted as a sum over a continuous index. Thus,

$$\delta\boldsymbol{\rho} = \boldsymbol{\chi}\delta\boldsymbol{v}_{\text{appl}} = \boldsymbol{\chi}_s\left(\delta\boldsymbol{v}_{\text{appl}} + \boldsymbol{f}_{\text{Hxc}}\delta\boldsymbol{\rho}\right), \tag{23}$$

is easily manipulated to give a Bethe–Salpeter-like equation (Sect. 3),

$$\boldsymbol{\chi} = \boldsymbol{\chi}_s + \boldsymbol{\chi}_s\boldsymbol{f}_{\text{Hxc}}\boldsymbol{\chi}, \tag{24}$$

or, written out more explicitly,

$$\chi(\mathbf{1},\mathbf{4}) = \chi_s(\mathbf{1},\mathbf{4}) + \int\chi_s(\mathbf{1},\mathbf{2})f_{\text{Hxc}}(\mathbf{2},\mathbf{3})\chi(\mathbf{3},\mathbf{4})\,d\mathbf{2}d\mathbf{3}. \tag{25}$$

Equation (23) may be solved iteratively for $\delta\rho$. Alternatively $\delta\rho$ may be obtained by solving

$$\left(\boldsymbol{\chi}_s^{-1} - \boldsymbol{f}_{\text{Hxc}}\right)\delta\boldsymbol{\rho} = \delta\boldsymbol{v}_{\text{appl}}, \tag{26}$$

which typically involves iterative Krylov space techniques because of the large size of the matrices involved.

This last equation may be manipulated to make the most common form of LR-TD-DFT used in quantum chemistry [38].[5] This is a pseudoeigenvalue problem,

$$\begin{bmatrix} \mathbf{A}(\omega) & \mathbf{B}(\omega) \\ \mathbf{B}^*(\omega) & \mathbf{A}^*(\omega) \end{bmatrix}\begin{pmatrix} \mathbf{X} \\ \mathbf{Y} \end{pmatrix} = \omega\begin{bmatrix} \mathbf{1} & \mathbf{0} \\ \mathbf{0} & -\mathbf{1} \end{bmatrix}\begin{pmatrix} \mathbf{X} \\ \mathbf{Y} \end{pmatrix}, \tag{27}$$

where

$$\begin{aligned} A_{ia,\,jb}(\omega) &= \delta_{i,\,j}\delta_{a,b}\varepsilon_{a,i} + \left(ia\middle|f_{\text{Hxc}}(\omega)\middle|jb\right) \\ B_{ia,\,bj}(\omega) &= \left(ia\middle|f_{\text{Hxc}}(\omega)\middle|bj\right). \end{aligned} \tag{28}$$

Here,

$$\left(pq\middle|f\middle|rs\right) = \iint\psi_p^*(1)\psi_q(1)f(1,2)\psi_r^*(2)\psi_s(2)\,d1d2, \tag{29}$$

is a two electron integral in Mulliken "charge-cloud" notation over the kernel f which may be the Hartree kernel [$f_H(1,2) = \delta_{\sigma_1,\sigma_2}/r_{12}$], the xc-kernel, or the sum of the two (Hxc). The index notation is $i,j,\ldots$ for occupied spin-orbitals, a,

[5] This equation is not infrequently called the "Casida equation" in the TD-DFT literature (e.g., as in [24], pp. 145–153.)

$b, \ldots$ for virtual spin-orbitals, and $p, q, \ldots$ for unspecified spin-orbitals (either occupied or unoccupied).[6] We have also introduced the compact notation

$$\varepsilon_{rs\cdots,uv\cdots} = (\varepsilon_r + \varepsilon_s + \cdots) - (\varepsilon_u + \varepsilon_v + \cdots). \tag{30}$$

Equation (28) has paired excitation and de-excitation solutions. Its eigenvalues are (de-)excitation energies, the vectors $\mathbf{X}$ and $\mathbf{Y}$ providing information about transition moments. In particular, the oscillator strength, of the transition with excitation energy ω_I may be calculated from $\mathbf{X}_I$ and $\mathbf{Y}_I$ [38]. When the adiabatic approximation (AA) to the xc-kernel is made, the $\mathbf{A}$ and $\mathbf{B}$ matrices become independent of frequency. As a consequence, the number of solutions is equal to the number of one-electron excitations, albeit dressed to include electron correlation effects. Allowing the $\mathbf{A}$ and $\mathbf{B}$ matrices to have a frequency dependence allows the explicit inclusion of two-electron (and higher) excited states.

The easiest way to understand what is missing in the AA is within the so-called Tamm–Dancoff approximation (TDA). The usual AA TDA equation,

$$\mathbf{AX} = \omega\mathbf{X}, \tag{31}$$

is restricted to single excitations. The configuration interaction (CI) equation [39],

$$(\mathbf{H} - E_0\mathbf{1})\mathbf{C} = \omega\mathbf{C}, \tag{32}$$

which includes all excitations of the system, can be put into the form of (31), but with a frequency-dependent $\mathbf{A}(\omega)$ matrix. This can be simply done by partitioning the full CI Hamiltonian into a singles excitations part ($\mathbf{A}_{1,1}$) and multiple-excitations part ($\mathbf{A}_{2+,2+}$) as

$$\begin{bmatrix} \mathbf{A}^{CI}_{1,1} & \mathbf{A}^{CI}_{1,2+} \\ \mathbf{A}^{CI}_{2+,1} & \mathbf{A}^{CI}_{2+,2+} \end{bmatrix} \begin{pmatrix} \mathbf{C}_1 \\ \mathbf{C}_{2+} \end{pmatrix} = \omega \begin{pmatrix} \mathbf{C}_1 \\ \mathbf{C}_{2+} \end{pmatrix}, \tag{33}$$

provided we can ignore any coupling between the ground state and excited states. Applying the standard Löwdin–Feshbach partitioning technique to (33) [40], we obtain

$$\left[\mathbf{A}^{CI}_{1,1} + \mathbf{A}^{CI}_{1,2+}\left(\omega\mathbf{1}_{2+,2+} - \mathbf{A}^{CI}_{2+,2+}\right)^{-1}\mathbf{A}^{CI}_{2+,1}\right]\mathbf{C}_1 = \omega\mathbf{C}_1, \tag{34}$$

in which it is clearly seen that multiple-excitation states arise from a frequency-dependent term missing in the AA xc-kernel [39].

[6] Sometimes we call this the FORTRAN index convention in reference to the default variable names for integers in that computer language.

In the remainder of this chapter we first show how MBPT may be used to derive expressions for the $\mathbf{A}^{CI}_{1,2+}$, $\mathbf{A}^{CI}_{2+,1}$, and $\mathbf{A}^{CI}_{2+,2+}$ blocks and show how this may be used in the form of dressed TD-DFT to correct the AA. Then we discuss localization of the terms beyond the AA in order to obtain some insight into the analytic behavior of the xc-kernel.

3 Many-Body Perturbation Theory (MBPT)

This section elaborates on the polarization propagator (PP) approach. As the PP was originally inspired by the Bethe–Salpeter equation (BSE) and as the BSE often crops up in articles from the solid-state physics community which are concerned with both TD-DFT and MBPT [41–47], we try to make the connection between the PP and BSE approaches as clear as possible. Although the two MBPT approaches are formally equivalent, differences emerge because the BSE approach emphasizes the time representation whereas the PP approach emphasizes the frequency representation. This can and typically does lead to different approximations. In particular, it seems to be easier to derive pole structure-conserving approximations needed for treating two-electron and higher excitations in the frequency representation than in the time representation. This and prior experience with the PP approach in the quantum chemistry community [48–53] have led us to favor the PP approach. We make extensive use of diagrams in order to give an overview of our manipulations. Whenever possible, more elaborate mathematical manipulations are relegated to the appendix.

3.1 Green's Functions

Perhaps the most common and arguably the most basic quantity in MBPT is the one-electron Green's function defined by

$$iG(\mathbf{1},\mathbf{2}) = \left\langle 0 \middle| \mathcal{T}\left\{ \hat{\psi}_H(\mathbf{1})\hat{\psi}^\dagger_H(\mathbf{2}) \right\} \middle| 0 \right\rangle . \tag{35}$$

Here, the subscript H indicates that the field operators are understood to be in the Heisenberg representation. Also $\mathcal{T}$ is the usual time-ordering operator, which includes anticommutation in our case (i.e., for fermions),

$$\mathcal{T}\left\{ \hat{\psi}_H(\mathbf{1})\hat{\psi}^\dagger_H(\mathbf{2}) \right\} = \theta(t_1 - t_2)\hat{\psi}_H(\mathbf{1})\hat{\psi}^\dagger_H(\mathbf{2}) - \theta(t_2 - t_1)\hat{\psi}^\dagger_H(\mathbf{2})\hat{\psi}_H(\mathbf{1}) . \tag{36}$$

The two-electron Green's function is (see p. 116 of [54])

$$G(\mathbf{1},\mathbf{2};\mathbf{3},\mathbf{4}) = (-i)^2\left\langle 0\middle|\mathcal{T}\left\{\hat{\psi}_H(\mathbf{1})\hat{\psi}_H(\mathbf{2})\hat{\psi}_H^\dagger(\mathbf{4})\hat{\psi}_H^\dagger(\mathbf{3})\right\}\middle|0\right\rangle. \tag{37}$$

The usual MBPT approach to evaluating the susceptibility, χ, uses the fact that it is the retarded form,

$$i\chi(\mathbf{1},\mathbf{2}) = \theta(t_1 - t_2)\left\langle 0\middle|[\widetilde{\rho}_H(\mathbf{1}),\widetilde{\rho}_H(\mathbf{2})]\middle|0\right\rangle, \tag{38}$$

of the time-ordered correlation function,

$$i\chi(\mathbf{1},\mathbf{2}) = \left\langle 0\middle|\mathcal{T}\{\widetilde{\rho}_H(\mathbf{1})\widetilde{\rho}_H(\mathbf{2})\}\middle|0\right\rangle, \tag{39}$$

where

$$\widetilde{\rho}_H(\mathbf{1}) = \hat{\psi}_H^\dagger(\mathbf{1})\hat{\psi}_H(\mathbf{1}) - \left\langle 0\middle|\hat{\psi}_H^\dagger(\mathbf{1})\hat{\psi}_H(\mathbf{1})\middle|0\right\rangle \tag{40}$$

is the density fluctuation operator. (See for example [54] pp. 151, 172–175.)

We will also need several generalizations of the susceptibility and the density fluctuation operator. The first is the particle-hole (ph) propagator [52], which we chose to write as

$$iL(\mathbf{1},\mathbf{2};\mathbf{3},\mathbf{4}) = \left\langle 0\middle|\mathcal{T}\{\widetilde{\gamma}(\mathbf{1},\mathbf{2})\widetilde{\gamma}(\mathbf{4},\mathbf{3})\}\middle|0\right\rangle, \tag{41}$$

where

$$\widetilde{\gamma}(\mathbf{1},\mathbf{2}) = \hat{\psi}_H^\dagger(\mathbf{2})\hat{\psi}_H(\mathbf{1}) - \left\langle 0\middle|\mathcal{T}\left\{\hat{\psi}_H^\dagger(\mathbf{2})\hat{\psi}_H(\mathbf{1})\right\}\middle|0\right\rangle \tag{42}$$

is a sort of density matrix fluctuation operator (or would be if we constrained $t_1 = t_2$ and $t_3 = t_4$). It should be noted that the ph-propagator is a four-time quantity.

[It may be useful to try to place L in the context of other two-electron propagators. The particle-hole response function [52]

$$R(\mathbf{1},\mathbf{2};\mathbf{3},\mathbf{4}) = G(\mathbf{1},\mathbf{2};\mathbf{3},\mathbf{4}) - G(\mathbf{1},\mathbf{3})G(\mathbf{2},\mathbf{4}). \tag{43}$$

Then L is related to R by the relation

$$L(\mathbf{1},\mathbf{2};\mathbf{3},\mathbf{4}) = iR(\mathbf{1},\mathbf{4};\mathbf{2},\mathbf{3})\ .] \tag{44}$$

We also need the polarization propagator (PP) which is the two-time quantity,

$$\Pi(1,2;3,4;t-t') = L(1t,2t;3t',4t'). \tag{45}$$

Written out explicitly,

$$
\begin{aligned}
&i\Pi(1,2;3,4;t-t') \\
&= \left\langle 0\middle|\mathcal{T}\left\{\hat{\psi}_H^\dagger(2t^+)\hat{\psi}_H(1t)\hat{\psi}_H^\dagger(3t'^+)\hat{\psi}_H(4t')\right\}\middle|0\right\rangle \\
&-\left\langle 0\middle|\mathcal{T}\left\{\hat{\psi}_H^\dagger(2t^+)\hat{\psi}_H(1t)\right\}\middle|0\right\rangle\left\langle 0\middle|\mathcal{T}\left\{\hat{\psi}_H^\dagger(3t'^+)\hat{\psi}_H(4t')\right\}\middle|0\right\rangle.
\end{aligned} \tag{46}
$$

The second term is often dropped in the definition of the PP. It is there to remove $\omega = 0$ excitations in the Lehmann representation. (See for example pp. 559–560 of [54].) The retarded version of the PP is the susceptibility describing the response of the one-electron density matrix,

$$\gamma(1,2;t) = \left\langle 0\middle|\hat{\psi}^\dagger(2t)\hat{\psi}(1t)\middle|0\right\rangle, \tag{47}$$

to a general (not necessarily local) applied perturbation,

$$\Pi(1,2;3,4;t-t') = \frac{\delta\gamma(1,2;t)}{\delta w_{\text{appl}}(3,4;t')}, \tag{48}$$

which is a convolution. After Fourier transforming,

$$\delta\gamma(1,2;\omega) = \int \Pi(1,2;3,4;\omega)\delta w_{\text{appl}}(3,4;\omega)\,d3d4, \tag{49}$$

or

$$\delta\boldsymbol{\gamma}(\omega) = \boldsymbol{\Pi}(\omega)\delta\boldsymbol{w}_{\text{appl}}(\omega) \tag{50}$$

in matrix form.

3.2 Diagram Rules

The representation of MBPT expansions in terms of diagrams is very convenient for bookkeeping purposes. Indeed, certain ideas such as the linked-cluster theorem [55] or the concept of a ladder approximation (see, e.g., [54] p. 136) are most naturally expressed in terms of diagrams. Diagrams drawn according to systematic rules also allow an easy way to check algebraic expressions. This is how we have used diagrams in our research. However, we introduce diagrams here for a different reason, namely because they provide a concise way to explain our work.

Several types of MBPT diagrams exist in the literature. These divide into four main classes which we call Feynman, Abrikosov, Goldstone, and Hugenholtz. Such diagrams can be distinguished by whether they are time-ordered (Goldstone and Hugenholtz) or not (Feynman and Abrikosov) and by whether they treat the electron repulsion interaction as a wavy or dotted line with an incoming and an

outgoing arrow at each end (Feynman and Goldstone) or in a symmetrized way as a point with two incoming and two outgoing arrows (Abrikosov and Hugenholtz). These differences affect how they are to be translated into algebraic expressions as does the nature of the quantity being expanded (wave function, one-electron Green's function, self-energy, polarization propagator, etc.). Given this plethora of types of diagrams and the difficulty of finding a clear explanation of how to read polarization propagator diagrams, we have chosen to present rules for how our diagrams should be translated into algebraic expressions. This is necessary because, whereas the usual practice in the solid-state literature is to use time-unordered diagrams with electron repulsions represented as wavy or dotted lines (i.e., Feynman diagrams), the usual practice in the quantum chemistry literature is using time-ordered diagrams with electron repulsions represented as points (i.e., Hugenholtz diagrams).

We limit ourselves to giving precise rules for the polarization propagator (PP) because these rules are difficult to find in the literature. The PP expressed in an orbital basis is

$$\Pi(1,2,3,4;t-t') = \sum\nolimits_{pqrs} \quad \Pi_{sr,qp}(t-t')\psi_r^*(2)\psi_s(1)\psi_q^*(3)\psi_p(4), \tag{51}$$

where

$$\begin{aligned}\Pi_{sr,qp}(t-t') = &-i\theta(t-t')\left\langle 0\middle|\hat{r}_H^\dagger(t)\hat{s}_H(t)\hat{q}_H^\dagger(t')\hat{p}_H(t')\middle|0\right\rangle \\ &- i\theta(t'-t)\left\langle 0\middle|\hat{q}_H^\dagger(t')\hat{p}_H(t')\hat{r}_H^\dagger(t)\hat{s}_H(t)\middle|0\right\rangle\end{aligned} \tag{52}$$

This makes it clear that the PP is a two time particle-hole propagator which either propagates forward in time or backward in time. To represent it we introduce the following rules:

1. Time increases vertically from bottom to top. This is in contrast to a common convention in the solid-state literature where time increases horizontally from right to left.
2. A PP is a two time quantity. Each of these twice is indicated by a horizontal dotted line. This is one type of "event" (representing the creation/destruction of an excitation).
3. Time-ordered diagrams use directed lines (arrows). Down-going arrows correspond to holes running backward in time, i.e., to occupied orbitals. Up-going arrows correspond to particles running forward in time, i.e., to unoccupied orbitals.

   At this point, the PP diagrams resemble Fig. 2. Fourier transforming leads us to the representation shown in Fig. 3. An additional rule has been introduced:
4. A downward ω arrow on the left indicates forward ph-propagation. An upward ω arrow on the right indicates backward ph-propagation.

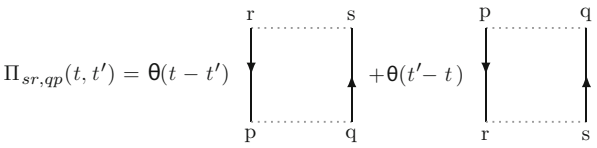

Fig. 2 Basic time-ordered finite basis set representation PP diagram

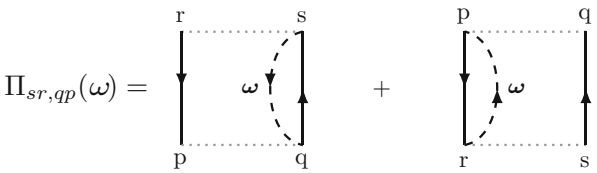

Fig. 3 Basic frequency and finite basis set representation PP diagram

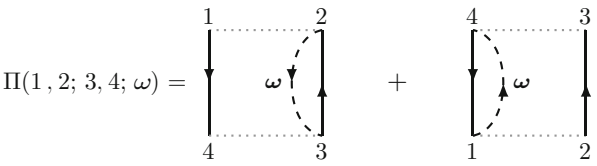

Fig. 4 Basic frequency and real space representation PP diagram

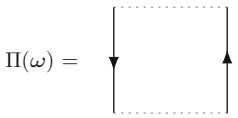

Fig. 5 Time-unordered representation PP diagram

Diagrams for the corresponding position space representation are shown in Fig. 4. Usually the labels (p, q, r, and s or 1, 2, 3, and 4) are suppressed. If the ω arrows are also suppressed, then there is no information about time-ordering and both diagrams may then be written as a single time-unordered diagram as in Fig. 5. Typical Feynman diagrams are unordered in time.

Perturbation theory introduces certain denominators in the algebraic expressions corresponding to the diagrams. These may be represented as cuts between events:

5. Each horizontal cut between events contributes a factor $\left(\pm\omega + \sum_p \varepsilon_p - \sum_h \varepsilon_h\right)^{-1}$, where $\sum_p \left(\sum_h\right)$ stands for the sum over all particle (hole) lines that are cut. The omega line only appears in the sum if it is also cut. It enters with a + sign if it is directed upwards and with a − sign if it is directed downwards.
6. There is also an overall sign given by the formula $(-1)^{h+l}$, where h is the number of hole lines and l is the number of closed loops, including the horizontal dotted event lines but ignoring the ω lines.

Diagrams are shown for the independent particle approximation in Fig. 6. The first diagram reads

Fig. 6 Zero-order PP diagrams

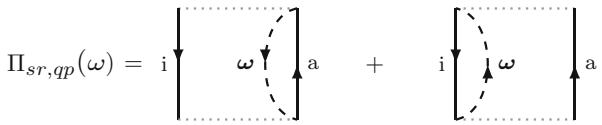

$$\Pi_{ai,ai}(\omega) = \frac{1}{\omega + \varepsilon_i - \varepsilon_a}. \tag{53}$$

The second diagram reads

$$\Pi_{ia,ia}(\omega) = \frac{1}{-\omega + \varepsilon_i - \varepsilon_a} = \frac{-1}{\omega + \varepsilon_a - \varepsilon_i}. \tag{54}$$

These two equations are often condensed in the literature as

$$\Pi_{pq,rs}(\omega) = \delta_{p,r}\delta_{q,s}\frac{n_q - n_p}{\omega + \varepsilon_q - \varepsilon_p}. \tag{55}$$

Let us now introduce one-electron perturbations in the form of M circles.

7. Each M circle in a diagram contributes a factor of $\langle p|\hat{M}_{\mathrm{xc}}|q\rangle$, where p is an incoming arrow, q is an outgoing arrow, and $\hat{M}_{\mathrm{xc}}$ is the "xc-mass operator" which is the difference between the Hartree–Fock exchange self-energy and the xc-potential – see (67). (Thus $\langle \mathrm{in}|\hat{M}_{\mathrm{xc}}|\mathrm{out}\rangle$.) For example, the term corresponding to Fig. 7b contains a factor of $\langle a|\hat{M}_{\mathrm{xc}}|c\rangle$, whereas the term corresponding to Fig. 7f contains a factor of $\langle k|\hat{M}_{\mathrm{xc}}|i\rangle$. This is a second type of "event" (representing "collision" with the quantity M_{xc}).

   For example, the term corresponding to Fig. 7j is

$$\Pi_{ck,cb}(\omega) = \frac{\langle k|\hat{M}_{\mathrm{xc}}|b\rangle}{(\omega - \varepsilon_k + \varepsilon_c)(\varepsilon_k - \varepsilon_b)}. \tag{56}$$

This brings us to the slightly more difficult treatment of electron repulsions.

8. When electron repulsion integrals are represented by dotted lines (Feynman and Goldstone diagrams), each end of the line corresponds to the labels corresponding to the same spatial point. The dotted line representation may be condensed into points (Abrikosov and Hugenholtz diagrams) as in Fig. 8. A point with two incoming arrows, labeled r and s, and two outgoing arrows, labeled p and q, contributes a factor of $(rs||pq) = (rp|f_H|sq) - (rq|f_H|sp)$. [Thus (in, in | | out, out) = (left in, right in | left in, right in) – (left in, right in | left in, right in). The minus sign is not part of the diagram as it is taken into account by other rules.] The integral notation is established in (29) and the integral

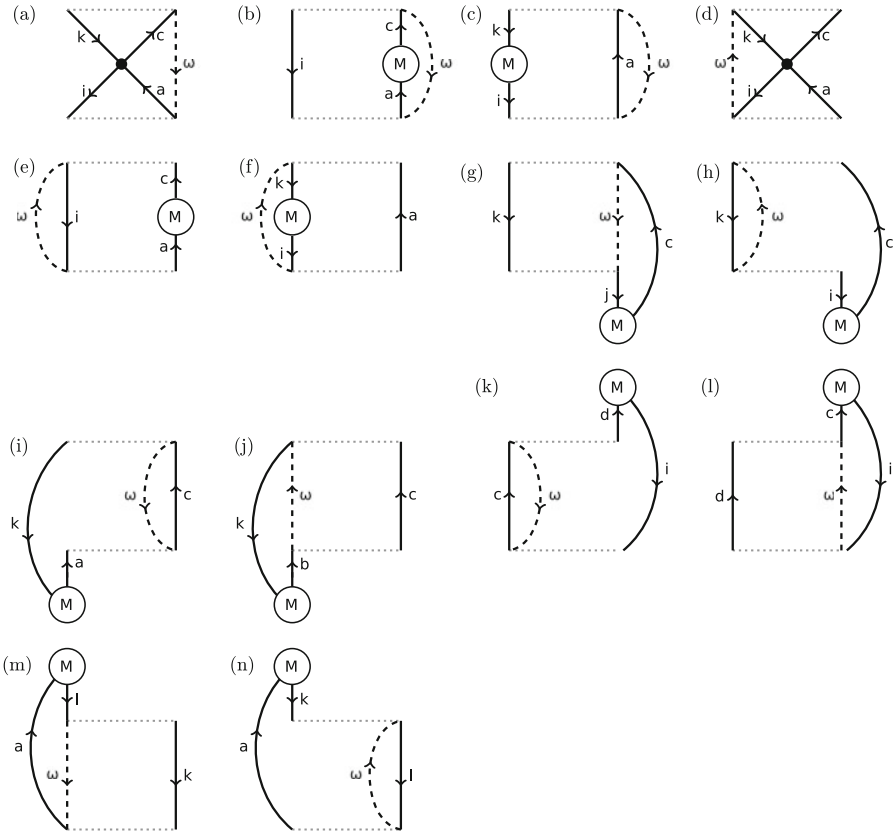

Fig. 7 First-order time-ordered diagrams Hugenholtz for $\boldsymbol{\Pi}(\omega) - \boldsymbol{\Pi}_s(\omega)$. **a–i** involve coupling between the particle-hole space; **g**, **h**, **m**, and **n** involve coupling between particle-hole space and particle-particle; **i–l** couple the particle-hole space with the hole-hole space

$$\left(pq||rs\right) = \int \psi_p^*(1)\psi_r^*(2)\frac{1}{r_{12}}(1-\mathcal{P}_{12})\psi_q(1)\psi_s(2)\,d1d2. \tag{57}$$

9. To determine the number of loops and hence the overall sign of a diagram in which electron repulsion integrals are expanded as dots, write each dot as a dotted line (it does not matter which one of the two in Fig. 8 is chosen) and apply rule 1. The order of indices in each integral $\left(rs\middle|\middle|pq\right)$ should correspond to the expanded diagrams. (When Goldstone diagrams are interpreted in this way, we call them Brandow diagrams.)

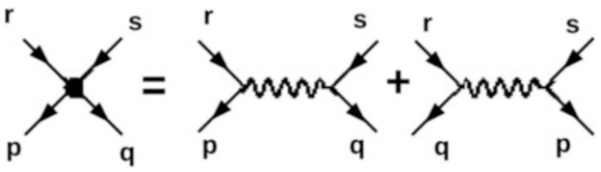

Fig. 8 Electron repulsion integral diagrams

10. An additional factor of 1/2 must be added for each pair of equivalent lines. These are directed lines whose interchange, in the absence of further labeling, leaves the Hugenholtz diagram unchanged.

For example, the term corresponding to Fig. 7a is

$$\Pi_{ck,ai}(\omega) = -\frac{(ka||ic)}{(-\omega+\varepsilon_k-\varepsilon_c)(-\omega+\varepsilon_i-\varepsilon_a)} = \frac{(ak||ic)}{(-\omega+\varepsilon_k-\varepsilon_c)(-\omega+\varepsilon_i-\varepsilon_a)}. \tag{58}$$

Additional information about Hugenholtz and other diagrams may be found, for example, in [56].

3.3 Dyson's Equation and the Bethe–Salpeter Equation (BSE)

Two of the most basic equations of diagrammatic MBPT are Dyson's equation for the one-electron Green's function and the BSE for the ph-propagator. Both require the choice of a zero-order picture which we take here to be the exact or approximate Kohn–Sham system of noninteracting electrons. We denote the zero-order quantities by the subscript s (for single particle).

Dyson's equation relates the true one-electron Green's function $\boldsymbol{G}$ to the zero-order Green's function $\boldsymbol{G}_s$ via the (proper) self-energy $\boldsymbol{\Sigma}$,

$$G(\mathbf{1},\mathbf{2}) = G_s(\mathbf{1},\mathbf{2}) + \int G_s(\mathbf{1},\mathbf{3})\Sigma(\mathbf{3},\mathbf{4})G(\mathbf{4},\mathbf{2})\,d\mathbf{3}d\mathbf{4}, \tag{59}$$

or, more concisely,

$$\boldsymbol{G} = \boldsymbol{G}_s + \boldsymbol{G}_s\boldsymbol{\Sigma}\boldsymbol{G}. \tag{60}$$

This is shown diagrammatically in Fig. 9. It is to be emphasized that these diagrams are *un*ordered in time as it is not possible to write a Dyson equation for time-ordered diagrams. Also shown in Fig. 9 are typical low-order self-energy approximations. Typical quantum chemistry approximations (Fig. 9b) involve

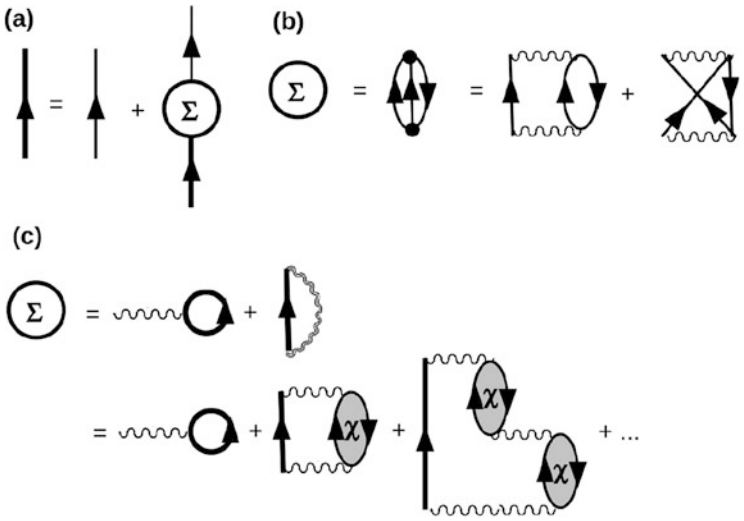

Fig. 9 Time-unordered (Feynman and Abrikosov) one-electron Green's function diagrams: (**a**) Dyson's equation; (**b**) second-order self-energy quantum chemistry approximation; (**c**) *GW* self-energy solid-state physics approximation

explicit antisymmetrization of electron-repulsion integrals whereas solid-state physics approximations (Fig. 9c) emphasize dynamical screening. Each approach has its strength and its weaknesses and so far the two approaches have defied any rigorous attempts at merger.

The BSE is "Dyson's equation" for the ph-propagator,

$$L(\mathbf{1},\mathbf{2};\mathbf{7},\mathbf{8}) = L_s(\mathbf{1},\mathbf{2};\mathbf{7},\mathbf{8}) + \int L_s(\mathbf{1},\mathbf{2};\mathbf{3},\mathbf{4})\Xi_{\mathrm{Hxc}}(\mathbf{3},\mathbf{4};\mathbf{5},\mathbf{6})L(\mathbf{5},\mathbf{6};\mathbf{7},\mathbf{8})\,d\mathbf{3}d\mathbf{4}d\mathbf{5}d\mathbf{6}, \tag{61}$$

or

$$\boldsymbol{L} = \boldsymbol{L}_s + \boldsymbol{L}_s\boldsymbol{\Xi}_{\mathrm{Hxc}}\boldsymbol{L}, \tag{62}$$

in matrix notation. Here

$$iL_s(\mathbf{1},\mathbf{2};\mathbf{3},\mathbf{4}) = G_s(\mathbf{1},\mathbf{3})G_s(\mathbf{4},\mathbf{2}) \tag{63}$$

is the ph-propagator for the zero-order picture (in our case, the exact or approximate Kohn–Sham fictitious system of noninteracting electrons), and the four-point quantity, $\boldsymbol{\Xi}_{\mathrm{Hxc}}$, may be deduced from a Feynman diagram expansion as the proper part of the ph-response function "self-energy". This is shown diagrammatically in Fig. 10. Again, the quantum chemical approximations emphasize antisymmetrization of the electron repulsion integrals which is needed for proper inclusion of double

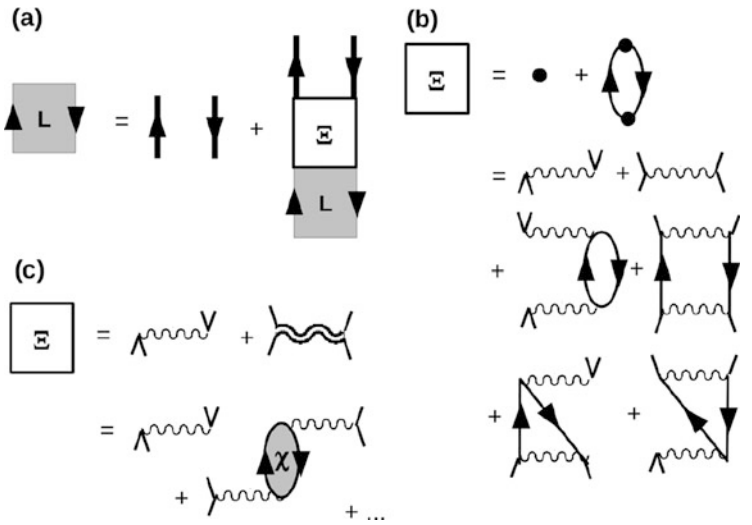

Fig. 10 Time-unordered (Feynman and Abrikosov) ph-propagator diagrams: (**a**) BSE; (**b**) second-order self-energy quantum chemistry approximation; (**c**) *GW* self-energy solid-state physics approximation. Note in part (**c**) that the solid-state physics literature often turns the *v* and *w wiggly lines* at right angles to each other to indicate the same thing that we have indicated here by adding *tab lines*

excitations whereas solid-state physics emphasizes use of a screened interaction. Although no rigorous way is yet known for combining screening and antisymmetrization, an interesting pragmatic suggestion may be found in [57].

3.4 Superoperator Equation-of-Motion (EOM) Polarization Propagator (PP) Approach

We now concentrate on the PP and show how to obtain a "Casida-like" equation for excitation energies and transition moments. This does not as yet give us correction terms to AA LR-TD-DFT but it does give us some important tools to help us build correction terms. The basic idea in this section is to take the exact or approximate Kohn–Sham system of independent electrons as the zero-order picture,

$$\hat{H}^{(0)} = \hat{h}_{KS}\,, \tag{64}$$

to add the perturbation,

$$\hat{H}^{(1)} = \hat{V} + \hat{M}_{\mathrm{xc}}. \tag{65}$$

and to do MBPT. Here, $\hat{V}$ is the fluctuation operator,

$$\hat{V} = \frac{1}{4}\sum_{pqrs}(pq||rs)\,\hat{p}^{\dagger}\hat{r}^{\dagger}\hat{s}\,\hat{q} - \sum_{pqr}(pr||rq)\,\hat{p}^{\dagger}\hat{q}\,, \tag{66}$$

$$\hat{M}_{\mathrm{xc}} = \sum_{pq}\left(p\middle|\hat{\Sigma}_{\mathrm{x}}^{\mathrm{HF}} - \hat{v}_{\mathrm{xc}}\middle|q\right)\hat{p}^{\dagger}\hat{q}\,, \tag{67}$$

and $\hat{\Sigma}_{\mathrm{x}}^{\mathrm{HF}}$ is the HF exchange operator defined in terms of the occupied Kohn–Sham orbitals. *Heuristically* this gives us a series of diagrams which we must resum to have the proper analytic structure of the exact PP so we can take advantage of this analytic structure to produce the desired "Casida-like" equation. *Rigorously* we actually first begin with some exact equations in the superoperator equation-of-motion (EOM) formalism to deduce the analytic structure of the PP. This exact structure is then developed in a perturbation expansion so that we can perform an order analysis of each of the terms entering into a basic "Casida-like" equation. As we can see, not every diagram is generated by this procedure, either because they are not needed or because of approximations which we have chosen to make.

Our MBPT expansions are in terms of the bare electron repulsion (or more exactly the "fluctuation potential" – see (66)), rather than the screened interaction used in solid-state physics [41, 47]. The main advantage of working with the bare interaction is a balanced treatment of direct and exchange diagrams, which is especially important for treating two- and higher-electron excitations. Although we automatically include what the solid state community refers to as vertex effects, the disadvantage of our approach is that it is likely to break down in solids when screening becomes important. The specific approach we take is the now well-established second-order polarization propagator approximation (SOPPA) of Nielsen, Jørgensen, and Oddershede [48–51]. The usual presentation of the SOPPA approach is based upon the superoperator equation-of-motion (EOM) approach previously used by one of us [58]. However, the SOPPA approach is very similar in many ways to the second-order algebraic diagrammatic construction [ADC(2)] approach of Schirmer [52, 53] and we do not hesitate to refer to this approach as needed (particularly with regard to the inclusion of various diagrammatic contributions). The only thing really new here is the change from a Hartree–Fock to a Kohn–Sham zero-order picture and the concomitant inclusion of (many) additional terms. Nevertheless, it is seen that the final working expressions are fairly compact.

Before going into the details of the superoperator EOM approach, let us anticipate some of the results by looking at some of the diagrams which emerge from this analysis. We have seen in (45) that the PP is just the restriction of the ph-propagator to twice rather than four times. Thus, heuristically, it suffices to take the ph-propagator diagrams, fix twice, and then take all possible time orderings.

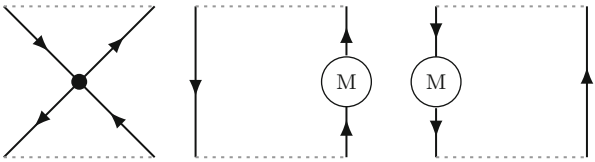

Fig. 11 Topologically different first-order time-unordered Abrikosov diagrams for the PP

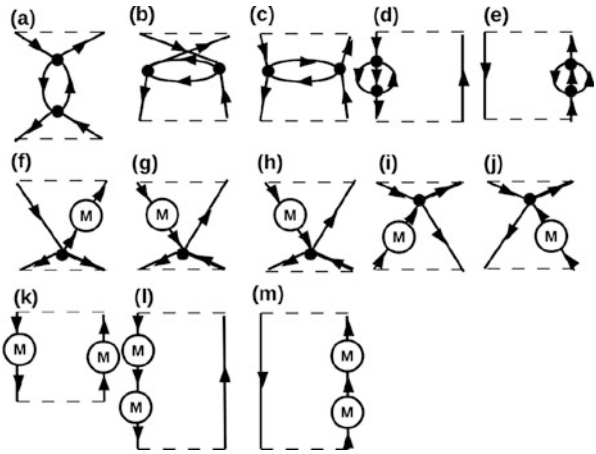

Fig. 12 Second-order time-unordered Abrikosov PP diagrams. Not all of the time-ordered Hugenholtz diagrams are generated by our procedure – only about 140 Hugenholtz diagrams

Defining order as the order in the number of times $\hat{V}$ and/or $\hat{M}_{\mathrm{xc}}$ appear, all of the time-unordered first-order terms are shown in Fig. 11. Fixing twice and restricting ourselves to an exchange-only theory gives the 14 time-ordered diagrams shown in Fig. 7. As we can see below in a very precise mathematical way, dangling parts below or above the horizontal dotted lines correspond respectively to Hugenholtz diagrams for initial-time and final-time perturbed wavefunctions. (Two other first-order Goldstone diagrams are found in [52] with the electron repulsion dot above or below the two dotted lines; however a more detailed analysis shows that these terms neatly cancel out in the final analysis.) The area between the dotted lines corresponds to time propagation. In this case, there are only one-hole/one-particle excitations between the two horizontal dotted lines. Our final results are in perfect agreement with diagrams appearing in the exact exchange (EXX) theory as obtained by Hirata et al. [59] which are equivalent to the more condensed form given by Görling [60].

Figure 12 shows all 13 second-order time-unordered diagrams. Although this may not seem to be very many, our procedure generates about 140 time-ordered Hugenholtz diagrams (and even more Feynman diagrams). A typical time-ordered Hugenholtz diagram is shown in Fig. 13. The corresponding equation,

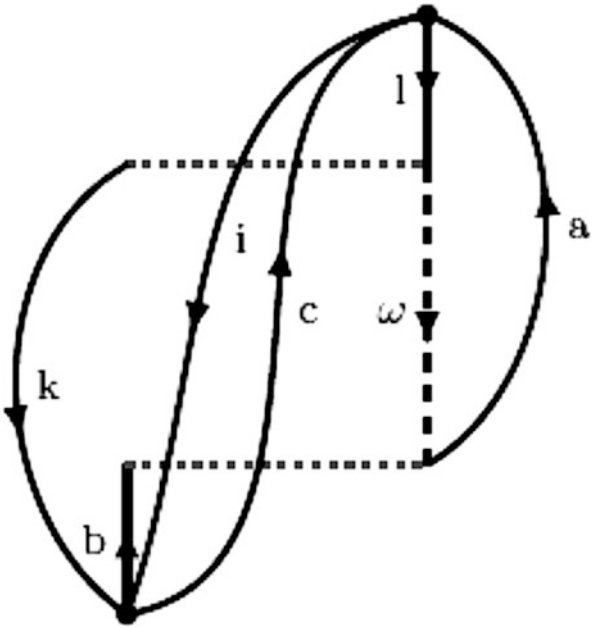

Fig. 13 An example of a second-order time-ordered Hugenholtz PP diagram

$$\Pi^{diag}_{sr,qp}(\omega) = \sum_{a,b,c,i,k,l} \frac{(pq||ba)(kl||rs)}{\varepsilon_{ik,bc}(\omega - \varepsilon_{ik,ca})\varepsilon_{il,ac}}, \tag{68}$$

shows that this diagrams has poles at the double excitations $\varepsilon_{ik,ca}$. Thus we see that the polarization propagator does have poles at double excitations, but we are not really ready to do calculations yet. There are two main reasons: (1) we need a more sophisticated formalism which allows the single and double excitations to mix with each other and (2) we would prefer a (pseudo)eigenvalue equation to solve. Thus we still have to do quite a bit more work to arrive at a "Casida-like" equation with explicit double excitations, but the basic idea is already present in what we have done so far.

To do so, it is first convenient to express the PP in a molecular orbital basis as

$$\Pi(1,2,3,4;t-t') = \sum\nolimits_{pqrs} \quad \Pi_{sr,qp}(t-t')\psi^*_r(2)\psi_s(1)\psi^*_q(3)\psi_p(4), \tag{69}$$

where

$$\begin{aligned} -\Pi_{sr,qp}(t-t') = {} & i\theta(t-t')\left\langle 0\middle|\hat{r}^\dagger_H(t)\hat{s}_H(t)\hat{q}^\dagger_H(t')\hat{p}_H(t')\middle|0\right\rangle \\ & + i\theta(t'-t)\left\langle 0\middle|\hat{q}^\dagger_H(t')\hat{p}_H(t')\hat{r}^\dagger_H(t)\hat{s}_H(t)\middle|0\right\rangle. \end{aligned} \tag{70}$$

As explained in [54], this change of convention with respect to that of (46) turns out to be more convenient. It should also be noted that, because the PP depends only

upon the time difference, $t - t'$, we can shift the origin of the time scale so that $t' = 0$ without loss of generality.

Equation (70) can be more easily manipulated by making use of the superoperator formalism. A (Liouville-space) superoperator $\breve{X}$ is defined by its action on a (Hilbert-space) operator $\hat{A}$ as

$$\breve{X}\hat{A} = \left[\hat{X}, \hat{A}\right] = \hat{X}\,\hat{A} - \hat{A}\,\hat{X}\,. \tag{71}$$

When $\breve{X}$ is the Hamiltonian operator, $\breve{H}$, one often speaks of the Liouvillian. An exception is the identity superoperator, $\breve{1}$, whose action is simply given by

$$\breve{1}\hat{A} = \hat{A}\,. \tag{72}$$

The Heisenberg form of orbital creation and annihilation operators is easily expressed in terms of the Liouvillian superoperator,

$$\hat{p}_{\,H}(t) = e^{i\hat{H}t}\,\hat{p}\,e^{-i\hat{H}t} = e^{i\breve{H}t}\,\hat{p}\,. \tag{73}$$

Then

$$\begin{aligned} -\Pi_{sr,qp}(t) = {} & i\theta(t)\left\langle 0\middle|\left[e^{i\breve{H}t}\left(\hat{r}^{\,\dagger}\hat{s}\right)\right]\hat{q}^{\,\dagger}\hat{p}\,\middle|0\right\rangle \\ & + i\theta(-t)\left\langle 0\middle|\hat{q}^{\,\dagger}\hat{p}\,\left[e^{i\breve{H}t}\left(\hat{r}^{\,\dagger}\hat{s}\right)\right]\middle|0\right\rangle. \end{aligned} \tag{74}$$

Taking the Fourier transform (with appropriate convergence factors (not shown)) gives,

$$-\Pi_{sr,qp}(\omega) = \left(\hat{p}^{\,\dagger}\hat{q}\,\middle|\left(\omega\breve{1} + \breve{H}\right)^{-1}\middle|\hat{r}^{\,\dagger}\hat{s}\right), \tag{75}$$

where we have introduced the superoperator metric,[7]

$$\left(\hat{A}\,\middle|\breve{X}\middle|\hat{B}\right) = \left\langle 0\middle|\left[\hat{A}^{\dagger}, \left[\hat{X}, \hat{B}\right]\right]\middle|0\right\rangle. \tag{76}$$

[It may be useful to note that

[7] Technically this is not a metric, because the overlap matrix is symplectic rather than positive definite. However, we will call it a metric as it can be used in much the same way as a true metric.

$$-\Pi_{sr,qp}(\omega) = \Pi_{rs,pq}(\omega), \tag{77}$$

follows as an easy consequence of the above definitions. Moreover, because we typically use real orbitals and a finite basis set, the PP is a real symmetric matrix. This allows us simply to identify Π as the superoperator resolvant,

$$\Pi_{pq,rs}(\omega) = \left(\hat{p}^\dagger \hat{q} \,\middle|\, \left(\omega \breve{1} + \breve{H}\right)^{-1} \middle| \hat{r}^\dagger \hat{s} \right) \Big]. \tag{78}$$

Because matrix elements of a resolvant superoperator are harder to manipulate than resolvants of a superoperator matrix, we transform (75) into the later form by introducing a complete set of excitation operators. The complete set

$$\left\{\mathbf{T}^\dagger\right\} = \left\{\mathbf{T}_1^\dagger \;;\; \mathbf{T}_2^\dagger \;;\; \ldots\right\} = \left\{\hat{a}^\dagger \hat{i} \;,\; \hat{i}^\dagger \hat{a} \;;\; \hat{a}^\dagger \hat{i} \hat{b}^\dagger \hat{j} \;,\; \hat{i}^\dagger \hat{a} \hat{j}^\dagger \hat{b} \;;\; \ldots\right\}, \tag{79}$$

leads to the resolution of the identity (RI):

$$\breve{\mathbf{1}} = \left|\mathbf{T}^\dagger\right) \left(\mathbf{T}^\dagger \middle| \mathbf{T}^\dagger\right)^{-1} \left(\mathbf{T}^\dagger\right|. \tag{80}$$

We have defined the operator space differently from the previous work of one of us [38] to be more consistent with the literature on the field of PP calculations. The difference is actually the commutation of two operators which introduces one sign change. Insertion into (75) and use of the relation

$$\left(\mathbf{T}^\dagger \middle| \left(\omega \breve{1} + \breve{H}\right)^{-1} \middle| \mathbf{T}^\dagger\right) = \left(\mathbf{T}^\dagger \middle| \mathbf{T}^\dagger\right) \left(\mathbf{T}^\dagger \middle| \omega \breve{1} + \breve{H} \middle| \mathbf{T}^\dagger\right)^{-1} \left(\mathbf{T}^\dagger \middle| \mathbf{T}^\dagger\right) \tag{81}$$

then gives

$$-\Pi_{sr,qp}(\omega) = \left(\hat{p}^\dagger \hat{q} \,\middle|\, \mathbf{T}^\dagger\right) \left(\mathbf{T}^\dagger \middle| \omega \breve{1} + \breve{H} \middle| \mathbf{T}^\dagger\right)^{-1} \left(\mathbf{T}^\dagger \middle| \hat{r}^\dagger \hat{s}\right). \tag{82}$$

This shows us the analytical form of the exact polarization propagator.
The corresponding "Casida-like" pseudoeigenvalue equation is

$$\left(\boldsymbol{T}^\dagger \middle| \breve{H} \middle| \boldsymbol{T}^\dagger\right) \mathbf{Z}_I = \omega_I \left(\boldsymbol{T}^\dagger \middle| \boldsymbol{T}^\dagger\right) \mathbf{Z}_I, \tag{83}$$

and with normalization

$$\mathbf{Z}_I^\dagger \left(\boldsymbol{T}^\dagger \middle| \boldsymbol{T}^\dagger\right) \mathbf{Z}_J = \delta_{I,J}. \tag{84}$$

Let us also seek a sum-over-states expression for the polarization propagator.
Spectral expansion tells us that

$$\boldsymbol{\Gamma}(\omega) = \omega\big(\boldsymbol{T}^\dagger\big|\boldsymbol{T}^\dagger\big) + \Big(\boldsymbol{T}^\dagger\Big|\breve{H}\Big|\boldsymbol{T}^\dagger\Big) = \sum_I \big(\boldsymbol{T}^\dagger\big|\boldsymbol{T}^\dagger\big)\mathbf{Z}_I(\omega+\omega_I)\mathbf{Z}_I^\dagger\big(\boldsymbol{T}^\dagger\big|\boldsymbol{T}^\dagger\big), \quad (85)$$

and

$$\boldsymbol{\Gamma}^{-1}(\omega) = \Big[\omega\big(\boldsymbol{T}^\dagger\big|\boldsymbol{T}^\dagger\big) + \Big(\boldsymbol{T}^\dagger\Big|\breve{H}\Big|\boldsymbol{T}^\dagger\Big)\Big]^{-1} = \sum_I \mathbf{Z}_I(\omega+\omega_I)^{-1}\mathbf{Z}_I^\dagger. \quad (86)$$

So (82) reads

$$-\Pi_{sr,qp}(\omega) = \sum_I \big(\hat{p}^\dagger\hat{q}\,\big|\mathbf{T}^\dagger\big)\mathbf{Z}_I(\omega+\omega_I)^{-1}\mathbf{Z}_I^\dagger\big(\mathbf{T}^\dagger\big|\hat{r}^\dagger\hat{s}\,\big). \quad (87)$$

This means that the PP has poles given at the pseudoeigenvalues of (83) and that the eigenvectors may be used to calculate oscillator strengths via (87).

As the "Casida-like" (83) is so important, let us rewrite it as

$$\begin{bmatrix} \boldsymbol{A} & \boldsymbol{B} \\ \boldsymbol{B}^* & \boldsymbol{A}^* \end{bmatrix}\begin{pmatrix} \mathbf{X} \\ \mathbf{Y} \end{pmatrix} = \omega\begin{bmatrix} \boldsymbol{S}_{A,A} & \boldsymbol{S}_{A,B} \\ \boldsymbol{S}_{B,A} & \boldsymbol{S}_{B,B} \end{bmatrix}\begin{pmatrix} \mathbf{X} \\ \mathbf{Y} \end{pmatrix}, \quad (88)$$

which is roughly

$$\begin{bmatrix} \boldsymbol{A} & \boldsymbol{B} \\ \boldsymbol{B}^* & \boldsymbol{A}^* \end{bmatrix}\begin{pmatrix} \mathbf{X} \\ \mathbf{Y} \end{pmatrix} = \omega\begin{bmatrix} \mathbf{1} & \mathbf{0} \\ \mathbf{0} & -\mathbf{1} \end{bmatrix}\begin{pmatrix} \mathbf{X} \\ \mathbf{Y} \end{pmatrix}. \quad (89)$$

The $\boldsymbol{A}$ and $\boldsymbol{B}$ matrices, as well as the $\mathbf{X}$ and $\mathbf{Y}$, partition according to whether they refer to one-electron excitations or two-electron excitations. In the Tamm–Dancoff approximation the $\boldsymbol{B}$ matrices are neglected so we can write

$$\begin{bmatrix} \boldsymbol{A}_{1,1}^{(0+1+2)} & \boldsymbol{A}_{1,2}^{(1)} \\ \boldsymbol{A}_{2,1}^{(1)} & \boldsymbol{A}_{2,2} \end{bmatrix}\begin{pmatrix} \mathbf{C}_1 \\ \mathbf{C}_2 \end{pmatrix} = \omega\begin{pmatrix} \mathbf{C}_1 \\ \mathbf{C}_2 \end{pmatrix} \quad (90)$$

Here $\mathbf{X}$ has been replaced by $\mathbf{C}$ as is traditional and to reflect the normalization $\mathbf{C}^\dagger\mathbf{C} = 1$.

The superscripts in (91) reflect a somewhat difficult order analysis which is carried out in the Appendix. This analysis consists of expanding the polarization propagator algebraically and then matching each term to a set of diagrams to see what order of each EOM matrix is needed to get a given order of polarization propagator.

The result in the case of the $\boldsymbol{A}$ matrices is

$$\begin{aligned}
\left(\boldsymbol{A}_{1,1}^{(0+1+2)}\right)_{kc,ia} &= \delta_{i,k}F_{a,c}^{(0+1+2)} - \delta_{a,c}F_{i,k}^{(0+1+2)} + \left(ai\middle||kc\right) \\
\left(\boldsymbol{A}_{2,1}^{(1)}\right)_{kc,jbia} &= -\delta_{i,k}\left(bc\middle||aj\right) + \delta_{j,k}\left(bc\middle||ai\right) \\
&\quad - \delta_{b,c}\left(ai\middle||kj\right) + \delta_{k,j}\left(bi\middle||kj\right) \\
\left(\boldsymbol{A}_{2,2}^{(0)}\right)_{ldkc,jbia} &= \delta_{i,k}\delta_{c,a}\delta_{d,b}\varepsilon_{ab,ij},
\end{aligned} \tag{91}$$

where $F_{r,s}^{(0+1)} = \delta_{r,s}\varepsilon_r + M_{r,s}^{xc}$ is the matrix of the Hartree–Fock operator constructed with Kohn–Sham orbitals and

$$\begin{aligned}
F_{a,c}^{(0+1+2)} &= F_{a,c}^{(0+1)} + \sum_{l}\frac{M_{l,a}M_{l,c}}{\varepsilon_{l,a}} - \frac{1}{2}\sum_{l,m,d}\frac{\left(ld\middle||mc\right)\left(dl\middle||am\right)}{\varepsilon_{lm,ad}} \\
F_{i,k}^{(0+1+2)} &= F_{i,k}^{(0+1)} + \sum_{d}\frac{M_{k,d}M_{d,i}}{\varepsilon_{i,d}} - \frac{1}{2}\sum_{l,d,e}\frac{\left(le\middle||kd\right)\left(dl\middle||ei\right)}{\varepsilon_{im,de}},
\end{aligned} \tag{92}$$

include second-order corrections. (Note that extra factors of 1/2 occur in these expressions when spin is taken explicitly into account.) In practice, a zero-order approximation to $\boldsymbol{A}_{2,2}$ is insufficient and we must use an expression correct through first order:

$$\begin{aligned}
\left(\boldsymbol{A}_{2,2}^{(0+1)}\right)_{aibj,ckdl} &= \delta_{i,k}\delta_{j,l}\left(\delta_{a,c}F_{b,d}^{(0+1)} + \delta_{b,d}F_{a,c}^{(0+1)}\right) - \delta_{a,c}\delta_{b,d}\left(\delta_{j,l}F_{i,k}^{(0+1)} - \delta_{i,k}F_{d,l}^{(0+1)}\right) \\
&\quad - \delta_{a,c}f_{i,j,k,l}(b,d) - \delta_{b,d}f_{i,j,k,l}(a,c) + \delta_{a,d}f_{i,j,k,l}(b,c) + \delta_{b,c}f_{i,j,k,l}(a,d) \\
&\quad - \delta_{a,c}\delta_{b,d}\left(kj\middle||li\right) - \delta_{j,l}\delta_{k,i}\left(ad\middle||bc\right),
\end{aligned} \tag{93}$$

where

$$f_{i,j,k,l}(p,q) = \delta_{i,k}\left(lj\middle||pq\right) + \delta_{j,l}\left(ki\middle||pq\right) - \delta_{k,j}\left(li\middle||pq\right) - \delta_{i,l}\left(kj\middle||pq\right). \tag{94}$$

We refer to the resultant method as extended SOPPA/ADC(2). It is immediately seen that truncating to first order recovers the usual configuration interaction singles (CIS) equations in a noncanonical basis set. We now have the essential tools to proceed with the rest of this chapter.

4 Dressed LR-TD-DFT

We now give one answer to the problem raised in the introduction – how to include explicit double excitations in LR-TD-DFT. This answer goes by the name "dressed LR-TD-DFT" and consists of a hybrid MBPT/AA LR-TD-DFT method. We first give the basic idea and comment on some of the early developments. We then go

into the practical details which are needed to make a useful implementation of dressed LR-TD-DFT. Finally, we introduce the notion of Brillouin corrections which are undoubtedly important for photochemistry.

4.1 Basic Idea

As emphasized in Sect. 2, simple counting arguments show that the AA limits LR-TD-DFT to single excitations, albeit dressed to include some electron correlation. However, explicit double excitations are sometimes needed when describing excited states. This was discussed in the introduction in the context of photochemistry (Fig. 1). It is well known in ab initio quantum chemistry that double excitations can be important when describing vertical excitations and the best known example is briefly discussed in the caption of Fig. 14.

At first this may seem a little perplexing because the fact that the oscillator strength is the transition matrix element of a one-electron operator – see (15) – means that the oscillator strength of a double excitation relative to a single-determinantal ground-state wavefunction should be zero – that is, the doubly excited state should be spectroscopically dark. What happens is easily explained by the two-level model shown in Fig. 15, which is sufficient to give a first explanation of the butadiene case, for example. (In the butadiene case, the singly-excited state to be used is already a mixture of two different one-hole/one-particle

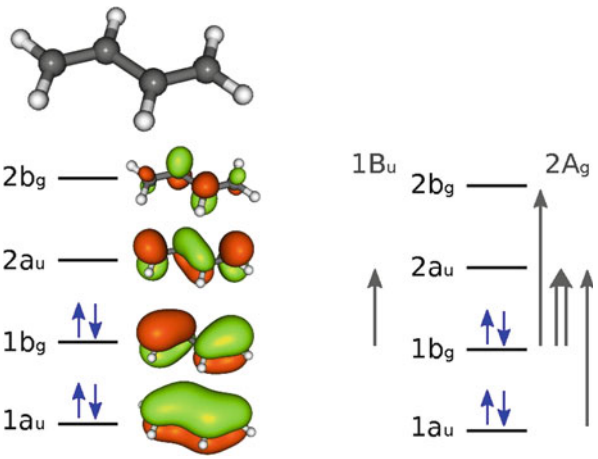

Fig. 14 Doubles contribution to the ^1A_g excited state of butadiene. Beecause the obvious two lowest singly-excited singlets $^1(1b_g, 2b_g)$ and $^1(1a_u, 2a_u)$ are quasidegenerate in energy, they mix to form new singly-excited singlets $\left(1/\sqrt{(2)}\right)\left[^1(1b_g, 2b_g) \pm {}^1(1a_u, 2a_u)\right]$. One of these is quasidegenerate with the doubly-excited singlet dark state $^1(1b_g^2, 2a_u^2)$. The resultant mixing modifies the energy and intensity of the observed ^1A_g excited state

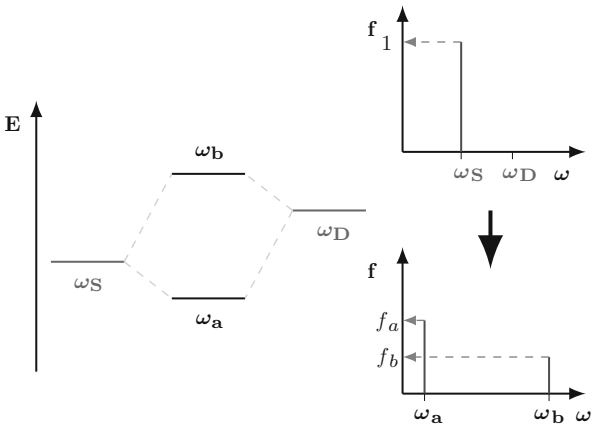

Fig. 15 Two-level model used by Maitra et al. in their *heuristic* derivation of dressed TDDFT. See explanation in text

states.) Figure 15 shows a bright singly-excited state with excitation energy ω_S and oscillator strength $f_S = 1$ interacting with a dark doubly-excited state with excitation energy ω_D and oscillator strength $f_D = 0$ via a coupling matrix element x. The CI problem is simply

$$\begin{bmatrix} \omega_S & x \\ x & \omega_D \end{bmatrix} \begin{pmatrix} C_S \\ C_D \end{pmatrix} = \omega \begin{pmatrix} C_S \\ C_D \end{pmatrix}, \tag{95}$$

which can be formally solved, obtaining

$$\begin{aligned} \omega_S &= \omega_a \cos^2\theta + \omega_b \sin^2\theta \\ \omega_D &= \omega_a \sin^2\theta + \omega_b \cos^2\theta, \end{aligned} \tag{96}$$

for some value of θ. It should be noted that the average excitation energy is conserved in the coupled problem ($\omega_a + \omega_b = \omega_S + \omega_D$) and that something similar occurs with the oscillator strengths. This leads to the common interpretation that the coupling "shatters the singly-excited peaks into two satellite peaks."

Now let us see how this wavefunction theory compares with LR-TD-DFT and how Maitra et al. [61] decided to combine the two into a hybrid method. Of course, the proper comparison with CI is LR-TD-DFT within the TDA. Applying the partitioning technique to (95), we obtain

$$\left(\omega_S + \frac{x^2}{\omega - \omega_D}\right) C_S = \omega C_S\,. \tag{97}$$

Comparing this with the diagonal TDA LR-TD-DFT within the two-orbital model,

$$\omega = \varepsilon_{a,i} + \left(ia\middle|f_{\mathrm{Hxc}}(\omega)\middle|ia\right), \tag{98}$$

shows that

$$\left(ia\middle|f_{\mathrm{Hxc}}(\omega)\middle|ia\right) = (\omega_S - \varepsilon_{a,i}) + \frac{x^2}{\omega - \omega_D}. \tag{99}$$

Maitra et al. [61] interpreted the first term as the adiabatic part,

$$f_{\mathrm{Hxc}}^{\mathrm{AA}} = \omega_S - \varepsilon_{a,i}, \tag{100}$$

and second term as the nonadiabatic correction,

$$f_{\mathrm{Hxc}}^{\mathrm{NA}}(\omega) = \frac{x^2}{\omega - \omega_D}. \tag{101}$$

Additionally, it is easy to show that

$$x^2 = \omega_S\omega_D - \omega_a\omega_b. \tag{102}$$

which is the form of the numerator used by Maitra et al. [61]. The suggestion of Maitra et al., which defines dressed LR-TD-DFT, is to calculate the nonadiabatic correction terms – see (101) – from MBPT [61]. Thus x and ω_D in (95) are to be calculated using MBPT rather than using DFT.

4.2 Practical Details and Applications

Applications of dressed LR-TD-DFT to the butadiene and related problems have proven to be very encouraging [61–64]. Nevertheless, several things were missing in these seminal papers. In the first place, they did not always use exactly the same formalism for dressed LR-TD-DFT and not always the same DFAs. Moreover, although the formalism showed encouraging results for a few molecules for those excitations which were thought to be most affected by explicit inclusion of double excitations, the same references failed to show that predominantly single excitations were left largely unaffected by the dressing of AA LR-TD-DFT. These questions were carefully addressed in [65], with some surprising answers.

The implementation of dressed LR-TD-DFT considered in [65] was to add just a few double excitations to AA LR-TD-DFT and solve the TDA equation

$$\begin{bmatrix} \boldsymbol{A}_{1,1}^{(\mathrm{AA})} & \boldsymbol{A}_{1,2}^{(1)} \\ \boldsymbol{A}_{2,1}^{(1)} & \boldsymbol{A}_{2,2}^{(0+1)} \end{bmatrix} \begin{pmatrix} \mathbf{C}_1 \\ \mathbf{C}_2 \end{pmatrix} = \omega \begin{pmatrix} \mathbf{C}_1 \\ \mathbf{C}_2 \end{pmatrix}. \tag{103}$$

Thus the calculation of the $\boldsymbol{A}_{1,1}$ block, which is one of the most difficult to calculate in the extended SOPPA/ADC(2) theory, is very much simplified by using AA LR-TD-DFT. The $\boldsymbol{A}_{2,2}$ block must, however, be calculated through first order in practice. It was confirmed that adding only a few (e.g., 100) double excitations led to little difference in calculated eigenvalues unless the double excitations were quasidegenerate with a single excitation. There is thus no significant problem in practice with double counting electron correlation effects when using this hybrid MBPT/LR-TD-DFT method. Tests were carried out on the test set of Schreiber et al. consisting of 28 organic chromophores with 116 well-characterized singlet excitation energies [66].

Note that the form of (103) was chosen instead of the form

$$\begin{aligned} &\left(\boldsymbol{A}_{1,1}^{(\mathrm{AA})} + \boldsymbol{K}_{1,1}^{\mathrm{NA}}(\omega)\right)\mathbf{C}_1 = \omega \mathbf{C}_1 \\ &\boldsymbol{K}_{1,1}^{\mathrm{NA}}(\omega) = \boldsymbol{A}_{1,2}^{(1)}\left(\omega \mathbf{1} - \boldsymbol{A}_{2,2}^{(0+1)}\right)^{-1} \boldsymbol{A}_{2,1}^{(1)}, \end{aligned} \tag{104}$$

for computational simplicity. However, (104) is the straightforward extension of the dressed kernel given at the end of the previous section and is easy to generalize to the full response theory case (i.e., without making the TDA).

We confirm the previous report that using the LDA for the AA LR-TD-DFT part of the calculation often gives good agreement with vertical excitation energies having significant double excitation contributions [67]. However, most excitations are dominated by singles and these are significantly underestimated by the AA LDA. Inclusion of double excitations tended to decrease the typically already too low AA LDA excitation energy. The AA LR-TD-DFT block was then modified to behave in the same way as a global hybrid functional with 20% Hartree–Fock exchange. The excitations with significant doubles character were then found to be overestimated but the addition of the doubles MBPT contribution again gave good agreement with benchmark ab initio results. This was consistent with previous experience with dressed LR-TD-DFT [61–64]. *The real surprise was the discovery that adding the MBPT to the hybrid functional made very little difference for the majority of excitations which are dominated by single excitation character*. It thus seems that a dressed LR-TD-DFT requires the use of hybrid functional.

4.3 Brillouin Corrections

So far, dressed LR-TD-DFT allows us to include explicit double excitations and so to describe photochemical funnels between excited states. However, a worrisome point remains, namely how to include doubles contributions to the ground state in

the same way that we include doubles contributions to excited states so that we may describe, for example, the photochemical funnel between S_1 and S_0 in Fig. 1. It is not clear how to do this in LR-TD-DFT where the excited-state potential energy surfaces are just obtained by adding the excitation energies at each geometry to the ground-state DFT energies. Not only does such a procedure lead to the excited states inheriting the convergence difficulties of the ground state surface coming from places with noninteracting *v*-representability difficulties, but also there is no coupling between the ground state and singly excited states. This is similar to what happens with Brillouin's theorem in CIS calculations and leads to problems describing conical intersections. However, adding in the missing nonzero terms (which we call Brillouin corrections) to dressed LR-TD-DFT is easy in the TDA.

It is good to emphasize at this point that we are making an ad hoc correction, albeit one which is eminently reasonable from a wavefunction point of view. Formally correct approaches might include: (1) acknowledging that part of the problem may lie in the fact that noninteracting *v*-representability in Kohn–Sham DFT often breaks down at key places on ground-state potential energy surfaces when bonds are formed or broken, so that conventional Kohn–Sham DFT may no longer be a good starting point; (2) examining nonadiabatic xc-kernels which seem to include some degree of multideterminantal ground-state character in their response such as that of Maitra and Tempel [68]; (3) introducing explicit multideterminantal character into the description of the Kohn–Sham DFT ground state. We return to this in our final section, but for now we just try the ad hoc approach of adding Brillouin corrections to TDA dressed LR-TD-DFT. Note that this also has an indirect effect on interactions between excited states, though the primary effect is between excited states and the ground state.

It is sufficient to add an extra column and row to the TDA problem to take into account the ground-state determinant in hybrid DFT. This gives

$$\begin{bmatrix} 0 & \boldsymbol{A}_{0,1} & \boldsymbol{A}_{0,2} \\ \boldsymbol{A}_{1,0} & \boldsymbol{A}_{1,1}^{(\mathrm{AA})} & \boldsymbol{A}_{1,2}^{(1)} \\ \boldsymbol{A}_{2,0} & \boldsymbol{A}_{2,1}^{(1)} & \boldsymbol{A}_{2,2}^{(0+1)} \end{bmatrix} \begin{pmatrix} C_0 \\ \mathbf{C}_1 \\ \mathbf{C}_2 \end{pmatrix} = \omega \begin{pmatrix} C_0 \\ \mathbf{C}_1 \\ \mathbf{C}_2 \end{pmatrix}. \tag{105}$$

where the extra matrix elements are calculated as

$$\left(\boldsymbol{A}_{0,1}\right)_{jb} = \left\langle j \middle| \hat{M}_{\mathrm{xc}} \middle| b \right\rangle, \tag{106}$$

and

$$\left(\boldsymbol{A}_{0,2}\right)_{kcld} = 2\left[\left(kc\middle||ld\right) - \left(kd\middle||lc\right)\right]. \tag{107}$$

Of course, we can also derive a corresponding nonadiabatic correction to the xc-coupling matrix:

$$\begin{aligned}
&\left(\boldsymbol{A}_{1,1}^{(\mathrm{AA})} + \boldsymbol{K}_{1,1}^{\mathrm{NA}}(\omega)\right)\mathbf{C}_1 = \omega\mathbf{C}_1 \\
&\boldsymbol{K}_{1,1}^{\mathrm{NA}}(\omega) = \begin{pmatrix} \boldsymbol{A}_{1,0} & \boldsymbol{A}_{1,2}^{(1)} \end{pmatrix} \begin{bmatrix} \omega 1 & -\boldsymbol{A}_{0,2} \\ -\boldsymbol{A}_{2,0} & \omega\mathbf{1} - \boldsymbol{A}_{2,2}^{(0+1)} \end{bmatrix}^{-1} \begin{pmatrix} \boldsymbol{A}_{0,1} \\ \boldsymbol{A}_{2,1}^{(1)} \end{pmatrix}.
\end{aligned} \tag{108}$$

The extension beyond the TDA is not obvious in this case.

4.3.1 Dissociation of Molecular Hydrogen

Molecular hydrogen dissociation is a prototypical case where doubly-excited configurations are essential for describing the potential energy surfaces of the lowest-lying excited states. The three lowest singlet states of Σ_g^+ symmetry can be essentially described by three CI configurations, namely $(1\sigma_g^2 1\sigma_u^0 2\sigma_g^0)$, $(1\sigma_g^1 1\sigma_u^0 2\sigma_g^1)$, and $(1\sigma_g^0 1\sigma_u^2 2\sigma_g^0)$, referred to as ground, single, and double configuration, respectively.

Obviously, the double configuration plays an essential role when a restricted single-determinant is used as reference. On the one hand, the mixing of ground and double configurations is necessary for describing the correct -1 Hartree dissociation energy of H_2. On the other hand, the single and double configurations mix at around 2.3 bohr, thus producing an avoided crossing. These features are shown in Fig. 16, where we compare different flavors of TD-DFT with the CISD benchmark (shown as solid lines in all graphs).

Adiabatic TD-DFT (shown in Fig. 16a) misses completely the double configuration, and so neither the avoided crossing nor the dissociation limit is described correctly. It should be noted, however, that CISD and adiabatic TD-DFT curves are superimposed for states $\mathrm{X}\,^1\Sigma_g^+$ and $1\,^1\Sigma_g^+$ at distances lower than 2.3 bohr, where the KS assumption is fully satisfied. At distances larger than 2.3 bohr, the $1\,^1\Sigma_g^+$ state corresponds to the CISD $2\,^1\Sigma_g^+$ state. This is because the $1\,^1\Sigma_g^+$ in TD-DFT is

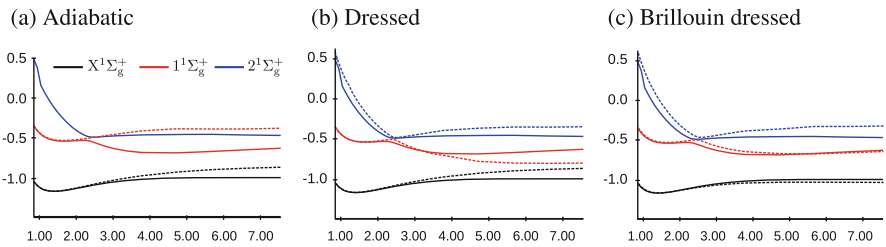

Fig. 16 Potential energy surfaces of the ground and two lowest excited states of Σ_g^+ symmetry. Comparison of CISD (*solid lines*) with adiabatic, dressed, and hybrid LR-TD-BH&HLYP/TDA (*dashed lines*). All calculations have been performed with a cc-pVTZ basis set. All axes are in Hartree atomic units (bohr for the *x*-axis and Hartree for the *y*-axis). Unlike the ethylene potential energy curves (Fig. 17), no shift has been made in the potential energy curves

diabatic, as it does not contain the doubly-excited configuration. The dissociation limit is also overestimated as it is usual from RKS with common xc functionals.

Dressed TD-DFT (Fig. 16b) includes the double configuration. On the one hand, the avoided crossing is represented correctly. However, the gap between the $1^1\Sigma_g^+$ and the $2^1\Sigma_g^+$ is smaller than the CISD crossing. The dissociation limit, however, is not correctly represented, as dressed TD-DFT does not include the ground- to excited-state interaction. Therefore, the double configuration dissociates at the same limit as the ground configuration.

Brillouin dressed TD-DFT (Fig. 16b) also includes the ground- and double configuration mixture additional to the single- and double mixing of dressed TD-DFT. On the one hand, the avoided crossing is represented more precisely, with a gap closer to that of CISD. Now the dissociation limit is more correctly described. Still there is a slight error in the dissociation energy limit, probably because of the double counting of correlation. This could be alleviated by a parameterization of the Brillouin-corrected dressed TD-DFT functional.

4.3.2 Ethylene Torsion

In Fig. 17 we show the potential energy surfaces of S_0, S_1, and S_2 of ethylene along the torsional coordinate. The static correlation of these three states can be essentially represented by three configurations, namely the ground-state configuration ($\pi^2\pi^{*,0}$), the singly-excited configuration ($\pi^1\pi^{*,1}$), and the doubly-excited configuration ($\pi^0\pi^{*,2}$).

From the CASSCF(2,2)/MCQDPT2, we observe that the ground- and doubly-excited configurations are heavily mixed at 90°, forming an avoided crossing. At this angle, the S_1 and S_2 states are degenerate. These features are not captured by adiabatic TD-DFT (Fig. 17a). Indeed, the doubly-excited configuration is missing,

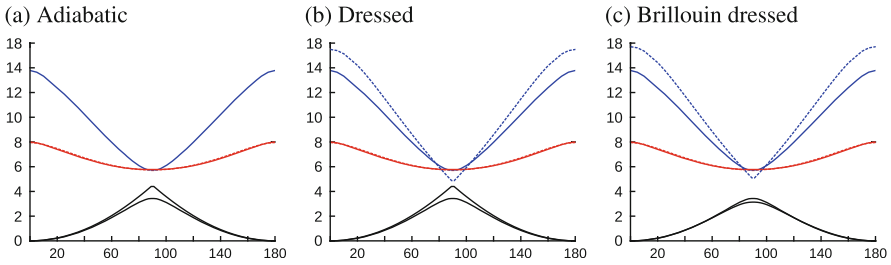

Fig. 17 Potential energy cuts of the S_0, S_1, and S_2 states of ethylene along the twisting coordinate: *x*-axis in degrees, *y*-axis in eV. All the curves have been shifted so that the ground-state curve at 0° corresponds to 0 eV. The *solid lines* correspond to a CASSCF(2,2)/MCQDPT2 calculation, and the *dashed lines* to the different models using the BH&HLYP functional and the Tamm–Dancoff approximation. The 6-31++G(d,p) basis set have been employed in all calculations. (Note that these curves are in good agreement with similar calculations previously reported in Fig. 7.3 of Chap. 7 of [69], albeit with a different functional)

and so the ground state features a cusp at the perpendicular conformation. The S_1, which is essentially represented by a single excitation, is virtually superimposed with the CASSCF(2,2)/MCQDPT2 result. The dressed TD-DFT (Fig. 17b) includes the double excitation, but the surfaces of S_0 and S_2 appear as diabatic states because the ground- to excited-state coupling term is missing. This is largely fixed by introducing the Brillouin corrections (Fig. 17c). The ground state is now in very good agreement with the CASSCF(2,2)/MCQDPT2 S_0 state, although the degeneracy of S_1 and S_2 at 90° is still not fully captured. Thus the picture given by Brillouin-corrected LR-TD-DFT is qualitatively correct with respect to the multi-reference results.

5 Effective Exchange-Correlation (xc) Kernel

We now have the tools to deduce an MBPT expression for the TD-DFT xc-kernel. It should be emphasized that this is not a new exercise but that we seem to be the only ones to do so within the PP formalism. We think this may have the advantage of making a rather complicated subject more accessible to Quantum Chemists already familiar with the PP formalism.

The problem of constructing xc-correlation objects such as the xc-potential v_{xc} and the xc-kernel $f_{\mathrm{xc}}(\omega)$ from MBPT for use in DFT has been termed "ab initio DFT" by Bartlet [70, 71]. At the exchange-only level, the terms optimized effective potential (OEP) [72, 73] or exact exchange [74, 75] are also used and OEP is also used to include the correlated case [76, 77]. At first glance, nothing much is gained. For example, the calculated excitation energies and oscillator strengths in ab initio TD-DFT must be, by construction, exactly the same as those from MBPT. This approach does not give explicit functionals of the density (though it may be thought of as giving implicit functionals). However it does allow us to formulate expressions for and to calculate purely (TD-) DFT objects and hence it can provide insight into, and computational checks of, the behavior of illusive objects such as v_{xc} and $f_{\mathrm{xc}}(\omega)$.

Here we concentrate on the latter, namely the xc-kernel. Previous work along these lines has been carried out for the kernel by directly taking the derivative of the OEP energy expression with the constraint that the orbitals come from a local potential. This was first done by Görling in 1998 [60] for the full time-dependent exchange-only problem. In 2002, Hirata et al. redid the derivation for the static case [78]. Later, in 2006, a diagrammatic derivation of the static result was given by Bokhan and Bartlett [71], and the functional derivative of the kernel g_x has been treated by Bokhan and Bartlett in the static exchange-only case [79].

In this section, we take a somewhat different and arguably more direct approach than that used in the previously mentioned articles, in that we make direct use of the fundamental relation

$$\chi(1,2) = L(1,1^+,2,2^+) = \Pi(1,1,2,2,t_1 - t_2) \tag{109}$$

where $\mathbf{i}^+$ is infinitesimally later than $\mathbf{i}$. This approach has been used by Totkatly, Stubner, and Pankaratov to develop a diagrammatic expression for $f_{\rm xc}(\omega)$ [80, 81]. It also leads to the "Nanoquanta approximation," so named by Lucia Reining because it was simultaneously derived by several different people [41–43, 46, 44] involved in the so-called Nanoquanta group. (See also pp. 318–329 of [24].)

The work presented here differs from previous work in two respects, namely (1) we make a direct connection with the PP formalism which is more common in quantum chemistry than is the full BSE approach (they are formally equivalent but differ in practice through the approximations used) and (2) we introduce a matrix formulation based upon Harriman's contraction $\hat{\Upsilon}$ and expansion operators $\hat{\Upsilon}^\dagger$. This allows us to introduce the concept of the localizer $\Lambda(\omega)$ which shows explicitly how localization in space results requires the introduction of additional frequency dependence. Finally, we recover the formulae of Görling and Hirata et al. and produce a rather trivial proof of the Gonze and Scheffler result [82] that this additional frequency dependence "undoes" the spatial localization procedure in particular cases.

We first seek a compact notation for (109). Harriman considered the relation between the space of kernels of operators and the space of functions [83, 84]. In order to main consistency with the rest of this chapter, we generalize Harriman's notion from space-only to space and spin coordinates. Then the collapse operator is defined by

$$\hat{\Upsilon} A(1,2) = A(1,1), \tag{110}$$

for an arbitrary operator kernel. The adjoint of the collapse operator is the so-called expansion operator

$$\hat{\Upsilon}^\dagger f(1) = f(1)\delta(1-2), \tag{111}$$

for an arbitrary function $f(1)$. Clearly $\hat{\Upsilon}^\dagger \hat{\Upsilon} A(1,2) = A(1,1)\delta(1-2) \neq A(1,2)$. The ability to express these operators as matrices ($\boldsymbol{\Upsilon}$ and $\boldsymbol{\Upsilon}^\dagger$) facilitates finite basis set applications.

We may now rewrite (109) as

$$\boldsymbol{\chi}(t_1 - t_2) = \boldsymbol{\Upsilon}\boldsymbol{L}\left(t_1, t_1^+, t_2, t_2^+\right)\boldsymbol{\Upsilon}^\dagger = \boldsymbol{\Upsilon}\boldsymbol{\Pi}(t_1 - t_2)\boldsymbol{\Upsilon}^\dagger \tag{112}$$

Comparing

$$\boldsymbol{\chi}(t_1 - t_2) = \boldsymbol{\chi}_s(t_1 - t_2) + \int \boldsymbol{\chi}_s(t_1 - t_3)\boldsymbol{f}_{\rm Hxc}(t_3 - t_4)\boldsymbol{\chi}(t_4 - t_2)\,dt_3 dt_4\,, \tag{113}$$

with the BSE

$$\boldsymbol{L}(t_1,t_2,t_3,t_4) = \boldsymbol{L}_s(t_1,t_2,t_3,t_4) + \int \boldsymbol{L}_s(t_1,t_2,t_5,t_6)\boldsymbol{\Xi}_{\mathrm{Hxc}}(t_5,t_6,t_7,t_8)\boldsymbol{L}(t_7,t_8,t_3,t_4)\,dt_5dt_6dt_7dt_8\,, \tag{114}$$

or, more precisely, with

$$\begin{aligned}\boldsymbol{\chi}(t_1-t_2) &= \boldsymbol{\Upsilon}\boldsymbol{L}\big(t_1,t_1^+,t_2,t_2^+\big)\boldsymbol{\Upsilon}^\dagger \\ &= \boldsymbol{\Upsilon}\boldsymbol{L}_s\big(t_1,t_1^+,t_2,t_2^+\big)\boldsymbol{\Upsilon}^\dagger \\ &\quad + \int \boldsymbol{\Upsilon}\boldsymbol{L}_s\big(t_1,t_1^+,t_5,t_6\big)\boldsymbol{\Xi}_{\mathrm{Hxc}}(t_5,t_6,t_7,t_8)\boldsymbol{L}\big(t_7,t_8,t_2,t_2^+\big)\,dt_5dt_6dt_7dt_8 \\ &= \boldsymbol{\chi}_s(t_1-t_2) \\ &\quad + \int \boldsymbol{\Upsilon}\boldsymbol{L}_s\big(t_1,t_1^+,t_5,t_6\big)\boldsymbol{\Xi}_{\mathrm{Hxc}}(t_5,t_6,t_7,t_8)\boldsymbol{L}\big(t_7,t_8,t_2,t_2^+\big)\,dt_5dt_6dt_7dt_8\,,\end{aligned} \tag{115}$$

then shows that

$$\begin{aligned}&\int \boldsymbol{\Upsilon}\boldsymbol{L}\big(t_1,t_1^+,t_3,t_3^+\big)\boldsymbol{\Upsilon}^\dagger \boldsymbol{f}_{\mathrm{Hxc}}(t_3-t_4)\boldsymbol{\Upsilon}\boldsymbol{L}\big(t_4,t_4^+,t_2,t_2^+\big)\boldsymbol{\Upsilon}^\dagger\,dt_3dt_4 \\ &\quad = \int \boldsymbol{\Upsilon}\boldsymbol{L}_s\big(t_1,t_1^+,t_5,t_6\big)\boldsymbol{\Xi}_{\mathrm{Hxc}}(t_5,t_6,t_7,t_8)\boldsymbol{L}\big(t_7,t_8,t_2,t_2^+\big)\,dt_5dt_6dt_7dt_8\,.\end{aligned} \tag{116}$$

If we take advantage of the Kohn–Sham reference giving us the exact density, then the Hartree part cancels out so that we actually get

$$\begin{aligned}&\int \boldsymbol{\Upsilon}\boldsymbol{L}\big(t_1,t_1^+,t_3,t_3^+\big)\boldsymbol{\Upsilon}^\dagger \boldsymbol{f}_{\mathrm{xc}}(t_3-t_4)\boldsymbol{\Upsilon}\boldsymbol{L}\big(t_4,t_4^+,t_2,t_2^+\big)\boldsymbol{\Upsilon}^\dagger\,dt_3dt_4 \\ &\quad = \int \boldsymbol{\Upsilon}\boldsymbol{L}_s\big(t_1,t_1^+,t_5,t_6\big)\boldsymbol{\Xi}_{\mathrm{xc}}(t_5,t_6,t_7,t_8)\boldsymbol{L}\big(t_7,t_8,t_2,t_2^+\big)\,dt_5dt_6dt_7dt_8\,.\end{aligned} \tag{117}$$

Although this is certainly a beautiful result, it is nevertheless plagued with four-time quantities which may be eliminated by using the PP:

$$\boldsymbol{\Pi}(t_1-t_2) = \boldsymbol{\Pi}_s(t_1-t_2) + \int \boldsymbol{\Pi}_s(t_1-t_3)\boldsymbol{K}_{\mathrm{Hxc}}(t_3-t_4)\boldsymbol{\Pi}(t_4-t_2)\,dt_3dt_4\,, \tag{118}$$

where we have introduced the coupling matrix defined by

$$\boldsymbol{K}_{\mathrm{Hxc}} = \boldsymbol{\Pi}_s^{-1} - \boldsymbol{\Pi}^{-1}. \tag{119}$$

The price we have to pay is that the coupling matrix cannot be easily expanded in Feynman diagrams, but that in no way prevents us from determining appropriate algebraic expressions for it. We may then write

$$\begin{aligned}&\int \boldsymbol{\Upsilon\Pi}_s(t_1-t_3)\boldsymbol{\Upsilon}^\dagger \boldsymbol{f}_{\rm xc}(t_3-t_4)\boldsymbol{\Upsilon\Pi}(t_4-t_2)\boldsymbol{\Upsilon}^\dagger dt_3 dt_4 = \\ &\int \boldsymbol{\Upsilon\Pi}_s(t_1-t_3)\boldsymbol{\Upsilon}^\dagger \boldsymbol{K}_{\rm xc}(t_3-t_4)\boldsymbol{\Upsilon\Pi}(t_4-t_2)\,dt_3 dt_4,\end{aligned} \tag{120}$$

which Fourier transforms to remove all the integrations,

$$\boldsymbol{\Upsilon\Pi}_s(\omega)\boldsymbol{\Upsilon}^\dagger \boldsymbol{f}_{\rm xc}(\omega)\boldsymbol{\Upsilon\Pi}(\omega)\boldsymbol{\Upsilon}^\dagger = \int \boldsymbol{\Upsilon\Pi}_s(\omega)\boldsymbol{\Upsilon}^\dagger \boldsymbol{K}_{\rm xc}(\omega)\boldsymbol{\Upsilon\Pi}(\omega)\boldsymbol{\Upsilon}^\dagger \tag{121}$$

5.1 Localizer

Evidently,

$$\boldsymbol{f}_{\rm xc}(\omega) = \boldsymbol{\Lambda}_s(\omega)\boldsymbol{K}_{\rm xc}(\omega)\boldsymbol{\Lambda}^\dagger(\omega), \tag{122}$$

where we have introduced the notion of noninteracting ($\boldsymbol{\Lambda}_s$) and interacting ($\boldsymbol{\Lambda}$) localizers,

$$\begin{aligned}\boldsymbol{\Lambda}_s(\omega) &= \left(\boldsymbol{\Upsilon\Pi}_s(\omega)\boldsymbol{\Upsilon}^\dagger\right)^{-1}\boldsymbol{\Upsilon\Pi}_s(\omega)\boldsymbol{\Upsilon}^\dagger \\ \boldsymbol{\Lambda}(\omega) &= \left(\boldsymbol{\Upsilon\Pi}(\omega)\boldsymbol{\Upsilon}^\dagger\right)^{-1}\boldsymbol{\Upsilon\Pi}(\omega)\boldsymbol{\Upsilon}^\dagger.\end{aligned} \tag{123}$$

The localizer arises quite naturally in the context of the time-dependent OEP problem. According to the Runge–Gross theory [25], the exact time-dependent xc-potential $v_{\rm xc}(t)$ is not only a functional of the density $\rho(t)$ but also of an initial condition which can be taken as the wavefunction $\Psi(t_0)$ at some prior time t_0. On the other hand, linear response theory begins with the static ground state case where the first Hohenberg–Kohn theorem tells us that the wavefunction is a functional of the density $\Psi(t_0) = \Psi\left[\rho_{t_0}\right]$. Görling has pointed out that this greatly simplifies the problem [60] because we can then show that

$$\int \Pi_s(1,1;2,2;\omega)v_x(2;\omega)\,d2 = \int \Pi_s(1,1;2,3;\omega)\Sigma_x(2,3)\,d2d3, \tag{124}$$

where Σ_x is the Hartree–Fock exchange operator. Equivalently, this may be written as

$$\boldsymbol{\Upsilon\Pi}_s(\omega)\boldsymbol{\Upsilon}^\dagger \boldsymbol{v}_x = \boldsymbol{\Upsilon\Pi}_s(\omega)\boldsymbol{\Sigma}_x, \tag{125}$$

or $\boldsymbol{\Sigma}_x$,

$$\boldsymbol{v}_x(\omega) = \boldsymbol{\Lambda}_s(\omega)\boldsymbol{\Sigma}_x. \tag{126}$$

Equations (122) and (126) are telling us something of fundamental importance, namely that the very act of spatially localizing the xc-coupling matrix involves introducing additional frequency dependence.

For the special case of noninteracting susceptibility, we can easily derive an expression for the dynamic localizer. Because

$$\begin{aligned}\Pi_s(1,2;3,4;\omega) = &\sum_i^{\text{occ}}\sum_a^{\text{virt}} \frac{\psi_i(1)\psi_a^*(2)\psi_i^*(3)\psi_a(4)}{\omega-\varepsilon_{a,i}} \\ &- \sum_i^{\text{occ}}\sum_a^{\text{virt}} \frac{\psi_a(1)\psi_i^*(2)\psi_a^*(3)\psi_i(4)}{\omega+\varepsilon_{a,i}},\end{aligned} \tag{127}$$

we can express the kernel of $\boldsymbol{\Upsilon\Pi}_s(\omega)$ as

$$\begin{aligned}(\Upsilon\Pi_s)(1;2,3;\omega) = &\sum_i^{\text{occ}}\sum_a^{\text{virt}} \frac{\psi_i(1)\psi_a^*(1)\psi_i^*(2)\psi_a(3)}{\omega-\varepsilon_{a,i}} \\ &- \sum_i^{\text{occ}}\sum_a^{\text{virt}} \frac{\psi_a(1)\psi_i^*(1)\psi_a^*(2)\psi_i(3)}{\omega+\varepsilon_{a,i}}.\end{aligned} \tag{128}$$

Also, the kernel of $\boldsymbol{\Upsilon\Pi}_s(\omega)\boldsymbol{\Upsilon}^\dagger$ is just

$$\begin{aligned}\left(\Upsilon\Pi_s\Upsilon^\dagger\right)(1;2;\omega) = &\sum_i^{\text{occ}}\sum_a^{\text{virt}} \frac{\psi_i(1)\psi_a^*(1)\psi_i^*(2)\psi_a(2)}{\omega-\varepsilon_{a,i}} \\ &- \sum_i^{\text{occ}}\sum_a^{\text{virt}} \frac{\psi_a(1)\psi_i^*(1)\psi_a^*(2)\psi_i(2)}{\omega+\varepsilon_{a,i}}.\end{aligned} \tag{129}$$

As with the susceptibility, the two operators have poles at the independent particle excitation energies $\omega = \pm\varepsilon_{a,i} = \pm(\varepsilon_a - \varepsilon_i)$.

In order to construct the dynamic localizer, the kernel (125) has to be inverted. It is not generally possible to do this analytically, though it can be done in a finite-basis representation with great care. However, Gonze and Scheffler have noted that exact inversion is possible in the special case of a frequency, $\omega = \varepsilon_{b,j}$, of a pole well separated from the other poles [82]. Near this pole, the kernels, $\boldsymbol{\Upsilon\Pi}_s(\omega)$ and $\boldsymbol{\Upsilon\Pi}_s(\omega)\boldsymbol{\Upsilon}^\dagger$, are each dominated by single terms

$$\begin{aligned}(\Upsilon\Pi_s) &\approx \frac{\psi_j(1)\psi_b^*(1)\psi_j^*(2)\psi_b(3)}{\omega-\varepsilon_{b,j}} \\ \left(\Upsilon\Pi_s\Upsilon^\dagger\right)(1;2;\omega) &\approx \frac{\psi_j(1)\psi_b^*(1)\psi_j^*(2)\psi_b(2)}{\omega-\varepsilon_{b,j}}.\end{aligned} \tag{130}$$

Thus (125) becomes

$$\frac{\psi_j(1)\psi_b^*(1)}{\omega-\varepsilon_{b,j}}\left\langle\psi_b\middle|v_x(\varepsilon_{b,j})\middle|\psi_j\right\rangle\approx\frac{\psi_j(1)\psi_b^*(1)}{\omega-\varepsilon_{b,j}}\left\langle\psi_b\middle|\hat{\Sigma}_x\middle|\psi_j\right\rangle, \tag{131}$$

with the approximation becoming increasingly exact as ω approaches $\varepsilon_{b,j}$. Hence,

$$\left\langle\psi_b\middle|v_x(\varepsilon_{b,j})\middle|\psi_j\right\rangle=\left\langle\psi_b\middle|\hat{\Sigma}_x\middle|\psi_j\right\rangle. \tag{132}$$

More generally for an arbitrary dynamic kernel, $K(1,2;\omega)$,

$$\left(\psi_b\psi_j^*\middle|\Lambda(\varepsilon_{b,j})K(\varepsilon_{b,j})\right)=\left(\psi_j\middle|K(\varepsilon_{b,j})\middle|\psi_b\right), \tag{133}$$

and we can do the same for $-\varepsilon_{b,j}$, obtaining

$$\left(\psi_j\psi_b^*\middle|\Lambda(-\varepsilon_{b,j})K(-\varepsilon_{b,j})\right)=\left(\psi_j\middle|K(-\varepsilon_{b,j})\middle|\psi_b\right). \tag{134}$$

We refer to these last two equations as Gonze–Scheffler (GS) relations, because they were first derived by these authors [82] and because we want to use them again. These GS relations show that the dynamic localizer, $\boldsymbol{\Lambda}_s(\omega)$, is pole free if the excitation energies, $\varepsilon_{a,i}$, are discrete and nondegenerate and suggest that the dynamic localizer may be a smoother function of ω than might at first be suspected. Equation (132) is also very significant because we see that, at a particular frequency, the matrix element of a local operator is the same as the matrix element of a nonlocal operator. Generalization to the xc-kernel requires an approximation.

5.1.1 First Approximation

Equation (122) is difficult to solve because of the need to invert an expression involving the correlated PP. However, it may instead be removed by using the approximate expression

$$\boldsymbol{f}_{\rm xc}(\omega)=\boldsymbol{\Lambda}_s(\omega)\boldsymbol{K}_{\rm xc}(\omega)\boldsymbol{\Lambda}_{1/2}^{+}(\omega), \tag{135}$$

where a localizer is used which is half way between the noninteracting and fully interacting form,

$$\boldsymbol{\Lambda}_{1/2}(\omega)=\left(\boldsymbol{\Upsilon}\boldsymbol{\Pi}_s(\omega)\boldsymbol{\Upsilon}^\dagger\right)^{-1}\boldsymbol{\Upsilon}\boldsymbol{\Pi}(\omega)\boldsymbol{\Upsilon}^\dagger. \tag{136}$$

Equation (135) then becomes

$$\mathbf{f}_{\mathrm{xc}}(\omega) = \left(\boldsymbol{\Upsilon}\boldsymbol{\Pi}_s(\omega)\boldsymbol{\Upsilon}^\dagger\right)^{-1}\left(\boldsymbol{\Pi}(\omega) - \boldsymbol{\Pi}_s(\omega)\right)\left(\boldsymbol{\Upsilon}\boldsymbol{\Pi}_s(\omega)\boldsymbol{\Upsilon}^\dagger\right)^{-1}. \tag{137}$$

Such an approximation is expected to work well in the off-resonant regime. As we can see, it does give Görling's exact exchange (EXX) kernel for TD-DFT [60]. On the other hand, the poles of the kernel in this approximation are a priori the poles of the exact and independent particle PPs – that is, the true and single-particle excitation energies – unless well-balanced approximations lead to fortuitous cancellations.

We can now return to a particular aspect of Casida's original PP approach [58] which was failure to take proper account of the localizer. This problem is rectified here. The importance of the localizer is made particularly clear by the GS relations in the case of charge transfer excitations. The single-pole approximation to the $i \rightarrow a$ excitation energy is

$$\begin{aligned}\omega &= \varepsilon_{a,i} + \left(ia\middle|\Lambda(\varepsilon_{a,i})K_{\mathrm{xc}}(\varepsilon_{a,i})\Lambda^\dagger(\varepsilon_{a,i})\middle|ai\right)\\ &= \varepsilon_{a,i} + \left(aa\middle|\Pi_s^{-1}(\varepsilon_{a,i}) - \Pi^{-1}(\varepsilon_{ai})\middle|ii\right).\end{aligned} \tag{138}$$

Thus once again we see that the frequency dependence of the localizer has transformed the matrix element of a spatially-local frequency-dependent operator into the matrix element of a spatially-nonlocal operator. Had the localizer been neglected, then we would have found, incorrectly, that

$$\omega = \varepsilon_{a,i} + \left(ia\middle|\Pi_s^{-1}(\varepsilon_{ai}) - \Pi^{-1}(\varepsilon_{a,i})\middle|ai\right). \tag{139}$$

Although the latter reduces to just ε_{ai} for charge transfer excitations at a distance (because $\psi_i\psi_a = 0$), the former does not [85]. However, for most excitations the overlap is non-zero. In such cases, and around a well-separated pole, the localizer can be completely neglected.

5.1.2 Exchange-Only Case

In order to apply (137) we need only the previously derived terms represented by the diagrams in Fig. 7. The resultant expressions agree perfectly with the expanded expressions of the TD-EXX kernel obtained by Hirata et al. [59], which are equivalent to the more condensed form given by Görling [60].

Use of the GS relation then leads to

$$\begin{aligned}\omega &= \varepsilon_{a,i}^{KS} + f_{\mathrm{xc}}\left(\varepsilon_{a,i}^{KS}\right)\\ &= \varepsilon_{a,i}^{KS} + \left\langle a\middle|\hat{M}_{\mathrm{xc}}\middle|a\right\rangle - \left\langle i\middle|\hat{M}_{xc}\middle|i\right\rangle + \left(ai\middle|\middle|ia\right)\\ &= \varepsilon_{a,i}^{HF} + \left(ai\middle|\middle|ia\right),\end{aligned} \tag{140}$$

which is exactly the configuration interaction singles (CIS, i.e., TDHF Tamm–Dancoff approximation) expression evaluated using Kohn–Sham orbitals.

This agrees with a previous exact result obtained using Görling–Levy perturbation theory [82, 86, 87].

5.1.3 Second Approximation

A second approximation, equivalent to the PP Born approximation,

$$\boldsymbol{\Pi}(\omega) = \boldsymbol{\Pi}_s(\omega) + \boldsymbol{\Pi}_s(\omega)\boldsymbol{K}_{\mathrm{Hxc}}(\omega)\boldsymbol{\Pi}_s(\omega)\,, \tag{141}$$

is useful because of its potential for preserving as much as possible of the basic algebraic structure of the exact equation at (122) although still remaining computationally tractable. This is our second approximation,

$$\boldsymbol{f}_{\mathrm{Hxc}}(\omega) = \boldsymbol{\Lambda}_s(\omega)\big(\boldsymbol{\Pi}_s^{-1}(\omega) - \boldsymbol{\Pi}^{-1}(\omega)\big)\boldsymbol{\Lambda}_s^{\dagger}(\omega). \tag{142}$$

Equation (142) simply reads that $\boldsymbol{f}_{\mathrm{Hxc}}(\omega)$ is a spatially localized form of $\boldsymbol{K}_{\mathrm{Hxc}}(\omega)$. This is nothing but the PP analogue of the basic approximation (117) used in the BSE approach on the way to the Nanoquanta approximation [41–46].

6 Conclusion and Perspectives

Time-dependent DFT has become part of the photochemical modeler's toolbox, at least in the FC region. However, extensions of TD-DFT are being made to answer the photochemical challenge of describing photochemical funnel regions where double and possibly higher excitations often need to be taken into account. This chapter has presented the dressed TD-D FT approach of using MBPT corrections to LR-TD-DFT in order to help address problems which are particularly hard for conventional TD-DFT. Illustrations have been given for the dissociation of H_2 and for *cis*/*trans* isomerization of ethylene. We have also included a section deriving the form of the TD-DFT xc-kernel from MBPT. This derivation makes it clear that localization in space is compensated for in the exact kernel by including additional frequency dependences. In the short run, it may be that such additional frequency dependences are easier to model with hybrid MBPT/LR-TD-DFT approaches. Let us mention in closing the very similar "configuration interaction-corrected Tamm–Dancoff approximation" of Truhlar and coworkers [88]. Yet another approach, similar in spirit, but different in detail is multiconfiguration TD-DFT based upon range separation [89]. In the future, if progress continues to be made at the current rate, we may very well be using some combination of these, including elements of dressed LR-TD-DFT, as well as other tricks such as a Maitra–Tempel form of the xc-kernel [68], constricted variational DFT for double excitations [90], DFT multi-reference configuration interaction (DFT-MRCI) [91], spin-flip theory [92–102], and restricted open-shell or spin-restricted ensemble-referenced Kohn–Sham

theory [97, 100, 101, 103–105] to attack difficult photochemical problems on a routine basis. Key elements to make this happen are the right balance between rigor and practicality, ease of automation, and last but not least ease of use if many users are going to try these techniques and if they can be routinely applied at every time step of a photochemical dynamics simulation.

Acknowledgements We thank Andrei Ipatov, Mathias Ljungberg, Hemanadhan Myneni, Valerio Olevano, Giovanni Onica, Lucia Reining, Pina Romaniello, Angel Rubio, Davide Sangalli, Jochen Schirmer, and Eric Shirley for useful discussions. M. H. R. would like to acknowledge an *Allocation de Recherche* from the French Ministry of Education. Over the years, this work has been carried out in the context of several programs: the French Rhône-Alpes *Réseau thématique de recherche avancée* (*RTRA*): *Nanosciences aux limites de la nanoélectronique*, the Rhône-Alpes Associated Node of the European Theoretical Spectroscopy Facility (ETSF), and, most recently, the grant ANR-12-MONU-0014-02 from the French *Agence Nationale de la Recherche* for the ORGAVOLT project (ORGAnic solar cell VOLTage by numerical computation).

Appendix: Order Analysis

We have presented the superoperator PP procedure as if we simply manipulated Feynman diagrams. In reality we expanded the matrices using Wick's theorem with the help of a home-made FORTRAN program. The result was a series of algebraic expressions which were subsequently analyzed by drawing the corresponding Feynman diagrams. This leads to about 200 diagrams which we ultimately resum to give a more compact expression. It is the generation of this expression that we now wish to discuss.

Let us analyze this expression for the PP according to the order of excitation operator. Following Casida [58], we partition the space as

$$-\Pi_{sr,qp}(\omega) = \left(\left(\hat{p}^{\dagger}\hat{q}\,\middle|\mathbf{T}_1^{\dagger}\right)\ \left(\hat{p}^{\dagger}\hat{q}\,\middle|\mathbf{T}_{2+}^{\dagger}\right)\right)\boldsymbol{\Gamma}^{-1}(\omega)\begin{pmatrix}\left(\mathbf{T}_1^{\dagger}\middle|\hat{r}^{\dagger}\hat{s}\right)\\ \left(\mathbf{T}_{2+}^{\dagger}\middle|\hat{r}^{\dagger}\hat{s}\right)\end{pmatrix}, \tag{143}$$

where $\mathbf{T}_{2+}^{\dagger}$ corresponds to the operator space of two-electron and higher excitations and

$$\boldsymbol{\Gamma}^{-1}(\omega) = \begin{bmatrix}\boldsymbol{\Gamma}_{1,1}(\omega) & \boldsymbol{\Gamma}_{1,2+}\\ \boldsymbol{\Gamma}_{2+,1} & \boldsymbol{\Gamma}_{2+,2+}(\omega)\end{bmatrix}^{-1}, \tag{144}$$

has been blocked:

$$\boldsymbol{\Gamma}_{i,j}(\omega) = \left(\mathbf{T}_i^\dagger \middle| \breve{\omega 1 + H} \middle| \mathbf{T}_j^\dagger\right). \tag{145}$$

Using the well-known expression for the inverse of a two-by-two block matrix allows us to transform (143) into

$$\begin{aligned} -\Pi_{sr,qp}(\omega) = &\left[\left(\hat{p}^\dagger\hat{q}\,\middle|\,\boldsymbol{T}_1^\dagger\right) - \left(\hat{p}^\dagger\hat{q}\,\middle|\,\boldsymbol{T}_{2+}^\dagger\right)\boldsymbol{\Gamma}_{2+,2+}^{-1}(\omega)\boldsymbol{\Gamma}_{2+,1}\right] \\ &\times \boldsymbol{P}^{-1}(\omega)\left[\left(\boldsymbol{T}_1^\dagger\middle|\hat{r}^\dagger\hat{s}\right) - \boldsymbol{\Gamma}_{1,2+}\boldsymbol{\Gamma}_{2+,2+}^{-1}(\omega)\left(\boldsymbol{T}_{2+}^\dagger\middle|\hat{r}^\dagger\hat{s}\right)\right] \\ &+\left(\hat{p}^\dagger\hat{q}\,\middle|\,\boldsymbol{T}_{2+}^\dagger\right)\boldsymbol{\Gamma}_{2+,2+}^{-1}(\omega)\left(\boldsymbol{T}_{2+}^\dagger\middle|\hat{r}^\dagger\hat{s}\right), \end{aligned} \tag{146}$$

where

$$\boldsymbol{P}(\omega) = \boldsymbol{\Gamma}_{1,1}(\omega) - \boldsymbol{\Gamma}_{1,2+}\boldsymbol{\Gamma}_{2+,2+}^{-1}(\omega)\boldsymbol{\Gamma}_{2+,1}\,. \tag{147}$$

Although (146) is somewhat complicated, it turns out that $\boldsymbol{P}(\omega)$ plays much the same role in the smaller $\boldsymbol{T}_1^\dagger$ space that $\boldsymbol{\Gamma}(\omega)$ plays in the full $\boldsymbol{T}^\dagger$ space. To see how this comes about, it is necessary to introduce the concept of order in the fluctuation operator – see (67) – and in $M_{\rm xc}$ – see (69). We can now perform an order-by-order expansion of (146). Through second order only the $\boldsymbol{T}_2^\dagger$ part of $\boldsymbol{T}_{2+}^\dagger$ contributes, so we need not consider higher than double excitation operators. However, we make some additional approximations. In particular, we follow the usual practice and drop the last term in (146) because it contributes only at second order and appears to be small when calculating excitation energies and transitions moments using the Hartree–Fock approximation as zero-order [52, 106–109]. For response functions such as dynamic polarizabilities, their inclusion is more critical, improving the agreement with experiments [49]. We also have no need to consider the second term in

$$\left(\hat{p}^\dagger\hat{q}\,\middle|\,\mathbf{T}_1^\dagger\right) - \left(\hat{p}^\dagger\hat{q}\,\middle|\,\mathbf{T}_{2+}^\dagger\right)\boldsymbol{\Gamma}_{2+,2+}^{-1}(\omega)\boldsymbol{\Gamma}_{2+,1}\,. \tag{148}$$

This means that for the purposes of this chapter we can treat the PP in the present work as given by

$$-\Pi_{sr,qp}(\omega) = \left(\hat{p}^\dagger\hat{q}\,\middle|\,\boldsymbol{T}_1^\dagger\right)\mathbf{P}^{-1}(\omega)\left(\boldsymbol{T}_1^\dagger\middle|\hat{r}^\dagger\hat{s}\right). \tag{149}$$

Comparing with (82) substantiates our earlier claim that $\boldsymbol{P}(\omega)$ plays the same role in the $\boldsymbol{T}_1^\dagger$ space that $\boldsymbol{\Gamma}(\omega)$ plays over the full $\boldsymbol{T}^\dagger$ space.

First-Order Exchange-Correlation Kernel

We now turn to the first-order exchange-correlation kernel. Our main motivation here is to verify that we obtain the same terms as in exact exchange (EXX) calculations when we evaluate $\boldsymbol{\Pi} - \boldsymbol{\Pi}_s$ [59, 60]. Because our approach is in some ways more general than previous approaches to the EXX kernel, this section may also provide some new insight into the meaning of the EXX equations.

Because we are limited to first order, only zero- and first-order wavefunction terms need be considered. This implies that all the contributions from the $\mathbf{T}^{\dagger}_{2+}$ space (the space of double- and higher-excitations) are zero and substantiates our claim that (149) is exact to first-order. An order-by-order expansion gives

$$\begin{aligned} -\Pi^{(0+1)}_{sr,qp}(\omega) = &\left(\hat{p}^{\dagger}\hat{q}\,\middle|\,\boldsymbol{T}^{\dagger}_1\right)^{(1)}\boldsymbol{P}^{(0),-1}(\omega)\left(\boldsymbol{T}^{\dagger}_1\middle|\hat{r}^{\dagger}\hat{s}\right)^{(0)} \\ &+\left(\hat{p}^{\dagger}\hat{q}\,\middle|\,\boldsymbol{T}^{\dagger}_1\right)^{(0)}\boldsymbol{P}^{(0),-1}(\omega)\left(\boldsymbol{T}^{\dagger}_1\middle|\hat{r}^{\dagger}\hat{s}\right)^{(1)} \\ &+\left(\hat{p}^{\dagger}\hat{q}\,\middle|\,\boldsymbol{T}^{\dagger}_1\right)^{(0)}\boldsymbol{P}^{(1),-1}(\omega)\left(\boldsymbol{T}^{\dagger}_1\middle|\hat{r}^{\dagger}\hat{s}\right)^{(0)} - \Pi^{s}_{sr,qp}(\omega), \end{aligned} \tag{150}$$

where

$$-\Pi^{s}_{sr,qp}(\omega) = \left(\hat{p}^{\dagger}\hat{q}\,\middle|\,\boldsymbol{T}^{\dagger}_1\right)^{(0)}\left(\boldsymbol{T}^{\dagger}_1\middle|\omega\breve{1} + \breve{h}_{KS}\middle|\boldsymbol{T}^{\dagger}_1\right)^{(0),-1}\left(\boldsymbol{T}^{\dagger}_1\middle|\hat{r}^{\dagger}\hat{s}\right)^{(0)}. \tag{151}$$

The evaluation of each of first-order block is straightforward using the basic definitions and Wick's theorem.

Let us first consider the $\boldsymbol{P}$ parts. The zeroth-order contribution is

$$P^{(0)}_{kc,ia}(\omega) = (\omega - \varepsilon_{i,a})\delta_{ik}\delta_{ac} \tag{152}$$

$$P^{(0)}_{ck,ia}(\omega) = 0, \tag{153}$$

and the first-order contribution gives

$$P^{(1)}_{kc,ia} = \big(ai\big|\big|kc\big) + M_{ac}\delta_{ik} - M_{ik}\delta_{ac} \tag{154}$$

$$P^{(1)}_{ck,ia} = \big(ci\big|\big|ak\big). \tag{155}$$

(It should be noted that $P_{kc,ia}$ is part of the $\boldsymbol{A}$ block, whereas $P_{ck,ia}$ is part of the $\boldsymbol{B}$ block.) The sum of $P^{(0)} + P^{(1)}$ gives the exact pole structure up to first-order in the SOPPA approach.

The zero-order contribution,

$$\left(\hat{p}^{\dagger}\hat{q}\left|\mathbf{T}_1^{\dagger}\right.\right)^{(0)} = \left(\mathbf{T}_1^{\dagger}\middle|\mathbf{T}_1^{\dagger}\right), \tag{156}$$

and the first-order contributions are given by

$$\left[\left(\hat{p}^{\dagger}\hat{q}\left|\mathbf{T}_1^{\dagger}\right.\right)\right]^{(1)}_{kc,\,ji} = -\frac{M_{jc}}{\varepsilon_{j,c}}\delta_{ik} \tag{157}$$

$$\left[\left(\hat{p}^{\dagger}\hat{q}\left|\mathbf{T}_1^{\dagger}\right.\right)\right]^{(1)}_{ck,\,ji} = \frac{M_{ic}}{\varepsilon_{i,c}}\delta_{kj} \tag{158}$$

$$\left[\left(\hat{p}^{\dagger}\hat{q}\left|\mathbf{T}_1^{\dagger}\right.\right)\right]^{(1)}_{kc,ba} = \frac{M_{ka}}{\varepsilon_{k,a}}\delta_{bc} \tag{159}$$

$$\left[\left(\hat{p}^{\dagger}\hat{q}\left|\mathbf{T}_1^{\dagger}\right.\right)\right]^{(1)}_{ck,ba} = -\frac{M_{kb}}{\varepsilon_{k,b}}\delta_{ca}\,. \tag{160}$$

The PP $\boldsymbol{\Pi}(\omega)$ is now easily constructed by simple matrix multiplication according to (150). Applying the first approximation from Sect. 5 and expanding $\boldsymbol{\Pi}_s(\omega) - \boldsymbol{\Pi}(\omega)$ through first order allows us to recover Görling's TD-EXX kernel [30]. The most convenient way to do this is to expand $\boldsymbol{P}^{(1),-1}$ using

$$\begin{aligned}\left(\mathbf{T}_1^{\dagger}\middle|\omega\breve{1} + \breve{H}\middle|\mathbf{T}_1^{\dagger}\right)^{-1} \approx{}& \left(\mathbf{T}_1^{\dagger}\middle|\omega\breve{1} + \breve{H}^{(0)}\middle|\mathbf{T}_1^{\dagger}\right)^{-1} \\ &+ \left(\mathbf{T}_1^{\dagger}\middle|\omega\breve{1} + \breve{H}^{(0)}\middle|\mathbf{T}_1^{\dagger}\right)^{-1}\left(\mathbf{T}_1^{\dagger}\middle|\breve{H}^{(1)}\middle|\mathbf{T}_1^{\dagger}\right)\left(\mathbf{T}_1^{\dagger}\middle|\omega\breve{1} + \breve{H}^{(0)}\middle|\mathbf{T}_1^{\dagger}\right)^{-1}.\end{aligned} \tag{161}$$

The result is represented diagrammatically in Fig. 7. The corresponding expressions agree perfectly with the expanded expressions of the TD-EXX kernel obtained by Hirata et al. [59] which are equivalent to the more condensed form given by Görling [60]. The diagrammatic treatment makes clear the connection with the BSE approach. There are in fact just three time-unordered diagrams, shown in Fig. 11, whose various time orderings generate the diagrams in Fig. 7. However the "hanging parts" above and below the horizontal dotted lines now have the physical interpretation of initial and final state wave function correlation. Had we applied the second approximation of Sect. 5, then only diagrams in Fig. 7a–f would have survived.

Use of the Gonze–Scheffler relation (see further Sect. 5) then leads to

$$\begin{aligned}\omega &= \varepsilon_{a,i}^{KS} + f_{\mathrm{xc}}\left(\varepsilon_{a,i}^{KS}\right) \\ &= \varepsilon_{a,i}^{KS} + \left\langle a\middle|\hat{M}_{\mathrm{xc}}\middle|a\right\rangle - \left\langle i\middle|\hat{M}_{\mathrm{xc}}\middle|i\right\rangle + \left(ai\middle|\middle|ia\right) \\ &= \varepsilon_{a,i}^{HF} + \left(ai\middle|\middle|ia\right),\end{aligned} \tag{162}$$

which is exactly the configuration interaction singles (CIS, i.e., TDHF Tamm–Dancoff approximation) expression evaluated using Kohn–Sham orbitals. This agrees with a previous exact result obtained using Görling–Levy perturbation theory [82, 86, 87].

Second-Order Exchange-Correlation Kernel

Having verified some known results, let us go on to do the MBPT necessary to obtain the pole structure of the xc-kernel through second order in the second approximation. That is, we need to evaluate $\boldsymbol{\Pi}_s^{-1}(\omega) - \boldsymbol{\Pi}^{-1}(\omega)$ through second order in such a way that its pole structure is evident. The SOPPA/ADC strategy for this is to make a diagrammatic $\boldsymbol{\Pi}_s(\omega) - \boldsymbol{\Pi}(\omega)$ expansion of this quantity and then resum the expansion in an order-consistent way having the form

$$[\boldsymbol{\Pi}_s(\omega) - \boldsymbol{\Pi}(\omega)]_{rs,qp}^{(0+1+\ldots+n)} = \sum_{k=0}^{n}\sum_{i=0}^{k}\sum_{j=0}^{k-i}\left(\hat{p}^\dagger\hat{q}\,\middle|\,\mathbf{T}_1^\dagger\right)^{(i)}\mathbf{P}^{(j),-1}(\omega)\left(\mathbf{T}_1^\dagger\middle|\hat{r}^\dagger\hat{s}\right)^{(k-i-j)},$$

when the Born approximation is applied to the $\mathbf{P}(\omega)$ in the same way as in Sect. 5. The number of diagrams contributing to this expansion is large and, for the sake of simplicity, we only give the resumed expressions for each block. Evidently, after the calculation of each block there is an additional step matrix inversion in order to apply the second approximation to the xc-kernel.

It should be emphasized that although the treatment below may seem simple, application of Wick's theorem is complicated and has been carried out using an in-house FORTRAN program written specifically for the purpose. The result before resummation is roughly 200 diagrams, which have been included as supplementary material.

It can be shown that the operator space may be truncated without loss of generality in a second-order treatment to only one- and two-electron excitation operators [52]. The wavefunction may also be truncated at second order. This truncation breaks the orthonormality of the $\mathbf{T}_1^\dagger$ space:

$$\left(\mathbf{T}_1^\dagger\middle|\mathbf{T}_1^\dagger\right) \approx \left(\mathbf{T}_1^\dagger\middle|\mathbf{T}_1^\dagger\right)^{(0)} + \left(\mathbf{T}_1^\dagger\middle|\mathbf{T}_1^\dagger\right)^{(2)} \neq \begin{pmatrix} 1 & 0 \\ 0 & -1 \end{pmatrix}. \tag{163}$$

This complication is dealt with by orthonormalizing our operator space. The new operator set expressed in terms of the original set contains only second-order corrections:

$$\begin{aligned}\left[\hat{a}^\dagger\hat{i}\right]^{(2)} &= \sum_b \left(\frac{1}{4}\sum_{kld}\frac{\left(kd\middle||lb\right)\left(dk\middle||al\right)}{\varepsilon_{kl,bd}\varepsilon_{kl,da}} + \sum_k \frac{M_{kb}M_{ka}}{\varepsilon_{k,b}\varepsilon_{k,a}}\right)\hat{b}^\dagger\hat{i} \\ &+ \sum_j \left(\frac{1}{4}\sum_{mcd}\frac{\left(md\middle||jc\right)\left(ci\middle||dm\right)}{\varepsilon_{mj,cd}\varepsilon_{im,cd}} + \sum_d \frac{M_{jd}M_{di}}{\varepsilon_{j,d}\varepsilon_{i,d}}\right)\hat{a}^\dagger\hat{j}\,.\end{aligned} \tag{164}$$

(It should be noted that we have used the linked-cluster theorem to eliminate contributions from disconnected diagrams. For a proof for the EOM of the one- and two-particle the Green's function, see [55].)

We may now proceed to calculate

$$\begin{aligned}-\Pi^{(2)}_{sr,qp}(\omega) &= \left(\hat{p}^\dagger\hat{q}\left|\mathbf{T}_1^\dagger\right.\right)^{(1)}\mathbf{P}^{(1),-1}(\omega)\left(\mathbf{T}_1^\dagger\middle|\hat{r}^\dagger\hat{s}\right)^{(0)} \\ &+ \left(\hat{p}^\dagger\hat{q}\left|\mathbf{T}_1^\dagger\right.\right)^{(0)}\mathbf{P}^{(1),-1}(\omega)\left(\mathbf{T}_1^\dagger\middle|\hat{r}^\dagger\hat{s}\right)^{(1)} \\ &+ \left(\hat{p}^\dagger\hat{q}\left|\mathbf{T}_1^\dagger\right.\right)^{(1)}\mathbf{P}^{(0),-1}(\omega)\left(\mathbf{T}_1^\dagger\middle|\hat{r}^\dagger\hat{s}\right)^{(1)} \\ &+ \left(\hat{p}^\dagger\hat{q}\left|\mathbf{T}_1^\dagger\right.\right)^{(0)}\mathbf{P}^{(2),-1}(\omega)\left(\mathbf{T}_1^\dagger\middle|\hat{r}^\dagger\hat{s}\right)^{(0)}.\end{aligned} \tag{165}$$

The only new contributions which arise at this level are from the block $\mathbf{P}^{(2)}$, which is given by

$$\mathbf{P}^{(2)} = \boldsymbol{\Gamma}^{(2)}_{1,1} - \boldsymbol{\Gamma}^{(1)}_{1,2}\boldsymbol{\Gamma}^{(0),-1}_{2,2}(\omega)\boldsymbol{\Gamma}^{(1)}_{2,1}\,. \tag{166}$$

(We are anticipating the ω-dependence of the various $\boldsymbol{\Gamma}$-blocks which are derived below.) Because the block $\boldsymbol{\Gamma}^{(2)}_{1,1}$ is affected by the orthonormalization procedure, it may be useful to provide a few more details. Expanding order-by-order,

$$
\begin{aligned}
\boldsymbol{\Gamma}^{(2)}_{1,1} = &\left\langle 0^{(1)}\right| \left[\mathbf{T}_1^{\dagger}, \left[\omega\breve{1} + \breve{H}^{(0)}, \mathbf{T}_1^{\dagger}\right]\right] \left|0^{(1)}\right\rangle \\
&+ \left\langle 0^{(0)}\right| \left[\mathbf{T}_1^{\dagger}, \left[\omega\breve{1} + \breve{H}^{(0)}, \mathbf{T}_1^{\dagger}\right]\right] \left|0^{(2)}\right\rangle \\
&+ \left\langle 0^{(2)}\right| \left[\mathbf{T}_1^{\dagger}, \left[\omega\breve{1} + \breve{H}^{(0)}, \mathbf{T}_1^{\dagger}\right]\right] \left|0^{(0)}\right\rangle \\
&+ \left\langle 0^{(0)}\right| \left[\mathbf{T}_1^{\dagger(2)}, \left[\omega\breve{1} + \breve{H}^{(0)}, \mathbf{T}_1^{\dagger}\right]\right] \left|0^{(0)}\right\rangle \\
&+ \left\langle 0^{(0)}\right| \left[\mathbf{T}_1^{\dagger}, \left[\omega\breve{1} + \breve{H}^{(0)}, \mathbf{T}_1^{\dagger(2)}\right]\right] \left|0^{(0)}\right\rangle \\
&+ \left\langle 0^{(1)}\right| \left[\mathbf{T}_1^{\dagger}, \left[\hat{H}^{(1)}, \mathbf{T}_1^{\dagger}\right]\right] \left|0^{(0)}\right\rangle \\
&+ \left\langle 0^{(0)}\right| \left[\mathbf{T}_1^{\dagger}, \left[\hat{H}^{(1)}, \mathbf{T}_1^{\dagger}\right]\right] \left|0^{(1)}\right\rangle,
\end{aligned}
\tag{167}
$$

where $\mathbf{T}_1^{\dagger(2)}$ is the vector of second-order operators defined in (164). It is easily shown that the first term cancels with the contributions coming from the second-order operators, and that the contributions from second-order wave function are exactly zero. Hence, that block is simply

$$
\boldsymbol{\Gamma}^{(2)}_{1,1} = \left\langle 0^{(1)}\right| \left[\mathbf{T}_1^{\dagger}, \left[\hat{H}^{(1)}, \mathbf{T}_1^{\dagger}\right]\right] \left|0^{(0)}\right\rangle + \left\langle 0^{(0)}\right| \left[\mathbf{T}_1^{\dagger}, \left[\hat{H}^{(1)}, \mathbf{T}_1^{\dagger}\right]\right] \left|0^{(1)}\right\rangle, \tag{168}
$$

which makes it frequency-independent. Its calculation gives

$$
\begin{aligned}
\left[\Gamma^{(2)}_{1,1}\right]_{kc,ia} = &\delta_{ac} \sum_d \frac{M_{kd} M_{di}}{\varepsilon_{i,d}} + \delta_{ik} \sum_l \frac{M_{la} M_{lc}}{\varepsilon_{l,a}} + \frac{\delta_{ac}}{2} \sum_{lde} \frac{\left(le\middle||kd\right)\left(dl\middle||ei\right)}{\varepsilon_{im,de}} \\
&- \frac{\delta_{ik}}{2} \sum_{lmd} \frac{\left(ld\middle||mc\right)\left(dl\middle||ma\right)}{\varepsilon_{lm,ad}},
\end{aligned}
\tag{169}
$$

$$
\begin{aligned}
\left[\Gamma^{(2)}_{1,1}\right]_{ck,ia} = &\frac{M_{ak} M_{id}}{\varepsilon_{i,d}} + \frac{M_{ci} M_{ka}}{\varepsilon_{k,a}} \\
&+ 2 \sum_d \frac{M_{dk}\left(ad\middle||ci\right)}{\varepsilon_{k,d}} + 2 \sum_l \frac{M_{lc}\left(lk\middle||ai\right)}{\varepsilon_{l,c}} \\
&- \sum_{md} \frac{\left(ce\middle||ad\right)\left(di\middle||em\right)}{\varepsilon_{im,de}} - \sum_{me} \frac{\left(ce\middle||mi\right)\left(ak\middle||me\right)}{\varepsilon_{km,ae}} \\
&- \frac{1}{2} \sum_{de} \frac{\left(ce\middle||ad\right)\left(dk\middle||ei\right)}{\varepsilon_{ik,de}} - \frac{1}{2} \sum_{ml} \frac{\left(ik\middle||ml\right)\left(ac\middle||ml\right)}{\varepsilon_{lm,ac}}.
\end{aligned}
\tag{170}
$$

The block $\boldsymbol{\Gamma}_{1,2}$ and its adjoint is of at least first order because the space is orthonormal. For that reason, it is not affected by the orthonormalization at this level of approximation. Its calculation gives

$$\begin{aligned}\left[\Gamma^{(2)}_{2,1}\right]_{kc,jbia} &= -\delta_{ik}\langle bc||aj\rangle + \delta_{jk}\langle bc||ai\rangle - \delta_{bc}\langle ai||kj\rangle + \delta_{ac}\langle bi||kj\rangle \\ \left[\Gamma^{(2)}_{2,1}\right]_{ck,jbia} &= 0\,.\end{aligned} \tag{171}$$

Finally, the block $\boldsymbol{\Gamma}_{2,2}(\omega)$ gives

$$\begin{aligned}\left[\Gamma^{(2)}_{2,2}(\omega)\right]_{ldkc,jbia} &= \left(\omega - \varepsilon_{ij,ab}\right)\delta_{jl}\delta_{ik}\delta_{ca}\delta_{db} \\ \left[\Gamma^{(2)}_{2,2}(\omega)\right]_{ckdl,jbia} &= 0\end{aligned} \tag{172}$$

It should be noted that double excitations are treated only to zeroth-order in a second-order approach. To obtain a consistent theory with first-order corrections to double excitations, one should go at least to third order. This however becomes computationally quite heavy.

It is interesting to speculate what would happen if we were to include the first-order doubles correction within the present second-order theory. There are, in fact, indications that this can lead to improved agreement between calculated and experimental double excitations, though the quality of the single excitations is simultaneously decreased because of an imbalanced treatment [110, 111].

We can now construct the PP necessary to construct the second approximation of the xc-kernel (142) according to (149). Because the localizers of both left- and right-sides are constructed from the noninteracting KS PP, we are only concerned with ph and hp contributions. This means that the blocks involving pp or hh indices, corresponding to density shift operators, can be ignored at this level of approximation. This simplifies the construction of $\boldsymbol{P}(\omega)$ in (149), which, up to second order, gives

$$\boldsymbol{\Pi}^{(0+1+2),-1}(\omega) = \left(\boldsymbol{T}_1^\dagger \middle| \boldsymbol{T}_1^\dagger\right)^{-1} \boldsymbol{P}^{(0+1+2)}(\omega) \left(\boldsymbol{T}_1^\dagger \middle| \boldsymbol{T}_1^\dagger\right)^{-1}. \tag{173}$$

Separating ph and hp contributions, the PP takes the form of a 2×2 block-matrix in the same spirit as the LR-TD-DFT formulation of Casida,

$$\begin{aligned}&\boldsymbol{\Pi}^{(0+1+2),-1}(\omega) \\ &= \begin{pmatrix} \mathbf{1} & \mathbf{0} \\ \mathbf{0} & -\mathbf{1} \end{pmatrix} \begin{pmatrix} \boldsymbol{P}^{(0+1+2)}(\omega) & \boldsymbol{P}^{(0+1+2)}(\omega) \\ \boldsymbol{P}^{(0+1+2)}(\omega) & \boldsymbol{P}^{(0+1+2)}(\omega) \end{pmatrix} \begin{pmatrix} \mathbf{1} & \mathbf{0} \\ \mathbf{0} & -\mathbf{1} \end{pmatrix} \\ &= \begin{pmatrix} \boldsymbol{P}^{(0+1+2)}(\omega) & -\boldsymbol{P}^{(0+1+2)}(\omega) \\ -\boldsymbol{P}^{(0+1+2)}(\omega) & \boldsymbol{P}^{(0+1+2)}(\omega) \end{pmatrix}.\end{aligned} \tag{174}$$

It follows that

$$\boldsymbol{\Pi}_s^{-1}(\omega) - \boldsymbol{\Pi}^{(0+1+2),-1}(\omega) = \begin{pmatrix} \boldsymbol{P}^{(1+2)}(\omega) & -\boldsymbol{\Gamma}_{1,1}^{(1+2)} \\ -\boldsymbol{\Gamma}_{1,1}^{(1+2)} & \boldsymbol{P}^{(1+2)}(\omega) \end{pmatrix}. \tag{175}$$

Note that the off-diagonal (ph,hp)- and (hp,ph)-blocks are frequency-independent and that the diagonal blocks are given by (166). Ignoring localization for the moment, we may now cast the present Kohn–Sham based second-order polarization propagator approximation (SOPPA/KS) into the familiar form of (27) with

$$\begin{aligned} A_{ia,\,jb}(\omega) &= \delta_{i,\,j}\delta_{a,b}\varepsilon_{a,i} + P_{ia,\,jb}^{(1+2)}(\omega) \\ B_{ia,bj}(\omega) &= -\left(\Gamma_{1,1}^{(1+2)}\right)_{ia,bj}. \end{aligned} \tag{176}$$

Localization – see (142) –complicates these formulae by mixing the $\boldsymbol{P}^{(1+2)}(\omega)$ and $\boldsymbol{\Gamma}_{1,1}^{(1+2)}$ terms,

$$\begin{aligned} A_{ia,\,jb}(\omega) &= \delta_{i,\,j}\delta_{a,b}(\varepsilon_a - \varepsilon_i) \\ &\quad + \left[(\boldsymbol{\Lambda}_s)_{hp,hp}(\omega)\boldsymbol{P}^{(1+2)}(\omega)\left(\boldsymbol{\Lambda}_s^{\dagger}\right)_{hp,hp}(\omega)\right]_{ia,\,jb} \\ &\quad + \left[(\boldsymbol{\Lambda}_s)_{hp,ph}(\omega)\boldsymbol{P}^{(1+2)}(\omega)\left(\boldsymbol{\Lambda}_s^{\dagger}\right)_{ph,hp}(\omega)\right]_{ia,\,jb} \\ &\quad - \left[(\boldsymbol{\Lambda}_s)_{hp,ph}(\omega)\boldsymbol{\Gamma}^{(1+2)}\left(\boldsymbol{\Lambda}_s^{\dagger}\right)_{hp,hp}(\omega)\right]_{ia,\,jb} \\ &\quad - \left[(\boldsymbol{\Lambda}_s)_{hp,hp}(\omega)\boldsymbol{\Gamma}^{(1+2)}\left(\boldsymbol{\Lambda}_s^{\dagger}\right)_{ph,hp}(\omega)\right]_{ia,\,jb} \\ B_{ia,bj}(\omega) &= \left[(\boldsymbol{\Lambda}_s)_{hp,hp}\boldsymbol{P}^{(1+2)}(\omega)\left(\boldsymbol{\Lambda}_s^{\dagger}\right)_{hp,ph}\right]_{ia,bj} \\ &\quad + \left[(\boldsymbol{\Lambda}_s)_{hp,ph}\boldsymbol{P}^{(1+2)}(\omega)\left(\boldsymbol{\Lambda}_s^{\dagger}\right)_{ph,ph}\right]_{ia,bj} \\ &\quad - \left[(\boldsymbol{\Lambda}_s)_{hp,ph}(\omega)\boldsymbol{\Gamma}^{(1+2)}\left(\boldsymbol{\Lambda}_s^{\dagger}\right)_{hp,ph}(\omega)\right]_{ia,bj} \\ &\quad - \left[(\boldsymbol{\Lambda}_s)_{hp,hp}(\omega)\boldsymbol{\Gamma}^{(1+2)}\left(\boldsymbol{\Lambda}_s^{\dagger}\right)_{ph,ph}(\omega)\right]_{ia,bj}. \end{aligned} \tag{177}$$

Of course, this extra complication is unnecessary if all we want to do is to calculate improved excitation energies and transition amplitudes by means of DFT-based many-body perturbation theory. It is only needed when our goal is to study the effect of localization on purely TDDFT quantities such as the xc-kernel and the TDDFT vectors $\boldsymbol{X}$ and $\boldsymbol{Y}$.

References

1. Rowlinson JS (2009) The border between physics and chemistry. Bull Hist Chem 34:1
2. Casida ME, Jamorski C, Casida KC, Salahub DR (1998) Molecular excitation energies to high-lying bound states from time-dependent density-functional response theory: characterization and correction of the time-dependent local density approximation ionization threshold. J Chem Phys 108:4439
3. Casida ME (2002) Jacob's ladder for time-dependent density-functional theory: some rungs on the way to photochemical heaven. In: Hoffmann MRH, Dyall KG (eds) Accurate description of low-lying molecular states and potential energy surfaces. ACS, Washington, p 199
4. Doltsinis NL, Marx D (2002) First principles molecular dynamics involving excited states and nonadiabatic transitions. J Theo Comput Chem 1:319
5. Cordova F, Doriol LJ, Ipatov A, Casida ME, Filippi C, Vela A (2007) Troubleshooting time-dependent density-functional theory for photochemical applications: oxirane. J Chem Phys 127:164111
6. Tapavicza E, Tavernelli I, Rothlisberger U, Filippi C, Casida ME (2008) Mixed time-dependent density-functional theory/classical trajectory surface hopping study of oxirane photochemistry. J Chem Phys 129(12):124108
7. Casida ME, Natarajan B, Deutsch T (2011) Non-Born-Oppenheimer dynamics and conical intersections. In: Marques M, Maitra N, Noguiera F, Gross EKU, Rubio A (eds) Fundamentals of time-dependent density-functional theory, Lecture Notes in Physics, vol 837. Springer, Berlin, p 279
8. Casida ME, Huix-Rotllant M (2012) Progress in time-dependent density-functional theory. Annu Rev Phys Chem 63:287
9. Hohenberg P, Kohn W (1964) Inhomogenous electron gas. Phys Rev 136:B864
10. Kohn W, Sham LJ (1965) Self-consistent equations including exchange and correlation effects. Phys Rev 140:A1133
11. Parr RG, Yang W (1989) Density-functional theory of atoms and molecules. Oxford University Press, New York
12. Dreizler DM, Gross EKU (1990) Density functional theory, an approach to the quantum many-body problem. Springer, New York
13. Koch W, Holthausen MC (2000) A chemist's guide to density functional theory. Wiley-VCH, New York
14. Perdew JP, Schmidt K (2001) Jacob's ladder of density functional approximations for the exchange-correlation energy. In: Doren VEV, Alseoy KV, Geerlings P (eds) Density functional theory and its applications to materials. American Institute of Physics, Melville, New York, p 1
15. Perdew JP, Ruzsinsky A, Constantin LA, Sun J, Csonka GI (2009) Some fundamental issues in ground-state density functional theory: a guide for the perplexed. J Chem Theor Comput 5:902
16. Perdew JP, Constantin LA (2007) Laplacian-level density functionals for the kinetic energy density and exchange-correlation energy. Phys Rev B 75:155109
17. Gill PM (2001) Obituary: density-functional theory (1927–1993). Aust J Chem 54:661
18. Becke A (1993) A new mixing of HartreeFock and local density functional theories. J Chem Phys 98:1372
19. Perdew JP, Ernzerhof M, Burke K (1996) Rationale for mixing exact exchange with density functional approximations. J Chem Phys 105:9982
20. Savin A (1995) Beyond the Kohn–Sham determinant. In: Chong DP (ed) Recent advances in density functional theory. World Scientific, Singapore, p 129
21. Baer R, Livshits E, Salzner U (2010) Tuned range-separated hybrids in density functional theory. Annu Rev Phys Chem 61:85
22. Marques MAL, Ullrich C, Nogueira F, Rubio A, Gross EKU (eds) (2006) Time-dependent density-functional theory, Lecture Notes in Physics, vol 706. Springer, Berlin

23. Marques M, Maitra N, Noguiera F, Gross EKU, Rubio A (2011) Fundamentals of time-dependent density-functional theory, Lecture Notes in Physics, vol 837. Springer, Berlin
24. Ullrich CA (2012) Time-dependent density-functional theory: concepts and applications. Oxford University Press, Oxford
25. Runge E, Gross EKU (1984) Density functional theory for time-dependent systems. Phys Rev Lett 52:997
26. van Leeuwen R (1999) Mapping from densities to potentials in time-dependent density-functional theory. Phys Rev Lett 82:3863
27. Maitra NT, Todorov TN, Woodward C, Burke K (2010) Density-potential mapping in time-dependent density-functional theory. Phys Rev A 81:042525
28. Ruggenthaler M, van Leeuwen R (2011) Global fixed-point proof of time-dependent density-functional theory. Europhys Lett 95:13001
29. Ruggenthaler M, Glesbertz KJH, Penz M, van Leeuwen R (2012) Density-potential mappings in quantum dynamics. Phys Rev A 85:052504
30. Ruggenthaler M, Nielsen SEB, van Leeuwen R (2013) Analytic density functionals with initial-state dependence. Phys Rev A 88:022512
31. Vignale G (2008) Real-time resolution of the causality paradox of time-dependent density-functional theory. Phys Rev A 77(6):1. doi:10.1103/PhysRevA.77.062511
32. Messud J, Dinh PM, Reinhard P, Suraud E (2011) The generalized SIC-OEP formalism and the generalized SIC-Slater approximation (stationary and time-dependent cases). Ann Phys (Berlin) 523:270
33. Rajagopal AK (1996) Time-dependent variational principle and the effective action in density-functional theory and Berrys phase. Phys Rev A 54:3916
34. van Leeuwen R (1998) Causality and symmetry in time-dependent density-functional theory. Phys Rev Lett 80:1280
35. van Leeuwen R (2001) Key concepts in time-dependent density-functional theory. Int J Mod Phys 15:1969
36. Mukamel S (2005) Generalized time-dependent density-functional-theory response functions for spontaneous density fluctuations and nonlinear response: resolving the causality paradox. Phys Rev A 024503
37. Mosquera MA (2013) Action formalism in time-dependent density-functional theory. Phys Rev B 88:022515
38. Casida ME (1995) Time-dependent density-functional response theory for molecules. In: Chong DP (ed) Recent advances in density functional methods, Part I. World Scientific, Singapore, p 155
39. Casida ME (1996) Time-dependent density functional response theory of molecular systems: theory, computational methods, and functionals. In: Seminario J (ed) Recent developments and applications of modern density functional theory. Elsevier, Amsterdam, p 391
40. Löwdin PO (1964) Studies in perturbation theory. Part VI. Contraction of secular equations. J Mol Spectr 14:112
41. Onida G, Reining L, Rubio A (2002) Electronic excitations: density-functional versus many-body Greens-function approaches. Rev Mod Phys 74:601
42. Reining L, Olevano V, Rubio A, Onida G (2002) Excitonic effects in solids described by time-dependent density-functional theory. Phys Rev Lett 88:066404
43. Sottile F, Olevano V, Reining L (2003) Parameter-free calculation of response functions in time-dependent density-functional theory. Phys Rev Lett 91:056402
44. Marini A, Sole RD, Rubio A (2003) Bound excitons in time-dependent density-functional theory: optical and energy-loss spectra. Phys Rev Lett 91:256402
45. Stubner R, Tokatly IV, Pankratov O (2004) Excitonic effects in time-dependent density-functional theory: an analytically solvable model. Phys Rev B 70:245119
46. von Barth U, Dahlen NE, van Leeuwen R, Stefanucci G (2005) Conserving approximations in time-dependent density functional theory. Phys Rev B 72:235109

47. Romaniello P, Sangalli D, Berger JA, Sottile F, Molinari LG, Reining L, Onida G (2009) Double excitations in finite systems. J Chem Phys 130:044108
48. Oddershede J, Jørgensen P (1977) An order analysis of the particle-hole propagator. J Chem Phys 66:1541
49. Nielsen ES, Jørgensen P, Oddershede J (1980) Transition moments and dynamic polarizabilities in a second order polarization propagator approach. J Chem Phys 73:6238
50. Nielsen ES, Jørgensen P, Oddershede J (1980) J Chem Phys 75:499; Erratum (1980): J Chem Phys 73:6238
51. Jørgensen P, Simons J (1981) Second quantization-based methods in quantum chemistry. Academic, New York
52. Schirmer J (1982) Beyond the random phase approximation: a new approximation scheme for the polarization propagator. Phys Rev A 26:2395
53. Trofimov AB, Stelter G, Schirmer J (1999) A consistent third-order propagator method for electronic excitation. J Chem Phys 111:9982
54. Fetter AL, Walecka JD (1971) Quantum theory of many-particle systems. McGraw-Hill, New York
55. Kobe DH (1966) Linked cluster theorem and the Green's function equations of motion for a many-fermion system. J Math Phys 7(10):1806
56. Wilson S (1984) Electron correlation in molecules. Clarendon, Oxford
57. Sangalli D, Romaniello P, Colò G, Marini A, Onida G (2011) Double excitation in correlated systems: a many-body approach. J Chem Phys 134:034115
58. Casida ME (2005) Propagator corrections to adiabatic time-dependent density-functional theory linear response theory. J Chem Phys 122:054111
59. Hirata S, Ivanov S, Bartlett RJ, Grabowski I (2005) Exact-exchange time-dependent density-functional theory for static and dynamic polarizabilities. Phys Rev A 71:032507
60. Görling A (1998) Exact exchange kernel for time-dependent density-functional theory. Int J Quant Chem 69:265
61. Maitra NT, Zhang F, Cave RJ, Burke K (2004) Double excitations within time-dependent density functional theory linear response theory. J Chem Phys 120:5932
62. Cave RJ, Zhang F, Maitra NT, Burke K (2004) A dressed TDDFT treatment of the ^1A_g states of butadiene and hexatriene. Chem Phys Lett 389:39
63. Mazur G, Włodarczyk R (2009) Application of the dressed time-dependent density functional theory for the excited states of linear polyenes. J Comput Chem 30:811
64. Gritsenko OV, Baerends EJ (2009) Double excitation effect in non-adiabatic time-dependent density functional theory with an analytic construction of the exchange-correlation kernel in the common energy denominator approximation. Phys Chem Chem Phys 11:4640
65. Huix-Rotllant M, Ipatov A, Rubio A, Casida ME (2011) Assessment of dressed time-dependent density-functional theory for the low-lying valence states of 28 organic chromophores. Chem Phys 391:120
66. Schreiber M, Silva-Junior MR, Sauer SPA, Thiel W (2008) Benchmarks for electronically excited states: CASPT2, CC2, CCSD, and CC3. J Chem Phys 128:134110
67. Hsu CP, Hirata S, Head-Gordon M (2001) Excitation energies from time-dependent density functional theory for linear polyene oligomers: butadiene to decapentaene. J Phys Chem A 105:451
68. Maitra NT, Tempel DG (2006) Long-range excitations in time-dependent density functional theory. J Chem Phys 125:184111
69. Huix-Rotllant M (2011) Improved correlation kernels for linear-response time-dependent density-functional theory. Ph.D. thesis, Université de Grenoble
70. Bokhan D, Schweigert IG, Bartlett RJ (2005) Interconnection between functional derivative and effective operator approaches in ab initio density functional theory. Mol Phys 103:2299
71. Bokhan D, Bartlett RJ (2006) Adiabatic ab initio time-dependent density-functional theory employing optimized-effective-potential many-body perturbation theory potentials. Phys Rev A 73:022502

72. Talman JD, Shadwick WF (1976) Optimized effective atomic central potential. Phys Rev A 14:36
73. Talman JD (1989) A program to compute variationally optimized effective atomic potentials. Comp Phys Commun 54:85
74. Görling A (1999) New KS method for molecules based on an exchange charge density generating the exact local KS exchange potential. Phys Rev Lett 83:5459
75. Ivanov S, Hirata S, Bartlett RJ (1999) Exact exchange treatment for molecules in finite-basis-set Kohn–Sham theory. Phys Rev Lett 83:5455
76. Casida ME (1995) Generalization of the optimized effective potential model to include electron correlation: a variational derivation of the Sham–Schlüter equation for the exact exchange-correlation potential. Phys Rev A 51:2505
77. Casida ME (1999) Correlated optimized effective potential treatment of the derivative discontinuity and of the highest occupied Kohn–Sham eigenvalue: a Janak-type theorem for the optimized effective potential method. Phys Rev B 59:4694
78. Hirata S, Ivanov S, Grabowski I, Bartlett RJ (2002) Time-dependent density functional theory employing optimized effective potentials. J Chem Phys 116:6468
79. Bokhan D, Barlett RJ (2007) Exact-exchange density functional theory for hyperpolarizabilities. J Chem Phys 127:174102
80. Tokatly IV, Pankratov O (2001) Many-body diagrammatic expansion in a Kohn–Sham basis: implications for time-dependent density functional theory of excited states. Phys Rev Lett 86: 2078
81. Tokatly IV, Stubner R, Pankratov O (2002) Many-body diagrammatic expansion of the exchange-correlation kernel in time-dependent density-functional theory. Phys Rev B 65: 113107
82. Gonze X, Scheffler M (1999) Exchange and correlation kernels at the resonance frequency: implications for excitation energies in density-functional theory. Phys Rev Lett 82:4416
83. Harriman JE (1983) Geometry of density-matrices. 4. The relationship between density-matrices and densities. Phys Rev A 27:632
84. Harriman JE (1986) Densities, operators, and basis sets. Phys Rev A 34:29
85. Heßelmann A, Ipatov A, Görling A (2009) Charge-transfer excitation energies with a time-dependent density-functional method suitable for orbital-dependent exchange-correlation functionals. Phys Rev A 80:012507
86. Filippi C, Umrigar CJ, Gonze X (1997) Excitation energies from density functional perturbation theory. J Chem Phys 107(23):9994
87. Görling A (1996) Density-functional theory for excited states. Phys Rev A 54(5):3912
88. Li SL, Marenich AV, Xu X, Truhlar DG (2014) Configuration interaction-corrected Tamm-Dancoff approximation: a time-dependent density functional method with the correct dimensionality of conical intersections. J Chem Phys Lett 5:322
89. Fromager E, Knecht S, Jensen HJA (2013) Multi-configuration time-dependent density-functional theory based upon range separation. J Chem Phys 138:084101
90. Seidu I, Krykunov M, Ziegler T (2014) The formulation of a constricted variational density functional theory for double excitations. Mol Phys 112:661
91. Böhm M, Tatchen J, Krügler D, Kleinermanns K, Nix MGD, LaGreve TA, Zwier TS, Schmitt M (2009) High-resolution and dispersed fluorescence examination of vibronic bands of tryptamine: spectroscopic signatures for L_a/L_b mixing near a conical intersection. J Phys Chem A 113:2456
92. Minezawa N, Gordon MS (2009) Optimizing conical intersections by spin-flip density-functional theory: application to ethylene. J Phys Chem A 113:12749
93. Huix-Rotllant M, Natarajan B, Ipatov A, Wawire CM, Deutsch T, Casida ME (2010) Assessment of noncollinear spin-flip Tamm-Dancoff approximation time-dependent density-functional theory for the photochemical ring-opening of oxirane. Phys Chem Chem Phys 12:12811

94. Rinkevicius Z, Vahtras O, Ågren H (2010) Spin-flip time dependent density functional theory applied to excited states with single, double, or mixed electron excitation character. J Chem Phys 133:114104
95. Minezawa N, Gordon MS (2011) Photoisomerization of stilbene: a spin-flip density functional theory approach. J Phys Chem A 115:7901
96. Casanova D (2012) Avoided crossings, conical intersections, and low-lying excited states with a single reference method: the restricted active space spin-flip configuration interaction approach. J Chem Phys 137:084105
97. Huix-Rotllant M, Filatov F, Gozem S, Schapiro I, Olivucci M, Ferré N (2013) Assessment of density functional theory for describing the correlation effects on the ground and excited state potential energy surfaces of a retinal chromophore model. J Chem Theory Comput 9:3917
98. Minezawa N (2014) Optimizing minimum free-energy crossing points in solution: linear-response free energy/spin-flip density functional theory approach. J Chem Phys 141:164118
99. Harabuchi Y, Keipert K, Zahariev F, Taketsugu T, Gordon MS (2014) Dynamics simulations with spin-flip time-dependent density functional theory: photoisomerization and photocyclization mechanisms of cis-stilbene in (π, π^*) states. J Phys Chem A 118:11987
100. Nikiforov A, Gamez JA, Thiel W, Huix-Rotllant M, Filatov M (2014) Assessment of approximate computational methods for conical intersections and branching plane vectors in organic molecules. J Chem Phys 141:124122
101. Gozem S, Melaccio F, Valentini A, Filatov M, Huix-Rotllant M, Ferré N, Frutos LM, Angeli C, Krylov AI, Granovsky AA, Lindh R, Olivucci M (2014) Shape of multireference, equation-of-motion coupled-cluster, and density functional theory potential energy surfaces at a conical intersection. J Chem Theory Comput 10:3074
102. Zhang X, Herbert JM (2014) Analytic derivative couplings for spin-flip configuration interaction singles and spin-flip time-dependent density functional theory. J Chem Phys 141: 064104
103. Frank I, Damianos K (2007) Restricted open-shell Kohn–Sham theory: simulation. J Chem Phys 126:125105
104. Friedrichs J, Darnianos K, Frank I (2008) Solving restricted open-shell equations in excited state molecular dynamics simulations. J Chem Phys 347:17
105. Filatov M (2015) Spin-restricted ensemble-referenced Kohn–Sham method: basic principles and application to strongly correlated ground and excited states of molecules. Comput Mol Sci 5:146
106. Shibuya T, Rose J, McKoy V (1973) Equations-of-motion method including renormalization and double-excitation mixing. J Chem Phys 58:500
107. Jørgensen P, Oddershede J, Ratner MA (1975) Two-particle, two-hole corrections to a self-consistent time-dependent Hartree-Fock scheme. Chem Phys Lett 32:111
108. Oddershede J, Sabin JR (1983) The use of modified virtual orbitals in perturbative polarization propagator calculations. J Chem Phys 79:2295
109. Oddershede J, Jørgensen P, Yeager DL (1984) Polarization propagator methods in atomic and molecular calculations. Comp Phys Rep 2:33
110. Oddershede J, Jørgensen P, Beebe NHF (1978) Analysis of excitation energies and transition moments. J Phys B Atom Mol Phys 11:1
111. Trofimov AB, Schirmer J (1995) An efficient polarization propagator approach to valence electron excitation spectra. J Phys B At Mol Opt Phys 28:2299

Top Curr Chem (2016) 368: 61–96
DOI: 10.1007/128_2014_611

Published online: 20 March 2015

Constricted Variational Density Functional Theory Approach to the Description of Excited States

Tom Ziegler, Mykhaylo Krykunov, Issaka Seidu, and Young Choon Park

Abstract We review the theoretical foundation of constricted variational density functional theory and illustrate its scope through applications.

Keywords Constricted variational density functional theory • Density functional theory • Time-dependent density functional theory

Contents

1 Introduction

Excited states have been studied in wave function theory by both excited state variational theories and ground state response methods [1, 2]. Either approach has been used extensively and is considered complementary and, in principle, able to

T. Ziegler (✉), M. Krykunov, I. Seidu, and Y.C. Park
Department of Chemistry, University of Calgary, Calgary, AB, Canada T2N1N4
e-mail: ziegler@ucalgary.ca

afford estimates to any desired degree of accuracy. Given the status of Kohn–Sham density functional theory (KS-DFT) as a ground state theory, the natural path to excited states in KS-DFT would seem to be the ground state response approach. In fact, Runge and Gross [3] have formulated a time-dependent density functional ground state response theory (TDDFT) which in principle should be able to describe excited state properties without approximations. TDDFT in its exact form requires knowledge of the "true" ground state functional and of the frequency dependence of the energy response kernel corresponding to this functional. In practical calculations, use is made of approximate ground state functionals and the frequency dependence of the kernel is neglected in what has now become known as the adiabatic TDDFT approach (ATDDFT) [4–9]. For more than two decades the ATDDFT approach has remained the method of choice in DFT-based studies of excited states and both its merits and limitations have been studied in great detail [10–33]. Progress beyond the adiabatic approximation has, on the other hand, been slow, although work in this direction is ongoing [34–36].

Long before TDDFT, Slater introduced a variational DFT approach to excited states called ΔSCF [37, 38]. Excited states are reached in this scheme by promoting electrons from occupied to virtual ground state levels followed by a KS calculation on the new electron configuration. The ΔSCF approach has met with considerable success for those lower excited states which can be represented by a single orbital replacement (SOR) [39–49]. However, it is plagued by SCF-convergence problems. Further, as it applies a ground state functional in a variational excited state calculation, it is considered somewhat ad hoc [50] and without any theoretical foundation [51–53]. Nevertheless, Van Voorhis et al. [39] have recently put forward some theoretical justifications for ΔSCF and Besley et al. [42, 43] and Park et al. [44] have addressed the SCF-convergence issue. Apart from ΔSCF, there are a number of interesting variational DFT approaches to the study of excited states. They include ensemble DFT [54–59], variation of bifunctionals [60], and excited state perturbation theory [61]. They are discussed elsewhere in this volume.

The use of a ground state functional in variational excited state calculations seems intuitively appealing from the point of view that electron correlation should be quite similar in the ground and excited states, at least in the lower valence region. In fact, based on this notion we introduced in 2009 the constricted variational DFT method (CV-DFT) for excited states [29]. In this theory we allow for an admixture of virtual ground state orbitals $\{\psi_a; a = 1, \mathrm{vir}\}$ into each of the occupied ground state orbitals $\{\psi_j; j = 1, \mathrm{occ}\}$, according to

$$\psi_i = \sum_a^{\mathrm{vir}} U_{ai}\psi_a \tag{1}$$

The ansatz in (1) makes it possible to construct occupied excited state orbitals and evaluate the corresponding excited state energies based on the ground state functional to any desired order n in the variational mixing matrix $\mathbf{U}$. Such a

procedure gives rise to the *n*th order CV-DFT scheme designated as CV(*n*)-DFT [26–28].

We start this review by an outline of the CV(*n*)-DFT theory. This framework enables us to identify ATDDFT and ΔSCF as special cases of the CV(*n*)-DFT scheme with ATDDFT being equivalent to CV(2)-DFT [29, 62] whereas ΔSCF corresponds to CV(∞)-DFT under the simplifying assumption that the excited state under investigation can be described by a single orbital replacement $(i \rightarrow a)$ [27, 44]. The theoretical exposition is followed by first assessing the general performance of CV(*n*)-DFT in connection with applications to $n \rightarrow \pi^*$ [26–67] and $\pi \rightarrow \pi^*$ [27] transitions in organic molecules. After that we demonstrate that CV(*n*)-DFT is able to deal with a number of transitions where the performance of ATDDFT based on local and hybrid functionals is problematic. These transitions involve $\pi \rightarrow \pi^*$ excitations in organic dyes [64, 65] as well as $\pi \rightarrow \pi^*$ transitions in charge transfer adducts [30] and Rydberg excitations for atoms and small molecules [66]. We finally discuss future directions for the development and application of the CV(*n*)-DFT scheme.

2 Constricted Variational Density Functional Theory

We have recently introduced a variational approach based on density functional theory for the description of excited states [29, 31]. In this constricted variational density functional theory, CV-DFT, we carry out a unitary transformation among occupied $\{\phi_i; i = 1, \mathrm{occ}\}$ and virtual $\{\phi_a; a = 1, \mathrm{vir}\}$ ground state orbitals:

$$Y\begin{pmatrix}\phi_{\mathrm{occ}}\\ \phi_{\mathrm{vir}}\end{pmatrix} = \mathrm{e}^{\mathbf{U}}\begin{pmatrix}\phi_{\mathrm{occ}}\\ \phi_{\mathrm{vir}}\end{pmatrix} = \left(\sum_{m=0}^{\infty}\frac{(\mathbf{U})^m}{m!}\right)\begin{pmatrix}\phi_{\mathrm{occ}}\\ \phi_{\mathrm{vir}}\end{pmatrix} = \begin{pmatrix}\phi'_{\mathrm{occ}}\\ \phi'_{\mathrm{vir}}\end{pmatrix} \tag{2a}$$

Here ϕ_{occ} and ϕ_{vir} are concatenated column vectors containing the sets $\{\phi_i; i = 1, \mathrm{occ}\}$ and $\{\phi_a; a = 1, \mathrm{vir}\}$ whereas ϕ'_{occ} and ϕ'_{vir} are concatenated column vectors containing the resulting sets $\{\phi'_i; i = 1, \mathrm{occ}\}$ and $\{\phi'_a; a = 1, \mathrm{vir}\}$ of occupied and virtual excited state orbitals, respectively. The unitary transformation matrix Y in (2a) is expressed in terms of a skew symmetric matrix $\mathbf{U}$ as

$$Y = \mathrm{e}^{\mathbf{U}} = \mathbf{I} + \mathbf{U} + \frac{\mathbf{U}^2}{2} + \cdots = \sum_{m=0}^{\infty}\frac{\mathbf{U}^m}{m!} = \sum_{m=0}^{\infty}\frac{\left(\mathbf{U}^2\right)^m}{2m!} + \mathbf{U}\sum_{m=0}^{\infty}\frac{\left(\mathbf{U}^2\right)^m}{(2m+1)!} \tag{2b}$$

If the summation in (2a) and (2b) over m is carried out to $m = n$ we talk about *n*th order CV-DFT or CV(*n*)-DFT. Above $U_{ij} = U_{ab} = 0$ where "*i*,*j*" refer to the occupied set $\{\phi_i; i = 1, \mathrm{occ}\}$ whereas "*a*,*b*" refer to $\{\phi_a; a = 1, \mathrm{vir}\}$. Further, U_{ai} are the variational mixing matrix elements of (1) which combines virtual and occupied ground state orbitals in the excited state with $U_{ai} = -U_{ia}$. Thus the entire

matrix **U** is made up of occ × vir independent elements U_{ai} which can also be organized in the column vector $\vec{U}$. For a given $\vec{U}$ we can, by means of (2a) and (2b), generate a set of "occupied" excited state orbitals:

$$\phi_i^{'} = \sum_{p}^{\text{occ+vir}} Y_{pi}\phi_p = \sum_{j}^{\text{occ}} Y_{ji}\phi_j + \sum_{a}^{\text{vir}} Y_{ai}\phi_a \tag{3}$$

which are orthonormal to any order in U_{ai}.

2.1 Second Order Constricted Variational Density Functional Theory

In the simple CV(2)-DFT theory [29] the unitary transformation of (2a) and (2b) is carried out to second order in **U**. We thus obtain the occupied excited state orbitals to second order as

$$\phi_i^{'} = \phi_i + \sum_{a}^{\text{vir}} U_{ai}\phi_a - \frac{1}{2}\sum_{j}^{\text{occ}}\sum_{a}^{\text{vir}} U_{ai}U_{aj} \tag{4}$$

from which we can generate the excited state Kohn–Sham density matrix to second order as

$$\begin{aligned}\rho'(1,1') = \rho^{(0)}(1,1') + \Delta\rho'(1,1') = \rho^{(0)}(1,1') \\ + \sum_{i}^{\text{occ}}\sum_{a}^{\text{vir}} U_{ai}\phi_a(1)\phi_i^*(1') + \sum_{i}^{\text{occ}}\sum_{a}^{\text{vir}} U_{ai}^*\phi_a^*(1')\phi_i(1) \\ + \sum_{i}^{\text{occ}}\sum_{a}^{\text{vir}}\sum_{b}^{\text{vir}} U_{ai}^*U_{bi}\phi_a(1')\phi_b^*(1') - \sum_{i}^{\text{occ}}\sum_{j}^{\text{occ}}\sum_{a}^{\text{vir}} U_{ai}^*U_{aj}\phi_i(1')\phi_j^*(1')\end{aligned} \tag{5}$$

The expression for $\rho'(1,1')$ now makes it possible to write down the corresponding excited state Kohn–Sham energy to second order as

$$\begin{aligned}E_{\text{KS}}[\rho'(1,1')] = E_{\text{KS}}[\rho^0] + \sum_{ai} U_{ai}U_{ai}^*\left(\varepsilon_a^0 - \varepsilon_i^0\right) + \sum_{ai}\sum_{bj} U_{ai}U_{bj}^*K_{ai,bj} \\ + \frac{1}{2}\sum_{ai}\sum_{bj} U_{ai}U_{bj}K_{ai,jb} + \frac{1}{2}\sum_{ai}\sum_{bj} U_{ai}^*U_{bj}^*K_{ai,jb} + O\left[U^{(3)}\right].\end{aligned} \tag{6}$$

Here $E_{\mathrm{KS}}[\rho^0]$ is the ground state energy and "a,b" run over virtual ground state canonical orbitals whereas "i,j" run over occupied ground state canonical orbitals. Further,

$$K_{ru,tq} = K^{C}_{ru,tq} + K^{XC}_{ru,tq} \tag{7}$$

where

$$K^{C}_{ru,tq} = \int\int \phi^*_r(1)\phi_u(1)\frac{1}{r_{12}}\phi_t(2)\phi^*_q(2)dv_1 dv_2 \tag{8}$$

whereas

$$K^{XC(\mathrm{HF})}_{ru,tq} = -\int\int \phi^*_r(1)\phi_t(2)\frac{1}{r_{12}}\phi_u(2)\phi^*_q(1)dv_1 dv_2 \tag{9a}$$

for Hartree–Fock exchange correlation and

$$K^{XC(\mathrm{KS})}_{ru,tq} = \delta(m_{sr},m_{su})\delta(m_{st},m_{sq})\int \phi^*_r\left(\vec{r}_1\right)\phi_u\left(\vec{r}_1\right)\left[f^{(m_{sr},m_{st})}(\rho^0)\right]\phi_t\left(\vec{r}_1\right)\phi^*_q\left(\vec{r}_1\right)d\vec{r}_1 \tag{9b}$$

for DFT exchange correlation. In (9a) $m_{sr} = 1/2$ for a spin orbital $\phi_r(1)$ of α-spin whereas $m_{sr} = -1/2$ for a spin orbital $\phi_r(1)$ of β-spin. In addition, the kernel $f^{(\tau,\upsilon)}(\rho^0)$ is the second functional derivative of E_{XC} with respect to ρ_α and ρ_β:

$$f^{\tau,\upsilon}\left(\rho^0_\alpha,\rho^0_\beta\right) = \left(\frac{\delta^2 E_{XC}}{\delta\rho_\tau\delta\rho_\upsilon}\right)_0 \quad \tau = \alpha,\beta\ ;\ \upsilon = \alpha,\beta. \tag{10}$$

Finally for KS exchange we have the case where $\phi_u\left(\vec{r}_1\right),\phi_q\left(\vec{r}_1\right)$ have the same (α) spin whereas $\phi_r\left(\vec{r}_1\right),\phi_t\left(\vec{r}_1\right)$ are of the other (β) spin. In this case we have, according to Wang and Ziegler [67–69],

$$K^{\mathrm{KS}(XC)}_{\bar{r}u,\bar{t}q} = \frac{1}{2}\int\left[\overline{\phi}^*_r\left(\vec{r}_1\right)\phi_u\left(\vec{r}_1\right)\overline{\phi}_t\left(\vec{r}_1\right)\phi^*_q\left(\vec{r}_1\right)\right]\left[\left(\frac{1}{s^0}\left(\frac{\delta E_{XC}}{\delta\rho_\alpha}-\frac{\delta E_{XC}}{\delta\rho_\beta}\right)\right)_{(\rho^0,s^0)}\right]d\vec{r}_1 \tag{11}$$

In (11) the integration is over space and $\overline{\phi}_r\left(\vec{r}_1\right),\overline{\phi}_t\left(\vec{r}_1\right)$ are the spatial parts of orbitals with β-spin. The evaluation of $K^{\mathrm{KS}(XC)}_{\bar{r}u,\bar{t}q}$ by numerical integration might lead to numerical instabilities if $s^0 = \rho^\alpha - \rho^\alpha \approx 0$. We can, in that case, carry out a Taylor expansion of $\partial E^{\mathrm{KS}}_{XC}/\partial\rho_\alpha, \partial E^{\mathrm{KS}}_{XC}/\partial\rho_\beta$ from $\rho = \rho^\alpha + \rho^\beta$ and $s^0 = 0$. Thus

$$K^{\mathrm{KS}(XC)}_{\bar{r}u,\bar{t}q} = \frac{1}{2}\int \left[\overline{\phi}^*_r(\bar{r}_1)\phi_u(\bar{r}_1)\overline{\phi}_t(\bar{r}_1)\phi^*_q(\bar{r}_1)\right]\frac{1}{2}\left[\left(\frac{\delta^2 E_{XC}}{\delta^2\rho_\alpha}+\frac{\delta^2 E_{XC}}{\delta^2\rho_\beta}-2\frac{\delta^2 E_{XC}}{\delta\rho_\alpha\delta\rho_\alpha}\right)_{(\rho^0,s^0)}\right]dr_1$$
$$= K^{\mathrm{KS},XC}_{ru,tq} - K^{\mathrm{KS},XC}_{\bar{r}t,uq} \tag{12}$$

where $K^{\mathrm{KS},XC}_{ru,tq}, K^{\mathrm{KS},XC}_{\bar{r}t,uq}$ are defined in (9a) and (9b). The expression in (12) is numerically stable and has no singularities for $s^0 = 0$. Finally, $\varepsilon^0_i, \varepsilon^0_a$ in (6) are the ground state orbital energies of $\phi_i(1)$ and $\phi_a(1)$, respectively.

2.2 Equivalence Between Adiabatic TDDFT and Second Order Constricted Variational Density Functional Theory

In second order variational density functional theory (CV(2)-DFT) we seek points on the energy surface $E_{\mathrm{KS}}[\rho']$ such that $\Delta E_{\mathrm{KS}}[\Delta\rho'] = E_{\mathrm{KS}}[\rho'] - E_{\mathrm{KS}}[\rho^0]$ represents transition energy. Obviously, a direct optimization of $\Delta E_{\mathrm{KS}}[\Delta\rho']$ without constraints results in $\Delta E_{KS}[\Delta\rho'] = 0$ and $U = 0$. We [29] now introduce the constraint that the electron excitation must represent a change in density $\Delta\rho'$ in which one electron in (5) is transferred from the occupied space represented by $\Delta\rho_{\mathrm{occ}} = -\sum_{ija} U_{ai}U^*_{aj}\varphi_i(1')\varphi^*_j(1)$ to the virtual space represented by $\Delta\rho_{\mathrm{vir}} = \sum_{iab} U_{ai}U^*_{bi}\varphi_a(1')\varphi^*_b(1)$. Integration of $\Delta\rho_{\mathrm{occ}}$ and $\Delta\rho_{\mathrm{vir}}$ over all space affords $-\Delta q_{\mathrm{occ}} = \Delta q_{\mathrm{vir}} = \sum_{ai} U_{ai}U^*_{ai}$. We thus introduce the constraint $\sum_{ai} U_{ai}U^*_{ai} = 1$. Constructing next the Lagrangian $L = E_{\mathrm{KS}}[\rho'] + \lambda\left(1 - \sum_{ai} U_{ai}U^*_{ai}\right)$ with λ being a Lagrange multiplier and demanding that L be stationary to any real variation in U results in the eigenvalue equation

$$\left(A^{\mathrm{KS}} + B^{\mathrm{KS}}\right)\vec{U}^{(I)} = \lambda_{(I)}\vec{U}^{(I)} \tag{13a}$$

where

$$A^{\mathrm{KS}}_{ai,bj} = \delta_{ab}\delta_{ij}\left(\varepsilon^0_a - \varepsilon^0_i\right) + K^{\mathrm{KS}}_{ai,bj}; \quad B^{\mathrm{KS}}_{ai,bj} = K^{\mathrm{KS}}_{ai,jb}. \tag{13b}$$

We can now from (13a) determine the sets of mixing coefficients $\left\{\vec{U}^{(I)}; I = 1, \mathrm{occ}\times\mathrm{vir}\right\}$ which make L stationary and represent excited states. The corresponding excitation energies are given by $\lambda_{(I)}$, as can be seen by

substituting $\vec{U}^{(I)}$ into (6) and making use of the constraint and normalization condition $\vec{U}^{(I)+}\vec{U}^{(I)} = 1$ after multiplying on both sides with $\vec{U}^{(I)+}$.

Within the Tamm–Dancoff approximation [70], (13a) reduces to

$$A^{\mathrm{KS}}\vec{U}^{(I)} = \lambda_{(I)}\vec{U}^{(I)} \tag{14}$$

which is identical in form to the equation obtained from ATDDFT in its adiabatic formulation [3–9] after applying the same Tamm–Dancoff [70] approximation (ATDDFT-TD). We have recently shown [62] that CV(2)-DFT without the Tamm–Dancoff approximation is equivalent to the full adiabatic TDDFT scheme developed by Gross [3], Casida [4], and others [5–9].

2.3 *Perturbative All Order Constricted Variational Density Functional Theory*

Having determined $\vec{U}^{(I)}$ from (14) allows us [28] to turn to a discussion of how we construct the proper energy expression for excited singlet states originating from a closed shell ground state. We first consider a spin-conserving transition from a close shell ground state and assume without loss of generality that the transition takes place in the α-manifold. In this case we can write the occupied excited state KS-orbitals generated from the unitary transformation of (2a) and (2b) as [28, 71]

$$\phi_i^{'} = \cos[\eta\gamma_i]\phi_i^{o_\alpha} + \sin[\eta\gamma_i]\phi_i^{v_\alpha}; \quad i = 1, \mathrm{occ}/2 \tag{15}$$

and

$$\phi_i^{'} = \phi_i; \quad i = \mathrm{occ}/2 + 1, \mathrm{vir} \tag{16}$$

whereas the corresponding KS-determinant is given by

$$\Psi_M = \left|\phi_1^{'}\phi_2^{'}\ldots\phi_i^{'}\phi_j^{'}\ldots\phi_n^{'}\right| \tag{17}$$

Here Ψ_M represents a mixed spin-state [40] which is half singlet and half triplet. Further, $\gamma_i(i = 1, \mathrm{occ}/2)$ is a set of eigenvalues to

$$(\mathbf{V}^{\alpha\alpha})^{\dagger}(\mathbf{U}^{\alpha\alpha})(\mathbf{W}^{\alpha\alpha}) = \mathbf{1}\gamma \tag{18}$$

where γ is a diagonal matrix of dimension occ/2 whereas $\mathbf{U}^{\alpha\alpha}$ is the part of the $\mathbf{U}$ matrix which runs over the occupied $\{\phi_i; i = 1, \mathrm{occ}\}$ and virtual $\{\phi_a; a = 1, \mathrm{vir}\}$ ground state orbitals of α-spin [28, 71]. Further,

$$\phi_i^{o_\alpha} = \sum_j^{\mathrm{occ}/2} \left(\mathbf{W}^{\alpha\alpha}\right)_{ji} \phi_j \tag{19}$$

and

$$\phi_i^{v_\alpha} = \sum_a^{occ/2} \left(\mathbf{V}^{\alpha\alpha}\right)_{ai} \phi_a \tag{20}$$

Finally, η is determined in such a way that $\sum_{i=1}^{\mathrm{occ}/2} \sin^2\left[\eta\gamma_i\right] = 1$, corresponding to the constraint that exactly one electron charge is involved in the transition [28]. The orbitals defined in (19) and (20) have been referred to as Natural Transition Orbitals (NTO) [72] because they give a more compact description of the excitations than the canonical orbitals. Thus, a transition involving several $i \rightarrow a$ replacements among canonical orbitals can often be described by a single replacement $\phi_i^{o_\alpha} \rightarrow \phi_i^{v_\alpha}$ in terms of NTOs. We note again that the set in (16) is obtained from the unitary transformation (2a) and (2b) among the occupied $\{\phi_i : i = \mathrm{vir}/2 + 1, \mathrm{vir}\}$ and virtual $\{\phi_a; i = 1, \mathrm{vir}/2\}$ ground state orbitals of α-spin with $\mathbf{U}$ represented by $\mathbf{U}^{\alpha\alpha}$.

For a spin-flip transition from a closed shell ground state the unitary transformation (2a) and (2b) among the occupied ground state orbitals $\{\phi_i; i = 1, \mathrm{occ}/2\}$ of α-spin and the virtual ground state orbitals $\{\phi_a; i = \mathrm{vir}/2 + 1, \mathrm{vir}\}$ of β-spin yields the occupied excited state orbitals

$$\phi_i^{''} = \cos\left[\eta\gamma_i^{'}\right]\phi_i^{o_\alpha} + \sin\left[\eta\gamma_i^{'}\right]\phi_i^{v_\beta}\ ; i = 1, \mathrm{occ}/2 \tag{21}$$

and

$$\phi_i^{''} = \phi_i\ ;\ i = \mathrm{occ}/2 + 1, \mathrm{vir} \tag{22}$$

whereas the corresponding KS-determinant is given by

$$\Psi_T = \left|\phi_1^{''}\phi_1^{''} \ldots \phi_i^{''}\phi_j^{''} \ldots \phi_n^{''}\right| \tag{23}$$

Here Ψ_T represents a triplet state. Further, $\gamma_i (i = 1, \mathrm{occ}/2)$ are the eigenvalues to

$$\left(\mathbf{V}^{\beta\alpha}\right)^{\dagger}\left(\mathbf{U}^{\beta\alpha}\right)\left(\mathbf{W}^{\beta\alpha}\right) = \mathbf{1}\gamma' \tag{24}$$

where $\mathbf{U}^{\beta\alpha}$ is the part of $\mathbf{U}$ which runs over the virtual ground state orbitals of β-spin and occupied ground state orbitals of α-spin. Finally

$$\phi_i^{o_\alpha} = \sum_j^{\text{occ}/2} \left(\mathbf{W}^{\beta\alpha}\right)_{ji} \phi_j \tag{25}$$

and

$$\phi_i^{v_\beta} = \sum_{a=\text{vir}/2+1}^{a=\text{vir}} \left(\mathbf{V}^{\beta\alpha}\right)_{ai} \phi_a \tag{26}$$

With the excitation energy of Ψ_T given by ΔE_T and that of Ψ_M by ΔE_M, we can write the singlet transition energy as [40]

$$\Delta E_S = 2\Delta E_M - \Delta E_T \tag{27}$$

provided that $\mathbf{U}^{\alpha\alpha} = \mathbf{U}^{\beta\alpha}$. This implies that $\mathbf{V}^{\alpha\alpha} = \mathbf{V}^{\beta\alpha}$, $\mathbf{W}^{\alpha\alpha} = \mathbf{W}^{\beta\alpha}$, and $\gamma = \gamma'$. As a result, $\phi_i^{o_\alpha}$ of (19) and (25) become identical as do the spatial parts of $\phi_i^{v_\alpha}$ in (20) and $\phi_i^{v_\beta}$ in (26). Straightforward manipulations [27, 28] allow us finally to write down the mixed state transition energy to all orders in $\mathbf{U}$ in a compact and closed form as

$$\begin{aligned}
\Delta E_M = & \sum_{i=1}^{\text{occ}/2} \sin^2\left[\eta\gamma_i\right]\left(\varepsilon_{i^{v_\alpha}} - \varepsilon_{i^{o_\alpha}}\right) \\
& + \frac{1}{2}\sum_{i=1}^{\text{occ}/2}\sum_{j=1}^{\text{occ}/2} \sin^2\left[\eta\gamma_i\right]\sin^2\left[\eta\gamma_j\right]\left(K_{i^{o_\alpha}i^{o_\alpha}j^{o_\alpha}j^{o_\alpha}} + K_{i^{v_\alpha}i^{v_\alpha}j^{v_\alpha}j^{v_\alpha}} - 2K_{i^{o_\alpha}i^{o_\alpha}j^{v_\alpha}j^{v_\alpha}}\right) \\
& + \sum_{i=1}^{\text{occ}/2}\sum_{j=1}^{\text{occ}/2} \sin\left[\eta\gamma_i\right]\cos\left[\eta\gamma_i\right]\sin\left[\eta\gamma_j\right]\cos\left[\eta\gamma_j\right]\left(K_{i^{o_\alpha}i^{v_\alpha}j^{o_\alpha}j^{v_\alpha}} + K_{i^{o_\alpha}i^{v_\alpha}j^{v_\alpha}j^{o_\alpha}}\right) \\
& + 2\sum_{i=1}^{\text{occ}/2}\sum_{j=1}^{\text{occ}/2} \sin\left[\eta\gamma_i\right]\sin\left[\eta\gamma_i\right]\sin\left[\eta\gamma_j\right]\cos\left[\eta\gamma_j\right]K_{i^{v_\alpha}i^{v_\alpha}j^{o_\alpha}j^{v_\alpha}} \\
& - 2\sum_{i=1}^{\text{occ}/2}\sum_{j=1}^{\text{occ}/2} \sin\left[\eta\gamma_i\right]\sin\left[\eta\gamma_i\right]\sin\left[\eta\gamma_j\right]\cos\left[\eta\gamma_j\right]K_{i^{o_\alpha}i^{o_\alpha}j^{o_\alpha}j^{v_\alpha}}
\end{aligned} \tag{28}$$

for spin-conserving transition from a close shell ground state. More details are given in Sect. 2.4. Here the indices $i^{o_\alpha}, j^{o_\alpha}, i^{v_\alpha}$, and j^{v_α} refer to α-spin orbitals with the spatial parts $\phi_i^{o_\alpha}, \phi_j^{o_\alpha}, \phi_i^{v_\alpha}$, and $\phi_j^{v_\alpha}$, respectively. The expression for the corresponding triplet transition energy reads

$$\Delta E_T = \sum_{i=1}^{occ/2} \sin^2\left[\eta' \gamma_i'\right] \left(\varepsilon_{i^{v\beta}} - \varepsilon_{i^{o\alpha}}\right)$$
$$+ \frac{1}{2} \sum_{i=1}^{occ/2} \sum_{j=1}^{occ/2} \sin^2\left[\eta' \gamma_i'\right] \sin^2\left[\eta' \gamma_i'\right] \left(K_{i^{o\alpha} i^{o\alpha} j^{o\alpha} j^{o\alpha}} + K_{i^{v\beta} i^{v\beta} j^{v\beta} j^{v\beta}} - 2K_{i^{o\alpha} i^{o\alpha} j^{v\beta} j^{v\beta}}\right) \quad (29)$$
$$+ \sum_{i=1}^{occ/2} \sum_{j=1}^{occ/2} \sin\left[\eta' \gamma_i'\right] \cos\left[\eta' \gamma_i'\right] \sin\left[\eta' \gamma_j'\right] \cos\left[\eta' \gamma_j'\right] K_{i^{o\alpha} i^{v\beta} j^{o\alpha} j^{v\beta}}$$

Here the indices $i^{v\beta}$ and $j^{v\beta}$ refer to β-spin orbitals with the spatial parts $\phi_i^{v\beta}$ and $\phi_i^{v\beta}$, respectively. More details are given in Sect. 2.4. From (28) and (29) we can readily express ΔE_S using (27).

In perturbative all order constricted variational DFT (P-CV(∞)-DFT) [27, 64] we make use of the **U** matrix optimized to second order according to (14), which is also the **U** obtained by ATDDFT-TD (CV(2)-DFT-TD). With this **U** we are able to generate Ψ_M of (17) and Ψ_T of (23) by means of (2a) and (2b). From that we can calculate ΔE_T and ΔE_S by means of (27)–(29).

2.3.1 Application of Perturbative All Order Constricted Variational Density Functional Theory to $\pi \rightarrow \pi^*$

We have carried out ATDDFT-TD, (CV(2)-DFT-TD), and P-CV(∞)-DFT calculations [27] on $\pi \rightarrow \pi^*$ transitions in the series of polyenes depicted in Fig. 1 using LDA. In the following we simplify the notation by referring to ATDDFT, ATDDFT-TD, CV(2)-DFT-TD, and P-CV(∞)-DFT-TD as TDDFT, TDDFT-TD, CV(2)-TD, and CV(∞)-TD, respectively, throughout Sect. 2.3.

The results are displayed in Table 1. We have divided the $\pi \rightarrow \pi^*$ transitions into a group A where each excitation is dominated by a single orbital replacement ($\gamma_{max} > 1.0$) and a group B where the excitation is best described by several orbital replacements ($\gamma_{max} < 1.0$). The group B transitions generally consist of two orbital replacements involving the HOMO → LUMO + 1 and the HOMO − 1 → LUMO transitions. It can be seen that the group B results for P-CV(∞)-TD with a root

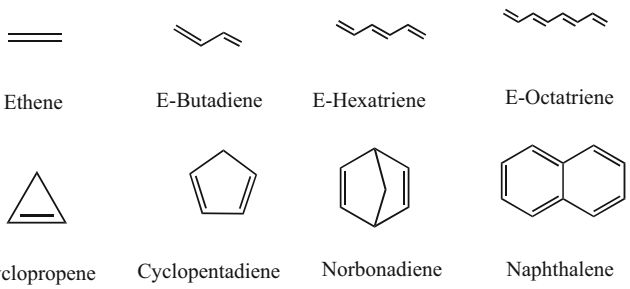

Fig. 1 Molecules used in the study of $\pi \rightarrow \pi^*$ transitions based on P-CV(∞)-DFT

Table 1 Results from TDDFT-TD and CV(∞)-TD calculations on excitation energies[a] for π to π* transitions in polyenes using LDA

	Group	State	Best[b]	TDDFT-TD[c]	CV(∞)-TD	γ_{max}[d]
Ethene	A	B_{1u}	7.80	8.44	8.39	1.177
Butadiene	A	B_u	6.18	6.16	6.10	1.174
	B	A_g	6.55	6.24	6.70	0.841
Hexatriene	B	A_g	5.09	5.03	5.36	0.787
	A	B_u	5.10	5.05	4.93	1.200
Octatetraene	B	A_g	4.47	4.17	4.42	0.799
	A	B_u	4.66	4.34	4.16	1.212
Cyclopropene	A	B_2	7.06	6.30	7.55	1.253
Cyclopentadiene	A	B_2	5.55	5.39	5.87	1.254
	B	A_1	6.31	6.05	6.45	0.809
Norbornadiene	A	A_2	5.34	4.52	5.10	1.158
	B	B_2	6.11	4.95	5.36	0.942
Naphthalene	B	B_{3u}	4.24	4.20	4.39	0.788
	A	B_{2u}	4.77	4.25	4.71	1.103
	B	B_{1g}	5.99	4.97	5.24	0.850
	B	A_g	5.87	5.80	6.02	0.854
	A	B_{2u}	6.33	6.12	6.09	1.043
	B	A_g	6.67	6.21	6.71	0.904
	B	B_{3u}	6.06	6.22	6.14	0.730
	B	B_{1g}	6.47	6.47	6.36	0.791
RMSD A[e]				0.48	0.35	
RMSD B				0.51	0.34	
RMSD A + B				0.50	0.35	

[a]Energies in eV
[b]Ab initio benchmark calculations [73]
[c]Identical to CV(2)-TD
[d]Maximum γ eigenvalue for this transition; see (18)
[e]Root mean square deviation in eV

mean square deviation (RMSD) of 0.34 eV compared to the best [73] wave function results constitute an improvement over the TDDFT-TD excitation energies with an RMSD of 0.51 eV. For the group A transitions we also note an improvement in going from TDDFT-TD with RMSD = 0.48 eV to CV(∞)-TD with RMSD = 0.35 eV. From experience so far [27, 64] it seems that CV(∞) can be used with advantage in studies of $\pi \rightarrow \pi^*$ transitions involving dyes employing simple local functionals.

2.3.2 Application of Perturbative All Order Constricted Variational Density Functional Theory to Acenes

The singlet ^1L_a and ^1L_b $\pi \rightarrow \pi^*$ excitations in linear polyacenes represent a set of benchmark excitations which have been studied extensively both experimentally

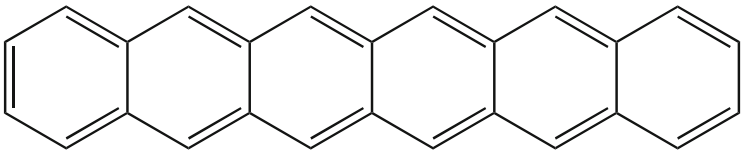

Fig. 2 Linear acenes with up to six fused rings ($n_r = 6$) considered in this study

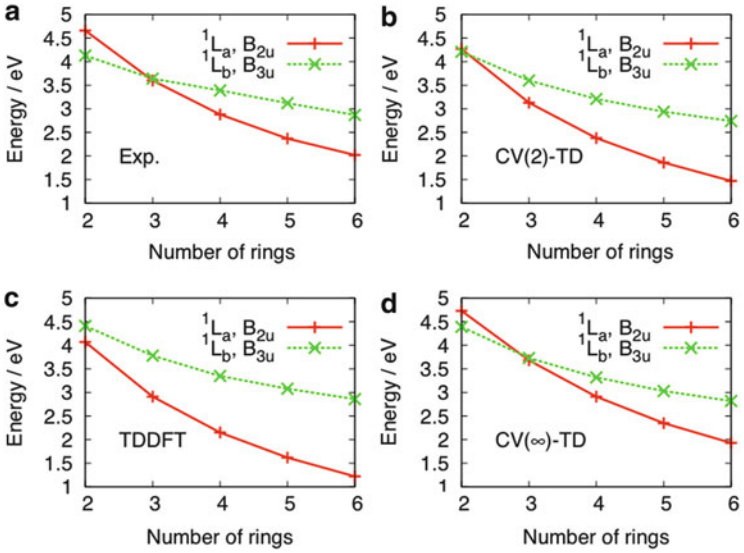

Fig. 3 Excitation energies for the ^1L_a and ^1L_b transitions in linear acenes as a function of the number of rings according to (**a**) experiment, (**b**) CV(2)-TD, (**c**) TDDFT, or (**d**) CV(∞)-TD

[74] and theoretically [75–78]. Here the acenes consist of a number (n_r) of fused benzene rings; see Fig. 2.

The distinct properties [74] of the ^1L_a and ^1L_b states for the linear acenes have already been described in the literature [75–78]. Essentially, the ^1L_a (or $^1B_{2u}$ when the x-axis corresponds to the long molecular axis state) is dominated by a single electron transition HOMO → LUMO, while the ^1L_b (or $^1B_{3u}$) state results from a combination of HOMO − 1 → LUMO and HOMO → LUMO + 1 transitions. Further, excitations to ^1L_a ($^1B_{2u}$) are short axis polarized with high intensity whereas the transitions to ^1L_b ($^1B_{3u}$) are long axis polarized with low intensity.

It follows from Fig. 3a that the experimental energy gap $\Delta E = \Delta E\left(^1B_{2u}2u\right) - \Delta E\left(^1B_{3u}3u\right)$ starts out positive at naphthalene ($n_r = 2$) with $\Delta E = 0.53$ eV before turning negative at anthracene ($n_r = 3$) where $\Delta E = 0.04$ eV. For larger linear acenes ΔE becomes increasingly negative, reaching $\Delta E = 0.85$ eV at hexacene. Thus, experimentally, $\Delta E(^1B_{2u})$ is seen to drop faster in energy than $\Delta E(^1B_{3u})$.

Table 2 Root mean square deviations ([d]RMSD) from experiment for ^1L_a and ^1L_b $\pi \rightarrow \pi^*$ excitations calculated by TDDFT, TDDFT-TD and CV(∞)-TD for linear and nonlinear acenes using LDA

	RMSD $^1B_{2u}$ (^1L_a)			RMSD $^1B_{3u}$ (^1L_b)		
Systems	TDDFT	TDDFT-TD[a]	CV(∞)-TD	TDDFT	TDDFT-TD[a]	CV(∞)-TD
Linear[b]	0.71	0.49	0.06	0.14	0.13	0.13
Nonlinear[c]	0.52	0.40	0.24	0.16	0.15	0.19

[a]Identical to CV(2)-TD
[b]Linear acenes of Fig. 2
[c]Nonlinear acenes of Fig. 4
[d]Ev

The ordering of the calculated CV(2)-TD (TDDFT-TD) excitation energies based on LDA(VWN) is correct for naphthalene as well as for all other linear acenes, although the gap differs from the experimental ΔE by almost 0.4 eV for naphthalene, anthracene, and hexacene. This difference is smaller for naphthacene and pentacene (Fig. 3b). It can be seen that the main contribution to this deviation comes from the underestimation of $\Delta E(^1B_{2u})$ Thus, the root mean square deviation (RMSD) value for $\Delta E(^1B_{2u})$ is 0.49 eV, while it is only 0.13 eV for $\Delta E(^1B_{3u})$; see Table 2.

As for the TDDFT results based on LDA(VWN), the deviation from the experimental gaps is larger in absolute terms and the calculated ΔE has the wrong sign for naphthalene (Fig. 3c). It happens because the $\Delta E(^1B_{2u})$ values for TDDFT are lower than those for CV(2)-TD while the $\Delta E(^1B_{3u})$ estimates for TDDFT are higher than for CV(2)-TD. As a result, the RMSD value for $\Delta E(^1B_{2u})$ increases for TDDFT by approximately 0.2 eV and reaches 0.71 eV; see Table 2. On the other hand, on average the TDDFT estimate of $\Delta E(^1B_{3u})$ is as accurate as for CV(2)-TD (TDDFT-TD). Thus, the TDDFT $\Delta E(^1B_{3u})$ values for naphthacene, pentacene, and hexacene are closer to experiment than those from CV(2)-TD while the opposite is true for naphthalene and anthracene. The RMSD value for TDDFT is 0.14 eV compare to 0.13 eV for CV(2)-TD; see Table 2.

It follows from the discussion given above that neither CV(2)-TD nor TDDFT are able to give a quantitative description of ΔE as a function of n_r with LDA, in line with previous TDDFT studies [75–78], using both pure density functionals and hybrids. The source of the error is in all cases primarily $\Delta E(^1B_{2u})$ which is too low compared to experiment. However, $\Delta E(^1B_{3u})$ is also seen to be slightly too high.

We note finally from Table 3 and Fig. 3d that the CV(∞)-TD results using LDA [64] are in excellent agreement with experiment for both $\Delta E(^1B_{3u})$ and $\Delta E(^1B_{2u})$ throughout the range of linear acenes (1–6 of Fig. 4). The RMSD for $\Delta E(^1B_{2u})$ is 0.06 eV whereas that for $\Delta E(^1B_{3u})$ is 0.13 eV; see Table 2. Thus, CV(∞)-TD clearly represents an improvement over TDDFT and CV(2)-TD for LDA. The improvement is, as anticipated, most noticeable for $\Delta E(^1B_{2u})$ where the RMSD was 0.71 eV for TDDFT and 0.49 eV for CV(2)-TD. For $\Delta E(^1B_{3u})$ all three methods have a similar RMSD.

We have extended [64] our benchmark calculations to include the 15 nonlinear acenes shown in Fig. 4. The RSMDs for the singlet transition energies involving ^1L_a

Table 3 CV(∞)-TD singlet excitation energies (in eV) for linear acenes with LDA

Number of rings	Experiment[a]			CV(∞)-TD		
	$^1B_{2u}$	$^1B_{3u}$	ΔE^b	$^1B_{2u}$	$^1B_{3u}$	ΔE^b
2	4.66	4.13	0.53	4.73	4.39	0.34
3	3.60	3.64	−0.04	3.68	3.73	−0.05
4	2.88	3.39	−0.51	2.91	3.32	−0.41
5	2.37	3.12	−0.75	2.35	3.03	−0.68
6	2.02	2.87	−0.85	1.93	2.82	−0.89

[a]Platt [74]
[b]$\Delta E = \Delta E(^1B_{2u}) - \Delta E(^1B_{3u})$

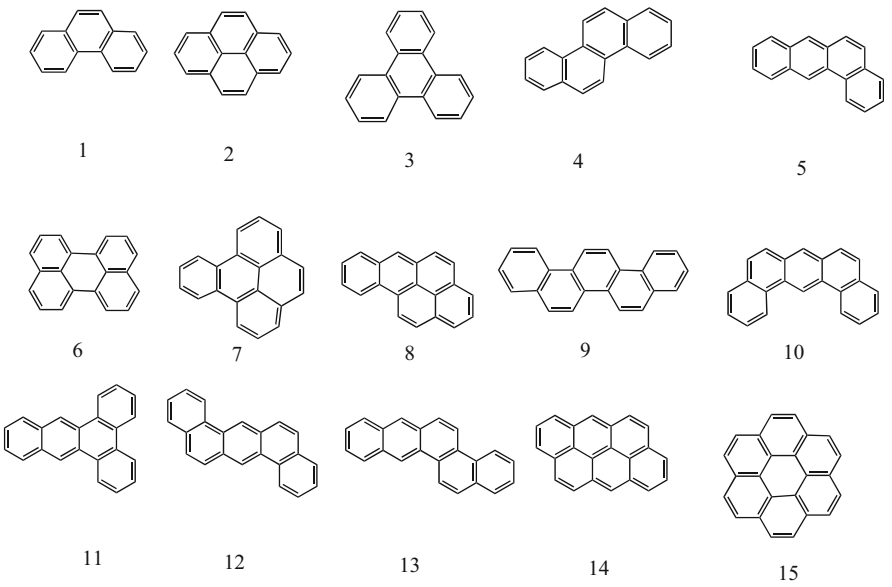

Fig. 4 Nonlinear acenes with up to six fused rings ($n_r = 6$) considered in this study

and ^1L_b are given in Table 2 for TDDFT, CV(2)-TD, and CV(∞)-TD based on LDA. ^1L_a CV(∞)-TD with an RMSD of 0.24 eV is seen to perform better than CV (2)-TD (RMSD = 0.40 eV) and especially TDDFT (0.52 eV). In fact our results are of a similar quality to the best results obtained by long-range corrected (LRC) functionals [79]. We note again that the ^1L_a transitions involves a single HOMO → LUMO orbital displacement with $\gamma_i = \pi/2$. For ^1L_b all three methods perform equally well with RMSDs of 0.16 eV (TDDFT), 0.15 eV(CV(2)-TD), and 0.19 eV (P-CV(∞)-DFT), respectively. It is interesting to note that the LRC-functionals [79] in this case perform much more poorly with RMSDs around 0.4 eV. Thus, CV(∞)-TD at the simple LDA level is the only scheme of the methods discussed here which gives a balanced description of $\pi \rightarrow \pi^*$ transitions involving a single orbital displacement (^1L_a) and $\pi \rightarrow \pi^*$ transitions with more than one displacement.

For the CV(∞)-scheme we note that the singlet excitation energy for a transition involving a single promotion $i \rightarrow a$ such as $^1A_{1g}1g \rightarrow {}^1B_{2u}2u$ according to (27)–(29) has the simple form [27]:

$$\Delta E_S^{CV(\infty)}(i \rightarrow a) = \varepsilon_a - \varepsilon_i + \left(\frac{1}{2}K_{aaaa} + \frac{1}{2}K_{iiii} + 2K_{aaii} - K_{i\overline{i}a\overline{a}}\right) \tag{30}$$

Here i is the HOMO π and a the LUMO π^* in the current study. Further, a bar "‾" indicates an orbital of β-spin. For CV(2)-TD we obtain for the same transition according to (14) and (27)

$$\Delta E_S^{CV(2)}(i \rightarrow a) = \varepsilon_a - \varepsilon_i + 2K_{aiai} - K_{\overline{a}i\overline{a}i} \tag{31}$$

For HF these two expressions are identical [27] because $K_{aaaa} = K_{iiii} = 0$ and $K_{aiai} = -K_{aaii}$. However, for any of the popular functionals this is not the case. Thus, the two expressions give rise to different excitation energies for the same functional. In the study at hand [27] on the $^1A_{1g}1g \rightarrow {}^1B_{2u}2u$ transition the sum of the K-integrals in (30) is larger than the sum of the K-integrals in (31) by 0.5 eV, giving rise to the better performance of CV(∞)-TD compared to CV(2)-TD for the $^1A_{1g}1g \rightarrow {}^1B_{2u}2u$ transition. We note that acenes have also been well described by the variational DFT-based spin-restricted ensemble referenced Kohn–Sham (REKS) method [57].[1]

2.4 *Self-Consistent All Order Constricted Variational Density Functional Theory*

Using the U matrix from TDDFT-TD or CV(2)-TD to calculate ΔE_M of (28) or ΔE_T of (29), as is done in P-CV(∞)-TD, might be a good approximation. However, ultimately, one would want to use a U matrix which actually minimizes ΔE_M of (28) or ΔE_T of (29). Such a procedure leads us to self-consistent CV(∞)-DFT (SCF-CV(∞)-DFT) [27] which we discuss next. We note that the **U** matrix can also be organized as a vector $\vec{U}$ with pairs "ai" of occupied and virtual orbitals as running numbers. The two formulations are used interchangeably in the following.

From the occupied excited state orbitals of (17) and (23) we can express the electron density and spin matrices.[2,3] Starting with a spin-conserving transition from a close shell ground state, we can, without loss of generality, assume that it

[1] See the chapter "Ensemble DFT approach to excited states of strongly correlated molecular systems" by M. Filatov.

[2] See Sect. 3.1 from part S1 of supporting information in Ziegler et al. [27].

[3] See Sect. 3.3 from part S1 of supporting information in Ziegler et al. [27].

takes place between orbitals of α-spin. Thus, for such a spin-conserving transition, the excited state orbitals $\phi_i^{'} = \cos[\eta\gamma_i]\phi_i^{o_\alpha} + \sin[\eta\gamma_i]\phi_i^{v_\alpha}$ (15) are obtained by the unitary transformation at (2a) and (2b) to all orders involving the part of the **U** matrix ($\mathbf{U}^{\alpha\alpha}$) which, according to (1), mixes occupied ground state orbitals of α-spin with virtual ground state orbitals of α-spin. We can now write (see footnote 3) the change in density within the α-manifold caused by the excitation as

$$\begin{aligned}\Delta\rho_M(1,1^{'}) = &\sum_j^{\mathrm{occ}/2} \sin^2\left[\eta^\alpha\gamma_j^\alpha\right]\left[\varphi_j^{v_\alpha}(1')\varphi_j^{v_\alpha}(1) - \varphi_j^{o_\alpha}(1')\varphi_j^{o_\alpha}(1)\right] \\ &+ \sum_j^{\mathrm{occ}/2} \sin\left[\eta^\alpha\gamma_j^\alpha\right]\cos\left[\eta^\alpha\gamma_j^\alpha\right]\left[\varphi_j^{v_\alpha}(1)\varphi_j^{o_\alpha}(1') + \varphi_j^{v_\alpha}(1')\varphi_j^{o_\alpha}(1)\right]\end{aligned} \tag{32a}$$

In (32a) the scaling factor η^α is introduced to ensure that $\Delta\rho^{\alpha(\infty)}(1,1')$ represents the transfer of a single electron from the occupied orbital space density $-\sum_j^{\mathrm{occ}/2} \sin^2\left[\eta^\alpha\gamma_j^\alpha\right]\varphi_j^{o_\alpha}(1')\varphi_j^{o_\alpha}(1)$ to the virtual orbital space density $\sum_j^{\mathrm{occ}/2} \sin^2\left[\eta^\alpha\gamma_j^\alpha\right]\varphi_j^{v_\alpha}(1')\varphi_j^{v_\alpha}(1)$ or

$$\sum_j^{\mathrm{occ}/2} \sin^2\left[\eta^\alpha\gamma_j^\alpha\right] = 1 \tag{32b}$$

Here the constraint of (32b) is a generalization of the corresponding second order constraint $\sum_{ai} U_{ai}U_{ai} = 1$ used to derive (14). The change in density $\Delta\rho^{\alpha(\infty)}(1,1')$ now allows us to write the excitation energy for the spin conserving excitation within the α-manifold as [27]

$$\begin{aligned}\Delta E_M &\equiv E_{\mathrm{KS}}[\rho^0/2 + \Delta\rho_M, \rho^0/2] - E_{\mathrm{KS}}[\rho^0/2, \rho^0/2] \\ &= \int F_{\mathrm{KS}}\left[\rho^0/2 + 1/2\Delta\rho_M, \rho^0/2)\right]\Delta\rho_M\end{aligned} \tag{33}$$

Here the right hand side of (33) is derived by Taylor expanding [80] $E_{\mathrm{KS}}[\rho^0/2 + \Delta\rho_M, \rho^0/2]$ and $E_{\mathrm{KS}}[\rho^0/2, \rho^0/2]$ from the intermediate point $(\rho^0/2 + \Delta\rho_M/2, \rho^0/2)$. Further, $F_{\mathrm{KS}}(\rho^0/2 + \Delta\rho_M/2, \rho^0/2)$ is a Kohn-Sham Fock operator defined with respect to the intermediate point. The expression in (33) is exact to third order in $\Delta\rho_M$ which is usually accurate enough [80]. However, its accuracy can be extended to any desired order [80]. Taylor expanding $F_{\mathrm{KS}}(\rho^0/2 + \Delta\rho_M/2, \rho^0/2)$ to second order in $\Delta\rho_M$ finally affords ΔE_M of (28) (see footnotes 2 and 3). The expression for ΔE_T of (29) can be derived along similar routes.[4,5]

[4] See Sect. 3.2 from part S1 of supporting information in Ziegler et al. [27].

[5] See Sect. 3.4 from part S1 of supporting information in Ziegler et al. [27].

2.4.1 Energy Gradient in SCF-CV(∞)-DFT

We now find vectors $\vec{U}^{(I)}$ which optimize ΔE_M and ΔE_T. In either case there are several which we order in terms of increasing energy with $I = 1, 2\ldots$. To this end, we need the energy gradient with respect to variations in $\vec{U}$. Considering first a spin-conserving transition[6] between orbitals of α-spin, we take as a starting point $\mathbf{U}^{\alpha\alpha}$ which generates $\phi_i' = \cos\left[\eta^\alpha \gamma_i^\alpha\right]\phi_i^{o_\alpha} + \sin\left[\eta^\alpha \gamma_i^\alpha\right]\phi_i^{v_\alpha}$ (15) the elements in $\vec{U}_{(2)}^{(I)} = \vec{U}^{(I)}$ which have been found by solving (14) for a spin conserving transition within the CV(2)-TD (TDDFT-TD) approximation for the Ith state. To the vector $\vec{U}^{(I)}$ corresponds the matrix $\tilde{\mathbf{U}}^{0,\alpha\alpha}$ and the set $\left\{\widetilde{\gamma}_k^{\alpha,0}; k = 1, \mathrm{occ}\right\}$. Next, scaling $\tilde{\mathbf{U}}^{0,\alpha\alpha}$ and $\left\{\widetilde{\gamma}_k^{\alpha,0}; k = 1, \mathrm{occ}\right\}$ by η^α such that $\sum_j^{\mathrm{occ}/2} \sin^2\left[\eta^\alpha \gamma_j^\alpha\right] = 1$ affords $\mathbf{U}^{0,\alpha\alpha} = \eta^\alpha \widetilde{\mathbf{U}}^{0,\alpha\alpha}$ and $\left\{\gamma_k^{\alpha,0} = \eta^\alpha \widetilde{\gamma}_k^{\alpha,0}; k = 1, \mathrm{occ}\right\}$ where now $\sum_j^{\mathrm{occ}/2} \sin^2\left[\eta^\alpha \gamma_j^\alpha\right] = 1$. The matrix $\tilde{\mathbf{U}}^{0,\alpha\alpha}$ is obtained from a CV(2)-TD (TDDFT-TD) calculation where $\mathbf{U}^{\alpha\alpha}$ and $-\mathbf{U}^{\alpha\alpha}$ afford the same energy according to (14). However, in CV(∞) with the energy expression given by (28), the sign matters through the terms containing cos $[\eta^\alpha \gamma_i^\alpha]sin[\eta^\alpha \gamma_i^\alpha]$. As we are dealing with a variational approach, we must pick the sign affording the lowest energy. The same considerations apply to the P-CV(∞)-DFT approach.

Next, a Taylor expansion of ΔE_M in (33) from $\mathbf{U}^{0,\alpha\alpha}$ to $\mathbf{U}^{\alpha\alpha} = \mathbf{U}^{0,\alpha\alpha} + \Delta\mathbf{U}^{\alpha\alpha}$ affords

$$\begin{aligned}\Delta E_M(\mathbf{U}^{\alpha\alpha}) &= E_M\left(\mathbf{U}^{0,\alpha\alpha}\right) + \sum_{ai}\left(\frac{d\Delta E_M}{d\Delta U_{ai}^{\alpha\alpha}}\right)_0 \Delta U_{ai}^{\alpha\alpha} \\ &+ \frac{1}{2}\sum_{ai}\sum_{bj}\left(\frac{d^2\Delta E_M}{d\Delta U_{ai}^{\alpha\alpha} d\Delta U_{bj}^{\alpha\alpha}}\right)_0 \Delta U_{ai}^{\alpha\alpha}\Delta U_{bj}^{\alpha\alpha} \\ &= \Delta E_M\left(\mathbf{U}^{0,\alpha\alpha}\right) + \sum_{ai} g_{ai}^{\alpha,e}\Delta U_{ai}^{\alpha\alpha} + \frac{1}{2}\sum_{ai}\sum_{bj} H_{ai,bj}^{\alpha,\alpha}\Delta U_{ai}^{\alpha\alpha}\Delta U_{bj}^{\alpha\alpha} + O^{(3)}[\Delta\mathbf{U}].\end{aligned} \tag{34}$$

A component of the gradient $g_{ai}^{\alpha,e}$ evaluated at $\mathbf{U}^{0,\alpha\alpha}$ reads

[6] See Sect. 4.1 from part S1 of supporting information in Ziegler et al. [27].

$$\begin{aligned}\overrightarrow{g}_{ai}^{\alpha,e}\left(U^{0,\alpha\alpha}\right) &= \left(\frac{d\Delta E_M}{d\Delta U_{ai}^{\alpha\alpha}}\right)_0 = \left(\frac{\delta\Delta E_M}{\delta\rho^\alpha}\right)_0\left(\frac{d\Delta\rho^\alpha}{d\Delta U_{ai}^{\alpha\alpha}}\right)_0 \\ &= \int F_{\mathrm{KS}}\left[\rho^0/2+1/2\Delta\rho_M^\alpha,\rho^0/2\right]\left(\frac{\partial\Delta\rho_M^\alpha}{dU_{ai}^{\alpha\alpha}}\right)_0 dv_1,\end{aligned} \tag{35}$$

Here $\Delta U_{ai}^{\alpha\alpha}$ is the change in $U_{ai}^{\alpha\alpha}$ in going from $U_{ai}^{0,\alpha\alpha}$ and $\Delta\rho^\alpha$ is the corresponding change in ρ^α. The subscript "0" in (35) indicates that the derivatives are evaluated at $U_{ai}^{\alpha\alpha}=U_{ai}^{0,\alpha\alpha}$. The calculation of $\overrightarrow{g}_{ai}^{\alpha,e}\left(U^{0,\alpha\alpha}\right)$ in (35) requires closed form expressions for $d\Delta\rho^\alpha/d\Delta U_{ai}^{\alpha\alpha}$ (see footnote 6).[7]

2.4.2 Optimization of U in SCF-CV(∞)-DFT

With the evaluation of $\overrightarrow{g}_{ai}^{\alpha,e}\left(\mathbf{U}^{0,\alpha\alpha}\right)$ we can now begin an iterative process from $\mathbf{U}^{0,\alpha\alpha}$ generated by $\overrightarrow{U}_{(2)}^{(I)}$ to the optimal $\mathbf{U}^{\alpha\alpha}$ matrix where $\Delta U^{\alpha\alpha}=0$. A differentiation of (35) by $\Delta\mathbf{U}^{\alpha\alpha}$ affords

$$\overrightarrow{g}^{e,\alpha}\left(\mathbf{U}^{0,\alpha\alpha}\right)+\mathbf{H}^{\alpha\alpha}\left(\mathbf{U}^{0,\alpha\alpha}\right)\Delta\mathbf{U}^{\alpha\alpha}=0 \tag{36}$$

from which we can find the next $\mathbf{U}^{\alpha\alpha}$. In the initial steps where $\left|\overrightarrow{\Delta U}^{\alpha\alpha}\right| \gg \delta_{\mathrm{tresh1}}$ the Hessian is calculated approximately by assuming that $\mathbf{H}^{\alpha\alpha}\left(\mathbf{U}^{0,\alpha\alpha}\right)=\varepsilon^D$ with $\left(\varepsilon^D\right)_{ai,bj}=\delta_{ij}\delta_{ab}(\varepsilon_a-\varepsilon_i)$. Here ε_i, ε_a are the energies of the occupied and virtual ground state orbitals, respectively. We thus get for each new step

$$\overrightarrow{\Delta U}^{\alpha\alpha}=\left(\varepsilon^D\right)^{-1}\overrightarrow{g}^{e,\sigma}\left(\mathbf{U}^{0,\alpha\alpha}\right) \tag{37}$$

If $\sum_j^{\mathrm{occ}/2}\sin^2\left[\eta^\alpha\gamma_j^\alpha\right]$ resulting from $\widetilde{\mathbf{U}}^{0,\alpha\alpha}=\mathbf{U}^{0,\alpha\alpha}+\Delta\mathbf{U}^{\alpha\alpha}$ does not satisfy (32b), we introduce a new η^α scaling so that $\sum_j^{\mathrm{occ}/2}\sin^2\left[\eta^\alpha\gamma_j^\alpha\right]$ constructed from $\widehat{\mathbf{U}}^{0,\alpha\alpha}=\eta^\alpha\widetilde{\mathbf{U}}^{0,\alpha\alpha}$ satisfies (32b). After that we finally ensure that $^{0,\alpha\alpha}$ satisfies $Tr\left(\widehat{U}^{0,\alpha\alpha}U^{K,\alpha\alpha}\right)=0$ for the excited states $K=1,\mathrm{I}-1$ which are below the excited state I for which we are optimizing $\mathbf{U}$. This is done by introducing the projection

$$\mathbf{U}^{0,\alpha\alpha}=\widehat{\mathbf{U}}^{0,\alpha\alpha}-\sum_{k=1}^{I-1}U^{K,\alpha\alpha}Tr\left(\mathbf{U}^{K,\alpha\alpha+}\widehat{\mathbf{U}}^{0,\alpha\alpha}\right)/Tr\left(\mathbf{U}^{K,\alpha\alpha+}\mathbf{U}^{K,\alpha\alpha}\right) \tag{38}$$

[7] See Sect. 3.0 from part S2 of supporting information in Ziegler et al. [27].

After that, we go back to (37) for a new step with $\mathbf{U}^{0,\alpha\alpha}$ defined in (38). When $\delta_{\text{tresh1}} \geq \left|\Delta\vec{U}^{\alpha\alpha}\right| \gg \delta_{\text{tresh2}}$, the iterative procedure is resumed by the help of the conjugated gradient technique described by Pople et al. [81]. It is not required in this procedure explicitly to know the Hessian. Instead, use is made of the fact that

$$\mathbf{H}^{\alpha\alpha}\left(\mathbf{U}^{0,\alpha\alpha}\right)\Delta\mathbf{U}^{\alpha\alpha} = \vec{g}^{e,\alpha}\left(\mathbf{U}^{0,\alpha\alpha} + \Delta\mathbf{U}\right) - \vec{g}^{e,\alpha}\left(\mathbf{U}^{0,\alpha\alpha}\right) + O^{[3]}(\Delta\mathbf{U}) \tag{39}$$

The value for δ_{tresh1} is typically 10^{-2} whereas $\delta_{\text{tresh2}} = 10^{-4}$. Convergence is obtained when the threshold δ_{tresh2} is reached. Typically 20–30 iterations are required to reach δ_{tresh1} and 5–10 to reach δ_{tresh2}. We have also attempted more advanced Hessians for the first part of the optimization, such as the one suggested by Fletcher [82] and implemented by Fischer and Almlöf [83]. However, it was found to be less robust than the simple procedure in (37). The optimization procedure outlined here for spin-conserving transitions can readily be formulated for spin-flip transitions [27].

2.4.3 Application of SCF-CV(∞)-DFT

We have applied SCF-CV(∞)-DFT to a number of $n_\sigma \rightarrow \pi^*$ transitions [63] where an electron is moved from an occupied lone-pair orbital n_σ to a virtual π^* orbital in the sample of molecules shown in Fig. 5. We present the results in Table. 4. For the sample of $n_\sigma \rightarrow \pi^*$ transitions studied here it can be seen that the perturbative P-CV (∞)-DFT approach with an RMSD of 1.14 eV is inadequate and one would hope that a full optimization of **U** would improve the RMSD. In fact, applying SCF-CV (∞) with complete optimization of **U** drops the RMSD to 0.50 eV, which is still poorer than CV(2)-TD (TDDFT-TD) with RMSD = 0.33 eV. At this point it is important to note that all the excitations in Table 4 can be represented by a single orbital replacement $n_\sigma \rightarrow \pi^*$. However, in going from P-CV(∞)-DFT to SCF-CV (∞) the π^* orbital is modified, leading to a lowering of the excitation energy and a reduction of RMSD.

On the other hand, all the other orbitals remain in P-CV(∞)-DFT and SCF-CV (∞) "frozen" as they are in the ground state. That this is a severe approximation can be seen from the ΔSCF results in Table 4 where RMSD = 0.32 eV. In the ΔSCF scheme we optimize not only n_σ and π^* but also all other occupied orbitals in the excited state with respect to the $(n_\sigma)^1(\pi^*)^1$ configuration. It is thus obvious that we must carry out a similar relaxation. This is done next in our SCF-CV(∞)-DFT scheme where we introduce full orbital relaxation on top of optimizing **U** (SCF-CV (∞)-DFT.

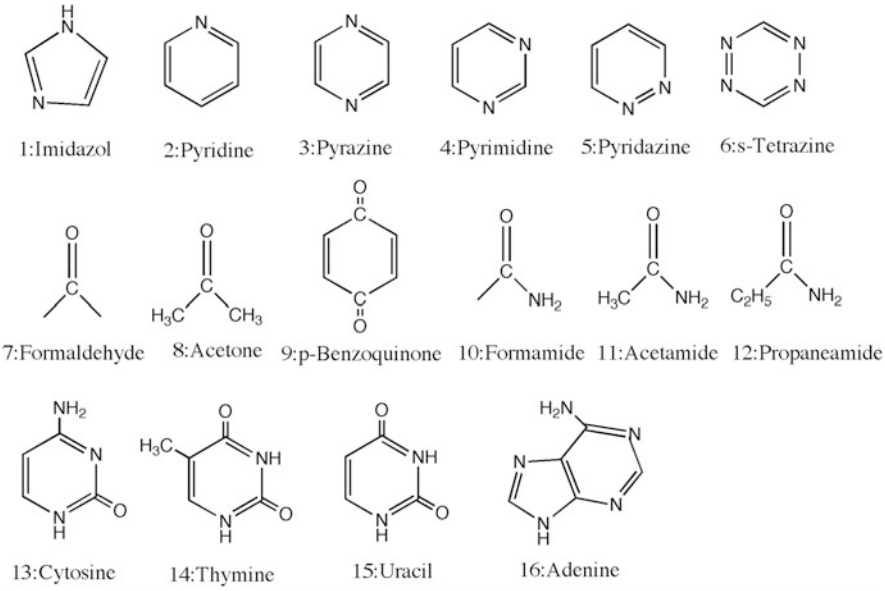

Fig. 5 Sample of molecules used in the study of $n_\sigma \rightarrow \pi^*$ transitions [26]

2.5 *Self-Consistent All Order Constricted Variational Density Functional Theory with Orbital Relaxation*

In the description of the excited state by the SCF-CV(∞)-DFT scheme all occupied β-orbitals are unchanged (frozen) from the ground state and the same is the case for a number of α-orbitals which do not directly participate in the transition. Thus in the case of the $n_\sigma \rightarrow \pi^*$ transitions, all α-orbitals other than n_σ, π^* are frozen. To remedy this, we allow in the RSCF-CV(∞)-DFT [26] scheme for a relaxation to second order in the mixing matrix $R^{\sigma\sigma}(\sigma = \alpha, \beta)$ of all occupied orbitals in the excited state [26]. Thus,

$$\psi_i^\sigma(1) \rightarrow \phi_i^\sigma(1) + \sum_c^{\mathrm{vir}/2} R_{ci}^{\sigma\sigma}\phi_c^\sigma(1) - \frac{1}{2}\sum_c^{\mathrm{vir}/2}\sum_k^{\mathrm{occ}/2} R_{ci}^{\sigma\sigma}R_{ck}^{\sigma\sigma}\phi_k^\sigma(1) + O^{(3)}[R^\sigma] \qquad (40a)$$

$$\psi_a^\sigma(1) \rightarrow \phi_a^\sigma(1) - \sum_k^{\mathrm{vir}/2} R_{ak}^{\sigma\sigma}\phi_k^\sigma(1) - \frac{1}{2}\sum_c^{\mathrm{vir}/2}\sum_k^{\mathrm{occ}/2} R_{ak}^{\sigma\sigma}R_{ck}^{\sigma\sigma}\phi_c^\sigma(1) + O^{(3)}[R^{\sigma\sigma}] \qquad (40b)$$

Replacing in (2a) the matrix $\tilde{\mathbf{U}}$ which combines occupied and virtual orbitals of the unrelaxed set $\{\phi_q; q = 1, \mathrm{occ} + \mathrm{vir}\}$ with the corresponding matrix U which mixes the occupied and virtual orbitals of the relaxed basis $\{\psi_q; q = 1, \mathrm{occ} + \mathrm{vir}\}$ leads to the unitary transformation

Table 4 Vertical singlet excitation energies[a] in $n \rightarrow \pi^*$ transitions based on B3LYP

Molecule	State	Best[b]	CV(2)[c]	P-CV(∞)[c]	SCF-CV(∞)	RSCF-CV(∞)	ΔSCF
1	A″	6.81	5.38	6.80	6.86	5.86	5.76
2	B_1	4.59	4.92	6.01	5.34	4.91	4.69
	A_2	5.11	5.17	7.20	6.26	5.10	5.15
3	B_{3u}	3.95	4.09	4.08	3.99	3.88	3.85
	A_u	4.81	4.74	5.49	5.30	4.52	4.63
	B_{2g}	5.56	5.67	5.92	5.81	5.56	5.48
	B_{1g}	6.6	6.40	7.92	7.78	6.20	6.38
4	B_1	4.55	4.37	4.94	4.72	4.19	4.14
	A_2	4.91	4.68	5.50	5.29	4.46	4.54
5	B_1	3.78	3.74	4.50	3.99	3.64	3.55
	A_2	4.31	4.26	5.75	5.29	3.96	4.15
	A_2	5.77	5.55	5.93	5.67	5.44	5.35
6	B_{3u}	2.29	2.41	2.43	2.30	2.11	2.15
	A_u	3.51	3.59	4.13	4.02	3.38	3.48
	B_{1g}	4.73	4.88	4.89	4.73	4.53	4.56
	A_u	5.5	5.20	5.22	5.16	4.92	4.96
	B_{2g}	5.2	5.40	5.34	5.31	5.16	5.17
7	A_2	3.88	3.93	4.53	4.30	3.53	3.52
8	A_2	4.4	4.41	5.19	4.84	4.01	4.02
9	B_{1g}	2.76	2.54	2.78	2.62	2.52	2.40
	A_u	2.77	2.69	3.15	2.97	2.72	2.55
	B_{3u}	5.64	5.47	6.82	6.18	5.40	5.40
10	A″	5.63	5.58	6.85	6.42	5.32	5.28
11	A″	5.69	5.59	6.94	6.43	5.33	5.31
12	A″	5.72	5.60	6.94	6.37	5.33	5.34
13	A″	4.87	4.78	7.56	5.90	4.92	4.83
	A″	5.26	5.17	7.32	6.43	5.58	–[d]
14	A″	4.82	4.74	6.75	5.73	4.78	4.59
	A″	6.16	5.63	6.66	6.64	5.96	5.82
15	A″	4.80	4.66	6.83	5.74	4.75	4.54
	A″	6.10	5.75	8.03	6.75	5.84	6.07
	A″	6.56	5.85	6.88	6.76	6.15	–[d]
16	A″	5.12	5.01	5.86	5.52	4.85	4.91
	A″	5.75	5.49	6.66	6.02	5.80	5.63
	RMSD		0.33	1.14	0.50	0.32	0.32

[a]Energies in eV
[b]Theoretical best estimates are from Schreiber et al. [73]
[c]Tamm-Dancoff approximation [70]
[d]Did not converge

$$Y\begin{pmatrix}\psi_{\text{occ}}\\ \psi_{\text{vir}}\end{pmatrix}=\mathrm{e}^{U}\begin{pmatrix}\psi_{\text{occ}}\\ \psi_{\text{vir}}\end{pmatrix}=\left(\sum_{m=0}^{\infty}\frac{U^m}{m!}\right)\begin{pmatrix}\psi_{\text{occ}}\\ \psi_{\text{vir}}\end{pmatrix}=\begin{pmatrix}\psi'_{\text{occ}}\\ \psi'_{\text{vir}}\end{pmatrix} \tag{41}$$

in which the sets of relaxed occupied $\{\psi_i; i=1,\text{occ}\}$ and virtual $\{\psi_a; a=1,\text{vir}\}$ ground state (reference) KS-orbitals are converted into the resulting sets $\{\psi'_i; i=1,\text{occ}\}$ and $\{\psi'_a; a=1,\text{vir}\}$ of relaxed occupied and virtual excited state orbitals, respectively. It should be noted that the relaxed orbital set is orthonormal to second order in **R**.

We now obtain for a spin conserving transition the excited state KS determinant which can be written as

$$\Psi_M=\left|\psi'_1\psi'_1\ldots\psi'_i\psi'_j\ldots\psi'_n\right| \tag{42}$$

The corresponding change in density $\Delta\rho_M$ expanded in terms of the unrelaxed ground state orbitals takes the form

$$\Delta\rho_M=\Delta\rho_M(U^{\alpha\alpha})+\Delta\rho_M^R \tag{43}$$

where

$$\begin{aligned}\Delta\rho_M(\mathbf{U}^{\alpha\alpha})=&\sum_{a}^{\text{vir}(\alpha)}\sum_{i}^{\text{occ}(\alpha)}\Delta P_{ai}(\mathbf{U}^{\alpha\alpha})\left[\phi_a^{\alpha}(1')\phi_i^{\alpha}(1)+\phi_a^{\alpha}(1')\phi_i^{\alpha}(1)\right]\\&+\sum_{ab}^{\text{vir}(\alpha)}\Delta P_{ab}(\mathbf{U}^{\alpha\alpha})\phi_a^{\alpha}(1')\phi_b^{\alpha}(1)+\sum_{ij}^{\text{occ}(\alpha)}\Delta P_{ij}(\mathbf{U}^{\alpha\alpha})\phi_i^{\alpha}(1')\phi_j^{\alpha}(1)\end{aligned} \tag{44}$$

is the change in density caused by $\mathbf{U}^{\alpha\alpha}$ alone and equivalent to (32a) but expressed in terms of unrelaxed ground state orbitals. On the other hand

$$\begin{aligned}\Delta\rho_M^R=&\sum_{\sigma}^{\alpha,\beta}\sum_{a}^{\text{vir}(\sigma)}\sum_{i}^{\text{occ}(\sigma)}T_{ai}^{(1)\sigma\sigma}\left[\phi_a^{\alpha}(1')\phi_i^{\alpha}(1)+\phi_a^{\alpha}(1')\phi_i^{\alpha}(1)\right]\\&+\sum_{ab}^{\text{vir}(\sigma)}T_{ab}^{(2)\sigma\sigma}\phi_a^{\sigma}(1')\phi_b^{\sigma}(1)+\sum_{ij}^{\text{occ}(\sigma)}T_{ij}^{(2)\sigma\sigma}\phi_i^{\sigma}(1')\phi_j^{\sigma}(1)\end{aligned} \tag{45}$$

is the change in density caused by the relaxation. Here

$$T_{ai}^{(1)\alpha\alpha}=R_{ai}^{\alpha\alpha}+\sum_{j}^{\text{occ}(\alpha)}\Delta P_{ij}^{\alpha\alpha}R_{aj}^{\alpha\alpha};\quad T_{ai}^{(1)\beta\beta}=R_{ai}^{\beta\beta} \tag{46a}$$

$$
\begin{aligned}
T^{(2)\alpha\alpha}_{ab} &= \sum_{i}^{\mathrm{occ}(\alpha)} R^{\alpha\alpha}_{ai} R^{\alpha\alpha}_{bi} + \sum_{i}^{\mathrm{occ}(\alpha)} \sum_{j}^{\mathrm{occ}(\alpha)} \Delta P^{\alpha\alpha}_{ij}(U^{\alpha\alpha}) R^{\alpha\alpha}_{ai} R^{\alpha\alpha}_{bj} \\
T^{(2)\beta\beta}_{ab} &= \sum_{a}^{\mathrm{vir}(\beta)} R^{\beta\beta}_{ai} R^{\beta\beta}_{bi}
\end{aligned}
\tag{46b}
$$

$$
\begin{aligned}
T^{(2)\alpha\alpha}_{ij} &= \sum_{a}^{\mathrm{vir}(\alpha)} R^{\alpha\alpha}_{ai} R^{\alpha\alpha}_{aj} - \sum_{l}^{\mathrm{occ}(\alpha)} \sum_{a}^{\mathrm{vir}(\alpha)} \Delta P^{\alpha\alpha}_{il}(\mathbf{U}^{\alpha\alpha}) R^{\alpha\alpha}_{al} R^{\alpha\alpha}_{aj} \\
T^{(2)\beta\beta}_{ij} &= -\sum_{i}^{\mathrm{vir}(\beta)} R^{\beta\beta}_{ai} R^{\beta\beta}_{aj}
\end{aligned}
\tag{46c}
$$

We obtain for the excitation energy

$$
\Delta E_M = \Delta E_M(U^{\alpha\alpha}) + \Delta E^R_M \tag{47}
$$

where

$$
\begin{aligned}
\Delta E_M(\mathbf{U}) = & \sum_{a}^{\mathrm{vir}(\alpha)} \varepsilon^{\alpha}_{a} \Delta P^{\alpha\alpha}_{aa}(\mathbf{U}^{\alpha\alpha})^2 - \sum_{i}^{\mathrm{occ}(\alpha)} - \varepsilon^{\alpha}_{i} \Delta P^{\alpha\alpha}_{ii}(\mathbf{U}^{\alpha\alpha})^2 \\
& + \sum_{ab}^{\mathrm{vir}(\alpha)} \sum_{i}^{\mathrm{occ}(\alpha)} \Delta P^{\alpha\alpha}_{ai}(\mathbf{U}^{\alpha\alpha}) \Delta P^{\alpha\alpha}_{bj}(\mathbf{U}^{\alpha\alpha}) \left[K_{a_\alpha i_\alpha b_\alpha j_\alpha} + K_{a_\alpha i_\alpha b_\alpha j_\alpha} \right] \\
& + \frac{1}{2} \sum_{ijkl}^{\mathrm{occ}(\alpha)} \Delta P^{\alpha\alpha}_{ij}(\mathbf{U}^{\alpha\alpha}) \Delta P^{\alpha\alpha}_{kl}(\mathbf{U}^{\alpha\alpha}) K_{i_\alpha j_\alpha k_\alpha l_\alpha} \\
& + \frac{1}{2} \sum_{abcd}^{\mathrm{vir}} \Delta P^{\alpha\alpha}_{ab}(\mathbf{U}^{\alpha\alpha}) \Delta P^{\alpha\alpha}_{cd}(\mathbf{U}^{\alpha\alpha}) K_{a_\alpha b_\alpha c_\alpha d_\alpha} \\
& + \sum_{ab}^{\mathrm{vir}(\alpha)} \sum_{ij}^{\mathrm{occ}(\alpha)} \Delta P^{\alpha\alpha}_{ab}(\mathbf{U}^{\alpha\alpha}) \Delta P^{\alpha\alpha}_{ij}(\mathbf{U}^{\alpha\alpha}) K_{a_\alpha b_\alpha i_\alpha j_\alpha} \\
& + 2 \sum_{abc}^{\mathrm{vir}(\alpha)} \sum_{k}^{\mathrm{occ}(\alpha)} \Delta P^{\alpha\alpha}_{ab}(\mathbf{U}^{\alpha\alpha}) \Delta P^{\alpha\alpha}_{ck}(\mathbf{U}^{\alpha\alpha}) K_{a_\alpha b_\alpha c_\alpha k_\alpha} \\
& + 2 \sum_{ijk}^{\mathrm{vir}(\alpha)} \sum_{c}^{\mathrm{occ}(\alpha)} \Delta P^{\alpha\alpha}_{ij}(\mathbf{U}^{\alpha\alpha}) \Delta P^{\alpha\alpha}_{ck}(\mathbf{U}^{\alpha\alpha}) K_{i_\alpha j_\alpha c_\alpha k_\alpha}
\end{aligned}
\tag{48}
$$

is the excitation caused by $\mathbf{U}^{\alpha\alpha}$ alone and equivalent to ΔE_M for the SCF-CV(∞)-DFT scheme of (28) but expressed in terms of canonical and unrelaxed ground state orbitals. Further

$$\Delta E_M^R = \sum_{\sigma}^{\alpha,\beta}\left(\sum_{a}^{\mathrm{vir}(\sigma)} T_{aa}^{(2)\sigma\sigma}\varepsilon_a^{\sigma} - \sum_{i}^{\mathrm{vir}(\sigma)} T_{ii}^{(2)\sigma\sigma}\varepsilon_i^{\sigma}\right)$$
$$+ \sum_{\sigma}^{\alpha,\beta}\sum_{\mu}^{\alpha,\beta}\sum_{a}^{\mathrm{vir}(\sigma)}\sum_{i}^{\mathrm{occ}(\sigma)}\sum_{c}^{\mathrm{vir}(\mu)} T_{ai}^{(1)\sigma\sigma}T_{bj}^{(1)\mu\mu}\left[K_{a_\sigma i_\sigma b_\mu j_\mu} + K_{a_\sigma b_\mu i_\sigma j_\mu}\right]$$
$$+ \sum_{\sigma}^{\alpha,\beta}\sum_{k}^{\mathrm{occ}(\sigma)}\sum_{c}^{\mathrm{vir}(\sigma)} T_{ck}^{(1)\sigma\sigma}\left[\sum_{ab}^{\mathrm{vir}(\alpha)} \Delta P_{ab}^{\alpha\alpha}(\mathbf{U}^{\alpha\alpha})K_{a_\alpha b_\alpha c_\sigma k_\sigma} + \sum_{ij}^{\mathrm{occ}(\alpha)} \Delta P_{ij}^{\alpha\alpha}(\mathbf{U}^{\alpha\alpha})K_{i_\alpha j_\alpha c_\sigma k_\sigma}\right] \tag{49}$$

is the relaxation contribution to the excitation energy. The total energy for Ψ_M is given as $E_M = E_0(\rho^0) + \Delta E_M(\mathbf{U}) + \Delta E_M^R$ where $E_0(\rho^0)$ is the ground state energy expressed in terms of unrelaxed orbitals. The expression for ΔE_M^R is derived after orthogonalization of Ψ_M to the ground state to second order in $\mathbf{R}$.

We optimize ΔE_M of (49) by first performing a Taylor expansion from the starting point reference $(\mathbf{U}^{0,\alpha\alpha}, \mathbf{R}^{0,\alpha\alpha}, \mathbf{R}^{0,\beta\beta})$ to $\left(\mathbf{U}^{\alpha\alpha}, \mathbf{R}^{\alpha\alpha}, \mathbf{R}^{\beta\beta}\right) = \left(\mathbf{U}^{0,\alpha\alpha} + \Delta\mathbf{U}^{\alpha\alpha}, \mathbf{R}^{0,\alpha\alpha} + \Delta\mathbf{R}^{\alpha\alpha}, \mathbf{R}^{0,\beta\beta} + \Delta\mathbf{R}^{\alpha\alpha}\right)$:

$$E_M\left(U^{\alpha\alpha},R^{\alpha\alpha},R^{\beta\beta}\right) = E_M\left(U^{0,\alpha\alpha},R^{0,\alpha\alpha},R^{0,\beta\beta}\right)$$
$$+\sum_{ai}\left(\frac{dE_M}{dU_{ai}^{\alpha\alpha}}\right)_0 \Delta U_{ai}^{\alpha\alpha} + \sum_{\sigma}^{\alpha,\beta}\sum_{ai}\left(\frac{dE_M}{dR_{ai}^{\sigma\sigma}}\right)_0 \Delta R_{ai}^{\sigma\sigma} + \frac{1}{2}\sum_{ai}\sum_{bj}\left(\frac{d^2E_M}{dU_{ai}^{\alpha\alpha}dU_{bj}^{\alpha\alpha}}\right)_0 \Delta U_{ai}^{\alpha\alpha}\Delta U_{bj}^{\alpha\alpha}$$
$$+\frac{1}{2}\sum_{ai}\sum_{bj}\sum_{\sigma}^{\alpha,\beta}\sum_{\tau}^{\alpha,\beta}\left(\frac{d^2E_M}{dR_{ai}^{\sigma\sigma}dR_{bj}^{\tau\tau}}\right)_0 \Delta R_{ai}^{\sigma\sigma}\Delta R_{bj}^{\tau\tau} + \sum_{ai}\sum_{bj}\sum_{\sigma}^{\alpha,\beta}\left(\frac{d^2E_M}{dU_{ai}^{\alpha\alpha}dR_{bj}^{\sigma\sigma}}\right)_0 \Delta U_{ai}^{\alpha\alpha}\Delta R_{bj}^{\sigma\sigma}$$
$$+\mathrm{O}^{[3]} \tag{50}$$

Here the subscript "0" indicates that the derivative is evaluated at the reference $(U^{0,\alpha\alpha},R^{0,\alpha\alpha},R^{0,\beta\beta})$. We can alternatively write the expansion in terms of energy gradients and energy Hessians as

$$E_M\left(U^{\alpha\alpha},R^{\alpha\alpha},R^{\beta\beta}\right) = E_M\left(U^{0,\alpha\alpha},R^{0,\alpha\alpha},R^{0,\beta\beta}\right) + \begin{pmatrix}\Delta\vec{U}^{\alpha\alpha} & \Delta\vec{R}^{\alpha\alpha} & \Delta\vec{R}^{\beta\beta}\end{pmatrix}\begin{pmatrix}\vec{g}^{U^{\alpha\alpha}}\\ \vec{g}^{R^{\alpha\alpha}}\\ \vec{g}^{R^{\beta\beta}}\end{pmatrix}$$
$$+\frac{1}{2}\begin{pmatrix}\Delta\vec{U}^{\alpha\alpha} & \Delta\vec{U}^{\alpha\alpha} & \Delta\vec{U}^{\alpha\alpha}\end{pmatrix}\begin{pmatrix}\mathbf{H}^{U^{\alpha\alpha},U^{\alpha\alpha}} & \mathbf{H}^{U^{\alpha\alpha},R^{\alpha\alpha}} & \mathbf{H}^{U^{\alpha\alpha},R^{\beta\beta}}\\ \mathbf{H}^{R^{\alpha\alpha},U^{\alpha\alpha}} & \mathbf{H}^{R^{\alpha\alpha},R^{\alpha\alpha}} & \mathbf{H}^{R^{\alpha\alpha},R^{\beta\beta}}\\ \mathbf{H}^{R^{\beta\beta},U^{\alpha\alpha}} & \mathbf{H}^{R^{\beta\beta},R^{\alpha\alpha}} & \mathbf{H}^{R^{\beta\beta},R^{\beta\beta}}\end{pmatrix}\begin{pmatrix}\mathbf{H}^{R^{\beta\beta},R^{\beta\beta}}\\ \Delta\vec{R}^{\alpha\alpha}\\ \Delta\vec{R}^{\beta\beta}\end{pmatrix} + O^{[3]} \tag{51}$$

where the expressions for the gradients $\vec{g}^{U^{\alpha\alpha}}, \vec{g}^{R^{\alpha\alpha}}, \vec{g}^{R^{\beta\beta}}$ and Hessians $\mathbf{H}^{U^{\alpha\alpha},U^{\alpha\alpha}}$, $H^{R^{\alpha\alpha},U^{\alpha\alpha}}$, etc. can be obtained by a comparison between (50) and (51). Specific

formula for $\vec{g}^{U^{\alpha\alpha}}$, $\vec{g}^{R^{\alpha\alpha}}$, and $\vec{g}^{R^{\beta\beta}}$ are also given in [26] for the spin-flip transition.

For the spin conserving transition, a differentiation of (51) with respect to the individual components of $\Delta\vec{U}^{\alpha\alpha}$, $\Delta\vec{R}^{\alpha\alpha}$, and $\Delta\vec{R}^{\beta\beta}$ affords, after rearrangement,

$$\begin{pmatrix} \vec{g}^{U^{\alpha\alpha}}(0) \\ \vec{g}^{R^{\alpha\alpha}}(0) \\ \vec{g}^{R^{\beta\beta}}(0) \end{pmatrix} + \begin{pmatrix} \mathbf{H}^{U^{\alpha\alpha},U^{\alpha\alpha}}(0) & \mathbf{H}^{U^{\alpha\alpha},R^{\alpha\alpha}}(0) & \mathbf{H}^{U^{\alpha\alpha},R^{\beta\beta}}(0) \\ \mathbf{H}^{R^{\alpha\alpha},U^{\alpha\alpha}}(0) & \mathbf{H}^{R^{\alpha\alpha},R^{\alpha\alpha}}(0) & \mathbf{H}^{R^{\alpha\alpha},R^{\beta\beta}}(0) \\ \mathbf{H}^{R^{\beta\beta},U^{\alpha\alpha}}(0) & \mathbf{H}^{R^{\beta\beta},R^{\alpha\alpha}}(0) & \mathbf{H}^{R^{\beta\beta},R^{\beta\beta}}(0) \end{pmatrix} \begin{pmatrix} \Delta\vec{U}^{\alpha\alpha} \\ \Delta\vec{R}^{\alpha\alpha} \\ \Delta\vec{R}^{\beta\beta} \end{pmatrix} = 0 \quad (52)$$

from which we can find $\left(\Delta\vec{U}^{\alpha\alpha}, \Delta\vec{R}^{\alpha\alpha}, \Delta\vec{R}^{\beta\beta}\right)$ iteratively. More details can be found in [26] which also covers the case of spin-flip transitions.

2.5.1 Application of RSCF-CV(∞)-DFT to $n_\sigma \rightarrow \pi^*$ Transitions

It follows from Table 4 that the RSCF-CV(∞)-DFT scheme with full orbital relaxation gives $n_\sigma \rightarrow \pi^*$ transition energies which on average are within 0.15 eV of the ΔSCF results. This is acceptable given the fact that the RSCF-CV(∞)-DFT scheme is only second order in relaxation and that it satisfies constraints not fulfilled by ΔSCF. In comparison to the "Best" ab initio results [73], RSCF-CV (∞)-DFT fares as well as ΔSCF and CV(2)-TD (TDDFT-TD) with an RMSD of 0.32 eV. Thus, although RSCF-CV(∞)-DFT is somewhat more costly (~twice) for each transition, it does not fare much better than CV(2)-TD in those cases where the latter is reliable and fares well. However, what we show shortly is that RSCF-CV (∞)-DFT has a similar accuracy (RMSD ~0.3–0.2 eV) where CV(2)-TD fails such as Rydberg and charge transfer transitions.

2.5.2 Application of RSCF-CV(∞)-DFT to Rydberg Transitions

We have benchmarked [66] the performance of RSCF-CV-DFT in studies on Rydberg transitions employing five different standard functionals and a diffuse basis; see Table 5. Our survey is based on 71 triplet or singlet Rydberg transitions distributed over 9 different species: N_2(5), CO (7), CH_2O (8), C_2H_2 (8), H_2O (10), C_2H_4 (13), Be (6), Mg (6), and Zn (8). The best performance comes from the long range corrected functional LCBP86 ($\omega = 0.4$.) with an average root mean square deviation (RMSD) of 0.23 eV. Of similar accuracy are LDA and B3LYP, both with an RMSD of 0.24 eV. The largest RMSD of 0.32 eV come from BP86 and LCBP86* ($\omega = 0.75$). The performance of RSCF-CV-DFT is considerably better than that of adiabatic time-dependent density functional theory (ATDDFT) and matches that of highly optimized long range corrected functionals. However, it is not as accurate as ATDDFT based on highly specialized functionals.

Table 5 Root mean square deviations of Rydberg excitation energies[a] calculated with RSCF-CV (∞)-DFT using five functionals with the extended basis set [66]

Species	Nr. of States	Functionals				
		LDA	BP86	B3LYP	LCBP86[b]	LCBP86*[c]
N_2	5	0.27	0.34	0.05	0.23	0.62
CO	7	0.22	0.43	0.13	0.12	0.37
CH_2O	8	0.21	0.28	0.12	0.20	0.34
C_2H_2	8	0.31	0.50	0.52	0.25	0.24
H_2O	10	0.27	0.17	0.14	0.21	0.24
C_2H_4	13	0.15	0.20	0.28[d]	0.28	0.29
Be	6	0.45	0.60	0.47	0.31	0.23
Mg	6	0.18	0.35	0.19	0.13	0.12
Zn	8	0.18	0.25	0.27	0.34	0.46
Average root mean square deviation		0.24	0.32	0.24	0.23	0.32

[a]Energies in eV
[b]Refers to LC functional combined with BP86 and $\omega = 0.4$
[c]Represents LC functional combined with BP86 and $\omega = 0.75$
[d]Comprised of 12 states

The reasonable success of RSCF-CV-DFT is based on its well documented ability to afford good estimates of ionization potentials (IP) and electron affinities (EA) even for simple local functionals after orbital relaxation has been taken into account [66]. In adiabatic time-dependent density functional theory (ATDDFT) based on regular functionals, both IP and -EA are poorly described with errors of up to 5 eV [66]. In the transition energy ($\Delta E = \text{IP} - \text{EA}$) these errors are cancelled to some degree. However, ΔE still carries an error exceeding 1 eV [66].

2.5.3 Application of RSCF-CV(∞)-DFT to Charge Transfer Transitions

It has been demonstrated that regular adiabatic TDDFT employing the general gradient approximation (GGA) as well as hybrid functionals with a fraction (α) of exact Hartree–Fock exchange included $(0.0 \leq \alpha \leq 0.5)$ underestimate charge transfer excitation energies by as much as 2–4 eV [24, 25, 33]. This failure has been discussed and analyzed extensively [24, 25, 32, 33]. By contrast, ATDDFT in conjunction with long range corrected (LC) functionals affords charge transfer excitation energies in good agreement with experiment [33]. In these functionals, Hartree–Fock exchange is given a growing weight towards longer inter-electronic distances.

We have recently [30] applied the RSCF-CV(∞)-DFT scheme to a series of charge transfer molecular complexes (CTMC) of the type X-TCNE where an aromatic molecule (X = benzene, toluene, *o*-xylene, naphthalene, anthracene) is bound to tetracyanoethylene (TCNE) [33]. All of these complexes have one or more distinct charge transfer transitions involving the excitation of an electron from an

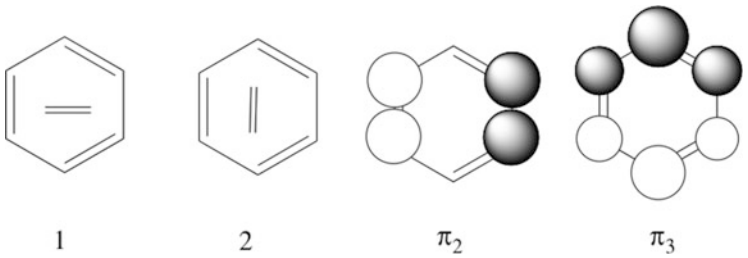

Fig. 6 Conformations and frontier orbitals in the benzene-TCNE adduct

occupied π-orbital on X to the empty π-orbital on TCNE. The X-TCNE complexes were first introduced by Stein et al. [33] as a benchmark set for CT-transitions in connection with their study on the performance of LC functionals.

The charge transfer spectrum for the series of adducts X-TCNE (X=benzene, toluene, *o*-xylene, and naphthalene, TCNE=tetracyanoethylene) has been studied extensively by experimental [84–88] and computational techniques [32, 89]. The experimental investigations include both gas phase [88] and solvation studies [85, 86] whereas the computational examinations have made use of high level ab initio schemes [89] and methods based on density functional theory [24, 25, 32, 33].

The simple adduct between benzene and TCNE has in the ground state two conformational minima of C_{2V} symmetry given as **1** and **2** in Fig. 6. The minima are calculated in both gas phase and solution to be separated by at most 0.7 kcal. Each conformation gives rise to one allowed and one forbidden transition. These transitions are to the same π^* LUMO orbital of TCNE but originate from two different HOMO orbitals on benzene; see π_2 and π_3 of Fig. 6. The four calculated transitions from π_2 and π_3 in **1** and **2** differ by less than 0.05 eV.

It is thus not surprising that the experimental spectrum in both gas phase and solution exhibits one (broad) CT-band at room temperature. The CT spectrum in gas phase has a halfwidth of 0.8 eV and a maximum at 3.59 eV [88]. This maximum is in a dichloromethane solution shifted to 3.25 eV. We exhibit in Table 6 [30] the calculated CT-excitation energies for CV(2)-DFT, CV(∞)-DFT, SCF-CV(∞)-DFT, and RSCF-CV(∞)-DFT using LDA, BP86, B3LYP, BHLYP, LCBP86, and HF.

We note in Table 6 for CV(2)-TD (ATDDFT-TD) that local functionals underestimate the experimental charge transfer excitation energy (3.59 eV [88]). The calculated excitation energies are still too low for the hybrids B3LYP and BHLYP, whereas the long range corrected functional LC-BP86 is now within 0.1 eV of experiment. For the perturbative P-CV(∞) approach, calculated ΔE_S values in Table 6 are in general seen to be higher than the observed excitation energy by more than 1 eV. This is understandable because the "excited state" determinants in P-CV(∞) are constructed from U vectors optimized with respect to CV(2)-TD. Further, all relaxation is neglected. In the SCF-CV(∞)-DFT scheme the excited state energy is minimized with respect to U while relaxation is still neglected. This leads to some improvement. However, the best results are obtained with RSCF-CV

Table 6 Calculated excitation energies[a] for benzene-TCNE[f]

	CV(2)-TD[b]	P-CV(∞)[c]	SCF-CV (∞)[d]	RSCF-CV (∞)[e]
LDA	1.40	4.99	3.64	3.30
BP86	1.37	4.92	3.69	3.32
B3LYP	1.85	4.89	4.38	3.56
BHLYP	2.75	4.80	4.76	3.31
LC-BP86	3.74	4.92	4.69	3.10
HF	4.70	4.72	4.53	2.85

[a]Energies in eV
[b]Second order energies identical to adiabatic TD-DFT within the Tamm–Dancoff approximation
[c]Energies to all orders in U. Matrix U taken from CV(2)
[d]Energies to all orders in U. Matrix U optimized with respect to the SCF-CV(∞) energy expression
[e]SCF-CV(∞) with orbital relaxation
[f]Allowed transition in conformation **2** involving the transition from π_2 of benzene to π^* of TCNE

Table 7 RSCF-CV(∞) calculations on the TCNE adducts I–IV from [30]

Functional	I	II	III	IV
LDA	3.30	2.91	2.70	2.40
BP86	3.32	2.93	2.73	2.42
B3LYP	3.56	3.19	3.05	2.44
BHLYP	3.31	3.10	2.84	2.40
LC-BP86	3.10	2.90	2.60	2.29
Exp	3.56	3.32	3.15	2.60

(∞)-DFT where the energy is minimized with respect to both R and U. After full optimization in RSCF-CV(∞)-DFT, the calculated excitation energies are lowered from CV(∞)-TD to values in reasonable agreement with experiment. The best fit is provided by B3LYP (3.56 eV) and the largest deviation is observed for LC-BP86 (3.10 eV). We must conclude that the RSCF-CV(∞)-DFT method in general gives reasonably good agreement with experiment for the different DFT schemes. Thus the RSCF-CV(∞)-DFT energy expressions of (28) and (29) seem to be relatively robust with respect to the choice of functional; see Table 6. The relaxation brings the calculated excitation energy to 2.85 eV for RSCF-CV(∞)-HF; see Table 6 [30].

We present in Table 7 [30] RSCF-CV(∞) results for calculations on X-TCNE adducts I-IV of Fig. 7 using both local functionals and hybrids together with long range corrected (LC) functionals. We notice again that the standard functionals LDA, BP86, B3LYP, and BHLYP all are close to experiment. The LC-BP86 functional fares somewhat worse here. However, we have not optimized the LC parameter which usually improves the results [33]. It should be noted that the corresponding ATDDFT results are off by 2 eV for LDA, BP86, 1 eV for B3LYP and BHLYP [30, 33]. For optimized LC functionals the ATDDFT results are in excellent agreement with experiment [33].

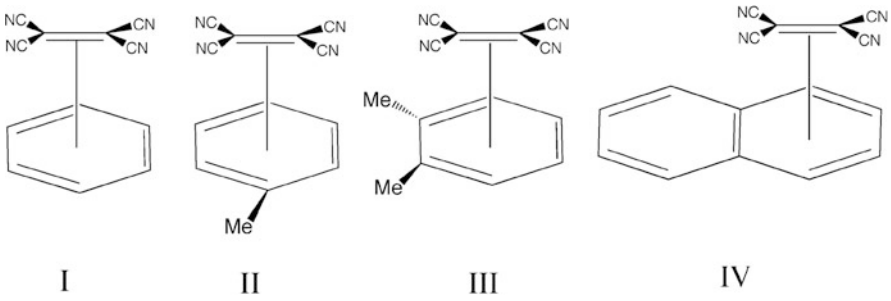

Fig. 7 Adducts I–IV of Table 7

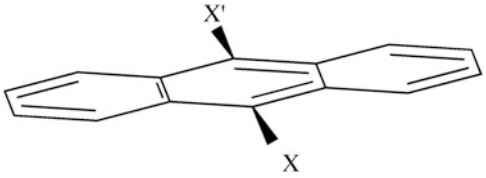

Fig. 8 Different anthracene complexes examined by the RP-CV(4)-DFT scheme

Table 8 Singlet excitation energies (in eV) for π (donor) to π^* (TCNE) transitions in X-anthracene complexes based on a TZP-basis and the RP-CV(4) scheme with different functionals

Substituents(X)	LDA	BP86	BLYP	BPErev	SAOP	GRAC	SKB	Exp.
None	1.69	1.71	1.66	1.73	1.60	1.71	1.82	1.73
9,10-Dimethyl	1.43	1.46	1.41	1.47	1.34	1.45	1.77	1.44
9-Carbo-methoxy	1.74	1.78	1.70	1.80	1.71	1.77	1.84	1.84
9-Chloro	1.74	1.78	1.71	1.80	1.66	1.78	1.82	1.74
9-Cyano	2.00	2.03	1.96	2.04	1.97	2.00	2.03	2.01
9-Formyl 10-chloro	2.02	2.06	1.99	2.08	1.80	2.06	1.96	1.96
9-Formyl	1.99	2.03	1.97	2.05	1.97	2.04	1.95	1.90
9-Methyl	1.48	1.50	1.45	1.51	1.44	1.49	1.71	1.55
9-Nitro	1.94	1.97	1.92	1.99	1.96	1.98	2.12	2.03
RMSD	0.06	0.07	0.08	0.07	0.10	0.07	0.10	1.73

VWN [90], BP86 [91, 92], BLYP [91, 93], revPBE [94–96], SAOP [97], SKB [33], GRAC [98]

In a method which predates RSCF-CV(∞) we combined P-CV(n) with orbital relaxation (RP-CV(n)) to study charge transfer transitions in a series of substituted anthracene–TCNE systems with various groups in the meso position where $n = 4$ [31]. Our results for the series X-anthracene of Fig. 8 are given in Table 8. Experimentally, X-anthracene with pure anthracene or alkyl substituted anthracenes have smaller excitation energies than X-anthracene systems with polar oxygen or a CN group. This order is more or less reproduced by R-CV(4)-DFT. The functional dependence shown in Table 8 is minor. Excitation energies

calculated by the GGA functionals BP86, BLYP, and revBEP differ on average by less than 0.05 eV from LDA estimates and introducing SAOP or GRAC with the right asymptotic 1/r behavior does not lead to any significant change. Charge transfer transitions can also be described well by the variational DFT-based spin-restricted ensemble referenced Kohn–Sham (REKS) method [57] (see footnote 1).

It is at this point important to note that the experimental excitation energies for the anthracene systems were all obtained in solution with CH_3Cl as the solvent. We do not expect the solvent effect to be significant. In fact, theoretical calculations [33] using a continuum model revealed that the excitation energies were lower by only 0.05 eV. We have, as a consequence, decided to compare our gas-phase results directly with the experimental solvent data. We obtain from such a comparison that the RMSD is 0.06 for LDA followed by 0.07 for BP86, revPBE, and 0.08 for BLYP. The two 1/r asymptotically corrected functionals afford 0.10 for SAOP and 0.07 for CRAC. Stein et al. [33] "SKB" introduced in their DZP gas-phase study a uniform correction of -0.32 eV to simulate solvation effects; see Table 8. The magnitude and sign of this correction was given without much explanation [33]. After applying their correction the authors obtained an RMSD of 0.1 which is quite similar to the one found here for our gas-phase results without any solvent correction. It should be noted that ATDDFT with the same functionals carries errors of up to 1 eV.

3 Concluding Remarks

We have here reviewed the theoretical foundation of constricted variational density functional theory and illustrated its scope through applications. CV(n)-DFT encompasses adiabatic TDDFT and ΔSCF-DFT as special cases. Thus our variational second order CV(2)-DFT is identical to adiabatic TDDFT ground state response theory [29, 62] and ΔSCF-DFT is the same as RSCF-CV(∞)-DFT in the case where the transition is described by a single orbital replacement with γ of (18) equal to $\pi/2$ [28]. CV(n)-DFT can be used as a natural extension of adiabatic TDDFT. The first step in this direction is the perturbative P-CV(∞)-DFT approach [64] in which the **U** from CV(2)-DFT is used to calculate the all order energy in CV(∞)-DFT [27, 64]. It is shown to work well for $\pi \rightarrow \pi^*$ transitions in conjugated systems. At a higher level, **U** is optimized with respect to the all order energy in CV(∞)-DFT scheme leading to SCF-CV(∞)-DFT [28]. Experience has shown [27, 63] that optimization of **U** alone is insufficient. One also has to relax all the other occupied orbitals which do not directly participate in the transition. This is done in SCF-CV (∞)-DFT by introducing orbital relaxation (RSCF-CV(∞)-DFT) [26]. The RSCF-CV(∞)-DFT scheme differs from adiabatic TDDFT (CV(2)-DFT) by going to all orders in **U** and by introducing orbital relaxation. The extra effort involved in connection with RSCF-CV(∞)-DFT compared to adiabatic TDDFT does not result in improved accuracy for cases where adiabatic TDDFT fares well, such as for the $\pi \rightarrow \pi^*$ transition [26]. However, it does not fail for charge transfer [30, 31] and Rydberg transitions [66] in the way adiabatic TDDFT does for regular functionals.

This is an important point in studies of absorption spectra where many different types of transitions are present.

In CV-DFT we use approximate ground state functionals in a variational description of the excited states. Such a procedure is consistent with AD-TDDFT in that this theory is equivalent to CV(2)-DFT within the TD-approximation. Going beyond the adiabatic approximation by introducing frequency-dependent kernels consistent with the approximate ground state functional in TDDFT has proven difficult. Here we go beyond CV(2)-DFT in a variational approach, still using an approximate ground state functional but introducing an optimization of U based on the KS-energy to all orders in $\mathbf{U}$ as well as relaxation of the inactive orbitals. It is hoped that going beyond CV(2) in this way is equivalent to introducing a frequency-dependent kernel in TDDFT. Obviously with such a kernel, inactive orbitals would be different from those of the ground state and vary between excited states as in the RSCF-CV(∞) scheme. Further, with a frequency-dependent kernel and related Hessian, the $\mathbf{U}$ matrix obtained for each excited state should be different from that determined by the ground state Hessian in AD-TDDFT, just as in the SCF-CV(∞)-DFT scheme. At present, CV-DFT has the same problems as TDDFT with regards to bond dissociation. Work is under way to introduce doubles into the description of one-electron transitions [99, 100]. This should ensure a prober bond dissociation and provides for a better description of the electron spectra of polyenes [36]. The perturbative P-CV(∞)-DFT approach doubles the time required for each excitation compared to TDDFT, whereas the increase is fivefold for RSCF-CV(∞). This might change with more efficient iterative procedures.

Acknowledgement T.Z. would like to thank the Canadian government for a Canada research chair in theoretical inorganic chemistry and NSERC for financial support.

References

1. Jensen F (2006) Introduction to computational chemistry. Wiley, New York
2. Helgaker T, Jørgensen P, Olsen J (2000) Molecular electronic-structure theory. Wiley, New York
3. Runge E, Gross EKU (1984) Density functional theory for time-dependent systems. Phys Rev Lett 52:997
4. Casida ME (1995) In: Chong DP (ed) Recent advances in density functional methods. World Scientific, Singapore, pp 155–193
5. van Gisbergen SJA, Snijders JG (1995) A density functional theory study of frequency dependent polarizabilities and Van der Waals dispersion coefficients for polyatomic molecules. J Chem Phys 103:9347
6. Petersilka M, Grossmann UJ, Gross EKU (1996) Excitation energies from time-dependent density-functional theory. Phys Rev Lett 76:12
7. Bauernschmitt R, Ahlrichs R (1996) Treatment of electronic excitations within the adiabatic approximation of time dependent density functional theory. Chem Phys Lett 256:454
8. Furche F (2001) On the density matrix based approach to time-dependent density functional response theory. J Chem Phys 114:5882

9. Furche F, Ahlrichs R (2002) Adiabatic time-dependent density functional methods for excited state properties. J Chem Phys 117:7433
10. Romaniello P, Sangalli D, Berger JA, Sottile F, Molinari LG, Reining L, Onida G (2009) Double excitations in finite systems. J Chem Phys 130:044108
11. Gritsenko O, Baerends EJ (2009) Double excitation effects in non-adiabatic time-dependent theory with an analytic construction of the exchange correlation kernel in the common energy denominator energy approximation. Phys Chem 11:4640
12. Jacquemin D, Wathelet V, Perpète EA, Adamo C (2009) Extensive TD-DFT benchmark: singlet excited states of organic molecules. J Chem Theory Comput 5:2420
13. Jacquemin D, Perpète EA, Ciofini I, Adamo C (2009) Accurate simulation of optical properties in dyes. Acc Chem Res 42:326
14. Jacquemin D, Perpete EA, Scuseria GE, Ciofini I, Adamo C (2008) TD-DFT performance for the visible absorption spectra of organic dyes: conventional versus long range hybrids. J Chem Theory Comput 4:123–135
15. Grimme S, Neese F (2007) Double-hybrid density functional theory for excited electronic states of molecules. J Chem Phys 127:154116
16. Send R, Valsson O, Filippi C (2011) Electronic excitations of simple cyanine dyes: reconciling density functional and wave function methods. J Chem Theory Comput 7:444
17. Jacquemin D, Perpete EA, Ciofini I, Adamo C, Valero R, Zhao Y, Truhlar DG (2010) On the performances of the M06 family of density functionals for electronic excitation energies. J Chem Theory Comput 6:2071
18. Moore B II, Autschbach J (2013) Longest-wavelength electronic excitations of linear cyanines: the role of electron delocalization and of approximations in time-dependent density functional theory. J Chem Theory Comput 9:4991
19. Schipper PRT, Gritsenko OV, van Gisberger SJA, Baerends EJ (2000) Molecular calculations of excitation energies and (hyper)polarizabilities with a statistical average of orbital model exchange-correlation potentials. J Chem Phys 112:1344
20. Likura H, Tsuneda T, Tanai T, Hirao K (2001) A long-range correction scheme for generalized-gradient-approximation exchange functionals. J Chem Phys 115:3540
21. Song J-W, Watson MA, Hirao K (2009) An improved long-range corrected hybrid functional with vanishing Hartree–Fock exchange at zero interelectronic distance (LC2gau-BOP). J Chem Phys 131:144108
22. Heyd J, Scuseria GE, Ernzerhof M (2003) Hybrid functionals based on a screened Coulomb potential. J Chem Phys 118:8207
23. Baer R, Neuhauser D (2005) Density functional theory with correct long-range asymptotic behavior. Phys Rev Lett 94:043002
24. Dreuw A, Weisman J, Head-Gordon M (2003) Long-range charge-transfer excited states in time-dependent density functional theory require non-local exchange. J Chem Phys 119:2943
25. Tozer D (2003) Relationship between long-range charge transfer error and integer discontinuity error in Kohn Sham theory. J Chem Phys 119:12697
26. Krykunov M, Ziegler T (2013) Self-consistent formulation of constricted variational density functional theory with orbital relaxation. Implementation and application. J Chem Theory Comput 9:2761
27. Ziegler T, Krykunov M, Cullen J (2012) The implementation of a self-consistent constricted variational density functional theory for the description of excited states. J Chem Phys 136:124107
28. Cullen J, Krykunov M, Ziegler T (2011) The formulation of a self-consistent constricted variational density functional theory for the description of excited states. Chem Phys 391:11
29. Ziegler T, Seth M, Krykunov M, Autschbach J, Wang F (2009) On the relation between time-dependent and variational density functional theory approaches for the determination of excitation energies and transition moments. J Chem Phys 130:154102
30. Krykunov M, Seth M, Ziegler T (2014) Derivation of the RPA (random phase approximation) equation of ATDDFT (adiabatic time dependent density functional ground state response

theory) from an excited state variational approach based on the ground state functional. J Chem Phys 140:18A502
31. Ziegler T, Krykunov M (2010) On the calculation of charge transfer transitions with standard density functionals using constrained variational density functional theory. J Chem Phys 133:074104
32. Ziegler T, Seth M, Krykunov M, Autschbach J, Wang F (2008) A revised electronic Hessian for approximate time-dependent density functional theory. J Chem Phys 129:184114
33. Stein T, Kronik L, Baer R (2009) Reliable prediction of charge transfer excitations in molecular complexes using time-dependent density functional theory. J Am Chem Soc 131:2818
34. Cave RJ, Zhang F, Maitra NT, Burke K (2004) A dressed time-dependent density functional treatment of the 2^1A states of butadiene and hexatriene. Chem Phys Lett 389:39
35. Mazur G, Wlodarczyk R (2009) Application of the dressed time-dependent density functional theory for the excited states of linear polyenes. J Comp Chem 30:811
36. Elliott P, Goldson S, Canahui C, Maitra NT (2011) Perspectives on double-excitations in TDDFT. Chem Phys 391:110
37. Slater JC, Wood JH (1971) Statistical exchange and the total energy of a crystal. Int J Quant Chem Suppl 4:3
38. Slater JC (1972) Statistical exchange-correlation in the self-consistent field. Adv Quant Chem 6:1
39. Kowalczyk T, Yost SR, Van Voorhis T (2011) Assessment of the ΔSCF density functional theory approach for electronic excitations in organic dyes. J Chem Phys 134:054128
40. Ziegler T, Rauk R, Baerends EJ (1977) On the calculation of multiplet energies by the Hartree-Fock-Slater method. Theor Chim Acta 43:261
41. Ziegler T, Rauk A, Baerends EJ (1976) The electronic structure of tetrahedral oxo-complexes. The nature of the "charge transfer" transitions. J Chem Phys 16:209
42. Gilbert A, Besley N, Gill P (2008) J Phys Chem A 122:13164
43. Besley N, Gilbert A, Gill P (2009) Self-consistent-field calculations of core excited states. J Chem Phys 130:124308-1
44. Park YC, Krykunov M, Seidu I, Ziegler T (2014) On the relation between adiabatic time dependent density functional theory (TDDFT) and the ΔSCF-DFT method. Introducing a numerically stable ΔSCF-DFT scheme for local functionals based on constricted variational DFT. Mol Phys 112:661
45. Gavnholt J, Olsen T, Engelund M, Schiøtz J (2008) Δ self-consistent field method to obtain potential energy surfaces of excited molecules on surfaces. J Phys Rev B 78:075441/1
46. Liu TQ, Han WG, Himo FG, Ullmann M, Bashford D, Toutchkine A, Hahn KM, Noodleman L (2004) Density functional vertical self-consistent reaction field theory for solvatochromism studies of solvent-sensitive dyes. Phys Chem A 108:3545
47. Ceresoli D, Tosatti E, Scandolo S, Santoro G, Serra S (2004) Trapping of excitons at chemical defects in polyethylene. J Chem Phys 121:6478
48. Zhekova H, Seth M, Ziegler T (2014) Application of time dependent and time independent density functional theory to the first π to π* transition in cyanine dyes. Int J Quant Chem 114:1019
49. Ziegler T (2011) A chronical about the development of electronic structure theories for transition metal complexes. Struct Bond 47:1
50. von Barth U (1979) Local-density theory of multiplet structure. Phys Rev A 20:1693
51. Gunnarsson O, Lundqvist BI (1976) Exchange and correlation in atoms, molecules, and solids by the spin-density-functional formalism. Phys Rev B 13:4274
52. Levy M, Perdew JP (1985) Hellmann-Feynman, virial, and scaling requisites for the exact universal density functionals. Shape of the correlation potential and diamagnetic susceptibility for atoms. Phys Rev A 32:2010
53. Gaudoin R, Burke K (2005) Lack of Hohenberg-Kohn theorem for excited states. Phys Rev Lett 93:173001

54. Oliveira LN, Gross EKU, Kohn W (1988) Density-functional theory for ensembles of fractionally occupied states. II. Application to the He atom. Phys Rev A 37:2821
55. Filatov M, Shaik S (1998) Spin-restricted density functional approach to the open-shell problem. Chem Phys Lett 288:689
56. Filatov M, Shaik S (1999) Spin-restricted density functional approach to the open-shell problem. Chem Phys Lett 304:429
57. Filatov M, Huix-Rotllant M (2014) Description of electron transfer in the ground and excited states of organic donor–acceptor systems by single-reference and multi-reference density functional methods. J Chem Phys 141:024112
58. Gidopoulos NI, Papaconstantinou PG, Gross EKU (2002) Density-functional theory for ensembles of fractionally occupied states. II. Application to the He atom. Phys Rev Lett 88:03300
59. Gross EKU, Oliveira LN, Kohn W (1988) Spurious interactions, and their correction, in the ensemble-Kohn-Sham scheme for excited states. Phys Rev A 37:2809
60. Levy M, Nagy A (1999) Variational density-functional theory for an individual excited state. Phys Rev Lett 83:4361
61. Görling A, Levy M (1993) Correlation-energy functional and its high-density limit obtained from a coupling-constant perturbation expansion. Phys Rev B 47:13105
62. Ziegler T, Krykunov M, Autschbach J (2014) Derivation of the RPA (random phase approximation) equation of ATDDFT (adiabatic time dependent density functional ground state response theory) from an excited state variational approach based on the ground state functional. J Chem Theory Comput 10:3980
63. Ziegler T, Krykunov M, Cullen J (2011) The application of constricted variational density functional theory to excitations involving electron transitions from occupied lone-pair orbitals to virtual π* orbitals. J Chem Theory Comput 7:2485
64. Krykunov M, Grimme S, Ziegler T (2012) Accurate theoretical description of the ^1L_a and ^1L_b excited states in acenes using the all order constricted variational density functional theory method and the local density approximation. J Chem Theory Comput 8:4434
65. Zhekova H, Krykunov M, Autschbach J, Ziegler T (2014) Applications of time dependent and time independent density functional theory to the first π to π* transition in cyanine dyes. J Chem Theory Comput 10:3299
66. Seidu I, Krykunov M, Ziegler T (2014) Applications of time--dependent and time-- independent density functional theory to Rydberg transitions. J Phys Chem A ASAP. doi:10.1021/jp5082802
67. Wang F, Ziegler T (2004) Time-dependent density functional theory based on a noncollinear formulation of the exchange-correlation potential. J Chem Phys 121:12191-1
68. Wang F, Ziegler T (2005) The performance of time-dependent density functional theory based on a noncollinear exchange-correlation potential in the calculations of excitation energies. J Chem Phys 122:074109-1
69. Wang F, Ziegler T (2006) Use of noncollinear exchange-correlation potentials in multiplet resolutions by time-dependent density functional theory. Int J Quant Chem 106:2545–2550
70. Hirata S, Head-Gordon M (1999) Time-dependent density functional theory within the Tamm-Dancoff approximation. Chem Phys Lett 291:314
71. Amos AT, Hall GG (1961) Single determinant wave functions. Proc R Soc A 263:483
72. Martin RLJ (2003) Natural transition orbitals. J Chem Phys 118:4775
73. Schreiber M, Silva-Junior M, Sauer S, Thiel W (2008) Benchmarks for electronically excited states: CASPT2, CC2, CCSD, and CC3. J Chem Phys 128:134110
74. Platt JR (1949) Classification of spectra of Cata condensed hydrocarbons. J Chem Phys 17:484
75. Grimme S, Parac M (2003) Substantial errors from time-dependent density functional theory for the calculation of excited states of large π systems. Chemphyschem 4:292
76. Parac M, Grimme S (2003) TDDFT of the lowest excitation energies of polycyclic aromatic hydrocarbons. Chem Phys 292:11

77. Jacquemin D, Wathelet V, Perpete EA, Adamo C (2009) Assessment of functionals for TD-DFT calculations of singlet-triplet calculations. J Chem Theory 5:2420
78. Goerigk L, Grimme S (2010) Assessment of TD-DFT methods and of various spin scaled CIS (D) and CC2 versions for the treatment of low-lying valence excitations of large organic dyes. J Chem Phys 132:184103
79. Richard RM, Herbert JM (2011) Time-dependent density-functional description of the 1La state in polycyclic aromatic hydrocarbons: charge-transfer character in disguise? J Chem Theory Comput 7:1296
80. Ziegler T, Rauk A (1977) On the calculation of bonding energies by the Hartree-Fock-Slater method. Theor Chim Acta (Berl) 46:1
81. Pople JA, Krishnan R, Schlegel HB, Binkley JS (1979) Derivative studies in configuration interaction theory. Int J Quant Chem S13:225
82. Fletcher R (1980) Practical methods of optimization, vol 1. Wiley, New York
83. Fischer H, Almlöf J (1992) General methods for geometry and wave function optimization. J Phys Chem 96:9768
84. Prochorow J, Tramer AJ (1967) Photoselection study of charge transfer complexes. J Chem Phys 47:775
85. Frey JE, Andrews AM, Ankoviac DG et al (1990) Charge-transfer complexes of tetracyanoethylene with cycloalkanes, alkenes, and alkynes and some of their aryl derivatives. J Org Chem 55:606
86. Merrifield RE, Phillips WD (1958) Cyanocarbon chemistry. II.1 Spectroscopic studies of the molecular complexes of tetracyanoethylene. J Am Chem Soc 80:2778
87. Masnovi JM, Seddon EA, Kochi JK (1984) Electron transfer from anthracenes. Comparison of photoionization, charge-transfer excitation and electrochemical oxidation. Can J Chem 62:2552
88. Hanazaki I (1972) Vapor-phase electron donor–acceptor complexes of tetracyanoethylene and of sulfur dioxide. J Phys Chem 76:1982
89. Garcia-Cuesta I, Sanchez de Meras AMJ, Koch H (2003) Coupled cluster calculations of the vertical excitation energies of tetracyanoethylene. J Chem Phys 118:8216
90. Vosko SH, Wilk L, Nusair M (1980) Accurate spin-dependent electron liquid correlation energies for local spin density calculations: a critical analysis. Can J Phys 58:1200
91. Becke AD (1988) Density-functional exchange-energy approximation with correct asymptotic behavior. Phys Rev A 38:3098
92. Perdew JP, Wang Y (1986) Density-functional approximation for the correlation energy of the inhomogeneous electron gas. Phys Rev B 33:8822
93. Lee C, Yang W, Parr RG (1988) Development of the Colle-Salvetti correlation-energy formula into a functional of the electron density. Phys Rev B 37:785
94. Perdew JP, Burke K, Ernzerhof M (1996) Generalized gradient approximation made simple. Phys Rev Lett 77:3865
95. Hammer B, Hansen LB, Norskøv JK (1999) Improved adsorption energetics within density-functional theory using revised Perdew-Burke-Ernzerhof functionals. Phys Rev B 59:7413
96. Zhang Y, Yang W (1998) Comment on "generalized gradient approximation made simple". Phys Rev Lett 80:890
97. Gritsenko OV, Schipper PRT, Baerends EJ (1999) Approximation of the exchange-correlation Kohn–Sham potential with a statistical average of different orbital model potentials. Chem Phys Lett 302:199
98. Grüning M, Gritsenko OV, van Gisbergen SJA, Baerends EJ (2001) Shape corrections to exchange-correlation Kohn-Sham potentials by gradient-regulated seamless connection of model potentials for inner and outer region. J Chem Phys 114:652
99. Filatov M (2013) Assessment of density functional methods for obtaining geometries at conical intersections in organic molecules. J Chem Theory Comput 9:4526
100. Ziegler T (1983) Extension of the statistical energy expression to multi-determinantal wave functions. In: Dahl JP, Avery J (eds) Density functional theory of atoms, molecules and solids. Plenum, New York

Top Curr Chem (2016) 368: 97–124
DOI: 10.1007/128_2015_630

Published online: 24 April 2015

Ensemble DFT Approach to Excited States of Strongly Correlated Molecular Systems

Michael Filatov

Abstract Ensemble density functional theory (DFT) is a novel *time-independent* formalism for obtaining excitation energies of many-body fermionic systems. A considerable advantage of ensemble DFT over the more common Kohn–Sham (KS) DFT and time-dependent DFT formalisms is that it enables one to account for strong non-dynamic electron correlation in the ground and excited states of molecular systems in a transparent and accurate fashion. Despite its positive aspects, ensemble DFT has not so far found its way into the repertoire of methods of modern computational chemistry, probably because of the perceived lack of practically affordable implementations of the theory. The spin-restricted ensemble-referenced KS (REKS) method is perhaps the first computationally feasible implementation of the ideas behind ensemble DFT which enables one to describe accurately electronic transitions in a wide class of molecular systems, including strongly correlated molecules (biradicals, molecules undergoing bond breaking/formation), extended π-conjugated systems, donor–acceptor charge transfer adducts, etc.

Keywords Charge transfer excitation energies · Ensemble density functional theory · Excited electronic states · Non-dynamic electron correlation

Contents

M. Filatov (✉)
Institut für Physikalische und Theoretische Chemie, Universität Bonn, Beringstr. 4, 53115 Bonn, Germany
e-mail: mike.filatov@gmail.com

1 Introduction

The founding principles of density functional theory (DFT) were initially formulated only for the ground states of fermionic many-body systems [1, 2]. It is therefore commonly accepted that the excited states in the context of DFT can be accessed by the use of some form of response formalism implemented, for instance, in the time-dependent DFT (TD-DFT) methods [3, 4]. In principle, TD-DFT is a rigorous formulation of the ground state DFT for time-dependent phenomena [5]. However the excitation energies of many-body systems are typically accessed with the use of the linear response (LR) formalism, which assumes that the time dependence stems from a weak (usually oscillatory) perturbing potential [3–5]. In practice, LR-TD-DFT yields a very reasonable description of optical absorption spectra with the use of the commonly available ground-state approximate density functionals [3, 4]; however, some spectacular failures of the formalism are also known. In particular, standard implementation of LR-TD-DFT relies on the adiabatic approximation (i.e., locality of the exchange-correlation (XC) kernel in the time domain) and consequently cannot take proper account of multiple excitations [6, 7], which become important, e.g., for excited states of conjugated molecular systems [8]. Yet another failure of the standard LR-TD-DFT to describe the excited states of strongly correlated systems, e.g., H_2 at stretched bondlength [9], can be traced back to the use of the standard ground-state Kohn–Sham (KS) formalism [2] which fails to take proper account of the non-dynamic electron correlation.

In the domain of wavefunction theory (WFT), the excited states of molecules can be obtained from the ground-state response formalism as well as the variational excited state formalism [10]. An appealing idea is to employ the (time-independent) variational formalism to obtaining excitation energies in the context of DFT. Indeed, the first attempts to calculate the excitation energies by taking the energy differences between the variationally obtained ground state energy and the energy of a state obtained by promoting an electron to unoccupied energy level, the so-called ΔSCF approach,[1] date back to the early 1970s [11, 12]. However, despite some attempts to justify the ΔSCF approach for computing the energies of one-electron transitions between the states of different spatial symmetry [13, 14], the idea of variationally obtaining the energy of an individual excited state in the context of DFT lacks firm theoretical background [15–17].

A rigorous way of developing time-independent formalism for obtaining excitation energies in the context of DFT is offered by *ensemble* DFT [18, 19] which

[1] For more details on ΔSCF, see the chapter "A Constricted Variational Density Functional Theory Approach to the Description of Excited States" by T. Ziegler, M. Krykunov, I. Seidu, and Y. C. Park.

operates with weighted sums (ensembles) of fractionally occupied (ground and excited) states. The ensemble representation of the density and the energy for an arbitrary many-body fermionic system was put on a firm theoretical ground by Lieb [20] and Englisch and Englisch [21, 22], and was later extended to the domain of excited states by Gross et al. [23–25].

A practical demonstration of the necessity to invoke the ensemble representation for mapping the density of a strongly correlated system onto a non-interacting KS reference was achieved by Baerends et al. [26, 27] in first-principles numeric simulations employing the (nearly) exact molecular densities, which was later confirmed by Morrison [28] in a series of first-principles atomic calculations. Although the ensemble formalism enables one to obtain excitation energies in a rigorous and computationally convenient way [5], the progress in this direction was extremely slow [29–33], perhaps because of the perceived lack of suitable density functionals capable to accommodate the densities with fractional occupation numbers (FONs).

A practically accessible approach to the calculation of the strongly correlated ground and excited states of molecules which employs the ideas behind ensemble DFT was achieved in the form of the spin-restricted ensemble-referenced KS (REKS) method [34–41]. The method was initially developed for the ground states of strongly correlated molecular systems [34–38] and was later extended to the domain of excited state calculations [39–41]. Although the REKS method is founded on a rigorous theoretical background [20, 21, 26] and was successfully applied to study situations often intractable with the use of the conventional KS DFT methods [37, 38, 40–61], the method has received a little attention in the literature and has been largely overlooked by the computational chemistry community. In this chapter, an overview of the REKS methodology and its connection to the ensemble DFT formalism is given with emphasis on the use of the method to obtain excited states of molecular systems.

2 Ensemble DFT

The basic tenet of KS DFT is that any physical fermionic ground state density $\rho(\mathbf{r})$ can be uniquely mapped onto the ground state density $\rho_s(\mathbf{r})$ of a fictitious system of non-interacting particles moving in a suitably modified external potential $v_s(\mathbf{r})$. If such a $v_s(\mathbf{r})$, which is also known as the KS potential, can be found, the respective KS Hamiltonian $\hat{H}_s$ is minimized by a single Slater determinant (KS determinant) constructed from the lowest-energy one-electron functions (KS orbitals) $\varphi_{s,i}(\boldsymbol{r})$ and the non-interacting density $\rho_s(\boldsymbol{r})$ is

$$\rho_s(\mathbf{r}) = \sum_i 2\left|\varphi_{s,i}(\mathbf{r})\right|^2; \quad \forall \varepsilon_i \leq \mu\,, \tag{1}$$

where ε_i are the respective eigenvalues, μ is the Fermi level, and a closed electronic

shell is assumed [1, 2]. The physical density $\rho(\mathbf{r})$ which can be mapped onto such a non-interacting density $\rho_s(\mathbf{r})$ is said to be non-interacting pure state v-representable, or PS-VR for brevity [21]. Naturally, in the case of non-interacting particles, such a pure state wavefunction is represented by a single KS determinant and one may speak of a determinantal v-representability (D-VR) as well [21].

A general proof of the existence of such a KS potential $v_s(\mathbf{r})$ and of the PS-VR property has never been achieved for an arbitrary physical density. By contrast, rigorous theoretical arguments have been given in favor of an alternative representation of an arbitrary fermionic density $\rho(\mathbf{r})$ by an ensemble (weighted sum) of a finite number (M) of the densities $\rho_K(\mathbf{r})$ originating from the same physical external potential $v_{\text{ext}}(\mathbf{r})$ [19–21]:

$$\rho(\mathbf{r}) = \sum_{K=1}^{M} \lambda_K \rho_K(\mathbf{r}), \quad \lambda_K \geq 0, \quad \sum_{K=1}^{M} \lambda_K = 1\,. \tag{2}$$

For the ensemble v-representable (E-VR) densities, the existence of a universal density functional $F[\rho]$ and its differentiability with respect to the density $\rho(\mathbf{r})$ were rigorously proved [20, 21], thus confirming the existence of the KS potential $v_s(\mathbf{r})$ and the respective non-interacting KS system.

Initially, ensemble DFT was formulated for ground state ensembles [20, 21], which implied that one could speak of averaging over degenerate electronic states. It is natural to assume that the degeneracy is imposed by the symmetry of the system. This seems a plausible assumption in the case of interacting particles, although for the non-interacting fermions (such as the KS reference system) there is a possibility of accidental degeneracy of several electronic configurations as was demonstrated in first principles numeric experiments by Schipper et al. [26] and by Morrison [28]. In these works it was shown that, when obtaining the KS potential $v_s(\mathbf{r})$ from the known (nearly) exact density [62], the fractional occupation numbers of several KS orbitals (i.e., the ensemble representation) have to be invoked. Thus, certain physical (i.e., interacting) PS-VR densities (the target densities were obtained from the accurate ab initio WFT calculations) can only be mapped onto the non-interacting E-VR densities. Remarkably, these target densities were obtained for molecular systems for which it was known that their electronic structure is dominated by the non-dynamic electron correlation; [63] in particular, the rectangular $H_2 + H_2$ system, the ground state of the C_2 molecule [26], and the ground state of a series of Be-like atomic ions [28] were investigated. For these atomic and molecular systems it is well established that, at the ab initio WFT level, their ground state wavefunctions require a multi-reference description, which is typically associated with the strong non-dynamic correlation [63].

The ensemble representation of the non-interacting KS reference system leads naturally to the fractional occupation numbers of KS orbitals:

$$\rho_s(\mathbf{r}) = \sum_i n_i \left|\varphi_{s,i}(\mathbf{r})\right|^2, \tag{3}$$

where the FONs satisfy the conditions

$$\begin{array}{cc} n_j = 2, & \varepsilon_j < \mu \\ 0 \le n_k \le 2, & \varepsilon_k = \mu \\ & \sum_i n_i = N \end{array}, \tag{4}$$

that is, only a few KS orbitals which degenerate at the Fermi level μ are allowed to have fractional occupations [26]. Alternatively, the ensemble density (*3*) can be written down as in (2) as a weighted sum of the densities $\rho_{s,K}$ (**r**) of several KS determinants constructed from a common set of KS orbitals; the ensemble weighting factors λ_K are then connected to the FONs in (*3*) via $\lambda_K = n_k/m$ where m is the number of electrons in the KS orbitals degenerate at the Fermi level and all the KS orbitals in the determinant yielding the $\rho_{s,K}$ (**r**) density are set doubly occupied. Recently, the degeneracy of the fractionally occupied KS orbitals at the Fermi level was rigorously proved [64].

For the ensemble density (2), Lieb proved [20] that the ground state energy is given by a weighted sum

$$E[\rho] = \sum_{K=1}^{M} \lambda_K E[\rho_K], \tag{5}$$

of the energies $E[\rho_K]$ of the ensemble components taken with the same weighting factors as in (2). Englisch and Englisch proved the differentiability of the ensemble energy $E[\rho]$ with respect to the ensemble density, thus demonstrating the existence of $v_s(\mathbf{r})$ and the ensemble KS reference system [21].

The energies of the non-interacting KS reference states constructed in [26] for the C_2 molecule and for the $H_2 + H_2$ system satisfy (5), provided that the ensemble densities are allowed. If, however, one insisted on having PS-VR (or D-VR) KS reference states for these molecular systems, holes below the Fermi level were observed which implied the breakdown of the basic assumption behind the KS method, namely that the density $\rho_s(\boldsymbol{r})$ is constructed from the *lowest* one-particle eigenstates of the non-interacting KS Hamiltonian. Besides that, the single determinant KS states found in [26] (and in [28]) had somewhat higher energies than the respective ensemble KS solutions. Thus, the ensemble KS solutions had to be preferred on the grounds of the variational principle. These conclusions have been fully confirmed by Morrison [28] in the study of Be isoelectronic series of atomic ions, for which mapping of the exact densities onto the KS reference could only be achieved with the use of ensemble densities, i.e., densities with the fractional occupation numbers of the valence 2s and 2p atomic orbitals. An attempt to formalize these observations and to develop ensemble variants of the KS theory

was undertaken in [30]; however this did not materialize in the form of a practically accessible computational scheme.

The ground-state ensemble DFT formalism was extended into the domain of excited state calculations in the works of Theophilou [18] and Gross et al. [23] who demonstrated that the Hohenberg–Kohn theorem is satisfied not only by the ground-state density and the energy but also by the density and the energy of an ensemble of several lowest energy states (i.e., the ground and excited states) of a many-body fermionic system. In particular, Gross et al. [23] proved that the ensemble energy (5) constructed from several lowest eigenstates of a many-body Hamiltonian $\hat{H}$ satisfies the variational principle

$$\sum_{K=1}^{M}\lambda_K\langle\Phi_K|\hat{H}|\Phi_K\rangle \geq \sum_{K=1}^{M}\lambda_K E_K; \quad 0 \leq \lambda_K \leq 1; \quad \sum_{K=1}^{M}\lambda_K = 1\,, \tag{6}$$

where Φ_k are the trial wavefunctions and E_K are the exact eigenvalues of the Hamiltonian $\hat{H}$ [23].

The variational character of the ensemble energy enables one to calculate excitation energies rigorously using (formally ground-state) density functionals. Considering only two state ensembles (the ground state E_0 and the lowest excited state E_1), for which the energy and the density are given by (7) and (8),

$$E_\omega = (1-\omega)E_0 + \omega E_1, \tag{7}$$

$$\rho_\omega(\mathbf{r}) = (1-\omega)\rho_0(\mathbf{r}) + \omega\rho_1(\mathbf{r}), \tag{8}$$

the excitation energy $\Delta E = E_1 – E_0$ can be obtained in two ways [5]. The first obtains ΔE for some fixed weighting factor ω, which trivially leads to

$$\Delta E = E_1 - E_0 = \frac{E_\omega - E_0}{\omega}, \tag{9}$$

and the second employs derivatives of E_ω with respect to the weighting factor [5, 29]

$$\Delta E = \frac{dE_\omega}{d\omega}, \tag{10}$$

A practical exploration of (10) was attempted by Gross et al. [29] who used the quasilocal density approximation (qLDA) [65] with fractional occupation numbers of the KS orbitals, although the excitation energies obtained for the He atom were unsatisfactory. Similarly poor results (with the errors on the order of a few eV) were obtained in several other works by employing various approximations for the exchange-correlation functional to calculate the excitation energies of atoms and small molecules [66–68].

Further theoretical developments of the ensemble DFT formalism for excited states were recently undertaken in [31–33]. Pernal et al. [31] demonstrated that the ensemble variational principle can be connected to the Helmholtz free-energy variational principle of the statistical mechanics. Ullrich et al. [33] used the ensemble formalism to construct the accurate exchange-correlation potentials for ensembles of ground and excited states of He atoms and several model systems that allow the exact solution (1D box and Hooke's atom). Fromager et al. [32] derived the generalized adiabatic connection formalism for ensemble DFT which can in principle provide a framework for the development of a rigorous multi-determinant DFT.

Perhaps the most significant realization in the aforementioned works on ensemble DFT is that not only the total ensemble energy E_ω but also its components should be kept linear in the ensemble weighting factors. Indeed, starting from (7) (or (5)) it is tempting to cast the ensemble energy into the traditional DFT form by splitting the energy functional into the familiar non-interacting kinetic energy T_s, the classical Hartree repulsion U_H, and the exchange-correlation E_{xc} terms, as in (11):

$$E_\omega = T_{s,\omega} + U_H[\rho_\omega] + E_{\mathrm{xc}}[\rho_\omega] + \int d^3 r v_{\mathrm{ext}}(\mathbf{r})\rho_\omega(\mathbf{r}), \tag{11}$$

where the Hartree electron–electron repulsion energy and E_{xc} are calculated for the total ensemble density,

$$U_H[\rho_\omega] = \frac{1}{2}\int d^3 r' \int d^3 r \frac{\rho_\omega(\mathbf{r})\rho_\omega(\mathbf{r}')}{|\mathbf{r} - \mathbf{r}'|}, \tag{12}$$

and a suitable approximate functional is employed for E_{xc} [29]. As the U_H energy depends nonlinearly on the density, the dependence of (12) on the ensemble weighting factors becomes nonlinear, which leads to the emergence of unphysical "ghost" contributions, i.e., cross-terms between the ensemble components. These terms are supposed to be eliminated by the XC functional, which should also become nonlinear in the ensemble weighting factors [31, 33]. The commonly available approximations for the XC functional were incapable of accurately compensating for the "ghost" contributions and, consequently, the results obtained with the use of these functionals were quite poor [29, 66–68].

Considerably better excitation energies from the ensemble DFT calculations were obtained by Pernal et al. [31], who employed a "ghost"-free formulation for the ensemble energy functional. The "ghost"-free Hartree electron–electron repulsion in [31] was calculated:

$$U_H[\rho_\omega] = \frac{1}{2}\sum_I \omega_I \int d^3r' \int d^3r \frac{\rho_I(\mathbf{r})\rho_I(\mathbf{r}')}{|\mathbf{r}-\mathbf{r}'|}, \tag{13}$$

where ρ_I are the densities of the individual components of the ensemble. In their work, Pernal et al. separated the ensemble XC energy into the long-range (lr) component which was treated at the multi-reference WFT level and the short-range (sr) XC energy approximated by a density functional:

$$E_\omega = \sum_I \omega_I \left(T_{s,I} + U_H[\rho_I] + \int d^3r\, v_{\text{ext}}(\mathbf{r})\rho_I(\mathbf{r}) + E^{lr}_{\text{xc},I} \right) + E^{\text{sr}}_{\text{xc,DFT}}[\rho_\omega]. \tag{14}$$

Although, with the use of this approach, the excitation energies of Be atom and LiH and BH molecules were considerably improved, there still remained substantial residual errors on the order of 0.6–0.8 eV. Furthermore, the sr-XC energy in (*14*) still remained nonlinear in the ensemble weighting factors and inseparable into the individual contributions of ensemble components. These shortcomings of the currently available implementations of ensemble DFT are not present in the REKS method which is described in the following section.

3 REKS Methodology

In this section the basic aspects of the REKS method are explained. The REKS method was initially developed to deal with the non-dynamic correlation in the ground electronic states of molecules [35, 38] and was later extended to treat the excited states [39–41]. The latter method is known as the state-averaged REKS (SA-REKS) [39] and the state interaction SA-REKS (SI-SA-REKS or SSR, for brevity) [40, 41].

3.1 REKS Method for Ground States

The REKS method for ground states is a practical implementation of ensemble DFT formalism that depends upon (2) and (5) [20]. Let us consider a situation that requires the use of the ensemble formalism at the DFT level and the multi-reference description at the WFT level. For instance, let us take two H_2 molecules in a rectangular arrangement as shown in Fig. 1. The $H_2 + H_2$ system was studied in [26] with the use of both the multi-reference configuration interaction (MRCI) method of WFT and the ensemble DFT formalism. In the latter case, the non-interacting KS reference state and the KS potential $v_s(\mathbf{r})$ were constructed from the MRCI density using the reverse engineering approach of Zhao, Morrison, and Parr [62]. It was found that one has to use the ensemble representation and the fractional

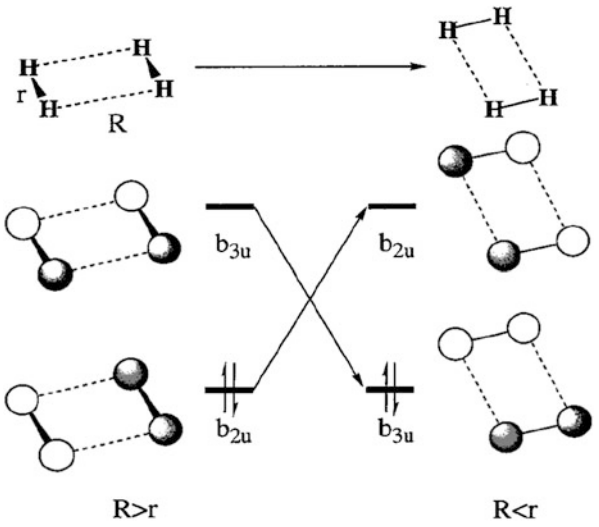

Fig. 1 Definition of geometry and frontier orbitals for the $H_2 + H_2$ system

occupations of the frontier orbitals to obtain the non-interacting KS reference system and $v_s(\mathbf{r})$ corresponding to the criteria behind the KS method of DFT; only the ensemble representation guaranteed the lowest-energy ground state of the KS system; otherwise there occurred holes below the Fermi level (not a ground state) and the resulting single determinant state lied at a somewhat higher energy [26].

At a long intermolecular separation R, the electronic structure of the system is dominated by the $(\ldots \phi_a^{(2)}\, \phi_b^{(0)})$ configuration, where ϕ_a corresponds to the b_{2u}-symmetric molecular orbital (MO) and ϕ_b to b_{3u}-symmetric MO (under the D_{2h} symmetry constraint). Such a situation is non-interacting PS-VR, i.e., it can be faithfully represented by a single KS determinant [26]. As the two molecules get closer, the gap between the highest occupied MO (HOMO) ϕ_a and the lowest unoccupied MO (LUMO) ϕ_b narrows down and, at a certain distance between the H_2 molecules, the non-dynamic correlation sets in, which is reflected in the character of the MRCI wavefunction which comprises two leading configurations, $(\ldots \phi_a^{(2)}\, \phi_b^{(0)})$ and $(\ldots \phi_a^{(0)}\, \phi_b^{(2)})$, and, at the KS DFT level, one has to switch over to the ensemble representation for the density. The frontier KS orbitals ϕ_a and ϕ_b become fractionally occupied and degenerate at the Fermi level of the system [26].

Thus, the density of the $H_2 + H_2$ system near the square conformation is given by a two-component ensemble (2) with the weighting factors λ_1 and λ_2 related to the FONs of the frontier KS orbitals, $\lambda_1 = n_a/2$ and $\lambda_2 = n_b/2$. The ensemble KS energy is given by (5) with the same weighting factors. The FONs of the frontier orbitals satisfy the condition of stationarity of the energy with respect to their variation [64]. Hence, the ensemble KS reference state obtained in [26] follows exactly theorems 4.2 and 4.3 and equations 4.5 and 4.7 of [20], and nicely illustrates the theoretical arguments behind the ensemble approach in DFT.

The ensemble KS solution obtained which comprises the densities and energies of two electronic configurations, where each is represented by a single KS determinant, corresponds to a system of non-interacting particles. To derive an energy expression that would conform with the ensemble representation and would yield the energy of a system of *interacting* electrons, let us make use of the adiabatic connection formalism [69], i.e., let us gradually switch the electron–electron interaction on and simultaneously modify the external potential in such a way that the total density remains unchanged [70]; see the Hamiltonian

$$\hat{H}_\alpha = \sum_i -\frac{1}{2}\nabla_i^2 + \sum_i v_{\mathrm{ext},\alpha}(\mathbf{r}_i) + \sum_{i>j}\frac{\alpha}{r_{ij}}, \tag{15}$$

where α is the variable coupling constant, $0 \le \alpha \le 1$, r_{ij} is the interelectronic distance, and the external potential $v_{\mathrm{ext},\alpha}$ satisfies the conditions $v_{\mathrm{ext},0} = v_s$ (the KS potential) and $v_{\mathrm{ext},1} = v_{\mathrm{ext}}$ (physical system of interacting electrons). When the electron–electron interaction is only infinitesimally switched on, such that it affects only the electrons in the degenerate orbitals at the Fermi level, the total energy with the Hamiltonian at $\alpha \approx 0$ can be obtained from quasi-degenerate perturbation theory [10] which leads to an expression which can be cast in the form of

$$\begin{aligned} E_\alpha = {} & \frac{n_a^\alpha}{2}E_\alpha\left[\ldots\phi_a\overline{\phi}_a\right] + \frac{n_b^\alpha}{2}E_\alpha\left[\ldots\phi_b\overline{\phi}_b\right] \\ & + \frac{1}{2}\left(n_a^\alpha n_b^\alpha\right)^{1/2}\left(E_\alpha[\ldots\phi_a\phi_b] - E_\alpha\left[\ldots\phi_a\overline{\phi}_b\right] + E_\alpha\left[\ldots\overline{\phi}_a\overline{\phi}_b\right] - E_\alpha\left[\ldots\overline{\phi}_a\phi_b\right]\right), \end{aligned} \tag{16}$$

where the energies of the electronic configurations are calculated using the Hamiltonian (15) and the barred orbitals and the unbarred orbitals are occupied with the beta-spin and the alpha-spin electrons, respectively. The energy term in parentheses in the second line of (16) represents the negative of the exchange integral $(\phi_a\phi_b|\phi_b\phi_a)$ expressed via the energy differences between the singlet and triplet configurations.[2]

Using the coupling strength integration [69] and making an assumption that the α-dependent occupation numbers n_a^α and n_b^α can be replaced by the respective median values, one arrives at the formula

[2] Note that the kinetic energy is independent of the spin and the total densities of the electronic configurations in the second line of (16) are identical.

$$E_{\text{ens}} = \frac{n_a}{2}E_{\text{DFT}}\left[\ldots\phi_a\overline{\phi}_a\right] + \frac{n_b}{2}E_{\text{DFT}}\left[\ldots\phi_b\overline{\phi}_b\right] + \frac{1}{2}(n_a n_b)^{1/2} \times \left(E_{\text{DFT}}[\ldots\phi_a\phi_b] - E_{\text{DFT}}\left[\ldots\phi_a\overline{\phi}_b\right] + E_{\text{DFT}}\left[\ldots\overline{\phi}_a\overline{\phi}_b\right] - E_{\text{DFT}}\left[\ldots\overline{\phi}_a\phi_b\right]\right), \tag{17}$$

where E_{DFT} denotes the total energy calculated for a single-determinant configuration using the conventional KS DFT formalism. It is noteworthy that the parenthesized term in the second line of (17) does not contribute to the total density, as the densities of these configurations cancel each other identically. Hence, the total density of a strongly correlated state can be calculated using

$$\begin{aligned}\rho_{\text{ens}} &= \frac{n_a}{2}\rho\left[\ldots\phi_a\overline{\phi}_a\right] + \frac{n_b}{2}\rho\left[\ldots\phi_b\overline{\phi}_b\right] \\ &+ \frac{1}{2}(n_a n_b)^{1/2}\left(\rho[\ldots\phi_a\phi_b] - \rho\left[\ldots\phi_a\overline{\phi}_b\right] + \rho\left[\ldots\overline{\phi}_a\overline{\phi}_b\right] - \left[\ldots\overline{\phi}_a\phi_b\right]\right), \\ &= \frac{n_a}{2}\rho\left[\ldots\phi_a\overline{\phi}_a\right] + \frac{n_b}{2}\rho\left[\ldots\phi_b\overline{\phi}_b\right]\end{aligned} \tag{18}$$

which is the weighted sum of the densities of the configurations in (17) taken with the same weighting factors.

To illustrate the derivation of (17), let us expand the ensemble energy (16) obtained from quasi-degenerate perturbation theory near $\alpha = 0$. Equation (16) is obtained as the most negative eigenvalue of the secular matrix

$$\begin{pmatrix} E_\alpha\left[\ldots\phi_a\overline{\phi}_a\right] & K^\alpha_{ab} \\ K^\alpha_{ab} & E_\alpha\left[\ldots\phi_b\overline{\phi}_b\right] \end{pmatrix}, \tag{19}$$

where $K^\alpha_{ab} = -\frac{1}{2}\left(E_\alpha[\ldots\phi_a\phi_b] - E_\alpha\left[\ldots\phi_a\overline{\phi}_b\right] + E_\alpha\left[\ldots\overline{\phi}_a\overline{\phi}_b\right] - E_\alpha\left[\ldots\overline{\phi}_a\phi_b\right]\right)$ $\left(K^\alpha_{ab} = \alpha\left(\phi_a\phi_b\middle|\phi_b\phi_a\right), \text{for } \alpha\to 0\right)$ is the coupling element between the configurations $\left|\ldots\phi_a\overline{\phi}_a\right\rangle$ and $\left|\ldots\phi_b\overline{\phi}_b\right\rangle$ (for a small α, the exchange integral between the orbitals ϕ_a and ϕ_b). Expanding this matrix with respect to α and keeping only the first term in the expansion, one obtains

(continued)

$$\begin{pmatrix} E_\alpha\left[\ldots\phi_a\overline{\phi}_a\right] & K^\alpha_{ab} \\ K^\alpha_{ab} & E_\alpha\left[\ldots\phi_b\overline{\phi}_b\right] \end{pmatrix} = \begin{pmatrix} E_0\left[\ldots\phi_a\overline{\phi}_a\right] & 0 \\ 0 & E_0\left[\ldots\phi_b\overline{\phi}_b\right] \end{pmatrix} + \alpha\begin{pmatrix} \frac{dE_\alpha\left[\ldots\phi_a\overline{\phi}_a\right]}{d\alpha} & \frac{dK^\alpha_{ab}}{d\alpha} \\ \frac{dK^\alpha_{ab}}{d\alpha} & \frac{dE_\alpha\left[\ldots\phi_b\overline{\phi}_b\right]}{d\alpha} \end{pmatrix} + O\left(\alpha^2\right), \tag{20}$$

the lowest energy solution of which is given by

$$E_\alpha = \frac{n^\alpha_a}{2}E_0\left[\ldots\phi_a\overline{\phi}_a\right] + \frac{n^\alpha_b}{2}E_0\left[\ldots\phi_b\overline{\phi}_b\right] + \alpha\left(\frac{n^\alpha_a}{2}\frac{dE_\alpha\left[\ldots\phi_a\overline{\phi}_a\right]}{d\alpha} + \frac{n^\alpha_b}{2}\frac{dE_\alpha\left[\ldots\phi_b\overline{\phi}_b\right]}{d\alpha} - \left(n^\alpha_a n^\alpha_b\right)^{1/2}\frac{dK^\alpha_{ab}}{d\alpha}\right). \tag{21}$$

In (21), it was used that $E_0\left[\ldots\phi_a\overline{\phi}_a\right] = E_0\left[\ldots\phi_b\overline{\phi}_b\right]$ and $n^\alpha_a + n^\alpha_b = 2$, where the occupation numbers $n^\alpha_a = 2\left|c^\alpha_1\right|^2$ and $n^\alpha_b = 2\left|c^\alpha_2\right|^2$ are obtained from the lowest eigenvector (c^α_1, c^α_2) of the matrix in the second line of (20).

Assuming that the occupation numbers n^α_a and n^α_b can be replaced by their respective median values, n_a and n_b, and performing the usual coupling constant integration [69, 70], one arrives at

$$E_{\text{ens}} = \frac{n_a}{2}E_0\left[\ldots\phi_a\overline{\phi}_a\right] + \frac{n_b}{2}E_0\left[\ldots\phi_b\overline{\phi}_b\right] + \int\rho_{\text{ens}}(\mathbf{r})(\nu_{\text{ext},1}(\mathbf{r}) - \nu_{\text{ext},0}(\mathbf{r}))d\mathbf{r} + \frac{n_a}{2}E_{\text{Hxc}}\left[\ldots\phi_a\overline{\phi}_a\right] + \frac{n_b}{2}E_{\text{Hxc}}\left[\ldots\phi_b\overline{\phi}_b\right] + \frac{1}{2}(n_a n_b)^{1/2} \times\left(E_{\text{Hxc}}\left[\ldots\phi_a\overline{\phi}_b\right] - E_{\text{Hxc}}\left[\ldots\phi_a\overline{\phi}_b\right] + E_{\text{Hxc}}\left[\ldots\overline{\phi}_a\overline{\phi}_b\right] - E_{\text{Hxc}}\left[\ldots\overline{\phi}_a\phi_b\right]\right), \tag{22}$$

where the E_{Hxc} terms comprise the Hartree and the XC energy of the given configuration. Equation (17) is obtained from (22) using the density ρ_{ens} in (18) and noting that the sum of the kinetic energy and the interaction with the external potential $v_{\text{ext},1}$ is the same for the four terms in parentheses in the third line of (22). When deriving (17), it was also assumed that no further degeneracies (except the point $\alpha = 0$) occur along the adiabatic connection path.

The formulae obtained for the density and the energy are valid for the case of strong non-dynamic correlation, where the occupation numbers of the fractionally occupied orbitals are close to unity, $n_a \approx n_b \approx 1$. When the multi-reference

character of the system subsides to a level commensurate with the pure-state v-representability, the ensemble energy in (17) should collapse to the usual KS DFT single-reference energy. Analyzing the dependence of the single-reference KS DFT energy on the FONs of the frontier orbitals near, say, $n_a \approx 2$ and $n_b \approx 0$, an expression similar to (17) can be obtained with the difference that the factor $(n_a n_b)^{1/2}$ approaches $(n_a n_b)^1$ [71, 72]. It is thus plausible to introduce a function that interpolates between the two asymptotes, the strong and the weak non-dynamic correlation, and to cast (17) in the form of [35]

$$E^{\mathrm{REKS}(2,2)} = \frac{n_a}{2} E_{\mathrm{DFT}}\left[\ldots \phi_a \overline{\phi}_a\right] + \frac{n_b}{2} E_{\mathrm{DFT}}\left[\ldots \phi_b \overline{\phi}_b\right] + f(n_a, n_b)\left(E_{\mathrm{DFT}}[\ldots \phi_a \phi_b] - E_{\mathrm{DFT}}\left[\ldots \phi_a \overline{\phi}_b\right] + E_{\mathrm{DFT}}\left[\ldots \overline{\phi}_a \overline{\phi}_b\right] - E_{\mathrm{DFT}}\left[\ldots \overline{\phi}_a \phi_b\right]\right), \tag{23}$$

where $f(n_a,n_b)$ is the interpolating function defined in [38]:

$$f(n_a, n_b) = \frac{1}{2}(n_a n_b)^{1-\frac{1}{2}\frac{n_a n_b + \delta}{1+\delta}}. \tag{24}$$

The damping factor in (24) is set to a value $\delta = 0.4$ to provide for a stable convergence of the REKS self-consistent field (SCF) iterations near the regime when E-VR solution collapses to the PS-VR solution [73]. In the described version of REKS, the FONs of the two frontier orbitals are restricted to sum up to two electrons; hence the name REKS(2,2), which is similar to the notation adopted for the complete active space SCF (CASSCF) method in multi-reference WFT.

In the strict implementation of KS theory, the derived REKS total energy should be minimized with respect to the REKS density (naturally, the FONs too). As the REKS energy is not an explicit functional of the density, such a minimization should inevitably rely on a variant of the optimized effective potential (OEP) approach [74], which is known to suffer from steep computation time scaling and certain stability issues when used in connection with the localized basis sets for expanding the KS orbitals [75]. Therefore, the REKS total energy is minimized with respect to the orbitals, as is being commonly done in connection with the hybrid and meta GGA density functionals, thus avoiding the need to tackle the density–density response function[3] used in the OEP formalism. The FONs are obtained variationally by minimizing the energy (23) under the constraint $n_a + n_b = 2$. The latter constraint is imposed explicitly, without using the method of Lagrange multipliers. The REKS orbitals are optimized using the coupling operator technique of the open-shell SCF theory [77]. For brevity, the REKS one-electron equations are not presented here and the reader is referred to the original publications [34, 35, 43]; see also a review article [73].

[3] See [76] for the derivation of density–density response function for ensemble densities.

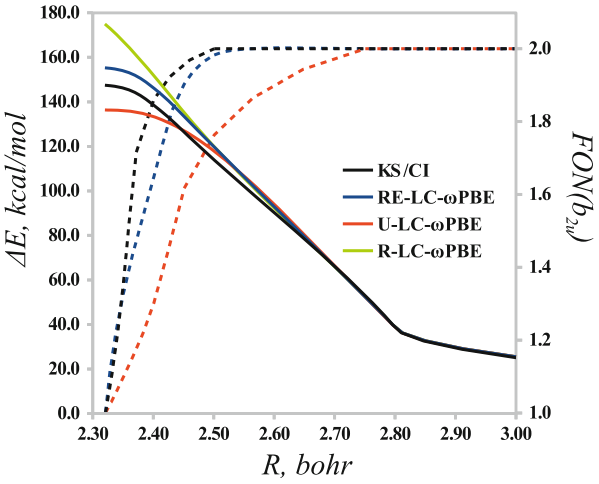

Fig. 2 Profile of the PES of $H_2 + H_2$ reaction and populations of the b_{2u} orbital as obtained from the KS/CI (*black*), BS-UKS (*red*), RKS (*green*), and REKS (*blue*) calculations. The relative energies are calculated with respect to two isolated H_2 molecules. *Solid curves* show the energies and *dashed curves* show the occupation numbers as a function of R (see Fig. 1 for definition). DFT calculations employ the LC-ωPBE functional

The derived REKS energy expression is based on a number of assumptions, of which the most severe is perhaps the assumption that the coupling strength dependent occupation numbers n_i^α in (16) can be replaced by their median values n_i in (17) to avoid the need to carry out their integration with respect to α. Although the coupling strength integration of the ensemble weighting factors for partially interacting Hamiltonians was attempted by Fromager et al. when deriving the generalized adiabatic connection for ensemble DFT [32], to keep the formalism simple we prefer to stick to the above assumption and to verify whether it is sufficiently accurate by comparing the results obtained using the REKS method with the reference (exact) data. In the following, an example is presented that illustrates the validity of the above assumptions.

The $H_2 + H_2$ reaction studied by Schipper et al. [26] is perhaps the simplest example of a 2+2 symmetry forbidden cycloaddition reaction [78–80]. This reaction was investigated using the MRCI/cc-pV5Z method and the ensemble KS reference was obtained from the MRCI density [26]. The potential energy surface (PES) profile along the direction of approach of the two H_2 molecules (see Fig. 1 for definitions) is shown in Fig. 2 along with the b_{2u} orbital population as obtained in the MRCI and DFT calculations. The DFT calculations in Fig. 2 employ the LC-ωPBE [81–83] range-separated density functional and three different computational techniques: the REKS method, the broken-symmetry spin-unrestricted KS (BS-UKS) method, and the conventional single-reference spin-restricted KS (RKS) method. All three DFT methods yield the same energy (−2.3574534 a.u.) for the two H_2 molecules at long distance from one another.

The RKS method fails to take proper account of the non-dynamic correlation arising from (near) degeneracy of the $(\ldots b_{2u}^{(2)} b_{3u}^{(0)})$ and $(\ldots b_{2u}^{(0)} b_{3u}^{(2)})$ configurations in the vicinity of the barrier summit and yields a cusp on the PES instead of a smooth transition state. The BS-UKS and REKS methods yield a smooth transition

between the configurations, although the BS-UKS curve deviates stronger from the target MRCI PES and underestimates the reaction barrier height. The FONs of the frontier orbitals (only the b_{2u} FON shown in Fig. 2) obtained by the REKS method are in a good agreement with the exact ensemble KS values, whereas the BS-UKS occupations (the natural orbital's occupation numbers are shown in lieu of FONs) deviate strongly from the exact ones, suggesting that BS-UKS overestimates the effect of the non-dynamic correlation. Furthermore, BS-UKS displays an abrupt onset of the non-dynamic correlation (after ca. $R = 2.75$ bohr), whereas the REKS method yields a smooth transition between the PS-VR and E-VR regimes and a more accurate description of the reaction PES profile.

The comparison vis-à-vis the exact ensemble KS results demonstrates the validity of the approximations made in the REKS working equations. Besides the $H_2 + H_2$ system, the REKS method was applied to study bond-breaking/bond-formation reactions in several chemical systems as well as the electronic structure of biradicals, magnetic coupling in metal complexes and organic charge transfer crystals. The reader is advised to inspect the original publications [37, 38, 42–53, 56, 57] for more examples of the method performance.

3.2 REKS Method for Excited States: SA-REKS and SI-SA-REKS

Let us consider a model system with two strongly correlated electrons in two orbitals, such as the H_2 molecule with the bond stretched beyond the Coulson–Fischer point [84]. Near the equilibrium bondlength, the electronic structure of H_2 is dominated by a single configuration $\left|1\sigma_g 1\overline{\sigma}_g\right\rangle$ and the doubly excited configuration $|1\sigma_u 1\overline{\sigma}_u\rangle$ lies high in energy ($1\sigma_g$ is the bonding MO and $1\sigma_u$ the anti-bonding MO). When the bond is stretched beyond the Coulson–Fischer point, the energy gap between the two electronic configurations narrows to a limit that allows for an efficient mixing of the configurations and the strong non-dynamic electron correlation ensues. In the minimal basis of the two orbitals (the bonding $1\sigma_g$ MO denoted to ϕ_a and the anti-bonding $1\sigma_u$ to ϕ_b), the ground-state wavefunction of stretched H_2 can be represented by a two-configurational wavefunction:

$$\Phi_0 = \sqrt{\frac{n_a}{2}}|\phi_a\overline{\phi}_a\rangle - \sqrt{\frac{n_b}{2}}|\phi_b\overline{\phi}_b\rangle, \tag{25}$$

where n_a and n_b are the FONs of the orbitals ϕ_a and ϕ_b. Promoting a single electron from ϕ_a to ϕ_b orbital leads to a singlet excited state Φ_1 which can be represented by the wavefunction

$$\Phi_1 = \frac{1}{\sqrt{2}}|\phi_a\overline{\phi}_b\rangle + \frac{1}{\sqrt{2}}|\phi_b\overline{\phi}_a\rangle, \tag{26}$$

For a homosymmetric molecule, such as H_2, the two states belong in different symmetry species and therefore do not interact with one another.

Using the ensemble DFT for excited states, described in Sect. 3.1, the excitation energy can be obtained from the variational optimization of the energy of an ensemble of the two states [5]. The ground state (25) can be described by the REKS(2,2) method and the excited state (26) by the spin-restricted open-shell KS (ROKS) method for an open-shell singlet (OSS) state [12, 34]. Within the latter approach, the energy of the OSS state is given by [12, 34]

$$E^{\text{ROKS}} = E_{\text{DFT}}\left[\ldots\phi_a\overline{\phi}_b\right] - \frac{1}{2}E_{\text{DFT}}\left[\ldots\phi_a\phi_b\right] + E_{\text{DFT}}\left[\ldots\overline{\phi}_a\phi_b\right] - \frac{1}{2}E_{\text{DFT}}\left[\ldots\overline{\phi}_a\overline{\phi}_b\right]. \tag{27}$$

The use of the REKS and ROKS energies in (7) leads to the SA-REKS energy expression [39]:

$$E_\omega^{\text{SA-REKS}} = (1-\omega)E^{\text{REKS(2,2)}} + \omega E^{\text{ROKS}}, \tag{28}$$

which is to be variationally optimized with respect to the density of the ensemble of the two states. Similar to the REKS(2,2) method, and to save the computational effort, the minimization with respect to the density is replaced by the minimization with respect to the orbitals and the orbitals' FONs (in the REKS(2,2) energy) [39]. Typically, equal weighting factors, i.e., $\omega = 1/2$, are employed in practical calculations with the SA-REKS method. Having completed the orbital optimization (carried out by the same open-shell SCF method as used in the ground-state REKS calculations) [73], the energies of the individual states are calculated using the common set of orbitals and the excitation energy is obtained by (9).

Let us illustrate how the SA-REKS method works by applying it to the H_2 molecule at varying bondlengths. Aryasetiawan et al. [9] found that the LR-TD-DFT approach in the adiabatic approximation is incapable of correctly describing the dependence of the ${}^1\Sigma_u^+ \leftarrow {}^1\Sigma_g^+$ excitation energy of H_2 on the bondlength. Figure 3 compares the exact excitation energy obtained from the data of [85] with the results of the TD-DFT and SA-REKS calculations carried out using the LC-ωPBE density functional and the cc-pV5Z basis set. Although the SA-REKS excitation energy curve in the lower panel of Fig. 3 is slightly shifted down with respect to the exact curve (the magnitude of the shift is dependent on the XC functional employed), it follows the shape of the exact curve sufficiently accurately and has a shallow minimum around $R_{\text{HH}} = 4.0$ bohr, which is comparable to the exact curve that minimizes at $R_{\text{HH}} = 4.1$ bohr. The adiabatic TD-DFT excitation energy curve does not have a minimum and, at long H–H bondlengths, goes

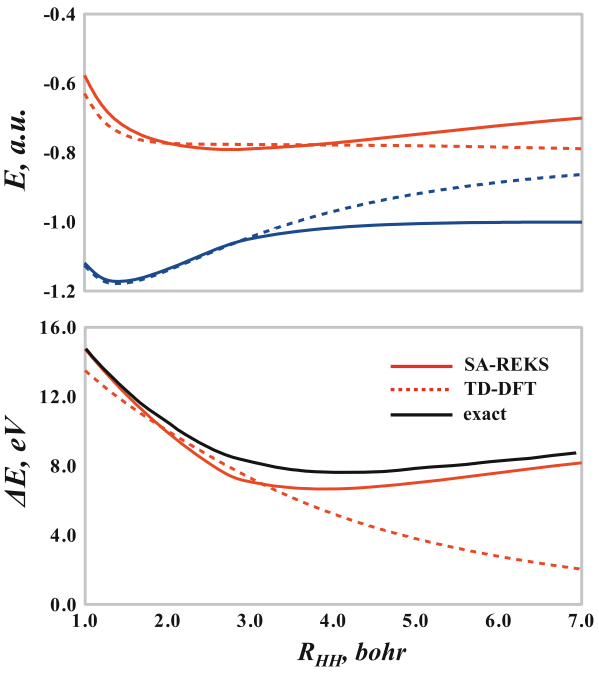

Fig. 3 Potential energy curves (*upper panel*) of the ${}^1\Sigma_g^+$ and ${}^1\Sigma_u^+$ states of H_2 and the ${}^1\Sigma_u^+ \leftarrow {}^1\Sigma_g^+$ excitation energy (*lower panel*) as a function of the H–H distance. *Solid colored curves* (*blue* for the ground state and *red* for the excited state) represent the results of the SA-REKS calculations, *dashed colored curves* refer to TD-DFT, and the *black curve* is the exact excitation energy from [85]. DFT calculations employ the LC-ωPBE density functional and the cc-pV5Z basis set

gradually to zero. As seen in the upper panel of Fig. 3, the SA-REKS method correctly describes the H–H bond dissociation, whereas the single-reference RKS approach fails to yield the correct dissociation limit for the H_2 molecule. Thus, it is the failure of the conventional KS DFT approach to describe the non-dynamic electron correlation for a dissociating covalent bond that is responsible for the failure of TD-DFT to describe correctly the excitation energy of a dissociating molecule.

The described SA-REKS method is capable of describing the ground and excited states of a homosymmetric molecule when the mixing of the two states is prevented by symmetry. In the case of a heterosymmetric molecule, e.g., dissociating LiH, the two states in (25) and (26) are allowed to mix and therefore their representation as a purely covalent state and a purely ionic state is no longer accurate. To correct for this deficiency of the SA-REKS description and to construct an ensemble of two decoupled states, one can obtain a pair of new states by solving a 2×2 secular problem with the Hamiltonian matrix that spans the $E^{\mathrm{REKS}(2,2)}$ and the E^{ROKS} energies as the diagonal elements and the off-diagonal (coupling) element given in (29):

$$H_{01} = \sqrt{n_a}\langle\phi_b|n_a\hat{F}_a|\phi_a\rangle - \sqrt{n_b}\langle\phi_a|n_b\hat{F}_b|\phi_b\rangle = (\sqrt{n_a} - \sqrt{n_b})\varepsilon_{ab} \qquad (29)$$

which was obtained in [40, 41] by applying the Slater–Condon rules in the space of the two CSFs Φ_0 and Φ_1 and the variational condition for the open-shell orbitals ϕ_a

and ϕ_b [34, 35, 77]. In (29), $\hat{F}_a$ and $\hat{F}_b$ are the Fock operators for the open-shell orbitals and ε_{ab} is the off-diagonal Lagrange multiplier[4] in the open-shell Lagrangian [73]. As the two states, Φ_0 and Φ_1, are mutually orthogonal, the average of the new energies E_0 and E_1 obtained from the above secular problem remains the same as the average of the REKS(2,2) and ROKS energies. This implies that the orbitals for the new approach, dubbed SI-SA-REKS or SSR, can still be obtained from the SA-REKS orbital optimization, provided that $\omega = 1/2$ was employed in the latter. In practical applications of the SI-SA-REKS method [40, 41, 59–61], it was found that the described state-interaction scheme is important for obtaining the correct shape of the ground and excited state PESs in the vicinity of conical intersections and near avoided crossings. For other situations, when the energy gap between the ground and excited states is sufficiently wide the SI-SA-REKS method yields nearly the same excitation energies as the SA-REKS method [59].

The argument leading to the SI-SA-REKS method can be proposed based on the adiabatic connection formalism for ensemble DFT as advocated by Fromager et al. [32]. Setting the coupling strength α in the Hamiltonian (15) to zero leads to the degeneracy of the states represented by (25) and (26). Applying the quasi-degenerate perturbation theory results in a 2×2 secular problem $\begin{pmatrix} E_0^\alpha & H_{01}^\alpha \\ H_{10}^\alpha & E_1^\alpha \end{pmatrix}$, where the off-diagonal elements are given by (29) for the intermediate coupling strength. Employing the coupling strength integration and invoking the assumptions used in (22) one arrives at the energy expressions for the ground and excited states of the SI-SA-REKS method (see the paragraph above). It should be noted that, for a homosymmetric molecule, such as H_2, the off-diagonal matrix element vanishes by symmetry and the SI-SA-REKS description collapses to the SA-REKS one.

To illustrate how the SI-SA-REKS method describes dissociation of a heteropolar chemical bond, let us briefly review the ground and the lowest excited singlet states of the LiH molecule. Near the equilibrium bondlength, the ground state of the LiH molecule has ionic character with ca. 0.3 ē shifted to the hydrogen atom. When the Li–H bond dissociates, the ground state undergoes an avoided crossing with the excited state, which has covalent character, and, at the dissociation limit, the ground state corresponds to a covalent configuration with two electrically neutral atoms.

The potential energy curves of the ground $x^1\Sigma^+$ and the excited $a^1\Sigma^+$ states of LiH are shown in Fig. 4. The results of the SI-SA-REKS calculations using the LC-

[4] The matrix of Lagrange multipliers in open-shell SCF becomes Hermitian (but not diagonal) upon convergence to the variational minimum [77].

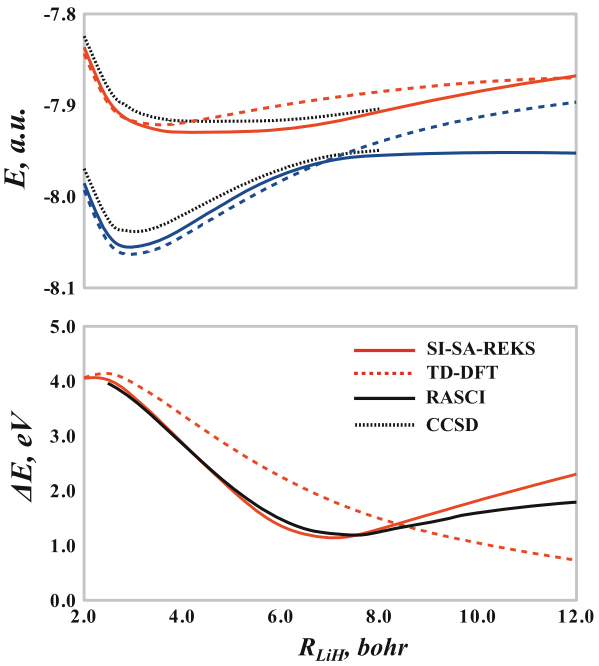

Fig. 4 Potential energy curves (*upper panel*) of the $x^1\Sigma^+$ and $a^1\Sigma^+$ states of LiH and the $x^1\Sigma^+ \leftarrow a^1\Sigma^+$ excitation energy (*lower panel*) as a function of the Li-H distance. *Solid curves* – SI-SA-REKS results, *dashed curves* – TD-DFT results. DFT calculations employ the LC-ωPBE functional and aug-cc-pVTZ basis set. *Solid black curve* in the lower panel shows the reference RASCI excitation energy [86] and the *dotted black curves* in the upper panel show the CCSD energies [31] of the two states

ωPBE functional and the aug-cc-pVTZ basis set are compared with the results of the conventional TD-DFT calculations (with the same basis set and functional) and with the literature data. The $x^1\Sigma^+ \leftarrow a^1\Sigma^+$ excitation energy of LiH was recently studied using an ab initio restricted active space CI (RASCI) method with the aug-cc-pVTZ basis set [86]. For the individual states, the $x^1\Sigma^+$ and the $a^1\Sigma^+$ states, the potential energy curves along the dissociation path were obtained in [31] using the CCSD method (presumably the EOM-CCSD was used to obtain the excited state curve).

As seen in Fig. 4, the SI-SA-REKS potential energy curves follow closely the ab initio results, whereas the conventional KS DFT curves fail to reproduce the correct dependence on distance. Near ca. $R_{\mathrm{LiH}} = 7$ bohr, the two states undergo an avoided crossing as seen in the curves obtained by the ab initio WFT calculations and the SI-SA-REKS calculations. The RKS ground-state curve does not converge to the correct dissociation limit and the ground state remains ionic along the whole dissociation path. The excitation energy from the SI-SA-REKS calculations closely follows the RASCI excitation energy curve and correctly yields the avoided crossing. The TD-DFT excitation energy, although close to the ab initio value near the equilibrium distance, fails to display the correct distance dependence and vanishes at the dissociation limit. This example illustrates yet another failure of the conventional KS DFT/TD-DFT approach to describe the ground and excited state potential energy surfaces of molecules with dissociating bonds (or, more generally, strongly correlated molecular systems). By contrast, the SI-SA-REKS method describes these situations with high accuracy and can be applied with confidence to study the excited states of strongly correlated molecules.

4 Applications of the REKS Method to Excited States

Although the application of the SA-REKS and SI-SA-REKS methods to diatomic molecules in Sect. 3.2 illustrates their capabilities in comparison with the (nearly) exact calculations, a more general benchmarking of the methods is needed to establish them as generally applicable computational schemes. In [59], the accuracy of the SI-SA-REKS method for valence excitations in ordinary (i.e., not strongly correlated) organic molecules was studied. For a set of 15 $\pi \rightarrow \pi^*$ and $n \rightarrow \pi^*$ excitations in aliphatic and aromatic hydrocarbons, it was found that SI-SA-REKS describes these excitations on a par with the widely used linear response methods, such as TD-DFT or ADC(2) [87–91] (second-order algebraic diagrammatic construction; a method based on second-order perturbation expansion of the linear-response polarization propagator).

Table 1 compares the results of the SI-SA-REKS calculations carried out with the BH&HLYP and LC-ωPBE functionals in connection with the aug-cc-pVTZ basis set with the traditional TD-DFT calculations and the best estimates of vertical excitation energies from [92]. The mean absolute deviation (MAD) shown by SI-SA-REKS is nearly the same as for the TD-DFT method with the same density functional. The ab initio WFT technique ADC(2) shows for the same excitation energies a mean deviation of 0.43 eV. These benchmarks show that the SI-SA-

Table 1 The $\pi \rightarrow \pi^*$ and $n \rightarrow \pi^*$ electronic excitation energies (eV) of organic molecules. Symmetry of the excited state is given parenthetically. MAD stands for "mean absolute deviation." All calculations employ the aug-cc-pVTZ basis set

			BH&HLYP[b]		LC-ωPBE[b]	
Molecule	Transition	Best estm.[a]	TD	SSR	TD	SSR
Ethylene	$\pi \rightarrow \pi^*(^1B_{1u})$	7.80	6.93	7.37	7.61	7.61
Butadiene	$\pi \rightarrow \pi^*(^1B_u)$	6.18	5.75	5.59	5.95	5.98
Hexatriene	$\pi \rightarrow \pi^*(^1B_u)$	5.10	4.83	4.64	5.03	5.11
Octatetraene	$\pi \rightarrow \pi^*(^1B_u)$	4.66	4.21	4.01	4.43	4.54
Cyclopropene	$\pi \rightarrow \pi^*(^1B_2)$	7.06	6.28	6.54	6.41	6.57
Cyclopentadiene	$\pi \rightarrow \pi^*(^1B_2)$	5.55	5.05	5.13	5.25	5.23
Norbornadiene	$\pi \rightarrow \pi^*(^1A_2)$	5.34	5.04	5.08	5.37	5.30
Furan	$\pi \rightarrow \pi^*(^1B_2)$	6.32	5.82	6.02	6.20	6.28
Pyrrole	$\pi \rightarrow \pi^*(^1B_2)$	6.57	6.08	6.03	6.35	6.48
Imidazole	$\pi \rightarrow \pi^*(^1A')$	6.19	6.33	6.30	6.56	6.58
	$n \rightarrow \pi^*(^1A'')$	6.81	7.02	6.87	6.86	6.81
Pyridine	$\pi \rightarrow \pi^*(^1B_2)$	4.85	5.64	5.91	5.54	6.24
	$n \rightarrow \pi^*(^1B_1)$	4.59	5.26	5.18	5.17	5.04
Uracil	$\pi \rightarrow \pi^*(^1A')$	5.35	5.54	5.53	5.49	5.71
	$n \rightarrow \pi^*(^1A'')$	4.80	5.26	5.13	5.12	5.20
MAD			0.47	0.43	0.28	0.30

[a]Best estimates of vertical excitation energies from [92]
[b]Geometries are taken from [92]

REKS method can be used as a general purpose computational scheme for describing the valence excitation energies.

Obviously, the ability of the SI-SA-REKS method to describe electronic transitions in strongly correlated molecules enables one to apply this method beyond the realm of applicability of the conventional adiabatic linear-response TD-DFT. Thus, the method was employed to study the optically bright ^1L_a electronic transitions ($^1B_{1u}$ symmetry) in a series of linear *n*-acenes (**1**) [59].

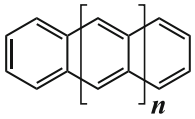

1

These transitions can be accurately described as HOMO → LUMO one-electron transitions and for a few members of the polyacene series the excitation energies were obtained experimentally either in the gas phase (or in solution and corrected for the solvent effects) or in inert gas matrices (see [59] and references cited therein). It was estimated that, with the growing number of fused rings, the ^1L_a excitation energy flattens out at a value of 1.18 ± 0.06 eV extrapolated in [93] from the matrix isolation values.

The results of the SI-SA-REKS calculations are compared in Table 2 with the TD-DFT results and the available experimental data. The TD-DFT excitation energies gradually approach zero as the number of fused rings increases. This

Table 2 ^1L_a ($^1B_{1u}$) excitation energy (eV) of polyacenes. The6-311 + G(2d,p) basis set is employed in DFT calculations

Molecule	Exp.[a]	BH&HLYP[b]		CAM-B3LYP[b]	
		TD	SSR	TD	SSR
Naphthalene	4.44	4.61	4.82	4.56	4.67
Anthracene	3.41	3.48	3.64	3.49	3.55
Tetracene	2.76	2.70	2.85	2.73	2.81
Pentacene	2.21	2.15	2.29	2.19	2.29
Hexacene	1.89	1.73	1.89	1.79	1.91
Heptacene	1.70	1.40	1.57	1.47	1.61
Octacene	1.54	1.11	1.35	1.20	1.40
Nonacene	1.43	0.89	1.20	1.00	1.26
Decacene		0.72	1.11	0.83	1.16
Dodecacene		0.45	1.00	0.59	1.05
Tetradecacene		0.22	0.95	0.40	0.99
Hexadecacene		0.10	0.92	0.29	0.95
Octadecacene		0.19	0.89	0.22	0.93
Icosacene		0.22	0.87	0.17	0.90

[a]Experimental gas phase or matrix isolation excitation energies cited in [59]

[b]Geometries were optimized in [59] using the RE-B3LYP/6-31G* method

feature of TD-DFT excitation energies is independent of the density functional employed (see [59] for more detail) and is another illustration of the failure of the conventional KS DFT approach to strongly correlated systems.

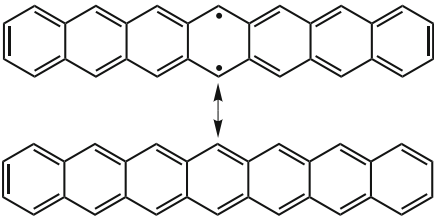

Polyacenes are known to have a strongly correlated ground state and this is illustrated by a sketch of the valence Lewis structures in the diagram above [94]. Therefore the use of multi-reference approaches is mandatory for proper description of their ground state. The single-reference KS DFT is incapable of taking accurate account of the non-dynamic correlation in the ground state of longer polyacenes and the TD-DFT excitation energies become unrealistically low for these molecules. The SI-SA-REKS method describes accurately the ground state of polyacenes and yields excitation energies in good agreement with the experimental figures.

Another situation where the description of the non-dynamic correlation in the ground state becomes important is the real crossing between the ground and lowest excited states of the same spin and space symmetry, the so-called conical intersections. The SI-SA-REKS method was successfully applied to study conical intersections in a series of organic molecules and models of biological chromophores [40, 41, 60, 95], molecular switches [55], and molecular motors [54, 58, 61]. In these applications and benchmarks, the SI-SA-REKS method was capable of describing the geometry at the minimum of the conical intersection seam (the so-called minimum energy conical intersection, MECI) with an accuracy matching high level ab initio multi-reference methods such as MRCI and CASPT2. The results of the application of SI-SA-REKS to conical intersections are described in another chapter of this book;[5] here it is only mentioned that the root mean square deviation of the SI-SA-REKS MECI geometries from the ab initio reference geometries is less than 0.1 Å on average (0.0609 Å was obtained in [95] for a set of 12 MECIs).

Besides being capable of describing excitations of strongly correlated molecular species, the SI-SA-REKS method displays an outstanding performance in other situations which proved to be difficult for standard linear response methods.

[5] See the chapter "Description of conical intersections with density functional methods" by M. Huix-Rotllant, A. Nikiforov, W. Thiel, and M. Filatov.

Table 3 Lowest electronic excitation energy (eV) of cyanine dyes. The aug-cc-pVTZ basis set is employed in DFT calculations

	BH&HLYP[a]		CAM-B3LYP[a]			
Molecule	TD	SSR	TD	SSR	CASPT2[b]	DMC[b]
CN5	5.35	4.87	5.19	4.71	4.69	5.03
CN7	4.19	3.72	4.07	3.65	3.52	3.83
CN9	3.49	3.06	3.39	3.03	2.81	3.09
CN11	3.02	2.62	2.93	2.62	2.46	2.62

[a]Geometries are taken from [96]
[b]CASPT2 and diffusion Monte–Carlo (DMC) data from [101]

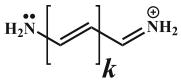

2

In cyanine dyes (**2**), the lowest singlet $^1B_1$ (in C_{2v} symmetry) excited state ($\pi \rightarrow \pi^*$ transition) is notoriously difficult for linear response methods [96–98]. TD-DFT with the commonly available density functionals overestimates the excitation energies by ca. 0.4–0.5 eV; this deviates from the trend typical for TD-DFT which has a tendency to underestimate the valence excitation energies by ca. 0.3–0.4 eV. The cyanine dyes do not have a strongly correlated ground state and it was the incorrect description of the differential correlation effects between the ground and excited states that was blamed for the poor performance of TD-DFT [99]. However, this conjecture was challenged by Ziegler et al. [100] who showed that going beyond the linear response approximation leads to considerable improvement of the calculated excitation energies.[6]

The $^1B_1$ excitation energies in a series of cyanine dyes were studied in [59] with the use of the SI-SA-REKS method in connection with a few commonly available density functionals and the aug-cc-pVTZ basis set. The results of the SI-SA-REKS calculations are compared in Table 3 with TD-DFT and with a number of high level ab initio calculations, the second-order complete active space perturbation theory (CASPT2), and the diffusion Monte–Carlo (DMC) calculations from [96]. The results in Table 3 show that SI-SA-REKS noticeably outperforms TD-DFT in the accuracy of description of the target excitation energies, thus demonstrating the advantage of the ensemble formalism. Indeed, the KS orbitals in the SI-SA-REKS method are variationally optimized for both states, the ground and the excited state, and the good performance of SI-SA-REKS seems to agree with the conclusions of Ziegler et al. [100, 102] drawn from the results of the application of the relaxed constricted variational DFT (RSCF-CV(∞)-DFT) method, a method that goes beyond the linear response and affords a variational optimization of the orbitals

[6] See the chapter "A Constricted Variational Density Functional Theory Approach to the Description of Excited States" by T. Ziegler, M. Krykunov, I. Seidu, and Y. C. Park.

Table 4 Excitation energies (eV) of the lowest CT transitions of the Ar-TCNE adducts. The cc-pVDZ basis set is employed in all DFT calculations

	BLYP[a]		BH&HLYP[a]		LC-ωPBE[a]			
Arene	TD	SSR	TD	SSR	TD	SSR	Lit.[b]	Exp.[c]
Benzene	1.54	3.53	2.96	3.52	4.00	3.69	3.80	3.59
Naphthalene	0.34	2.28	1.84	2.46	3.01	2.74	2.70	2.60
Toluene	1.37	2.72	2.67	3.26	3.65	3.30	3.40	3.36
o-Xylene	1.47	2.61	2.42	2.85	3.40	3.01	3.00	3.15
MAD[d]	2.00	0.39	0.70	0.15	0.34	0.11	0.13	

[a]Geometries are taken from [101]
[b]Literature data: results of TD-DFT calculations using the tuned range separated BNL functional from [101]
[c]Gas phase excitation energies of CT transitions from [106]
[d]Mean absolute deviations from the experimental data

partaking in the electronic transition [100, 102]. The SI-SA-REKS method achieves the same effect by using the ensemble formalism.

The use of ensemble formalism based on the variational principle also turns out to be beneficial for the description of charge transfer transitions. Linear response methods, such as TD-DFT, experience considerable difficulties when describing this type of electronic excitation, especially when used in connection with the commonly available approximate density functionals [103, 104]. Although it was not designed with these particular excitations in mind, the SI-SA-REKS method was found to be surprisingly accurate for charge transfer excitations, even when used in connection with the stock parameterization of the commonly available GGA and hybrid density functionals [105].

Table 4 reports excitation energies of the lowest charge transfer transitions of a series of arene–TCNE (tetracyanoethylene) adducts, for which the gas phase optical absorption spectra are available [106]. For these electronic transitions, the TD-DFT excitation energies obtained with the use of the usual density functionals deviate from the experimental figures by a wide margin and only the use of individually tuned range-separated density functionals brings these errors down to an acceptable level [101]. However, the accuracy achieved with the fine-tuned density functionals is easily surpassed by the SI-SA-REKS method employed in connection with the standard parameterizations of commonly available density functionals. Even when used in connection with the GGA functional, such as BLYP, the SI-SA-REKS method yields more accurate charge transfer excitation energies than does TD-DFT with the use of range-separated hybrid functional (see Table 4). The observed excellent performance of SI-SA-REKS is consistent with the analysis of the description of various types of excitations undertaken by Ziegler et al. [100, 104] who showed that it is the use of approximate density functionals in connection with the adiabatic linear response approximation that is to blame for ludicrous performance of the adiabatic TD-DFT and not the density functional alone.

To conclude this section, ensemble DFT for excited states as implemented in the SI-SA-REKS method is a versatile and accurate approach to the calculation of

various types of excitations in molecular systems. A wide range of excited states, which are otherwise inaccessible with the use of TD-DFT, can be studied, including the charge transfer excitations [105], excitations in extended π-conjugated systems [59], excitations in molecules undergoing bond breaking/bond formation [39], conical intersections between the ground and excited electronic states [40, 41, 54, 55, 58, 60, 61, 95], etc. It is also noteworthy that the SI-SA-REKS results can be obtained at an essentially mean-field cost, avoiding a steeper scaling of the linear response formalism of TD-DFT.

5 Conclusions and Outlook

Ensemble DFT [18, 20, 21, 23, 29] holds considerable promise for theoretical description of the excited states of strongly correlated molecular systems. Although it was conceived more than three decades ago, ensemble DFT still did not find its way to the repertoire of the methods used by computational chemists on a daily basis. Perhaps it is the perceived lack of practical implementations of ensemble DFT that holds down its adoption by a wider computational chemistry community. Although there is a renewed interest in developing ensemble DFT further [31–33] and in implementing it in the form of practically affordable computational schemes, these approaches are largely unknown to ordinary computational chemists.

The REKS computational method, reviewed in this chapter, makes ensemble DFT affordable. The method has already been used to study various types of electronic transitions occurring in usual as well as strongly correlated molecular systems and its ability to describe excitation energies in these systems with a remarkable accuracy has been demonstrated. Although the currently available implementation of the REKS formalism is not free of certain limitations, in particular the size of the active space and the number of excited states are restricted, these limitations will be removed in the near future and this should considerably improve the prospects for practical use of the method. Especially promising for obtaining multiple excited states and for simulating the entire excitation spectra of strongly correlated molecules appears to be a merger of the REKS methodology with the variational constricted DFT formalism proposed by Ziegler et al. [102, 104] (see Footnote 6). The work in these directions is currently in progress and will continue in the future.

References

1. Hohenberg P, Kohn W (1964) Phys Rev 136:B864
2. Kohn W, Sham LJ (1965) Phys Rev 140:A1133
3. Casida ME, Jamorski C, Bohr F, Guan JG, Salahub DR (1994) In: Karna SP, Yeates AT (eds) Nonlinear optical materials: theory and modeling, ACS symposium series, vol. 628, (Am Chem Soc, Div Comp Chem, 1996), ACS Symposium Series, vol. 628, pp 145–163.

Symposium on nonlinear optical materials – theory and modeling, at the 208th National Meeting of the American Chemical Society, Washington, DC
4. Casida ME, Huix-Rotllant M (2012) Annu Rev Phys Chem 63:287
5. Marques MAL, Gross EKU (2003) In: Fiolhais C, Nogueira F, Marques MAL (eds) A primer in density-functional theory, lecture notes in physics, vol 620. Springer, Berlin, pp 144–184
6. Maitra NT, Zhang F, Cave R, Burke K (2004) J Chem Phys 120:5932
7. Cave RJ, Zhang F, Maitra NT, Burke K (2004) Chem Phys Lett 389:39
8. Huix-Rotllant M, Ipatov A, Rubio A, Casida ME (2011) Chem Phys 391:120
9. Aryasetiawan F, Gunnarsson O, Rubio A (2002) Europhys Lett 57:683
10. McWeeny R (1992) Methods of molecular quantum mechanics. Academic, San Diego
11. Slater JC, Wood JH (1970) Int J Quantum Chem S4:3
12. Ziegler T, Rauk A, Baerends EJ (1977) Theor Chim Acta 43:261
13. Gunnarsson O, Lundqvist BI (1976) Phys Rev B 13:4274
14. Kowalczyk T, Yost SR, Van Voorhis T (2011) J Chem Phys 134:054128
15. Gaudoin R, Burke K (2004) Phys Rev Lett 93:173001
16. Gaudoin R, Burke K (2005) Phys Rev Lett 94:029901
17. Li YQ, Pan XY, Li B, Sahni V (2012) Phys Rev A 85:032517
18. Theophilou AK (1979) J Phys C Solid State Phys 12:5419
19. Valone SM (1980) J Chem Phys 73:4653
20. Lieb EH (1983) Int J Quantum Chem 24:243
21. Englisch H, Englisch R (1984) Phys Stat Sol (b) 123:711
22. Englisch H, Englisch R (1984) Phys Stat Sol (b) 124:373
23. Gross EKU, Oliveira LN, Kohn W (1988) Phys Rev A 37:2805
24. Gross EKU, Oliveira LN, Kohn W (1988) Phys Rev A 37:2809
25. Oliveira LN, Gross EKU, Kohn W (1988) Phys Rev A 37:2821
26. Schipper PRT, Gritsenko OV, Baerends EJ (1998) Theor Chem Acc 99:329
27. Schipper PRT, Gritsenko OV, Baerends EJ (1999) J Chem Phys 111:4056
28. Morrison RC (2002) J Chem Phys 117:10506
29. Oliveira LN, Gross EKU, Kohn W (1990) Int J Quantum Chem Quantum Chem Symp 24:707
30. Ullrich CA, Kohn W (2001) Phys Rev Lett 87:093001
31. Pastorczak E, Gidopoulos NI, Pernal K (2013) Phys Rev A 87:062501
32. Franck O, Fromager E (2014) Mol Phys 112:1684
33. Pribram-Jones A, Yang ZH, Trail JR, Burke K, Needs RJ, Ullrich CA (2014) J Chem Phys 140:18A541
34. Filatov M, Shaik S (1998) Chem Phys Lett 288:689
35. Filatov M, Shaik S (1999) Chem Phys Lett 304:429
36. Filatov M, Shaik S (2000) Chem Phys Lett 332:409
37. Filatov M, Shaik S (2000) J Phys Chem A 104:6628
38. Moreira IDPR, Costa R, Filatov M, Illas F (2007) J Chem Theory Comput 3:764
39. Kazaryan A, Heuver J, Filatov M (2008) J Phys Chem A 112:12980
40. Filatov M (2013) J Chem Theory Comput 9:4526
41. Huix-Rotllant M, Filatov M, Gozem S, Schapiro I, Olivucci M, Ferré N (2013) J Chem Theory Comput 9:3917
42. Filatov M, Shaik S (1999) J Phys Chem A 103:8885
43. Filatov M, Shaik S (1999) J Chem Phys 110:116
44. De Visser SP, Filatov M, Shaik S (2000) Phys Chem Chem Phys 2:5046
45. Filatov M, Shaik S, Woeller M, Grimme S, Peyerimhoff SD (2000) Chem Phys Lett 316:135
46. De Visser SP, Filatov M, Shaik S (2001) Phys Chem Chem Phys 3:1242
47. Kraka E, Anglada J, Hjerpe A, Filatov M, Cremer D (2001) Chem Phys Lett 348:115
48. Cremer D, Filatov M, Polo V, Kraka E, Shaik S (2002) Int J Mol Sci 3:604
49. Gräfenstein J, Kraka E, Filatov M, Cremer D (2002) Int J Mol Sci 3:360
50. Filatov M, Cremer D (2003) Phys Chem Chem Phys 5:2320
51. De Visser SP, Filatov M, Schreiner PR, Shaik S (2003) Eur J Org Chem 21:4199

52. Illas F, Moreira IDPR, Bofill JM, Filatov M (2004) Phys Rev B 70:132414
53. Illas F, Moreira IDPR, Bofill JM, Filatov M (2006) Theor Chem Acc 116:587
54. Kazaryan A, Kistemaker JCM, Schäfer LV, Browne WR, Feringa BL, Filatov M (2010) J Phys Chem A 114:5058
55. Filatov M (2011) ChemPhysChem 12:3348
56. Filatov M (2011) Phys Chem Chem Phys 13:12328
57. Filatov M (2011) Phys Chem Chem Phys 13:144
58. Kazaryan A, Lan Z, Schäfer LV, Thiel W, Filatov M (2011) J Chem Theory Comput 7:2189
59. Filatov M, Huix-Rotllant M (2014) J Chem Phys 141:024112
60. Gozem S, Melaccio F, Valentini A, Filatov M, Huix-Rotllant M, Ferré N, Frutos LM, Angeli C, Krylov AI, Granovsky AA, Lindh R, Olivucci M (2014) J Chem Theory Comput 10:3074
61. Filatov M, Olivucci M (2014) J Org Chem 79:3587
62. Zhao Q, Morrison RC, Parr RG (1994) Phys Rev A 50:2138
63. Sinanoglŭ O (1964) Adv Chem Phys 6:315
64. Giesbertz KJH, Baerends EJ (2010) J Chem Phys 132:194108
65. Kohn W (1986) Phys Rev A 34:737
66. Andrejkovics I, Nagy Á (1998) Chem Phys Lett 296:489
67. Paragi G, Gyémánt IK, Van Doren VE (2000) Chem Phys Lett 324:440
68. Paragi G, Gyémánt IK, Van Doren VE (2001) J Mol Struct Theochem 571:153
69. Noziéres P, Pines D (1966) The theory of quantum liquids. Perseus Books Publishing LLC, Cambridge
70. Becke AD (1988) J Chem Phys 88:1053
71. Wang SG, Schwarz WHE (1996) J Chem Phys 105:4641
72. Csányi G, Arias T (2000) Phys Rev B 61:7348
73. Filatov M (2015) WIREs Comput Mol Sci 5:146
74. Lathiotakis NN, Helbig N, Rubio A, Gidopoulos NI (2014) Phys Rev A 90:032511
75. Fernandez JJ, Kollmar C, Filatov M (2010) Phys Rev A 82:022508
76. Farid B (1998) J Phys Condens Matter 10:L1
77. Hirao K, Nakatsuji H (1973) J Chem Phys 59:1457
78. Hoffmann R, Woodward RB (1965) J Am Chem Soc 87:395
79. Hoffmann R, Woodward RB (1965) J Am Chem Soc 87:2046
80. Woodward RB, Hoffmann R (1969) Angew Chem Int Ed 8:781
81. Vydrov OA, Heyd J, Krukau A, Scuseria GE (2006) J Chem Phys 125:074106
82. Vydrov OA, Scuseria GE (2006) J Chem Phys 125:234109
83. Vydrov OA, Scuseria GE, Perdew JP (2007) J Chem Phys 126:154109
84. Coulson CA, Fischer I (1949) Philos Mag 40:386
85. Kolos W, Wolniewicz L (1965) J Chem Phys 43:2429
86. Van Meer R, Gritsenko OV, Baerends EJ (2014) J Chem Phys 140:024101
87. Schirmer J (1982) Phys Rev A 26:2395
88. Schirmer J, Trofimov AB (1995) J Phys B At Mol Opt Phys 28:2299
89. Trofimov AB, Stelter G, Schirmer J (1999) J Chem Phys 111:9982
90. Trofimov AB, Stelter G, Schirmer J (2002) J Chem Phys 117:6402
91. Schirmer J, Trofimov AB (2004) J Chem Phys 120:11449
92. Silva-Junior MR, Schreiber M, Sauer SPA, Thiel W (2008) J Chem Phys 129:104103
93. Tönshoff C, Bettinger HF (2010) Angew Chem Int Ed 49:4125
94. Plasser F, Pašalić H, Gerzabek MH, Libisch F, Reiter R, Burgdörfer J, Müller T, Shepard R, Lischka H (2013) Angew Chem Int Ed 52:2581
95. Nikiforov A, Gamez JA, Thiel W, Huix-Rotllant M, Filatov M (2014) J Chem Phys 141: 124122
96. Send R, Valsson O, Filippi C (2011) J Chem Theory Comput 7:444
97. Jacquemin D, Zhao Y, Valero R, Adamo C, Ciofini I, Truhlar DG (2012) J Chem Theory Comput 8:1255
98. Moore B II, Autschbach J (2013) J Chem Theory Comput 9:4991

99. Grimme S, Neese F (2007) J Chem Phys 127:154116
100. Zhekova H, Krykunov M, Autschbach J, Ziegler T (2014) J Chem Theory Comput 10:3299
101. Stein T, Kronik L, Baer R (2009) J Am Chem Soc 131:2818
102. Krykunov M, Ziegler T (2013) J Chem Theory Comput 9:2761
103. Dreuw A, Weisman JL, Head-Gordon M (2003) J Chem Phys 119:2943
104. Krykunov M, Seth M, Ziegler T (2014) J Chem Phys 140:18A502
105. Filatov M (2014) J Chem Phys 141:124123
106. Hanazaki I (1972) J Phys Chem 76(14):1982

Top Curr Chem (2016) 368: 125–184
DOI: 10.1007/128_2015_624

Published online: 14 May 2015

Reduced Density Matrix Functional Theory (RDMFT) and Linear Response Time-Dependent RDMFT (TD-RDMFT)

Katarzyna Pernal and Klaas J.H. Giesbertz

Abstract Recent advances in reduced density matrix functional theory (RDMFT) and linear response time-dependent reduced density matrix functional theory (TD-RDMFT) are reviewed. In particular, we present various approaches to develop approximate density matrix functionals which have been employed in RDMFT. We discuss the properties and performance of most available density matrix functionals. Progress in the development of functionals has been paralleled by formulation of novel RDMFT-based methods for predicting properties of molecular systems and solids. We give an overview of these methods. The time-dependent extension, TD-RDMFT, is a relatively new theory still awaiting practical and generally useful functionals which would work within the adiabatic approximation. In this chapter we concentrate on the formulation of TD-RDMFT response equations and various adiabatic approximations. None of the adiabatic approximations is fully satisfactory, so we also discuss a phase-dependent extension to TD-RDMFT employing the concept of phase-including-natural-spinorbitals (PINOs). We focus on applications of the linear response formulations to two-electron systems, for which the (almost) exact functional is known.

Keywords Density matrix functional · Reduced density matrix · Density matrix functional theory · Time-dependent density matrix functional · Electron correlation

K. Pernal (✉)
Institute of Physics, ul. Wolczanska 219, 90-924 Lodz, Poland
e-mail: pernalk@gmail.com

K.J.H. Giesbertz
Theoretical Chemistry, VU University, De Boelelaan 1083, 1081 HV Amsterdam, The Netherlands
e-mail: k.j.h.giesbertz@vu.nl

Contents

1 Introduction

The most widely used methods in quantum chemistry are either wavefunction-based or they exploit density functional theory (DFT). The former class of methods offers high accuracy, but unfavorable scaling of the computational cost with system size limits their scope of applicability to relatively small systems. Density functional approximations are known to offer a good balance between computational efficiency and accuracy. Nevertheless, most approximations to DFT are plagued by generic problems related to the fact that DFT employs a simple local object – the electron density. Accurate description of the electronic structure of multireference systems or predicting multiple electronic excitations are examples of problems that still await satisfactory solutions in DFT. There has recently been growing interest in approaches embracing simplicity (in the sense that a wavefunction is not involved), computational efficiency, and versatility of DFT, while lacking the drawbacks. Functionals of one-electron reduced density matrix (1-RDM) γ, defined for an N-electron wavefunction Ψ as

$$\gamma(\mathbf{x},\mathbf{x}') = N\int\cdots\int \Psi(\mathbf{x},\mathbf{x}_2,\ldots,\mathbf{x}_N)\Psi^*(\mathbf{x}',\mathbf{x}_2,\ldots,\mathbf{x}_N)\mathrm{d}\mathbf{x}_2\cdots\mathrm{d}\mathbf{x}_N, \qquad (1)$$

where $\mathbf{x} = (\mathbf{r}, s)$ is a combined spatial and spin coordinate, should, in principle, lead to formulating methods superior to existing density functional approximations, especially when static electron correlation effects cannot be neglected. An immediate advantage of using 1-RDM as a main variable instead of the electron density, ρ, is that the kinetic energy is an explicit functional of γ but not of ρ. Thus, in

reduced (one-electron) density matrix functional theory (RDMFT) there is no need to introduce a fictitious noninteracting system. Moreover, orbitals present in RDMFT are fractionally occupied so functionals of γ seem to be better suited than their density counterparts to account for static correlation and, for example, describe correctly a covalent bond-breaking process. As discussed in this chapter, this presumption has been confirmed by a good performance of the most successful density matrix functionals.

Although the theoretical foundations of RDMFT were set a long time ago [1–11], functionals of practical usefulness which can compete with density functionals in accuracy have only recently been proposed. In this section we present the main ingredients of RDMFT (theorems, definitions, and conditions) and first approximate density matrix functionals proposed for electronic systems. In the following sections more recent and successful developments in RDMFT are shown.

Self-adjointness of γ defined in (1) allows for its spectral representation, namely [12]

$$\gamma(\mathbf{x},\mathbf{x}') = \sum_p n_p \varphi_p(\mathbf{x}) \varphi_p^*(\mathbf{x}'). \tag{2}$$

Eigenvalues of 1-RDM, $\{n_p\}$, are called natural occupation numbers, whereas its eigenfunctions, $\{\varphi_p\}$, are known as natural spinorbitals. Throughout the chapter we assume a convention that the indices p, q, r, s pertain to natural spinorbitals and a, b, c, d to arbitrary one-electron functions. Self-adjointness of γ implies orthonormality of the natural spinorbitals. Additionally, because γ is assumed to be normalized to a number of electrons N, cf. definition given in (1), the natural occupancies sum up to N. Taking into account that each n_p is nonnegative and not greater than 1 [2, 3], the overall properties of the natural spinorbitals and occupation numbers read

$$\forall_{p,q} \int \varphi_p^*(\mathbf{x}) \varphi_q(\mathbf{x}) \mathrm{d}\mathbf{x} = \delta_{pq}, \tag{3}$$

$$\forall_p \quad 0 \le n_p \le 1, \tag{4}$$

$$\sum_p n_p = N. \tag{5}$$

Coleman [2] has proved that if a given Hermitian 1-RDM satisfies the conditions (3)–(5) there exists an ensemble of N-electron antisymmetric wavefunctions that yield γ. The conditions are called N-representability conditions. It should be noted that similar sufficient and necessary conditions that would ensure pure-state N-representability are not known, though some significant progress has been reported by Klyachko [A.A. Klyachko, J. Phys. Conf. Ser. 36, 72–86 (2006), doi: 10.1088/1742-6596/36/1/014].

A one-to-one mapping between pure-state v-representable 1-RDMs and non-degenerate ground state wavefunctions has been demonstrated by Gilbert who extended the Hohenberg–Kohn theorem to nonlocal potentials [1, 13]. This establishes existence of a 1-RDM functional [1, 11]

$$E_v^{\mathrm{HK}}[\gamma] = \mathrm{Tr}\left[\hat{h}\,\hat{\gamma}\right] + \left\langle \Psi[\gamma] \middle| \hat{V}_{\mathrm{ee}} \middle| \Psi[\gamma] \right\rangle, \tag{6}$$

where $\hat{h}$ stands for a one-electron Hamiltonian comprising kinetic energy and external potential operators,

$$\hat{h} = \hat{t} + \hat{v}_{\mathrm{ext}}, \tag{7}$$

$\hat{V}_{\mathrm{ee}} = \sum_{i>j}^{N} \frac{1}{r_{ij}}$ is an electron interaction operator (note that atomic units are employed throughout the chapter), and $\Psi[\gamma]$ denotes a ground state wavefunction pertinent to a v-representable γ. A variational principle for the functional defined in (6) exists and reads

$$\forall_{\gamma \in v\text{-rep}} \quad E_v[\gamma] \geq E_0\,, \tag{8}$$

where "v-rep" denotes a set of pure-state v-representable 1-RDMs. The equality is achieved for a ground state density matrix. Levy extended the domain of a density matrix functional to all pure-state N-representable 1-RDMs by defining the electron repulsion functional as [4, 5]

$$E_{\mathrm{ee}}^{L}[\gamma] = \min_{\Psi \to \gamma} \left\langle \Psi \middle| \hat{V}_{\mathrm{ee}} \middle| \Psi \right\rangle. \tag{9}$$

The minimization is carried out in a set of all physically admissible wavefunctions Ψ that yield a given 1-RDM γ. Levy's constrained search definition has been further extended to ensemble N-representable 1-RDMs (belonging to a set "N-rep") by Valone [7, 8] and the exact functional reads

$$E_{\mathrm{ee}}[\gamma] = \min_{\Gamma^{(N)} \to \gamma} Tr\left[\hat{\mathrm{H}}\,\hat{\Gamma}^{(N)}\right], \tag{10}$$

where the minimization is carried out with respect to N-electron density matrices $\Gamma^{(N)}$ that yield γ. Because of the linearity of the map $\Gamma^{(N)} \to \gamma$ and the fact that the set of N-representable γ is convex, a functional $E_{\mathrm{ee}}[\gamma]$ is also convex [6]. For a given external potential $\hat{v}_{\mathrm{ext}}$, minima of the Hohenberg–Kohn functional given in (6), the Levy functional $\mathrm{Tr}\left[\hat{h}\,\hat{\gamma}\right] + E_{\mathrm{ee}}^{\mathrm{L}}[\gamma]$ (9), and the functional $\mathrm{Tr}\left[\hat{h}\,\hat{\gamma}\right] + E_{\mathrm{ee}}[\gamma]$ (10), defined, respectively, for v-rep, pure-state N-representable, and ensemble N-representable (N-rep) 1-RDMs, coincide [7, 9]. Therefore, taking into account a variational principle given in (8), one concludes that a functional defined for N-rep 1-RDMs yields a ground state energy at minimum, i.e.,

$$E_0 = \min_{\gamma \in N\text{-rep}} \left\{ \mathrm{Tr}\left[\hat{h}\,\hat{\gamma}\right] + E_{\mathrm{ee}}[\gamma] \right\}. \tag{11}$$

A great advantage of working with functionals defined for (ensemble) N-representable γs is that sufficient and necessary conditions for N-representability are known. Equation (11) together with (3)–(5) are a foundation for RDMFT.

The definition of the exact functional (10) is of little practical use in developing approximate functionals. However, in two cases exact forms of $E_{\mathrm{ee}}[\gamma]$ are known, providing some guidelines for developing generally applicable approximate functionals. The first case corresponds to N-electron noninteracting systems. The 1-RDM corresponding to a single determinantal wavefunction is idempotent which implies integer (0 or 1) values of the natural occupation numbers, i.e.,

$$\hat{\gamma}^2 = \hat{\gamma} \quad \Leftrightarrow \quad \forall_p \quad n_p = 0 \quad \bigvee \quad n_p = 1\,. \tag{12}$$

A two-electron reduced density matrix Γ (2-RDM), defined for a general wavefunction Ψ as

$$\Gamma\left(\mathbf{x}_1, \mathbf{x}_2, \mathbf{x}_1'\mathbf{x}_2'\right) = N(N-1)\int\cdots\int \Psi(\mathbf{x}_1, \mathbf{x}_2, \mathbf{x}_3, \ldots, \mathbf{x}_N)\Psi^*\left(\mathbf{x}_1', \mathbf{x}_2', \mathbf{x}_3, \ldots, \mathbf{x}_N\right)\mathrm{d}\mathbf{x}_3\cdots\mathrm{d}\mathbf{x}_N, \tag{13}$$

is explicitly expressible in terms of 1-RDM if the wavefunction takes the form of a Slater determinant, namely

$$\Gamma\left(\mathbf{x}_1, \mathbf{x}_2, \mathbf{x}_1'\mathbf{x}_2'\right) = \gamma\left(\mathbf{x}_1, \mathbf{x}_1'\right)\gamma\left(\mathbf{x}_2, \mathbf{x}_2'\right) - \gamma\left(\mathbf{x}_1, \mathbf{x}_2'\right)\gamma\left(\mathbf{x}_2, \mathbf{x}_1'\right). \tag{14}$$

The electron interaction functional corresponding to such a noninteracting 2-RDM reads

$$E_{\mathrm{ee}}^{\mathrm{HF}}[\gamma] = E_{\mathrm{H}}[\gamma] + E_{\mathrm{x}}[\gamma]. \tag{15}$$

We refer to it as Hartree–Fock functional (thus the superscript HF) because optimization of the functional which is a sum of the one-electron part and $E_{\mathrm{ee}}^{\mathrm{HF}}$ with respect to N-representable γ leads to an idempotent density matrix coinciding with the solution to the Hartree–Fock equations [14]. The HF functional (15) comprises two components. The Hartree functional, E_{H}, describes the classical part of electron interaction, namely

$$E_{\mathrm{H}}[\gamma] = \frac{1}{2}\int\int \frac{\gamma(\mathbf{x}, \mathbf{x})\gamma(\mathbf{x}', \mathbf{x}')}{|\mathbf{r} - \mathbf{r}'|}\mathrm{d}\mathbf{x}\mathrm{d}\mathbf{x}', \tag{16}$$

whereas the exchange functional, E_{x}, reads

$$E_{\mathrm{x}}[\gamma] = -\frac{1}{2}\int\int \frac{\gamma(\mathbf{x}, \mathbf{x}')\gamma(\mathbf{x}', \mathbf{x})}{|\mathbf{r} - \mathbf{r}'|}\mathrm{d}\mathbf{x}\mathrm{d}\mathbf{x}'. \tag{17}$$

Another paradigm case for which an exact density matrix functional is known, is a two-electron closed-shell system. We discuss this case extensively in Sect. 2.1.

The two cases, namely a noninteracting N-electron system and an interacting two-electron species, cover two extreme regimes of electron correlation for an electron pair: the former pertains to an uncorrelated pair, whereas the latter, applied to electrons separated in space (e.g., H_2 molecule in a dissociation limit), describes strongly correlated electrons. In other words, exact density matrix functionals for an uncorrelated and a strongly correlated electron pair are known. Ideally, a valid approximate functional should reduce to exact functionals for both cases.

In developing approximate functionals it is convenient to separate out the Hartree functional given in (16) from the electron repulsion E_{ee} functional defined in (10) and to search for approximations to the exchange-correlation complement E_{xc} defined as

$$E_{xc}[\gamma] = E_{ee}[\gamma] - E_H[\gamma]. \tag{18}$$

The exchange-correlation functional can be further decomposed into an exchange part given in (17) and the remainder called the correlation functional E_c

$$E_c[\gamma] = E_{xc}[\gamma] - E_x[\gamma]. \tag{19}$$

A number of conditions satisfied by the exact E_{ee} functional or its correlation component E_c have been revealed, cf. [5, 15–17], and some of them are invoked in this chapter.

The first realization of the approximate density matrix functional has been given by Müller [18] and it was later independently derived from more physical arguments by Buijse and Baerends [19, 20]. The exchange-correlation part of the functional called either Müller functional or BB (we adhere to the latter name) reads

$$E_{xc}^{BB}[\gamma] = -\frac{1}{2}\sum_{pq}\sqrt{n_p n_q}\langle pq|qp\rangle, \tag{20}$$

where the natural occupation numbers $\{n_p\}$ and the spinorbitals $\{\varphi_p\}$ are eigenvalues and eigenfunctions of γ and the exchange integrals $\{\langle pq|qp\rangle\}$ are written in the representation of the natural spinorbitals. The following notation is adopted in this chapter for two-electron integrals

$$\langle pq|rs\rangle = \iint \varphi_p^*(\mathbf{x}_1)\varphi_q^*(\mathbf{x}_2)|\mathbf{r}_1 - \mathbf{r}_2|^{-1}\varphi_r(\mathbf{x}_1)\varphi_s(\mathbf{x}_2)\,d\mathbf{x}_1 d\mathbf{x}_2. \tag{21}$$

The BB functional is convex [21] and reduces to the exchange functional (17) for an idempotent γ. It is not exact for two-electron systems, though. It has been shown that this functional severely overestimates correlation energy of atoms and molecules [22–27]. However, the BB functional has been successfully used as a base for developing more sophisticated functionals, as discussed in Sect. 2.1.

Goedecker and Umrigar (GU) have modified the BB functional by removing diagonal ($p = q$) terms, called electron self-interaction, from the Hartree and the

exchange-correlation BB functionals [28, 29], and thus the xc part of the GU functional reads

$$E_{\mathrm{xc}}^{\mathrm{GU}}[\gamma] = -\frac{1}{2}\sum_{pq}\sqrt{n_p n_q}\langle pq|qp\rangle + \frac{1}{2}\sum_{p}\left(n_p - n_p^2\right)\langle pp|pp\rangle. \tag{22}$$

GU offers an improvement to the BB functional for atoms and molecules around their equilibrium geometries [28, 30] but it is in large error in the bond dissociation region of diatomic molecules [22, 25, 27]. Another simple xc functional – corrected Hartree–Fock (CHF) – has been proposed by Csanyi and Arias [31]

$$E_{\mathrm{xc}}^{\mathrm{CHF}} = -\frac{1}{2}\sum_{pq}\left(n_p n_q + \sqrt{n_p(1-n_p)n_q(1-n_q)}\right)\langle pp|pp\rangle. \tag{23}$$

Even though the correlation part of the CHF functional satisfies the particle-hole symmetry condition, cf. (30), which is also satisfied by the exact functional [15], it provides little or no improvement over the HF method for molecules around the equilibrium distances, and it breaks down in the dissociation limit [22, 32].

Although the aforementioned first generation of density matrix functionals has not turned out to be overall competitive with DFT approximations, understanding the origins of their failures has provided insight to developing more advanced and successful functionals described in the next section.

2 Construction of Density Matrix Functionals

Because of the two-particle nature of the electron interaction, given a system described by a ground state wavefunction $|0\rangle$, the electronic repulsion energy E_{ee} results from contraction of the two-electron reduced density matrix elements Γ_{abcd} with two-electron integrals $\langle ab|cd\rangle$, namely

$$E_{\mathrm{ee}} = \frac{1}{2}\sum_{abcd}\Gamma_{abcd}\langle cd|ab\rangle, \tag{24}$$

where, for a given basis set $\{\chi_a\}$ and the pertinent sets of the creation and annihilation operators $\{\hat{a}^\dagger\}$, $\{\hat{a}\}$, the elements of the 2-RDM are defined as

$$\Gamma_{abcd} = \langle 0|\hat{c}^\dagger\hat{d}^\dagger\hat{b}\,\hat{a}\,|0\rangle. \tag{25}$$

Formally, the 2-RDM is a functional of the 1-RDM. Most approaches to approximating the electron–electron interaction functional (10) exploit the formula given in (24) and assume that the elements of Γ are functions of the natural occupation numbers $\{n_p\}$. Consequently, if natural spinorbitals $\{\varphi_p\}$ are used as a basis set, the

whole dependence of the E_{ee} functional on the natural spinorbitals is included in two-electron integrals, which gives rise to the form

$$E_{\mathrm{ee}}[\gamma] = \frac{1}{2}\sum_{pqrs} \Gamma_{pqrs}[\{n_t\}]\langle rs|\, pq\rangle. \tag{26}$$

This assumption is borrowed from the Hartree–Fock approximation, cf. (14), in which elements of the 2-RDM in the representation of the natural spinorbitals are given solely in terms of the occupation numbers, i.e.,

$$\Gamma^{\mathrm{HF}}_{pqrs} = n_p n_q \big(\delta_{pr}\delta_{qs} - \delta_{ps}\delta_{qr}\big). \tag{27}$$

The functional $E_{\mathrm{ee}}[\gamma]$ in most approximations proposed so far is an explicit function of the occupation numbers and the natural spinorbitals.

Developing an approximate correlation functional, cf. (19), begins with assuming a cumulant expansion of 2-RDM [33] which consists of writing Γ as the antisymmetrized product of γ and the cumulant part, λ being a functional of γ,

$$\Gamma_{pqrs} = n_p n_q \big(\delta_{pr}\delta_{qs} - \delta_{ps}\delta_{qr}\big) + \lambda_{pqrs}[\gamma]. \tag{28}$$

A cumulant expansion gives rise to the following expression for E_{c}

$$E_{\mathrm{c}}[\gamma] = \frac{1}{2}\sum_{pqrs} \lambda_{pqrs}[\gamma]\langle rs|\, pq\rangle. \tag{29}$$

It has been shown that the exact correlation 1-RDM functional possesses a particle-hole symmetry [15]

$$E_{\mathrm{c}}[\gamma] = E_{\mathrm{c}}[1-\gamma] \tag{30}$$

(this symmetry should be understood as invariance of E_{c} to the following replacement $\forall_p\ n_p \to (1-n_p)$) and scales linearly under homogeneous scaling of coordinates in $\gamma(\mathbf{x}, \mathbf{x}')$ [5]

$$E_{\mathrm{c}}\big[\gamma_\eta\big] = \eta E_{\mathrm{c}}[\gamma], \tag{31}$$

where coordinates in γ_η are scaled with a real number η and the normalization is preserved, i.e.,

$$\gamma_\eta(\mathbf{x}, \mathbf{x}') = \eta^3 \gamma(\eta\mathbf{x}, \eta\mathbf{x}'). \tag{32}$$

Some density matrix functionals rely on the reconstruction scheme given in (28). In other cases, the exchange-correlation functional (18) is not partitioned any further and is modeled as a whole. Different approaches to approximating electron–electron density matrix functionals proposed in recent years are discussed in the remaining part of this section.

2.1 Functionals Based on a Paradigm Two-Electron Case

Homogeneous electron gas (HEG) is a paradigm system for density functionals. This is because the exact form of the exchange density functional for this system is known and a highly accurate correlation energy functional is available. Consequently, electron gas has been a reference system for most approximate density functionals and their forms are such that exact energy for a homogeneous electron density is recovered. The situation is different in RDMFT because the exchange-correlation density matrix functional for HEG is not known. However, the exact density matrix functional is available for a two-electron system [29, 34], so it is now considered to be a paradigm in RDMFT. A two-electron molecule seems to be even a more adequate reference than the homogeneous electron gas if one aims at developing a functional accurately describing electronic structure of molecules.

A form of the two-electron density matrix functional can be immediately formulated based on the work of Löwdin and Shull (LS) [35] who showed that in a basis of the natural spinorbitals $\{\varphi_p\}$ a Slater-determinant-expansion of a singlet wavefunction (assumed to be real-valued) is entirely given by "diagonal" determinants composed of spinorbitals sharing spatial parts, i.e.,

$$\Psi^{\mathrm{LS}} = \sum_p c_p \left|\varphi_p \varphi_{\overline{p}}\right|, \tag{33}$$

where p and $\overline{p}$ are spinorbitals of the opposite spin and $\left|\varphi_p \varphi_{\overline{p}}\right|$ denotes a normalized Slater determinant. The normalization of the wavefunction imposes the following condition of the expansion coefficients $\{c_p\}$

$$\sum_p c_p^2 = 1. \tag{34}$$

Employing the LS wavefunction given in (33) in (1) defining 1-RDM, one immediately obtains γ in its spectral representation, which indicates that squares of the expansion coefficients are simply the natural occupation numbers, i.e.,

$$\forall_p \quad n_p = c_p^2 . \tag{35}$$

Taking the expectation value of the Hamiltonian with the LS wavefunction (33) leads to a simple expression for the energy

$$E = \sum_p c_p^2 h_{pp} + \frac{1}{2}\sum_{pq} c_p c_q \langle pp|qq\rangle, \tag{36}$$

where the indices p, q correspond to indices of the natural spinorbitals. It should be noted that (36) is valid for a closed-shell system so it is assumed that the coefficients corresponding to spinorbitals of opposite spins and same spatial parts are equal.

The exact ground state energy for a two-electron system follows by minimizing the energy with respect to the expansion coefficients $\{c_p\}$ and the natural spinorbitals $\{\varphi_p\}$ under the orthonormality condition for the orbitals and a normalization condition given in (34). An exact electron interaction density matrix functional can be immediately written as

$$E_{\mathrm{ee}}^{\mathrm{LS}}[\gamma] = \frac{1}{2} \min_{\{f_q\}} \sum_{pq} f_p f_q \sqrt{n_p n_q} \langle pq|qp\rangle, \tag{37}$$

$$\forall_p \quad f_p = \pm 1\,, \tag{38}$$

where it has been taken into account that the orbitals are real so the integrals $\langle pp|qq\rangle$ are equal to the exchange integrals $\langle pq|qp\rangle$, and the relation (35) between expansion coefficients in the LS wavefunction and the occupation numbers have been exploited. It is known that for two-electron atoms and molecules at equilibrium geometry the sign of the factor f_1 corresponding to the highest occupation n_1 is predominantly opposite to signs $\{f_p\}$ of all other factors corresponding to weakly occupied $\left(n_p < \frac{1}{2}\right)$ orbitals [29]. It should be noted that cases when this rule is violated are known and they include, for example, a hydrogen molecule far from equilibrium bond distance [36–38] or a strongly correlated Hooke's atom [39]. In such cases, natural orbitals that violate the phase rule, i.e., those orbitals whose phase factor coincides with f_1, are very weakly occupied and their contribution to the energy is small. Consequently, a two-electron functional explicitly depending on the occupation numbers defined as

$$\widetilde{E}_{\mathrm{ee}}^{\mathrm{LS}}[\gamma] = \frac{1}{2} \sum_{pq} G_{pq}^{\mathrm{LS}} \langle pq|qp\rangle, \tag{39}$$

$$G_{pq}^{\mathrm{LS}} = \begin{cases} n_p & p = q \\ -\sqrt{n_p n_q} & p = 1, q > 1 \quad \text{or} \quad p > 1, q = 1\,, \\ \sqrt{n_p n_q} & \text{otherwise} \end{cases} \tag{40}$$

is not always fully equivalent to the exact LS functional (37) but it provides a very good approximation to it. Inspecting the structure of the functional (39), it is evident that terms corresponding to two weakly occupied orbitals (p, $q > 1$) are treated differently (enter the functional with a different signs) from products of strongly-weakly occupied orbitals ($p = 1$, $q > 1$ or $p > 1$, $q = 1$).

Evidently the form of the BB functional given in (20) does not reflect the orbital structure of the functional for two electrons given in (39). Restoring this structure and correcting for the overcorrelation by the BB functional have been motivations behind proposing a number of corrections to it [27]. This has resulted in the development of BB-corrected (BBC) functionals consisting of the Hartree part (16) and the exchange-correlation functional comprising products of exchange integrals and occupation number depending factors G_{pq}^{BBC}, namely

$$E_{\mathrm{ee}}^{\mathrm{BBC}}[\gamma] = \frac{1}{2}\sum_{pq} n_p n_q \langle pp|qq\rangle + \frac{1}{2}\sum_{pq} G_{pq}^{\mathrm{BBC}} \langle pq|qp\rangle. \tag{41}$$

In definitions of the BBC functionals, spinorbitals of the occupancies smaller than 1/2 are called weakly occupied, although those with occupation numbers exceeding 1/2 belong to a set of strongly occupied orbitals (it should be noted that only in the limit of strong correlation are some natural occupation numbers exactly equal to 1/2). Note also that the BB functional is recovered from (41) upon setting $G_{pq}^{\mathrm{BBC}} = -\sqrt{n_p n_q}$. A comparison of the orbital structure of the BB functional with that of the accurate two-electron functional (39) has led to proposing a correction restoring positive signs of cross products between weakly occupied natural spinorbitals. Such a corrected BB functional, named BBC1, conforms to a general form of (41) after assuming

$$G_{pq}^{\mathrm{BBC1}} = \begin{cases} \sqrt{n_p n_q} & p \neq q, \quad p,q \in \text{weak}, \\ -\sqrt{n_p n_q} & \text{otherwise}, \end{cases} \tag{42}$$

where p, $q \in$ weak denotes that both spinorbitals are weakly occupied. Self-consistent calculations revealed that, similar to BB, BBC1 overbinds diatomic molecules, which indicates a need for further repulsive corrections [27]. The BBC2 functional emerged after correcting interaction between two different strongly occupied orbitals and replacing square roots of products of the pertinent occupancies with products $n_p n_q$. The third functional, BBC3, is a result of adding another two corrections to the BBC2 functional. In the BBC3 functional a pair of bonding and antibonding (both called frontier) spinorbitals which form a breaking bond is distinguished. It is assumed that a bonding orbital belongs only to a set of frontier orbitals, and that, at the same time, antibonding orbitals belong to sets of frontier and weakly occupied orbitals. The first BBC3 correction, added on top of the BBC1 and BBC2 corrections, replaces square roots of products of occupation numbers with pertinent products if one occupancy corresponds to an antibonding orbital and the other to a strongly occupied one. The replacement does not affect pairs of antibonding-bonding orbitals. The second correction removes self-interaction from all orbitals except the frontier (i.e., bonding and antibonding) orbitals. The form of the G_{pq} elements in the BBC3 functional therefore read

$$G_{pq}^{\mathrm{BBC3}} = \begin{cases} \sqrt{n_p n_q} & \begin{array}{l} p \neq q, \quad p,q \in \text{weak}, \\ p \in \text{weak}, \quad q \in \text{frontier (weak)} \\ p \in \text{frontier (weak)}, \quad q \in \text{weak} \end{array} \\ -n_p n_q & \begin{array}{l} p \neq q, \quad p,q \in \text{strong}, \\ p \in \text{strong}, \quad q \in \text{frontier}, \\ p \in \text{frontier}, \quad q \in \text{strong}, \end{array} \\ -n_p^2 & p = q, \quad p \notin \text{frontier}, \\ -\sqrt{n_p n_q} & \text{otherwise}, \end{cases} \tag{43}$$

where the frontier (weak) spinorbitals are those that belong to a set of frontier orbitals and their occupancy number is smaller than 1/2 (antibonding orbitals). BBC3 functional possesses a correct orbital structure of the two-electron functional (39) if applied to hydrogen molecule in the dissociating limit and it is able to reproduce very accurately the whole dissociation curve [27]. Moreover, based on examples of small atoms and diatomic molecules at equilibrium geometries and in their dissociation limits, it has been shown that BBC3 accounts for both dynamic and static correlation yielding correct potential energy and recovering most of the correlation energy.

A difficulty with practical usage of the BBC3 functional is a need to select bonding and antibonding orbitals. In a computer implementation a strongly occupied orbital of the lowest occupancy is taken as bonding although a weakly occupied orbital of the highest occupancy is taken as an antibonding with a straightforward extension for this selection rule for molecules with more than one bond. This, however, leads to numerical problems because in the optimization procedure occupation numbers are varied and the antibonding character of orbitals may change, which may cause problems with convergence or may result in obtaining discontinuities in potential energy curves. To avoid the previously described problems with selecting frontier orbitals and to improve the overall accuracy of the BBC3 functional, it has been proposed to replace the elements G_{pq} present in the BBC functional, cf. (41), with a function $G(n_p,n_q)$. The function mimics the behavior of the G_{pq}^{BBC3} elements but does it automatically, based on the values of its arguments. The optimal function has been found by introducing two parameters and fitting the resulting AC3 functional to accurate energies of two molecules at equilibrium and stretched-bond geometries [40]. The AC3 functional yields decent quality potential energy curves for ten-electron molecules, although for some molecules a small hump in the curve is visible.

A two-electron wavefunction (33) is a special case of the more general closed-shell N-electron ansatz (N assumed to be even) involving, apart from a reference determinant Φ_0, all determinants arising from diagonal double, diagonal quadruple, etc., excitations; cf. (67). Taking the expectation value of the Hamiltonian with such a wavefunction yields an energy expression involving only Coulomb, exchange, and integrals of the $\langle pp|qq\rangle$ type [41]. In [42] the previously mentioned ansatz for the wavefunction has been used in development of the extended Löwdin–Shull (ELS) functional. The functional is applicable to systems for which a set of the natural spinorbitals can be partitioned into "inner" orbitals localized on atoms and the occupancies close to 1 and "outer" orbitals including a bonding orbital and all weakly occupied orbitals, i.e., orbitals localized on a single bond. For N-electron (N being even) systems $(N/2-1)$ strongly occupied orbitals (in a spin-restricted formulation each orbital gives rise to two spinorbitals with opposite spins) would be considered "inner" and the remaining strongly occupied orbital of the lowest occupancy would belong to the "outer" orbital set. By analyzing a structure of the energy expression resulting from the assumed ansatz, the following form of the ELS functional has been proposed

$$E_{\mathrm{ee}}^{\mathrm{ELS}}[\gamma] = \frac{1}{2}\sum_{p,q\in\mathrm{outer}} f_p f_q \sqrt{n_p n_q}\langle pp|qq\rangle + \frac{1}{2}\sum_{p\in\mathrm{inner}} n_p \langle pp|pp\rangle + \sum_{p\in\mathrm{inner}}\sum_{\substack{q>p \\ q\in\mathrm{inner}}} n_p n_q\left(\langle pq|pq\rangle - \langle pq|qp\rangle\right) + \sum_{p\in\mathrm{inner}}\sum_{q\in\mathrm{outer}} \left[n_p n_q\left(\langle pq|pq\rangle - \langle pq|qp\rangle\right) + F_{\mathrm{L}}(n_p, n_q)\langle pp|qq\rangle\right], \tag{44}$$

where the phase factors $\{f_p\}$ for the outer orbitals are set according to the rule valid for two-electron systems, namely

$$\forall_{p\in\mathrm{outer}} \quad f_p = \begin{cases} 1 & \text{if} \quad n_p > \frac{1}{2} \\ -1 & \text{if} \quad n_p < \frac{1}{2} \end{cases}. \tag{45}$$

Note that even though the exchange integrals $\langle pq|qp\rangle$ are identical to $\langle pp|qq\rangle$ if the spinorbitals are real, the two types of integrals make different contributions to time-dependent linear response equations so they are kept separately in the ELS functional. It is evident that for a two-electron system the set of inner spinorbitals is empty and, unlike the BBC3 or AC3 functionals, the ELS reduces to the accurate functional given in (39). A few models have been tried for the function F_{L}, which is responsible for correlating inner and outer orbitals. The most successful ones include one or two empirical parameters fitted to reproduce potential energy curves of LiH, Li_2, and BH^+ molecules. Very accurate potential energy curves have been obtained for these molecules [42]. Unfortunately, applications to other systems have not been presented, because the functional has been designed to treat only molecules with one single bond and no lone electron pairs. Nevertheless, ELS is a promising step towards extending the Löwdin–Shull functional to more than two electrons, aiming at providing a balanced description of the dynamic and static correlation.

2.2 *Functionals Based on Reconstruction of 2-RDM in Terms of 1-RDM*

One of the possible strategies towards development of novel one-electron density matrix functionals consists of assuming the cumulant expansion for the 2-RDM (28) and finding approximations for the cumulant part, γ, by imposing known conditions which the exact cumulant satisfies. The first naive proposition one might try is neglecting γ completely. This would result in the electron interaction functional being just a sum of the Hartree (16) and exchange (17) functionals, with no correlation part. One might then hope that some portion of correlation could still

be recovered by allowing nonidempotent γ in the optimization, in other words by allowing fractional occupancies of the natural orbitals. However, it has been shown by Lieb, that for electronic systems the minimum of the functional involving only Hartree and exchange contributions to the electronic repulsion, cf. (15), is achieved at an idempotent 1-RDM [14]. Thus, the minimum of the functional free of the correlation part simply coincides with the Hartree–Fock energy. To go beyond the Hartree–Fock approximation requires not only admitting nonidempotent γ but also including nonzero cumulant part in the reconstructed 2-RDM. Recently, Piris and collaborators proposed a series of natural orbital functionals known as PNOFi ($i = 1$–6) [43–48] by finding approximations to the cumulant matrix γ in terms of the natural occupation numbers [49, 50]. In reconstructing RDM defined in (25) in terms of 1-RDM the equality conditions satisfied by the N-representable 2-RDM are such that Hermiticity

$$\Gamma_{pqrs} = \Gamma^*_{rspq}, \tag{46}$$

antisymmetry

$$\Gamma_{pqrs} = -\Gamma_{qprs} = -\Gamma_{pqsr}, \tag{47}$$

and a sum rule

$$\sum_q \Gamma_{pqrq} = (N-1) n_p \delta_{pr} \tag{48}$$

have been imposed. To narrow down the possible form of the 2-RDM as a function of the occupation numbers, it has been required that the final correlation energy functional includes only Coulomb integrals $\langle pq|pq\rangle$, exchange integrals $\langle pq|qp\rangle$, and integrals of the type $\langle pp|qq\rangle$. It should be noted that the last two sets are identical if the orbitals are real, which is the case in practical calculations, but they enter the time-dependent density matrix functional equations in different terms as discussed in Sect. 5. Piris and Ugalde [49, 50] proposed the following structure of the spin-blocks of the cumulant matrix in a spin-restricted formalism

$$\lambda^{\sigma\sigma}_{pqrs} = -\Delta^{\sigma\sigma}_{pq}\left(\delta_{pr}\delta_{qs} - \delta_{ps}\delta_{qr}\right), \tag{49}$$

$$\lambda^{\alpha\beta}_{pqrs} = -\Delta^{\alpha\beta}_{pq}\delta_{pr}\delta_{qs} + \Pi_{rp}\delta_{pq}\delta_{rs}, \tag{50}$$

where $\sigma = \alpha, \beta$, the Δ matrices are symmetric, and the Π matrix is Hermitian. Such an ansatz for the cumulant results in the 2-RDM given in (28) satisfying the symmetry and antisymmetry conditions; cf. (46) and (47). For Systems in a singlet state, for which $n_{p_\alpha} = n_{p_\beta} = n_p$, and $\lambda^{\alpha\alpha}_{pqrs} = \lambda^{\beta\beta}_{pqrs}$, PNOF functionals, resulting from employing a reconstruction of Γ given in (28) with the ansatz (49) and (50), are of the following spin-summed form:

$$E_{\mathrm{ee}}^{\mathrm{PNOF}}[\gamma] = \sum_{pq} n_p n_q \left(2\langle pq|pq\rangle - \langle pq|qp\rangle\right) - \sum_{pq} \left[\left(\Delta_{pq}^{\alpha\alpha} + \Delta_{pq}^{\alpha\beta}\right)\langle pq|pq\rangle - \Delta_{pq}^{\alpha\alpha}\langle pq|qp\rangle\right] + \sum_{pq} \Pi_{pq}\langle pp|qq\rangle, \tag{51}$$

where the indices p, q pertain to spatial parts of the natural spinorbitals. Diagonal elements of the $\Delta^{\alpha\beta}$ and Π matrices have been fixed by imposing conservation of spin [51] which for high-spin states amounts to requiring that the expectation value of the $\hat{S}^2$ operator computed with the assumed form of the 2-RDM is equal to $M_s(M_s+1)$, with $M_s = (N^\alpha - N^\beta)/2$, $N_\alpha \geq N_\beta$. The pertinent diagonal elements read [50]

$$\Delta_{pp}^{\alpha\beta} = n_p^\alpha n_p^\beta, \tag{52}$$

$$\Pi_{pp} = n_p^\beta. \tag{53}$$

The final forms of the off-diagonal elements of the Δ and Π matrices have been proposed by further imposing a sum rule given in (48) and exploiting the so-called D, G, Q-conditions that state that 2-RDM, the electron–hole density matrix G, and two-hole density matrix Q must be positive [50]. The first PNO functional, PNOF1 [43], has been proposed for singlets after setting $\Delta^{\alpha\alpha} = \Delta^{\alpha\beta}$, assuming dependence of the cumulant matrix on two occupation numbers with relevant indices, i.e.,

$$\lambda_{pq} = \lambda_{pq}(n_p, n_q), \tag{54}$$

and defining symmetric functions $\Pi_{pq}(n_p,n_q) = \Pi_{pq}(n_q,n_p)$. Three possible cases have been considered for pairs of indices p, q: (1) p and q pertain to strongly occupied spinorbitals of occupancies greater than 1/2, (2) p and q pertain to weakly occupied spinorbitals of occupancies smaller than 1/2, and (3) one orbital is strongly occupied while the other is weakly occupied. Each of the cases is treated with a different function Π_{pq} with the form deduced from the structure of the 2-RDM for two-electron systems. It is worth mentioning that the PNOF1 functional has also been extended to high-spin multiplet states [51]. Despite the fact that PNOF1 has been designed to resemble an exact functional for two-electron systems in singlet state, its performance for potential energy curves is poor [40]. However, it has to be admitted that despite its simple form PNOF1 has turned out to be reliable in reproducing equilibrium bond distances, harmonic vibrational frequency, ionization potentials, and polarizabilities of small molecules [52].

A more involved form of the cumulant than that shown in (54) has been employed in the PNOF3 functional [45]. The same-spin block of the Δ matrix (49) was set to 0 and only the opposite-spin block, cf. (50), has been considered for singlet and high-spin multiplet states. Analogously to the PNOF1 functional

different forms of the λ_{pq} and $\Delta_{pq}^{\alpha\beta}$ functions of $\{n_p\}$ have been proposed depending on the values of occupation numbers of the pertinent spinorbitals p and q. The elements $\Delta_{pq}^{\alpha\beta}$ for the strongly-weakly occupied pair of orbitals p, q are functions not only of the corresponding occupancies n_p and n_q but also of the sum of occupation numbers of all weakly occupied spinorbitals. PNOF3 has been applied to computing high/low-spin energy splitting of atoms and atomization energies of molecules showing a remarkable agreement with the accurate coupled cluster accurate data [45]. PNOF3 has also correctly reproduced potential energy surfaces of challenging isomerization reactions [53]. Despite the proved usefulness of PNOF3 for systems dominated by dynamic electron correlation it fails in describing near-degenerate systems which has been illustrated by the breakdown of the functional in reproducing the energy of the Li_2 molecule with the stretched bond [46]. This failure has been attributed to violation of the positivity condition of the electron–hole density matrix G corresponding to the reconstruction scheme assumed in PNOF3. This problem has been addressed in [46] and a new form of the $\Pi_{pq}(\{n_r\})$ function has been proposed which resulted in a PNOF4 functional. PNOF4 accurately reproduces potential energy surfaces of diatomic molecules. Unfortunately, it has been reported recently that the products of homolytic dissociated molecules may have a non-integer number of electrons [50].

The PNOF5 functional formulated for closed-shell systems [47] can be seen as a simplification to PNOF4, because both the elements Δ_{pq} and Π_{pq} are functions of only the occupation numbers n_p and n_q (and not of the whole vector $\mathbf{n}$), yet the proposed ansatz for the two-electron reduced density matrix laying the foundation for PNOF5 satisfies the symmetry conditions and the sum rule (46)–(48), as well as the positivity conditions. This has been achieved by assuming that for an N-electron system (N being even) only for N natural orbitals ($2N$ natural spinorbitals) the occupation numbers are different from zero, the rest of orbitals being unoccupied. Additionally, the set of occupied orbitals has been partitioned into $N/2$ pairs. Each orbital belongs to only one pair and for the p, q orbitals coupled in a pair P the pertinent occupation numbers sum up to 1, i.e.,

$$\forall_{p,q\in P} \quad n_p + n_q = 1. \tag{55}$$

It should be noted that imposing the condition (55) immediately implies that the normalization condition for 1-RDM, namely

$$2\sum_{P=1}^{N/2}\sum_{p\in P} n_p = N \tag{56}$$

is satisfied. In (56) the first summation runs over pairs of electrons and the condition (55) has been employed. Analogously to other PNOF functionals, the diagonal elements of the Δ and Π matrices employed in PNOF5 are given by (52) and (53), whereas the off-diagonal elements for the coupled indices p and q have been proposed to take the form

$$\forall_{p,q\in P} \quad \Delta_{pq} = n_p n_q, \tag{57a}$$

$$\forall_{p,q\in P} \quad \Pi_{pq} = -\sqrt{n_p n_q}. \tag{57b}$$

The resulting spin-summed expression of the PNOF5 functional reads [47, 49]

$$\begin{aligned} E_{\mathrm{ee}}^{\mathrm{PNOF5}}[\gamma] \quad &= \sum_{P\neq Q}^{N/2}\sum_{p\in P}\sum_{q\in Q} n_p n_q \left(2\langle pq|pq\rangle - \langle pq|qp\rangle\right) \\ &- \sum_{P}^{N/2}\sum_{p\in P}\sum_{\substack{q\in P \\ q\neq p}} \sqrt{n_p n_q}\langle pp|qq\rangle + \sum_p n_p \langle pp|pp\rangle, \end{aligned} \tag{58}$$

where P and Q stand for indices of pairs of coupled orbitals. PNOF5 has outperformed all its PNOF predecessors in describing multireference systems. In particular it has been shown that it describes qualitatively correctly dissociation curves yielding accurate dissociation energies [54–56] and products of dissociation are of integer numbers of electrons [47, 56]. Dissociating of molecules with multiple bonds, e.g., N_2 or CO, leads to products of a correct high-spin symmetry [56]. The ability of the PNOF5 functional to treat homolytic bond cleavage has been exploited in its application to radical formation reactions [54]. Unfortunately, good performance of PNOF5 in recovering static correlation in nearly degenerate systems is paralleled by its insufficient inclusion of the dynamic correlation [49, 57, 58]. Application of the PNOF5 functional for such challenging systems as Cr_2, Mo_2, and W_2 dimers revealed that, although it yields energies of an accuracy between that of the CASSCF and CASPT2 methods, the lack of an important portion of dynamic correlation energy spoils the results [55]. In order to add the missing interpair dynamic correlation to PNOF5 Piris has considered a second-order multiconfiguration perturbation theory [59] and has adopted it for a wavefunction which leads to the PNOF5 energy expression [57]. The method has been named PNOF5-SC2-MCPT. Quite unexpectedly, its application to description of the helium dimer has led to a curve with multiple minima. Moreover, homolytic dissociation of diatomic molecules with the perturbation method resulted in breakdown of the dissociation curves because of singularities in the second-order energy appearing for quasi-degenerate systems. The former problem has been avoided by excluding from the perturbative expansion determinants corresponding to double excitations from spinorbitals of the same spatial parts, whereas singularities have been eliminated by removing second-order terms corresponding to quasi-degenerate orbitals [57]. Such a modified perturbation method has been called PNOF5-PT2. Application of PNOF5-SC2-MCPT and PNOF5-PT2 to the G2/97 test set of molecules has shown that, on average, the methods recover, respectively, around 80% and 70% of the correlation energy (with respect to Hartree–Fock energies) [58].

Good performance of the uncorrected PNOF5 for chemical reactions is a consequence of the observation that the functional can also be derived within the

antisymmetrized product of strongly orthogonal geminals (APSG) theory [60]. APSG has not only proven to be successful in describing dissociation curves of singly-bonded molecules [61] but it is also very accurate in predicting equilibrium geometries, vibrational frequencies, and dipole moments of diatomic molecules from G2/97 test set [62, 63]. In the APSG theory a wavefunction for an N-electron system in a singlet state is given by the antisymmetrized product of geminals $\{\psi_P(\mathbf{x}_{2P-1},\mathbf{x}_{2P})\}$

$$\Psi^{\mathrm{APSG}}(\mathbf{x}_1,\ldots,\mathbf{x}_N) = \hat{A}\prod_{P=1}^{N/2}\psi_P(\mathbf{x}_{2P-1},\mathbf{x}_{2P}), \tag{59}$$

which are strongly orthogonal, i.e., $\forall_{P\neq Q}\int \psi_P(\mathbf{x}_1,\mathbf{x}_2)\psi_Q(\mathbf{x}_1',\mathbf{x}_2)\mathrm{d}\mathbf{x}_2 = 0$ [64, 65]. It can be shown that if geminals are expanded in the natural orbitals $\{\varphi_p(\mathbf{r})\}$ corresponding to the 1-RDM obtained from the ansatz (59), then the expansion for each geminal P is diagonal, i.e.,

$$\psi_P(\mathbf{x}_1,\mathbf{x}_2) = 2^{-1/2}\sum_{p\in P} c_p\varphi_p(\mathbf{r}_1)\varphi_p(\mathbf{r}_2)[\alpha(1)\beta(2)-\alpha(2)\beta(1)], \tag{60}$$

the coefficients $\{c_p\}$ are simply square roots of the corresponding occupation numbers taken with "+" or "−" sign

$$\forall_p \quad n_p = c_p^2 \tag{61}$$

and the strong orthogonality of geminals implies that the sets of orbitals belonging to individual geminals are disjointed, i.e., each natural orbital belongs to only one geminal [66]. It should be noted that for a closed-shell two-electron system the APSG wavefunction is exact and identical with the Löwdin and Shull function given in (33). The expectation value of the Hamiltonian with the APSG wavefunction yields the following spin-summed electron–electron repulsion energy expression

$$\begin{aligned} E_{\mathrm{ee}}^{\mathrm{APSG}}\left[\{f_p\},\{n_p\},\{\varphi_p\}\right] &= \sum_{P}^{N/2}\sum_{p,q\in P} f_p f_q\sqrt{n_p n_q}\langle pp|qq\rangle \\ &+\sum_{P\neq Q}^{N/2}\sum_{p\in P,\,q\in Q} n_p n_q\left(2\langle pq|pq\rangle - \langle pq|qp\rangle\right), \end{aligned} \tag{62}$$

where $\{f_p\}$ are phase factors of the value +1 or −1. The APSG ground state energy follows from optimization of the total energy with respect to phase factors, occupation numbers, and the orbitals. Actually, it turns out that typically each geminal is composed of one strongly occupied orbital of the occupation number greater than 1/2 and a pertinent phase factor $f_1 = +1$, and all other orbitals, which are weakly

occupied ($n_p < 1/2$), of the corresponding phase factors $f_p = -1$ [61, 67]. As already mentioned in Sect. 2.1 for two-electron singlet systems (described within the APSG theory by one geminal), exceptions to this rule have been observed [36, 39], but they occur for very weakly occupied orbitals. Practically, fixing the phases in the APSG functional given in (62) according to the aforementioned rule, instead of finding them variationally, has only a small effect on the APSG energy. The APSG functional with the phase factors fixed can be seen as a density matrix functional. Comparison of the PNOF5 functional defined by (58) and (55) with (62) immediately reveals that they are identical if the dimension of the expansion space for each geminal in the APSG approach is limited to 2 and the phase factors of the two orbitals which form a given geminal are opposite, i.e., $f_1 = -f_2$ [60]. Because PNOF5 is equivalent to such constrained APSG approximation, it inherits its features from the latter, which explains the good performance of the PNOF5 functional for predicting dissociation energy curves of molecules [47] and the localized character of its optimal orbitals [68].

Lifting the restriction on the dimensionality of expansion spaces for the geminals in PNOF5 functional should allow one to recover a part of the correlation energy missing in this functional. This procedure has been proposed in [69] but clearly such extended PNOF5 functional (PNOF5e) is identical to the APSG functional (62) with fixed phases. For PNOF5 and PNOF5e functionals a systematic reconstruction of the 2-RDM in terms of the 1-RDM has merged with a theory based on the ansatz for the wavefunction [49]. On one hand this may seem to be a desirable result – the functionals are N-representable and bound by the exact ground state energy, but the drawback is that the functionals suffer from the same deficiencies as the APSG approximation.

An interesting idea that leads to incorporating the dynamic correlation that PNOF5 lacks has been proposed in [48]. The intrapair correlation is included in PNOF5 by proposing the elements Δ_{pq} (57a) and Π_{pq} (57b) corresponding to uncoupled orbitals p and q (belonging to different pairs) to be nonzero and expressing them as functions of the occupation numbers. The new functional, PNOF6, employs, similarly to PNOF5, a paired-orbitals picture. Compared to PNOF5, the PNOF6 functional underestimates the dissociation energies to a lesser degree. Unlike its predecessor, PNOF6 yields delocalized orbitals and it avoids spatial symmetry breaking of the benzene equilibrium geometry [48].

An ongoing development of natural orbital functionals, PNOF, originating from reconstruction of 2-RDM in terms of 1-RDM, has already resulted in functionals competing in accuracy with MP2 method for single-reference systems. Unlike the MP2 method, the PNOF4, PNOF5, and PNOF6 functionals are useful in describing potential energy surface also when bonds are stretched and dissociation potential energy curves are often of the quality of the much more expensive CASSCF approach.

2.3 Going Beyond Explicit Density Matrix Functionals

Approximate density matrix functionals discussed so far are explicitly expressed in terms of natural spinorbitals and natural occupation numbers. Ground state energy results from minimization of a functional with respect to orbitals and occupancies under N-representability conditions given in (3)–(5). To afford greater versatility, over the years efforts have been made to develop functionals the forms of which involve other quantities than only spectral components of 1-RDM. The quantities (typically being parameters) are found for a given γ by solving some auxiliary equations. The overall dependence of such functionals on γ is only implicit.

One of the first functionals of this kind has been proposed by Yasuda [15] who, by considering a contracted Schrödinger equation, derived a set of equations yielding, for given sets $\{n_p\}$ and $\{\varphi_p\}$, values of partially contracted products of cumulant elements λ (28) and two-electron integrals $\{\langle pq|rs\rangle\}$, i.e.,

$$\sum_{qrs} \lambda_{pqrs}[\gamma] \langle rs|\, pq\rangle = \varepsilon_p. \tag{63}$$

The resulting Yasuda correlation functional, cf. Eq.(29), $E_c[\gamma] = \sum_p \varepsilon_p[\gamma]$ is therefore implicitly dependent on spectral components of γ. Parameters $\{\varepsilon_p\}$ are found from a set of auxiliary equations. Despite the fact that the Yasuda correlation functional possesses a number of desirable features, i.e., it satisfies the exact conditions given in (30) and (31), it gives rise to dispersion interaction [70] and recovers a logarithmic divergence of the correlation energy of the homogeneous electron gas in high-density limit [71], its usefulness in practical electronic structure calculations has been undermined by showing that it does not seem to be bound from below even for two-electron systems [72].

Quite a different approach has been assumed in [41, 73–76] where explicit density matrix functionals have been derived by assuming a configuration interaction (CI) ansatz for a wavefunction and parameterizing CI coefficient. In all cases the CI wavefunctions were such that the resulting expression for the energy involved only Coulomb and exchange two-electron integrals. Because the former integrals are often denoted with the letter J and the latter with K, the functionals involving only these two types of integrals are sometimes called "JK-only" functionals. The idea of constructing functionals by parameterizing the CI ansatz is evidently directly related to the Levy constrained search functional (9) which for the CI wavefunction

$$\Psi = \sum_I C_I \Phi_I, \tag{64}$$

where $\{\Phi_I\}$ is a set of Slater determinants, turns into

$$E_{\mathrm{ee}}^{\mathrm{CI}}[\gamma] = \min_{C\to\gamma} \langle \Psi(\mathbf{C}) | \hat{V}_{\mathrm{ee}} | \Psi(\mathbf{C}) \rangle. \tag{65}$$

C stands for a vector of all CI coefficients and the minimization in the functional (65) is carried out with respect to all vectors **C** corresponding to the assumed ansatz for a wavefunction (64) which yield a given density matrix γ. Were the expansion in (64) complete, the functional (65) would be exact, i.e., it would be equivalent to the Levy functional (9). Otherwise, for truncated CI expansion, the functional is only approximate. The strategy adopted in [41, 73–76] was to use a CI ansatz leading to a "*JK*-only" approximation and to replace the whole set of the CI parameters by auxiliary variational matrices, say **A** and **B**, such that the functional (65) turns into

$$E_{\mathrm{ee}}\left[\{n_p\},\{\varphi_p\}\right] = \min_{\mathbf{A},\mathbf{B}\to\mathbf{n}} \left\{ \sum_{pq} A_{pq}\langle pq|pq\rangle + \sum_{pq} B_{pq}\langle pq|qp\rangle \right\}, \qquad (66)$$

where the two-electron integrals are computed with the natural spinorbitals $\{\varphi_p\}$. The minimization is done with respect to the matrices **A**, **B** constrained to yield a given vector of occupation numbers **n** and to satisfy some conditions, for example conditions imposing size-consistency on the functional. If the conditions are such that there is a mapping from **A** and **B** to the CI coefficients **C**, the functional given in (66) is variational, i.e., it constitutes an upper bound to the functional (65) and the exact Levy functional (9). If, however, the matrices **A**, **B** are constructed to ensure that the underlying 2-RDM only satisfies some of the necessary *N*-representability conditions, the functional (66) is not necessarily variational. The main advantage of replacing functionals (65) with approximations (66) is to obtain a more efficient method than CI, because the complex objects (CI coefficients) are replaced by matrices of much smaller dimensionalities. Moreover, if the starting CI ansatz (64) is not size-consistent, the proposed reparameterization in terms of **A**, **B** could restore this property (but then variationality is lost).

In [74] Kollmar and Hess considered a CI wavefunction being a combination of a closed-shell reference Slater determinant Φ_0 and determinants arising from Φ_0 by doubly exciting electrons from spinorbitals of the same spatial parts to virtual orbitals also sharing spatial functions, i.e., $\Phi_{i_\alpha i_\beta}^{a_\alpha a_\beta}$, where i and a stand for, respectively, occupied and unoccupied orbitals in the reference state. Such an ansatz leads to an energy expression involving only Coulomb and exchange integrals but it lacks size-consistency. To recover this property a normalization condition has been replaced by a new condition on the CI coefficients. The resulting functional of the form of (66) has been applied to the description of symmetric dissociation of water molecule which has led to a potential energy curve of a reasonable shape. At the same time, it became evident that the functional misses dynamic correlation.

In [41] the most general form of the closed-shell CI wavefunction which leads only to Coulomb and exchange integrals in the energy expression has been considered. The wavefunction can be called pair-excited CI because it includes all possible Slater determinants, each built of $N/2$ spatial orbitals entering a determinant with the α and β spin component, i.e.,

$$\Psi = \frac{1}{\sqrt{(N/2)!}} \sum_{Q_{N/2}} A_{Q_{N/2}} \left| \phi_{q_1} \phi_{\overline{q}_1} \cdots \phi_{q_{N/2}} \phi_{\overline{q}_{N/2}} \right|, \tag{67}$$

where $Q_{N/2} = q_1, \ldots, q_{N/2}$ is a string of indices, and $\left| \phi_{q1} \phi_{\overline{q}1} \cdots \phi_{qN/2} \phi_{\overline{q}N/2} \right|$ is a Slater determinant built of $N/2$ elements from the set of one-electron spatial functions $\{\phi_p\}$. The coefficients $\left\{ A_{Q_{N/2}} \right\}$ are symmetric with respect to exchanging two indices in a string $Q_{N/2}$ and they satisfy a normalization condition. The wavefunction (67) is size-consistent and it yields a diagonal 1-RDM, i.e.,

$$\gamma_{pq} = 2\delta_{pq} N \sum_{Q_{N/2-1}} \left(A_{pQ_{N/2-1}} \right)^2 = 2\delta_{pq} n_p. \tag{68}$$

Therefore one immediately recognizes that the orbitals $\{\phi_p\}$ are simply the natural orbitals, i.e., $\varphi_p(\mathbf{r}) \equiv \phi_p(\mathbf{r})$. As already mentioned, another property of the ansatz (67) is that the spin-summed electron interaction part of the corresponding energy reading

$$E_{\mathrm{ee}} = \sum_{pq} F_{pq} \left[2\langle pq|pq\rangle - \langle pq|qp\rangle \right] + \sum_{pq} G_{pq} \langle pp|qq\rangle, \tag{69}$$

where

$$F_{pq} = \frac{N}{2} \left(\frac{N}{2} - 1 \right) \sum_{Q_{N/2-2}} \left(A_{pqQ_{N/2-1}} \right)^2, \tag{70}$$

$$G_{pq} = \frac{N}{2} \sum_{Q_{N/2-1}} A_{pQ_{N/2-1}} A_{qQ_{N/2-1}}, \tag{71}$$

takes a simple "*JK*-only" form. A reparameterization of the energy expression (69) proposed in [41] consists of replacing the coefficients $\{A_{QN/2}\}$ by a new variational object: an idempotent matrix ω having occupation numbers on its diagonal and additional phase factors $\left\{ f_{Q_{N/2}} \right\}$ (of values 1 or -1). The parameterization preserves the variationality of the energy so the resulting functional

$$E_{\mathrm{ee}}[\gamma] = \min_{\omega \to \mathbf{n}} \min_{\left\{ f_{Q_{N/2}} \right\}} \left\{ \sum_{pq} F_{pq}(\omega) \left[2\langle pq|pq\rangle - \langle pq|qp\rangle \right] + \sum_{pq} G_{pq} \left(\omega, \mathbf{f}_{Q_{N/2}} \right) \langle pp|qq\rangle \right\} \tag{72}$$

is a strict upper bound to the exact energy functional. A large number of possible phase factors makes minimization of the functional practically impossible. Introducing some fixed pattern for signs of those factors could destroy variationality of the functional. This has been called a "phase dilemma" in [41] and identified as a serious bottleneck in constructing density matrix functionals. A functional free of the phase factors has been obtained by Kollmar and Hess by reconstructing 2-RDM in terms of 1-RDM by imposing N-representability condition (a strategy similar to the one adopted in construction of PNOF functionals presented in Sect. 2.2 [75]). The Kollmar–Hess functional is identical to (72) if a simple approximation for phase factor products is assumed [41]. The functional is therefore not variational in general (except for two-electron systems for which the functional is exact). Numerical applications showed that it is very accurate for four-electron systems [75]. The results for water molecule undergoing symmetric dissociation are much less satisfactory. They are very close, however, to those corresponding to the closed-shell MC-SCF approach with the CI ansatz given in (67). One can therefore conclude that the phase dilemma is not such a serious limitation if a proper model is assumed for the phase factors. Another confirmation of this conclusion comes from considering the exact functional for a two-electron closed-shell system which is a special case of the functional given in (72) for $N = 2$. As has already been mentioned, fixing the signs of the phase factors corresponding to the weakly occupied orbitals to be opposite to the sign of the phase factor associated with the strongly occupied orbitals leads to only a small change in the energy.

In [76] it has been shown that a computationally hard MC-SCF problem can be replaced by the optimization of a simple 1-RDM functional which parallels the MC-SCF method in accuracy. However, it has also been pointed out that the ansatz (67), i.e., the best possible wavefunction leading to a "*JK*-only" expression for the energy (67), recovers only a small fraction of the correlation energy for systems as small as a ten-electron molecule. Any variational (or based on an N-representable 2-RDM) "*JK*-only" functional suffers from the same deficiency. The density matrix functionals tested in [76] developed by imposing basic necessary N-representability conditions on the underlying 2-RDM do not recover more correlation than the wavefunction-based approach, even though they are not variational. In other words, results of parallel accuracy are obtained by minimizing the CI energy given by (69)–(71) with respect to the CI coefficients and the orbitals $\{\phi_p\}$ and by optimizing "*JK*-only" functionals proposed as approximations to (69) [76]. This poses a question as to whether the pair-excited CI ansatz (67) is a good starting point for developing functionals. This question is addressed in Sect. 6.

Apart from the implicit density matrix functionals discussed earlier which involve some auxiliary parameters, cf. (66), a promising class of functionals depending on γ and electron density ρ has been proposed by combining density-functional and density matrix functional theory [77, 78]. The method is based on the range-separation of electron–electron interaction operator, $\hat{V}_{\mathrm{ee}}$, into short- and long-range parts, $\hat{V}_{\mathrm{ee}}^{\mathrm{sr}}$ and $\hat{V}_{\mathrm{ee}}^{\mathrm{lr}}$, respectively [79, 80]. Dynamic correlation energy should mostly be described by the short-range density functional, and static

correlation energy by the long-range density matrix functional. A formal definition of the exact range-separated functional is possible by exploiting Levy constrained-search construction [4] and it reads [77]

$$E[\gamma] = T[\gamma] + V_{\text{ext}}[\rho_\gamma] + E_{\text{ee}}^{\text{lr}}[\gamma] + F^{\text{sr}}[\rho_\gamma], \tag{73}$$

where the long-range functional is defined analogously to the full-range functional in (9), namely

$$E_{\text{ee}}^{\text{lr}}[\gamma] = \min_{\Psi\to\gamma} \langle \Psi | \hat{V}_{\text{ee}}^{\text{lr}} | \Psi \rangle, \tag{74}$$

ρ_γ is a diagonal part of the density matrix γ and the definition of the short-range universal density functional F^{sr} also employs Levy constrained search construction. Partitioning the long- and short-range functionals into Hartree and exchange-correlation parts results in obtaining the following srDFT-lrRDMFT energy functional

$$E[\gamma] = T[\gamma] + V_{\text{ext}}[\rho_\gamma] + E_{\text{H}}[\rho_\gamma] + E_{\text{xc}}^{\text{lr}}[\gamma] + E_{\text{xc}}^{\text{sr}}[\rho_\gamma]. \tag{75}$$

Ground state energy follows from minimizing the range-separated functional with respect to N-representable γ. A short-range PBE exchange-correlation functional [81] has been used for $E_{\text{xc}}^{\text{sr}}[\rho]$. This is a short-range version of the PBE functional derived for the error function employed in range-separation of electronic interaction. The long-range density matrix functional, $E_{\text{xc}}^{\text{lr}}$, has been approximated by the long-range BB functional $E_{\text{xc}}^{\text{lrBB}}$ obtained by simply replacing two-electron integrals in the full-range BB functional, cf. (20), by their long-range counterparts, namely the spin-summed expression which reads

$$E_{\text{XC}}^{\text{lrBB}}[\gamma] = -\sum_{pq} \sqrt{n_p n_q} \langle pq|qp\rangle^{\text{lr}}, \tag{76}$$

$$\langle pq|qp\rangle^{\text{lr}} = \iint \varphi_p^*(\mathbf{r}_1)\varphi_q^*(\mathbf{r}_2) \frac{\text{erf}(\mu r_{12})}{r_{12}} \varphi_q(\mathbf{r}_1)\varphi_p(\mathbf{r}_2) \text{d}\mathbf{r}_1 \text{d}\mathbf{r}_2, \tag{77}$$

where $r_{12} = |\mathbf{r}_1 - \mathbf{r}_2|$ and erf stands for the error function. Both short- (sr) and long-range (lr) functionals involve a range-separation parameter μ, the value of which has been empirically chosen to be 0.4 bohr^{-1}. Such an obtained srPBE-lrBB functional has been applied to a few diatomic molecules and, in contrast to full-range BB or PBE functional, the range-separated density matrix functional turned out to be capable of reproducing correct dissociation energy curves [78]. Another direct advantage of range-separated functionals over full-range density matrix functionals is that the former, unlike the latter, are weakly basis set dependent which adds to their favorable computational efficiency.

2.4 Empirical Density Matrix Functionals

Approximate density matrix functionals cannot be rigorously derived. Rather, the form of the functional is proposed by taking into account properties of the exact functional. The applicability of density matrix functionals is not limited to finite systems (atoms and molecules); in principle, most of them could also be applied to solids. However, functionals such as BBC, AC3, or the recent PNOF approximations account for a sophisticated interplay between orbitals which is necessary to predict bond stretching and breaking. It is therefore not so surprising that performance of BBC1 and BBC2 functionals for a model extended system, namely the homogeneous electron gas (HEG), is quite poor. The accuracy of predicted correlation energy and the quality of momentum distribution for the HEG described with these functionals are unsatisfactory even for metallic densities. Admittedly, they still perform better than the other simple density matrix functionals defined in (20) and (23) such as BB or CHF [82, 83]. It should be noted that an exact exchange-correlation density matrix functional working for the HEG is not known even for a high-density limit, which is the reason why this system does not serve as a starting point for developing new density matrix functionals. In order to develop functionals for extended systems one could try introducing some empirical parameters into known approximate functionals and fitting them to experimental data.

Such an approach has been tried in [82, 84–86]. Adopting plane-waves as natural orbitals of the homogeneous electron gas turns a spectral representation of 1-RDM into

$$\gamma(\mathbf{r},\mathbf{r}') = \frac{2}{V}\sum_{\mathbf{k}} n(k)\mathrm{e}^{\mathrm{i}\mathbf{k}\cdot(\mathbf{r}-\mathbf{r}')}, \tag{78}$$

where $k = |\mathbf{k}|$, $n(k)$ is called momentum distribution, and V is the volume of the system ($V \to \infty$). BBC functionals, cf. (41)–(43), developed for molecules involve in their definition partitioning natural orbitals into strongly and weakly occupied, which is based on the value of the pertaining occupation number. A straightforward generalization of the BBC functionals to extended systems would assume establishing a type of the natural orbital (a plane wave) on the basis of the k-number i.e., whether it is smaller or greater than some reference value k_c [82]. The most obvious choice would be $k_\mathrm{c} = k_\mathrm{F}$, where k_F is the Fermi wave vector. As mentioned before, this choice implemented in the BBC1 or BBC2 functionals does not lead to accurate correlation energy of HEG. Lathiotakis et al. proposed two variants of the BBC1 modifications [82]. In the first, k_c was treated as a parameter, whereas the second variant assumes keeping $k_\mathrm{c} = k_\mathrm{F}$, multiplying the exchange-correlation terms of the BBC1 functional corresponding to two weakly occupied orbitals by a parameter s (s-functional). In both cases, values of parameters were chosen to reproduce the exact correlation energy of HEG. Unfortunately, momentum distributions resulting from such proposed functionals obtained for metallic densities, even though they show discontinuity, quantitatively still deviate strongly from the

accurate references. Adaptation of the *s*-functional developed for the electron gas to finite systems has led to surprisingly accurate values of energy for molecules at their equilibrium geometry but it has been also revealed that the functional is not size-consistent and it fails in the description of potential energy curves [85].

Motivated by the fact that the exchange-correlation functional (18) in many density matrix functionals is approximated by an expression involving only exchange integrals multiplied by factors depending on two pertinent occupation numbers, i.e.,

$$E_{\mathrm{xc}}[\gamma] = -\frac{1}{2}\sum_{pq} G\left(n_p, n_q\right)\left\langle pq|qp\right\rangle, \tag{79}$$

Marques and Lathiotakis (ML) proposed to find the function G fully empirically by using a Padé approximant depending on a variable $x = n_p n_q$ [87]. Coefficients in the Padé approximant were found by minimizing the error of the correlation energies of selected test-molecules. Computing the correlation energies of molecules in a G2 test with different methods has revealed that the empirical ML functional is on average the most accurate of all functionals tested, competing with or being superior to the MP2 method [87]. However, because the exchange-correlation part depends only on products of two occupation numbers, it inevitably lacks the structure needed to describe the breaking of a two-electron bond. The ML functional is not appropriate for describing molecules at geometries far from their equilibrium.

In the quest to develop a computationally efficient 1-RDM functional which is useful for solids, a very simple idea has been proposed and leads to remarkable results. The first and simplest approximate density matrix functional proposed is the BB functional (also known as the Müller functional) [18, 19], cf. (20). Müller has arrived at the particular form for the exchange-correlation functional given in (18) by considering a generalization of the Hartree–Fock exchange functional (17), which assumes replacing $|\gamma(\mathbf{x}, \mathbf{x}')|^2$ present in the HF two-particle density matrix and, consequently, in the functional (17), by a product $\gamma^{1-\alpha}(\mathbf{x}, \mathbf{x}')\gamma^{\alpha}(\mathbf{x}, \mathbf{x}')^*$. The power α was constrained to belong to the interval $\langle 0, 1\rangle$, to assure convexity of the functional and integrating of the corresponding exchange-correlation hole to -1 [18]. The BB functional results from choosing $\alpha = 1/2$. Sharma et al. proposed to consider an approximate exchange-correlation functional of the form [84]

$$E_{\mathrm{xc}}^{\alpha}[\gamma] = -\frac{1}{2}\sum_{pq} \left(n_p n_q\right)^{\alpha}\left\langle pq|qp\right\rangle, \tag{80}$$

that for $\alpha = 1$ is just an exchange Hartree–Fock functional (17) whereas for $\alpha = 1/2$ it turns into a BB form (20). It should be mentioned that a 2-RDM

$$\Gamma_{pqrs} = n_p n_q \delta_{pr}\delta_{qs} - \left(n_p n_q\right)^{\alpha}\delta_{ps}\delta_{qr}, \tag{81}$$

giving rise (via (26)) to the exchange-correlation power functional (80) satisfies the sum rule (48) only for $\alpha = 1/2$. Application of the power functional to the homogeneous electron gas revealed that momentum distribution resulting from the functional optimization not only lacks a step structure but is very different from the exact distributions in general [83, 88]. Even though the power functional does not recover the exact high-density limit of the correlation energy of the HEG [83, 89], it has been shown that with a carefully chosen value of α it is possible to obtain rather accurate values of the correlation energy for this system in the broad range of densities [86]. Moreover, the power functional performs remarkably well in predicting accurate band gaps of semiconductors and insulators [84]. The test set included materials of covalent or ionic character with band gaps ranging from 1 to 14.2 eV. It is striking that all these systems are incorrectly predicted to be metallic if described with the $\alpha = 1/2$ power functional, whereas choosing $\alpha = 0.65$ or $\alpha = 0.7$ results in obtaining nonzero gaps deviating on average from experimental values by less than 10%. Reducing α below the value 0.65 leads to zero energy gap for some materials, so it seems the range of admissible values of α is quite narrow.

Performance of the simple power functional (80) with $\alpha \in (0.65, 0.7)$ when applied to transition metal oxides (TMO) is even more impressive. TMOs can be regarded as prototypes of strongly correlated Mott insulators, the nonzero band gap of which is a result of strong Mott–Hubbard correlations. Most approximate density functionals incorrectly predict TMO to be metallic. The power density matrix functional, however, yields finite values for band gaps of nonmagnetic TMOs, although deviations of the computed gaps from their experimental counterparts are larger than in the case of conventional insulators [84]. Sharma et al. also showed that apart from band gaps the power functional is capable of accurately predicting other properties of solids such as equilibrium lattice constants. Another successful application of the power functional includes predicting the photoelectron spectra of strongly correlated Mott insulators within a density matrix functional method proposed in [90]. Despite its very simplistic form, the power functional has been shown to be a useful tool for studying solids, including those for which most density functionals provide unreliable results.

3 Predicting Properties of Electronic Systems with Density Matrix Functionals

Reduced density matrix functionals give immediate access to total energies of systems under investigation and, because the 1-RDM is known, to expectation values of local or nonlocal one-electron operators. However, in recent years a number of methods have been formulated within RDMFT allowing one to obtain properties of systems which are not mere traces of products of 1-RDM with one-electron operators. The properties accessible within static RDMFT include second- and higher-order static response properties, photoelectron spectra, or fundamental gaps.

3.1 Response Properties

Response properties follow from RDMFT by considering a one-electron perturbation of the strength λ

$$\hat{H}' = \sum_{i}^{N} \hat{w}(\lambda, \mathbf{x}_i), \tag{82}$$

where $\lambda = 0$ corresponds to the lack of perturbation [91]. Because 1-RDM is obtained variationally, the Hellman–Feynman theorem is satisfied and the first-order response properties result from taking a trace of 1-RDM with the first-order perturbation, i.e.,

$$\frac{\partial E[\gamma]}{\partial \lambda} = \sum_{p} n_p \left\langle \varphi_p \middle| \frac{\partial \hat{w}}{\partial \lambda} \middle| \varphi_p \right\rangle, \tag{83}$$

where the occupancies $\{n_p\}$ and the natural spinorbitals $\{\varphi_p\}$ correspond to unperturbed γ. Second-order properties are given by the expression (valid for real orbitals)

$$\frac{\partial^2 E[\gamma]}{\partial \lambda^2} = \sum_{p} n_p \left\langle \varphi_p \middle| \frac{\partial^2 \hat{w}}{\partial \lambda^2} \middle| \varphi_p \right\rangle + \sum_{pq} \left[n_p^{(1)} \delta_{pq} + (n_q - n_p) U_{pq}^{(1)} \right] \left\langle \varphi_p \middle| \frac{\partial \hat{w}}{\partial \lambda} \middle| \varphi_p \right\rangle, \tag{84}$$

where $\{n_p^{(1)}\}$ and $\mathbf{U}^{(1)}$ are components of the first-order response of γ, namely

$$\gamma_{pq}^{(1)} = n_p^{(1)} \delta_{pq} + (n_q - n_p) U_{pq}^{(1)}. \tag{85}$$

They can be found by solving a set of linear coupled-perturbed equations [91]. If the perturbation is particle-number-conserving then a condition must be imposed that a sum of perturbations $\{n_p^{(1)}\}$ vanishes. Applying the response equations to compute the static polarizabilities has revealed that even functionals which perform well in predicting energies of atoms and diatomic molecules, e.g., BBC3, do not provide satisfactory results for the second-order response properties [91]. The values for polarizabilities are of comparable or even worse quality than those obtained within the coupled-perturbed Hartree–Fock method [91]. Much more encouraging results have been obtained for hyperpolarizabilities of the H_2 molecule using the PNOF5 functional within a finite field approach [92]. Good accuracy could have been expected though, because the PNOF5 functional, cf. (58), is equivalent to the two-electron functional (39) if the number of orbitals with nonzero occupancy is restricted to two [60]. Despite this constraint, the PNOF5 functional captures the right physics of two-electron systems.

3.2 Ionization Potentials

A number of methods for predicting vertical ionization potentials (IPs) have been proposed within RDMFT. The most straightforward approach involves performing calculations of energies for a neutral and ionized species [93–95]. Apart from the fact that such multiple calculations are time consuming, it has been pointed out in [95] that inaccuracy may arise because of different treatment of closed- and open-shell systems in RDMFT.

Another way of computing IPs is provided by the Extended Koopmans' Theorem (EKT) which connects 1- and 2-RDM of a Coulombic system with its ionization potentials [96–98]. It has been shown in [99] that the Lagrangian matrix λ related to imposing orthonormality of the natural orbitals in optimizing a density matrix functional, reading

$$\lambda_{pq} = n_p h_{qp} + \int \frac{\delta E_{\mathrm{ee}}[\gamma]}{\delta \varphi_p^*(\mathbf{x})} \varphi_q^*(\mathbf{x})\, \mathrm{d}\mathbf{x}, \tag{86}$$

is equivalent to the generalized Fock matrix of the EKT equations. This implies that diagonalization of a Hermitian matrix Λ defined as

$$\Lambda_{pq} = -\frac{\lambda_{pq}}{\sqrt{n_p n_q}} \tag{87}$$

yields IPs as eigenvalues. For small molecules the BBC and GU functionals employed in the EKT formalism yield ionization energies with errors with respect to experimental references of the order of 4–6%. Similar accuracy has been obtained with the PNOF functionals [93, 100]. On average the accuracy is higher than that of the standard Koopmans' theorem.

The EKT method is not practical for solids as it would require diagonalization of a very large matrix. Sharma et al. proposed an alternative method [90]. This consists of assigning to each natural spinorbital an orbital energy ε_p obtained as a derivative of the total energy with respect to the pertinent occupation n_p. The derivative is taken at $n_p = 1/2$ with the rest of occupation numbers set equal to their ground state optimal values, i.e.,

$$\varepsilon_p = \left.\frac{\partial E[\gamma]}{\partial n_p}\right|_{n_p=1/2}. \tag{88}$$

Employing orbital energies obtained in this way for predicting densities of states of transition metal oxides has led to excellent agreement with experimental data. The orbital energies defined in (88) have also been used as approximations to ionization energies and electron affinities of molecules. Performance of density matrix functionals within such an approach is satisfactory and for IPs the errors are of the same order as those obtained from the much more theoretically grounded EKT method [95].

A central feature of one-electron approximations such as Hartree–Fock or Kohn–Sham DFT methods is existence of an effective Hamiltonian, the spectrum of which provides approximate ionization potentials. In HF this approximation is justified by Koopmans' theorem. In the KS-DFT formulation, although only the negative of the HOMO orbital energy yields the exact first IP if the exact potential is employed, it has been shown and theoretically justified that other orbital energies of occupied orbitals also approximate well ionization potentials, on condition that an accurate potential with a correct asymptotics is employed in KS equations [101, 102]. In RDMFT the effective Hamiltonian whose eigenfunctions correspond to natural spinorbitals also exists but its spectrum is infinitely degenerate [1, 103]. Recently, however, a local reduced density matrix functional method has been proposed which, for a given functional, searches for an optimal local potential, such that eigenfunctions of the corresponding effective Hamiltonian minimize a functional (for a fixed set of the occupation numbers) [104]. Although formulation of the local variant of RDMFT is not theoretically grounded, it offers at least two advantages over the standard optimization of the density matrix functional via a nonlocal potential. The first is better computational efficiency of the optimization of the energy functional (see Sect. 4). The other advantage is that local RDMFT formulation yields approximations to IPs as eigenvalues of the effective Hamiltonian with a local potential. Namely, it has been shown that photoelectron spectra of molecular systems obtained from the local-RDMFT with the BB [19], BBC3 [27], power [84], and empirical functional of Marques and Lathiotakis [87] compare well with experiment and are superior to spectra obtained from the Hartree–Fock Koopmans' method [105].

3.3 *Fundamental Gap*

Another quantity of key importance for solids accessible in RDMFT is the band gap or more generally the fundamental gap, which is defined as the difference between the ionization potential I and the electron affinity A as

$$\Delta = I - A. \tag{89}$$

Helbig et al. proved that within exact formulation of RDMFT a Lagrange multiplier μ, used to impose the normalization condition (5) on the occupation numbers in variational equations, possesses a discontinuity at integer particle numbers. This discontinuity amounts to the fundamental gap [106, 107], i.e.,

$$\Delta = \lim_{\eta \to 0} [\mu(N+\eta) - \mu(N-\eta)]. \tag{90}$$

A system with a fractional number of electrons $N+\eta$ should be understood as an ensemble of N- and $(N+1)$-electron states mixed with the corresponding weights $1-\eta$ and η so that the 1-RDM of the ensemble reads

$$\gamma^{N+\eta} = (1-\eta)\gamma^{N} + \eta\gamma^{N+1}, \tag{91}$$

where $0 \leq \eta \leq 1$, and γ^N and γ^{N+1} are one-electron reduced density matrices corresponding to N- and $(N+1)$-electron states. $\gamma^{N+\eta}$ is normalized to $N+\eta$. Necessary and sufficient N-representability conditions for $\gamma^{N+\eta}$, i.e., conditions under which there is a link between a density matrix $\gamma^{N+\eta}$ with a fractional number of electrons and an ensemble of N- and $(N+1)$-states, have been a proved [108]. They are of the same form as N-representability conditions for an integer-particle system, namely $\sum_p n_p = N+\eta$ and $\forall_p\ 0 \leq n_p \leq 1$.

To find a chemical potential (a Lagrange multiplier) $\mu(N+\eta)$ one just carries out minimization of the density matrix functional under standard N-representability conditions, imposing the normalization of $\{n_p\}$ to $N+\eta$. Applying approximate functionals to estimation of the fundamental gap of finite systems shows that μ does not possess a discontinuity. However, for functionals with self-interaction removed, e.g., the GU functional, μ plotted as a function of η displays a steep increase close to $\eta = 0$. This increase usually begins with a kink of the function $\mu\,(\eta)$ which occurs for η larger than 0 [106–108]. Its origin is related to the fact that by adding excess charge η the "HOMO" natural orbital (the orbital whose occupation number is the smallest among all strongly occupied orbitals) is filling up till its occupancy reaches 1. Increasing η further, the "LUMO" natural orbital (the orbital whose occupation number is the largest among all weakly occupied orbitals) begins increasing its occupancy which shows up on a $\mu(\eta)$ plot as a kink from which a steep increase of μ begins. Taking into account the origin of the step-like structure of μ for approximate functionals, it is rather surprising that a crude extrapolation of μ from large η (close to 1) to small η (close to 0) provides very reasonable estimations for the gaps [106, 107]. Formulation of the method for computing Δ within the open-shell RDMFT leads to obtaining a more pronounced step-like structure of the chemical potential μ, which makes the process of estimating Δ by extrapolating less ambiguous [107].

As mentioned in Sect. 2.4, satisfactory band gaps have been obtained for semiconductors, insulators, and even Mott insulators by employing the aforementioned method of finding approximate discontinuity of μ, cf. the formula (90), together with the power functional (80) [84]. Clearly, for periodic solids, the energy and the number of electrons are infinite and adding a charge η to each unit cell would result in an infinitely charged unstable system. It has therefore been proposed in [84] to find band gaps by adding excess charge η per unit cell and, at the same time, adding a constant charge background to keep the total system charge neutral. A band gap corresponds to a difference $\widetilde{\mu}(\eta \to 0^+) - \widetilde{\mu}(\eta \to 0^-)$, where $\widetilde{\mu} = \partial \widetilde{E}_{V+\delta v}(\eta)/\partial\eta$ and $\widetilde{E}_{V+\delta v}$ is the energy per volume unit computed self-consistently at the external potential V with the charge neutralizing potential δv added. A chemical potential obtained with the power functional lacks the discontinuity but its curvature changes the sign around $\eta = 0$ for nonmetallic systems. It allows the estimation of band gaps by constructing two tangent lines [84].

4 Optimization of Density Matrix Functionals

As mentioned in the introduction, the RDMFT approximations, apart from being accurate, are expected to be competitive with one-electron methods in terms of computational efficiency. RDMFT is based on the variational principle given in (11) according to which a ground state energy of a given system can be obtained by minimizing the energy functional on the set of N-representable density matrices. Thus, the optimization is of the constrained-type, because it must take into account N-representability conditions provided in (3)–(5). Because the conditions are given in the forms of equalities and inequalities involving eigenvalues and eigenvectors of 1-RDM, it implies that imposing N-representability conditions would require carrying out diagonalization of γ even for explicit functionals of γ.

An efficient algorithm offering optimization of the functional directly with respect to the whole density matrix or its square root has been proposed [109]. The N-representability of γ is imposed in each iteration step by projecting γ resulting from unconstrained directional optimization onto the space of N-representable 1-RDMs. An advantage of the proposed projected gradient algorithm is that, because the gradient is taken with respect to the elements of γ, changes in natural orbitals are coupled with variations of the occupancies which should lead to faster convergence. The proposed projection algorithm has been shown to work efficiently for Hartree–Fock (15) or BB (20) functionals. For other functionals, which are given in terms of orbitals and occupation numbers and are not proper functionals of γ (e.g., GU or BBC functionals), it is still possible to compute the gradient with respect to γ but the projected gradient algorithm converges disappointingly slowly [109].

The most robust and universal optimization approach consists of minimizing a functional with respect to the natural orbitals and the natural occupation numbers successively in separate steps. Natural orbitals are typically parameterized using, for a given orthonormal basis set $\{\chi_a\}$, the exponential function of a skew-symmetric matrix $\mathbf{X}$, i.e.,

$$\varphi = \mathrm{e}^{\mathbf{X}}\chi \tag{92}$$

which assures orthonormality of the orbitals φ, cf. (3), [26, 27]. To satisfy the N-representability condition given in (4) the natural occupation numbers may be parameterized by cosine functions, namely $\forall_p \; n_p = \cos^2(x_p)$ where parameters $\{x_p\}$ are unconstrained. The normalization condition (5) is taken into account by means of a Lagrange multiplier. A bottleneck of a two-step procedure is optimization of the orbitals. It takes many iterations to meet tight convergence criteria, because energy is almost completely insensitive to variations of very weakly occupied orbitals.

Because of unsatisfactory efficiency of the gradient orbital optimization algorithms, efforts have been made to turn the optimization problem for orbitals into an eigenproblem for an effective Hamiltonian [1, 103, 110–113]. For a given

functional and a fixed set of the natural occupation numbers, a one-electron Hamiltonian can be constructed in a self-consistent way such that its eigenfunctions minimize the functional (for fixed occupancies) [103, 110, 112]. The problem is that the self-consistent procedure of calculating orbitals from diagonalization of the effective Hamiltonian is highly divergent [103]. Moreover, the spectrum of this Hamiltonian is infinitely degenerate if it is constructed from optimal natural orbitals and occupation numbers. However, by proper combination of level-shifting and scaling off-diagonal elements of the Hamiltonian matrix, optimal orbitals can be obtained from iterative diagonalization [103, 111]. Such an approach does not, however, seem to surpass gradient methods significantly in terms of speed of convergence.

It has recently been proposed to employ an optimal effective potential (OEP) method formulated originally for optimization of orbital-dependent density functionals [114, 115] in RDMFT [104]. For a given density matrix functional, a local potential is sought such that its orbitals minimize the functional for fixed occupation numbers. The main difference from the above-mentioned scheme which employs a nonlocal Hamiltonian is that in local-RDMFT the potential is constrained to be local and to possess proper asymptotic behavior. Replacing a nonlocal potential with a local one and employing the OEP approach formulated originally for DFT (cf. [116]) leads to an efficient optimization method which enlarges scopes of applicability of the density matrix functionals to larger molecules and provides good estimations for the ionization potentials [105]. These advantages notwithstanding, it should also be noted that there is no theoretical justification for local-RDMFT. Moreover, by definition, the method does not provide a solution to the original variational problem given in (11) and for a given functional the optimal energy resulting from the local method is higher (although not much) than that obtained by solving the "nonlocal" RDMFT optimization problem [104].

5 Time-Dependent RDMFT

The extension of ground state RDMFT to the time domain was recently considered [117–121]. The main motivation to develop time-dependent RDMFT (TD-RDMFT) is the poor performance of time-dependent DFT (TDDFT) in the adiabatic approximation in combination with the approximate ground state density functionals. The best known failure is the inability of approximate TDDFT to capture charge transfer excitations [122, 123], though this deficiency has been remedied with some success using range-separated hybrid functionals [123, 124] and by an explicit reconstruction of the spatial divergence in the kernel [125, 126]. Other failures of adiabatic TDDFT are bond-breaking excitations which are predicted to be too low in energy upon dissociation (they can even go to zero) [127, 128] and a lack of double excitations [128–130]. All these failures are connected to the inability of approximate adiabatic density functionals to deal with static

correlation effects. Because approximate 1-RDM functionals have been quite successful in dealing with static correlation effects on the ground state level, we also expect an improvement for the calculation of excitations when using the full 1-RDM in our formalism instead of only the density. It turns out, however, that the formulation of a satisfactory adiabatic approximation in TD-RDMFT is not as straightforward as in TDDFT. Most of the research has therefore been done on formulating an adequate adiabatic approximation, so the formulation of an adiabatic approximation forms the major content of this TD-RDMFT section.

5.1 Equation of Motion of the 1-RDM

The time-dependent 1-RDM is obtained by using the time-dependent wavefunction in the definition of the 1-RDM (1)

$$\gamma(\mathbf{x},\ \mathbf{x}';t) = N\int\cdots\int \Psi\big(\mathbf{x},\mathbf{x}_2,\ \ldots,\mathbf{x}_N;t\big)\Psi^*(\mathbf{x}',\mathbf{x},\ldots,\mathbf{x}_N;t)\mathrm{d}\mathbf{x}_2\cdots\mathrm{d}\mathbf{x}_N. \tag{93}$$

The equation of motion for the 1-RDM is readily obtained from the time-dependent Schrödinger equation

$$\begin{aligned}\mathrm{i}\partial_t\gamma(\mathbf{x},\mathbf{x}';t) = \big(\hat{h}\,(\mathbf{x};t) - \hat{h}\,(\mathbf{x}';t)\big)\gamma(\mathbf{x},\mathbf{x}';t) + \\ \int\left(\frac{1}{|\mathbf{r}-\mathbf{r}_2|} - \frac{1}{|\mathbf{r}'-\mathbf{r}_2|}\right)\Gamma(\mathbf{x}\mathbf{x}_2,\mathbf{x}'\mathbf{x}_2;t)\mathrm{d}\mathbf{x}_2,\end{aligned} \tag{94}$$

where ∂_t denotes a time derivative and the time-dependent 2-RDM is defined as

$$\begin{aligned}\Gamma\big(\mathbf{x}_1\mathbf{x}_2,\mathbf{x}_1'\mathbf{x}_2';t\big) = N(N-1)\int\cdots\int\Psi(\mathbf{x}_1,\mathbf{x}_2,\mathbf{x}_3,\ldots,\mathbf{x}_N;t) \\ \times\Psi^*\big(\mathbf{x}_1',\mathbf{x}_2',\mathbf{x}_3,\ldots,\mathbf{x}_N;t\big)\mathrm{d}\mathbf{x}_3\ldots\mathrm{d}\mathbf{x}_N.\end{aligned} \tag{95}$$

So we find that we need the 2-RDM to determine the evolution of the 1-RDM. It turns out that the evolution of the 2-RDM is coupled to the 3-RDM and so on, till we hit the full N-RDM. This chain of p-RDMs coupled to each other is known as the Bogoliubov–Born–Green–Kirkwood–Yvon (BBGKY) hierarchy [131–137]. To be of any practical use, the BBGKY hierarchy needs to be truncated at some level. In TD-RDMFT the hierarchy is truncated already at the level of the 1-RDM and it is assumed that the time-dependent 2-RDM is a functional of the 1-RDM, $\Gamma[\gamma]$. For Hamiltonians with only local potentials, we know from the Runge–Gross theorem [138] and its extension [139, 140] that this is indeed true, because all observables are already functionals of the density, so they are also functionals of the 1-RDM. The use of density for the formal foundations of TD-RDMFT is not satisfactory, however, because we would have to limit ourselves to local-potential representable

1-RDMs. The formulation of a solid foundation for TD-RDMFT which allows for non-local potentials is still an open challenge.

The time-dependent 1-RDM can be diagonalized at each time t, allowing one to consider the time-dependent natural spinorbitals, $\varphi_p(\mathbf{x}t)$, and time-dependent occupation numbers, $n_p(t)$. The equation of motion for the 1-RDM (94) can be transformed to the time-dependent natural spinorbital basis, which gives the equations of motion for the natural spinorbitals and occupation numbers separately [118, 119]

$$\mathrm{i}\big(n_q(t)-n_p(t)\big)\big\langle\varphi_p(t)|\dot{\varphi}_q(t)\big\rangle=\big(n_q(t)-n_p(t)\big)h_{pq}(t)+\Big(W^{\dagger}_{pq}(t)-W_{pq}(t)\Big)\forall_{p\neq q}, \tag{96a}$$

$$\mathrm{i}\dot{n}_p(t)=\Big(W^{\dagger}_{pp}(t)-W_{pp}(t)\Big), \tag{96b}$$

where the dot indicates a time-derivative and we introduced a short-hand notation for the partial contraction of the 2-RDM with the two-electron integrals

$$W_{pq}(t)=\sum_{rst}\Gamma_{prst}(t)\big\langle st\big|qr\big\rangle(t). \tag{97}$$

It should be noted that the two-electron integrals are also time-dependent here, because they are evaluated with the time-dependent natural spinorbitals.

5.2 Time-Dependent Response Equations

The time-dependent response equations can be derived from the equation of motion of the 1-RDM (96) by considering a small time-dependent perturbation to a stationary system, with the stationary 1-RDM γ^0. The first-order perturbation in the 1-RDM is directly related to perturbation in the natural spinorbitals and occupation numbers as [compare with (85)]

$$\delta\gamma_{pq}(t)=\delta n_p(t)\delta_{pq}+\big(n_q-n_p\big)\delta U_{pq}(t), \tag{98}$$

where the indices refer to the natural spinorbital basis at $t=0$ and $\delta U_{pq}(t)=\langle\varphi_p|\delta\varphi_q(t)\rangle$. Collecting the perturbations in all the quantities up to first order, we obtain the first-order time-dependent response equation for the 1-RDM

$$\begin{aligned}\mathrm{i}\delta\dot{\gamma}_{pq}(t)=&\sum_r\big(h_{pr}(t)\delta\gamma_{rq}(t)-\delta\gamma_{pr}(t)h_{rq}(t)\big)+\\&\sum_{rs}\int_{-\infty}^{\infty}K_{pq,rs}\big[\gamma^0\big](t-t')\delta\gamma_{rs}(t')\mathrm{d}t'+\big(n_q-n_p\big)\delta v_{pq}(t).\end{aligned} \tag{99}$$

The response matrix $\mathbf{K}[\gamma^0](\tau)$ is the coupling matrix defined as [117, 119, 121, 141, 142]

$$K_{pq,rs}[\gamma^0](t-t') = \left.\frac{\delta\left(W^{\dagger}_{pq}(t) - W_{pq}(t)\right)}{\delta\gamma_{rs}(t')}\right|_{\gamma^0} \tag{100}$$

and plays the same role as the Hartree-exchange-correlation kernel, f_{Hxc} ($\mathbf{r}$, $\mathbf{r}'$, $t-t'$), in TDDFT [138, 143]. To obtain the frequency-dependent response equations, we simply need to take the Fourier transform of the time-dependent response equations. Because the time-integral over the coupling matrix $\mathbf{K}(t-t')$ and the perturbation in the 1-RDM has the form of a convolution, the Fourier transform turns this integral into a simple product. If we further assume that the natural spinorbitals of the unperturbed 1-RDM can be chosen to be real (no magnetic fields), the frequency-dependent response equations can be cast into a particular simple matrix form

$$\begin{pmatrix} \omega\mathbf{1}_M & -\mathbf{A}^{+}_{MM}(\omega) & \mathbf{0} \\ -\mathbf{N}^{-1}\mathbf{A}^{-}(\omega)\mathbf{N}^{-1} & \omega\mathbf{1}_M & -\mathbf{N}^{-1}\mathbf{C}(\omega) \\ \mathbf{0} & -\mathbf{A}^{+}_{mM}(\omega) & \omega\mathbf{1}_m \end{pmatrix} \begin{pmatrix} \delta\gamma^R(\omega) \\ \mathrm{i}\delta\mathbf{U}^I(\omega) \\ \delta\mathbf{n}(\omega) \end{pmatrix} = \begin{pmatrix} \mathbf{0} \\ \delta\mathbf{v}^R(\omega) \\ \mathbf{0} \end{pmatrix}, \tag{101}$$

where $N_{pq,rs} = (n_q - n_p)\delta_{pr}\delta_{qs}$ and 1_M denotes an $M \times M$ unit matrix. The sub-matrices $\delta\gamma^R(\omega) = \mathcal{F}[Re\gamma](\omega)$ and $\delta\mathbf{U}^R(\omega) = \mathcal{F}[Im\mathbf{U}](\omega)$ denote the Fourier transforms of the real and imaginary parts of the unique off-diagonal parts of $\delta\gamma(t)$ and $\delta\mathbf{U}(t)$, respectively, and likewise, $\delta\mathbf{v}^R(\omega) = \mathcal{F}[Re\mathbf{v}](\omega)$ denotes the Fourier transform of the real part of the unique off-diagonal parts of the perturbing potential $\delta\mathbf{v}(t)$. The matrix on the left is therefore an $(M, M, m) \times (M, M, m)$ matrix, where m denotes the number of basis functions and $M = m(m-1)/2$ the number of unique off-diagonal elements. The submatrix $\mathbf{A}^{+}$ has labels MM and mM to indicate which parts of this matrix need to be used. The response matrices $\mathbf{A}(\omega)$ and $\mathbf{C}(\omega)$ combine the one-body and two-body effects to the response of the 1-RDM and are defined as

$$A_{pq,rs}(\omega) = (n_s - n_r)\left(\left(h_{pr}\delta_{sq} - \delta_{pr}h_{sq}\right) + K_{pq,rs}(\omega)\right), \tag{102a}$$

$$C_{pq,r}(\omega) = h_{pq}\left(\delta_{rq} - \delta_{rp}\right) + K_{pq,rr}(\omega). \tag{102b}$$

Positive and negative combinations of the response matrix $\mathbf{A}(\omega)$ enter the frequency-dependent RDMFT response equations (101) as

$$A^{\pm}_{pq,rs}(\omega) = A_{pq,rs}(\omega) \pm A_{pq,sr}(\omega). \tag{103}$$

5.3 Standard Adiabatic Approximation

To turn the frequency-dependent RDMFT linear response equations (101) into a practical scheme, we need to be able to evaluate the coupling matrix **K** in some manner. In the standard adiabatic approximation (the one also used in TDDFT), one assumes that the history dependence for slow processes is not very important, so a good approximation would be

$$\mathbf{K}\left[\gamma^0\right](t-t') \approx \mathbf{K}\left[\gamma^0\right]\delta(t-t'). \tag{104}$$

If the initial state of the system was the ground state, a ground state functional would probably provide a reasonable approximation and the full standard adiabatic approximation becomes

$$\mathbf{K}\left[\gamma^0\right](t-t') \approx \mathbf{K}^{\mathrm{gs}}\left[\gamma^0\right]\delta(t-t'). \tag{105}$$

An additional advantage of the adiabatic approximation for the frequency-dependent response RDMFT equations (101) is that all the response matrices $\mathbf{A}^{\pm}$ and **C** become frequency independent, which greatly simplifies the calculation of response properties (excitation energies), because we only need to solve a linear system of equations (eigenvalue equation), instead of a complicated set of coupled nonlinear equations.

The standard adiabatic approximation, however, implies that the natural occupation numbers do *not* change in time. This is a particularly disappointing result, because the time-evolution of the natural occupation numbers is expected to be important to handle strongly correlated systems such as stretched chemical bonds. For "*JK*-only" approximate functionals the stationarity of the occupation numbers is easily demonstrated [118, 120, 121]. The "*JK*-only" 2-RDM is of the general form

$$\Gamma_{pqrs} = F_{\mathrm{H}}\left(n_p, n_q\right)\delta_{pr}\delta_{qs} + F_{\mathrm{x}}\left(n_p, n_q\right)\delta_{ps}\delta_{qr}. \tag{106}$$

Using this approximate 2-RDM in the definition for $\mathbf{W}(t)$ (97), and inserting the result into the equation of motion of the natural occupation numbers (96b), we find that they are time-independent, $\mathrm{i}\dot{n}_p(t) = 0$.

More work is needed to demonstrate that the use of a ground state functional for the 2-RDM always leads to stationary occupation numbers in the standard adiabatic approximation [117, 144, 145]. First we note that, because the natural orbitals are the eigenfunctions of the self-adjoint kernel, $\gamma(\mathbf{x},\mathbf{x}';t)$, their phases are undetermined by the 1-RDM. Therefore, a 1-RDM functional formulated in terms of the natural orbitals and occupation numbers is not allowed to depend on the phase of the natural orbitals. Making the phase of the natural orbital explicit $\varphi_p(\mathbf{x}t) = \mathrm{e}^{\mathrm{i}\alpha_p(t)}\phi_p(\mathbf{x}t)$, we have the following condition on the derivative of any 1-RDM functional, F

$$0 = \frac{\mathrm{d}F}{\mathrm{d}\alpha_p(t)} = i\int \mathrm{d}\mathbf{x}\left(\varphi_p^*(\mathbf{x}t)\frac{\partial F}{\partial \varphi_p^*(\mathbf{x}t)} - \frac{\partial F}{\partial \varphi_p(\mathbf{x}t)}\varphi_p(\mathbf{x}t)\right). \tag{107}$$

To connect these derivatives with the contractions $\mathbf{W}(t)$ (97) in the adiabatic approximation, we express the exact ground state functional as [99]

$$W\left[\{\varphi_p\},\left\{\varphi_p^*\right\},\{n_p\}\right] = \frac{1}{2}\min_{\{\xi_i\}}\sum_{pqrs}\Gamma_{pqrs}\left[\{\xi_i\},\{n_p\}\right]\langle rs|pq\rangle, \tag{108}$$

where the set of variables $\{\xi_i\}$ indicates the additional degrees of freedom over which we can vary the 2-RDM, keeping the 2-RDM ensemble N-representable and such that it yields the prescribed 1-RDM (48). This expression assumes that only the occupation numbers are part of the N-representability conditions for the 2-RDM and not the natural orbitals. This is reasonable, because N-representability should not depend on the particular orthonormal basis we are working in. An advantage of expressing the exact interaction-energy function in this manner is that the functional W is even defined for non-orthogonal natural spinorbitals. Although the value of the functional W does not make any physical sense for non-orthonormal orbitals, it allows us to define derivatives with respect to $\phi_p(\mathbf{x})$ and $\phi_q^*(\mathbf{x})$ separately in an unambiguous manner and impose the orthonormality conditions afterwards with the help of Lagrange multipliers or in other ways, e.g., (92).

The optimal 2-RDM parameters which attain the minimum are functionals of the natural orbitals and occupation numbers, and we write these optimal value for the parameters as $\bar{\xi}_i\left[\{\varphi_p\},\left\{\varphi_p^*\right\},\{n_p\}\right]$. Using $\{\bar{\xi}_i\}$ the exact interaction-energy functional can also be written as

$$W\left[\{\varphi_p\},\left\{\varphi_p^*\right\},\{n_p\}\right] = \frac{1}{2}\sum_{pqrs}\Gamma_{pqrs}\left[\{\bar{\xi}_i\},\{n_p\}\right]\langle rs|pq\rangle, \tag{109}$$

where we suppressed the explicit dependence of the optimal 2-RDM parameters on the natural spinorbitals and occupation numbers. Assuming that the gradient of $\Gamma[\{\xi_i\},\{n_p\}]$ with respect to the parameters ξ_i exists, we can work out the functional derivative of W with respect to the natural orbitals as

$$\frac{\delta W}{\delta\varphi_t(\mathbf{x})} = \frac{1}{2}\sum_i \frac{\delta\xi_i}{\delta\varphi_t(\mathbf{x})}\sum_{pqrs}\frac{\partial\Gamma_{pqrs}}{\partial\xi_i}\bigg|_{\bar{\xi}}\langle rs|pq\rangle + \frac{1}{2}\sum_{pqrs}\Gamma_{pqrs}\frac{\delta\langle rs|pq\rangle}{\delta\varphi_t(\mathbf{x})}. \tag{110}$$

Because we minimize over the parameters ξ_i in the functional W, the derivatives with respect to ξ_i vanish at the minimum $\{\bar{\xi}_i\}$, so the first term on the right-hand side does not give any contribution. Projecting the functional derivative against natural spinorbitals, we have

$$\int \mathrm{d}\mathbf{x} \frac{\delta W}{\delta \varphi_p(\mathbf{x})} \varphi_q(\mathbf{x}) = \sum_{rst} \Gamma_{prst} \langle st|qr\rangle = W_{pq}. \tag{111}$$

Using this result together with the phase invariance condition (107) in the equation of motion for the occupation numbers (96b) in the standard adiabatic approximation, we find the claimed result

$$\mathrm{i}\dot{n}_p(t) = \int \mathrm{d}\mathbf{x} \left(\varphi_p^*(\mathbf{x}t) \frac{\partial W}{\partial \varphi_p^*(\mathbf{x}t)} - \frac{\partial W}{\partial \varphi_p(\mathbf{x}t)} \varphi_p(\mathbf{x}t) \right) = 0. \tag{112}$$

A shorter, though more handwaving argument has been given in [146].

Because the occupation numbers are not perturbed in the standard adiabatic approximation, they drop out of the response equations and the standard adiabatic response equations reduce to

$$\begin{pmatrix} \omega \mathbf{1}_M & -\mathbf{A}^+_{MM} \\ -\mathbf{N}^{-1}\mathbf{A}^-\mathbf{N}^{-1} & \omega \mathbf{1}_M \end{pmatrix} \begin{pmatrix} \delta\gamma^R(\omega) \\ \mathrm{i}\delta\mathbf{U}^I(\omega) \end{pmatrix} = \begin{pmatrix} \mathbf{0} \\ \delta\mathbf{v}^R(\omega) \end{pmatrix}. \tag{113}$$

Because no $\delta\mathbf{n}(\omega)$ term is present, we find that even in the static limit $\omega \to 0$ the occupation numbers are not perturbed, in contrast to the time-*in*dependent response equations presented in Sect. 3.1 [120, 121, 142]. This discrepancy has been demonstrated to be sizable by calculating the polarizability of HeH^+ [117, 120, 144, 145]. The Löwdin–Shull functional has been exclusively used for these calculations. There are two possible variants of this functional: one with the exchange integrals (39) and one where we restore the original integrals $\langle pp|qq\rangle$ of the singlet two-electron system (36) and replace products $c_p c_q$ with G^{LS}_{pq} given in (40). For real natural spinorbitals there is no difference, but in the time-dependent case the natural orbitals are complex and hence the two different integrals give rise to different coupling matrices. The advantage of using exchange integrals is that the functional is phase invariant, which is a requirement for a proper 1-RDM functional. Therefore, this variant is called the density matrix LS (DMLS). The variant with the original $\langle pp|qq\rangle$ integrals is not phase invariant, so not a proper 1-RDM functional. Because of its phase dependence it is called the phase including LS (PILS). Though the PILS is not a proper 1-RDM functional, its use is appealing, because the breaking of phase invariance implies that the natural occupation numbers do change.

One would expect that the DMLS functional should give superior results. This is indeed the case for the polarizability of HeH^+ if only a limited number of transitions between the natural orbitals are taken into account [117, 144, 147], typically only the transitions from the two highest occupied NOs to all the others. If all transitions between the natural orbitals are taken into account, the DMLS functional has spurious divergences in the polarizability at low frequencies [117, 145, 147], severely deteriorating the DMLS result. Though the polarizability from the PILS

functional does not follow the exact polarizability as closely as the DMLS, it has the main advantage that no spurious divergences emerge, even when all natural orbital transitions are taken into account in the response calculation [117, 121, 147].

Another disadvantage of the standard adiabatic approximation is that we effectively lose excitation energies. Because the original frequency-dependent response matrix has $M+M+m=m^2$ entries, the standard adiabatic approximation yields m^2 excitation energies, because the response matrices $\mathbf{A}$ and $\mathbf{C}$ are frequency independent. However, we only obtain $2M=m(m-1)$ sensible excitation energies and m roots $\omega=0$, which are physically meaningless, so, effectively, these m excitation energies are lost in the standard adiabatic approximation [142].

Test calculations on the excitation spectrum of the hydrogen molecule as a function of the bond length have been carried out to test the performance of both LS functionals. Because divergences in the polarizability correspond to excitations, the spurious divergences of the DMLS functional already indicate that the performance of the DMLS functional for the calculation of excitation energies is not very good. Indeed, the test calculations on H_2 have shown that the DMLS functional predicts many spurious low lying excitations which completely clutter the excitation spectrum when all natural orbital transitions are taken into account [117, 145, 148]. Reducing the number of transitions to only transitions from the two heaviest occupied natural orbitals is very effective in cleaning up the DMLS excitation spectrum [117]. Such an approach would not be desirable in practice, because it is orthogonal to the idea that expanding a basis brings one closer to the desired result.

Because the PILS functional is dependent on the phase of the natural orbitals, the occupation numbers are not necessarily stationary any more in the standard adiabatic approximation. However, it can be demonstrated that there are still only $2M=m(m-1)$ non-trivial roots of the response equations (113) and m zero excitations [117]. Nevertheless, the PILS functional gives a huge improvement over the DMLS functional for excitation energies. Most notably, no spurious low lying excitations appear when we exhaust the response basis by including more natural orbital transitions. Furthermore, one can show that the ${}^1\Sigma_u^+$, ${}^1\Pi_g$ and ${}^1\Pi_u$ excitations become equal to the full CI result when all natural orbital transitions are taken into account [117, 141, 142]. This is caused by the fact that these excitations do not need any perturbation in the natural occupation numbers to be described exactly, which is related to symmetry. This also holds for excitations in other irreducible representations (irreps) that do not couple to the completely symmetric irreducible part of the response matrix, such as the xy component of the Δ_g excitations. The x^2-y^2 component does couple to the occupation numbers, however, so the Δ_g excitations of the H_2 molecule is symmetry broken when using the PILS functional: the xy components are equal to the full CI result and the x^2-y^2 components are not [117]. Symmetry breaking does not occur for the DMLS functional, because the occupation numbers are never involved in the standard adiabatic response.

5.4 Alternative Adiabatic Approximation

Because the standard adiabatic approximation used in TD-RDMFT has the undesirable features of stationary occupation numbers and a mismatch with the static response equations (Sect. 3.1) in the $\omega \to 0$ limit, an alternative adiabatic approximation has been proposed. The idea is to replace the dynamic equation for the occupation numbers (96b) by its static counterpart and to make the perturbed quantities frequency-dependent, which leads to the following equation

$$0 = 2\sum_{r>s} C^T_{p,rs}\delta\gamma^R_{rs}(\omega) + 2\sum_r \overline{W}_{p,r}\delta n_r(\omega) + \delta v_{pp}(\omega), \tag{114}$$

where we use

$$C^T_{p,rs} = C_{rs,\,p} \quad \text{and} \quad \overline{W}_{p,q} = \frac{1}{2}\frac{\partial^2 W}{\partial n_p \partial n_q}. \tag{115}$$

Though the occupation numbers are not determined by an equation of motion, but follow instantaneously from $\delta\gamma^R(\omega)$ and the diagonal elements of the potential $\delta\mathbf{v}^D(\omega)$, there is at least a response of the occupation numbers. The fact that this alternative adiabatic approximation is an instantaneous relaxation of the natural occupation numbers at each time t has been stressed in [149] where the more descriptive name "instantaneous occupation number relaxation" was introduced. The frequency-dependent response equations in this alternative adiabatic approximation become

$$\begin{pmatrix} \omega\mathbf{1}_M & -\mathbf{A}^+_{MM} & \mathbf{0} \\ -\mathbf{N}^{-1}\mathbf{A}^-\mathbf{N}^{-1} & \omega\mathbf{1}_M & -\mathbf{N}^{-1}\mathbf{C} \\ -\mathbf{C}^T\mathbf{N}^{-1} & \mathbf{0} & -\overline{\mathbf{W}} \end{pmatrix} \begin{pmatrix} \delta\gamma^R(\omega) \\ \mathrm{i}\delta\mathbf{U}^I(\omega) \\ \delta\mathbf{n}(\omega) \end{pmatrix} = \begin{pmatrix} \mathbf{0} \\ \delta\mathbf{v}^R(\omega) \\ \delta\mathbf{v}^D(\omega)/2 \end{pmatrix}. \tag{116}$$

The correction for the $\omega \to 0$ limit to the standard adiabatic approximation proves to be quite effective and improves the description of the polarizability for small frequencies [117, 120, 121]. Additionally, because the frequency-dependent response equations now reduce correctly to the static response equations in the $\omega \to 0$ limit, both the DMLS and PILS functionals coincide at $\omega = 0$. The general trend from the standard adiabatic approximation remains: the DMLS is closer to the exact polarizability, though has some spurious divergences which are absent in the PILS calculations [117].

Because ω is only present in the upper two $M \times M$ blocks, the determinant of the response matrix is only a $2M = m(m-1)$ order polynomial in ω. We therefore find that the alternative adiabatic approximation does not restore the lost roots in the standard adiabatic approximation. Calculations on the H_2 and HeH^+ have demonstrated that the excitation spectrum does not change much compared to the standard adiabatic approximation for both the DMLS and PILS functionals [117]. The lowest

excitation energies decrease somewhat when correcting the incorrect $\omega \to 0$ limit in the adiabatic approximation and it depends on the particular system whether this is an improvement. For H_2 the results are slightly worse in the alternative adiabatic approximation, whereas for HeH^+ they are slightly better [117, 142].

Although the alternative adiabatic approximation is successful in correcting the $\omega \to 0$ limit of the standard adiabatic approximation, this adiabatic approximation is still not very satisfactory, because the occupation numbers are still not truly dynamic variables and we still lose m excitations. These m excitations correspond to excitations which require a significant response of the occupation numbers. Because the response of the occupation numbers corresponds to the response of the diagonal of the 1-RDM (98), so they are referred to as the diagonal double excitations. Other double excitations related to perturbations in the off-diagonal parts of the 1-RDM are well accounted for, as the excitation energies in the ${}^1\Sigma_u^+$ and ${}^1\Pi_u$ are perfectly accounted for [117, 142]. It turns out that these diagonal double excitations are important for the correct description of the lowest ${}^1\Sigma_g^+$ excitation energy in stretched H_2 [141, 142], so including the diagonal double excitations is important.

5.5 *Phase Including Natural Orbitals*

It is unlikely that the missing m diagonal double excitations can be restored with any decent adiabatic approximation to the TD-RDMFT equations. The problem is that the excitation energies should come out of the response equations in pairs $+\omega$ and $-\omega$. This pairing of the frequencies is dictated by an important symmetry of the response function $\chi(\omega) = \chi^*(-\omega)$, which follows directly from the Lehmann [150] (sum-over-states) representation. We therefore need to increase the number of roots by m in some manner, because m is not necessarily even. Increasing the number of roots to $2(M+m)$ results in an even number of roots, which in turn ensures that all excitations are present in both the positive and negative parts of the spectrum.

This partially explains why we had m zero excitations in the standard adiabatic approximation, because $\omega = 0$ is the only number which is its own negative, so it does not destroy the $\chi(\omega) = \chi^*(-\omega)$ symmetry even if an odd number of these roots is present. This does not explain why we could not have $\lfloor m/2 \rfloor$ excitation energies occurring both at $+\omega$ and $-\omega$ in an adiabatic approximation. To explain this, we observe that for a proper quantum evolution a quantity needs to be able to have a complex phase. All the off-diagonal elements of the 1-RDM are able to obtain a complex phase-factor, but because the diagonal is necessarily real, the occupation numbers do not have a quantum phase [117]. This lack of a corresponding quantum phase for the natural occupation numbers is not limited to the 1-RDM, but exists for the diagonal of any p-RDM if the BBGKY hierarchy is truncated at the pth order [151].

The way to solve all these problems together is to include an additional set of m complex phase factors which can act as the conjugate variables for the natural

occupation numbers to facilitate a true quantum evolution. It is obvious that the ideal candidate would be the phase factors of the natural orbitals, which is corroborated by the reconstruction of the exact frequency-dependent coupling matrices of the $\mathbf{K}(\omega)$ for singlet two-electron systems [117, 142]. To distinguish these special natural orbitals with a specific phase from those defined as eigenfunctions of the 1-RDM, we call them phase-including natural orbitals (PINOs) and give them their own symbols, $\not{\pi}_p(\mathbf{x}t)$. Using PINOs, the functionals are also allowed to depend explicitly on the phase of the orbitals, so the PILS functional becomes a legal functional.

To derive equations of motion for the PINOs and their occupation numbers, we start from the following quantum mechanical action [152]

$$A\left[\left\{\not{\pi}_p, n_p\right\}\right] = \int_0^T \mathrm{d}t \left\langle \Psi\left[\left\{\not{\pi}_p, n_p\right\}\right](t) \middle| \mathrm{i}\partial_t - \hat{\mathrm{H}}(t) \middle| \Psi\left[\left\{\not{\pi}_p, n_p\right\}\right](t) \right\rangle, \tag{117}$$

where we assume that the action can be considered as a functional of the PINOs and occupation numbers. The equations of motion for the PINOs and their occupation numbers follow by making the action stationary with respect to all variations. However, we have to keep in mind that the action is now only a functional of the PINOs and occupation numbers and *not* of the full many-body wavefunction. Therefore, we cannot set the variation at the end-point $t = T$ to zero and need to take this term into account explicitly [153], so the variational principle becomes

$$\delta A = \mathrm{i}\left\langle \Psi(T) \middle| \delta\Psi(T) \right\rangle. \tag{118}$$

Neglect of the variations in the boundary term at $t = T$ leads to violation of causality as was shown by Vignale in [153], where he showed that explicit treatment of the boundary term solves the causality paradox which has haunted TDDFT for so many years [154].

To obtain more practical and explicit equations, we follow the same approach as in TDDFT [138] and partition the action of the fully interaction system into a non-interacting part, A_0 and a remainder A_{Hxc}

$$A\left[\left\{\not{\pi}_p, n_p\right\}\right] = A_0\left[\left\{\not{\pi}_p, n_p\right\}\right] - A_{\mathrm{Hxc}}\left[\left\{\not{\pi}_p, n_p\right\}\right]. \tag{119}$$

Because the occupation numbers of non-interacting pure-states are stationary by construction, we need to use the action for an ensemble for the non-interacting system to allow for occupation numbers that vary in time

$$A_0\left[\left\{\not{\pi}_p, n_p\right\}\right] = \int_0^T \mathrm{d}t \sum_P d_P(t) \langle \Phi_P(t) | i\partial_t - \hat{\mathrm{H}}_0(t) | \Phi_P(t) \rangle, \tag{120}$$

where $0 \leq d_P(t) \leq 1$ are time-dependent weights, $\Sigma_P d_P(t) = 1$, and $\hat{\mathrm{H}}_0(t)$ is the one-body part of the fully interacting Hamiltonian, $\hat{\mathrm{H}}(t)$, so corresponding to a

noninteracting system. The states $\Phi_P(t)$ are time-dependent Slater determinants constructed out of the PINOs. Because the states $\Phi_P(t)$ are constructed out of PINOs, the expectation values can be worked out as

$$\langle \Phi_P(t)|\mathrm{i}\partial_t - \hat{\mathrm{H}}_0(t)|\Phi_P(t)\rangle = \sum_{p\in P} \big\langle \text{ɸ}_p(t)\big|\mathrm{i}\partial_t - \hat{h}(t)\big|\text{ɸ}_p(t)\big\rangle, \tag{121}$$

where $p \in P$ means that the sum runs over all PINOs present in the determinant Φ_P. Because the 1-RDM of the ensemble should have the prescribed occupation numbers, all the weights of the states which contain a particular ɸ_p need to sum to the corresponding occupation number, $n_p(t)$. The non-interacting action therefore simplifies even further to

$$A_0\big[\{\text{ɸ}_p, n_p\}\big] = \int_0^T \mathrm{d}t \sum_p n_p(t) \big\langle \text{ɸ}_p(t)\big|\mathrm{i}\partial_t - \hat{h}(t)\big|\text{ɸ}_p(t)\big\rangle, \tag{122}$$

and the variational principle becomes

$$\delta A_0 = \mathrm{i}\sum_P \big\langle \Phi_P(T)\big|\delta\Phi_P(T)\big\rangle = \mathrm{i}\sum_p n_p(T)\big\langle \text{ɸ}_p(T)\big|\delta\text{ɸ}_p(T)\big\rangle. \tag{123}$$

Considering variations in δA_0 separately, we find the expected result that the PINOs are solutions of one-electron Schrödinger equations $\mathrm{i}\partial_t \text{ɸ}_p(\mathbf{x}t) = \hat{h}(t)\,\text{ɸ}_p(\mathbf{x}t)$ and that the occupation numbers (weights) are time-*in*dependent. We are not interested in the solutions of the non-interacting system, however, but we want the solutions of the interacting system. Therefore, we should add a "bath" term which takes into account that the electrons do not behave independently but move in the "bath" of other electrons. Hence, we subtract the following term

$$\begin{aligned}\delta\mathcal{W}\big[\{\text{ɸ}_p, n_p\}\big] &= \delta A_{\mathrm{Hxc}}\big[\{\text{ɸ}_p, n_p\}\big] \\ &+ \mathrm{i}\big\langle \Psi\big[\{\text{ɸ}_p, n_p\}\big](T)\big|\delta\Psi\big[\{\text{ɸ}_p, n_p\}\big](T)\big\rangle - \mathrm{i}\sum_p n_p(T)\big\langle \text{ɸ}_p(T)|\delta\text{ɸ}_p(T)\big\rangle\end{aligned} \tag{124}$$

from the left-hand side, to make the variational principle equal to the interacting one (118)

$$\delta A_0\big[\{\text{ɸ}_p, n_p\}\big] - \delta\mathcal{W}\big[\{\text{ɸ}_p, n_p\}\big] = \mathrm{i}\sum_p n_p(T)\big\langle \text{ɸ}_p(T)|\delta\text{ɸ}_p(T)\big\rangle. \tag{125}$$

Enforcing the orthonormality of the PINOs with the standard Lagrange multiplier technique, we can work out the variations in the action produced by perturbations in the PINOs [117, 145], which recovers the equation of motion for the 1-RDM in the natural orbital basis (96)

$$\begin{aligned} &\mathrm{i}\Big[\dot{n}_p(t) + \big(n_q(t) - n_p(t)\big)\Big\langle \phi_p(t)|\dot{\phi}_q(t)\Big\rangle\Big] \\ &\quad = \big(n_q(t) - n_p(t)\big)h_{pq}(t) + \Big(\mathcal{W}^{\phi^\dagger}_{pq}(t) - \mathcal{W}^{\phi}_{pq}(t)\Big), \end{aligned} \tag{126}$$

where the effects of the electron–electron interaction are now expressed as variations $\delta\mathcal{W}$ produced by perturbations in the PINOs

$$\mathcal{W}^{\phi}_{pq}(t) = \int \mathrm{d}\mathbf{x}\, \frac{\delta\mathcal{W}}{\delta\phi_p(\mathbf{x}t)}\,\phi_q(\mathbf{x}t). \tag{127}$$

An equation of motion for the phase factors of the PINOs is obtained by considering variations produced by perturbations in the occupation numbers, which give [117, 144, 145]

$$\mathrm{i}\Big\langle \phi_p(t)|\dot{\phi}_p(t)\Big\rangle = h_{pp}(t) + \frac{\delta\mathcal{W}}{\delta n_p(t)}. \tag{128}$$

One can combine the equation of motion for the PINO phase factors with the off-diagonal terms of the equation of motion for the 1-RDM (126) to write a Schrödinger equation for the PINOs with an effective potential, $\hat{v}^{\,\mathrm{PINO}}\big[\{\phi_p, n_p\}\big](t)$, [117, 144, 145]

$$\mathrm{i}\partial_t \phi_p(\mathbf{x}t) = \big(\hat{h}(t) + \hat{v}^{\,\mathrm{PINO}}[\{\phi_r, n_r\}](t)\big)\,\phi_p(\mathbf{x}t), \tag{129}$$

where $\hat{v}^{\,\mathrm{PINO}}\big[\{\phi_p, n_p\}\big](t)$ is an effective potential which takes the two-body effects into account and is defined via its matrix elements which can be read off from (126) and (128)

$$v^{\mathrm{PINO}}_{pq}[\{\phi_r, n_r\}](t) = \begin{cases} \dfrac{\mathcal{W}^{\phi^\dagger}_{pq}(t) - \mathcal{W}^{\phi}_{pq}(t)}{n_q(t) - n_p(t)} & \text{for } p \neq q \\ \dfrac{\delta\mathcal{W}}{\delta n_p(t)} & \text{for } p = q \end{cases}. \tag{130}$$

It is interesting to consider the effective time-dependent Schrödinger equation for the PINOs (129) in the case of a stationary (ground) state. In that case, the time-dependence of the PINOs factors out as a simple exponential, $\phi_p(\mathbf{x}t) = \mathrm{e}^{-\mathrm{i}\varepsilon_p t}\phi_p(\mathbf{x})$, and the exponential factors, ε_p, are related to the time-independent Schrödinger for the PINOs

$$\Big(\hat{h} + v^{\mathrm{PINO}}_{pq}[\{\phi_r, n_r\}]\Big)\,\phi_p(\mathbf{x}) = \varepsilon_p\,\phi_p(\mathbf{x}). \tag{131}$$

The degeneracy of the natural spinorbitals [103] mentioned in Sect. 4 can therefore also be regarded as the complete in-phase time evolution of the PINOs. This makes

complete sense, especially for the two-electron system, because the phase factors of the PINOs can be used to reconstruct completely the two-electron wavefunction as [117, 155]

$$\Psi(\mathbf{x}_1,\mathbf{x}_2;t) = \frac{1}{\sqrt{2}}\sum_{p=1}^{m}\sqrt{n_p(t)}\left[\phi\!\!\!^{-}_{p}(\mathbf{x}_1 t)\phi\!\!\!^{-}_{-p}(\mathbf{x}_2 t) - \phi\!\!\!^{-}_{-p}(\mathbf{x}_1 t)\phi\!\!\!^{-}_{p}(\mathbf{x}_2 t)\right], \tag{132}$$

so the PINOs are coupled in pairs in the two-electron wavefunction. This expression is valid for an arbitrary spin state. In the case of a singlet state, the spin-up and spin-down components of the same spatial part form the PINO pairs and, in the case of triplet states, two PINO which are spatially different are coupled together [117]. It is clear from this expression that for all $n_p \neq 0$, all the PINOs need to have the same time-dependent phase factor in order for the full two-electron wavefunction to be a stationary state, $\Psi(\mathbf{x}_1,\mathbf{x}_2;t) = \mathrm{e}^{-\mathrm{i}Et}\Psi(\mathbf{x}_1,\mathbf{x}_2)$.

The equations of motion can be used again to formulate time-dependent response equations. Because the zeroth-order time-dependent PINOs already have a (time-dependent) phase factor, we expand the perturbation in the PINO in the order of the perturbation as

$$\phi\!\!\!^{-}_{p}(\mathbf{x}t) = \mathrm{e}^{\mathrm{i}\varepsilon_p t}\left(\phi\!\!\!^{-}_{p}(\mathbf{x}) + \delta\phi\!\!\!^{-}_{p}(\mathbf{x}t) + \cdots\right) \tag{133}$$

The first order of the perturbation in the PINOs, $\delta\phi\!\!\!^{-}_{p}(\mathbf{x}t)$ is expanded in the time-independent PINO basis as

$$\delta\phi\!\!\!^{-}_{p}(\mathbf{x}t) = \sum_{r}\phi\!\!\!^{-}_{r}(\mathbf{x})\delta U_{rp}(t). \tag{134}$$

The advantage of expressing the first-order perturbation in this manner is that the connection between and $\delta\boldsymbol{\gamma}(t)$ used in the TD-RDMFT response equations at (98) is still valid. Following the same procedure as before, collecting all perturbations up to first order and taking the Fourier transform, the frequency-dependent PINO response equations in the standard adiabatic approximation, $\mathcal{W} \approx W$ can be cast in the following form [117, 144, 145, 156]

$$\begin{pmatrix} \omega\mathbf{1}_M & \mathbf{0} & -\mathbf{A}^{+}_{MM} & -\mathbf{A}^{+}_{Mm} \\ \mathbf{0} & \omega\mathbf{1}_m & -\mathbf{A}^{+}_{mM} & -\mathbf{A}^{+}_{mm} \\ -\mathbf{N}^{-1}\mathbf{A}^{-}\mathbf{N}^{-1} & -\mathbf{N}^{-1}\mathbf{C} & \omega\mathbf{1}_M & \mathbf{0} \\ -\mathbf{C}^{T}\mathbf{N}^{-1} & -\overline{\mathbf{W}} & \mathbf{0} & \omega\mathbf{1}_m \end{pmatrix} \begin{pmatrix} \delta\gamma^{R}(\omega) \\ \delta\mathbf{n}(\omega) \\ \mathrm{i}\delta\mathbf{U}^{I}(\omega) \\ \mathrm{i}\delta\mathbf{U}^{D}(\omega)/2 \end{pmatrix} = \begin{pmatrix} \mathbf{0} \\ \mathbf{0} \\ \delta\mathbf{v}^{R}(\omega) \\ \delta\mathbf{v}^{D}(\omega)/2 \end{pmatrix}. \tag{135}$$

These PINO response equations in the adiabatic approximation have all the desired properties:

- The $\omega \to 0$ exactly coincides with the linear response equations of static RDMFT (see Sect. 3.1)

- The diagonal double excitations are properly accounted for without destroying the important symmetry of the response function, $\chi(\omega) = \chi^*(-\omega)$
- The PILS functional is a proper PINO functional, so the exact PINO functional is known for the two-electron system

The dimensionality of the response equations can be reduced by half by eliminating the imaginary components from the response equations, giving

$$\left[\omega^2 - \mathbf{A}^+ \begin{pmatrix} \mathbf{N}^{-1}\mathbf{A}^-\mathbf{N}^{-1} & \mathbf{N}^{-1}\mathbf{C} \\ \mathbf{C}^T\mathbf{N}^{-1} & \overline{\mathbf{W}} \end{pmatrix}\right] \begin{pmatrix} \delta\gamma^R(\omega) \\ \delta\mathbf{n}(\omega) \end{pmatrix} = \mathbf{A}^+ \begin{pmatrix} \delta\mathbf{v}^R(\omega) \\ \delta\mathbf{v}^D(\omega)/2 \end{pmatrix}, \quad (136)$$

which immediately demonstrates that indeed all the roots occur both at $+\omega$ and $-\omega$. The dimensionality of the TD-PINO response equations ($m(m+1)/2$) is significantly larger than in TDDFT, where only the transitions between the occupied and unoccupied KS orbitals need to be taken into account (so the dimension would be only $m-1$ for two electrons). Though the results from the adiabatic TD-PINO equations are far superior to those from adiabatic TDDFT, the computational cost is equivalent to a full CI calculation. However, one would expect that the transitions between all the low occupied PINOs are not important for the description of low lying excited states. Test calculations have been performed where only transitions from the k highest occupied PINOs to all other PINOs are taken into account. No reduction was made in $\delta\mathbf{n}(\omega)$, because its full treatment turned out to be important for particle number conservation.

Indeed, calculations with low values of k demonstrated that the polarizabilities [147], excitations [156], and oscillator strengths [157] are in excellent agreement with the exact results. Taking transitions from only the highest occupied PINO into account ($k=1$) gives reasonable results for the low lying excitations of the hydrogen molecule at its equilibrium. To take properly into account the static correlation effects on the excitation spectrum, one also needs transition from the $1\sigma_u$ PINO, because that PINO also obtains a significant occupation when the bond is stretched. The truncation to $k=2$ already gives results very close to the exact ones along the complete bond-breaking coordinate. Going to $k=3$ only provides a small additional improvement over $k=2$.

The same idea has also been tested in the time-domain [155, 158]. The same effect as in the frequency-domain has been observed: only a small number of the highest occupied PINOs need explicitly to be taken into account to give a reliable description of the physical processes. This is particularly interesting for the calculation of the double ionization yield of He in strong laser fields, which needs an accurate description of non-sequential double ionization, a highly correlated process [159, 160]. An accurate account of the non-sequential double ionization process has only been given in one dimension by solving the full many-body Schrödinger equation for a one-dimensional He model [161]. A full three-dimensional treatment is still out of reach, because the grid (number of basis functions) needs to be very large to describe the electrons moving very far away from the nucleus and coming back. In a one-dimensional pilot study it has been

demonstrated that only ten PINOs are sufficient to give a quantitative prediction of the double ionization yield [162], so an accurate three-dimensional calculation should now come within reach.

The main challenge is to make the PINO approach applicable to systems with more than two electrons. For the two-electron system it is clear how to define the PINO phase factors which gives a very simple expression for the two-body effects, W, and is even exact. For systems with more electrons, it is not so clear what a suitable and convenient definition for the PINO phase would be and which preferably reduces to the exact functional for two electrons. For multi-electron systems which only have one electron pair constituting a chemical bond (Li_2 and LiH for example), one can try to use a Hartree–Fock (HF) functional for the core electrons and the PILS functional for the "HONO" which is the highest strongly occupied natural orbital and some encouraging results have already been obtained for diatomic molecules with a single chemical bond [163].

A different route is also explored by combining features from the PINO response equations to the extended RPA equations [164, 165] obtained from Rowe's equation of motion framework [166]. The advantage is that the response matrices are now formulated as partial contractions of the 1-RDM and 2-RDM instead of functional derivatives with respect to PINOs and occupation numbers. This makes it easier to use other sources for approximate 2-RDMs such as the APSG wavefunction or other correlated methods. However, the APSG wavefunction can also be used to construct a PINO functional (62). The adiabatic PINO response equations with the APSG functional are actually identical to those obtained by applying time-dependent response theory to the APSG wavefunction directly [165]. Calculations on small molecular systems have demonstrated that the lowest excitation energies for the APSG functional (62) are in very good agreement with more sophisticated approaches. Higher excitation energies seem to be less reliable. Experiments using a range-separated version of the APSG functional indicate a shortcoming of the APSG functional rather than an inherent limitation of the adiabatic TD-PINO linear response equations [165]. However, more evidence needs to be gathered before we can make any conclusive statement.

6 Summary and Outlook

Reduced density matrix functional theory is a promising approach to the problem of electron correlation based on the existence of a functional of the one-electron reduced density matrix (1-RDM). One-electron components of the total energy, i.e. the kinetic part and the external potential interaction, are explicitly given in terms of 1-RDM. The electron–electron interaction functional, the two-electron part of the energy, is well defined, cf. (10), but its practical exact realization remains unknown. A formalism that would lead to systematically more accurate and efficient approximations to $E_{ee}[\gamma]$ is not available. By "efficient" we mean approximations that would avoid searching for minimizing wavefunctions or ensembles

proposed in constructions given in (9) or (10), and would be competing in computational efficiency with one-electron methods. Over the years different approaches to construct approximate functionals have been explored, some of them leading to successful functionals. The first generation of functionals such as BB (20), GU (22), or CHF (23) has turned out to be insufficiently accurate for molecules and extended systems. Their failure in predicting potential energy curves of diatomic molecules has led to realizing the importance of incorporating orbital structure of the exact two-electron functional into approximate *N*-electron functionals. A series of BBC (41)–(43) functionals and the recent ELS (44) functional have emerged as a result of a careful analysis of the orbital structure of the energy expression obtained from a size-consistent CI ansatz. The orbital structure of the most accurate BBC functional – BBC3 – leads to accurate potential energy curves of simple molecules. Because of numerical problems with selecting bonding and antibonding orbitals, assumed in a definition of BBC3 [see (43)], an "automated" version has been proposed – the AC3 functional [40]. The orbital structures of the BBC3, AC3, and ELS functionals account for that of the exact two-electron functional necessary to provide a correct description of electron-pair dissociation.

Almost all approximate electron–electron interaction functionals proposed so far are the so-called "*JK*-only" functionals, i.e., they include only two-electron integrals of the Coulomb and exchange type. In [76] Kollmar addressed the question of accuracy of the most general "*JK*-only" variational energy expression. Based on his findings, one is driven to a conclusion of fundamental importance for functional development. Namely, the limits of accuracy of the variational "*JK*-only" functionals are set by a pair-excited CI ansatz (67) that leads to the best "*JK*-only" energy expression [41]. This ansatz is known to be insufficiently accurate for chemical problems. It has been shown in [76] that variational (bounded from below by an exact ground state energy) "*JK*-only" functionals unavoidably miss a significant portion of the dynamic electron correlation. Therefore, successful variational functionals should include other than Coulomb and exchange integrals or one should not try to impose variationality in developing accurate and versatile "*JK*-only" functionals.

Another class of functionals – Piris natural orbital functionals (PNOF's) [cf. (51)] – are also of "*JK*-only" type. They have been proposed by employing a cumulant expansion given in (28) and approximating two-electron reduced density matrix elements in terms of the natural occupation numbers. Reconstruction of 2-RDM in terms of 1-RDM is guided by *N*-representability conditions for 2-RDM. PNOFs, especially one of the latest ones, PNOF5, have been extensively tested for predicting energy and different properties of molecules of diversified electronic structure. PNOF5 is particularly successful in describing systems for which static electron correlation is nonnegligible. At the same time, it has become apparent that this functional misses an important part of dynamic correlation, which seriously plagues its performance for some systems. These findings are perfectly understandable because, as a variational "*JK*-only" functional, PNOF5 inherits the aforementioned limitations of the best "*JK*-only" functional. Thinking about the possible ways of developing functionals based on reconstructing 2-RDM in terms of

1-RDM, it is evident that retaining solely Coulomb and exchange integrals in the functional and reconstructing N-representable 2-RDM would lead to a variational functional deficient in accounting for dynamic electron correlation. However, N-representability conditions for 2-RDM employed in developing novel functionals are of necessary but insufficient character. Consequently, functionals resulting from employing a reconstructional approach are not necessarily variational. As a result, they can yield lower energy than the best "*JK*-only" functional if the limited "*JK*-only" form is properly compensated by the lack of N-representability of the underlying 2-RDM.

BBC, ELS, or PNOF functionals are orbital-dependent and, by incorporating a subtle orbital structure of the exact two-electron functional, they are more appropriate for molecular systems than for solids. A functional proposed to work mainly for extended systems is the power functional (80) with the value of the power α found empirically. Because of a simple form of the power functional its optimization is highly efficient. Taking into account that its form has been proposed rather ad hoc without imposing any exact conditions, it is remarkable how well it works for solids. The most spectacular application of the power functional is for Mott insulators which are properly predicted to be nonmetallic [84]. In general, power functional cannot compete with the BBC3 or the recent PNOF functionals in describing the electronic structure of molecular systems.

It should be mentioned that most of the functionals have been proposed in spin-restricted formulation but extensions to open-shell systems are also available [167]. So far, RDMFT for high-spin systems has been tested for only a limited set of systems.

Size-consistency is another property that a useful functional should possess. Apart from the BB or power functionals, most of the other available approximations are, in principle, not size-consistent. However, in [168] it has been shown that violation of size-consistency is negligible for BBC, AC3, and ML functionals.

Undoubtedly there has been significant progress in the last 10 years in the development of methods in RDMFT. More accurate and versatile functionals have been proposed. Surprisingly, the "*JK*-only" form has not yet been fully exploited and the most recent functionals, ELS [42] and PNOF6 [48], still stay within this form. As has been discussed, future functionals can either include other integrals than Coulomb and exchange or stay within the "*JK*-only" form at the price of abandoning variationality from the start. Unfortunately, development of RDMFT-based methods is hindered by slow advances in improving computational efficiency of optimization algorithms for density matrix functionals. The lack of sufficiently fast methods has not allowed for application of the existing functionals to systems consisting of more than a few tens of electrons. Only the very recently proposed local-RDMFT approach [104] holds any promise of extending limits of the size of systems that can be treated with RDMFT by at least one order of magnitude.

The practical use of a time-dependent version of RDMFT has recently been explored to calculate excitation energies and other frequency-dependent response properties. A rigorous mathematical foundation for TD-RDMFT is still lacking,

because the Runge–Gross proof [138] cannot straightforwardly be extended to 1-RDMs and non-local potentials. Not only is the mathematical foundation of TD-RDMFT more challenging than in TDDFT, but also the formulation of a satisfactory adiabatic approximation has turned out to be rather involved. The standard adiabatic approximation (same as in TDDFT) leads to a mismatch between the static response equations and the frequency-dependent response equations in their $\omega \to 0$ limit. This problem can be mitigated by assuming an instantaneous response of the natural occupation numbers. Nevertheless, important diagonal double excitations are still missing and a justification for the use of the PILS functional, which is not a proper 1-RDM functional, is still lacking. All these problems are solved by augmenting the time-dependent 1-RDM with explicit phase-factors for the natural spinorbitals. The TD-PINO equations have all the desired properties of a decent adiabatic approximation. In contrast to TDDFT, even in the adiabatic approximation, the TD-PINO response equations are able to describe excitations of double and bond-breaking character and charge transfer excitations are also recovered without difficulty. A confirmation of this statement has been delivered by the results for the H_2 and HeH^+ molecules, obtained within the adiabatic TD-PINO formalism with the PILS functional and the extended RPA results with the APSG density matrices. The latter approach has been shown to be equivalent to the adiabatic TD-PINO if the APSG functional is employed [165] and has been tested on several small molecules. Even though it recovers certain double excitations, its overall accuracy is not satisfactory. The main challenges in the time-dependent direction are to formulate a general definition for the PINO phase factors to develop functionals for N-electron systems and to establish a proper mathematical foundation.

Acknowledgements The authors wish to acknowledge Dr. Ewa Pastorczak for critically reading the manuscript. KJHG gratefully acknowledges a VENI grant by the Netherlands Foundation for Research NWO (722.012.013). KP acknowledges support by the National Science Centre of Poland under grant DEC-2012/07/E/ST4/03023.

References

1. Gilbert TL (1975) Hohenberg–Kohn theorem for nonlocal external potentials. Phys Rev B 12 (6):2111–2120. doi:10.1103/PhysRevB.12.2111
2. Coleman AJ (1963) Structure of fermion density matrices. Rev Mod Phys 35(3):668–687. doi:10.1103/RevModPhys.35.668
3. Smith DW (1966) N-representability problem for fermion density matrices. II. The first-order density matrix with N even. Phys Rev 147(4):896–898. doi:10.1103/PhysRev.147.896
4. Levy M (1979) Universal variational functionals of electron-densities, first-order density-matrices, and natural spin-orbitals and solution of the v-representability problem. Proc Natl Acad Sci U S A 76(12):6062–6065. doi:10.1073/pnas.76.12.6062
5. Levy M (1987) Correlation energy functionals of one-matrices and Hartree–Fock densities. In: Erdahl R, Smith VHJ (eds) Density matrices and density functionals. Reidel, Dordrecht, pp 479–498

6. Zumbach G, Maschke K (1985) Density-matrix functional theory for the N-particle ground-state. J Chem Phys 82(12):5604–5607. doi:10.1063/1.448595
7. Valone SM (1980) Consequences of extending 1 matrix energy functionals from pure-state representable to all ensemble representable 1 matrices. J Chem Phys 73(3):1344–1349. doi:10.1063/1.440249
8. Valone SM (1980) A one-to-one mapping between one-particle densities and some normal-particle ensembles. J Chem Phys 73(9):4653–4655. doi:10.1063/1.440656
9. Nguyen-Dang TT, Ludeña EV, Tal Y (1985) Variation of the energy functional of the reduced first-order density operator. J Mol Struct (THEOCHEM) 120:247–264. doi:10.1016/0166-1280(85)85114-9
10. Donnelly RA (1979) Fundamental difference between energy functionals based on 1st-order and on 2nd-order density matrices. J Chem Phys 71(7):2874–2879. doi:10.1063/1.438678
11. Donnelly RA, Parr RG (1978) Elementary properties of an energy functional of first-order reduced density matrix. J Chem Phys 69(10):4431–4439. doi:10.1063/1.436433
12. Löwdin PO (1955) Quantum theory of many-particle systems. I. Physical interpretations by means of density matrices, natural spin-orbitals, and convergence problems in the method of configurational interaction. Phys Rev 97(6):1474–1489. doi:10.1103/PhysRev.97.1474
13. Hohenberg P, Kohn W (1964) Inhomogeneous electron gas. Phys Rev B 136(3B):B864–B871. doi:10.1103/PhysRev.136.B864
14. Lieb EH (1981) Variational principle for many-fermion systems. Phys Rev Lett 46 (7):457–459. doi:10.1103/PhysRevLett.46.457
15. Yasuda K (2001) Correlation energy functional in the density-matrix functional theory. Phys Rev A 63:032517. doi:10.1103/PhysRevA.63.032517
16. Cioslowski J (2005) New constraints upon the electron–electron repulsion energy functional of the one-electron reduced density matrix. J Chem Phys 123:164106
17. Cioslowski J, Pernal K, Ziesche P (2002) Systematic construction of approximate one-matrix functionals for the electron–electron repulsion energy. J Chem Phys 117(21):9560–9566. doi:10.1063/1.1516804
18. Müller AMK (1984) Explicit approximate relation between reduced two-particle and one-particle density-matrices. Phys Lett A 105(9):446–452. doi:10.1016/0375-9601(84)91034-X
19. Buijse MA, Baerends EJ (2002) An approximate exchange-correlation hole density as a functional of the natural orbitals. Mol Phys 100(4):401–421. doi:10.1080/00268970110070243
20. Buijse MA (1991) Ph.D. thesis, Electron correlation. Fermi and Coulomb holes, dynamical and nondynamical correlation. Vrije Universiteit, Amsterdam
21. Frank RL, Lieb EH, Seiringer R, Siedentop H (2007) Muller's exchange-correlation energy in density-matrix-functional theory. Phys Rev A 76(5):052517. doi:10.1103/PhysRevA.76.052517
22. Staroverov VN, Scuseria GE (2002) Assessment of simple exchange-correlation energy functionals of the one-particle density matrix. J Chem Phys 117(6):2489–2495. doi:10.1063/1.1491395
23. Herbert JM, Harriman JE (2003) Self-interaction in natural orbital functional theory. Chem Phys Lett 382(1–2):142–149. doi:10.1016/j.cplett.2003.10.057
24. Herbert JM, Harriman JE (2003) N-representability and variational stability in natural orbital functional theory. J Chem Phys 118(24):10835–10846. doi:10.1063/1.1574787
25. Cohen AJ, Baerends EJ (2002) Variational density matrix functional calculations for the corrected Hartree and corrected Hartree–Fock functionals. Chem Phys Lett 364 (3–4):409–419. doi:10.1016/S0009-2614(02)01345-3
26. Cioslowski J, Pernal K (2001) Response properties and stability conditions in density matrix functional theory. J Chem Phys 115(13):5784–5790. doi:10.1063/1.1383292

27. Gritsenko O, Pernal K, Baerends E (2005) An improved density matrix functional by physically motivated repulsive corrections. J Chem Phys 122(20):204102. doi:10.1063/1.1906203
28. Goedecker S, Umrigar CJ (1998) Natural orbital functional for the many-electron problem. Phys Rev Lett 81(4):866–869. doi:10.1103/PhysRevLett.81.866
29. Goedecker S, Umrigar CJ (2000) Natural orbital functional theory. In: Cioslowski J (ed) - Many-electron densities and reduced density matrices. Kluwer, New York, p 165
30. Lathiotakis NN, Marques MAL (2008) Benchmark calculations for reduced density-matrix functional theory. J Chem Phys 128(18):184103. doi:10.1063/1.2899328
31. Csanyi G, Arias TA (2000) Tensor product expansions for correlation in quantum many-body systems. Phys Rev B 61(11):7348–7352. doi:10.1103/PhysRevB.61.7348
32. Staroverov VN, Scuseria GE (2002) Optimization of density matrix functionals by the Hartree-Fock-Bogoliubov method. J Chem Phys 117(24):11107–11112. doi:10.1063/1.1523060
33. Kutzelnigg W, Mukherjee D (1999) Cumulant expansion of the reduced density matrices. J Chem Phys 110(6):2800–2809. doi:10.1063/1.478189
34. Kutzelnigg W (1963) Die losung des quantenmechanischen zwei-elektronenproblems durch unmittelbare bestimmung der naturlichen einelektronenfunktionen. I. Theorie. Theor Chim Acta 1(4):327–342. doi:10.1007/BF00528764
35. Shull H, Löwdin PO (1956) Correlation splitting in helium-like ions. J Chem Phys 25 (5):1035–1040. doi:10.1063/1.1743093
36. Cioslowski J, Pernal K (2006) Unoccupied natural orbitals in two-electron Coulombic systems. Chem Phys Lett 430(1–3):188–190. doi:10.1016/j.cplett.2006.08.011
37. Sheng XW, Mentel LM, Gritsenko OV, Baerends EJ (2013) A natural orbital analysis of the long range behavior of chemical bonding and van der Waals interaction in singlet H2: the issue of zero natural orbital occupation numbers. J Chem Phys 138(16):164105. doi:10.1063/1.4801431
38. Giesbertz KJH, van Leeuwen R (2013) Long-range interactions and the sign of natural amplitudes in two-electron systems. J Chem Phys 139(10):104110. doi:10.1063/1.4820418
39. Cioslowski J, Pernal K (2000) The ground state of harmonium. J Chem Phys 113 (19):8434–8443. doi:10.1063/1.1318767
40. Rohr DR, Pernal K, Gritsenko OV, Baerends EJ (2008) A density matrix functional with occupation number driven treatment of dynamical and nondynamical correlation. J Chem Phys 129(16):164105. doi:10.1063/1.2998201
41. Pernal K, Cioslowski J (2004) Phase dilemma in density matrix functional theory. J Chem Phys 120(13):5987–5992. doi:10.1063/1.1651059
42. Mentel LM, van Meer R, Gritsenko OV, Baerends EJ (2014) The density matrix functional approach to electron correlation: dynamic and nondynamic correlation along the full dissociation coordinate. J Chem Phys 140(21):214105. doi:10.1063/1.4879776
43. Piris M (2006) A new approach for the two-electron cumulant in natural orbital functional theory. Int J Quant Chem 106(5):1093–1104. doi:10.1002/qua.20858
44. Piris M, Lopez X, Ugalde JM (2007) Dispersion interactions within the Piris natural orbital functional theory: the helium dimer. J Chem Phys 126(21):214103. doi:10.1063/1.2743019
45. Piris M, Matxain JM, Lopez X, Ugalde JM (2010) Communications: accurate description of atoms and molecules by natural orbital functional theory. J Chem Phys 132(3):031103. doi:10.1063/1.3298694
46. Piris M, Matxain JM, Lopez X, Ugalde JM (2010) Communication: the role of the positivity N-representability conditions in natural orbital functional theory. J Chem Phys 133 (11):111101. doi:10.1063/1.3481578
47. Piris M, Lopez X, Ruiperez F, Matxain JM, Ugalde JM (2011) A natural orbital functional for multiconfigurational states. J Chem Phys 134(16):164102. doi:10.1063/1.3582792
48. Piris M (2014) Interacting pairs in natural orbital functional theory. J Chem Phys 141:044107. doi:10.1063/1.4890653

49. Piris M, Ugalde JM (2014) Perspective on natural orbital functional theory. Int J Quant Chem 114(18, SI):1169–1175. doi:10.1002/qua.24663
50. Piris M (2013) A natural orbital functional based on an explicit approach of the two-electron cumulant. Int J Quant Chem 113(5, SI):620–630. doi:10.1002/qua.24020
51. Piris M, Matxain JM, Lopez X, Ugalde JM (2009) Spin conserving natural orbital functional theory. J Chem Phys 131(2):021102. doi:10.1063/1.3180958
52. Leiva P, Piris M (2006) Calculation of vertical ionization potentials with the Piris natural orbital functional. J Mol Struct (THEOCHEM) 770(1–3):45–49. doi:10.1016/j.theochem.2006.05.001
53. Lopez X, Piris M, Matxain JM, Ugalde JM (2010) Performance of PNOF3 for reactivity studies: X[BO] and X[CN] isomerization reactions (X = H, Li) as a case study. Phys Chem Chem Phys 12(40):12931–12934. doi:10.1039/c003379k
54. Lopez X, Ruiperez F, Piris M, Matxain JM, Matito E, Ugalde JM (2012) Performance of PNOF5 natural orbital functional for radical formation reactions: hydrogen atom abstraction and C-C and O-O homolytic bond cleavage in selected molecules. J Chem Theory Comput 8 (8):2646–2652. doi:10.1021/ct300414t
55. Ruiperez F, Piris M, Ugalde JM, Matxain JM (2013) The natural orbital functional theory of the bonding in Cr2, Mo2 and W2. Phys Chem Chem Phys 15(6):2055–2062. doi:10.1039/c2cp43559d
56. Matxain JM, Piris M, Ruiperez F, Lopez X, Ugalde JM (2011) Homolytic molecular dissociation in natural orbital functional theory. Phys Chem Chem Phys 13 (45):20129–20135. doi:10.1039/c1cp21696a
57. Piris M (2013) Interpair electron correlation by second-order perturbative corrections to PNOF5. J Chem Phys 139(6):064111. doi:10.1063/1.4817946
58. Piris M, Ruiperez F, Matxain JM (2014) Assessment of the second-order perturbative corrections to PNOF5. Mol Phys 112(5–6, SI):1–8. doi:10.1080/00268976.2013.854933
59. Szabados Á, Rolik Z, Tóth G, Surján PR (2005) Multiconfiguration perturbation theory: size consistency at second order. J Chem Phys 122(11):114104. doi:10.1063/1.1862235
60. Pernal K (2013) The equivalence of the Piris Natural Orbital Functional 5 (PNOF5) and the antisymmetrized product of strongly orthogonal geminal theory. Comput Theor Chem 1003 (SI):127–129. doi:10.1016/j.comptc.2012.08.022
61. Surján PR (1999) An introduction to the theory of geminals. In: Surján PR (ed) Correlation and localization, vol 203, Topics in current chemistry. Springer, Berlin/Heidelberg, pp 63–88
62. Rassolov V (2002) A geminal model chemistry. J Chem Phys 117(13):5978–5987. doi:10.1063/1.1503773
63. Rassolov VA, Xu F (2007) Geminal model chemistry. IV. Variational and size consistent pure spin states. J Chem Phys 127(4):044104. doi:10.1063/1.2755738
64. Hurley AC, Lennard-Jones J, Pople JA (1953) The molecular orbital theory of chemical valency. A theory of paired-electrons in polyatomic molecules. Proc R Soc Lond A Math Phys Sci 220(1143):446–455. doi:10.1098/rspa.1953.0198
65. Kutzelnigg W (1964) Direct determination of natural orbitals and natural expansion coefficients of many-electron wavefunctions. I. Natural orbitals in geminal product approximation. J Chem Phys 40(12):3640–3647. doi:10.1063/1.1725065
66. Arai T (1960) Theorem on separability of electron pairs. J Chem Phys 33(1):95–98. doi:10.1063/1.1731142
67. Mehler EL, Reudenberg K, Silver DM (1970) Electron correlation and separated pair approximation in diatomic molecules. II. Lithium hydride and boron hydride. J Chem Phys 52(3):1181–1205. doi:10.1063/1.1673115
68. Matxain JM, Piris M, Uranga J, Lopez X, Merino G, Ugalde JM (2012) The nature of chemical bonds from PNOF5 calculations. Chemphyschem 13(9):2297–2303. doi:10.1002/cphc.201200205
69. Piris M, Matxain JM, Lopez X (2013) The intrapair electron correlation in natural orbital functional theory. J Chem Phys 139(23):234109. doi:10.1063/1.4844075

70. Cioslowski J, Pernal K (2002) Density matrix functional theory of weak intermolecular interactions. J Chem Phys 116(12):4802–4807. doi:10.1063/1.1446028
71. Cioslowski J, Ziesche P, Pernal K (2001) Description of a high-density homogeneous electron gas with the Yasuda density matrix functional. J Chem Phys 115(19):8725–8730. doi:10.1063/1.1412604
72. Cioslowski J, Pernal K (2002) Variational density matrix functional theory calculations with the lowest-order Yasuda functional. J Chem Phys 117(1):67–71. doi:10.1063/1.1481384
73. Cioslowski J, Buchowiecki M, Ziesche P (2003) Density matrix functional theory of four-electron systems. J Chem Phys 119(22):11570–11573. doi:10.1063/1.1623741
74. Kollmar C, Hess BA (2003) A new approach to density matrix functional theory. J Chem Phys 119(9):4655–4661. doi:10.1063/1.1590635
75. Kollmar C, Hess BA (2004) The structure of the second-order reduced density matrix in density matrix functional theory and its construction from formal criteria. J Chem Phys 120 (7):3158–3171. doi:10.1063/1.1634554
76. Kollmar C (2004) The "JK-only" approximation in density matrix functional and wave function theory. J Chem Phys 121(23):11581–11586. doi:10.1063/1.1819319
77. Pernal K (2010) Long-range density-matrix-functional theory: application to a modified homogeneous electron gas. Phys Rev A 81(5):052511. doi:10.1103/PhysRevA.81.052511
78. Rohr DR, Toulouse J, Pernal K (2010) Combining density-functional theory and density-matrix-functional theory. Phys Rev A 82(5):052502. doi:10.1103/PhysRevA.82.052502
79. Stoll H, Savin A (1985) Density functionals for correlation energies of atoms and molecules. In: Dreizler R, da Providencia J (eds) Density functional methods in physics. Plenum, New York, pp 177–207
80. Toulouse J, Colonna F, Savin A (2004) Long-range-short-range separation of the electron–electron interaction in density-functional theory. Phys Rev A 70(6):062505. doi:10.1103/PhysRevA.70.062505
81. Goll E, Werner HJ, Stoll H (2005) A short-range gradient-corrected density functional in long-range coupled-cluster calculations for rare gas dimers. Phys Chem Chem Phys 7 (23):3917–3923. doi:10.1039/b509242f
82. Lathiotakis NN, Helbig N, Gross EKU (2007) Performance of one-body reduced density-matrix functionals for the homogeneous electron gas. Phys Rev B 75(19):195120. doi:10.1103/PhysRevB.75.195120
83. Cioslowski J, Pernal K (2000) Description of a homogeneous electron gas with simple functionals of the one-particle density matrix. Phys Rev A 61(3):034503
84. Sharma S, Dewhurst JK, Lathiotakis NN, Gross EKU (2008) Reduced density matrix functional for many-electron systems. Phys Rev B 78(20):201103. doi:10.1103/PhysRevB.78.201103
85. Lathiotakis NN, Helbig N, Zacarias A, Gross EKU (2009) A functional of the one-body-reduced density matrix derived from the homogeneous electron gas: performance for finite systems. J Chem Phys 130(6):064109. doi:10.1063/1.3073053
86. Lathiotakis NN, Sharma S, Dewhurst JK, Eich FG, Marques MAL, Gross EKU (2009) Density-matrix-power functional: performance for finite systems and the homogeneous electron gas. Phys Rev A 79(4):040501. doi:10.1103/PhysRevA.79.040501
87. Marques MAL, Lathiotakis NN (2008) Empirical functionals for reduced-density-matrix-functional theory. Phys Rev A 77(3):032509. doi:10.1103/PhysRevA.77.032509
88. Cioslowski J, Ziesche P, Pernal K (2001) On the exactness of simple natural spin-orbital functionals for a high-density homogeneous electron gas. Phys Rev B 63(20):205105
89. Cioslowski J, Pernal K (1999) Constraints upon natural spin orbital functionals imposed by properties of a homogeneous electron gas. J Chem Phys 111(8):3396–3400. doi:10.1063/1.479623
90. Sharma S, Dewhurst JK, Shallcross S, Gross EKU (2013) Spectral density and metal-insulator phase transition in Mott insulators within reduced density matrix functional theory. Phys Rev Lett 110(11):116403. doi:10.1103/PhysRevLett.110.116403

91. Pernal K, Baerends EJ (2006) Coupled-perturbed density-matrix functional theory equations. Application to static polarizabilities. J Chem Phys 124(1):14102. doi:10.1063/1.2137325
92. Lopez X, Piris M, Nakano M, Champagne B (2014) Natural orbital functional calculations of molecular polarizabilities and second hyperpolarizabilities. The hydrogen molecule as a test case. J Phys B At Mol Opt Phys 47(1):015101. doi:10.1088/0953-4075/47/1/015101
93. Leiva P, Piris M (2005) Assessment of a new approach for the two-electron cumulant in natural-orbital-functional theory. J Chem Phys 123(21):214102. doi:10.1063/1.2135289
94. Leiva P, Piris M (2005) Natural orbital functional theory: ionization potentials, equilibrium geometries and vibrational frequencies. J Mol Struct (THEOCHEM) 719(1–3):63–67. doi:10.1016/j.theochem.2005.01.023
95. Zarkadoula EN, Sharma S, Dewhurst JK, Gross EKU, Lathiotakis NN (2012) Ionization potentials and electron affinities from reduced-density-matrix functional theory. Phys Rev A 85(3):032504. doi:10.1103/PhysRevA.85.032504
96. Smith DW, Day OW (1975) Extension of Koopmans theorem. I. Derivation. J Chem Phys 62 (1):113–114. doi:10.1063/1.430253
97. Day OW, Smith DW, Morrison RC (1975) Extension of Koopmans theorem. II. Accurate ionization energies from correlated wavefunctions for closed-shell atoms. J Chem Phys 62 (1):115–119. doi:10.1063/1.430254
98. Morrell MM, Parr RG, Levy M (1975) Calculation of ionization-potentials from density matrices and natural functions, and long-range behavior of natural orbitals and electron-density. J Chem Phys 62(2):549–554. doi:10.1063/1.430509
99. Pernal K, Cioslowski J (2005) Ionization potentials from the extended Koopmans' theorem applied to density matrix functional theory. Chem Phys Lett 412(1–3):71–75. doi:10.1016/j.cplett.2005.06.103
100. Piris M, Matxain JM, Lopez X, Ugalde JM (2012) The extended Koopmans' theorem: vertical ionization potentials from natural orbital functional theory. J Chem Phys 136 (17):174116. doi:10.1063/1.4709769
101. Gritsenko OV, Braida B, Baerends EJ (2003) Physical interpretation and evaluation of the Kohn-Sham and Dyson components of the ε-I relations between the Kohn-Sham orbital energies and the ionization potentials. J Chem Phys 119(4):1937–1950. doi:10.1063/1.1582839
102. Chong DP, Gritsenko OV, Baerends EJ (2002) Interpretation of the Kohn-Sham orbital energies as approximate vertical ionization potentials. J Chem Phys 116(5):1760–1772. doi:10.1063/1.1430255
103. Pernal K (2005) Effective potential for natural spin orbitals. Phys Rev Lett 94(23):233002. doi:10.1103/PhysRevLett.94.233002
104. Lathiotakis NN, Helbig N, Rubio A, Gidopoulos NI (2014) Local reduced-density-matrix-functional theory: incorporating static correlation effects in Kohn-Sham equations. Phys Rev A 90(3):032511. doi:10.1103/PhysRevA.90.032511
105. Lathiotakis NN, Helbig N, Rubio A, Gidopoulos NI (2014) Quasi-particle energy spectra in local reduced density matrix functional theory. J Chem Phys 141(16):164120
106. Helbig N, Lathiotakis NN, Albrecht M, Gross EKU (2007) Discontinuity of the chemical potential in reduced-density-matrix-functional theory. EPL 77(6):67003. doi:10.1209/0295-5075/77/67003
107. Helbig N, Lathiotakis NN, Gross EKU (2009) Discontinuity of the chemical potential in reduced-density-matrix-functional theory for open-shell systems. Phys Rev A 79(2):022504. doi:10.1103/PhysRevA.79.022504
108. Lathiotakis NN, Sharma S, Helbig N, Dewhurst JK, Marques MAL, Eich F, Baldsiefen T, Zacarias A, Gross EKU (2010) Discontinuities of the chemical potential in reduced density matrix functional theory. Z Phys Chem 224(3–4, SI):467–480. doi:10.1524/zpch.2010.6118
109. Cancès E, Pernal K (2008) Projected gradient algorithms for Hartree-Fock and density matrix functional theory calculations. J Chem Phys 128(13):134108. doi:10.1063/1.2888550

110. Giesbertz KJH, Baerends EJ (2010) Aufbau derived from a unified treatment of occupation numbers in Hartree-Fock, Kohn-Sham, and natural orbital theories with the Karush-Kuhn-Tucker conditions for the inequality constraints $n_i \leq 1$ and $n_i \geq 0$. J Comput Chem 132 (19):194108. doi:10.1063/1.3426319
111. Piris M, Ugalde JM (2009) Iterative diagonalization for orbital optimization in natural orbital functional theory. J Comput Chem 30(13):2078–2086. doi:10.1002/jcc.21225
112. Requist R, Pankratov O (2008) Generalized Kohn-Sham system in one-matrix functional theory. Phys Rev B 77(23):235121. doi:10.1103/PhysRevB.77.235121
113. Baldsiefen T, Gross EKU (2013) Minimization procedure in reduced density matrix functional theory by means of an effective noninteracting system. Comput Theor Chem 1003 (SI):114–122. doi:10.1016/j.comptc.2012.09.001
114. Talman JD, Shadwick WF (1976) Optimized effective atomic central potential. Phys Rev A 14(1):36–40. doi:10.1103/PhysRevA.14.36
115. Kümmel S, Kronik L (2008) Orbital-dependent density functionals: theory and applications. Rev Mod Phys 80(1):3–60. doi:10.1103/RevModPhys.80.3
116. Gidopoulos NI, Lathiotakis NN (2012) Nonanalyticity of the optimized effective potential with finite basis sets. Phys Rev A 85(5):046502. doi:10.1103/PhysRevA.85.052508
117. Giesbertz KJH (2010) Time-dependent one-body reduced density matrix functional theory; adiabatic approximations and beyond. Ph.D. thesis, Vrije Universiteit, Amsterdam
118. Appel H (2007) Time-dependent quantum many-body systems: linear response, electronic transport and reduced density matrices. Ph.D. thesis, Freie Universität, Berlin
119. Pernal K, Gritsenko O, Baerends EJ (2007) Time-dependent density-matrix-functional theory. Phys Rev A 75(1):012506. doi:10.1103/PhysRevA.75.012506
120. Pernal K, Cioslowski J (2007) Frequency-dependent response properties and excitation energies from one-electron density matrix functionals. Phys Chem Chem Phys 9(45):5956. doi:10.1039/b704797e
121. Pernal K, Giesbertz K, Gritsenko O, Baerends EJ (2007) Adiabatic approximation of time-dependent density matrix functional response theory. J Chem Phys 127:214101. doi:10.1063/1.2800016
122. Tozer DJ, Amos RD, Handy NC, Roor BO, Serrano-Andrés L (1999) Does density functional theory contribute to the understanding of excited states of unsaturated organic compounds? Mol Phys 97(7):859–868
123. Dreuw A, Weisman JL, Head-Gordon M (2003) Long-range charge-transfer excited states in time-dependent density functional theory require non-local exchange. J Chem Phys 119 (6):2943. doi:10.1063/1.1590951
124. Yanai T, Tew DP, Handy NC (2004) A new hybrid exchange-correlation functional using the Coulomb-attenuating method (CAM-B3LYP). Chem Phys Lett 393(1–3):51
125. Gritsenko O, Baerends EJ (2004) Asymptotic correction of the exchange-correlation kernel of time-dependent density functional theory for long-range charge-transfer excitations. J Chem Phys 121(2):655
126. Neugebauer J, Gritsenko O, Baerends EJ (2006) Assessment of a simple correction for the long-range charge-transfer problem in time-dependent density-functional theory. J Chem Phys 124(21):214102
127. Gritsenko O, van Gisbergen SJA, Görling A, Baerends EJ (2000) Excitation energies of dissociating H2: a problematic case for the adiabatic approximation of time-dependent density functional theory. J Chem Phys 113(19):8478
128. Giesbertz KJH, Baerends EJ (2008) Failure of time-dependent density functional theory for excited state surfaces in case of homolytic bond dissociation. Chem Phys Lett 461:338. doi:10.1016/j.cplett.2008.07.018
129. Maitra NT, Zhang F, Cave RJ, Burke K (2004) Double excitations within time-dependent density functional theory linear response. J Chem Phys 120(13):5932

130. Neugebauer J, Baerends E (2004) Vibronic coupling and double excitations in linear response time-dependent density functional calculations: dipole allowed states of N_2. J Chem Phys 121 (13):6155. doi:10.1063/1.1785775
131. Yvon J (1935) Theorie statistique des fluides et l'equation et l'equation d'etat (French). In: Actes Sientifique et Industrie, vol. 203. Hermann, Paris
132. Bogoliubov NN (1946) Kinetic equations. J Phys USSR 10(3):265 (in English)
133. Bogoliubov NN (1946) Kinetic equations. J Exp Theor Phys 16(8):691 (in Russian)
134. Kirkwood JG (1946) The statistical mechanical theory of transport processes I. General theory. J Chem Phys 14(3):180
135. Born M, Green HS (1946) A general kinetic theory of liquids. I. The molecular distribution functions. Proc R Soc Med 188(1012):10–18
136. Kirkwood JG (1947) The statistical mechanical theory of transport processes II. Transport in gases. J Chem Phys 15(1):72
137. Bogoliubov NN, Gurov KP (1947) Kinetic equations in quantum mechanics (rus.). J Exp Theor Phys 17(7):614
138. Runge E, Gross EKU (1984) Density-functional theory for time-dependent systems. Phys Rev Lett 52(12):997. doi:10.1103/PhysRevLett.52.997
139. Ruggenthaler M, van Leeuwen R (2011) Global fixed-point proof of time-dependent density-functional theory. Europhys Lett 95(1):13001. doi:10.1209/0295-5075/95/13001
140. Ruggenthaler M, Giesbertz KJH, Penz M, van Leeuwen R (2012) Density-potential mappings in quantum dynamics. Phys Rev A 85(5):052504. doi:10.1103/PhysRevA.85.052504
141. Giesbertz KJH, Baerends EJ, Gritsenko OV (2008) Charge transfer, double and bond-breaking excitations with time-dependent density matrix functional theory. Phys Rev Lett 101:033004. doi:10.1103/PhysRevLett.101.033004
142. Giesbertz KJH, Pernal K, Gritsenko OV, Baerends EJ (2009) Excitation energies with time-dependent density matrix functional theory: singlet two-electron systems. J Chem Phys 130 (11):114104. doi:10.1063/1.3079821
143. Peuckert V (1978) A new approximation method for electron systems. J Phys C 11(24):4945
144. Giesbertz KJH, Gritsenko OV, Baerends EJ (2010) Response calculations with an independent particle system with an exact one-particle density matrix. Phys Rev Lett 105(1):013002. doi:10.1103/PhysRevLett.105.013002
145. Giesbertz KJH, Gritsenko OV, Baerends EJ (2010) The adiabatic approximation in time-dependent density matrix functional theory: response properties from dynamics of phase-including natural orbitals. J Chem Phys 133(17):174119. doi:10.1063/1.3499601
146. Requist R, Pankratov O (2011) Time-dependent occupation numbers in reduced-density-matrix-functional theory: application to an interacting Landau–Zener model. Phys Rev A 83 (5):052510. doi:10.1103/PhysRevA.83.052510
147. Giesbertz KJH, Gritsenko OV, Baerends EJ (2014) Response calculations based on an independent particle system with the exact one-particle density matrix: polarizabilities. J Chem Phys 140(18):18A517. doi:10.1063/1.4867000
148. Giesbertz KJH, Gritsenko OV, Baerends EJ (2012) Time-dependent reduced density matrix functional theory. In: Marques MAL, Maitra N, Nogueira F, Gross EKU, Rubio A (eds) Fundamentals of time-dependent density functional theory, vol 837, Lecture notes in physics. Springer, Berlin, pp 485–498. doi:10.1007/978-3-642-23518-4
149. Requist R, Pankratov O (2010) Adiabatic approximation in time-dependent reduced-density-matrix functional theory. Phys Rev A 81(4):042519. doi:10.1103/PhysRevA.81.042519
150. Lehmann H (1954) Über Eigenschaften von Ausbreitungsfunktionen und Renormierungs-konstanten quantisierter Felder. Nuovo Cimento 11(4):342
151. Requist R (2012) Hamiltonian formulation of nonequilibrium quantum dynamics: geometric structure of the Bogoliubov–Born–Green–Kirkwood–Yvon hierarchy. Phys Rev A 86 (2):022117. doi:10.1103/PhysRevA.86.02211

152. Kramer P, Saraceno M (1980) Geometry of the time-dependent variational principle in quantum mechanics. In: Group theoretical methods in physics. Lecture notes in physics, vol 135. Springer, Berlin, pp 112–121
153. Vignale G (2008) Real-time resolution of the causality paradox of time-dependent density-functional theory. Phys Rev A 77:062511. doi:10.1103/PhysRevA.77.062511
154. Gross EKU, Dobson JF, Petersilka M (1996) Density functional theory of time-dependent phenomena. In: Nalewajsk RF (ed) Density functional theory II, vol 181, Topics in current chemistry. Springer, Berlin, pp 81–172. doi:10.1007/BFb0016643
155. Rapp J, Brics M, Bauer D (2014) Equations of motion for natural orbitals of strongly driven two-electron systems. Phys Rev A 90(1):012518. doi:10.1103/PhysRevA.90.012518
156. Giesbertz KJH, Gritsenko OV, Baerends EJ (2012) Response calculations based on an independent particle system with the exact one-particle density matrix: excitation energies. J Chem Phys 136:094104. doi:10.1063/1.3687344
157. van Meer R, Gritsenko OV, Giesbertz KJH, Baerends EJ (2013) Oscillator strengths of electronic excitations with response theory using phase including natural orbital functionals. J Chem Phys 138(9):094114. doi:10.1063/1.4793740
158. Brics M, Bauer D (2013) Time-dependent renormalized natural orbital theory applied to the two-electron spin-singlet case: ground state, linear response, and autoionization. Phys Rev A 88(5):052514. doi:10.1103/PhysRevA.88.052514
159. de Morisson Faria CF, Liu X (2011) Electron–electron correlation in strong laser fields. J Opt Phys 58(13):1076. doi:10.1080/09500340.2010.543958
160. Becker W, Liu X, Ho PJ, Eberly JH (2012) Theories of photoelectron correlation in laser-driven multiple atomic ionization. Rev Mod Phys 84(3):1011. doi:10.1103/RevModPhys.84.1011
161. Lappas DG, van Leeuwen R (1998) Electron correlation effects in the double ionization of He. J Phys B 31(6):L249. doi:10.1088/0953-4075/31/6/001
162. Brics M, Rapp J, Bauer D (2014) Nonsequential double ionization with time-dependent renormalized-natural-orbital theory. Phys Rev A 90(5):053418. doi:10.1103/PhysRevA.90.053418
163. van Meer R, Gritsenko OV, Baerends EJ (2014) Excitation energies with linear response density matrix functional theory along the dissociation coordinate of an electron-pair bond in *N*-electron systems. J Chem Phys 140(2):024101. doi:10.1063/1.4852195
164. Chatterjee K, Pernal K (2012) Excitation energies from extended random phase approximation employed with approximate one- and two-electron reduced density matrices. J Chem Phys 137(20):204109. doi:10.1063/1.4766934
165. Pernal K, Chatterjee K, Kowalski PH (2014) How accurate is the strongly orthogonal geminal theory in predicting excitation energies? Comparison of the extended random phase approximation and the linear response theory approaches. J Chem Phys 140(1):014101. doi:10.1063/1.4855275
166. Rowe DJ (1968) Equations-of-motion method and the extended shell model. Rev Mod Phys 40(1):153–166. doi:10.1103/RevModPhys.40.153
167. Lathiotakis NN, Helbig N, Gross EKU (2005) Open shells in reduced-density-matrix-functional theory. Phys Rev A 72(3):030501. doi:10.1103/PhysRevA.72.030501
168. Lathiotakis NN, Gidopoulos NI, Helbig N (2010) Size consistency of explicit functionals of the natural orbitals in reduced density matrix functional theory. J Chem Phys 132(8):084105. doi:10.1063/1.3324699

Top Curr Chem (2016) 368: 185–218
DOI: 10.1007/128_2014_610

Published online: 25 March 2015

Excitons in Time-Dependent Density-Functional Theory

Carsten A. Ullrich and Zeng-hui Yang

Abstract This chapter gives an overview of the description of the optical and dielectric properties of bulk insulators and semiconductors in time-dependent density-functional theory (TDDFT), with an emphasis on excitons. We review the linear-response formalism for periodic solids, discuss excitonic exchange-correlation kernels, calculate exciton binding energies for various materials, and compare the treatment of excitons with TDDFT and with the Bethe–Salpeter equation.

Keywords Bethe–Salpeter equation · Dielectric function · Exchange-correlation kernel · Excitons · Time-dependent density-functional theory

Contents

C.A. Ullrich (✉)
Department of Physics and Astronomy, University of Missouri, Columbia, MO 65211, USA
e-mail: ullrichc@missouri.edu

Z.-h. Yang
Department of Physics and Astronomy, University of Missouri, Columbia, MO 65211, USA

Department of Physics, Temple University, Philadelphia, PA 19122, USA

1 Introduction

Time-dependent density-functional theory (TDDFT) is a universal approach to the dynamical many-body problem. A detailed, up-to-date coverage of TDDFT can be found in two books [1, 2]. An easy and concise introduction is given in a recent review article by Ullrich and Yang [3].

At present, the majority of applications of TDDFT take place in the field of computational (bio)chemistry, to obtain excitation energies and excited-state properties of molecules. However, applications in condensed-matter physics and materials science are emerging at a rapid rate. In this chapter we give an introduction and overview of TDDFT for extended periodic systems, focusing on the optical properties of semiconducting and insulating systems. In particular, we address the question of how TDDFT can be used to calculate excitonic binding energies and optical spectra with excitonic features. The present state-of-the-art approach in this field is given by Green's function-based many-body techniques, most notably, the combination of GW [4, 5] and the Bethe–Salpeter equation (BSE) [6–13]. We compare and contrast this approach with TDDFT and discuss their performance and the various pros and cons for bulk semiconductors and insulators.

TDDFT for periodic solids was reviewed a few years ago by Onida et al. [14] and Botti et al. [15]. Since then, many new developments have occurred, and in this chapter we attempt to cover the more recent progress in this field, including our own recent work [16–19]. We use atomic units ($\hbar = m = e = 4\pi\varepsilon_0 = 1$) unless otherwise indicated.

2 What Is an Exciton?

The optical properties of materials are determined by the way in which the electrons and the ions respond to light. In this chapter we focus exclusively on the electronic response and ignore the lattice dynamics or any effects related to the coupling of electronic and lattice excitations (such as polarons; for details see, e.g., Yu and Cardona [20]).

The response of a system of N electrons is often characterized as having either "single-particle" or "collective" character. What do we mean by this? If a system consists of noninteracting particles, the response is always purely single-particle, or can be viewed as the sum of many individual, uncorrelated single-particle excitations. In the presence of interactions this simple picture is no longer valid, because any change of state of one electron has an immediate influence on all other electrons

in the system; the response is collective and involves, in principle, all electrons. The question is how dominant these effects are.

There are many situations where the interactions give rise to rather straightforward behavior. Imagine an experiment where we can turn off the interactions between the electrons in a molecule, and measure the resulting excitation spectrum. If we now gradually turn the interactions back on, all the while keeping an eye on the excitation spectrum, we find that the peaks in the spectrum shift, but we can keep track of each of them and hence can in principle interpret them as single particle excitations of an effective system such as Kohn–Sham.

On the other hand, interacting systems have certain excitations without a counterpart in any corresponding noninteracting system. A most drastic example is plasmons in a metal, where all electrons respond collectively and with a fixed phase relationship. A plasmon requires dynamical electron–electron interactions at least at the level of the random-phase approximation (RPA).

An exciton is another example of a collective excitation, occurring in nonmetallic systems. The ideal exciton can be described [21] as an electrically neutral quantum of electronic excitation energy travelling in the periodic structure of a crystal. It can be viewed as a bound electron–hole pair and can hence be associated with the transportation of energy, but not of net charge. Excitons are a crucial stage in the photovoltaic process, where free carriers are generated after separation of the electron–hole pairs.

Excitons come in different types [22]:

- Frenkel excitons [23, 24] are excitations localized at the atomic sites of wide-gap insulators such as solid rare gases (neon, argon) or certain ionic solids (e.g., LiF).
- Davydov excitons [25] are found in molecular crystals with ring units, such as benzene and anthracene. Because the excitations remain localized on the individual molecules, Davydov excitons can be viewed as a subclass of Frenkel excitons.
- Mott–Wannier excitons [26, 27] typically occur in semiconductors such as GaAs, CdSe, or Cu_2O. They tend to be delocalized over several atomic unit cells.

The concept of excitons was originally introduced in bulk crystals, but they also exist in many lower-dimensional systems such as surfaces, quantum wells, quantum wires, nanotubes, polymers, nanocrystals, and quantum dots [28–33]. In this chapter we limit ourselves to three-dimensional periodic crystals.

Excitons are usually described as bound electron–hole pairs, i.e., as an effective two-particle system. Within the effective-mass approximation [34, 35], where conduction band electrons have effective mass m_e^* and valence band holes have effective mass m_h^*, we can define a reduced effective mass $m_r = m_e^* m_h^* / \left(m_e^* + m_h^*\right)$. Next, we separate center-of-mass and relative degrees of freedom. The former describes how the exciton travels through the crystal, and the latter determines the exciton binding energy according to the following hydrogen-like Schrödinger equation:

$$\left\{ -\frac{\hbar^2 \nabla^2}{2m_r} - \frac{e^2}{4\pi\varepsilon_0 \varepsilon r} \right\} \psi_j(\mathbf{r}) = E_j \psi_j(\mathbf{r}). \tag{1}$$

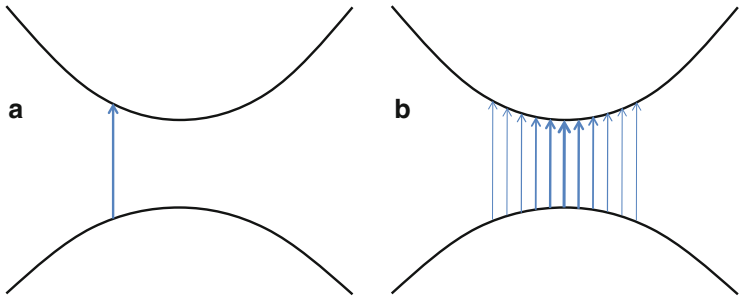

Fig. 1 Optical transitions in a two-band insulator, where the lower (valence) band is filled and the upper (conduction) band is empty. The vertical direction is energy, the horizontal direction is wavevector. (**a**) A single-particle transition, in which only one single-particle state gets excited and all other states do not participate. The associated excitation energy is the difference of the initial and final single-particle states. (**b**) Excitonic transition, which is a collective excitation in which many states participate. The thickness of the arrows indicates that transitions close to the band gap are dominant. The associated excitation energy can be *lower* than the band gap, because the collective nature of the response is energetically favorable

Here, ε_0 is the vacuum permittivity, e is the free electron charge, and ε is the dielectric constant of the material (we talk about the dielectric constant in greater detail in the following section). Equation (1) is also known as the Wannier equation. It yields a Rydberg series of bound states as well as a continuum of unbound states [36]. The lowest (1s) excitonic state determines the exciton binding energy E_0^{ex} and the exciton Bohr radius a_0^*. In GaAs, a material in which the Wannier equation works particularly well, one obtains $E_0^{\mathrm{ex}} = 4.6\,\mathrm{meV}$ and $a_0^* = 118\,\text{Å}$, which clearly shows that Wannier excitons are weakly bound and extend over many lattice constants which, a posteriori, justifies the simplified treatment via (1).

The Wannier picture of excitons as bound electron–hole pairs, described by (1), is generally not quantitatively accurate, and breaks down completely if the exciton radius becomes comparable to a lattice constant. In this chapter we present an ab initio approach, based on TDDFT and/or other many-body techniques, which is universally valid and in principle exact. This approach reveals an alternative point of view, in which excitons are described as collective excitations of the many-electron system. This picture is schematically illustrated in Fig. 1.

The left panel of Fig. 1 shows a single-particle transition in a simple model of an insulator, going vertically from the filled valence band to the empty conduction band. The energy associated with this transition is just the difference between the levels in the two bands. By contrast, an exciton arises from a superposition of many single-particle transitions, as illustrated in the right panel of Fig. 1. Not all transitions contribute with equal weight, as indicated by the different thicknesses of the arrows, but all of them have a fixed phase relationship; hence, the exciton is a collective excitation. The energy of the exciton (i.e., the energy of this collective excitation) is *lower* than the lowest single-particle transition. This happens because the collective behavior induced by the dynamical many-body effects is energetically favorable compared to any single-particle transition. We see later how the two viewpoints of the nature of an exciton can be reconciled with each other [18].

3 A Tale of Three Gaps

The defining characteristic of insulators and semiconductors is that they have an electronic band gap (we only consider materials at zero temperature) which dominates their optical and transport properties. Before we deal with the optical response of solids, it is crucial to have a clear understanding and a good description of the gap. However, it turns out that there are in fact three different kinds of gap (for the nonmagnetic materials we are interested in), and it is important to distinguish carefully between them [37].

The fundamental band gap E_{g} of an N-electron system is defined as follows:

$$E_{\mathrm{g}}(N) = I(N) - A(N), \tag{2}$$

where $I(N)$ and $A(N)$ are the ionization potential and the electron affinity of the system, respectively. These two quantities can be obtained in a straightforward manner from ground-state DFT: the ionization potential is formally exactly given by the highest occupied Kohn–Sham eigenvalue of the N-electron system, $\varepsilon_N(N)$, and the electron affinity is the corresponding quantity of the $N+1$-electron system. Hence, we obtain

$$E_{\mathrm{g}}(N) = \varepsilon_{N+1}(N+1) - \varepsilon_N(N). \tag{3}$$

It is important to note that the right-hand side of (3) contains the highest occupied Kohn–Sham eigenvalues of two different systems, namely with N and with $N+1$ electrons. In a macroscopic solid with 10^{23} electrons, it would be impossible (or at least highly impractical) to calculate the band gap according to this definition.

The band gap in the noninteracting Kohn–Sham system, also known as the Kohn–Sham gap, is defined as

$$E_{\mathrm{g,s}}(N) = \varepsilon_{N+1}(N) - \varepsilon_N(N). \tag{4}$$

In contrast with the interacting gap E_{g}, the Kohn–Sham gap $E_{\mathrm{g,s}}$ is simply the difference between the highest occupied and lowest unoccupied single-particle levels in the *same* N-particle system. This quantity is what is usually taken as the band gap in standard DFT band-structure calculations. We can relate the two gaps by

$$E_{\mathrm{g}} = E_{\mathrm{g,s}} + \Delta_{\mathrm{xc}}, \tag{5}$$

which defines Δ_{xc} as a many-body correction to the Kohn–Sham gap. By making use of the previous relations, we find $\Delta_{\mathrm{xc}} = \varepsilon_{N+1}(N+1) - \varepsilon_{N+1}(N)$. It turns out that the many-body gap correction Δ_{xc} can be related to a very fundamental property of density functionals, known as derivative discontinuities [38–42].

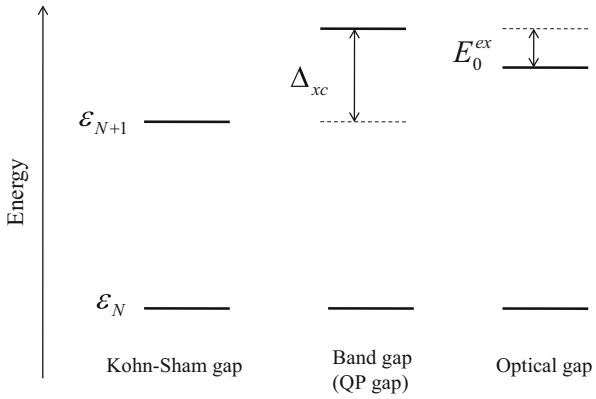

Fig. 2 Schematic illustration of the different types of gaps in DFT and TDDFT. The Kohn–Sham gap is defined as the difference of the highest occupied and lowest unoccupied Kohn–Sham eigenvalues of the N-electron system; see (4). The fundamental band gap [or quasiparticle (QP) gap] is the Kohn–Sham gap plus the derivative discontinuity; see (5). The optical gap is the band gap minus the lowest exciton binding energy E_0^{ex}. The Kohn–Sham gap can be viewed as an approximation for the optical gap

The so-called band-gap problem of DFT reflects the fact that in practice $E_{\mathrm{g,s}}$ is often a poor approximation to E_{g}, typically underestimating the exact band gap by as much as 50%. The reason for this is twofold: commonly used approximate xc functionals (such as LDA and GGA) tend to underestimate the *exact* Kohn–Sham gap $E_{\mathrm{g,s}}$, and they do not yield any discontinuity correction Δ_{xc}. An extreme example for the second failure is Mott insulators, which are typically predicted to be metallic by DFT. This is no accident: in Mott insulators, the exact Kohn–Sham system is metallic (i.e., $E_{\mathrm{g,s}} = 0$) so that $E_{\mathrm{g}} = \Delta_{\mathrm{xc}}$. Clearly, standard xc functionals (where Δ_{xc} vanishes) are unfit to describe Mott insulators.

It is important to distinguish between the fundamental band gap and the optical gap [43]. The band gap describes the energy which an electron must have so that, when it is added to an N-electron system, the result is an $N+1$ electron system in its ground state. The total charge of the system changes by -1 in this process. By contrast, the optical gap describes the lowest neutral excitation of an N-electron system: here, the number of electrons remains unchanged. The two gaps are schematically illustrated in Fig. 2 together with the Kohn–Sham gap.

The band gap of insulators can be accurately obtained from the so-called quasiparticle energies, which are defined as the single-particle energies of a noninteracting system whose one-particle Green's function is the same as that of the real interacting system (it should be noted that this effective noninteracting system is very different from the Kohn–Sham system, which is defined as that noninteracting system which reproduces the exact density). In practice, quasiparticle calculations are often done using the GW method [4, 5, 14]. GW calculations are more demanding than DFT, but they produce band structures of solids which agree very well with experiment.

In recent years, generalized Kohn–Sham schemes [37, 44, 45] have become quite popular for calculating band gaps of solids. Generalized Kohn–Sham theory means, in essence, using exchange-correlation (xc) functionals which contain an admixture of Hartree–Fock (HF) nonlocal exchange. These functionals (for instance B3LYP [46] or PBE0 [47]) have been crucial for the enormous success of DFT in theoretical chemistry. Hybrid xc functionals for solids are not unproblematic: HF exchange is difficult to implement in periodic systems, and B3LYP fails for metals [48]. However, for insulators, hybrid functionals generally produce excellent results, comparable to what can be achieved by more sophisticated many-body calculations [49–59]. Another promising approach is meta-GGA functionals such as the Tran–Blaha exchange potential [60–64], which gives good band structures and band gaps and is much less costly than hybrid functionals. However, it has the drawback of not being derivable from an energy functional.

It should be emphasized that current implementations of hybrid xc functionals do not actually calculate the *Kohn–Sham* gap (this would require a self-consistent calculation with a local potential); instead, hybrid functionals yield an approximation to the *quasiparticle* gap. Local xc potentials can, in principle, be constructed from hybrid functionals using the OEP (optimized effective potential) method, which was successfully done for the case of exact exchange (see Betzinger et al. [65] and references therein).

While the band gap can be measured using techniques in which electrons are added or removed from the system (such as photoemission spectroscopy), the optical gap refers to the lowest neutral excitation. The difference between quasiparticle band gap and optical gap is the lowest exciton binding energy, E_0^{ex}. In the previous section we have seen that excitons can be viewed as bound electron–hole pairs, whose bound states form a Rydberg series, analogous to the hydrogen atom. The band gap is given by the asymptotic limit of the excitonic Rydberg series [66] (at least for direct-gap insulators and semiconductors).

4 Linear Response and Optical Properties in Periodic Solids

4.1 Microscopic and Macroscopic Dielectric Functions

The interactions of electromagnetic fields and matter are governed by Maxwell's equations,

$$\nabla \cdot \mathbf{D} = n_{\mathrm{f}}, \tag{6}$$

$$\nabla \times \mathbf{E} = -\frac{\partial \mathbf{B}}{\partial t}, \tag{7}$$

$$\nabla \cdot \mathbf{B} = 0, \tag{8}$$

$$\nabla \times \mathbf{H} = \mathbf{j}_{\mathrm{f}} + \frac{\partial \mathbf{D}}{\partial t}, \tag{9}$$

where all fields (**D**, **E**, **B**, and **H**) and all source terms (the density of free charges n_{f} and the free current density $\mathbf{j}_{\mathrm{f}}$) are functions of position **r** and time t. We consider situations where all time dependence is periodic, and we Fourier transform from time t to frequency ω. Of main interest to us (because we are concerned with nonmagnetic materials) is the relationship between the electric displacement **D** and the total electric field **E**:

$$\mathbf{D}(\mathbf{r},\omega) = \int d^3r' \, \underline{\underline{\varepsilon}}(\mathbf{r},\mathbf{r}',\omega)\mathbf{E}(\mathbf{r}',\omega), \tag{10}$$

where $\underline{\underline{\varepsilon}}(\mathbf{r},\mathbf{r}',\omega)$ is the nonlocal, frequency-dependent dielectric tensor. In lattice-periodic systems, translational symmetry implies $\underline{\underline{\varepsilon}}(\mathbf{r},\mathbf{r}',\omega) = \underline{\underline{\varepsilon}}(\mathbf{r}+\mathbf{R},\mathbf{r}'+\mathbf{R},\omega)$, where **R** is a lattice vector. We can then Fourier analyze $\underline{\underline{\varepsilon}}(\mathbf{r},\mathbf{r}',\omega)$ and obtain

$$\underline{\underline{\varepsilon}}(\mathbf{r},\mathbf{r}',\omega) = \frac{1}{V}\sum_{\mathbf{k}\in \mathrm{BZ}} \sum_{\mathbf{G},\mathbf{G}'} \mathrm{e}^{-i(\mathbf{k}+\mathbf{G})\cdot\mathbf{r}} \mathrm{e}^{i(\mathbf{k}+\mathbf{G}')\cdot\mathbf{r}'} \underline{\underline{\varepsilon}}(\mathbf{k}+\mathbf{G},\mathbf{k}+\mathbf{G}',\omega), \tag{11}$$

where V is the crystal volume, **k** is a wave vector in the first Brillouin zone (BZ), and **G** and **G**′ are reciprocal lattice vectors. In the following we use the notation

$$\underline{\underline{\varepsilon}}_{\mathbf{G}\mathbf{G}'}(\mathbf{k},\omega) = \underline{\underline{\varepsilon}}(\mathbf{k}+\mathbf{G},\mathbf{k}+\mathbf{G}',\omega). \tag{12}$$

Using these definitions, we can recast (10) into

$$\mathbf{D}_{\mathbf{G}}(\mathbf{k},\omega) = \sum_{\mathbf{G}'} \underline{\underline{\varepsilon}}_{\mathbf{G}\mathbf{G}'}(\mathbf{k},\omega)\mathbf{E}_{\mathbf{G}'}(\mathbf{k},\omega). \tag{13}$$

For comparison with experiment, one is usually interested in macroscopic quantities, i.e., quantities which are defined as averages over the unit cell of the crystal. For instance, the macroscopic limit of (13) is defined as

$$\mathbf{D}_{\mathrm{mac}}(\omega) = \underline{\underline{\varepsilon}}_{\mathrm{mac}}(\omega)\mathbf{E}_{\mathrm{mac}}(\omega). \tag{14}$$

An important observation from (13) is that the microscopic $\underline{\underline{\varepsilon}}_{\mathbf{G}\mathbf{G}'}(\mathbf{k},\omega)$ is in general nondiagonal in **G** and **G**′, for inhomogeneous systems. Therefore, even a uniform external field induces nonuniform microscopic fluctuations in the solid; these are called local-field effects. As a consequence, the macroscopic $\underline{\underline{\varepsilon}}_{\mathrm{mac}}(\omega)$ cannot be calculated directly; instead, one must take a detour via microscopic linear-response theory. Otherwise, local-field effects would not be properly included.

In the following we restrict the discussion to crystals with cubic symmetry because this leads to the considerable simplification that the dielectric tensor becomes isotropic in the long-wavelength limit and one can carry out a decomposition into longitudinal and transverse components similar to that for the homogeneous case. It can then be shown that the macroscopic dielectric constant is given by [67–69]

$$\varepsilon_{\mathrm{mac}}(\omega) = \lim_{k\to 0}\left[\varepsilon_{\mathbf{G}\mathbf{G}'}(\mathbf{k},\omega)^{-1}\big|_{\mathbf{G}=0,\,\mathbf{G}'=0}\right]^{-1}, \tag{15}$$

where $\varepsilon_{\mathbf{G}\mathbf{G}'}(\mathbf{k},\omega)$, the longitudinal component of the dielectric tensor for the cubic system, is often called the dielectric matrix. Calculating the macroscopic dielectric tensor without imposing cubic symmetry is technically more involved [70].

In the optical spectroscopy of materials, a central quantity is the complex refractive index $\tilde{n}$, defined as [20]

$$\varepsilon_{\mathrm{mac}}(\omega) = \tilde{n}^2. \tag{16}$$

The real and imaginary parts of $\tilde{n}$ determine two key optical properties of materials: the refractive index n and the extinction coefficient κ, where

$$\Re\varepsilon_{\mathrm{mac}} = n^2 + \kappa^2, \tag{17}$$

$$\Im\varepsilon_{\mathrm{mac}} = 2n\kappa. \tag{18}$$

The extinction coefficient κ is proportional to the optical absorption coefficient; therefore, optical absorption spectra are essentially determined by $\Im\varepsilon_{\mathrm{mac}}(\omega)$.

4.2 Linear-Response Theory and TDDFT

We now make a connection between the dielectric function and the linear-response formalism. The linear density response $n_1(\mathbf{r}, \omega)$ caused by a frequency-dependent scalar perturbation v_1 $(\mathbf{r}, \omega)$ is given by

$$n_1(\mathbf{r},\omega) = \int d^3r'\chi(\mathbf{r},\mathbf{r}',\omega)v_1(\mathbf{r}',\omega), \tag{19}$$

where $\chi(\mathbf{r},\mathbf{r}',\omega)$ is the density–density response function of the interacting many-body system. In analogy with (10), the scalar dielectric function can be introduced as follows [71]:

$$v_1(\mathbf{r},\omega) = \int d^3r' \varepsilon(\mathbf{r},\mathbf{r}',\omega)\left[v_1(\mathbf{r}',\omega) + \int d^3r'' \frac{n_1(\mathbf{r}'',\omega)}{|\mathbf{r}'-\mathbf{r}''|}\right]. \tag{20}$$

Combining (19) and (20), we obtain the inverse dielectric function as

$$\varepsilon^{-1}(\mathbf{r},\mathbf{r}',\omega) = \delta(\mathbf{r}-\mathbf{r}') + \int d^3r'' \frac{\chi(\mathbf{r}'',\mathbf{r}',\omega)}{|\mathbf{r}'-\mathbf{r}''|}, \tag{21}$$

and for a periodic system we have

$$\varepsilon^{-1}_{\mathbf{G}\mathbf{G}'}(\mathbf{k},\omega) = \delta_{\mathbf{G}\mathbf{G}'} + v_{\mathbf{G}}(\mathbf{k})\chi_{\mathbf{G}\mathbf{G}'}(\mathbf{k},\omega), \tag{22}$$

where the Fourier transform of the 3D Coulomb potential is given by

$$v_{\mathbf{G}}(\mathbf{k}) = \frac{4\pi}{|\mathbf{k}+\mathbf{G}|^2}. \tag{23}$$

Thus, the inverse dielectric function follows directly from the response function.

In linear-response TDDFT [72], the interacting response function χ can be expressed in terms of the response function of the Kohn–Sham system χ_s and the Hartree and xc kernels:

$$\chi(\mathbf{r},\mathbf{r}',\omega) = \chi_s(\mathbf{r},\mathbf{r}',\omega) + \int d^3x \int d^3x' \chi_s(\mathbf{r},\mathbf{x},\omega)\left\{\frac{1}{|\mathbf{x}-\mathbf{x}'|} + f_{xc}(\mathbf{x},\mathbf{x}',\omega)\right\}\chi(\mathbf{x}',\mathbf{r}',\omega). \tag{24}$$

Here, χ_s is the response function of the noninteracting Kohn–Sham system, given by

$$\chi_s(\mathbf{r},\mathbf{r}',\omega) = \sum_{j,k=1}^{\infty} (f_k - f_j)\frac{\varphi_j(\mathbf{r})\varphi_k^*(\mathbf{r})\varphi_j^*(\mathbf{r}')\varphi_k(\mathbf{r}')}{\omega - \omega_{jk} + i\eta}, \tag{25}$$

where f_j and f_k are occupation numbers referring to the configuration of the Kohn–Sham ground state (1 for occupied and 0 for empty Kohn–Sham orbitals), $\varphi_j(\mathbf{r})$ are the Kohn–Sham orbitals, and the ω_{jk} are defined as the differences of the Kohn–Sham eigenvalues,

$$\omega_{jk} = \varepsilon_j - \varepsilon_k. \tag{26}$$

The key quantity in linear-response TDDFT is the xc kernel, defined as the functional derivative of the time-dependent xc potential with respect to the time-dependent density, evaluated at the ground-state density:

$$f_{\mathrm{xc}}(\mathbf{r},t,\mathbf{r}',t') = \left.\frac{\delta v_{\mathrm{xc}}[n](\mathbf{r},t)}{\delta_n(\mathbf{r}',t')}\right|_{n_0(\mathbf{r})} . \tag{27}$$

The frequency-dependent xc kernel, $f_{\mathrm{xc}}(\mathbf{r}, \mathbf{r}', \omega)$, is the Fourier transform of this with respect to $(t–t')$.

In lattice-periodic systems, (24) can be cast into the following form:

$$\chi_{\mathbf{G}\mathbf{G}'}(\mathbf{k},\omega) = \chi_{\mathrm{s}\mathbf{G}\mathbf{G}'}(\mathbf{k},\omega) + \sum_{\mathbf{G}_1,\mathbf{G}_2} \chi_{\mathrm{s}\mathbf{G}\mathbf{G}_1}(\mathbf{k},\omega)\left\{v_{\mathbf{G}_1}(\mathbf{k})\delta_{\mathbf{G}_1\mathbf{G}_2} + f_{\mathrm{xc}\mathbf{G}_1\mathbf{G}_2}(\mathbf{k},\omega)\right\}\chi_{\mathbf{G}_2\mathbf{G}'}(\mathbf{k},\omega) , \tag{28}$$

where the Kohn–Sham response function (25) is transformed into

$$\chi_{\mathrm{s}\mathbf{G}\mathbf{G}'}(\mathbf{k}) = \frac{1}{V}\sum_{\mathbf{k}'\in \mathrm{BZ}} \sum_{j,l=1}^{\infty} \frac{f_{l\mathbf{k}+\mathbf{k}'} - f_{j\mathbf{k}'}}{\omega + \varepsilon_{j\mathbf{k}'} - \varepsilon_{l\mathbf{k}+\mathbf{k}'} + i\eta} \int d^3r \varphi^*_{j\mathbf{k}'}(\mathbf{r}) \mathrm{e}^{-i(\mathbf{k}+\mathbf{G})\cdot\mathbf{r}} \varphi_{l\mathbf{k}+\mathbf{k}'}(\mathbf{r}) \times \int d^3r' \varphi^*_{l\mathbf{k}+\mathbf{k}'}(\mathbf{r}') \mathrm{e}^{i(\mathbf{k}+\mathbf{G}')\cdot\mathbf{r}'} \varphi_{j\mathbf{k}'}(\mathbf{r}'), \tag{29}$$

featuring the Kohn–Sham band structure $\varepsilon_{j\mathbf{k}}$ and Bloch functions $\varphi_{j\mathbf{k}}(\mathbf{r})$. The so-called head ($\mathbf{G} = \mathbf{G}' = 0$) of the xc kernel $f_{\mathrm{xc}\mathbf{G}\mathbf{G}'}(\mathbf{k},\omega)$ gives the largest contribution to the change from χ_{s} to χ; the contributions from bigger $\mathbf{G}$s decay rapidly. Thus the sums in (28) can usually be restricted to a small number of reciprocal lattice vectors, which reduces the computational effort significantly.

Let us now come back to the macroscopic dielectric constant. It can be shown [1, 14, 15] that $\varepsilon_{\mathrm{mac}}(\omega)$ takes on the following form:

$$\varepsilon_{\mathrm{mac}}(\omega) = 1 - \lim_{k\to 0} v_0(\mathbf{k})\overline{\chi}_{00}(\mathbf{k},\omega). \tag{30}$$

Here, $\overline{\chi}_{\mathbf{G}\mathbf{G}'}(\mathbf{k},\omega)$ differs from the full response function $\chi_{\mathbf{G}\mathbf{G}'}(\mathbf{k},\omega)$, as defined in (28), in the following way: instead of using the full Coulomb interaction $v_{\mathbf{G}}(\mathbf{k})$ [see (23)], it uses the modified Coulomb interaction

$$\overline{v}_{\mathbf{G}}(\mathbf{k}) = \begin{cases} 0 & \text{for } \mathbf{G} = 0, \\ \dfrac{4\pi}{|\mathbf{k}+\mathbf{G}|^2} & \text{for } \mathbf{G} \neq 0, \end{cases} \tag{31}$$

in which the long-range part $v_0(\mathbf{k}) = 4\pi/k^2$ has been left out. This seemingly small modification turns out to be quite important.

5 TDDFT for Excitons in Solids

5.1 Why Are Excitons a Difficult Problem?

Until a few years ago, common wisdom held that TDDFT may be good for molecular excitations but fails for excitons in solids. We now know better, as we see in this section. However, let us first discuss why excitons are such a hard problem for TDDFT.

Figure 3 shows the imaginary part of the macroscopic dielectric function of bulk silicon [73], comparing experimental data with calculations using the RPA (where $f_{xc} = 0$) and the adiabatic local-density approximation (ALDA), which is the simplest and most commonly used approximation of TDDFT. There are drastic deviations between theory and experiment. First, the onset of absorption is red-shifted in RPA and ALDA by about half an eV; this is not very surprising, and reflects the "band gap problem" of ground-state DFT: as discussed in Sect. 3, the Kohn–Sham gap of standard local and semilocal xc functionals is smaller than the quasiparticle gap. One can correct for this error and shift the empty bands via a scissors operator [74, 75] or one can use other methods to obtain band structures with a better gap, such as GW or hybrid functionals (see Sect. 3).

The second deviation is more problematic: both RPA and ALDA lack the first excitonic peak (labeled E_1 in the experimental data), and instead only have a weak shoulder. This discrepancy persists even if a better band structure (such as GW) is used as input to calculate the noninteracting response function χ_s [14]. This failure of the ALDA as well as the GGA xc functionals is by no means unique to silicon,

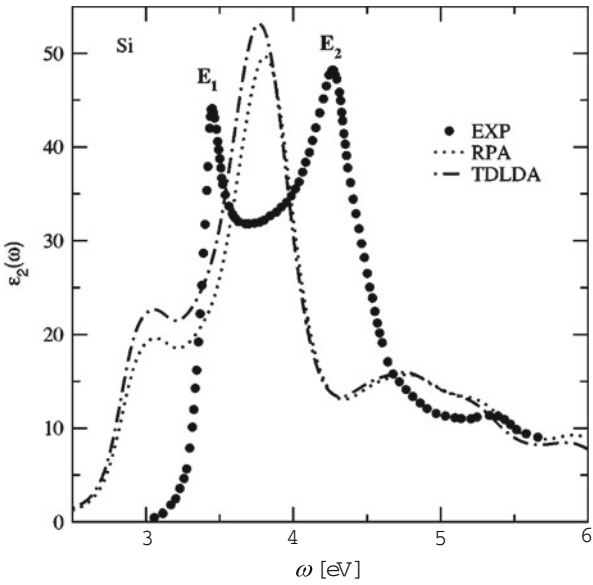

Fig. 3 Optical absorption spectrum of bulk Si. RPA and ALDA fail to reproduce the optical gap and the excitonic peak. Reproduced with permission from APS from Botti et al. [73]. © 2004

but systematically occurs in bulk insulators and semiconductors. The underlying reason is the long-range behavior of the xc kernel: in reciprocal space, the head of f_{xc} should diverge as $1/q^2$ for small q, but semilocal approximations instead approach a constant. In the next sections we explain this in more detail.

The main reason why excitons in TDDFT are a hard problem is thus that the standard local and semilocal xc kernels don't work, and one needs to resort to nonstandard kernels or even develop new ones. We discuss this in Sect. 5.4 and show some results.

Another reason is of a more practical nature. Even if very good approximations for the xc kernel are available, the calculations can be numerically difficult because convergence in reciprocal space can be slow. This problem also affects the standard many-body approaches (GW-BSE) [76, 77].

5.2 *Formalism: Direct Calculation of Exciton Binding Energies*

The Kohn–Sham response function χ_{s} has poles at the single-particle Kohn–Sham excitation energies, which can be clearly seen in (25) and (29). On the other hand, the full many-body response function χ has poles at the exact excitation energies of the system [1, 71]. This is true for any type of system, finite or extended. The Hartree and xc kernels in (24) and (28) are responsible for transforming the Kohn–Sham excitation spectrum into the exact one; this includes the creation of excitations which have no counterpart in the Kohn–Sham spectrum, such as plasmons in metals or excitons in semiconductors and insulators.

It is convenient to describe electronic excitations as electronic eigenmodes of the system. The associated mode frequencies – the excitation energies of the system – are then obtained via the so-called Casida equation [78]:

$$\begin{pmatrix} \mathbf{A} & \mathbf{B} \\ \mathbf{B} & \mathbf{A} \end{pmatrix} \begin{pmatrix} \mathrm{X} \\ \mathrm{Y} \end{pmatrix} = \Omega \begin{pmatrix} -\mathbf{1} & \mathbf{0} \\ \mathbf{0} & \mathbf{1} \end{pmatrix} \begin{pmatrix} \mathrm{X} \\ \mathrm{Y} \end{pmatrix}, \tag{32}$$

where the elements of the matrices $\mathbf{A}$ and $\mathbf{B}$ are

$$A_{ia\sigma,\, jb\sigma'}(\omega) = (\varepsilon_{a\sigma} - \varepsilon_{i\sigma})\delta_{ij}\delta_{ab}\delta_{\sigma\sigma'} + K^{\mathrm{Hxc}}_{ia\sigma,\, jb\sigma'}(\omega), \tag{33}$$

$$B_{ia\sigma,\, jb\sigma'}(\omega) = K^{\mathrm{Hxc}}_{ia\sigma,\, jb\sigma'}(\omega), \tag{34}$$

with the Hartree-exchange-correlation (Hxc) matrix elements

$$K^{\mathrm{Hxc}}_{ia\sigma,\, jb\sigma'}(\omega) = \int d^3r \int d^3r' \varphi^*_{i\sigma}(\mathbf{r})\varphi_{a\sigma}(\mathbf{r}) f_{\mathrm{Hxc},\sigma\sigma'}(\mathbf{r},\mathbf{r}',\omega)\varphi_{j\sigma'}(\mathbf{r}')\varphi^*_{b\sigma'}(\mathbf{r}'). \tag{35}$$

The indices i, j and a, b run over occupied and unoccupied Kohn–Sham orbitals, respectively. f_{Hxc} denotes the sum of the Hartree and xc kernels.

Most of the currently available xc kernels are frequency independent, in which case (32) becomes a (pseudo-)eigenvalue problem. The excitation frequencies of the system are explicitly given by the eigenvalues Ω. The eigenvector X together with Y describes how the Kohn–Sham excitations combine to form the excitation in the real system. The optical spectrum can be calculated with X and Y.

The widely used Tamm–Dancoff approximation (TDA) sets the matrix $\mathbf{B}$ to zero and hence neglects the correlation between excitations and de-excitations. Within the TDA and using the adiabatic approximation for the xc kernel, (32) becomes

$$\sum_{jb\sigma'} \left[\delta_{ij}\delta_{ab}\delta_{\sigma\sigma'}(\varepsilon_{a\sigma} - \varepsilon_{i\sigma}) + K^{\mathrm{Hxc}}_{ia\sigma,\, jb\sigma'} \right] X_{jb\sigma'} = \Omega X_{ia\sigma}. \tag{36}$$

The real space representation of the Hxc kernel is related to the momentum space representation as

$$f_{\mathrm{Hxc}\sigma\sigma'}(\mathbf{r},\mathbf{r}',\omega) = \frac{1}{V}\sum_{\mathbf{q}\in\mathrm{FBZ}}\sum_{\mathbf{G},\mathbf{G}'} \mathrm{e}^{i(\mathbf{q}+\mathbf{G})\cdot\mathbf{r}} f_{\mathrm{Hxc}\sigma\sigma'}(\mathbf{q},\mathbf{G},\mathbf{G}',\omega)\mathrm{e}^{-i(\mathbf{q}+\mathbf{G}')\cdot\mathbf{r}'}. \tag{37}$$

With (37), the Hxc kernel in transition space, (35), becomes

$$K^{\mathrm{Hxc}}_{ia\sigma,\, jb\sigma'} = \frac{1}{V}\sum_{\mathbf{q}\in\mathrm{FBZ}}\sum_{\mathbf{G},\mathbf{G}'} \langle i\mathbf{k}_i\sigma|\mathrm{e}^{i(\mathbf{q}+\mathbf{G})\cdot\mathbf{r}}|a\mathbf{k}_a\sigma\rangle f_{\mathrm{Hxc}\sigma\sigma'}(\mathbf{q},\mathbf{G},\mathbf{G}')\times$$

$$\langle b\mathbf{k}_b\sigma'|\mathrm{e}^{-i(\mathbf{q}+\mathbf{G}')\cdot\mathbf{r}'}|j\mathbf{k}_j\sigma'\rangle \delta_{\mathbf{k}_a-\mathbf{k}_i+\mathbf{q},\,\mathbf{G}_0}\delta_{\mathbf{k}_b-\mathbf{k}_j+\mathbf{q},\,\mathbf{G}'_0}, \tag{38}$$

with the matrix elements defined as

$$\langle i\mathbf{k}_i\sigma|\mathrm{e}^{i(\mathbf{q}+\mathbf{G})\cdot\mathbf{r}}|a\mathbf{k}_a\sigma\rangle \equiv \int d^3r \varphi^*_{i\mathbf{k}_i\sigma}(\mathbf{r})\mathrm{e}^{i(\mathbf{q}+\mathbf{G})\cdot\mathbf{r}}\varphi_{a\mathbf{k}_a\sigma}(\mathbf{r}), \tag{39}$$

where the $\mathbf{k}$s are the Bloch wavevectors of the corresponding wavefunctions, and $\mathbf{G}_0$, $\mathbf{G}'_0$ can be any reciprocal lattice vector. The Kronecker-δs in (38) are a consequence of Bloch's theorem.

In the following, we do not consider any spin-dependent excitations (see Yang and Ullrich [19] for a discussion of triplet excitons within TDDFT). Because we are interested in optical absorption, only vertical single-particle transitions need to be considered, so that $\mathbf{k}_i = \mathbf{k}_a$ and $\mathbf{k}_j = \mathbf{k}_b$, which implies $\mathbf{q} = 0$ in (38). Equation (36) then becomes, in reciprocal space,

$$\sum_{jb\mathbf{k}'} \left[\delta_{i\mathbf{k},\,j\mathbf{k}'}\delta_{a\mathbf{k},\,b\mathbf{k}'}(\varepsilon_{a\mathbf{k}} - \varepsilon_{i\mathbf{k}}) + K^{\mathrm{Hxc}}_{ia\mathbf{k},\, jb\mathbf{k}'} \right] X_{jb\mathbf{k}'} = \Omega X_{ia\mathbf{k}}. \tag{40}$$

Here, i, j and a, b denote occupied and unoccupied band indices, respectively. This includes, in principle, all empty bands including continuum states; in practice, however, only a limited number of valence and conduction bands in the vicinity of the band gap need to be included if (40) is to be solved numerically.

The Hartree part of the coupling matrix is given by

$$K^{\mathrm{H}}_{ia\mathbf{k},\,jb\mathbf{k}'} = \frac{2}{V}\sum_{\mathbf{G}\neq 0}\frac{4\pi}{|\mathbf{G}|^2}\langle i\mathbf{k}|\mathrm{e}^{i\mathbf{G}\cdot\mathbf{r}}|a\mathbf{k}\rangle\langle b\mathbf{k}'|\mathrm{e}^{-i\mathbf{G}\cdot\mathbf{r}}|j\mathbf{k}'\rangle. \tag{41}$$

The long-range part ($\mathbf{G}=0$) of the Coulomb interaction is omitted so that the eigenvalues of (40) correspond to the poles in the macroscopic dielectric function, as discussed at the end of Sect. 4.2. The xc part is given by

$$K^{\mathrm{xc}}_{ia\mathbf{k},\,jb\mathbf{k}'} = \frac{2}{V}\lim_{\mathbf{q}\to 0}\sum_{\mathbf{G}\mathbf{G}'} f_{\mathrm{xc},\mathbf{G}\mathbf{G}'}(\mathbf{q})\langle i\mathbf{k}|\mathrm{e}^{i(\mathbf{q}+\mathbf{G})\cdot\mathbf{r}}|a\mathbf{k}\rangle\langle b\mathbf{k}'|\mathrm{e}^{-i(\mathbf{q}+\mathbf{G})\cdot\mathbf{r}}|j\mathbf{k}'\rangle. \tag{42}$$

The solutions of (40) can be used to calculate the macroscopic dielectric function, using the following expression [l labels the lth eigenvalue of (40)]:

$$\varepsilon_{\mathrm{mac}}(\omega) = 1 - \lim_{q\to 0}\frac{4\pi}{q^2}\sum_{l}\frac{\left|\sum ia\mathbf{k}\langle i\mathbf{k}|\mathrm{e}^{-i\mathbf{q}\cdot\mathbf{r}}|a\mathbf{k}\rangle X^{(l)}_{ia\mathbf{k}}\right|^2}{\omega-\Omega_l+i\eta}. \tag{43}$$

5.3 Why Does ALDA Fail?

Now let us discuss the behavior of the head, wings, and body of the coupling matrix (42). For $\mathbf{G}=0$, the matrix element $\langle i\mathbf{k}|\mathrm{e}^{i(\mathbf{q}+\mathbf{G})\cdot\mathbf{r}}|a\mathbf{k}\rangle$ vanishes as $\mathcal{O}(q)$ when $\mathbf{q}\to 0$, and similarly for the other matrix element, $\langle b\mathbf{k}'|\mathrm{e}^{-i(\mathbf{q}+\mathbf{G}')\cdot\mathbf{r}}|j\mathbf{k}'\rangle$. This means that the head ($\mathbf{G}=\mathbf{G}'=0$) of $K^{\mathrm{xc}}_{ia\mathbf{k},\,jb\mathbf{k}'}$ vanishes unless the head of $f_{\mathrm{xc},\mathbf{G}\mathbf{G}'}(\mathbf{q})$ diverges at least as q^{-2}. Likewise, the wings ($\mathbf{G}=0$ and $\mathbf{G}'$ finite, or vice versa) vanish unless the wings of the xc kernel diverge at least as q^{-1}.

All local and semilocal xc kernels (ALDA and adiabatic GGAs) remain finite for all $\mathbf{G}$, $\mathbf{G}'$, and $\mathbf{q}$. This is easy to see for the ALDA, whose real-space form is

$$f^{\mathrm{ALDA}}_{\mathrm{xc}}(\mathbf{r},\mathbf{r}') = \left.\frac{d^2 e_{\mathrm{xc}}(n)}{dn^2}\right|_{n-n_0(\mathbf{r})}\delta(\mathbf{r}-\mathbf{r}'), \tag{44}$$

where $e_{\mathrm{xc}}(n)$ is the xc energy density of a homogeneous electron gas of uniform density n and $n_0(\mathbf{r})$ is the ground-state density of the material. Carrying out the Fourier transform we find that the $\mathbf{q}$-dependence simply drops out [79]:

$$f_{\mathrm{xc},\mathbf{G}\mathbf{G}'}^{\mathrm{ALDA}}(\mathbf{q}) = \frac{1}{V_{\mathrm{cell}}}\int d^3r\, \mathrm{e}^{-i(\mathbf{G}-\mathbf{G}')\cdot\mathbf{r}}\ \left.\frac{d^2e_{\mathrm{xc}}(n)}{dn^2}\right|_{n=n_0(\mathbf{r})}, \tag{45}$$

where the integral runs over one unit cell with volume V_{cell}. The adiabatic GGA xc kernels exhibit similar behavior. If $f_{\mathrm{xc},\mathbf{G}\mathbf{G}'}^{\mathrm{ALDA}}(\mathbf{q})$ is substituted into (42), then the contribution from the head and wings of f_{xc} to $K_{ia\mathbf{k},\,jb\mathbf{k}'}^{\mathrm{xc}}$ vanishes. For ALDA and GGA kernels, all changes to the Kohn–Sham spectrum can thus only come from the *body* of $K_{ia\mathbf{k},\,jb\mathbf{k}'}^{\mathrm{xc}}$ (where both $\mathbf{G}\neq 0$ and $\mathbf{G}'\neq 0$), but these are not sufficiently strong to produce excitons.

The case $\mathbf{q}\to 0$ in reciprocal space corresponds to $r\to\infty$ in real space. The long-range behavior of the xc kernel is relatively unimportant for low-lying excitations in finite systems such as atoms and molecules, which means that local and semilocal xc kernels work reasonably well (an exception to this statement are charge-transfer excitations [80–86]). However, for extended and periodic systems it is crucial to have xc kernels with the proper long-range behavior to obtain correct optical spectra [14, 73]. Gonze et al. [87, 88] pointed out that the head of f_{xc} has to diverge as q^{-2} for $q\to 0$ to describe correctly the polarization of periodic insulators. With the q^{-2} divergence, the head of f_{xc} contributes in the sum of (42), dominating the other parts of f_{xc} (the wings and the body). Local and semilocal xc kernels do not have this long-range behavior, and there is no obvious and consistent way of modifying them to include the long-rangedness. Hence, a different class of approximate xc kernels – excitonic xc kernels – is needed.

5.4 *Excitonic xc Kernels*

Because TDDFT is formally rigorous, it should in principle yield exact optical absorption spectra for insulators. However, even if we start from an exact ground-state Kohn–Sham calculation (which would give the exact independent-particle spectrum), the xc kernel $f_{\mathrm{xc}\mathbf{G}\mathbf{G}'}(\mathbf{k},\omega)$ has to carry a heavy burden: it has to open the gap and shift the Kohn–Sham band edge to the true band edge, and it has to cause an effective electron–hole attraction, leading to excitonic features in the spectrum. Formally, the xc kernel can be separated into a *quasiparticle* and an *excitonic* part [89–91],

$$f_{\mathrm{xc}} = f_{\mathrm{xc}}^{\mathrm{qp}} + f_{\mathrm{xc}}^{\mathrm{ex}}. \tag{46}$$

The two parts are responsible for the opening of the gap and the excitonic effects, respectively. Further justification of (46) is given in Sect. 5.4.6. Let us now focus on the excitonic part and give some examples of how it can be approximated.

5.4.1 Contact Exciton

Let us begin with an apparent paradox, namely, the so-called contact exciton. Even though we have stressed that the proper long-range behavior of the xc kernel is crucial, an ultra-short-range xc kernel of the general form

$$f_{\mathrm{xc}}^{\mathrm{cont}}(\mathbf{r},\mathbf{r}') = -A_{\mathrm{cont}}\delta(\mathbf{r}-\mathbf{r}') \tag{47}$$

can produce excitonic features if the constant A_{cont} is properly chosen [15, 18, 92]. By the same token, an ad hoc scaled ALDA, $\alpha f_{\mathrm{xc},\mathbf{GG}'}^{\mathrm{ALDA}}$, can, in principle, produce excitons, although the scaling factor α would have to be rather absurdly large (typically of the order of $\sim 10^3$).

The resolution of the contact-exciton paradox is that the contact kernel and the scaled ALDA work via the *body* of the coupling matrix $K_{ia\mathbf{k},\,jb\mathbf{k}'}^{\mathrm{xc}}$. In other words, the missing long-range behavior is, somewhat unphysically, compensated by an ultrastrong short-range electron–hole interaction. It is found [15, 90] that the contact xc kernel can be tuned to reproduce certain features of the optical spectrum (for instance, a bound-exciton peak) but at the cost of a poor description of other parts of the spectrum.

5.4.2 Long-Range Corrected Kernel

Because we know from Sect. 5.3 that the long-range $1/q^2$ behavior of the head of the xc kernel is the key to excitonic effects, it is straightforward to construct a simple ad hoc approximation which captures the right physics for the right reason. The resulting so-called long-range corrected (LRC) kernel has the following form:

$$f_{\mathrm{xc},\mathbf{GG}'}^{\mathrm{LRC}}(\mathbf{q}) = -\frac{A_{\mathrm{LRC}}}{|\mathbf{q}+\mathbf{G}|^2}\delta_{\mathbf{GG}'}, \tag{48}$$

where A_{LRC} is a system-dependent fitting parameter. Despite its simple form, LRC spectra (with properly chosen A_{LRC}) can be in good agreement with experiment [73, 92] because the head contribution of the kernel tends to dominate over the local-field effects contained in the contributions of the body of $K_{ia\mathbf{k},\,jb\mathbf{k}'}^{\mathrm{xc}}$. A simple connection with the high-frequency dielectric constant ε_∞ has been suggested [73]:

$$A_{\mathrm{LRC}} = 4.651\varepsilon_\infty^{-1} - 0.213. \tag{49}$$

The purpose of this empirical formula was to reproduce the continuum spectrum; hence, it cannot be expected to (and, in fact, does not) perform well for bound excitons (see Sect. 5.4.9).

5.4.3 Exact Exchange

The frequency-dependent xc kernel can be formally constructed from many-body perturbation theory, using a diagrammatic expansion [93, 94]. The first-order term of this expansion is the exact exchange kernel $f_x(\mathbf{r}, \mathbf{r}', \omega)$, which can be represented as the sum of five diagrams (see Fig. 4a). Translated into formulas using the standard diagrammatic rules, one obtains [95, 96]

$$\int d^3r_1 \int d^3r_2 \chi_s(\mathbf{r}, \mathbf{r}_1, \omega) f_x(\mathbf{r}_1, \mathbf{r}_2, \omega) \chi_s(\mathbf{r}_2, \mathbf{r}', \omega) = R_V(\mathbf{r}, \mathbf{r}', \omega) + R_\Sigma(\mathbf{r}, \mathbf{r}', \omega). \tag{50}$$

R_v is the first-order vertex diagram (third on the right-hand side in Fig. 4a),

$$R_V(\mathbf{r}, \mathbf{r}', \omega) = -2 \sum_{ijkl} \varphi_i(\mathbf{r}) \varphi_j^*(\mathbf{r}) \varphi_k^*(\mathbf{r}') \varphi_l(\mathbf{r}') \langle il|w|jk\rangle \frac{(f_i - f_j)(f_k - f_l)}{(z - \omega_{ij})(z - \omega_{lk})}, \tag{51}$$

where $z = \omega + i0^+$, and the f_j are the usual occupation factors. R_Σ denotes the sum of all the remaining four diagrams (the self-energy diagrams):

$$R_\Sigma(\mathbf{r}, \mathbf{r}', \omega) = 4 \sum_{ijk} \frac{\varphi_i(\mathbf{r}) \varphi_i^*(\mathbf{r}') \varphi_j(\mathbf{r}) \varphi_k^*(\mathbf{r}') \langle j|\Delta|k\rangle}{\omega_{kj}} \left\{ \frac{(f_k - f_i)\omega_{ik}}{z^2 - \omega_{ik}^2} - \frac{(f_j - f_i)\omega_{ij}}{z^2 - \omega_{ij}^2} \right\}, \tag{52}$$

where $\Delta(\mathbf{r}_1, \mathbf{r}_2) = \Sigma_x(\mathbf{r}_1, \mathbf{r}_2) - v_x(\mathbf{r}_1)\delta(\mathbf{r}_1 - \mathbf{r}_2)$. Here, Σ_x is the exchange part of the self-energy, and v_x is the exact exchange potential of DFT, defined as an orbital functional via the optimized effective potential (OEP) method [45, 97]. It is also

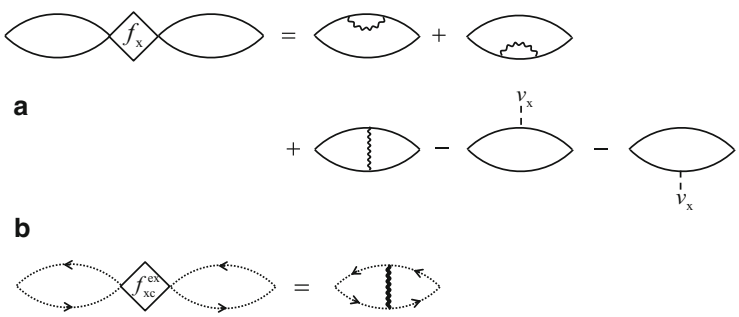

Fig. 4 Diagrammatic representations of (**a**) the exact exchange kernel f_x (50) and (**b**) the excitonic xc kernel f_{xc}^{ex} (61), the so-called nanoquanta kernel. Full lines represent noninteracting Kohn–Sham Green's functions and dashed lines represent quasiparticle Green's functions. Thin wavy lines are bare Coulomb interactions and the thick wavy line is a screened interaction

possible to derive the exact exchange kernel directly as the functional derivative $f_x(\omega) = \delta v_x(\omega)/\delta n(\omega)$ [98, 99].

In periodic insulators, the exact-exchange kernel has the long-range behavior necessary for the formation of excitons [100, 101]. However, the resulting unscreened electron–hole interaction tends to lead to a dramatic overbinding of the excitons; in extreme cases this causes a collapse of the optical spectra (i.e., the exciton would be so strongly bound that it falls below the valence band edge). This collapse can be prevented by a cutoff of the Coulomb singularity [100, 101]; this is equivalent to an evaluation of the xc kernel with a screened interaction [15, 102].

5.4.4 Hybrid Functionals and Meta GGAs

Hybrid xc functionals [46–59] replace a portion of the semilocal exchange energy with the exact exchange energy, so the long-range part of the corresponding xc kernel resembles a screened exact exchange kernel; as we saw above, this can produce bound excitons. In practice, however, hybrid functionals are used in a different manner [103]: the exact exchange part is treated nonlocally, similar to the time-dependent HF approach, instead of using the exact exchange kernel in (42).

The B3LYP hybrid functional has been used by Bernasconi et al. to calculate optical spectra in several semiconductor materials [104–106]; they achieve a generally good description of optical gaps, including excitonic features. Indeed, we have obtained some preliminary results [107] which confirm that B3LYP can be reasonably accurate for exciton binding energies in semiconductors, despite the fact that the 0.2 mixing parameter of the exact exchange is optimized for finite systems [46].

Range-separated hybrid functionals [50, 108, 109] are based on the idea of separating the Coulomb interaction into different spatial ranges, which are then treated differently, using either exact exchange or approximate semilocal exchange functionals. Recent applications of range-separated hybrids to solids have produced good quasiparticle gaps [51, 52, 54, 55, 57, 61]. In linear response, these functionals are again closely related to the exact exchange kernel. However, if the range-separated functional uses semilocal exchange for the long-range part, it cannot produce bound excitons for the same reason as in ALDA. Therefore, the popular HSE06 functional [50, 51, 110] cannot yield bound excitons, although it may still produce decent looking optical spectra of insulators [111].

The so-called meta-GGA functionals [112–115] depend not only on the density and its gradients but also on the kinetic-energy density, which is expressed in terms of Kohn–Sham orbitals and, hence, depends nonlocally on the density. This nonlocality produces good quasiparticle gaps in solids [60–64], and opens up the possibility of describing excitonic interactions with meta-GGAs. Nazarov and Vignale [116] tested two types of meta-GGAs, TPSS [112] and VS98 [113, 114]. They found TPSS to be unsuited for describing dielectric properties of solids; VS98, on the other hand, performed rather well. Further tests are needed;

however, the implementation of meta-GGAs for the linear response in solids turns out to be technically rather difficult.

5.4.5 The PGG Kernel

The exact exchange kernel can be approximated in various ways. The simplest approximation is known as the PGG kernel (after Petersilka, Gossmann, and Gross [117, 118]). In real space, it is defined as

$$f_{\mathrm{x}}^{\mathrm{PGG}}(\mathbf{r},\mathbf{r}') = -\frac{2\left|\sum_i^{\mathrm{occ}} \varphi_i^*(\mathbf{r})\varphi_i(\mathbf{r}')\right|^2}{|\mathbf{r}-\mathbf{r}'|n(\mathbf{r})n(\mathbf{r}')}, \tag{53}$$

where n is the ground-state electronic density. In this form, the PGG kernel has been successfully applied to calculate atomic and molecular excitation energies as well as plasmons in nanostructures [119]. Thus, one might be optimistic regarding its performance for excitons.

We convert the PGG kernel into reciprocal space, assuming that the Kohn–Sham orbitals have the form $\varphi_{i\mathbf{k}}(\mathbf{r}) = N_{\mathrm{cell}}^{-1/2} u_{i\mathbf{k}}(\mathbf{r})\mathrm{e}^{i\mathbf{k}\cdot\mathbf{r}}$, where N_{cell} is the number of unit cells in the crystal and $u_{i\mathbf{k}}(\mathbf{r})$ are Bloch functions. $f_{\mathrm{x}}^{\mathrm{PGG}}$ can then be written as

$$f_{\mathrm{x}}^{\mathrm{PGG}}(\mathbf{r},\mathbf{r}') = -\sum_{i\mathbf{k}}^{\mathrm{occ}}\sum_{m\mathbf{k}'}^{\mathrm{occ}} \frac{2\mathrm{e}^{-i(\mathbf{k}-\mathbf{k}')\cdot(\mathbf{r}-\mathbf{r}')}}{|\mathbf{r}-\mathbf{r}'|} H_{i\mathbf{k}m\mathbf{k}'}(\mathbf{r},\mathbf{r}'), \tag{54}$$

where $H_{i\mathbf{k}m\mathbf{k}'}(\mathbf{r},\mathbf{r}')$ is periodic within one unit cell and defined as

$$H_{i\mathbf{k}m\mathbf{k}'}(\mathbf{r},\mathbf{r}') = \frac{u_{i\mathbf{k}}^*(\mathbf{r})u_{i\mathbf{k}}(\mathbf{r}')u_{m\mathbf{k}'}(\mathbf{r})u_{m\mathbf{k}'}^*(\mathbf{r}')}{N_{\mathrm{cell}}^2 n(\mathbf{r})n(\mathbf{r}')} \tag{55}$$

The Fourier transform of $f_{\mathrm{x}}^{\mathrm{PGG}}$ yields

$$f_{\mathrm{x}}^{\mathrm{PGG}}(\mathbf{q},\mathbf{G},\mathbf{G}') = -\frac{8\pi}{V}\sum_{i\mathbf{k}}^{\mathrm{occ}}\sum_{m\mathbf{k}'}^{\mathrm{occ}}\sum_{\mathbf{G}_0} \frac{\widetilde{H}_{i\mathbf{k}m\mathbf{k}'}(\mathbf{G}-\mathbf{G}_0,\mathbf{G}'-\mathbf{G}_0)}{|\mathbf{q}-(\mathbf{k}'-\mathbf{k})+\mathbf{G}_0|^2}, \tag{56}$$

where $\widetilde{H}$ is obtained by numerical Fourier transform of expression (55) within one unit cell. For simplicity, we ignore the local-field effects and only use the head of the PGG kernel, which is given by

$$f_{\mathrm{x}}^{\mathrm{PGG}}(\mathbf{q},0,0) = -\frac{8\pi}{V}\sum_{i,m,\mathbf{k}}^{\mathrm{occ}} \frac{\widetilde{H}_{i\mathbf{k}m\mathbf{k}}(0,0)}{q^2}. \tag{57}$$

Unfortunately, explicit calculations show that the performance of the PGG kernel is disappointing for solids: it does not produce any bound excitons at all, despite having a nonzero head contribution with the correct $1/q^2$ behavior [19]. How can this be reconciled with the fact that the PGG kernel seems to work well in finite systems such as atoms and molecules? Periodic systems are dominated by the head of the xc kernel in reciprocal space; however, the situation is very different in finite systems, where the electron dynamics can be viewed as coming entirely from local-field effects. Thus, the strongly attractive nature of the PGG kernel in finite systems would at most translate into a strong body of the xc matrix in periodic systems (which, however, is irrelevant for excitons), but does not necessarily guarantee a strong head. Indeed, if one fits the head of the PGG kernel to the LRC kernel (48), one finds that the resulting constant $A_{\mathrm{LRC}}^{\mathrm{PGG}}$ is orders of magnitude too weak [19].

The underlying reason for the failure of the PGG kernel for periodic insulators can be inferred from its real-space definition (53), which can be written in the form $f_{\mathrm{x}}^{\mathrm{PGG}} = -\left|\rho(\mathbf{r},\mathbf{r}')\right|^2 / \left[2\left|\mathbf{r}-\mathbf{r}'\right| n(\mathbf{r}) n(\mathbf{r}')\right]$, where $\rho(\mathbf{r}, \mathbf{r}')$ is the Kohn–Sham density matrix. For periodic solids, the long-range behavior of $f_{\mathrm{x}}^{\mathrm{PGG}}$ is determined by both the Coulomb singularity and the density matrix. It is a well-known fact [120–124] that the one-particle density matrix in insulators decays exponentially as $\rho(\mathbf{r}, \mathbf{r}') \sim \exp(-\gamma|\mathbf{r}–\mathbf{r}'|)$. This effectively cuts off the required long-range behavior and explains why the head of the PGG kernel is so weak.

5.4.6 The "Nanoquanta" Kernel

Let us introduce the so-called *proper* response function $\widetilde{\chi}$ as

$$\widetilde{\chi} = \chi_{\mathrm{s}} + \chi_{\mathrm{s}} f_{\mathrm{xc}} \widetilde{\chi} \tag{58}$$

(for simplicity, we drop all arguments and integrals). At the beginning of this section we defined the quasiparticle and excitonic parts of the xc kernel; see (46). It is then easy to write down the following relations for the two parts of f_{xc} [91]:

$$\chi_{\mathrm{qp}} = \chi_{\mathrm{s}} + \chi_{\mathrm{s}} f_{\mathrm{xc}}^{\mathrm{qp}} \chi_{\mathrm{qp}}, \tag{59}$$

$$\widetilde{\chi} = \chi_{\mathrm{qp}} + \chi_{\mathrm{qp}} f_{\mathrm{xc}}^{\mathrm{ex}} \widetilde{\chi}. \tag{60}$$

Here, χ_{qp} is the *quasiparticle* response function, which uses quasiparticle states as input. Hence, χ_{qp} has the quasiparticle gap built in by default, and the roles of $f_{\mathrm{xc}}^{\mathrm{qp}}$ and $f_{\mathrm{xc}}^{\mathrm{ex}}$ are clear from (59) and (60). Our focus here is on the excitons: all we need to do, then, is start with a good approximation for χ_{qp}. Usually, one obtains it from the GW approach (see Sect. 3), but other approximations that yield good quasiparticle gaps (such as hybrids or the scissors operator) can be used as well.

The exact proper response function $\widetilde{\chi}$ is, of course, unknown. To construct an approximation for $f_{\mathrm{xc}}^{\mathrm{ex}}$ from (60) one can proceed in two steps. First, replace

$\chi_{\rm qp} f_{\rm xc}^{\rm ex} \widetilde{\chi} \approx \chi_{\rm qp} f_{\rm xc}^{\rm ex} \chi_{\rm qp}$. Second, find a diagrammatic representation of $\widetilde{\chi} - \chi_{\rm qp}$; the details of this representation are quite technical and are not given here (in essence, it involves two-particle Green's functions and four-point vertex functions [1, 14, 15, 125]). The key point is that this diagrammatic representation can be very easily approximated, and one ends up with the following expression:

$$\int d3 \int d4 \chi_{\rm qp}(1,3) f_{\rm xc}^{\rm ex}(3,4) \chi_{\rm qp}(4,2) = \int d3 \int d4 G_{\rm qp}(1,3) G_{\rm qp}(4,1) W(3,4) G_{\rm qp}(3,2) G_{\rm qp}(2,4). \tag{61}$$

This is the xc kernel of Reining et al. [89] and many others [also known as the "nanoquanta" kernel (http://www.cmt.york.ac.uk/nanoquanta/)]. Figure 4b shows its diagrammatic representation. The numbers in (61) represent space-time arguments, e.g., $1 = (\mathbf{r}_1, t_1)$. $G_{\rm qp}$ is a quasiparticle Green's function, and W is a screened interaction, formally defined as

$$W(1,2) = w(1,2) + \int d3 \int d4 w(1,3) \widetilde{\chi}(3,4) W(4,2), \tag{62}$$

where $w(1,2)$ is the bare Coulomb interaction, and $\widetilde{\chi}$ is approximated by $\chi_{\rm qp}$.

The excitonic xc kernel $f_{\rm xc}^{\rm ex}$ of (61) has been widely applied in a variety of systems [14, 89, 90, 102, 126–131]. Its performance is, in general, found to be excellent, at par with results obtained from solving the full BSE. This provided an important proof of concept that TDDFT is very well capable of capturing excitonic properties. The price to be paid, however, is that the many-body xc kernel (61) is not simple to implement and is computationally costly (it is, essentially, as expensive as the BSE when it comes to calculating optical spectra, but somewhat more favorable if the full dielectric matrix is needed).

5.4.7 The "Bootstrap" Kernel

Compared to the exact exchange and nanoquanta kernels, the simplicity of the LRC kernel is desirable for practical use. The adjustable parameter $A_{\rm LRC}$ requires prior knowledge to the system, however, and therefore the LRC kernel cannot be used as a black-box method. The bootstrap kernel proposed by Sharma et al. [132, 133] can be seen as an attempt to determine the $A_{\rm LRC}$ parameter (which now depends on $\mathbf{q}$, $\mathbf{G}$, and $\mathbf{G}'$) self-consistently while retaining the simplicity of the LRC kernel. The original definition [132] is written in terms of symmetrized quantities to avoid singularities: for example, $f_{\rm xc}^{\rm sym}(\mathbf{q},\mathbf{G},\mathbf{G}') = v_{\mathbf{G}}^{-1/2}(\mathbf{q}) f_{\rm xc}(\mathbf{q},\mathbf{G},\mathbf{G}') v_{\mathbf{G}'}^{-1/2}(\mathbf{q})$ and $\chi^{\rm sym}(\mathbf{q},\mathbf{G},\mathbf{G}') = v_{\mathbf{G}}^{1/2}(\mathbf{q}) \chi(\mathbf{q},\mathbf{G},\mathbf{G}') v_{\mathbf{G}'}^{1/2}(\mathbf{q})$. In terms of regular, non-symmetrized quantities, the kernel is defined as

$$f_{\mathrm{xc}}^{\mathrm{boot}}(\mathbf{q},\mathbf{G},\mathbf{G}') = \frac{|\mathbf{q}|^2\left[\delta_{\mathbf{G}\mathbf{G}'} + v_{\mathbf{G}}^{1/2}(\mathbf{q})v_{\mathbf{G}'}^{1/2}(\mathbf{q})\chi(\mathbf{q},\mathbf{G},\mathbf{G}')\right]}{|\mathbf{q}+\mathbf{G}||\mathbf{q}+\mathbf{G}'|\chi_{\mathrm{s}}(\mathbf{q},0,0)}, \tag{63}$$

where $v_{\mathbf{G}}(\mathbf{q}) = 4\pi/|\mathbf{q}+\mathbf{G}|^2$ is the Coulomb potential, χ_{s} is the Kohn–Sham linear response function of (29), and χ is the TDDFT linear response function obtained via (28). Equations (28) and (63) are solved self-consistently for the xc kernel. The $q \to 0$ behavior of $\chi_{\mathrm{s}}(\mathbf{q}, 0, 0)$ is $O(q^2)$, and it is canceled by the $|\mathbf{q}|^2$ in the numerator. Thus the bootstrap f_{xc} has the correct $q \to 0$ behavior because of the presence of $|\mathbf{q}+\mathbf{G}|\,|\mathbf{q}+\mathbf{G}'|$ in the denominator.

The bootstrap kernel has been reported to yield good continuum spectra (including the enhancement of the band-edge spectra by continuum excitons) for a wide range of materials [132]. Unfortunately, numerical applications of this xc kernel are plagued by its slow convergence with respect to the total number of bands included in χ_{s}. When convergence is finally achieved (which may require including dozens of unoccupied bands), the results for bound excitons tend to be disappointing, with exciton binding energies typically orders of magnitude smaller than the experimental values [19]. In fact, contrary to Sharma et al. [132], the bootstrap kernel does not yield bound excitons for wide-gap insulators such as LiF and solid Ar (we present numerical results in Sect. 5.4.9). Improving the performance of the bootstrap kernel by suitable modification is a subject of ongoing research.

5.4.8 The Jellium-with-a-Gap Model

Trevisanutto et al. recently developed an xc kernel based on the jellium-with-a-gap model (JGM) [134]. Although the JGM kernel depends on the local density, it differs from local and semilocal xc kernels by having the correct $1/q^2$ and $1/q$ behavior of head and wings as $q \to 0$, and it can therefore in principle produce bound excitons. The JGM kernel is an empirical kernel because it requires the band gap as input. The kernel is defined as

$$\begin{aligned} f_{\mathrm{xc}}^{\mathrm{JGM}}(q;n,E_{\mathrm{g}}) = {} & \frac{4\pi\left[B(n)+E_{\mathrm{g}}\right]}{q^2\left(1+E_{\mathrm{g}}\right)}\left(\mathrm{e}^{-k\left(n,E_{\mathrm{g}}\right)q^2}-1\right) \\ & - \frac{4\pi C(n)}{(3\pi^2 n)^{2/3}(1+1/q^2)\left(1+E_{\mathrm{g}}\right)}, \end{aligned} \tag{64}$$

where [135]

$$C(n) = -\frac{\pi}{2(3\pi^2 n)^{1/3}}\frac{d[r_{\mathrm{s}}\varepsilon_{\mathrm{c}}(r_{\mathrm{s}})]}{dr_{\mathrm{s}}}, \tag{65}$$

$$k(n, E_g) = -\frac{\alpha n^{\beta}}{B(n)} + \frac{E_g^2\left(1 + E_g\right)}{4\pi q^2 n\left[B(n) + E_g\right]}, \tag{66}$$

and [136]

$$B(n) = \frac{1 + a_1 r_s^{1/2} + a_2 r_s^{3/2}}{3 + b_1 r_s^{1/2} + b_2 r_s^{3/2}}. \tag{67}$$

Here, $r_s = [3/(4\pi n)]^{1/3}$, ε_c is the LDA correlation energy per particle [137], and $\alpha = -0.02552$, $\beta = -0.6916$, $a_1 = 2.15$, $a_2 = 0.435$, $b_1 = 1.57$, and $b_2 = 0.409$. The performance of the JGM kernel is similar to that of the bootstrap kernel for continuum spectra; unfortunately, it also severely underestimates exciton binding energies.

5.4.9 Some Results

We now present some results for exciton binding energies, obtained using (40), to demonstrate the performance of several of the xc kernels we have discussed. All TDDFT calculations are done on top of scissor-corrected [74, 75] LDA band structures, so that only the excitonic part of the exact xc kernel is approximated by the functionals that we consider. All calculations include only the head of the xc coupling matrix $K^{xc}_{ia\mathbf{k},\, jk\mathbf{k}'}$. Ignoring the wings and the body of the xc coupling matrix gives an estimated error of less than 5%. Other details specific to our numerical implementation are described in Yang and Ullrich [19].

Experimental and calculated exciton binding energies for several materials are collected in Table 1. We compare the performance of three different xc kernels: the LRC kernel (48), evaluated using (49), the bootstrap kernel (63),[1] and the JGM

Table 1 Exciton binding energies calculated with different TDDFT xc kernels, compared with experimental values (all energies in meV)

	GaAs	β-GaN	α-GaN	CdS	CdSe	Ar	Ne	LiF	AlN	ZnO	MgO
Exp.	3.27	26.0	20.4	28.0	15.0	1,900	4,080	1,600	75	60	80
LRC	0.858	0.514	0	0.513	1.40	0.304	0.127	1.14	0	0.810	0.076
Boot	0.332	0.199	0	0.461	0.895	1.70	852	32.2	0	1.09	0.051
JGM	0.833	0.382	0	0.741	1.42	41.0	0.593	993	0	4.45	1.79

[1] We find that the convergence of the bootstrap kernel strongly depends on the number of bands used in the iterative calculation of the kernel. The results for solid Ar, solid Ne, and LiF are obtained by calculating the bootstrap kernel with 30 bands. It turns out that some of our previous results reported in Yang and Ullrich [19], where the bootstrap kernel seemed to work very well for Ar, Ne, and LiF, were in fact not fully converged.

Table 2 Top row: fitted A_{LRC} parameter which reproduces the experimental exciton binding energies with the LRC kernel. Second and third rows: heads of the xc coupling matrix of the bootstrap and JGM kernels

	GaAs	β-GaN	α-GaN	CdS	CdSe	Ar	Ne	LiF	AlN	ZnO	MgO
Fit	0.595	2.409	3.6285	4.244	2.144	21.45	96.5	9.5	3.0006	1.6285	4.0405
Boot	0.0884	0.3048	0.2147	0.5895	0.3183	6.448	46.34	4.236	0.3412	0.3620	1.230
JGM	0.2056	0.5245	0.5782	0.7829	0.4631	9.685	10.76	7.78	1.568	0.8008	2.357

kernel (64). Except for α-GaN and AlN, all three TDDFT methods produce a bound exciton; however, the results are quantitatively not very accurate. By and large, the excitons are significantly underbound, sometimes by up to two to three orders of magnitude.

The LRC kernel contains the adjustable parameter A_{LRC}, which can be fitted to reproduce the experimental exciton binding energy. The fitted values of A_{LRC} are given in the first row of Table 2. From the head of the bootstrap and the JGM xc coupling matrices, we can extract the corresponding A_{LRC} parameters; the results are given in the second and third rows of Table 2. Clearly, the bootstrap and JGM kernels produce heads which are significantly too weak in comparison with what would be needed to reproduce the experimental data. Clearly, the exciton binding energy depends crucially on the strength of the head of the xc coupling matrix.

Figure 5 shows optical absorption spectra of solid Ar. The spectra in the top panel were calculated from the solutions of (40) using (43). The bottom panel (adapted from Sottile et al. [128]) was calculated via (30). The top panel compares RPA and LRC, both of them using a scissor-corrected LDA band structure as input. The LRC kernel clearly produces a very strong bound exciton, but the continuum part is too weak compared to the excitonic peak. The bottom panel compares experimental results with calculations using GW-BSE and GW-TDDFT, using the nanoquanta kernel. Clearly, BSE and the nanoquanta kernel are in excellent agreement, and both agree well with the experimental data (the splitting of the peaks is caused by spin-orbit coupling, which is not included in the calculations). It should be noted that a second bound exciton is present, which is missing in the LRC calculation. For comparison, the bottom panel of Fig. 5 also shows ALDA results, based on an uncorrected LDA band structure. Clearly, the ALDA bears no resemblance whatsoever to experiment.

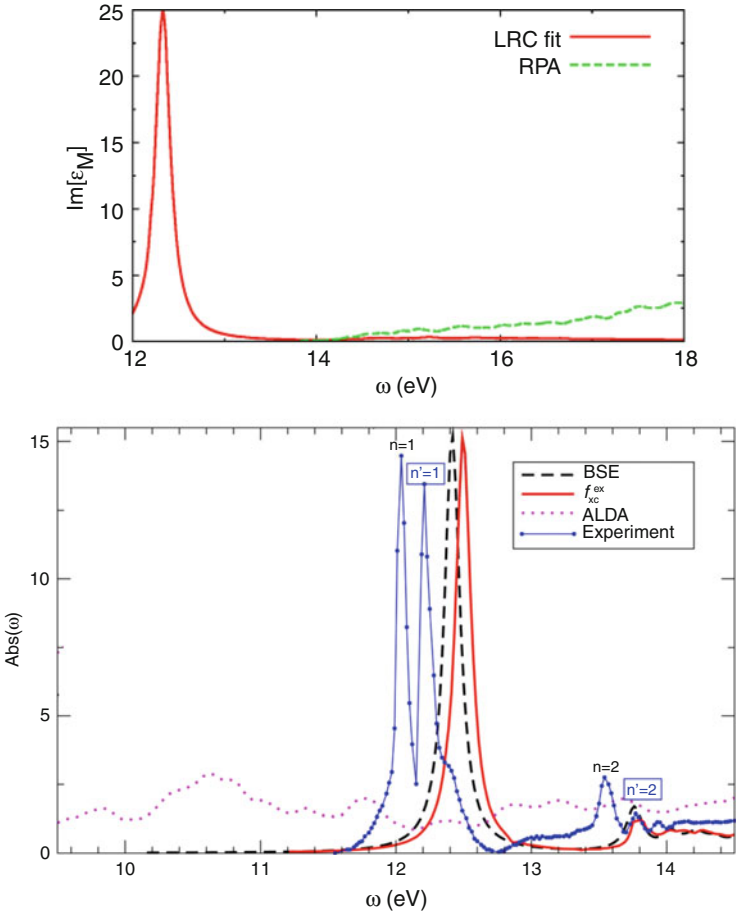

Fig. 5 Absorption spectra of solid Ar obtained from (43) (*top panel*) and from (30) (*bottom panel*, adapted from Sottile et al. [128]). Reproduced with permission from APS from Sottile et al. [128]. ©2007

6 Comparison of TDDFT and the BSE

Exciton binding energies in TDDFT are determined via (40). The Hxc coupling matrix is given by

$$K^{\mathrm{Hxc}}_{ia\mathbf{k},\,jb\mathbf{k}'} = K^{\mathrm{H}}_{ia\mathbf{k},\,jb\mathbf{k}'} + K^{\mathrm{xc}}_{ia\mathbf{k},\,jb\mathbf{k}'}, \tag{68}$$

where the Hartree and xc matrices are defined in (41) and (42). It turns out that the BSE leads to an equation for exciton binding energies which is formally identical to (40), except that it features the coupling matrix

$$K^{\mathrm{BSE}}_{ia\mathbf{k},\,jb\mathbf{k}'} = K^{\mathrm{H}}_{ia\mathbf{k},\,jb\mathbf{k}'} + K^{\mathrm{W}}_{ia\mathbf{k},\,jb\mathbf{k}'}, \tag{69}$$

where

$$K^{\mathrm{W}}_{ia\mathbf{k},\,jb\mathbf{k}'} = -\frac{1}{V}\sum_{\mathbf{G}\mathbf{G}'} W_{\mathbf{G}\mathbf{G}'}(\mathbf{q})\langle i\mathbf{k}|\mathrm{e}^{i(\mathbf{q}+\mathbf{G})\cdot\mathbf{r}}|j\mathbf{k}\rangle\langle b\mathbf{k}'|\mathrm{e}^{-i(\mathbf{q}+\mathbf{G}')\cdot\mathbf{r}}|a\mathbf{k}'\rangle. \tag{70}$$

The Hartree part is the same as in TDDFT, but the xc part is replaced by a coupling matrix featuring the screened interaction (62). In practice, one ignores the frequency dependence of W; explicitly, one finds

$$W_{\mathbf{G}\mathbf{G}'}(\mathbf{q},\omega=0) = \frac{4\pi\varepsilon^{-1}_{\mathbf{G}\mathbf{G}'}(\mathbf{q},\omega=0)}{|\mathbf{q}+\mathbf{G}'|^2}. \tag{71}$$

Let us now compare the two coupling matrices K^{xc} and K^{W}. Two main differences become apparent: first, the order of the band indices i, j, a, b is different; second, the xc matrix only depends on the long-range ($q=0$) behavior, while the W matrix also depends on other values of $\mathbf{q}$.

Figure 6 shows contour plots of the xc and W coupling matrices, calculated for a one-dimensional model insulator with a soft-Coulomb interaction [18]. The xc kernel here is the long-range corrected kernel $f^{\mathrm{LRC}}_{\mathrm{xc}}$ with a fitting parameter chosen such that the lowest exciton binding energy in TDDFT and BSE is the same.

The two coupling matrices shown in Fig. 6 are strikingly different. This is not surprising, because the screened interaction $W_{\mathbf{G}\mathbf{G}'}(\mathbf{q})$ has an extra degree of freedom over $f_{\mathrm{xc}\mathbf{G}\mathbf{G}'}(\mathbf{q}=0)$; hence, it cannot be expected that an adiabatic xc kernel can be found that reproduces the full BSE coupling matrix. One can only hope to reproduce a portion of the BSE coupling matrix, unless the xc kernel is made frequency-dependent so that at least some of the information from the

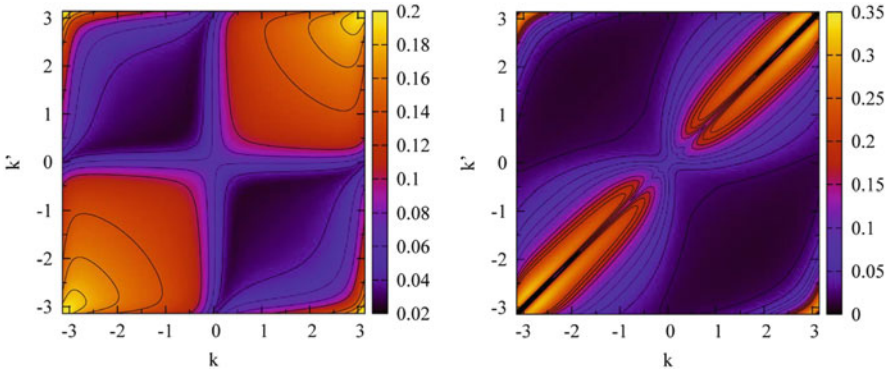

Fig. 6 Contour plots of the coupling matrices K^{xc} (*left panel*) and K^{W} (*right panel*). Reproduced with permission from AIP from Yang et al. [18]. ©2012

q-dependence in the screened interaction is mapped into the frequency dependence of the xc kernel [89]. As a consequence, adiabatic xc kernels can be made to produce a single bound exciton, but not an excitonic Rydberg series (at least, not just with the head of the xc matrix) [18].

The question then arises how TDDFT can produce bound excitons at all, given the fact that the xc and BSE coupling matrices are so drastically different. To illustrate how this is possible, we now make a connection with the Wannier model discussed in Sect. 2, and ask: what is the TDDFT and BSE analog of the Wannier equation, (1)?

Let us consider, for simplicity, a two-band model in which there is only one filled valence band (v) and one empty conduction band (c). We define an effective two-body potential via the Fourier transform of the xc coupling matrix:

$$V^{\rm xc}_{\rm e-h}(\mathbf{R},\mathbf{R}') = \sum_{\mathbf{k},\mathbf{k}'\in {\rm BZ}} {\rm e}^{-i\mathbf{k}\cdot\mathbf{R}} K^{\rm xc}_{{\rm vc}\mathbf{k},{\rm vc}\mathbf{k}'} {\rm e}^{i\mathbf{k}\cdot\mathbf{R}'}, \tag{72}$$

where $\mathbf{R}$, $\mathbf{R}'$ are direct lattice vectors. Because Wannier exciton radii extend over many lattice constants, one may replace $\mathbf{R}$ by a continuous spatial variable $\mathbf{r}$. Assuming, furthermore, parabolic valence and conduction bands, and using the effective-mass approximation, (40) becomes, after Fourier transformation,

$$\frac{\nabla^2}{2m_r} X(\mathbf{r}) + \int d^3r' V^{\rm xc}_{\rm e-h}(\mathbf{r},\mathbf{r}') X(\mathbf{r}') = EX(\mathbf{r}), \tag{73}$$

where E is the exciton binding energy, and the integration goes over all space. This shows that the TDDFT analog of the Wannier equation (1) is a nonlocal Schrödinger equation. With a proper choice of the xc kernel, the nonlocal effective electron–hole interaction potential $V^{\rm xc}_{\rm e-h}$ supports bound excitonic states.

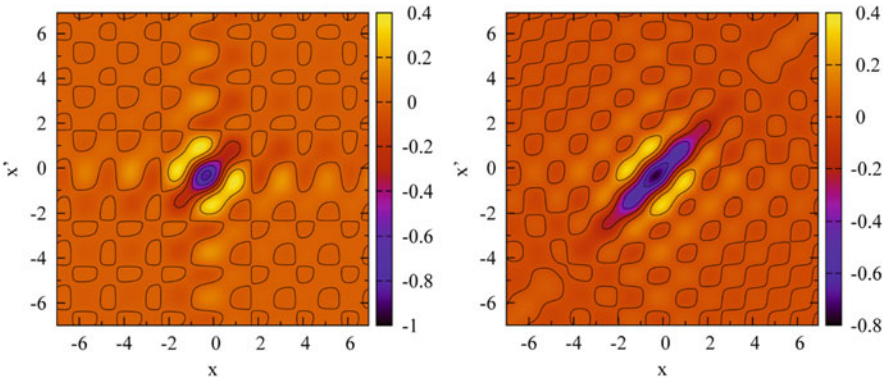

Fig. 7 Contour plots of the effective nonlocal electron–hole interaction potentials in TDDFT (*left panel*) and BSE (*right panel*). Reproduced with permission from AIP from Yang et al. [18]. ©2012

Because of the formal similarity between BSE and TDDFT in the transition space representation, we can also define a BSE effective electron–hole interaction potential $V^{\mathrm{BSE}}_{\mathrm{e-h}}$ in analogy to (72), using the BSE kernel K^{W}. Figure 7 shows a comparison of $V^{\mathrm{xc}}_{\mathrm{e-h}}$ and $V^{\mathrm{BSE}}_{\mathrm{e-h}}$ for our one-dimensional model insulator. It can clearly be seen that the nonlocal potentials in both cases are dominated by the diagonal part; however, under further examination it turns out that $V^{\mathrm{xc}}_{\mathrm{e-h}}$ is shallower than $V^{\mathrm{BSE}}_{\mathrm{e-h}}$, and hence is only able to sustain a single bound exciton.

7 Conclusions

There exist two alternative, complementary first-principles methods to calculate optical spectra and excitonic effects in extended periodic solids. The more traditional approach is based on many-body Green's function techniques, exemplified by the GW-BSE method; the other approach is based on TDDFT. The Green's function approach is formally straightforward, in the sense that excitonic particle–hole interactions are built in by construction; however, it is computationally costly. TDDFT, on the other hand, is computationally cheaper (provided that the approximate xc functionals are simple enough), but the price one has to pay is that intrinsically nonlocal electron–hole interaction effects have to be described via linearized local xc potentials; this is a somewhat unnatural way of dealing with excitonic interactions, which makes it non-straightforward to construct good approximations.

In this chapter we have focused on the TDDFT approach for excitons, and have tried to bring across the following points:

- Excitons in TDDFT are a difficult problem, because they require an xc kernel which has the long-range property $f_{\mathrm{xc},00}(\mathbf{q},\omega) \sim q^{-2}$ for $q \to 0$. The popular local and semilocal approximations such as ALDA and standard GGAs do not have this property: although they work well for finite systems such as atoms and molecules, they do not produce excitons in extended systems. New approximations are therefore required.
- There exist several approximate "excitonic" xc kernels, with various degrees of sophistication. Some kernels involve adjustable parameters, others don't. A typical behavior of the simpler kernels is that they can reproduce some part of the optical spectrum reasonably well (e.g., a bound exciton, or the continuum part), but not all of it at the same time. The best excitonic xc kernel, the "nanoquanta" kernel, is computationally not much simpler than the BSE.
- Adiabatic (i.e., frequency-independent) xc kernels cannot produce an excitonic Rydberg series. At best, they can generate a single bound exciton (if only the head of the xc coupling matrix is used). The TDDFT analog of the excitonic Wannier equation features a nonlocal potential, which is too shallow to produce more than one bound level.

Despite the difficulties of developing accurate and efficient TDDFT approaches for excitons, much progress has been made over the past few years. The path forward is most likely to bring TDDFT and traditional many-body theory even closer together, the outcome being xc kernels that are functionals of occupied as well as unoccupied bands, similar in spirit to the nanoquanta and bootstrap kernels.

Hybrid xc kernels are another promising way forward; however, this means abandoning pure TDDFT and admitting nonlocal exchange. This has been an extremely successful strategy for finite systems: indeed, standard hybrid functionals are widely used for excitons in polymers and other nanoscale systems [138–141]. For periodic solids, the standard hybrid functionals may have to be suitably modified to describe excitonic properties; work along these lines is in progress [107].

Acknowledgments This work was supported by NSF grant DMR-1408904. We thank Lucia Reining and Francesco Sottile for many helpful discussions. C.U. thanks the ETSF-Palaiseau group for its hospitality and the Ecole Polytechnique for its support during an extended visit in 2014.

References

1. Ullrich CA (2012) Time-dependent density-functional theory: concepts and applications. Oxford University Press, Oxford
2. Marques MAL, Maitra NT, Nogueira FMS, Gross EKU, Rubio A (2012) Fundamentals of time-dependent density functional theory. Springer, Berlin
3. Ullrich CA, Yang ZH (2014) Brazil J Phys 44:154
4. Hedin L (1965) Phys Rev 139:A796
5. Aryasetiawan F, Gunnarsson O (1998) Rep Prog Phys 61:237
6. Sham LS, Rice TM (1966) Phys Rev 144:708
7. Hanke W, Sham L (1979) Phys Rev Lett 43:387
8. Hanke W, Sham LS (1980) Phys Rev B 21:4656
9. Strinati G (1982) Phys Rev Lett 49:1519
10. Strinati G (1984) Phys Rev B 29:5718
11. Strinati G (1988) Riv Nuovo Cimento 11:1
12. Rohlfing M, Louie SG (1998) Phys Rev Lett 81:2312
13. Rohlfing M, Louie S (2000) Phys Rev B 62:4927
14. Onida G, Reining L, Rubio A (2002) Rev Mod Phys 74:601
15. Botti S, Schindlmayr A, Del Sole R, Reining L (2007) Rep Prog Phys 70:357
16. Turkowski V, Ullrich CA (2008) Phys Rev B 77:075204
17. Turkowski V, Leonardo A, Ullrich CA (2009) Phys Rev B 79:233201
18. Yang ZH, Li Y, Ullrich CA (2012) J Chem Phys 137:014513
19. Yang ZH, Ullrich CA (2013) Phys Rev B 87:195204
20. Yu P, Cardona M (2010) Fundamentals of semiconductors. Springer, Berlin
21. Liang WY (1970) Phys Educ 5:226
22. Knox RS (1963) Theory of excitons. Academic, New York
23. Frenkel J (1931) Phys Rev 37:17; 1276
24. Peierls R (1932) Ann Phys (Leipzig) 13:905
25. Davydov AS (1948) Zh Eksperim i Teor Fiz 18:210
26. Wannier GH (1937) Phys Rev 52:191

27. Mott NF (1938) Trans Faraday Soc 34:500
28. Glutsch S (1994) Excitons in low-dimensional semiconductors. Springer, Berlin
29. Koch SW, Kira M, Khitrova G, Gibbs HM (2006) Nat Mater 5:523
30. Scholes GD, Rumbles G (2006) Nat Mater 5:683
31. Dresselhaus MS, Dresselhaus G, Saito R, Jorio A (2007) Annu Rev Phys Chem 58:719
32. Wheeler DA, Zhang JZ (2013) Adv Mater 25:2878
33. Bardeen CJ (2014) Annu Rev Phys Chem 65:127
34. Dresselhaus G (1956) J Phys Chem Solid 1:14
35. Elliott RJ (1957) Phys Rev 108:1384
36. Haug H, Koch SW (2004) Quantum theory of the optical and electronic properties of solids. World Scientific, Singapore
37. Baerends EJ, Gritsenko OV, van Meer R (2013) Phys Chem Chem Phys 15:16408
38. Perdew JP, Parr RG, Levy M, Balduz JL (1982) Phys Rev Lett 49:1691
39. Perdew JP, Levy M (1983) Phys Rev Lett 51:1884
40. Kohn W (1986) Phys Rev B 33:4331
41. Godby RW, Schlüter M, Sham LJ (1986) Phys Rev Lett 56:2415
42. Capelle K, Vignale G, Ullrich CA (2010) Phys Rev B 81:125114
43. Kronik L, Stein T, Refaely-Abramson S, Baer R (2012) J Chem Theor Comput 8:1515
44. Seidl A, Görling A, Vogl P, Majewski JA, Levy M (1996) Phys Rev B 53:3764
45. Kümmel S, Kronik L (2008) Rev Mod Phys 80:3
46. Stephens PJ, Devlin FJ, Chabalowski CF, Frisch MJ (1994) J Phys Chem 98:11623
47. Ernzerhof M, Scuseria GE (1999) J Chem Phys 110:5029
48. Paier J, Marsman M, Kresse G (2007) J Chem Phys 127:024103
49. Muscat J, Wander A, Harrison NN (2001) Chem Phys Lett 342:397
50. Heyd J, Scuseria GE, Ernzerhof M (2003) J Chem Phys 118:8207
51. Heyd J, Peralta JE, Scuseria GE, Martin RL (2005) J Chem Phys 112:174101
52. Gerber IC, Ángyán JC, Marsman M, Kresse G (2007) J Chem Phys 127:054101
53. Moussa JE, Schultz PE, Chelikowsky JR (2011) J Chem Phys 136:204117
54. Schimka L, Harl J, Kresse G (2011) J Chem Phys 134:024116
55. Henderson TM, Paier P, Scuseria GE (2011) Phys State Solid B 248:767
56. Marques MAL, Vidal J, Oliveira MCT, Reining L, Botti S (2011) Phys Rev B 83:035119
57. Matsushita Y, Nakamura K, Oshiyama A (2011) Phys Rev B 84:075205
58. Friedrich C, Betzinger M, Schlipf M, Blügel S, Schindlmayr A (2012) J Phys Condens Matter 24:293201
59. Waroquiers D, Lherbier A, Miglio A, Stankovski M, Poncé S, Oliveira MJT, Fiantomassi M, Rignanese G-M, Gonze X (2013) Phys Rev B 87:075121
60. Tran F, Blaha P (2009) Phys Rev Lett 102:226401
61. Kim Y-S, Marsman M, Kresse G, Tran F, Blaha P (2010) Phys Rev B 82:205212
62. Koller D, Tran F, Blaha P (2011) Phys Rev B 83:195134
63. Koller D, Tran F, Blaha P (2012) Phys Rev B 85:155109
64. Jiang H (2013) J Chem Phys 138:134115
65. Betzinger M, Friedrich C, Blügel S, Görling A (2011) Phys Rev B 83:045105
66. Perdew JP, Ruzsinszky A, Constantin LA, Sun J, Czonka GI (2009) J Chem Theor Comput 5:902
67. Adler SL (1962) Phys Rev 126:413
68. Wiser N (1963) Phys Rev 129:62
69. Hanke W (1978) Adv Phys 27:187
70. Del Sole R, Fiorino E (1984) Phys Rev B 29:4631
71. Giuliani GF, Vignale G (2005) Quantum theory of the electron liquid. Cambridge University Press, Cambridge
72. Gross EKU, Kohn W (1985) Phys Rev Lett 55:2850
73. Botti S, Sottile F, Vast N, Olevano V, Reining L, Weissker H-C, Rubio A, Onida G, Del Sole R, Godby RW (2004) Phys Rev B 69:155112

74. Levine ZH, Allan DC (1989) Phys Rev Lett 63:1719
75. Del Sole R, Girlanda R (1993) Phys Rev B 48:11789
76. Fuchs F, Rödl C, Schleife A, Bechstedt F (2008) Phys Rev B 78:085103
77. Erhart P, Schleife A, Sadigh B, Åberg D (2014) Phys Rev B 89:075132
78. Casida ME (1995) Recent advances in density functional methods. In: Chong DE (ed) Recent advances in computational chemistry, vol 1. World Scientific, Singapore, p 155
79. Gurtubay IG, Pitarke JM, Ku W, Eguiluz AG, Larson BC, Tischler J, Zschack P, Finkelstein KD (2005) Phys Rev B 72:125117
80. Tozer DJ, Amos RD, Handy NC, Roos BO, Serrano-Andrés L (1999) Mol Phys 97:859
81. Tozer DJ (2003) J Chem Phys 119:12697
82. Casida ME, Gutierrez F, Guan J, Gadea F-X, Salahub D, Daudey J-P (2000) J Chem Phys 113:7062
83. Dreuw A, Weisman JL, Head-Gordon M (2003) J Chem Phys 119:2943
84. Dreuw A, Head-Gordon M (2004) J Am Chem Soc 126:4007
85. Gritsenko O, Baerends EJ (2004) J Chem Phys 121:655
86. Autschbach J (2009) Chemphyschem 10:1757
87. Gonze X, Ghosez P, Godby RW (1995) Phys Rev Lett 74:4035
88. Ghosez P, Gonze X, Godby RW (1997) Phys Rev B 56:12811
89. Reining L, Olevano V, Rubio A, Onida G (2002) Phys Rev Lett 88:066404
90. Sottile F, Olevano V, Reining L (2003) Phys Rev Lett 91:056402
91. Stubner R, Tokatly IV, Pankratov O (2004) Phys Rev B 70:245119
92. Sottile F, Karlsson K, Reining L, Aryasetiawan F (2003) Phys Rev B 68:205112
93. Tokatly IV, Pankratov O (2001) Phys Rev Lett 86:2078
94. Tokatly IV, Stubner R, Pankratov O (2002) Phys Rev B 65:113107
95. Hellgren M, von Barth U (2008) Phys Rev B 78:115107
96. Hellgren M, von Barth U (2009) J Chem Phys 131:044110
97. Talman JD, Shadwick WF (1976) Phys Rev A 14:36
98. Görling A (1998) Phys Rev A 57:3433
99. Görling A (1998) Int J Quant Chem 69:265
100. Kim Y-H, Görling A (2002) Phys Rev B 66:035114
101. Kim Y-H, Görling A (2002) Phys Rev Lett 89:096402
102. Bruneval F, Sottile F, Olevano V, Reining L (2006) J Chem Phys 124:144113
103. Izmaylov A, Scuseria GE (2008) J Chem Phys 129:034101
104. Bernasconi L, Tomić S, Ferrero M, Rérat M, Orlando R, Dovesi R, Harrison NM (2011) Phys Rev B 83:195325
105. Bernasconi L, Webster R, Tomić S, Harrison NM (2012) J Phys Conf Ser 367:012001
106. Tomić S, Bernasconi L, Searle BG, Harrison NM (2014) J Phys Chem C 118:14478
107. Yang ZH, Sottile F, Ullrich CA, arXiv:1501.05631
108. Yanai T, Tew DP, Handy NC (2004) Chem Phys Lett 393:51
109. Vydrov OA, Scuseria GE (2006) J Chem Phys 125:234109
110. Heyd J, Scuseria GE, Ernzerhof M (2006) J Chem Phys 124:219906
111. Paier J, Marsman M, Kresse G (2008) Phys Rev B 78:121201 (R)
112. Tao JM, Perdew JP, Staroverov VN, Scuseria GE (2003) Phys Rev Lett 91:146401
113. Voorhis TV, Scuseria GE (1998) J Chem Phys 109:400
114. Voorhis TV, Scuseria GE (2008) J Chem Phys 129:219901
115. Becke AD, Johnson ER (2006) J Chem Phys 124:221101
116. Nazarov VU, Vignale G (2011) Phys Rev Lett 107:216402
117. Petersilka M, Gossmann UJ, Gross EKU (1996) Phys Rev Lett 76:1212
118. Petersilka M, Gossmann UJ, Gross EKU (1998) In: Dobson JF, Vignale G, Das MP (eds) Electronic density functional theory: recent progress and new directions. Plenum, New York, p 177
119. Karimi S, Ullrich CA (2014) Phys Rev B 90:245304
120. Kohn W (1959) Phys Rev 115:809

121. des Cloiseaux J (1964) Phys Rev 135:A685; A698
122. Kohn W (1996) Phys Rev Lett 76:3168
123. Zhang W, Drabold DA (2001) Phys Rev B 63:233109
124. Taraskin SN, Drabold DA, Elliott SR (2002) Phys Rev Lett 88:196405
125. Stefanucci G, van Leeuwen R (2013) Nonequilibrium many-body theory of quantum systems. Cambridge University Press, Cambridge
126. Adragna G, Del Sole R, Marini A (2003) Phys Rev B 68:165108
127. Marini A, Del Sole R, Rubio A (2003) Phys Rev Lett 91:256401
128. Sottile F, Marsili M, Olevano V, Reining L (2007) Phys Rev B 76:161103
129. Gatti M, Olevano V, Reining L, Tokatly IV (2007) Phys Rev Lett 99:057401
130. Varsano D, Marini A, Rubio A (2008) Phys Rev Lett 101:133002
131. Sagmeister S, Ambrosch-Draxl C (2009) Phys Chem Chem Phys 11:4451
132. Sharma S, Dewhurst JK, Sanna A, Gross EKU (2011) Phys Rev Lett 107:186401
133. Sharma S, Dewhurst JK, Gross EKU (2014) Top Curr Chem 347:235
134. Trevisanutto PE, Terentjevs A, Constantin LA, Olevano V, Della Sala F (2013) Phys Rev B 87:205143
135. Constantin LA, Pitarke JM (2007) Phys Rev B 75:245127
136. Corradini M, Del Sole R, Onida G, Palummo M (1998) Phys Rev B 57:14569
137. Perdew JP, Wang Y (1992) Phys Rev B 45:13244
138. Tretiak S, Igumenshchev K, Chernyak V (2005) Phys Rev B 71:033201
139. Kilina S, Badaeva E, Piryatinski A, Tretiak S, Saxena A, Bishop AR (2009) Phys Chem Chem Phys 11:4113
140. Wong BM (2009) J Phys Chem C 113:21921
141. Zimmerman PM, Bell F, Casanova D, Head-Gordon M (2011) J Am Chem Soc 133:19944

Top Curr Chem (2016) 368: 219–272
DOI: 10.1007/128_2014_616

Published online: 10 April 2015

Dynamical Processes in Open Quantum Systems from a TDDFT Perspective: Resonances and Electron Photoemission

Ask Hjorth Larsen, Umberto De Giovannini, and Angel Rubio

Abstract We present a review of different computational methods to describe time-dependent phenomena in open quantum systems and their extension to a density-functional framework. We focus the discussion on electron emission processes in atoms and molecules addressing excited-state lifetimes and dissipative processes. Initially we analyze the concept of an electronic resonance, a central concept in spectroscopy associated with a metastable state from which an electron eventually escapes (electronic lifetime). Resonances play a fundamental role in many time-dependent molecular phenomena but can be rationalized from a time-independent context in terms of scattering states. We introduce the method of complex scaling, which is used to capture resonant states as localized states in the spirit of usual bound-state methods, and work on its extension to static and time-dependent density-functional theory. In a time-dependent setting, complex scaling can be used to describe excitations in the continuum as well as wave packet dynamics leading to electron emission. This process can also be treated by using open boundary conditions which allow time-dependent simulations of emission processes without artificial reflections at the boundaries (i.e., borders of the simulation box). We compare in detail different schemes to implement open boundaries, namely transparent boundaries using Green functions, and absorbing boundaries in

A.H. Larsen (✉) and U. De Giovannini (✉)
Nano-bio Spectroscopy Group and European Theoretical Spectroscopy Facility (ETSF), Centro de Física de Materiales CSIC-UPV and DIPC, Universidad del País Vasco UPV/EHU, E-20018 Donostia–San Sebastián, Spain
e-mail: asklarsen@gmail.com; umberto.degiovannini@gmail.com

A. Rubio (✉)
Nano-bio Spectroscopy Group and European Theoretical Spectroscopy Facility (ETSF), Centro de Física de Materiales CSIC-UPV and DIPC, Universidad del País Vasco UPV/EHU, E-20018 Donostia–San Sebastián, Spain

Max Planck Institute for the Structure and Dynamics of Matter, Hamburg, Germany
e-mail: angel.rubio@ehu.es

the form of complex absorbing potentials and mask functions. The last two are regularly used together with time-dependent density-functional theory to describe the electron emission dynamics of atoms and molecules. Finally, we discuss approaches to the calculation of energy and angle-resolved time-dependent pump–probe photoelectron spectroscopy of molecular systems.

Keywords Absorbing boundaries · Complex scaling · Photoemission · Resonances

Contents

1 Introduction

All natural phenomena occur away from equilibrium. Non-equilibrium systems can range in scale from microscopic (such as nanostructures and bacteria) to geological phenomena, and away-from-equilibrium processes occur on timescales ranging from nanoseconds to millennia. Despite the ubiquitous non-equilibrium systems and processes, most of the current understanding of physical and biological systems is based on equilibrium concepts. In fact, in interacting many-body systems, more

often than not we face the fact that the electronic states have finite lifetimes because of the coupling to the environment or to a continuum of states (*resonance processes*). Even if we were able to prepare a perfectly isolated quantum system, we would need to regard a measurement of the system as bringing the system into contact with an environment. Already a single atom in vacuum cannot be regarded as completely isolated, because the atom is embedded in the surrounding photon field (spontaneous emission). Other examples where the coupling to the surrounding plays a prominent role include hot electron relaxation in bulk systems and surfaces after laser irradiation, thermalization caused by electron–phonon coupling, decoherence in pump–probe experiments, exciton propagation and relaxation in biological chromophores, and vibrational relaxation in nanomaterials and molecular systems. Understanding these decay mechanisms provides important information about electron correlations, quantum coherence, dissipative and decoherence processes, and control of these processes has important implications. For instance, this would make it possible to enhance the performance of molecular/solid-based optoelectronic devices.

In this context, density-functional theory (DFT) provides an exact theoretical framework which could yield observable quantities directly, by-passing the need to calculate the many-body wavefunction Ψ. Hohenberg and Kohn [1] proved that all observable properties of a static many-electron system can be extracted exactly from the one-body ground-state density alone (*density–potential mapping*). Later, Runge and Gross extended this theorem to time-dependent systems [2]. Time-dependent density-functional theory (TDDFT) is a rigorous reformulation of the non-relativistic time-dependent quantum mechanics of many-body systems. The central theorem of TDDFT is the Runge–Gross theorem which proves a one-to-one correspondence between the time-dependent external potential $\nu_{\text{ext}}(\mathbf{r}, t)$ and the electronic one-body density $n(\mathbf{r}, t)$ for many-body systems evolving from a fixed initial state Ψ_0. This implies that the time-dependent electronic density determines all properties of the interacting many-electron system: all observable properties of a many-electron system can be extracted from the one-body time-dependent density alone [2]. What has made both DFT and TDDFT so successful is the Kohn–Sham scheme [3]: the density of the interacting many-electron system is obtained as the density of an auxiliary system of non-interacting fermions, living in a one-body potential. Because of the excellent balance between the computational load it requires and the accuracy it provides, TDDFT is now a tool of choice for quite accurate and reliable predictions for excited-state properties in solid state physics, chemistry, and biophysics, in both the linear and nonlinear regimes. However, there exist many situations where the electronic degrees of freedom are not isolated but must be treated as a subsystem embedded in an environment, which influences it in a non-negligible way. Those situations go beyond the realm of the original formulation of TDDFT which is meant to tackle the isolated dynamics of electronic systems. It is therefore clear that there is a need to extend density-functional approaches to the realm of open quantum systems to allow us to treat the processes described above.

Burke and co-workers recently introduced a TDDFT approach based on a Kohn–Sham master equation [4], and in recent work this has been pursued by the group of

Aspuru-Guzik [5–7]. This group also proposed a description of open quantum systems in terms of a unitarily evolving closed Kohn–Sham system [7, 8]. The theory of open quantum systems (OQS) mostly deals with the situation where the environment exchanges energy and momentum with the system but particle number is conserved ([9, Chap. 10]). What happens in the case when the environment exchanges particles with the system is an equivalently important problem which has been less developed. Here we intend to review methods developed to address this kind of problem. We describe the theoretical frameworks and approximations that can be used to describe particle exchange.

Solving the problem of describing a system which exchanges electrons with the environment is only half the challenge. In fact, even in the ideal case where one is able to calculate the correct time-dependent wavefunction, one is faced with the additional problem that some observables may require the knowledge of the complete wavefunction or of eigenstates in the continuum. This includes ionization products such as photoelectron spectra and resonance lifetimes/widths, and is also connected to the measurement process of an open system. These problems are even more severe in the case of DFT and TDDFT, where the density is the only physical object, and where finding the explicit density-functional linking to a physical observable is a daunting task.

This review is structured as follows. We first introduce the general concept of resonance in Sect. 2 and describe how it can be observed in many different physical situations. Then in Sect. 3 we introduce the reader to the basic concepts of the complex scaling theory which is one of the most important tools for studying shape resonances in a static framework. In Sect. 4 we review the successful extension of the complex scaling theory to the realm of DFT, including some recent work adapting the method to the time-dependent realm. In Sect. 5 we review several methods for the incorporation of boundary conditions with the TDDFT equations in order to include the dynamic exchange of electrons with an environment/reservoir. We discuss the strategies for describing specific observables in Sect. 6 where we focus on the case of electron photoemission.

Unless otherwise specified, atomic units are used throughout ($\hbar = m_e = e = 4\pi\varepsilon_0 = 1$).

2 Resonances

Consider a system acted upon by an external oscillating force characterized by some energy and corresponding frequency. If the system responds particularly strongly close to a particular frequency, we call that a *resonance* process. The typical textbook case is that of a classical damped harmonic oscillator acted upon by an external sinusoidal force. For each frequency the system responds by oscillating with some amplitude, and the resonances appear as strong narrow peaks in the amplitude.

This simple model has two important properties that are very general to any type of resonance: First, if the oscillatory force is turned off, the resonant oscillation

decays as governed by the damping force, and the rate of decay is proportional to the *width* of the resonance peak. Second, if we consider the *phase* of the oscillation of the system with respect to that of the external force, we see that it shifts quickly by up to π as the energy passes that of the resonance. The rate with which it shifts is inversely proportional to the decay rate.

We mention here a few commonly studied types of resonance in atomic, molecular, and condensed-matter physics:

- Plasmon resonances where the whole electron charge density in a material resonates with incoming light. Surface plasmon resonances are central to the field of plasmonics.
- Scattering resonances where incident electrons interact with an atom or molecule. Near a resonance energy, the electrons couple strongly and the scattering cross-section shows a peak. The process may be understood as the incoming electron becoming temporarily trapped in a metastable state before escaping.
- Asymmetric Fano resonances [10]. These occur when two coupled excitation pathways interfere with each other.
- Autoionizing resonances, wherein a system such as an atom or molecule is unstable with respect to the ejection of one or more electrons. These are similar to those that would be observed in time-resolved spectroscopies and electron scattering experiments as mentioned above.
- Electron transport processes with molecular junctions, where a bias voltage causes electrons to jump from one metallic lead across a metastable state at a molecule, then escapes through another lead. Such processes have, for example, been studied using DFT plus non-equilibrium Green functions represented with atomic basis sets [11–14].
- Adsorption of an atom onto a surface where the continuum states of the surface couple with the discrete atomic states which then become unstable, broadening into resonances. The Newns–Anderson model [15] describes this process for a one-electron adsorbate.

There are many further classes of resonance which we do not mention here. Below we consider only a small class of resonances, namely scattering or autoionizing ones. In this context, a resonance is a metastable quantum mechanical state that the system possesses, and which can be associated with a wavefunction. Below we describe some mathematical properties of such resonances, with the objective of eventually calculating them from static or time-dependent DFT.

2.1 Definition and Properties of Resonant States

Let us consider a typical scattering experiment where an incoming electron is captured by atom and is temporarily trapped before it escapes again. Whereas scattering processes are clearly time-dependent, resonances can nevertheless be captured from time-independent methods as static properties of the system. A conceptually simple method is to study the phase δ of the wavefunction in the

asymptotic region, taking in one dimension the form $\cos(kx+\delta)$. See for instance the simple demonstration by Gellene [16] which we consider again later. A resonance energy and width can be estimated by locating the energy where the phase shift δ changes most rapidly, and the width can be estimated from the maximum rate of change. This intuitively relates the resonance to a strong coupling of the system with continuum states in a narrow energy interval, as we noted in the beginning.

A more mathematically precise way of identifying a resonance is, following the work of Siegert [17], to search for complex energies corresponding to singularities of the scattering cross section. A pole close to the real energy axis would produce a peak in the scattering cross-section for real energies, consistent with a resonance. As noted by Siegert, the corresponding condition on a wavefunction[1] $\psi(r)$ is that far away from the scattering region:

$$\frac{\mathrm{d}\psi(r)}{\mathrm{d}r} = ik\psi(r), \tag{1}$$

with the energy

$$k^2/2 = \varepsilon - i\Gamma/2, \tag{2}$$

where $\varepsilon > 0$ is the real resonance energy, and $\Gamma > 0$ its width. This yields a discrete set of resonant states characterized by being purely outgoing waves. States obeying the boundary condition (1) are frequently called Siegert or Gamow–Siegert states, and they diverge as $r \to \infty$. See, for example, Hatano et al. [18] for a detailed description of resonant states.

Most computational methods in quantum mechanics work in terms of square integrable states, and thus cannot straightforwardly represent a resonance wavefunction. An elegant solution to this problem is the *complex scaling method*, where one uses complex spatial coordinates to suppress the exponential divergence. One thus solves for functions that obey the usual boundary conditions, $\psi(r) \to 0$ for $r \to \infty$. This also has the convenient advantage that the boundary conditions no longer depend on k. The method relies on the properties of analytic functions to transform the Hamiltonian into a non-Hermitian operator whose point spectrum consists exactly of that of the bound states along the negative real axis plus the complex resonance energies which have positive real part and negative imaginary part. The wavefunctions of bound as well as resonance states are square integrable analytic continuations of the original ones. These properties make the complex scaling method a powerful computational tool as it can make use of many existing methods which do not otherwise apply to unbounded scattering states.

[1] We mention for completeness that Siegert worked in a spherical system where the represented quantity is really r times the wavefunction; this however happens to yield the same equation as in the one-dimensional case.

Although the complex scaling method clearly works with any kind of particles in a finite system, here we explicitly assume that we are dealing with electrons temporarily trapped by simple potentials representing atoms or molecules. The electrons eventually tunnel out to a far-away region which we do not wish to represent explicitly in the calculation. We are thus dealing with the specific case of an open quantum system where we only have particles leaving the system.

3 Calculation of Resonances from Complex Scaling

The complex scaling method was initially developed by Aguilar, Balslev, Combes, and Simon [19–21], and is based on a scaling $\mathbf{r} \to \mathbf{r}e^{i\theta}$ of the position variable in the Schrödinger equation. This is referred to as *uniform* complex scaling. Here we review uniform complex scaling in the simple case of independent particles. Most recent work is based on a later generalization called *exterior* complex scaling [22], which we consider later. The following is a rather informal description of complex scaling, focusing on a few important cases. More information can be found in any of the many existing reviews.[23–27]

3.1 Formalism

Consider the standard independent-particle time-independent Schrödinger equation for a finite system:

$$\hat{H}\psi(\mathbf{r}) = \varepsilon\psi(\mathbf{r}). \tag{3}$$

The Hamiltonian is $\hat{H} = -\frac{1}{2}\nabla^2 + v(\mathbf{r})$, where $v(\mathbf{r})$ is some reasonably well-behaved potential which approaches zero as $r \to \infty$. Formally, the potential has to be *dilation* or *dilatation analytic* [19], but the method has been applied successfully to potentials that are not, an example of which is the Stark effect [28–30]. For our informal review we only insist that it be *analytic* in relevant parts of the complex plane.

The spectrum of $\hat{H}$ consists of a negative point spectrum corresponding to the bound states, and the continuum $\varepsilon \geq 0$. The goal of complex scaling is to identify resonances associated with positive energies somewhere within the continuum.

The complex scaling operation is implemented by the operator $\hat{R}_\theta$ defined by

$$\hat{R}_\theta\psi(\mathbf{r}) = e^{iN\theta/2}\psi\left(\mathbf{r}e^{i\theta}\right), \tag{4}$$

where N is the number of spatial coordinates on which the scaling is applied (thrice the number of particles in the 3D many-body case). θ, the *scaling angle*, is a fixed

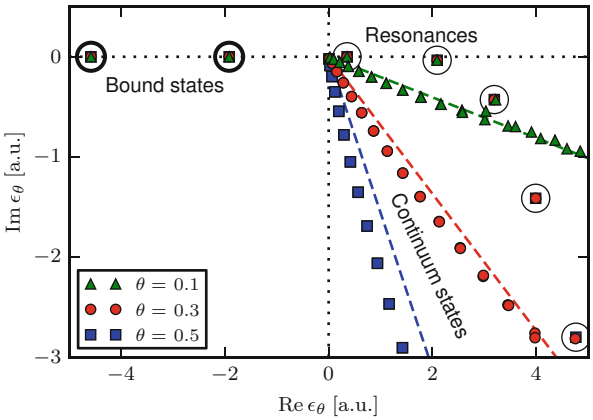

Fig. 1 Effect of complex scaling on the spectrum for the 1D potential $v(x) = 3(x^2 - 2)\exp(-x^2/4)$. Bound-state eigenvalues (*bold circles*) are independent of θ while the continuous spectrum rotates by -2θ around the threshold 0. Because of the finite size of the simulation box, the numerically calculated unbound states (*uncircled*) do not fall exactly on the line $\arg z = -2\theta$. Resonances (*thin circles*) are resolved when θ is sufficiently large for them to segregate from the continuum states. Calculated using a uniform real-space grid from -18 to 18 a.u. with 250 points and fourth-order Laplacian finite-difference stencil

number formally supposed to lie within $0 \leq \theta \leq \pi/4$, although this depends on the analyticity of the potential. The scaling operation transforms the position and momentum operators as $x \to x\mathrm{e}^{i\theta}$ and $\mathrm{d}/\mathrm{d}x \to \mathrm{e}^{-i\theta}\mathrm{d}/\mathrm{d}x$, wherefore the Hamiltonian transforms to

$$\hat{H}_\theta \psi_\theta(\mathbf{r}) = \varepsilon_\theta \psi_\theta(\mathbf{r}) \tag{5}$$

with

$$\hat{H}_\theta = \hat{R}_\theta \hat{H} \hat{R}_\theta^{-1} = -\frac{1}{2}\mathrm{e}^{-i2\theta}\nabla^2 + v\left(\mathbf{r}\mathrm{e}^{i\theta}\right). \tag{6}$$

The transformation maps the potential to its analytic continuation on $\mathbf{r}\mathrm{e}^{i\theta}$ in the complex plane. The interesting property of $\hat{H}_\theta$ is how its spectrum and eigenstates are related to that of $\hat{H}$. First of all, $\hat{H}_\theta$ is non-Hermitian and therefore admits complex eigenvalues. The continuous spectrum "swings down" by an angle of 2θ as shown in Fig. 1. Meanwhile, the energies of any bound states remain unaffected. Finally, for sufficiently large θ, new eigenvalues materialize which are independent of further increase of θ and which are taken to represent resonances. Let us have a closer look at each of these three effects separately.

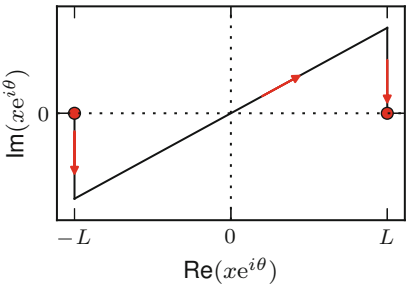

Fig. 2 Complex integration path with directions indicated by *arrows*. If the integrand is suitably localized and analytic on the integration path, the indicated path becomes equivalent to that over the real axis from $-\infty$ to ∞ as $L \to \infty$. This ensures that the unphysical complex scaling angle does not affect matrix elements or expectation values

3.2 Bound States

Suppose $\phi(\mathbf{r})$ and $\psi(\mathbf{r})$ are square-integrable and reasonably well-behaved states. We consider first the scaling operation $\hat{U}_\eta\ \psi(\mathbf{r}) = \mathrm{e}^{N\eta/2}\ \psi(\mathbf{r}\mathrm{e}^{\eta})$ where η is a real number. This operation is easily seen to be unitary; for example it preserves scalar products:

$$\left\langle \phi \middle| \hat{U}_\eta^{\dagger} \hat{U}_\eta \middle| \psi \right\rangle = \int \phi^*(\mathbf{r}\mathrm{e}^{\eta}) \psi(\mathbf{r}\mathrm{e}^{\eta}) \mathrm{d}\mathbf{r}\mathrm{e}^{N\eta} = \int \phi^*(\mathbf{r}') \psi(\mathbf{r}') \mathrm{d}\mathbf{r}' = \left\langle \phi \middle| \psi \right\rangle, \tag{7}$$

where we used the substitution $\mathbf{r}' = \mathbf{r}\mathrm{e}^{\eta}$. A real scaling therefore preserves matrix elements and eigenvalues.

The derivation of the complex scaling method starts with the unitarity of the real scaling, then considers the extension to the complex plane of the scaling parameter η. However, as we see, the situation becomes radically different when the scaling is complex. In order for the method to be correct, the scaling operation must retain some property resembling unitarity to make sure that observables do not arbitrarily change with the scaling parameter. The analytic continuations of functions defined originally on the real axis are not always within the Hilbert space (hence breaking unitarity). However, for suitable states and operators, as we see later, the complex scaling operation corresponds simply to a change of integration path which preserves scalar products. Let us consider a matrix element of some local operator

$$\left\langle \phi \middle| \hat{O} \middle| \psi \right\rangle = \int \phi^*(\mathbf{r}) \hat{O}(\mathbf{r}) \psi(\mathbf{r}) \mathrm{d}\mathbf{r}. \tag{8}$$

This integral is taken for each coordinate axis over all real numbers $-\infty$ to ∞. Imagine now that we liberate each position coordinate and allow it to take complex values. Then, instead, we take the integral over some complex path, such as the one in Fig. 2 with three segments. If the diagonal segment is long enough ($L \to \infty$ in the

figure), and the integrand is analytic and sufficiently localized, then the integral along the vertical segments is zero. Thus the integral over the diagonal $z = x\mathrm{e}^{i\theta}$ is independent of θ and equal to that along the real line:

$$\int \cdot \mathrm{d}x = \lim_{a\to\infty} \int_{-a\mathrm{e}^{i\theta}}^{a\mathrm{e}^{i\theta}} \cdot \mathrm{d}x. \tag{9}$$

The substitution $\mathbf{r}' = \mathbf{r}\mathrm{e}^{i\theta}$ then transforms the integral back so the integration variable is (unlike the integrand) real:

$$\left\langle \phi \middle| \hat{O} \middle| \psi \right\rangle = \int \overline{\phi}_\theta(\mathbf{r}) \hat{O}_\theta(\mathbf{r}) \psi_\theta(\mathbf{r}) \mathrm{d}\mathbf{r}, \tag{10}$$

with

$$\psi_\theta(\mathbf{r}) = \mathrm{e}^{iN\theta/2} \psi\left(\mathbf{r}\mathrm{e}^{i\theta}\right) = \hat{R}_\theta \psi(\mathbf{r}), \tag{11}$$

$$\overline{\phi}_\theta(\mathbf{r}) = \mathrm{e}^{iN\theta/2} \phi^*\left(\mathbf{r}\mathrm{e}^{i\theta}\right) = \left[\hat{R}_{-\theta} \phi(\mathbf{r})\right]^*, \tag{12}$$

$$\hat{O}_\theta(\mathbf{r}) = \hat{O}\left(\mathbf{r}\mathrm{e}^{i\theta}\right) = \hat{R}_\theta \hat{O} \hat{R}_\theta^{-1}. \tag{13}$$

Note how (1) the complex prefactors of $\mathrm{e}^{iN\theta/2}$ from (4) serve to "absorb" exactly the volume element $\mathrm{e}^{iN\theta}$ produced by the variable substitution, and (2) the left states or bras are effectively rotated by $-\theta$. Furthermore, if the unscaled state $\phi(\mathbf{r})$ is real, the cumbersome notation for $\overline{\phi}_\theta(\mathbf{r})$ of (12) can be avoided:

$$\overline{\phi}_\theta(\mathbf{r}) = \phi_\theta(\mathbf{r}) \quad \text{if } \phi(\mathbf{r}) \text{ is real.} \tag{14}$$

We can then calculate the matrix element without conjugating anything.

What we have established is that the complex scaling operation corresponds to a change of integration path when calculating matrix elements. For states and operators that produce a sufficiently localized integrand and do not possess poles that interfere with the integration path, it preserves values of matrix elements. In particular this guarantees that observables or eigenvalues of bound states under complex scaling, at least for sufficiently small values of θ, are independent of θ.

3.3 Continuum States

The previous discussion does not apply to states that are not localized, such as continuum states. Let us consider the complex-scaled Schrödinger equation for a free particle in one dimension:

$$-\frac{1}{2}\frac{\mathrm{d}^2\psi_\theta(x)}{\mathrm{d}x^2}\mathrm{e}^{-i2\theta} = \varepsilon_\theta\psi_\theta(x). \tag{15}$$

We immediately see that this is the *same* differential equation as the unscaled one, and thus has the usual set of solutions:

$$\psi_\theta(x) = A\exp(ikx) + B\exp(-ikx). \tag{16}$$

As per the standard procedure, let us say that the particle is confined to some finite box. We then require that $\psi_\theta(x)$ be 0 on the boundaries, which quantizes k to a set of real positive numbers. Taking the limit of large boxes, we see that solutions exist for all $k > 0$. It follows that the energy ε_θ in (15) must become complex according to

$$\varepsilon_\theta = \frac{1}{2}k^2\mathrm{e}^{-i2\theta}, \quad k > 0. \tag{17}$$

Evidently the spectrum has been rotated by an angle of -2θ into the fourth quadrant of the complex plane. Meanwhile, the solution wavefunctions for the free particle have the same form as without the complex scaling operation.

What, then, is so interesting about the complex-scaled solutions $\psi_\theta(x)$? Because they are not normalizable, and because their energy depends on the scaling angle θ, they are not of much use computationally. However, we can gain some insight by scaling them back to $\theta = 0$ to obtain

$$\hat{R}_{-\theta}\psi_\theta(x) = \mathrm{e}^{-i\theta/2}\left(A\mathrm{e}^{ikx\cos\theta}\mathrm{e}^{kx\sin\theta} + B\mathrm{e}^{-ikx\cos\theta}\mathrm{e}^{-kx\sin\theta}\right). \tag{18}$$

For $x \to \infty$ the right-going term diverges whereas the left-going one dies out. For $x \to -\infty$ it is the left-going one which survives. The solution $\psi_\theta(x)$ to the complex-scaled problem therefore resembles an outgoing, exponentially diverging state. We see intuitively that the complex scaling operation may have something to say about the outgoing character of states. However, as mentioned, the states $\psi_\theta(x)$ are not normalizable and their energies depend on θ. The main effect of the complex scaling operation was to move the continuous spectrum of the Hamiltonian away from the real axis, close to which we find the resonance eigenvalues as we see later.

If the system consists of a central, (almost) localized potential surrounded by vacuum, an unbound state still has the form (16) almost everywhere in space. Importantly and non-trivially, this also works with the Coulomb potential in spite of its long range. The complex scaling transformation still causes the continuous spectrum to rotate by exactly -2θ. In numerical representations this is only approximately true because of incompleteness of the basis and in particular finite simulation boxes as in Fig. 1.

We note here that the method cannot in general be combined with extended (periodic) systems, because complex scaling fundamentally works in terms of the asymptotic form of decaying functions. For example, a metal would possess occupied continuum states which do not decay at the end of the cell. This makes

their properties depend on the scaling angle θ as we saw for free particles. However, from what we have seen so far, one could well imagine using complex scaling in some directions and not others – for example, to describe electrons escaping in the z direction from a surface which is periodic along x and y, or radially from a one-dimensional nanowire.

3.4 Resonant States

From standard scattering theory we know that resonances are associated with wavefunctions that diverge exponentially at increasing distances. If the resonance is generated by a short-range potential, the resonance wavefunction must far away equal or approach that of a free particle.

In one dimension the resonance wavefunction must therefore have the form

$$\psi(x) = A\mathrm{e}^{ikx} = A\mathrm{e}^{i(p-iq)x}, \quad x \to \infty, \tag{19}$$

where we have used the complex wavenumber $k = p - iq$ with positive p (so the wave is outgoing) and q (so it diverges exponentially). Now apply the complex scaling transformation to this function:

$$\hat{R}_\theta \psi(x) = \mathrm{e}^{i\theta/2}\mathrm{e}^{i(p-iq)x\mathrm{e}^{i\theta}} = \mathrm{e}^{i\theta/2}\mathrm{e}^{i(p\cos\theta+q\sin\theta)x}\mathrm{e}^{(-p\sin\theta+q\cos\theta)x}. \tag{20}$$

This function is square integrable if $q < p \tan\theta$. Physically we would expect a resonance peak to be located at a positive energy, and that the resonance width is much smaller than the resonance energy. The energy of this wave is $(p-iq)^2/2 = (p^2 - q^2 - 2ipq)/2$, and we would thus expect p to be well greater than q for any resonance. Some intermediate value of θ therefore easily ensures that $q < p \tan\theta$, i.e., that the resonance wavefunction is square integrable.

We conclude from this that the Siegert wavefunction representing a resonant state indeed becomes square integrable under adequate complex scaling. This makes matrix elements with resonant states invariant to variations in θ, similarly to bound states, as long as the variation of θ does not make them unbounded.[2]

The numerical convergence of resonance energies and widths is a non-trivial issue with complex scaling. When using a numerical representation such as a finite basis set, matrix elements are not perfectly independent of θ. For a given system it is standard practice to compare calculated resonance energies and widths over a range of different θ-values, looking for a stationary point or a cusp which, following the

[2] The above discussion is, of course, very informal. Scrinzi and Piraux have presented a more complete argument on the link between outgoing wavefunctions and square integrability after complex scaling; see Scrinzi and Piraux [31], Appendix A.

"complex virial theorem," would best approximate the fully converged complex energy [32, 33].

3.5 *Exterior Complex Scaling*

We established previously that the complex scaling operation preserves scalar products of square integrable states because it corresponds to a change of integration contour of an analytic function. Suppose we want to calculate a resonance of a molecule in the Born–Oppenheimer approximation. The nuclear point charges cause poles in the Coulomb potential at each nuclear position. Uniform complex scaling does not work because of these poles. A solution to this problem is to change the integration contour to avoid the poles. From complex analysis we know that we could have chosen many other integration paths, corresponding to other definitions of the scaling operation $\hat{R}_\theta$, and those contours would equally well preserve scalar products as long as the integration contours have the same start and end points and do not enclose poles. This is the basis for *exterior complex scaling* which was proposed by Simon [22] to solve exactly this problem. Another method is to use the analytic continuation of matrix elements within a basis set representation [34–36], which effectively approximates the exterior complex scaling approach [37].

We thus complex-scale the *exterior* of a region containing all the point charges by an operation, here written in one dimension, of the form

$$\hat{R}_\theta^a \psi(x) = \begin{cases} \psi\left(-a + (x+a)\mathrm{e}^{i\theta}\right), & x < -a, \\ \psi(x), & -a \le x < a, \\ \psi\left(a + (x-a)\mathrm{e}^{i\theta}\right), & a \le x. \end{cases} \tag{21}$$

The uniform and exterior scaling integration contours are shown in Fig. 3. The important condition for exterior scaling is that the scaling retains the asymptotic form $x \to x\mathrm{e}^{i\theta}$ which ensures outgoing-wave boundary conditions. Because the integration contour is not differentiable, neither is an exterior complex-scaled function that corresponds to a smooth original function. Recall from uniform scaling that we needed to multiply by $\mathrm{e}^{i\theta/2}$ to "absorb" the now complex volume element when integrating. We have not done anything to the volume element in (21), and therefore we need to apply a factor of $\mathrm{e}^{i\theta}$ when calculating integrals over the complex segments. Alternatively, most authors define the exterior scaling operation so the wavefunction in the exterior segments includes the complex prefactor; the functions then become discontinuous [38], but we do not need to consider the volume element when integrating. Here we have followed the original convention of Simon [22] where the function is always continuous. As long as the discontinuities of the complex-scaled functions or their derivatives are well incorporated into the numerical basis set used to represent them, they are harmless.

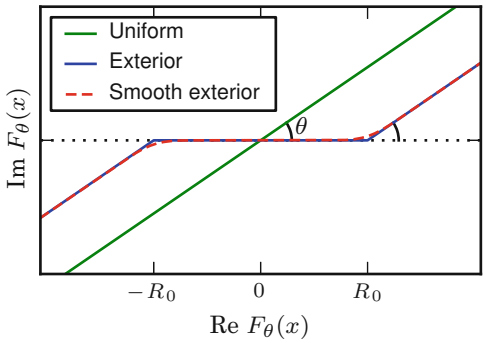

Fig. 3 Possible complex integration contours for uniform, exterior and smooth exterior complex scaling. $\theta = 0.6$. The contours must be continuously deformable (without crossing any poles) back to the real axis in order for them to be equivalent to a real integration. Note that, as per basic complex analysis, the contours themselves do not have to be differentiable – it is sufficient that the integrand be analytic

If for numerical reasons we want smooth functions everywhere, we can equally well choose a smooth integration contour. This is called *smooth-exterior* complex scaling. The scaling operator here acts by applying a smooth function $x \to z = F(x)$ to the position coordinate, with $F(x) \sim x e^{i\theta}$ for large $|x|$.

Once again we have the choice of where to include the smoothly varying volume element: either in the definition of the scaling operation, or explicitly when integrating. This yields different expressions which are given, for example, by Moiseyev [39]. If we include the volume element in the scaling operation, it reads

$$\hat{R}^{F}_{\text{smooth}}\psi(x) = [F'(x)]^{1/2}\psi(F(x)). \tag{22}$$

The Hamiltonian subject to this transformation is

$$H^F = -\frac{1}{2}[F'(x)]^{-2}\frac{\partial^2}{\partial x^2} + V_1^F(x)\frac{\partial}{\partial x} + V_0^F(x) + V[F(x)], \tag{23}$$

where

$$V_0^F(x) = \frac{1}{4}[F'(x)]^{-3}F'''(x) - \frac{5}{8}[F'(x)]^{-4}[F''(x)]^2, \tag{24}$$

$$V_1^F(x) = [F'(x)]^{-3}F''(x). \tag{25}$$

An example contour is shown in Fig. 3. The contour defined by F can be quite general, but one would choose $F(x) = x$ within the interior region such that $V_0^F(x) = V_1^F(x) = 0$ and $[F'(x)]^{-2} = 1$. Note how (23) then reduces to the usual Schrödinger equation as it should. With this formulation we do not need to mind

any discontinuities of wavefunctions, their derivatives, or the Jacobian, and standard methods such as finite-difference stencils can be applied straightforwardly as long as F is adequately differentiable.

How do the different types of complex scaling discussed above compare computationally? The basic equations of exterior and smooth exterior complex scaling are clearly more complicated than those for uniform scaling. However, as mentioned, the purpose of exterior complex scaling is that it admits potentials that are not analytic within the interior region. This includes any strictly localized function such as most atomic pseudopotentials – a major advantage for advanced self-consistent field methods such as DFT. One other advantage of exterior scaling is that. within the interior region, quantities such as the density retain their true physical values rather than a difficult-to-interpret complex continuation which is also numerically difficult to rotate back to real space.

For real-space methods, an advantage of smooth exterior complex scaling is that one can transparently use finite-difference stencils as per (23). Standard finite-difference stencils, representing, for instance, the kinetic operator, do not work on a non-differentiable contour although one can derive special stencils for this case [40]. Basis sets should also make sure to take the discontinuity into account. Finite-element representations involving some kind of basis are commonly used; see, for example, Rescigno et al. [41] and Scrinzi and Elander [42]. Rescigno and co-workers have reported that finite-element calculations with a basis set which properly takes the discontinuity of "sharp" exterior scaling into account require less functions than a purely analytic basis set using smooth scaling [41]. A more detailed discussion of the numerical representations and basis sets can be found in work by McCurdy et al. [24], who also argue that grid-based methods enjoy a similar advantage with sharp exterior complex scaling, provided the scaling onset is exactly on a grid point.[3]

3.6 Example: Resonance in One Dimension

Let us perform an analytic calculation of a resonance using complex scaling to see how exactly the resonance emerges. We consider a barrier formed by the piece-wise constant potential

[3] This would be less of an advantage in Cartesian 3D calculations where a smooth scaling could be applied spherically, whereas the sharp scaling would need a cube to align its boundary with the grid.

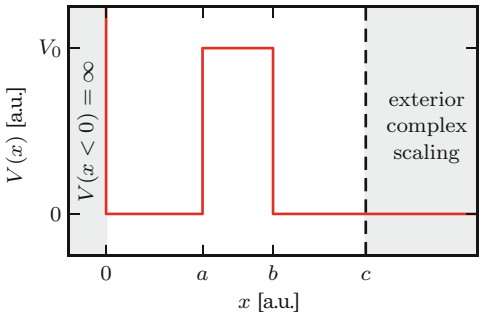

Fig. 4 Rectangular potential barrier supporting resonances. Exterior complex scaling ensures that resonance wavefunctions localize and appear as eigenstates of the scaled Hamiltonian

$$V(x) = \begin{cases} 0, & 0 \leq x < a, \\ V_0, & a \leq x < b, \\ 0, & b \leq x, \end{cases} \tag{26}$$

seen in Fig. 4. Both Gellene [16] and Simons [43] have considered this problem previously. As the rectangular barrier is not an analytic function, we cannot use uniform complex scaling. However, nothing stops us from using exterior scaling, with the scaling transformation starting somewhere outside the barrier at $x = c > b$.

We thus use the contour

$$F_\theta^c(x) = \begin{cases} x, & 0 \leq x < c, \\ c + \mathrm{e}^{i\theta}(x - c), & c \leq x. \end{cases} \tag{27}$$

For $x \geq c$ the Hamiltonian is therefore $-\frac{1}{2}\mathrm{e}^{-i2\theta}\frac{\mathrm{d}^2}{\mathrm{d}x^2}$. This gives us four regions, within each of which the wavefunction must be a solution to the Schrödinger equation for a free particle but with different local momenta k_1, k_2, and k_3^θ which may be complex:

$$\psi_1(x) = -iA\left(\mathrm{e}^{ik_1x} - \mathrm{e}^{-ik_1x}\right) = 2A\sin(k_1x), \quad 0 \leq x < a, \tag{28}$$

$$\psi_2(x) = C\mathrm{e}^{ik_2x} + D\mathrm{e}^{-ik_2x}, \quad a \leq x < b, \tag{29}$$

$$\psi_3(x) = F\mathrm{e}^{ik_1x} + G\mathrm{e}^{-ik_1x}, \quad b \leq x < c, \tag{30}$$

$$\psi_4^\theta(x) = I\mathrm{e}^{ik_3^\theta x} + J\mathrm{e}^{-ik_3^\theta x}, \quad c \leq x. \tag{31}$$

The expression for $\psi_1(x)$ has been chosen to fulfill the boundary condition $\psi_1(0) = 0$, and A eventually determines the normalization of the state. To relate the three wavenumbers k_1, k_2, and k_3^θ, we note that applying the Hamiltonian to the wavefunction must yield the same energy eigenvalue $\varepsilon_\theta = k_1^2/2 = k_2^2/2 + V_0 = \left(\mathrm{e}^{-i\theta}k_3^\theta\right)^2/2$ within each segment. From this may take $k_3^\theta = k_1\mathrm{e}^{i\theta}$.

The segments must be joined continuously and differentiably, i.e., $\psi_1(a) = \psi_2(a)$ and $\psi_1'(a) = \psi_2'(a)$ at $x = a$. Likewise $\psi_2(b) = \psi_3(b)$ and $\psi_2'(b) = \psi_3'(b)$. At $x = c$,

the onset of the scaled exterior region, the derivative $\psi'_3(c)$ must match the *scaled* derivative $\psi_4^{\theta\,\prime}(c)$, so the derivative becomes discontinuous [22]:

$$\psi_3(c) = \psi_4^{\theta}(c), \tag{32}$$

$$\psi'_3(c) = \mathrm{e}^{-i\theta}\psi_4^{\theta\prime}(c). \tag{33}$$

(We have here, for esthetic reasons, chosen not to include the square root of the volume element or Jacobian in the definition of $\psi_4^{\theta}(x)$; if we had, the function itself would have been discontinuous as discussed in Sect. 3.5.)

We thus have two equations at each of the points a, b, and c, for a total of six equations. A seventh equation follows from the requirement that the function be square integrable. These seven equations determine the six unknown coefficients C, D, F, G, I, and J, and further quantize the energy so that we get solutions only for specific wavenumbers k_1, k_2, and k_3^{θ}.

Gellene [16] provides expressions for the coefficients C, D, F, and G in terms of A so that $\psi_1(x)$, $\psi_2(x)$, and $\psi_3(x)$ match at the points a and b. The resonances are then found by considering the phase shift between the incoming and outgoing coefficients F and G of $\psi_3(x)$. However, this is very different in our case using complex scaling; here, the coefficients I and J of $\psi_4^{\theta}(x)$ must ensure square integrability.

Physically, we would expect of a resonance that its energy is much greater than its width. The wavenumber k_1 then has real and imaginary parts $k_1 = p - iq$ such that $p \gg q$. The wavefunction can thus be written as

$$\begin{aligned}\psi_4^{\theta}(x) = {} & I\mathrm{e}^{(-p\sin\theta+q\cos\theta)x}\mathrm{e}^{i(p\cos\theta+q\sin\theta)x} \\ & +J\mathrm{e}^{(p\sin\theta-q\cos\theta)x}\mathrm{e}^{-i(p\cos\theta+q\sin\theta)x}.\end{aligned} \tag{34}$$

For scaling angles θ not too close to zero, the first term converges whereas the second diverges as $x \to \infty$, and so we conclude that $J = 0$. Relating the right and left values and derivatives of $\psi_3(x)$ and $\psi_4^{\theta}(x)$ at $x = c$ we get

$$F\mathrm{e}^{ik_1c} + G\mathrm{e}^{-ik_1c} = I\mathrm{e}^{ik_1\mathrm{e}^{i\theta}c}, \quad \text{(values)} \tag{35}$$

$$ik_1\left(F\mathrm{e}^{ik_1c} - G\mathrm{e}^{-ik_1c}\right) = ik_1I\mathrm{e}^{ik_1\mathrm{e}^{i\theta}c}, \quad \text{(derivatives)} \tag{36}$$

and it immediately follows that $G = 0$, i.e., there is no incoming wave component. This is very different from the Hermitian treatment demonstrated by Gellene which yields $F = G^*$, exactly balancing the outgoing and incoming flux. We see that, as previously discussed, the square integrability requirement of the complex-scaled solution ensures that waves are purely outgoing. In a simple model we could just as easily have forgotten everything about complex scaling and set $G = 0$ immediately. However, in a numerical calculation things are not so simple, and we have to rely on the complex scaling transformation to ensure square integrability and to extract the resonant states in a tractable form.

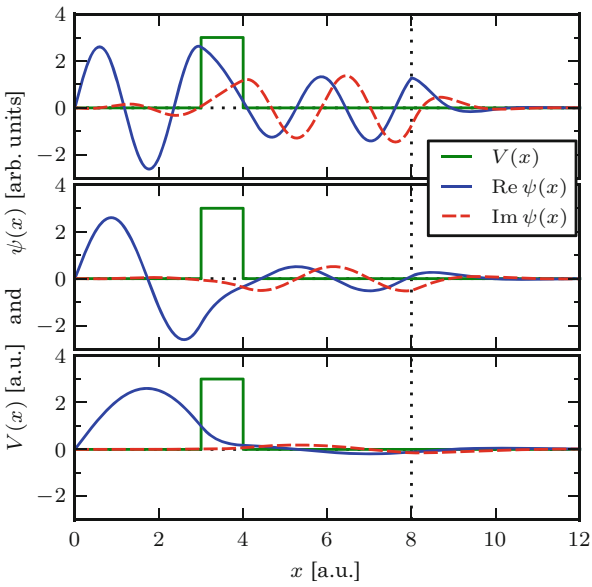

Fig. 5 The first (*bottom*), second (*middle*), and third (*top*) lowest-energy resonances of the model potential. Exterior scaling is applied for $x \geq 8$ which exponentially damps the resonance wavefunctions. Otherwise they would be exponentially increasing

In a more complicated potential generated by multiple atoms, the situation would be similar sufficiently far away from the system. The asymptotic form of the wavefunctions may differ slightly because of long-range interactions such as the Coulomb interaction, but this doesn't prevent the exponentially localizing effect of the complex scaling operation from functioning.

However, let us get back to the determination of the resonance eigenvalues. The requirement that $G = 0$ allows us to proceed, linking F, D, and C by means of the differentiability and continuity requirements. Once all coefficients are eliminated, the condition for resonance is

$$\left(1 - \frac{k_2}{k_1}\right)\left(\tan k_1 a - i\frac{k_1}{k_2}\right)e^{2ik_2(b-a)} + \left(1 + \frac{k_2}{k_1}\right)\left(\tan k_1 a + i\frac{k_1}{k_2}\right) = 0. \qquad (37)$$

For any energy $\varepsilon - i\Gamma/2$, the wavenumbers k_1 and k_2 are uniquely determined. The solutions can then be determined numerically. The three complex resonance energies closest to 0 are given by the real parts $\varepsilon = 0.421$, 1.65, 3.57, and half-widths $\Gamma/2 = 0.00138$, 0.0189, 0.138. Figure 5 shows the corresponding resonance wavefunctions. The eigenvalues slightly disagree with those by Gellene who works effectively on the real axis. This is because the two methods are different: With complex scaling we find an eigenvalue in the complex plane which corresponds exactly to an outgoing wave. Working on the real axis, we would find the real energy which responds most strongly to that eigenvalue. However, as the complex eigenvalue gets further away from the real axis, location and width soon begin to differ.

4 Density Functional Resonance Theory

As the complex scaling formalism is based on the many-particle Schrödinger equation, the method inherits the same exponential computational cost with respect to the number of particles. The method in the original form is therefore practical only for systems with very few particles, such as small atoms or molecules, using, for example, correlated basis sets [44, 45]. However, larger systems require more scalable computational methods, of which many have been investigated. Of particular interest are self-consistent field methods such as Hartree–Fock [46], post-Hartree–Fock methods [47, 48], and DFT [49, 50]. DFT as always has the drawback that it relies on a complicated formalism including an approximation of the exchange and correlation effects which is difficult to control, but its inarguable performance advantages nevertheless make it more than worthy of consideration. Below we describe the extension of DFT with complex scaling.

4.1 Complex Scaling and DFT

DFT is based on the minimization of a functional of the real electron density. The minimum of the functional and the corresponding electron density are the ground-state energy and electron density [1, 3]. For practical calculations one uses a set of single-particle states or Kohn–Sham states to facilitate evaluation of the kinetic part of the functional. The Kohn–Sham energy functional contains the following contributions: the kinetic energy, the Hartree energy, the exchange–correlation (XC) energy, and the energy from a system-dependent external potential. The kinetic energy functional depends explicitly on the Kohn–Sham wavefunctions whereas the others depend on them only through the density. Either way, all the terms can be understood as sums of matrix elements of operators. We know from Sect. 3.2 how the complex scaling operation conserves matrix elements of states that are spatially localized, provided that the operators are analytic. We can therefore reasonably expect complex scaling to be made to work within DFT, once we know how each term in the energy functional scales. The combination has been dubbed density functional resonance theory (DFRT) [50].

One would thus propose a complex-valued energy functional

$$E_\theta = -\frac{1}{2}\mathrm{e}^{-i2\theta}\sum_n f_n \int \overline{\psi}_{\theta n}(\mathbf{r})\nabla^2\psi_{\theta n}(\mathbf{r})\mathrm{d}\mathbf{r} + \frac{1}{2}\mathrm{e}^{-i\theta}\int\int \frac{\rho_\theta(\mathbf{r})\rho_\theta(\mathbf{r}')}{\|\mathbf{r}-\mathbf{r}'\|}\mathrm{d}\mathbf{r}\mathrm{d}\mathbf{r}' + E_{\mathrm{xc}}^{\theta}[n_\theta] + \int v_{\mathrm{ext}}\left(\mathbf{r}\mathrm{e}^{i\theta}\right)n_\theta(\mathbf{r})\mathrm{d}\mathbf{r} \tag{38}$$

with the complex-scaled density

$$n_\theta(\mathbf{r}) = \sum_n f_n \overline{\psi}_{\theta n}(\mathbf{r}) \psi_{\theta n}(\mathbf{r}) \mathrm{d}\mathbf{r} = \mathrm{e}^{iN\theta} n\left(\mathbf{r}\mathrm{e}^{i\theta}\right), \tag{39}$$

where f_n are occupation numbers, and N the number of dimensions in which the coordinates are complex-scaled. In (38) the kinetic and external contributions are complex-scaled as normal. In the Hartree energy, $\rho_\theta(\mathbf{r})$ denotes the complex-scaled charge density which is the electron density $n_\theta(\mathbf{r})$ plus any other contributions such as pseudopotential charges (whose complex-scaled form is uniquely determined by requiring that their Hartree potential scales as normal). The Hartree energy itself scales as $E_\mathrm{H}^\theta[n_\theta] = \mathrm{e}^{-i\theta} E_\mathrm{H}[n_\theta]$, i.e., the standard Hartree functional is applied to the *complex* density, with the factor $\mathrm{e}^{-i\theta}$ appearing because of the $1/r$ kernel. We discuss the complex XC energy functional $E_\mathrm{xc}^\theta[n_\theta]$ later.

Being complex, "minimizing" the energy functional (38) does not strictly make sense. Nevertheless, the lowest-energy resonance is obtainable as a stationary point of the complex energy functional [51]. An equation for the stationary point can, as normal, be obtained by taking the derivative with respect to the wavefunctions plus a set of Lagrange multipliers which ensure normalization. This yields the complex scaled Kohn–Sham equations

$$H_\mathrm{KS}^\theta \psi_{\theta n}(\mathbf{r}) = \left[-\frac{1}{2}\mathrm{e}^{-i2\theta}\nabla^2 + v_\theta(\mathbf{r})\right]\psi_{\theta n}(\mathbf{r}) = \varepsilon_{\theta n}\psi_{\theta n}(\mathbf{r}) \tag{40}$$

for $\psi_{\theta n}(\mathbf{r})$ and $\varepsilon_{\theta n}$, where we have taken the derivative with respect to the left states $\overline{\psi}_{\theta n}(\mathbf{r})$. If the unscaled Hamiltonian is real, the states can be chosen to be real so that $\overline{\psi}_{\theta n}(\mathbf{r}) = \psi_{\theta n}(\mathbf{r})$. In general, however, we could equally well have derived a Hamiltonian for the left states $\overline{\psi}_{\theta n}(\mathbf{r})$.

In the Kohn–Sham equations (40) we have introduced the effective potential

$$v_\theta(\mathbf{r}) = v_\mathrm{H}^\theta(\mathbf{r}) + v_\mathrm{xc}^\theta(\mathbf{r}) + v_\mathrm{ext}\left(\mathbf{r}\mathrm{e}^{i\theta}\right) \tag{41}$$

defined as the density-derivatives of terms in the energy functional. The Hartree potential is

$$v_\mathrm{H}^\theta(\mathbf{r}) = \mathrm{e}^{-i\theta}\frac{\delta E_\mathrm{H}[\rho_\theta]}{\delta\rho_\theta(\mathbf{r})} = \mathrm{e}^{-i\theta}\int \frac{\rho_\theta(\mathbf{r}')}{\|\mathbf{r}' - \mathbf{r}\|}\mathrm{d}\mathbf{r}', \tag{42}$$

which allows the potential to be determined from the charge density by solving a complex Poisson problem using standard techniques. What remains to be discussed now is the XC functional.

4.2 Complex Scaling of Exchange and Correlation

The first DFRT calculations were carried out in a one-dimensional model potential with two electrons in the same (singlet) state [50]. The method was demonstrated using the exact KS potential, which in this case is

$$v^{\theta}_{\text{exact}}(x) = \mathrm{e}^{-i2\theta}\frac{\nabla^2\psi_\theta(x)}{2\psi_\theta(x)} + \varepsilon_\theta, \tag{43}$$

along with exact exchange (EXX) which, in this case, simply cancels out half the Coulomb energy. However, for systems with more particles, and indeed for realistic numerical calculations in the style of modern DFT software, the XC functional would have to be one of the many commonly used approximations. For simplicity we ignore any notion of spin below. The simplest functional is the local density approximation (LDA), the complex scaling of which was studied by Larsen et al. [49]. The first question is whether the functional is analytic. The exchange energy is given by

$$E_{\text{x}}[n] = -\frac{3}{4}\left(\frac{3}{\pi}\right)^{1/3}\int n^{4/3}(\mathbf{r})\mathrm{d}\mathbf{r}, \tag{44}$$

where the fractional power $n^{4/3}$ is three-valued on the complex numbers and we must mind the branch cuts. Following the arguments of Sect. 3.2 for handling the change in complex contour, the integral scales as follows as long as we do not run into a branch cut:

$$\begin{aligned}\int n^{4/3}(\mathbf{r})\mathrm{d}\mathbf{r} &= \int n^{4/3}\left(\mathbf{r}\mathrm{e}^{i\theta}\right)\mathrm{d}\mathbf{r}\mathrm{e}^{iN\theta} = \int\left[\mathrm{e}^{-iN\theta}n_\theta(\mathbf{r})\right]^{4/3}\mathrm{d}\mathbf{r}\mathrm{e}^{iN\theta}\\ &= \mathrm{e}^{-iN\theta/3}\int n_\theta^{4/3}(\mathbf{r})\mathrm{d}\mathbf{r}.\end{aligned} \tag{45}$$

The complex-scaled XC potential is naturally defined as

$$v^{\theta}_{\text{xc}}(\mathbf{r}) = \frac{\delta E^{\theta}_{\text{xc}}[n_\theta]}{\delta n_\theta(\mathbf{r})}. \tag{46}$$

Taking the derivative with respect to $n_\theta(\mathbf{r})$ we get the exchange potential

$$v^{\text{LDA}}_{\text{x}\theta}(\mathbf{r}) = -\left(\frac{3}{\pi}\right)^{1/3}\mathrm{e}^{-iN\theta/3}n_\theta^{1/3}(\mathbf{r}) = v^{\text{LDA}}_{\text{x}}\left(\mathbf{r}\mathrm{e}^{i\theta}\right), \tag{47}$$

i.e., the expression is consistent with analytically continuing the expression for the unscaled potential.

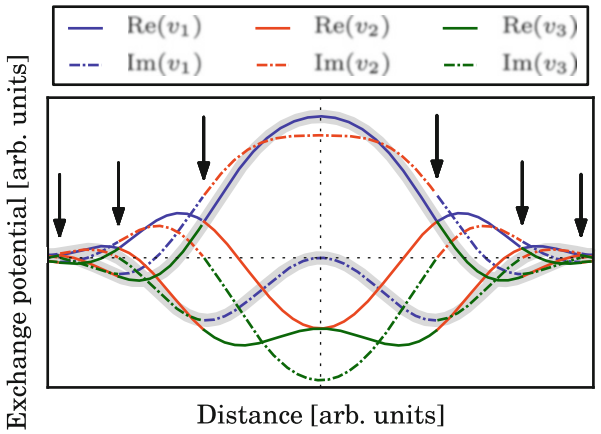

Fig. 6 "Stitching" branches of the cube root for the LDA exchange potential. The procedure starts at $x = 0$ where we know that the potential must be real. When the density takes the value of a branch cut of the cube root (indicated by *arrows*), the function must switch to a different branch to retain analyticity. The stitched function, indicated by the *shaded gray band*, is analytic everywhere and always follows one of the three branches of the cube root. In this example the density is a Gaussian function. From Larsen et al. [49]

As already noted, the expressions are three-valued because of the fractional power. In Larsen et al. [49] this was resolved by "stitching" the potential from the three branches of the cube root: In the origin, the potential must be real as the spatial co-ordinate is real. Further away, whenever the cube root encounters a branch cut, one of the other branches is chosen to restore analyticity. This procedure is illustrated in Fig. 6.

Following the Perdew–Wang parametrization of the LDA correlation functional [52], the correlation potential is given by

$$v_c(r_s) = \varepsilon_c(r_s) - \frac{1}{3}\frac{\mathrm{d}\varepsilon_c(r_s)}{\mathrm{d}r_s} r_s, \tag{48}$$

where

$$\varepsilon_c(r_s) = -2A(1 + \alpha_1 r_s)\ln(1 + 1/Q_1(r_s)), \tag{49}$$

$$Q_1(r_s) = 2A\sum_{i=1}^{4} \beta_i r_s^{i/2}, \tag{50}$$

and r_s is the Wigner–Seitz radius, i.e., $r_s(\mathbf{r}) = [3/(4\pi n(\mathbf{r}))]^{1/3}$. The complex logarithm can be stitched quite analogously to the cube root. Other XC functionals can be stitched similarly, provided that they do not contain poles that get in the way of the integration contour. With exterior complex scaling we avoid scaling the regions of space where most of the action happens, potentially avoiding these problems. We

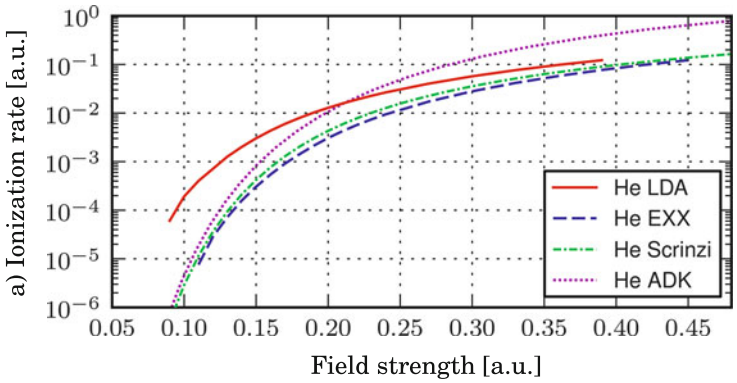

Fig. 7 Ionization rates of the helium atom in static electric fields from different methods. The accuracy at low field strengths is determined by how well the XC functional predicts the energy of the highest occupied orbital, which LDA is known to greatly overestimate. From Larsen et al. [49]

mention a recent time-dependent study [53] which uses smooth exterior complex scaling with the LB94 [54] XC model potential for spin σ:

$$v_{\mathrm{xc},\sigma}^{\mathrm{LB94}}(\mathbf{r}) = v_{\mathrm{xc},\sigma}^{\mathrm{LDA}}(\mathbf{r}) - \frac{\beta x_\sigma^2(\mathbf{r}) n_\sigma^{1/3}(\mathbf{r})}{1 + 3\beta x_\sigma(\mathbf{r}) \sinh^{-1} x_\sigma(\mathbf{r})} \tag{51}$$

with

$$x_\sigma(\mathbf{r}) = \frac{\|\nabla n_\sigma(\mathbf{r})\|}{n_\sigma^{4/3}(\mathbf{r})}. \tag{52}$$

This expression also has several issues with analyticity as it involves both division and fractional powers. In Telnov et al. [53] the exterior scaling contour was probably chosen so as to avoid these, but unfortunately the issue was not mentioned.

4.3 Resonance Lifetimes in DFRT

In this section we present a few results from DFRT on physical systems. Figure 7 shows the ionization rate of a helium atom in an electric field as a function of field strength calculated with different methods: LDA, EXX (Hartree–Fock), ADK [55], and an accurate correlated-electron calculation by Scrinzi [45].

ADK is a simple approximation which is correct in the limit of weak fields. The ionization potential of the atom entirely determines the form of the curve in this limit. Precisely because low-field asymptotics are determined by the value of the ionization potential, the utility of a functional in this limit is directly linked to the

precision with which it estimates the ionization potential, i.e., which energy it assigns to the highest occupied state.

LDA is well known to overestimate this energy, and therefore calculates too high ionization rates for low fields. This problem is attributed to the wrong asymptotic decay of the LDA potential [54]. Meanwhile, Hartree–Fock is known to produce accurate orbital energies, and the decay of the exact exchange potential has the correct asymptotic form. EXX also yields results that are close to the reference by Scrinzi. This all suggests that a good XC functional for DFRT resonance lifetime calculations is one retaining the correct asymptotic form of the potential, such as the previously mentioned LB94 functional.

4.4 Time-Dependence in Complex Scaling

In this section we consider the extension of complex scaling to time-dependent simulations. Most obviously, one could simulate the dynamics of a system whose initial state is derived from a resonance. However, the method has been found useful for another practical reason, namely that complex scaling can be used to avoid the effects of waves reflecting from the boundaries. An early approach by Parker and McCurdy [56] showed that a complex basis set, with properties closely related to the complex scaling method, reduced the amount of basis functions necessary to represent properly a Gaussian wave packet under time evolution. The authors found that the representation avoided reflection effects produced by incompleteness of the basis sets as the wave packet moved away from the central region.

Exterior complex scaling is now widely used as a practical absorber to prevent reflections of waves because of the finite size of the simulation box. Details of its use in this context are given in Sect. 5.6.

Let us go back to the basic question of how to time evolve complex-scaled states. Bengtsson and co-workers [57, 58] have considered this problem in detail. The time evolution of a state vector and its corresponding functional (or bra) are determined by

$$i\frac{\partial\psi(\mathbf{r}t)}{\partial t} = \hat{H}\,\psi(\mathbf{r}t). \tag{53}$$

We apply the complex rotation operator and get

$$i\frac{\partial\psi_\theta(\mathbf{r}t)}{\partial t} = i\hat{R}_\theta\frac{\partial\psi(\mathbf{r}t)}{\partial t} = \hat{R}_\theta\hat{H}\hat{R}_\theta^{-1}\hat{R}_\theta\psi(\mathbf{r}t) = \hat{H}_\theta\psi_\theta(\mathbf{r}t). \tag{54}$$

A general state $\psi_\theta(\mathbf{r}t)$ can be time-evolved according to its expansion in eigenstates. If $\phi_\theta^0(\mathbf{r})$ is an eigenstate with energy ε_θ, then

$$\phi_\theta(\mathbf{r}t) = \mathrm{e}^{-i\hat{H}_\theta t}\phi^0_\theta(\mathbf{r}) = \mathrm{e}^{-i\epsilon_\theta t}\phi^0_\theta(\mathbf{r}). \tag{55}$$

If, further, the eigenstate represents a resonance, so that its energy has a negative imaginary part, $\phi_\theta(\mathbf{r}t)$ decays exponentially while everywhere maintaining its shape. To calculate a general expectation value after a certain time, we would, according to (10), need to apply the *left* state $\overline{\psi}_\theta(\mathbf{r}t) = [\psi_{-\theta}(\mathbf{r}t)]^*$ as per (12). The left state can be time evolved using (54) with $-\theta$. The Hamiltonian $\hat{H}_{-\theta}$ is the conjugate of $\hat{H}_\theta$ so all eigenvalues are likewise conjugated. If $\psi_\theta(\mathbf{r}t)$ contains exponentially decaying components, the corresponding components of $\psi_{-\theta}(\mathbf{r}t)$ exponentially increase at the same rate (one could equivalently say that they propagate backward in time [59]). In principle the increase of the left state would be cancelled by the decay of the right so that the norm, calculated using both left and right states, is time independent, but any numerical error accumulates over the course of the time evolution and eventually causes the procedure to break down.

Although Bengtsson and co-workers have demonstrated that a complex time propagation path can be used to stabilize the time evolution [58], most applications of complex scaling with time evolution have been handled differently. The typical approach is to use exterior complex scaling and time evolve only the right states, then calculate all physical quantities using only the right states although this in general is not formally justified. This approach is discussed further in Sect. 5.6.

5 Open Boundary Conditions

In the previous sections we showed how it is possible to capture intrinsically time-dependent properties such as the lifetime of a resonance using a static, time-independent approach. Now we turn instead to the class of problems where the explicit time-dependence must be taken into account. As we see, the concepts introduced in the previous sections reemerge in the description of physical processes where the total number of particles is no longer a conserved quantity. In particular, insistence on describing an infinitely extended problem in a bounded domain naturally results in dynamics governed by a non-Hermitian Hamiltonian.

Let us divide space into two parts as in Fig. 8 where we have a bounded region we call A and its complement B. We want to solve the equations of motion in A without having to describe explicitly the environment in B. In other words, the problem we have is finding the appropriate boundary conditions for the equations in A, such that the localized solution $\Psi_A(t)$ is equal to the full solution $\Psi(t)$ evaluated in A at all times t.

The class of processes which can be described by the scheme in Fig. 8 includes all the scattering problems where electrons enter A from one side and escape after having interacted with the system. This encompasses, for instance, electron diffraction or molecular transport. It also includes scattering problems where electrons are scattered by other kinds of particles such as photons or protons, thus leading to

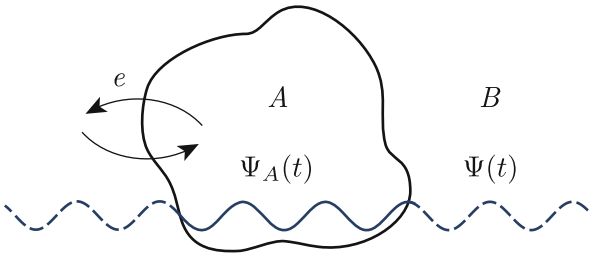

Fig. 8 A system localized in a bounded region A exchanges electrons with the environment B. We look for the correct boundary conditions for the TDSE in A such that the bounded wavefunction $\Psi_A(t)$ matches the complete wavefunction $\Psi(t)$ at all times t

photoionization or proton impact ionization. This last class of processes is sometimes called half-scattering processes because, from the point of view of the electron, the scattering happens with another kind of particle. The main difference between scattering and half-scattering processes is that the boundary conditions for describing the half process are simpler because there is no need to inject charge but only to absorb it. We must, however, note that if nonlinear effects are dominant, for instance when strong laser fields are involved, this distinction is less clear and one may also need to account for incoming electrons for half-scattering problems.

Below we review some of the most notable methods in the literature that have been employed to address this problem. We anticipate that, in all the approaches we discuss, the boundary conditions are implemented by modifying the Hamiltonian with the addition of a complex term that explicitly breaks Hermiticity.

5.1 *Transparent Boundary Conditions Using Green Functions*

Transparent boundary conditions include, by definition, all boundary conditions that allow an exact solution of the open boundary problem. As such, they allow electrons to move back and forth between A and B without reflection. We examine below the class of boundary conditions that can be defined in terms of Green functions. This is not the only possible solution, and other instances of transparent boundaries can be constructed, for example, by using *time dependent exterior complex scaling* or *split propagation schemes* as we show in Sects. 5.6 and 6.3, respectively. So-called *decimation* techniques have also been employed to describe transparent boundaries; see, for instance, García-Moliner and Flores [60] and Kudrnovský et al. [61].

Green function boundary conditions are based on the idea of matching the inner solution Ψ_A of the Schrödinger equation with the outer one Ψ_B expressed in terms of Green functions. Underlying this strategy is the hypothesis that the Hamiltonian describing the system in B is easier to handle than the one describing the system in A.

In general, the problem of finding the Green function for an arbitrary system is hard to solve. However, including in A most of the atomic and molecular structure leaves us in B with a problem which, in many cases, can be easily solved.

The simplest case consists of choosing B to represent the empty space, and the method lends itself to the description of scattering or ionization [62, 63]. On a more advanced level, one may choose B to represent a bulk system and, in conjunction with a time-dependent potential, create a base model for electron transport [64, 65]. Alternatively, by mixing both bulk and empty space Green functions, the frameworks can adapt to the description of ionization from surfaces [66, 67].

The approach is adaptable to a large variety of situations. This versatility has, however, to face the fact that discretizing the otherwise exact equations often leads to computationally demanding implementations with limited application. On the practical level, either one introduces an approximation which affects the quality of the results, or one just uses a simple time propagation of a full-dimensional system, which represents a challenging task [68].

In spite of the technical limitations, the approach provides a fundamental and illustrative description of the open boundary problem. Below we discuss two of the most notable derivations present in the literature.

5.2 Time-Dependent Embedding

The original Green function embedding was developed in the context of surface and solid state physics for the static Schrödinger equation by Inglesfield [69]. It was subsequently extended to the time-dependent case in Inglesfield [67, 70] by the same author, but similar derivations have been proposed earlier in different fields, for instance, to describe the interaction of a strong laser with atoms in Boucke et al. [62] and Ermolaev et al. [63], and for electron transport in Hellums and Frensley [64].

Below we introduce the theory following an approach similar to the one used to describe molecular transport with TDDFT by Kurth [65].[4] We first restrict ourselves to the single-electron case and then discuss the extension to the many-electron one with TDDFT.

Let us consider the case of a system in contact with a reservoir as shown in Fig. 9. We want to find a closed set of conditions that have to be imposed on the equations for a wavefunction in A such that it correctly matches its outer part in B for all times. Following the division in the figure, we can write the time-dependent Schrödinger equation for the system A coupled with a reservoir/environment B using a block matrix representation:

[4] An analogous approach was first presented by Hellums [64] in a single-particle picture.

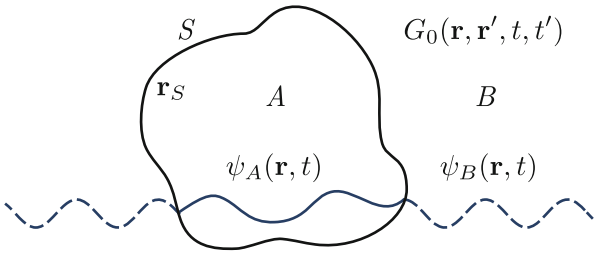

Fig. 9 Time-dependent embedding. Embedding consists in modifying the Hamiltonian in A in such a way that, solving the associated time-dependent Schrödinger equation in A only, it automatically imposes the matching of $\psi_A(\mathbf{r},t)$ with $\psi_B(\mathbf{r},t)$ for all t. The modification is made using an embedding operator derived in terms of the Green function $G_0(\mathbf{r},\mathbf{r}',t,t')$ of the environment B

$$i\frac{\partial}{\partial t}\begin{bmatrix}\psi_A(\mathbf{r},t)\\ \psi_B(\mathbf{r},t)\end{bmatrix} = \begin{bmatrix}\hat{H}_{A,A}(t)\hat{H}_{A,B}(t)\\ \hat{H}_{B,A}(t)\hat{H}_{B,B}(t)\end{bmatrix}\begin{bmatrix}\psi_A(\mathbf{r},t)\\ \psi_B(\mathbf{r},t)\end{bmatrix}, \tag{56}$$

where $\psi_A(\mathbf{r},t)$ and $\psi_B(\mathbf{r},t)$ are the wavefunctions projected onto each separate region. Here we consider the general case where the Hamiltonian is time-dependent, and its components include two diagonal terms $\hat{H}_{A,A}(t)$ and $\hat{H}_{B,B}(t)$ operating within each separate region and two coupling terms $\hat{H}_{A,B}(t)$ and $\hat{H}_{B,A}(t)$ connecting the environment to the system.

To derive the embedded time-dependent equations we introduce the retarded Green function G_0 for the reservoir, defined as

$$\left[i\frac{\partial}{\partial t} - \hat{H}_{B,B}(t)\right]G_0(\mathbf{r},\mathbf{r}',t,t') = \delta(\mathbf{r}-\mathbf{r}')\delta(t-t'), \tag{57}$$

with boundary conditions $G_0(\mathbf{r},\mathbf{r}',t^+,t) = -i$, $G_0(\mathbf{r},\mathbf{r}',t,t^+) = 0$, and where t^+ represents a time approaching t from above. Because of the explicit time dependence of $\hat{H}_{B,B}(t)$, it generally depends on both the time variables t and t'. We note however that the solution greatly simplifies if we consider B to represent empty space. In this case, $G_0(\mathbf{r},\mathbf{r}',t,t')$ is the free propagator, which depends only on the time difference $t-t'$ and is known analytically.

Using $G_0(\mathbf{r},\mathbf{r}',t,t')$ we can directly build the solution of the differential equations in B. This corresponds to considering only the second row in (56), and results in[5]

[5] To simplify notation we avoid explicitly writing out all the coordinates. We also use the same convention used in Kurth et al. [65] where operators are thought of as matrices with continuous indices along the spatial coordinates. We thus omit explicit reference to $\mathbf{r}$ and $\mathbf{r}'$ and interpret operator products as integrals.

$$\psi_B(t) = iG_0(t,0)\psi_B(0) + \int_0^t \hat{G}_0(t,t')\hat{H}_{B,A}(t)\psi_A(t')\mathrm{d}t'. \tag{58}$$

The final equation governing the time evolution for $\psi_A(t)$ can be written in a closed form simply by plugging (58) into the first row of (56). After that we obtain

$$i\frac{\partial\psi_A(t)}{\partial t} = \hat{H}_{A,A}(t)\psi_A(t) + \hat{H}_\Sigma[\psi_A](t) \tag{59}$$

with

$$\hat{H}_\Sigma[\psi_A](t) = \int_0^t \hat{\Sigma}(t,t')\psi_A(t')\mathrm{d}t' + i\hat{H}_{A,B}(t)\hat{G}_0(t,0)\psi_B(0). \tag{60}$$

In this equation, $\hat{\Sigma}(t,t') = \hat{H}_{A,B}(t)\hat{G}_0(t,t')\hat{H}_{B,A}(t')$ can be identified with the self-energy responsible for the hopping in and out of the system, whereas the last term is responsible for imposing the initial conditions in the reservoir. It is zero if the wavefunction is completely localized in A at $t=0$. The time evolution of $\psi_A(t)$ is thus governed by a modified Hamiltonian containing an additional time-dependent embedding operator $\hat{H}_\Sigma[\psi_A](t)$. The dependence on the wavefunction is written in square brackets to stress the fact that $\hat{H}_\Sigma[\psi_A](t)$ is not just a simple local potential but involves a more general non-local action.

The kernel $\hat{\Sigma}(t,t')$ of the time integral in (60) is, in the most general case, an explicit function of t and t'. This is the case, for instance, when one wants to apply this method to model molecular transport and B represents an electrode with a time-dependent voltage bias. Evaluating (60) thus requires one to keep track of $\psi_A(t)$ for all times up to t. This is one of the biggest drawbacks of the approach as it restricts the propagation to short times because of storage limitations. Direct approximations of the kernel intended to mitigate this problem have to face the fact that the kernel is often non-analytical and highly oscillating, especially for $t \to t'$ [65]. However, we note that when the Hamiltonian in B is not explicitly time-dependent, $\hat{\Sigma}(t,t')$ depends only on the time difference $t-t'$ and we are left with a much easier convolution integral.

In this last case, i.e., when the Hamiltonian in B is time-independent, an alternative but equivalent form for the embedding operator can be obtained following the derivation of Inglesfield [67]. In this approach we are given two wavefunctions $\psi_A(\mathbf{r},t)$ and $\psi_B(\mathbf{r},t)$ which have equal amplitude on the surface S separating A and B, but arbitrary derivative as illustrated in Fig. 9. Assuming that $\psi_B(\mathbf{r},t)$ is a solution of the time-dependent Schrödinger equation in B, we need to find a closed set of equations for $\psi_A(\mathbf{r},t)$ to connect perfectly to $\psi_B(\mathbf{r},t)$ on S for all t.

The problem is solved with the use of what in the field of partial differential equations goes under the name of Dirichlet-to-Neumann and its inverse Neumann-to-Dirichlet maps [68, 71, 72]. These maps allow one to transform Dirichlet

boundary conditions, fixing the value of a function on a surface, into Neumann boundary conditions, fixing the normal derivative over a surface, and vice versa. The resulting time-dependent equations for $\psi_A(\mathbf{r},t)$ can be written in the same way as (59) with an embedding operator defined as [67, 70]

$$\hat{H}_{\mathcal{E}}[\psi_A](t) = \delta(\mathbf{r}-\mathbf{r}_S)\left[\frac{1}{2}\frac{\partial\psi_A(\mathbf{r}_S,t)}{\partial n_S} + \int_S\int_0^t \overline{G}_0^{-1}(\mathbf{r}_S,\mathbf{r}'_S,t-t')\frac{\partial\psi_A(\mathbf{r}'_S,t')}{\partial t'}\mathrm{d}t'\mathrm{d}\mathbf{r}'_S\right], \tag{61}$$

where $\partial/\partial n_s$ denotes the directional derivative out of A and perpendicular to S, and

$$\overline{G}_0^{-1}(\mathbf{r}_S,\mathbf{r}'_S,t) = \frac{1}{2\pi}\int_{-\infty}^{\infty} \mathrm{e}^{-i\varepsilon t}G_0^{-1}(\mathbf{r}_S,\mathbf{r}'_S,\varepsilon)\mathrm{d}\varepsilon. \tag{62}$$

Here $G_0^{-1}(\mathbf{r}_S,\mathbf{r}'_S,\varepsilon)$ is the inverse of the Green function defined by (57) evaluated on the boundary surface S with $\mathbf{r}_S,\mathbf{r}'_S \in S$. Because $G_0(\mathbf{r},\mathbf{r}',t-t')$ depends only on time differences it is conveniently expressed in the energy domain ε with a Fourier transform over the time domain. Because of the presence of the $\delta(\mathbf{r}-\mathbf{r}_S)$, the embedding operator (61) is non-zero only on the boundary surface and involves normal and time derivatives of $\psi_A(\mathbf{r},t)$ over that surface.

Because of the equivalence of $\hat{H}_{\mathcal{E}}$ and $\hat{H}_{\Sigma}$ defined in (60) and (61), we refer in the following to an embedding operator with the symbol $\hat{\mathcal{E}}[\psi_A](t)$ for simplicity. We are now in the position to comment on the most characteristic features of $\hat{\mathcal{E}}[\psi_A](t)$. In general, it involves complex quantities which make it an explicitly non-Hermitian operator. This fact implies that the total number of electrons is no longer conserved during the propagation. Furthermore, it contains a memory term in the form of a time integral. In Frensley [73] it was postulated that transparent boundary conditions should break time reversal symmetry. The presence of a memory term in (59) turns the time propagation into a non-Markovian process and precisely breaks this symmetry.

The extension to the many-electron case is straightforward using the same 2×2 block structure of (56) with the difference that the entries must be interpreted as operators acting on the N-body Hilbert space. The previous steps of the derivation hold in a completely equivalent way up to (59) and (60) provided the interacting many-body Green function G is used in place of G_0.

Formulating this in the language of TDDFT, the OQS-TDDFT theory establishes a one-to-one connection between potential and density for non-unitary dynamics [5–7]. The evolution from an initial state is uniquely defined if we find a way to write the coupling with the environment as a functional $\nu^B[n]$ of the total density n. Once again the equations retain the block structure of (56) with entries interpreted as multi-index tensors, each index being associated with a Kohn–Sham orbital. The result is a set of equations equivalent to (59) for each orbital, where the exact embedding operator $\hat{\mathcal{E}}[n]$ depends on the total density of the system (i.e., in $A\cup B$)

through each orbital and the full many-body Green function $G[n]$. The total embedding operator can thus be interpreted as the coupling functional $\nu^B[n]$ with the environment. Obviously, this connection involving the full many-body Green function is of little use in practical situations, but it provides a clear starting point for further approximations.

5.3 Absorbing Boundaries

Describing charge transfer between a system and its environment implies a modification of the isolated Hamiltonian. In the previous section we showed how the exact condition requires the addition of an embedding operator $\hat{\mathcal{E}}[\psi_A](t)$ that turns the Hamiltonian non-Hermitian. The evaluation of such an operator can, however, be very demanding and one needs to resort to simpler strategies.

Absorbing boundaries (ABs) or boundary absorbers are cheaper options. They can be defined as any approximation of the form

$$\hat{H}_{\mathrm{AB}}[\psi_A(t)](t) \approx \hat{\mathcal{E}}[\psi_A](t) \tag{63}$$

to an embedding operator such as the one given by (60) or (61). This approximation is specific to the case where B represents the empty space and we only have to absorb outgoing electrons. We know that $\hat{\mathcal{E}}[\psi_A](t)$ can be spatially localized on the boundary surface. The absorbing boundary operator is instead generally allowed to act on the wavefunctions over a larger region close to the boundaries, as illustrated in Fig. 10. In the large majority of approximations, this operator is taken to be a local potential:

$$\hat{H}_{\mathrm{AB}}[\psi_A(t)](t) = \hat{V}_{\mathrm{AB}}(t)\psi_A(t). \tag{64}$$

Its purpose is to absorb completely any outgoing wave packet entering the region (striped in the figure) of its support. The main goal here is to apply the absorber that best simulates the exact embedding operator with the minimum computational cost.

From a TDDFT perspective, when we apply $\hat{H}_{\mathrm{AB}}$ to each Kohn–Sham orbital, on top of all the approximations which might be involved in the description of the embedding operator, we are also approximating the interaction between the system and the environment by setting it to zero.

The absorbing properties of a boundary depend strongly on the numerical implementation. We do not enter any specific implementation here but just point out the fact that none of the absorbers presented in the literature are completely free from reflections. We refer to De Giovannini et al. [74] for a recent review on the reflection properties of members of each boundary family.

We discuss below two of the most popular families of absorbing boundaries: the complex absorbing potentials (CAPs) and the mask function absorbers (MFAs).

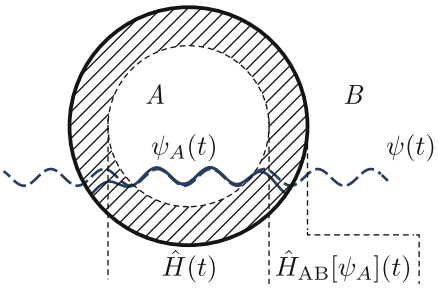

Fig. 10 Absorbing boundaries. An absorbing boundary Hamiltonian $\hat{H}_{\mathrm{AB}}(t)$ acting on the striped region is added to the original one $\hat{H}(t)$ to prevent reflections from the boundaries during time propagation. The perfect absorber is the one that matches the full solution $\psi(t)$ with $\psi_A(t)$ in the inner (*non-striped*) region for all times t

These families are substantially phenomenological approximations to the open boundary problem for which the main point of attraction rests on their simplicity of implementation and limited computational costs.

5.4 Complex Absorbing Potentials (CAPs)

We already noted above that the exact embedding potential has to be a complex quantity to turn the Hamiltonian non-Hermitian, and the fundamental mechanism of CAPs is precisely based on this observation. The idea was originally introduced from a different standpoint by Neuhauser and Baer [75, 76] with the use of negative imaginary potentials for the Schrödinger equation. This was in connection with the so-called optical potentials or perfectly matched layers developed for electromagnetic waves [77].

The effect of a CAP can be easily understood by observing the action of the infinitesimal time evolution operator on a wavefunction

$$\hat{U}(t + \mathrm{d}t, t)\psi_A(t) = \exp\left[-i\left(\hat{H}(t) + \hat{V}_{\mathrm{CAP}}\right)\mathrm{d}t\right]\psi_A(t), \tag{65}$$

when $\hat{V}_{\mathrm{CAP}}$ is a negative imaginary potential with support on a region close to the boundaries of A. In this case, the effect simply results in an exponential suppression of the wavefunction in the absorbing region. In other words, the time evolution operator associated with the non-Hermitian Hamiltonian modified with $\hat{V}_{\mathrm{CAP}}$ is non-unitary and no longer conserves the wavefunction norm. The norm decreases if $\hat{V}_{\mathrm{CAP}}$ is negative and increases if it is positive. In the latter case it becomes possible to simulate charge injection, and this fact has been used to mimic reservoirs acting as sinks or sources in the attempt to simulate electron transport [78–80].

CAPs are by no means restricted to purely imaginary potentials and there is a huge body of literature describing their different forms and declinations [81]. We

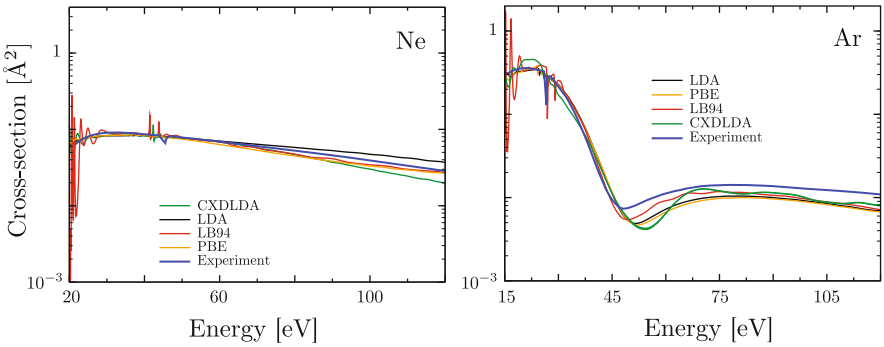

Fig. 11 Neon and argon atom absorption cross-sections above the first ionization threshold calculated with TDDFT and different exchange and correlation functionals: LDA, CXD-LDA [82], PBE [83], and LB94 [54]. A CAP is introduced to reduce reflections in an energy window centered around $E = 93$ eV (Ne) and $E = 105$ eV (Ar). Adapted from Crawford-Uranga et al. [84]

stress the fact that their properties strongly depend both on their mathematical form and the specific implementation, and, without exception, they all reflect in some energy range [74]. For practical purposes it is thus very important to ensure that the CAP we choose for our calculations has good absorption properties in the range of interest.

As an example, in Fig. 11 we show the absorption cross-sections for argon and neon in the continuum, above the first ionization threshold, calculated in linear response with TDDFT and a CAP. The CAP is chosen to minimize reflections around $E = 93$ eV for neon and $E = 105$ eV for argon. The spectra are in good agreement with the experimental ones in a fairly large range around those energies and reflections appear as oscillations.

What is interesting about this result is that we are able to calculate a quantity involving transitions to infinitely extended continuum states just performing a time propagation in a bounded volume. Although at first it might seem counterintuitive, the explanation is actually quite intuitive. In fact, we are calculating here a quantity involving the dipole matrix element between an initial state, the ground state of our system Ψ_0, to a final state, a continuum state $\Psi_{E>0} : \langle \Psi_0 | \hat{d} | \Psi_{E>0} \rangle$. The main contribution to this matrix element comes from an integration over the overlap region between the two wavefunctions and, because the ground state is bounded, this region is safely included in A. The extent to which we manage to remove reflection thus directly relates to the quality with which we calculate this integral and, eventually, the quality of the absorption cross-section.

5.5 Mask Function Absorbers (MFAs)

MFAs are an alternative formulation of CAPs. They have been employed to study a variety of phenomena including high harmonic generation [85], electron and proton emission [86], and above-threshold ionization [87].

They are defined by directly modifying the infinitesimal time evolution operator with a mask function $M(\mathbf{r})$ as follows:

$$\hat{U}_{\mathrm{M}}(t+\mathrm{d}t,t) = \mathrm{M}(\mathbf{r})\hat{U}(t+\mathrm{d}t,t). \tag{66}$$

The effect of this modification can be easily understood by choosing $M(\mathbf{r})$ to be a real function equal to 1 in the inner part of A and smoothly decaying to zero close to the boundaries. With this choice, recursive application of $U_{\mathrm{M}}(t+\mathrm{d}t,t)$ to $\psi_A(t)$ directly suppresses the part of the wavefunction in the decay region.

This is only one of the possible choices of MFA and, in general, $M(\mathbf{r})$ can be a complex function. We illustrate the effect of using complex $M(\mathbf{r})$ by showing the equivalence between MFAs and CAPs. In fact, given a $\hat{V}_{\mathrm{CAP}}$, we can obtain the corresponding $M_{\mathrm{CAP}}(\mathbf{r})$ straightforwardly by expanding the exponential in (65). To first order in dt the MFA $M^{(1)}_{\mathrm{CAP}}$ associated with $\hat{V}_{\mathrm{CAP}}$ is

$$M^{(1)}_{\mathrm{CAP}}(\mathbf{r}) = \mathrm{e}^{-iV_{\mathrm{CAP}}(\mathbf{r})\mathrm{d}t}. \tag{67}$$

The mask function can thus be a complex function, and becomes real when $\hat{V}_{\mathrm{CAP}}$ is purely imaginary. The inverse relation can be obtained in a similar way, and to first order it reduces to

$$V^{(1)}_{\mathrm{MFA}}(\mathbf{r}) = \frac{i}{\mathrm{d}t}\ln[M(\mathbf{r})]. \tag{68}$$

In De Giovannini et al. [74] it was shown that the first-order relations above, for a given pair of CAP and MFA, yield reflection properties in excellent agreement with each other.

One important feature of the MFA approach is that by multiplying $M(\mathbf{r})$ and $1-M(\mathbf{r})$ by a wavefunction it is possible to split its propagation in two different components moving in separate regions. This property is fundamental for split-domain propagation schemes initially derived in Chelkowski et al. [88] and Grobe et al. [89] and later extended to the study of electron photoemission with TDDFT in De Giovannini et al. [90]. We return to this point in Sect. 6.3.

5.6 Time-Dependent Exterior Complex Scaling

In Sect. 3.5 we introduced *exterior complex scaling* as an extension of *complex scaling* where the transformation is only applied outside a certain region. It was noted that it shares an important feature with the global transformation: it naturally imposes outgoing boundary conditions on the Schrödinger equation. We discuss here to what extent this property applies to the time-dependent case.

Let us consider a scaling transformation similar to those illustrated in Fig. 3. We further select a path on the real axis deep into region A that departs for the complex plane at some point close to the boundary and eventually reaches the asymptotic form $\mathbf{r} \to \mathbf{r}e^{i\theta}$. Following this scaling transformation, the time-dependent Schrödinger equation can be formally cast into a set of equations:

$$i\frac{\partial \psi_\theta(\mathbf{r},t)}{\partial t} = \hat{H}_\theta^{\mathrm{ECS}}(t)\psi_\theta(\mathbf{r},t) \tag{69}$$

$$-i\frac{\partial \overline{\psi}_\theta(\mathbf{r},t)}{\partial t} = \hat{H}_\theta^{\mathrm{ECS}}(t)\overline{\psi}_\theta(\mathbf{r},t). \tag{70}$$

for left $\overline{\psi}_\theta(\mathbf{r},t)$ and right states $\psi_\theta(\mathbf{r},t)$, where $\hat{H}_\theta^{\mathrm{ECS}}(t)$ represents the scaled Hamiltonian. Extrapolating from the discussion in Sect. 4.4 we can interpret (69) as imposing purely outgoing boundary conditions and (70) as the incoming counterpart.

In the theory of *complex scaling*, the calculation of the expectation value of an observable $\hat{O}_\theta$ on the scaled path as of (10) involves left and right states on an equal footing. This extends to the time-dependent case with the requirement of having both left and right states at the same time to calculate $\hat{O}_\theta$. Hence, we need, in principle, to solve (69) and (70) simultaneously.

The fact that the scaling path lies exactly on the real axis in a certain region simplifies the equations. In fact, on the real axis, left and right states are complex conjugates: $\overline{\psi}_\theta(\mathbf{r},t) \equiv [\psi_{-\theta}(\mathbf{r},t)]^* = \psi_\theta(\mathbf{r},t)^*$ for $\mathbf{r}$ in the interior region. This is particularly true when the system contains only a local potential and the propagation is initialized with a state localized in the unscaled region at $t=0$ and propagating outward. If we restrict ourselves to observables in the unscaled region and we want to describe a purely outgoing process, we resolve to use the right state $\psi_\theta(\mathbf{r},t)$ only. This state can be obtained by propagating (69) which involves only right states [38]. Following this, most applications of *exterior complex scaling* are limited to a use with the decaying right states and observables evaluated in the unscaled region.

Equation (69) perfectly describes problems where imposing purely outgoing boundary conditions represents an exact condition similar to that, for example, in ionization processes. In those cases it can be regarded as equivalent to a transparent boundary condition described with a Green function. Here, because we are dealing with purely outgoing conditions, we should note that the title of perfect absorber is

more appropriate than that of transparent boundary, because electrons can flow in only one direction.

However, we note an important difference between the two approaches. Whereas the Green function embedding defines the exact matching conditions at the boundary of a finite volume A, the scaled (69) acts on a wavefunction defined in the full space $A \cup B$. This makes the size of the simulation box a weakness in numerical simulations if a wave is capable of reaching the end of the box. The scaling transformation imposes an asymptotic form which can be efficiently captured by exponential functions $e^{-\alpha r}$. By employing a finite element approach with an element at infinity which captures the exponential tail, it was numerically shown by Scrinzi [38] that *exterior complex scaling* indeed provides perfectly absorbing conditions for numerical precision.

Restricting (69) to A otherwise implies a truncation which irrevocably breaks its perfect properties. In this case the scaling transformation reduces to an absorbing boundary which can be regarded as a simple CAP and, as such, presents reflections [74, 91]. We should mention that the use of (69) restricted to A in combination with a *smooth exterior complex scaling* in the literature has been going under the misleading name of reflection-free CAP, in spite of presenting a certain degree of reflection [39, 91–93].

In the context of TDDFT, *exterior complex scaling* has been applied purely as an absorbing boundary [53, 94].

6 Electron Photoemission

We focus here on the approaches that can be employed in the description of multi-electron ionization initiated by external electromagnetic fields within TDDFT. As in previous sections, we are interested only in electronic processes, neglecting any ionic motion, and we restrict ourselves to the class of methods that requires knowledge of the wavefunctions only on a bounded region of space A much as in Fig. 8.

We are interested in the family of problems characterized by time-dependent electronic Hamiltonians with the structure

$$\hat{H}(t) = \frac{1}{2}\left[-i\nabla - \frac{\boldsymbol{\mathcal{A}}(t)}{c}\right]^2 + v_{\text{ext}} + v_{\text{ee}}, \tag{71}$$

where v_{ee} is the electron–electron Coulomb interaction, v_{ext} is the external potential which generally consists of a static potential produced by the nuclei, $\boldsymbol{\mathcal{A}}(t)$ is the vector potential of the external field, and c is the speed of light. In writing (71) we implied the choice of the velocity gauge to describe the action of the field. The associated electric field can easily be obtained as a time derivative: $\boldsymbol{\mathcal{E}}(t) = -\partial_t \boldsymbol{\mathcal{A}}(t)$. Typically, one would want to perform a simulation by choosing

a vector potential representing one or more laser pulses, then investigate the induced dynamic.

Ionization takes place whenever the field is capable of inducing a bound-to-continuum transition, resulting in electrons escaping with a given kinetic energy. Calculation of observables characterizing these ionized electrons is at the center of our interest here.

To some extent we already approached this problem in Sect. 5. In fact, total ionization can be naturally described using only information contained in a bounded volume A surrounding our system. The total number of electrons contained in A can be simply calculated from the knowledge of the time-dependent density as

$$N(t) = \int_A n(\mathbf{r}, t) \mathrm{d}\mathbf{r}. \tag{72}$$

Combined with the use of one of the boundary conditions described above, (72) implements a practical strategy for the calculation of $N(t)$. The total ionization probability, i.e., the probability of ejecting an electron in the long-time limit, is thus naturally obtained using only quantities defined in A as

$$\mathcal{P} = \lim_{t\to\infty} \frac{N - N(t)}{N}, \tag{73}$$

where N represents the total number of electrons in the system before ionization. Being a direct functional of the density, $\mathcal{P}$ is an exact quantity within TDDFT and does not present any further approximation besides the one involved with the use of the boundary conditions.

In many situations the quantities containing relevant physical information are more complex objects than the simple total ionization probability, and one would wish to access differential probabilities with respect to energy or momentum:

$$P(E) = \frac{\partial \mathcal{P}}{\partial E}, \quad P(\mathbf{k}) = \frac{\partial^3 \mathcal{P}}{\partial k_x \partial k_y \partial k_z}. \tag{74}$$

The calculation of these observables within TDDFT is, however, not as straightforward as the evaluation of $\mathcal{P}$.

The first reason is the intrinsic complexity of the ionization process already with only one electron. There are situations, especially when strong laser fields are involved, where the electron dynamics are so complex that one has to propagate explicitly the wavefunction in time to account for the process. In principle, the differential probabilities can then be obtained by projecting the scattering wavefunction $\Psi_s(t)$ onto the appropriate set of scattering wavefunctions ϕ_E as

$$P(E) = \lim_{t\to\infty} \left|\left\langle \phi_E \middle| \Psi_s(t) \right\rangle\right|^2 \quad \text{with } E > 0. \tag{75}$$

Besides the issues related to the correct evaluation of the projecting set, owing to their large spatial extension, the propagation of the total electronic wavefunction at long times can be practically performed only for highly symmetrical systems, such as atoms and small molecules, or for short times. Alternative approaches, such as those we describe below, involve the knowledge of the wavefunction only in a bounded region of space.

The second reason has to do with the multi-electron nature of ionization at the TDDFT level. In fact, whereas the connection between $\mathcal{P}$ and the total density is explicitly known, the differential quantities (74) cannot be easily expressed in terms of the density. The derivation and the use of appropriate density functionals to describe $P(E)$ and $P(\mathbf{k})$ from (74) are thus important and have to take into account in our model.

In the following we discuss the methods that have been developed to tackle these problems numerically.

6.1 Sampling Point Method

A simple scheme to evaluate the energy-resolved photoelectron distribution $P(E)$ was proposed by Pohl et al. [95]. Lacking clear theoretical foundations, this method has some limitations to its range of applicability. We briefly review it here for historical reasons connected to the fact that, together with the mask method of Sect. 6.3, it is the only method that has been employed to calculate $P(E)$ from (74) for molecular systems with TDDFT.

The method consists in recording the time evolution of each Kohn–Sham orbital $\psi_i(\mathbf{r}_S,t)$ at given points in space $\mathbf{r}_S$ as shown in Fig. 12. This time evolution is then turned into an energy dependence by Fourier transforming the time series

$$\widetilde{\psi}_i(\mathbf{r}_S, E) = \frac{1}{\sqrt{2\pi}} \int \mathrm{e}^{-iEt} \psi_i(\mathbf{r}_S, t) \mathrm{d}t, \tag{76}$$

and the photoelectron energy distribution is postulated to be proportional to a sum over the orbitals in the following fashion:

$$P_{\mathbf{r}_S}(E) \propto \frac{1}{\sqrt{E}} \sum_{i=1}^{N} |\widetilde{\psi}_i(\mathbf{r}_S, E)|^2. \tag{77}$$

Because photoelectrons are in general emitted with different probabilities at different angles, a more accurate definition of the total probability is to sample the boundary densely with points $\mathbf{r}_S$ so that (77) becomes an integral over a surface S enclosing the system

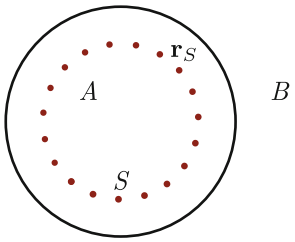

Fig. 12 Electron photoemission with the sampling method. The energy-resolved photoelectron probability is calculated by recording the time evolution of the wavefunction at the *points marked in red*

$$P(E) \propto \int_S P_{\mathbf{r}_S}(E) \mathrm{d}\mathbf{r}_S. \tag{78}$$

In practical calculations, the integral over the S is of course still discretized, and open boundary conditions, often in the form of absorbing boundaries, may be employed. The choice of the absorber must be such that it efficiently removes reflected wave packets in the energy range where photoelectrons are simulated.

In the original paper, (78) was introduced without the energy density factor $1/\sqrt{E}$ and the surface integral [95]. The results where thus, in general, strongly dependent on the choice of the sample point $\mathbf{r}_s$ and applicable only in the situations where the electrons are emitted as s-waves, hence not presenting any angular fluctuations. Even taking into account the integral over S, the method is not free from problems. It requires S to be placed at a distance from the parent system such that two conditions are fulfilled: (i) the electronic wave packets can be considered to be composed of outgoing waves only, and (ii) photoelectrons must hit the surface at a time for which the external field is turned off. It was later realized that a time- and energy-dependent phase $e^{i\Phi(E,t)}$ must be included in the integral (76) to account for the wrong kinetic energy reference when the external field is still active [96].

Although this method is straightforward and easy to implement in existing TDDFT codes, the above drawbacks render it of limited use in many interesting physical situations, especially when strong laser fields are employed.

6.2 *Surface Flux Approach*

This method is based on the idea that differential photoemission probabilities (74) can be calculated by recording the electron flux through a surface. It was originally introduced by Scrinzi and co-workers in Caillat et al. [97] in the context of multi-configuration Hartree–Fock and then further developed in Scrinzi [98] and Tao and Scrinzi [99] for one- and two-electron problems. Although no applications in the context of TDDFT have been attempted so far, it presents an interesting approach for the calculation of photoelectron differential probabilities in bounded volumes.

Let us consider the case of a one-electron system governed by a Hamiltonian $\hat{H}(t)$ (71) such that at large distances it matches an exactly solvable one $\hat{H}_{\mathrm{v}}(t)$,

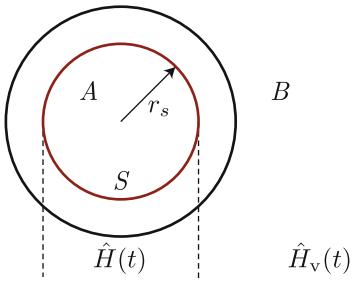

Fig. 13 The setup for the calculation of electron photoemission with the surface flux method. The emission probability is calculated by recording the flux through the closed surface *S marked in red*

$$\hat{H}(t) = \hat{H}_{\mathrm{v}}(t) \quad \text{for } |\mathbf{r}| \geq r_s \text{ and all } t, \tag{79}$$

as shown in Fig. 13. We are assuming here for simplicity that the surface S separating the Hamiltonians is spherical, but what follows can be easily extended to a generic surface. If we consider the case of a short range external potential $\nu_{\mathrm{ext}}(\mathbf{r}) = 0$ for $|\mathbf{r}| > r_s$, $\hat{H}_{\mathrm{v}}$ is the Volkov Hamiltonian, i.e., the Hamiltonian governing the motion of free electrons in an external field:

$$\hat{H}_{\mathrm{v}}(t) = \frac{1}{2}\left[-i\nabla - \frac{\boldsymbol{\mathcal{A}}(t)}{c}\right]^2. \tag{80}$$

Provided the external field has no spatial dependence, i.e., $\boldsymbol{\mathcal{A}}(t)$ is constant in space, the associated TDSE can be solved exactly. The solutions can then be expressed as plane waves with an additional time and momentum-dependent phase:

$$\phi_{\mathbf{k}}(\mathbf{r}, t) = \frac{1}{(2\pi)^{\frac{3}{2}}} e^{i\mathbf{k}\cdot\mathbf{r}} e^{-i\Phi(\mathbf{k},t)}, \quad \Phi(\mathbf{k}, t) = \frac{1}{2}\int_{-\infty}^{t} \left[\mathbf{k} - \frac{\boldsymbol{\mathcal{A}}(t)}{c}\right]^2 \mathrm{d}t'. \tag{81}$$

Let us imagine the situation where a laser pulse ionizes our system. In the long time limit $t > T$, some time after the field as been turned off, $\boldsymbol{\mathcal{A}}(t > T) = 0$, the electronic configuration is described by a scattering wavefunction which can be partitioned into bound and scattering components,

$$\Psi(\mathbf{r}, t) = \Psi_A(\mathbf{r}, t) + \Psi_B(\mathbf{r}, t), \tag{82}$$

which are approximately localized in the bound and unbound regions A and B of Fig. 8. The quality of this approximation is ultimately connected to r_s and T, and the time that it takes the slowest components of the scattering wave packet $\Psi_B(\mathbf{r},t)$ to cross S.

In order to calculate the emission amplitude, we just need to evaluate the projection of $\Psi(\mathbf{r},t)$ over the asymptotic wavefunctions $\phi_{\mathbf{k}}(\mathbf{r})$ as in (75). The information about the scattering process is contained only in $\Psi_B(\mathbf{r},t)$. Because $\Psi_B(\mathbf{r},t)$ is exponentially vanishing in A for $t \geq T$, we can write the emission amplitude as

$$S(\mathbf{k},T) = \langle \phi_{\mathbf{k}}(T)|\theta(\mathbf{r},r_s)|\Psi(T)\rangle = \big\langle \phi_{\mathbf{k}}(T)\big|\Psi_B(T)\big\rangle, \tag{83}$$

with $\theta(\mathbf{r},r_s)$ being a step function with support in B defined as

$$\theta(\mathbf{r},r_s) = \begin{cases} 0 & \text{for } |\mathbf{r}| < r_s \\ 1 & \text{for } |\mathbf{r}| \geq r_s \end{cases}. \tag{84}$$

Equation (83) can be written as a time integral of the derivative of $S(\mathbf{k},t)$. Combined with the Ehrenfest theorem and the fact that both states in (83) evolve with the same Hamiltonian $\hat{H}_{\mathrm{v}}$ within the support of $\theta(\mathbf{r},r_s)$ we obtain

$$S(\mathbf{k},T) = i\int_0^T \big\langle \phi_{\mathbf{k}}(t)\big|\big[\hat{H}_{\mathrm{v}},\theta(\mathbf{r},r_s)\big]\big|\Psi(t)\big\rangle \mathrm{d}t. \tag{85}$$

The dependence on T of the emission amplitude $S(\mathbf{k}, T)$ becomes negligible for large values of T. The momentum-resolved probability is then defined by taking the square modulus of the emission amplitude $P(\mathbf{k}) = |S(\mathbf{k}, T)|^2$ and dropping the dependence on T.

Equation (85) can be interpreted as the time integral of a surface flux, hence the name of the method. This interpretation can be established by observing that the commutator in (85) is non-zero only for $|\mathbf{r}| = r_s$, and that the expectation value reduces to an integral over S. We can also proceed one step further and explicitly write the emission amplitude as a flux integral

$$S(\mathbf{k},T) = \int_0^T \int_S \mathbf{J}_{\mathbf{k}}(t)\cdot \mathrm{d}\mathbf{r}_s \mathrm{d}t \tag{86}$$

of the momentum-resolved current density

$$\mathbf{J}_{\mathbf{k}}(t) = \frac{1}{2}\left[\Psi(t) i\nabla\phi^*_{\mathbf{k}}(t) - \phi^*_{\mathbf{k}}(t) i\nabla\Psi(t) - 2\frac{\boldsymbol{\mathcal{A}}(t)}{c}\phi^*_{\mathbf{k}}(t)\Psi(t)\right]. \tag{87}$$

In practical calculations the time propagation of $\Psi(t)$ can be spatially truncated, imposing open boundary conditions in the region outside S. The evaluation of $P(\mathbf{k})$ can then be safely performed in a bounded volume.

In order to obtain (85) we only need to find a Hamiltonian $\hat{H}_{\mathrm{v}}$ that satisfies the asymptotic condition (79). The method can, in principle, be extended to handle the long-range Coulomb potential just by modifying (80) to match the Coulomb tails. In this case, however, the calculation of $\phi_{\mathbf{k}}(\mathbf{r},t)$ is complicated by the absence of an exact solution for time-dependent $\boldsymbol{\mathcal{A}}(t)$ and the Coulomb–Volkov solutions provide a poor approximation [99]. In practical situations, the use of free Volkov wavefunctions (81) as asymptotic solution combined with a convergence on the surface radius r_s is nevertheless enough to provide high-quality results.

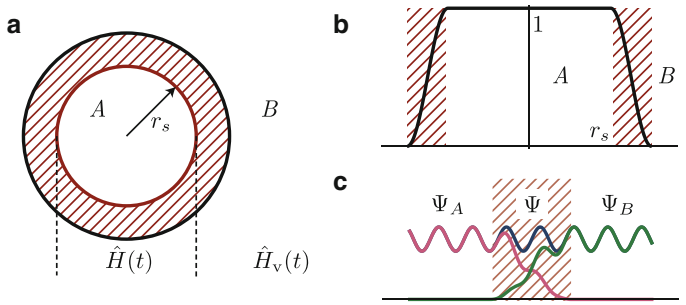

Fig. 14 The main traits of the mask method. In this method, photoelectrons are time propagated with a mixed real and momentum-space representation. A *red striped area* identifies the region where the matching between the two representations is performed. (**a**) Spatial and Hamiltonian partitioning. (**b**) The mask function. (**c**) A wavefunction Ψ is split into two parts, Ψ_A and Ψ_B, using the mask function

6.3 Mask Method

This *mask method* is based on the idea that the photoelectron emission probability can be calculated by explicitly propagating the ionized electron wave packets as a superposition of plane waves. The problem of matching inner and outer solutions is solved here with the aid of a mask function [90]. This approach as been successfully employed within TDDFT in situations involving atoms and molecules under the influence of a variety of external fields ranging from strong and weak laser fields [90] to pump and probe configurations [100, 101].

We begin here by introducing the equations governing time propagation for the single-electron case and then turn to the many-electron one. Let us consider the case where the Hamiltonian $\hat{H}(t)$ is of short range and satisfies the asymptotic condition (79), i.e., it coincides with $\hat{H}_v(t)$ for $|\mathbf{r}| \geq r_s$ as illustrated in Fig. 14a.

As discussed in the previous section, in the long-time limit of an ionization process, we can assume the electronic wavefunction splits into two spatially separated parts, namely the bound and the scattering parts (82). A practical way to implement this splitting for a generic time t is to use a mask function $M(\mathbf{r})$ similar to what was discussed in Sect. 5.5:

$$\Psi(\mathbf{r},t) = M(\mathbf{r})\Psi(\mathbf{r},t) + [1 - M(\mathbf{r})]\Psi(\mathbf{r},t) = \Psi_A(\mathbf{r},t) + \Psi_B(\mathbf{r},t). \qquad (88)$$

We consider here the case where $M(\mathbf{r})$ is a continuous function equal to 1 in an inner part of A, where $|\mathbf{r}| \leq r_s$, equal to 0 in B, and smoothly decays over the intermediate region as shown in Fig. 14b. The splitting defined with this procedure is smooth and the wavefunctions $\Psi_A(\mathbf{r},t)$ and $\Psi_B(\mathbf{r},t)$ are not sharply separated but are allowed to overlap in the region where the mask decays to zero, as illustrated in Fig. 14c. The mask function $M(\mathbf{r})$ is such that this overlap region is entirely contained in A.

The solution of the TDSE associated with the full Hamiltonian $\hat{H}(t)$ in the whole space $A \cup B$ can be formally written as a set of coupled equations:

$$\begin{cases} |\Psi_A(t')\rangle = \hat{M}\,\hat{U}\,(t',t)[|\Psi_A(t)\rangle + |\Psi_B(t)\rangle] \\ |\Psi_B(t')\rangle = \left[1-\hat{M}\right]\hat{U}\,(t',t)[|\Psi_A(t)\rangle + |\Psi_B(t)\rangle] \end{cases}, \tag{89}$$

using the time evolution operator

$$\hat{U}\,(t',t) = \exp\left\{-i\int_t^{t'} \hat{H}\,(\tau)\mathrm{d}\tau\right\}, \tag{90}$$

and imposing the boundary condition $|\Psi_B(t=0)\rangle = 0$. Here the mask operator is given by $\langle \mathbf{r}|\mathrm{P}\hat{M}\,|\mathbf{r}'\rangle = M(\mathbf{r})\delta(\mathbf{r}-\mathbf{r}')$.

Owing to the asymptotic condition (79) on the Hamiltonian, $|\Psi_B(t)\rangle$ evolves under the action of $\hat{H}_\mathrm{v}$ defined in (80). In what follows we indicate with $U_\mathrm{v}(t',t)$ the evolution operator associated with $\hat{H}_\mathrm{v}$. Because $\hat{H}_\mathrm{v}$ is diagonal in momentum, the action of $U_\mathrm{v}(t',t)$ is easily described in this space. It is thus convenient to expand the equations for $|\Psi_B(t)\rangle$ using plane waves: $\langle \mathbf{r}|\mathbf{k}\rangle = (2\pi)^{-3/2}\exp\{i\mathbf{k}\cdot\mathbf{r}\}$. On the other hand, owing to the presence in $\hat{H}(t)$ of $V(\mathbf{r})$, which has an explicit dependence on $\mathbf{r}$, the equations for $|\Psi_A(t)\rangle$ are better solved in real space. The use of a mixed real and momentum space representation seems the more natural one for the problem.

Using a mixed representation we can integrate (89) by recursively applying the discrete time evolution operator $\hat{U}(\Delta t) \equiv \hat{U}(t+\Delta t,t)$ as

$$\begin{cases} \langle \mathbf{r}|\Psi_A(t+\Delta t)\rangle = \langle \mathbf{r}|\hat{M}\,\hat{U}\,(\Delta t)|\Psi_A(t)\rangle + \langle \mathbf{r}|\hat{M}\,\hat{U}_\mathrm{v}(\Delta t)|\Psi_B(t)\rangle \\ \langle \mathbf{k}|\Psi_B(t+\Delta t)\rangle = \langle \mathbf{k}|\left[1-\hat{M}\right]\hat{U}\,(\Delta t)|\Psi_A(t)\rangle + \langle \mathbf{k}|\left[1-\hat{M}\right]\hat{U}_\mathrm{v}(\Delta t)|\Psi_B(t)\rangle \end{cases}, \tag{91}$$

with initial condition $\langle \mathbf{k}|\Psi_B(t=0)\rangle = 0$. These equations can be written in a closed form for $\langle \mathbf{r}|\Psi_A(t)\rangle$ and $\langle \mathbf{k}|\Psi_B(t)\rangle$ by including the additional set

$$\begin{cases} \langle \mathbf{r}|\hat{M}\,\hat{U}\,(\Delta t)|\Psi_A(t)\rangle = M(\mathbf{r})\langle \mathbf{r}|\hat{U}\,(\Delta t)|\Psi_A(t)\rangle \\ \langle \mathbf{r}|\hat{M}\,\hat{U}_\mathrm{v}(\Delta t)|\Psi_B(t)\rangle = M(\mathbf{r})\displaystyle\int \langle \mathbf{r}|\mathbf{k}\rangle\langle \mathbf{k}|\hat{U}_\mathrm{v}(\Delta t)|\Psi_B(t)\rangle \mathrm{d}\mathbf{k} \\ \langle \mathbf{k}|\left[1-\hat{M}\right]\hat{U}\,(\Delta t)|\Psi_A(t)\rangle = \displaystyle\int \langle \mathbf{k}|\mathbf{r}\rangle[1-M(\mathbf{r})]\langle \mathbf{r}|\hat{U}\,(\Delta t)|\Psi_A(t)\rangle \mathrm{d}\mathbf{r} \\ \langle \mathbf{k}|\left[1-\hat{M}\right]\hat{U}_\mathrm{v}(\Delta t)|\Psi_B(t)\rangle = \langle \mathbf{k}|\hat{U}_\mathrm{v}(\Delta t)|\Psi_B(t)\rangle - \displaystyle\int \langle \mathbf{k}|\mathbf{r}\rangle\langle \mathbf{r}|\hat{M}\,\hat{U}_\mathrm{v}(\Delta t)|\Psi_B(t)\rangle \mathrm{d}\mathbf{r} \end{cases}. \tag{92}$$

The equations in (92) have an intuitive interpretation in terms of electron flow. The first and second equations account, respectively, for electrons leaving and returning to A. The third equation is responsible for introducing charge in B whereas the fourth is composed of a term of pure time evolution minus a term balancing the backward flow of the second equation. In the limit of infinitesimal steps $\Delta t = dt$, the complete set defined by (91) and (92) is equivalent to (89), and it fully accounts

for the description of outgoing and incoming particle flows. In this respect it directly relates to the exact boundary conditions of Sect. 5.1.

Once (91) and (92) are propagated up to a time T such that the external field has vanished and the bound and scattering components of $\Psi(t)$ are well separated, the momentum-resolved probability can be obtained just by taking the square modulus of the wavefunction in B: $P(\mathbf{k}) = |\langle \mathbf{k}|\Psi_B(T)\rangle|^2$. This definition is consistent with that of the surface flux method, noting that, at time T, Volkov and plane waves differ only by a phase $|\phi_{\mathbf{k}}(T)\rangle = |\mathbf{k}\rangle \exp\{i\Phi(\mathbf{k},T)\}$. Extending the mask method to the case of infinite-range potentials incurs the same approximation errors as in the flux method with Volkov states.

The extension of the method to the many-electron case, on the other hand, is less trivial. It can be derived from a phase-space standpoint given the interpretation of the Wigner transform of the one-body density matrix $\rho(\mathbf{r},\mathbf{r}',t)$,

$$W(\mathbf{R},\mathbf{k},t) = \int \frac{\mathrm{e}^{i\mathbf{k}\cdot\mathbf{s}}}{(2\pi)^{\frac{3}{2}}} \rho\left(\mathbf{R}+\frac{\mathbf{s}}{2},\mathbf{R}-\frac{\mathbf{s}}{2},t\right)\mathrm{d}\mathbf{s} \quad \text{with} \quad \begin{cases} \mathbf{R} = (\mathbf{r}+\mathbf{r}')/2 \\ \mathbf{s} = \mathbf{r}-\mathbf{r}' \end{cases}, \tag{93}$$

as a quasi-probability distribution. With this interpretation it is natural to define the photoemission probability as the integral over B of $W(\mathbf{R},\mathbf{k},t)$, i.e.,

$$P(\mathbf{k}) = \lim_{t\to\infty} \int_B W(\mathbf{R},\mathbf{k},t)\mathrm{d}\mathbf{R}. \tag{94}$$

The connection with TDDFT can be established using the Kohn–Sham one-body density matrix

$$\rho_{\mathrm{KS}}(\mathbf{r},\mathbf{r}',t) = 2\sum_{i=1}^{N/2} \psi_i^*(\mathbf{r},t)\psi_i(\mathbf{r}',t) \tag{95}$$

in (93) to calculate the Wigner distribution. For simplicity we assume here a closed-shell system where each orbital $\psi_i(\mathbf{r},t)$ is doubly occupied. There is no fundamental restriction in extending to the more general case where spin polarization is taken into account.

We now assume that it is possible to establish an approximate asymptotic connection, similar to (79), between the Kohn–Sham Hamiltonian $\hat{H}_{\mathrm{KS}}(t)$ and $\hat{H}_{\mathrm{v}}(t)$ after a certain radius $|\mathbf{r}| > r_s$ (see De Giovannini et al. [90]). Under this assumption we can partition each orbital according to (88) and use (91) and (92) to propagate them in time. By plugging the Wigner distribution obtained from $\rho_{\mathrm{KS}}(\mathbf{r},\mathbf{r}',t)$ into (94) we then obtain that the momentum-resolved probability distribution can be expressed as an sum of orbital densities

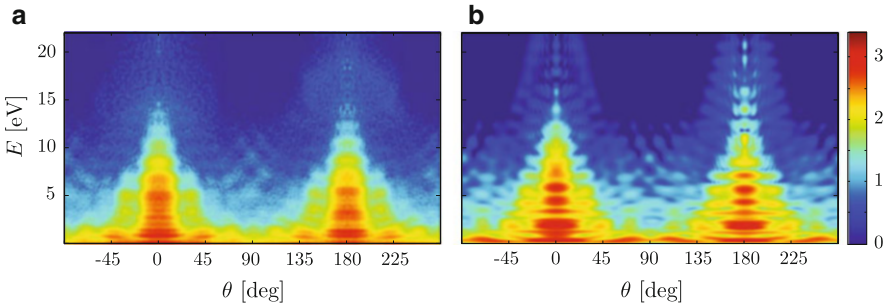

Fig. 15 Ionization of randomly oriented N_2 molecules by a strong infrared laser field. Angle and energy-resolved photoelectron probability $P(E,\theta)$ (log scale) obtained from the experiment [102] (**a**) and with the theory (**b**) using the mask method of (91) and (92). The laser is a six-cycle pulse with wavelength $\lambda = 750$ nm and intensity $I = 4.3 \times 10^{13}$ W/cm^2. Adapted from De Giovannini et al. [90]

$$P(\mathbf{k}) = 2\sum_{i=1}^{N/2} \left| \langle \mathbf{k} | \psi_{i,B}(T) \rangle \right|^2. \tag{96}$$

The quality of this approximation is now limited by the error committed by truncating the exchange and correlation potential contained in $\hat{H}_{\mathrm{KS}}(t)$ for $\mathbf{r} \geq r_s$. In atoms and molecules this adds to the error from truncating the tails of the Coulomb potential and strongly depends on the dynamics induced by the external field. It should be noted that for independent electrons in short-range potentials the method is exact. The validity of this approximation in more general situations may be assessed on the basis of the success in reproducing experiments. The example constituted by the strong field ionization of N_2 in Fig. 15 offers a good argument in favor of its success.

In numerical implementations the evaluations of the integrals in (92) must undergo some level of discretization. In spite of the fact that the integrands can be safely assumed to be well localized both in real and momentum space, the discretization process turns out to be a limiting factor. In fact, substituting Fourier integrals by Fourier series introduces unwanted periodic boundaries conditions that reintroduce ionized wave packets into the simulation box. This results in a limit for the maximum time a simulation can be carried on as the time needed for the fastest wave packet to reenter A. For a more detailed discussion see the appendix of De Giovannini et al. [90].

A more stable scheme can be obtained by simplifying (92) under the assumption that the electron flow is only outward from A. In this case we can set to zero the term responsible for the introduction of charge from B, and obtain a modified set of equations:

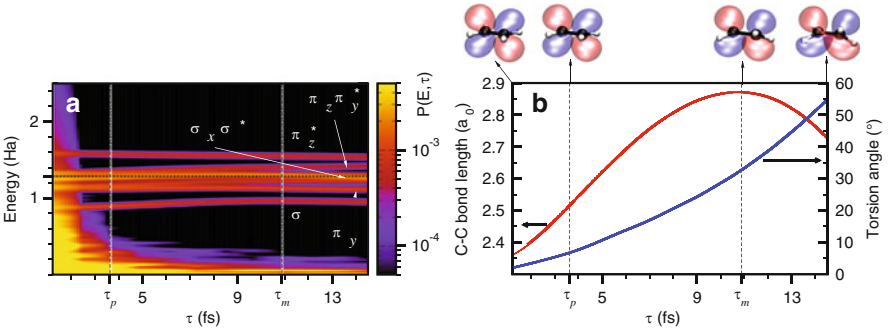

Fig. 16 Relaxation of a $\pi_z \rightarrow \pi_z^*$ excitation in ethylene observed with photoelectrons calculated with (91) and (97). (**a**) Time-resolved photoelectron spectrum $P(E, \tau)$ as a function of electron energy E and time delay τ from the initial excitation measured with an XUV probe pulse of energy $\omega = 1.8$ a.u., with a 40-cycle trapezoidal shape (8-cycle ramp), and an intensity of $I = 1.02 \times 10^{11}$ W/cm^2. (**b**) Carbon–carbon bond length in *red* and torsion angle in *blue* as a function of the time delay τ. Nuclear motion is modeled classically with an initial temperature of 300 K. Adapted from Crawford-Uranga et al. [100]

$$\begin{cases} \langle \mathbf{r}|\hat{M}\,\hat{U}\,(\Delta t)|\Psi_A(t)\rangle = M(\mathbf{r})\langle \mathbf{r}|\hat{U}\,(\Delta t)|\Psi_A(t)\rangle \\ \langle \mathbf{r}|\hat{M}\,\hat{U}_{\mathrm{v}}(\Delta t)|\Psi_B(t)\rangle = 0 \\ \langle \mathbf{k}|\left[1-\hat{M}\right]\hat{U}\,(\Delta t)|\Psi_A(t)\rangle = \int \langle \mathbf{k}|\mathbf{r}\rangle[1-M(\mathbf{r})]\langle \mathbf{r}|\hat{U}\,(\Delta t)|\Psi_A(t)\rangle \mathrm{d}\mathbf{r} \\ \langle \mathbf{k}|\left[1-\hat{M}\right]\hat{U}_{\mathrm{v}}(\Delta t)|\Psi_B(t)\rangle = \langle \mathbf{k}|\hat{U}_{\mathrm{v}}(\Delta t)|\Psi_B(t)\rangle \end{cases} . \tag{97}$$

Together with (91), it defines a modified scheme completely equivalent to the previous one in the limit where r_s is big enough to justify the outgoing flow condition. The distance at which this condition is satisfied ultimately depends on the electron dynamics induced by the external fields.

In (97) the first two equations, which govern the evolution of the real-space components of the wavefunction in A, are no longer connected with the momentum-space ones, and the propagation is thus equivalent to a time propagation with a mask function absorber similar to that in (66). The new more stable scheme thus comes at the price of introducing spurious reflections. Such reflections can, in principle, be reduced by using the most appropriate MFA or a CAP connected via equation (67). In the energy range where the MFA is absorbing, it is possible to carry out stable simulations for long times. As an example, in Fig. 16 we show the time-resolved photoelectron spectrum for an ethylene molecule where the ionic degrees of freedom are included at a classical level [100].

7 Summary

We have discussed a selection of methods which in different ways allow the calculation of properties of open quantum systems, with the objective of describing electron emission processes.

In scattering experiments and spectroscopy, the concept of resonances is of particular importance, and we have taken care to describe in detail the complex scaling method which, by a transformation of the real-space coordinates, causes the exponentially divergent resonant states to localize and become representable as square integrable states which emerge as eigenstates of the transformed, non-Hermitian Hamiltonian. This, to a large extent, makes them accessible using standard bound-state methods. The extension of ordinary ground-state DFT with complex scaling allows for a computationally tractable means of extracting resonant states and properties such as energy and lifetimes in many-body systems.

Although resonances can be captured from static calculations reminiscent of ground-state DFT, truly dynamic processes require explicit time propagation approaches. We have subsequently examined several methods used to describe dynamics leading to electron emission. We have studied these methods from the perspective of a complex system A which is in contact with a different system B that acts as a reservoir. Representing the wavefunction in B by means of Green functions provides a flexible way of accessing the full open-boundary problem, allowing transfer of particles into and out of a system. Using Green function embedding, one can calculate the wavefunctions in A that automatically satisfy the boundary conditions emulating their contact with B. However such embedding techniques suffer the disadvantage of being computationally demanding when employed to solve fully three-dimensional problems with first-principles methods.

Absorbing boundaries provide more computationally practical ways of accessing ionization processes in which charge leaves the system. We have considered absorbing boundaries and mask functions which are simple methods to absorb outgoing waves in time-dependent simulations. The boundary absorbers are meant to absorb waves that leave the system, so that an outgoing wave disappears rather than reflects on the simulation box. The complex scaling method provides a particularly elegant way to absorb outgoing waves, allowing one, in principle, to impose perfectly absorbing boundaries.

Having discussed the problem of describing total ionization with the appropriate choice of boundary conditions, we turned to the problem of describing electron photoemission probabilities with TDDFT. We examined three approaches suitable for the task. The sampling point method, where the energy-resolved probability is calculated by Fourier transforming the time evolution of each Khon–Sham orbital in the energy domain; the surface flux method, where the photoelectron probability is generated by recording the electron flux through a closed surface surrounding the system; and finally we discussed the mask method where, by means of a mask function, it is possible to generate a split real/momentum-space propagation scheme where electrons, moving from a bounded volume into the empty space, seamlessly

change from real space to momentum space representation. This scheme allows for the description of a wide range of processes and time resolved pump–probe spectroscopies.

Acknowledgments We acknowledge financial support from the European Research Council Advanced Grant DYNamo (ERC-2010-AdG-267374), Ministerio de Economía y Competitividad or MINECO, Spanish Grant (FIS2013-46159-C3-1-P), Grupos Consolidados UPV/EHU del Gobierno Vasco (IT578-13), European Commission FP7 project CRONOS (Grant number 280879-2), COST Actions CM1204 (XLIC), and MP1306 (EUSpec).

References

1. Hohenberg P, Kohn W (1964) Inhomogeneous electron gas. Phys Rev 136:B864–B871. doi:10.1103/PhysRev.136.B864, http://link.aps.org/doi/10.1103/PhysRev.136.B864
2. Runge E, Gross EKU (1984) Density-functional theory for time-dependent systems. Phys Rev Lett 52(12):997–1000
3. Kohn W, Sham LJ (1965) Self-consistent equations including exchange and correlation effects. Phys Rev 140:A1133–A1138. doi:10.1103/PhysRev.140.A1133, http://link.aps.org/doi/10.1103/PhysRev.140.A1133
4. Burke K, Car R, Gebauer R (2005) Density functional theory of the electrical conductivity of molecular devices. Phys Rev Lett 94(14):146803
5. Tempel DG, Aspuru-Guzik A (2011) Relaxation and dephasing in open quantum systems time-dependent density functional theory: properties of exact functionals from an exactly-solvable model system. Chem Phys 391(1):130–142
6. Tempel DG, Watson MA, Olivares-Amaya R, Aspuru-Guzik A (2011) Time-dependent density functional theory of open quantum systems in the linear-response regime. J Chem Phys 134(7):074116
7. Yuen-Zhou J, Rodríguez-Rosario C, Aspuru-Guzik A (2009) Time-dependent current-density functional theory for generalized open quantum systems. Phys Chem Chem Phys 11(22):4509–4522
8. Yuen-Zhou J, Tempel DG, Rodríguez-Rosario CA, Aspuru-Guzik A (2010) Time-dependent density functional theory for open quantum systems with unitary propagation. Phys Rev Lett 104(4):043001
9. Marques MAL, Maitra NT, Nogueira F, Gross EKU, Rubio A (2011) Fundamentals of time-dependent density functional theory. Springer, Berlin
10. Fano U (1961) Effects of configuration interaction on intensities and phase shifts. Phys Rev 124(6):1866–1878
11. Brandbyge M, Mozos JL, Ordejón P, Taylor J, Stokbro K (2002) Density-functional method for nonequilibrium electron transport. Phys Rev B 65:165401. doi:10.1103/PhysRevB.65.165401
12. Chen J, Thygesen KS, Jacobsen KW (2012) Ab initio. Phys Rev B 85:155140. doi:10.1103/PhysRevB.85.155140, http://link.aps.org/doi/10.1103/PhysRevB.85.155140
13. Larsen AH, Vanin M, Mortensen JJ, Thygesen KS, Jacobsen KW (2009) Localized atomic basis set in the projector augmented wave method. Phys Rev B 80:195112. doi:10.1103/PhysRevB.80.195112, http://link.aps.org/doi/10.1103/PhysRevB.80.195112
14. Soler JM, Artacho E, Gale JD, García A, Junquera J, Ordejón P, Sánchez-Portal D (2002) The SIESTA method for ab initio order-N materials simulation. J Phys Condens Matter 14:2745–2779. doi:10.1088/0953-8984/14/11/302, http://iopscience.iop.org/0953-8984/14/11/302

15. Newns DM (1969) Self-consistent model of hydrogen chemisorption. Phys Rev 178: 1123–1135. doi:10.1103/PhysRev.178.1123, http://link.aps.org/doi/10.1103/PhysRev.178.1123
16. Gellene GI (1995) Resonant states of a one-dimensional piecewise constant potential. J Chem Educ 72(11):1015. doi:10.1021/ed072p1015, http://dx.doi.org/10.1021/ed072p1015
17. Siegert AJF (1939) On the derivation of the dispersion formula for nuclear reactions. Phys Rev 56:750–752. doi:10.1103/PhysRev.56.750, http://link.aps.org/doi/10.1103/PhysRev.56.750
18. Hatano N, Sasada K, Nakamura H, Petrosky T (2008) Some properties of the resonant state in quantum mechanics and its computation. Prog Theor Phys 119(2):187–222. doi:10.1143/PTP.119.187, http://ptp.oxfordjournals.org/content/119/2/187.abstract
19. Aguilar J, Combes J (1971) A class of analytic perturbations for one-body Schrödinger Hamiltonians. Commun Math Phys 22:269–279. doi:10.1007/BF01877510, http://dx.doi.org/10.1007/BF01877510
20. Balslev E, Combes JM (1971) Spectral properties of many-body Schrödinger operators with dilatation-analytic interactions. Commun Math Phys 22(4):280–294
21. Simon B (1973) Resonances in n-body quantum systems with dilatation analytic potentials and the foundations of time-dependent perturbation theory. Ann Math 97:247–274
22. Simon B (1979) The definition of molecular resonance curves by the method of exterior complex scaling. Phys Lett A 71(2):211–214
23. Ho Y (1983) The method of complex coordinate rotation and its applications to atomic collision processes. Phys Rep 99(1):1–68. doi:10.1016/0370-1573(83)90112-6, http://www.sciencedirect.com/science/article/pii/0370157383901126
24. McCurdy CW, Baertschy M, Rescigno TN (2004) Solving the three-body Coulomb breakup problem using exterior complex scaling. J Phys B At Mol Opt 37(17):R137, http://stacks.iop.org/0953-4075/37/i=17/a=R01
25. Moiseyev N (1998) Quantum theory of resonances: calculating energies, widths and cross-sections by complex scaling. Phys Rep 302(5–6):212–293. doi:10.1016/S0370-1573(98)00002-7, http://www.sciencedirect.com/science/article/pii/S0370157398000027
26. Reinhardt WP (1982) Complex coordinates in the theory of atomic and molecular structure and dynamics. Annu Rev Phys Chem 33(1):223–255. doi:10.1146/annurev.pc.33.100182.001255, http://www.annualreviews.org/doi/abs/10.1146/annurev.pc.33.100182.001255
27. Simon B (1978) Resonances and complex scaling: a rigorous overview. Int J Quantum Chem 14(4):529–542. doi:10.1002/qua.560140415, http://dx.doi.org/10.1002/qua.560140415
28. Cerjan C, Hedges R, Holt C, Reinhardt WP, Scheibner K, Wendoloski JJ (1978) Complex coordinates and the Stark effect. Int J Quantum Chem 14(4):393–418. doi:10.1002/qua.560140408, http://dx.doi.org/10.1002/qua.560140408
29. Herbst IW (1979) Dilation analyticity in constant electric field. Commun Math Phys 64(3): 279–298. doi:10.1007/BF01221735
30. Herbst IW, Simon B (1978) Stark effect revisited. Phys Rev Lett 41:67–69. doi:10.1103/PhysRevLett.41.67, http://link.aps.org/doi/10.1103/PhysRevLett.41.67
31. Scrinzi A, Piraux B (1998) Two-electron atoms in short intense laser pulses. Phys Rev A 58: 1310–1321. doi:10.1103/PhysRevA.58.1310, http://link.aps.org/doi/10.1103/PhysRevA.58.1310
32. Junker BR (1983) Complex virial theorem and complex scaling. Phys Rev A 27:2785–2789. doi:10.1103/PhysRevA.27.2785, http://link.aps.org/doi/10.1103/PhysRevA.27.2785
33. Moiseyev N, Friedland S, Certain PR (1981) Cusps, θ trajectories, and the complex virial theorem. J Chem Phys 74(8):4739–4740. doi:10.1063/1.441624, http://scitation.aip.org/content/aip/journal/jcp/74/8/10.1063/1.441624
34. McCurdy CW (1980) Complex-coordinate calculation of matrix elements of the resolvent of the Born–Oppenheimer Hamiltonian. Phys Rev A 21:464–470. doi:10.1103/PhysRevA.21.464, http://link.aps.org/doi/10.1103/PhysRevA.21.464
35. McCurdy CW, Rescigno TN (1978) Extension of the method of complex basis functions to molecular resonances. Phys Rev Lett 41:1364–1368. doi:10.1103/PhysRevLett.41.1364, http://link.aps.org/doi/10.1103/PhysRevLett.41.1364

36. Moiseyev N, Corcoran C (1979) Autoionizing states of H_2 and H_2^- using the complex-scaling method. Phys Rev A 20:814–817. doi:10.1103/PhysRevA.20.814, http://link.aps.org/doi/10.1103/PhysRevA.20.814
37. Morgan JD, Simon B (1981) The calculation of molecular resonances by complex scaling. J Phys B At Mol Opt 14(5):L167
38. Scrinzi A (2010) Infinite-range exterior complex scaling as a perfect absorber in time-dependent problems. Phys Rev A 81(5):053845
39. Moiseyev N (1999) Derivations of universal exact complex absorption potentials by the generalized complex coordinate method. J Phys B At Mol Opt 31(7):1431–1441
40. Krylstedt P, Carlsund C, Elander N (1989) On the calculation of electron–atom collision properties using exterior complex dilatated *s*-matrix expansions. J Phys B At Mol Opt 22(7): 1051, http://stacks.iop.org/0953-4075/22/i = 7/a = 014
41. Rescigno TN, Baertschy M, Byrum D, McCurdy CW (1997) Making complex scaling work for long-range potentials. Phys Rev A 55:4253–4262. doi:10.1103/PhysRevA.55.4253, http://link.aps.org/doi/10.1103/PhysRevA.55.4253
42. Scrinzi A, Elander N (1993) A finite element implementation of exterior complex scaling for the accurate determination of resonance energies. J Chem Phys 98(5):3866–3875. doi:10.1063/1.464014, http://scitation.aip.org/content/aip/journal/jcp/98/5/10.1063/1.464014
43. Simons J (1980) The complex coordinate rotation method and exterior scaling: a simple example. Int J Quantum Chem 18(S14):113–121. doi:10.1002/qua.560180814, http://dx.doi.org/10.1002/qua.560180814
44. Kar S, Ho YK (2009) Isotope shift for the $^1D^e$ autodetaching resonance in H^- and D^-. J Phys B At Mol Opt 42(5):055001, http://stacks.iop.org/0953-4075/42/i = 5/a = 055001
45. Scrinzi A, Geissler M, Brabec T (1999) Ionization above the Coulomb barrier. Phys Rev Lett 83:706–709. doi:10.1103/PhysRevLett.83.706, http://link.aps.org/doi/10.1103/PhysRevLett.83.706
46. McCurdy CW, Rescigno TN, Davidson ER, Lauderdale JG (1980) Applicability of self-consistent field techniques based on the complex coordinate method to metastable electronic states. J Chem Phys 73(7):3268–3273. doi:10.1063/1.440522, http://scitation.aip.org/content/aip/journal/jcp/73/7/10.1063/1.440522
47. Samanta K, Yeager DL (2008) Investigation of ^2P Be^- shape resonances using a quadratically convergent complex multiconfigurational self-consistent field method. J Phys Chem B 112(50):16214–16219. doi:10.1021/jp806998n, http://dx.doi.org/10.1021/jp806998n
48. Zdánská PR, Moiseyev N (2005) Hartree–Fock orbitals for complex-scaled configuration interaction calculation of highly excited Feshbach resonances. J Chem Phys 123(19):194105. doi:10.1063/1.2110169, http://scitation.aip.org/content/aip/journal/jcp/123/19/10.1063/1.2110169
49. Larsen AH, Whitenack DL, De Giovannini U, Wasserman A, Rubio A (2013) Stark ionization of atoms and molecules within density functional resonance theory. J Phys Chem Lett 4:2734–2738
50. Whitenack DL, Wasserman A (2011) Density functional resonance theory of unbound electronic systems. Phys Rev Lett 107(16):163002
51. Wasserman A, Moiseyev N (2007) Hohenberg-Kohn theorem for the lowest-energy resonance of unbound systems. Phys Rev Lett 98:093003. doi:10.1103/PhysRevLett.98.093003, http://link.aps.org/doi/10.1103/PhysRevLett.98.093003
52. Perdew JP, Wang Y (1992) Accurate and simple analytic representation of the electron-gas correlation energy. Phys Rev B 45:13244–13249. doi:10.1103/PhysRevB.45.13244, http://link.aps.org/doi/10.1103/PhysRevB.45.13244
53. Telnov DA, Sosnova KE, Rozenbaum E, Chu SI (2013) Exterior complex scaling method in time-dependent density-functional theory: multiphoton ionization and high-order-harmonic generation of Ar atoms. Phys Rev A 87(5):053406

54. van Leeuwen R, Baerends EJ (1994) Exchange–correlation potential with correct asymptotic behavior. Phys Rev A 49:2421–2431. doi:10.1103/PhysRevA.49.2421, http://link.aps.org/doi/10.1103/PhysRevA.49.2421
55. Ammosov MV, Delone NB, Krainov VP (1986) Tunnel ionization of complex atoms and atomic ions in a varying electromagnetic-field. Zh Éksp Teor Fiz 91:2008–2013
56. Parker SD, McCurdy C (1989) Propagation of wave packets using the complex basis function method. Chem Phys Lett 156(5):483–488. doi:10.1016/S0009-2614(89)87316-6, http://www.sciencedirect.com/science/article/pii/S0009261489873166
57. Bengtsson J, Lindroth E, Selstø S (2008) Solution of the time-dependent Schrödinger equation using uniform complex scaling. Phys Rev A 78:032502. doi:10.1103/PhysRevA.78.032502, http://link.aps.org/doi/10.1103/PhysRevA.78.032502
58. Bengtsson J, Lindroth E, Selstø S (2012) Wave functions associated with time-dependent, complex-scaled Hamiltonians evaluated on a complex time grid. Phys Rev A 85:013419. doi:10.1103/PhysRevA.85.013419, http://link.aps.org/doi/10.1103/PhysRevA.85.013419
59. Gilary I, Fleischer A, Moiseyev N (2005) Calculations of time-dependent observables in non-Hermitian quantum mechanics: the problem and a possible solution. Phys Rev A 72:012,117. doi:10.1103/PhysRevA.72.012117, http://link.aps.org/doi/10.1103/PhysRevA.72.012117
60. García-Moliner F, Flores F (2009) Introduction to the theory of solid surfaces. Cambridge University Press, Cambridge
61. Kudrnovský J, Drchal V, Turek I, Weinberger P (1994) Magnetic coupling of interfaces: a surface-Green's-function approach. Phys Rev B 50:16105–16108. doi:10.1103/PhysRevB.50.16105, http://link.aps.org/doi/10.1103/PhysRevB.50.16105
62. Boucke K, Schmitz H, Kull HJ (1997) Radiation conditions for the time-dependent Schrödinger equation: application to strong-field photoionization. Phys Rev A 56(1):763–771
63. Ermolaev A, Puzynin I, Selin A, Vinitsky S (1999) Integral boundary conditions for the time-dependent Schrödinger equation: atom in a laser field. Phys Rev A 60(6):4831–4845
64. Hellums J, Frensley W (1994) Non-Markovian open-system boundary conditions for the time-dependent Schrödinger equation. Phys Rev B 49(4):2904–2906
65. Kurth S, Stefanucci G, Almbladh CO, Rubio A, Gross EKU (2005) Time-dependent quantum transport: a practical scheme using density functional theory. Phys Rev B 72(3):035308
66. Inglesfield JE (2001) Embedding at surfaces. Comput Phys Commun 137(1):89–107
67. Inglesfield JE (2011) A time-dependent embedding calculation of surface electron emission. J Phys Condens Matter 23(30):305004
68. Antoine X, Arnold A, Besse C, Ehrhardt M, Schädle A (2008) A review of transparent and artificial boundary conditions techniques for linear and nonlinear Schrödinger equations. Commun Comput Phys 4:729–796
69. Inglesfield JE (1981) A method of embedding. J Phys C Solid State 14(26):3795–3806
70. Inglesfield J (2008) Time-dependent embedding. J Phys Condens Matter 20:095215
71. Ehrhardt M (1999) Discrete transparent boundary conditions for general Schrödinger-type equations. VLSI Des 9(4):325–338
72. Szmytkowski R, Bielski S (2004) Dirichlet-to-Neumann and Neumann-to-Dirichlet embedding methods for bound states of the Schrödinger equation. Phys Rev A 70(4):042103
73. Frensley W (1990) Boundary conditions for open quantum systems driven far from equilibrium. Rev Mod Phys 62(3):745–791
74. De Giovannini U, Larsen AH, Rubio A (2015) Modeling electron dynamics coupled to continuum states in finite volumes. Eur Phys J B 88(3):56. doi:10.1140/epjb/e2015-50808-0
75. Neuhauser D, Baer M (1989) The application of wave packets to reactive atom–diatom systems: a new approach. J Chem Phys 91(8):4651–4657
76. Neuhauser D, Baer M (1989) The time-dependent Schrödinger equation: application of absorbing boundary conditions. J Chem Phys 90(8):4351
77. Berenger JP (1994) A perfectly matched layer for the absorption of electromagnetic waves. J Comput Phys 114(2):185–200

78. Elenewski JE, Chen H (2014) Real-time transport in open quantum systems from PT-symmetric quantum mechanics. Phys Rev B 90(8):085104
79. Varga K, Pantelides S (2007) Quantum transport in molecules and nanotube devices. Phys Rev Lett 98(7):076804
80. Wibking BD, Varga K (2012) Quantum mechanics with complex injecting potentials. Phys Lett A 376(4):365–369
81. Muga J, Palao JP, Navarro B, Egusquiza IL (2004) Complex absorbing potentials. Phys Rep 395(6):357–426
82. Andrade X, Aspuru-Guzik A (2011) Prediction of the derivative discontinuity in density functional theory from an electrostatic description of the exchange and correlation potential. Phys Rev Lett 107(18):183002
83. Perdew JP, Burke K, Ernzerhof M (1996) Generalized gradient approximation made simple. Phys Rev Lett 77(18):3865–3868
84. Crawford-Uranga A, De Giovannini U, Räsänen E, Oliveira MJT, Mowbray DJ, Nikolopoulos GM, Karamatskos ET, Markellos D, Lambropoulos P, Kurth S, Rubio A (2014) Time-dependent density-functional theory of strong-field ionization of atoms by soft X-rays. Phys Rev A 90(3):033412
85. Krause J, Schafer K, Kulander K (1992) Calculation of photoemission from atoms subject to intense laser fields. Phys Rev A 45(7):4998–5010
86. Kulander K, Mies F, Schafer K (1996) Model for studies of laser-induced nonlinear processes in molecules. Phys Rev A 53(4):2562–2570
87. Lein M, Marangos J, Knight P (2002) Electron diffraction in above-threshold ionization of molecules. Phys Rev A 66(5):051404R
88. Chelkowski S, Foisy C, Bandrauk AD (1998) Electron–nuclear dynamics of multiphoton H_2^+ dissociative ionization in intense laser fields. Phys Rev A 57(2):1176–1185
89. Grobe R, Haan S, Eberly J (1999) A split-domain algorithm for time-dependent multi-electron wave functions. Comput Phys Commun 117(3):200–210
90. De Giovannini U, Varsano D, Marques MAL, Appel H, Gross EKU, Rubio A (2012) *Ab initio* angle- and energy-resolved photoelectron spectroscopy with time-dependent density-functional theory. Phys Rev A 85:062515
91. Shemer O, Brisker D, Moiseyev N (2005) Optimal reflection-free complex absorbing potentials for quantum propagation of wave packets. Phys Rev A 71(3):032716
92. McCurdy CW, Stroud C, Wisinski M (1991) Solving the time-dependent Schrödinger equation using complex-coordinate contours. Phys Rev A 43(11):5980–5990
93. Riss UV, Meyer HD (1995) Reflection-free complex absorbing potentials. J Phys B At Mol Opt 28(8):1475–1493
94. Sosnova KE, Telnov DA, Rozenbaum EB, Chu SI (2014) Exterior complex scaling method in TDDFT: HHG of Ar atoms in intense laser fields. J Phys Conf Ser 488(1):012022
95. Pohl A, Reinhard PG, Suraud E (2000) Towards single-particle spectroscopy of small metal clusters. Phys Rev Lett 84(22):5090–5093
96. Dinh PM, Romaniello P, Reinhard PG, Suraud E (2013) Calculation of photoelectron spectra: a mean-field-based scheme. Phys Rev A 87(3):032514
97. Caillat J, Zanghellini J, Kitzler M, Koch O, Kreuzer W, Scrinzi A (2005) Correlated multielectron systems in strong laser fields: a multiconfiguration time-dependent Hartree–Fock approach. Phys Rev A 71(1):012712
98. Scrinzi A (2012) t-SURFF: fully differential two-electron photo-emission spectra. New J Phys 14(8):085008
99. Tao L, Scrinzi A (2012) Photo-electron momentum spectra from minimal volumes: the time-dependent surface flux method. New J Phys 14(1):013021
100. Crawford-Uranga A, De Giovannini U, Mowbray DJ, Kurth S, Rubio A (2014) Modelling the effect of nuclear motion on the attosecond time-resolved photoelectron spectra of ethylene. J Phys B At Mol Phys 47(12):124018

101. De Giovannini U, Brunetto G, Castro A, Walkenhorst J, Rubio A (2013) Simulating pump-probe photoelectron and absorption spectroscopy on the attosecond timescale with time-dependent density functional theory. Chemphyschem 14(7):1363–1376
102. Gazibegović-Busuladžić A, Hasović E, Busuladžić M, Milosevic D, Kelkensberg F, Siu W, Vrakking M, Lepine F, Sansone G, Nisoli M, Znakovskaya I, Kling M (2011) Above-threshold ionization of diatomic molecules by few-cycle laser pulses. Phys Rev A 84(4): 043426

Top Curr Chem (2016) 368: 273–346
DOI: 10.1007/128_2014_618

Published online: 12 April 2015

Nonlinear Spectroscopy of Core and Valence Excitations Using Short X-Ray Pulses: Simulation Challenges

Yu Zhang, Weijie Hua, Kochise Bennett, and Shaul Mukamel

Abstract Measuring the nonlinear response of electrons and nuclei to attosecond broadband X-ray radiation has become possible by newly developed free electron lasers and high harmonic generation light sources. The design and interpretation of these novel experiments poses considerable computational challenges. In this chapter we survey the basic description of nonlinear X-ray spectroscopy signals and the electronic structure protocols which may be used for their simulation.

Keywords Core excitation · DFT · Double excitation · Double-quantum-coherence · MCSCF · Nonlinear spectroscopy · Real-time TDDFT · Stimulated X-ray Raman spectroscopy · TDDFT · X-ray

Contents

Y. Zhang, W. Hua, K. Bennett, and S. Mukamel (✉)
Department of Chemistry, University of California, Irvine, CA 92697, USA
e-mail: smukamel@uci.edu

Abbreviations

ADC	Algebraic diagrammatic construction
AES	Auger electron spectroscopy
AIMD	*ab initio* molecular dynamics
ASRS	Attosecond stimulated Raman spectroscopy
BO	Bohn–Oppenheimer
CAP	Complex absorption potential
CASPT2	Complete active space second-order perturbation theory
CASSCF	Complete active space self-consistent field
CASSI	Complete active space state interaction
CC	Coupled cluster
CCSD	Coupled cluster singles and doubles
CEO	Collective electronic oscillator
CFM	Crystal field multiplet
CI	Configuration interaction
CIS	Configuration interaction singles
CoIn	Conical intersection
CPP	Complex polarization propagator
CSF	Configuration state function
CV	Core-valence
CV-DFT	Constricted variational density functional theory
DCH	Double core hole
DFT	Density functional theory
DMRG	Density matrix renormalization group
DQC	Double-quantum-coherence
ECH	Equivalent core hole
EET	Excitation energy transfer
EOM	Equation of motion
ET	Electron transfer
EXAFS	Extended X-ray absorption fine structure
FC	Frank–Condon
FCH	Full core hole
FORS	Full optimization reaction space
GGA	Generalized gradient approximation
GSB	Ground state bleaching

HCH	Half core hole
HHG	High harmonic generation
IR	Infrared
LCM	Linear coupling model
LFT	Ligand field theory
MCSCF	Multiconfigurational self-consistent field
MLFT	Multiplet ligand field theory
MMUT	Modified midpoint unitary transform
MO	Molecular orbital
MOM	Maximum overlap method
MRCC	Multireference coupled cluster
MRCI	Multireference configuration interaction
MRPT	Multireference perturbation theory
NEO	Norm-extended optimization
NMA	*N*-methylacetamide
NR	Newton–Raphson
NTO	Natural transition orbital
OEP	Optimal effective potential
PAD	Photoelectron angular distribution
PES	Potential energy surface
RAS	Restricted active space
RASPT2	Restricted active space second-order perturbation theory
RASSCF	Restricted active space self-consistent field
RASSI	Restricted active space state interaction
REW	Restricted excitation window
RIXS	Resonant inelastic X-ray scattering
ROCIS	Restricted open-shell configuration interaction singles
ROHF	Restricted open-shell Hartree–Fock
RT	Real-time
SA	State-averaged
SAC-CI	Symmetry-adapted cluster configuration interaction
SCF	Self-consistent field
SF	Spin-flip
SIC	Self-interaction correction
SLE	Stochastic Liouville equation
SO	Spin-orbit
SOS	Sum over state
SS-MRCC	State-specific multireference coupled cluster
STEX	Static exchange
SXRS	Stimulated X-ray Raman spectroscopy
TDA	Tamm–Dancoff approximation
TDDFT	Time-dependent density functional theory
TDHF	Time-dependent Hartree–Fock
TDM	Transition dipole moments
TP	Transition potential
TRPES	Time-resolved photoelectron spectroscopy

TS	Transition state
TSH	Trajectory surface hopping
TXAS	Transient X-ray absorption spectroscopy
XANES	X-Ray absorption nearedge structure
XCH	Excited core hole
XDQC	X-Ray double-quantum-coherence
XES	X-Ray emission spectroscopy
XFEL	X-Ray free electron laser
XPS	X-Ray photoelectron spectroscopy

1 Introduction

In linear spectroscopy experiments, the incident light field interacts with the studied system only once and is relatively weak compared to the intrinsic interaction potential of the system. The signal can be considered as the linear response of the system to the perturbation of the light field. Linear spectroscopy provides useful information about the atomic and electronic structure of the system. Nonlinear spectroscopy techniques provide more detailed information. Nonlinear spectroscopy [1] employs multiple light fields to probe the correlations between different spectral features. Many controlling factors, such as the frequencies, wavevectors, and polarizations of the light fields and the time delays between them, can be varied so that detection of the correlation between certain spectroscopy features and their dynamics is possible.

Nonlinear optical spectroscopy became feasible soon after the invention of the laser in the 1960s. With the development of laser technology, pulse durations were reduced from picoseconds (1970s) to femtoseconds (1980s) [2], and now to attoseconds [3]. Nonlinear infrared and optical spectroscopy techniques have proved to be very successful for studying various excited state couplings and dynamics in molecules and materials [4, 5]. Nonlinear spectroscopy techniques in the X-ray regime made possible by new X-ray free electron lasers (XFEL) and high harmonic generation (HHG) sources provide a unique window into the motions of electrons, holes, and excitons in molecules and materials. Because of their broad bandwidth (about 10 eV for a 100-attosecond pulse), X-ray pulses can create coherent superpositions of many excited states localized at the target atoms. In analogy to how optical pulses manipulate molecular vibrations, attosecond X-ray pulses triggering and probing valence excited state dynamics have been considered recently [6] and explored experimentally [7–10]. Sequences of coherent broadband X-ray pulses can reveal the dynamics of nuclei and electrons in molecules with attosecond temporal, and nanometer spatial resolution.

X-Ray pulses can be used in various ways:

- Off-resonant diffraction detects the charge density. This technique can be extended to multiple dimensions to provide multipoint correlations of the charge density [11, 12].

- Core resonant spectroscopy offers a fast and versatile way to trigger valence excitations at selected positions and times via a stimulated Raman process [6] and to study their dynamics.
- Multiple cores can be excited at various delays, allowing the study of nonlinear response of valence electrons.

The complex nature of excited state correlations and dynamics leads to characteristic patterns in nonlinear spectroscopy signals, whose interpretation calls for state-of-the-art theoretical simulation methods. The simulation of time-domain nonlinear X-ray spectroscopy signals poses numerous challenges to quantum chemists. First, resonant X-ray spectroscopy involves core excited state. Most computational molecular electronic structure activity had focused on the ground state and valence excitations. Core excitations received much less attention because they do not participate in typical chemical processes. Core excited states lie well above many valence excited states, and calculating them directly with bottom-up algorithms is not practical. Core electrons also have special asymptotic behavior (cusp condition) close to the nuclei and large relativistic effects. Second, signals obtained by broadband X-ray pulses require many excited states. A state-by-state calculation scheme is tedious and it is better to obtain all excited states with an energy range in one shot. Third, resonant X-ray signals require not only the energies of excited states but also the transition dipoles between them. It is usually necessary to calculate high order excited state energy gradients to determine these quantities, which complicates the simulation. Furthermore, multiple X-ray pulses can easily create excited states with multiple core holes, which are not well described by single-reference-based excited state quantum chemistry methods such as adiabatic time-dependent density functional theory (TDDFT). Most of the discussions in this chapter are based on adiabatic TDDFT. Non-adiabatic frequency-dependent kernels are discussed in Sect. 4.3. Finally, many electrons may respond to the core hole created by the X-ray pulses (e.g., shake-up and shake-off processes) [13], so that many-body effects are very important in these signals. The single-particle picture may break down and high level methods such as multireference configuration interaction (MRCI) or multireference perturbation theory (MRPT) are often necessary to account for electron correlation. These challenges are addressed in the following sections. We focus on the theoretical methods (mainly DFT/TDDFT) which have been extensively used in X-ray spectroscopy simulation. There are excellent reviews on using TDDFT to simulate linear X-ray spectroscopy signals [13–15]. Here we emphasize the specific issues associated with nonlinear X-ray spectroscopy simulations and mainly discuss the methods applied to molecules.

This chapter is organized as follows. We first briefly describe the calculation of various nonlinear X-ray spectroscopy signals, and then review existing quantum chemistry simulation methods. We then discuss several key issues in nonlinear X-ray spectroscopy simulation. Finally, conclusions and future directions are outlined.

2 Nonlinear X-Ray Spectroscopies

A system of interacting electrons is described by the Hamiltonian

$$\hat{H} = \sum_i \frac{\hat{p}_i^2}{2m_i} + \frac{1}{2}\sum_{ij} \hat{\mathcal{V}}\left(|\mathbf{r}_i - \mathbf{r}_j|\right), \tag{1}$$

where $\hat{p}_i$ is the momentum of the ith electron and $\hat{\mathcal{V}}$ is the Coulomb potential. In the minimal-coupling Hamiltonian, the effects of an external electromagnetic field are included by the substitution $\hat{p}_i \rightarrow \hat{p}_i - \frac{q_i}{c}\hat{\mathbf{A}}$ where q_i is the charge and $\hat{\mathbf{A}}$ is the electronic magnetic vector potential [1, 16]. The minimal coupling is well-suited to discuss X-ray diffraction, which arises from the $\mathbf{A}^2$ term, but it is often more convenient to work with the electric and magnetic fields (which are gauge invariant) rather than the vector potential. This is accomplished by the Power–Zienau canonical transformation [1, 16]. The Hamiltonian of the system then becomes

$$\hat{H}_S(t) = \hat{H} + \hat{H}_{\text{int}}(t), \tag{2}$$

where H is the material Hamiltonian and, in the dipole approximation, the interaction Hamiltonian is

$$\hat{H}_{\text{int}}(t) = -\int d\mathbf{r}\left(\hat{\mathcal{E}}(\mathbf{r},t) + \hat{\mathcal{E}}^\dagger(\mathbf{r},t)\right)\cdot\hat{\mu}\,, \tag{3}$$

with $\hat{\mu}$ the dipole operator and $\left(\hat{\mathcal{E}} + \hat{\mathcal{E}}^\dagger\right) \equiv \hat{\mathbf{E}}$ is the electric field which is separated into positive and negative Fourier components. Within the rotating wave approximation, the dipole moment is also separated into positive and negative Fourier components $\hat{\mu} = \hat{V} + \hat{V}^\dagger$ and only the terms $\hat{\mathcal{E}}\hat{V}^\dagger + \hat{\mathcal{E}}^\dagger\hat{V}$ are retained [1]. Throughout, we work in the interaction picture with respect to this Hamiltonian and in the Hartree units, which simplifies the coefficients in the resulting expressions. The detected quantity in the signals coincided here is the integrated photon number

$$S(\Lambda) = \int dt\left\langle\dot{\hat{N}}(t)\right\rangle = \int dt d\mathbf{r}\Im\left[\hat{\mathcal{E}}^\dagger(\mathbf{r},t)\cdot\langle\hat{\mu}(t)\rangle\right], \tag{4}$$

where the last equality follows from the Heisenberg equation of motion for the photon number operator and the signal is a function of the parameters defining the pulse envelope (collectively denoted Λ). In the following, we take the field to be polarized along the dipole and avoid the tensor notation (this restriction is easily relaxed). Note that this form for the signal does not include any frequency- or time-resolved detection. This could be done by adding gating functions [11, 17, 18] in nonlinear spectroscopic applications; the electric field is a superposition of more

than one externally applied pulses or continuous wave (CW) laser field. To simulate such experiments, we calculate the propagated wavefunction of the driven system

$$|\psi(t)\rangle = \hat{U}(t)|\psi_0\rangle, \tag{5}$$

where the time-evolution operator $\hat{U}(t)$ follows from the Schrödinger equation

$$\mathrm{i}\frac{\partial}{\partial t}|\psi(t)\rangle = \hat{H}_{\mathrm{int}}|\psi(t)\rangle \rightarrow \hat{U}(t) = \exp_+\left(-\mathrm{i}\int_0^t d\tau \hat{H}_{\mathrm{int}}(\tau)\right), \tag{6}$$

where e_+ stands for the positive time-ordered exponential. As a reminder, we work in the interaction picture where the states carry the interaction propagation and the operators carry the field-free propagators so that the time-dependent dipole moment is

$$\hat{\mu}(t) = e^{\mathrm{i}\hat{H}t}\hat{\mu}\, e^{-\mathrm{i}\hat{H}t}, \tag{7}$$

and its expectation value is then written

$$\langle\hat{\mu}(t)\rangle = \langle\psi(t)|\hat{\mu}(t)|\psi(t)\rangle = \langle\psi_0|\hat{U}^{\dagger}(t)\hat{\mu}(t)\hat{U}(t)|\psi_0\rangle. \tag{8}$$

To analyze particular experiments, we expand the interaction propagator (time-ordered exponential) perturbatively in powers of the electric field. Together with an explicit form for the material Hamiltonian H, the previous equations form the basis for the perturbative description of the nonlinear signals considered below.

2.1 Time-Resolved Four-Wave Mixing

Linear signals are determined by the first order $\hat{H}_{\mathrm{int}}$. In the X-ray regime, such signals include X-ray absorption near edge structure (XANES) and extended X-ray absorption fine structure (EXAFS) [19–21]. The third order techniques (four-wave mixing) provide more detailed information [6, 22]. In this section, we describe a class of techniques that utilize four pulses well-separated in time. The pulses interact with the molecule sequentially and the signal is defined as the change in transmission of the final pulse. In the limit of ultrashort pulses, the signal is parameterized by the time delays between successive pulses. In the semiclassical approximation (where the electric field is treated classically and the molecule is quantum), we have

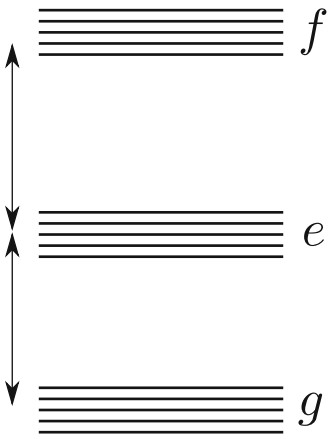

Fig. 1 Schematic depiction of the energy levels under consideration. The g, e, and f are ground state, single core excitation, and double core excitation manifolds. The fine structures of the manifolds are given by valence excitations on *top* of the core excited states whereas in the optical regime they represent vibrational excitations on *top* of the valence excited states

$$E(t) = \sum_{p=1,2,3,4} \tilde{\mathcal{E}}\left(t-\bar{\tau}_p\right) e^{i\mathbf{k}_p\cdot\mathbf{r}-i\omega_p\left(t-\bar{\tau}_p\right)+i\phi_p} + \text{c.c.} \tag{9}$$

where ϕ_p is the phase of the pth pulse, $\bar{\tau}_p$, ω_p the central times and frequencies of the temporal and spectral pulse envelopes and $\tilde{\mathcal{E}}_p(t)$ the temporal pulse envelopes centered at $t=0$. The system interacts once with each pulse and the signal can then be plotted as a function of the pulse parameters. The terms in the perturbative expansions are conveniently depicted diagrammatically. Besides facilitating enumeration of all terms, this procedure allows one to write quickly the signal corresponding to a particular diagram and to discern in which time periods particular coherences appear. For macroscopic samples longer than the relevant radiation wavelength a delta function $\delta(-\mathbf{k}_4 \pm \mathbf{k}_3 \pm \mathbf{k}_2 \pm \mathbf{k}_1)$ results. This is known as phase matching for our level and dipole scheme. The ground state, singly excited state and doubly excited state manifolds involved in these four-wave mixing experiment are shown in Fig. 1. The three possible signals are denoted $\mathbf{k}_{\mathrm{I}} \equiv -\mathbf{k}_1 + \mathbf{k}_2 + \mathbf{k}_3$, $\mathbf{k}_{\mathrm{II}} \equiv \mathbf{k}_1 - \mathbf{k}_2 + \mathbf{k}_3$, and $\mathbf{k}_{\mathrm{III}} \equiv \mathbf{k}_1 + \mathbf{k}_2 - \mathbf{k}_3$. Below we focus on two techniques: the double quantum coherence four wave mixing, and the stimulated Raman simulations, and analysis of these signals are given later. The diagrams of other two four-wave mixing techniques are also provided in Fig. 2 for reference.

2.2 *Double-Quantum-Coherence Signal*

We focus on the DQC $\mathbf{k}_{\mathrm{III}}$ signal, which is particularly sensitive to electron correlations. The pulse order and the diagrams corresponding to the DQC signal are depicted in Figs. 3 and 4, respectively. During the time period $t_2 \equiv \tau_2 - \tau_1$, the system is in a coherence between the doubly-excited states and the ground state.

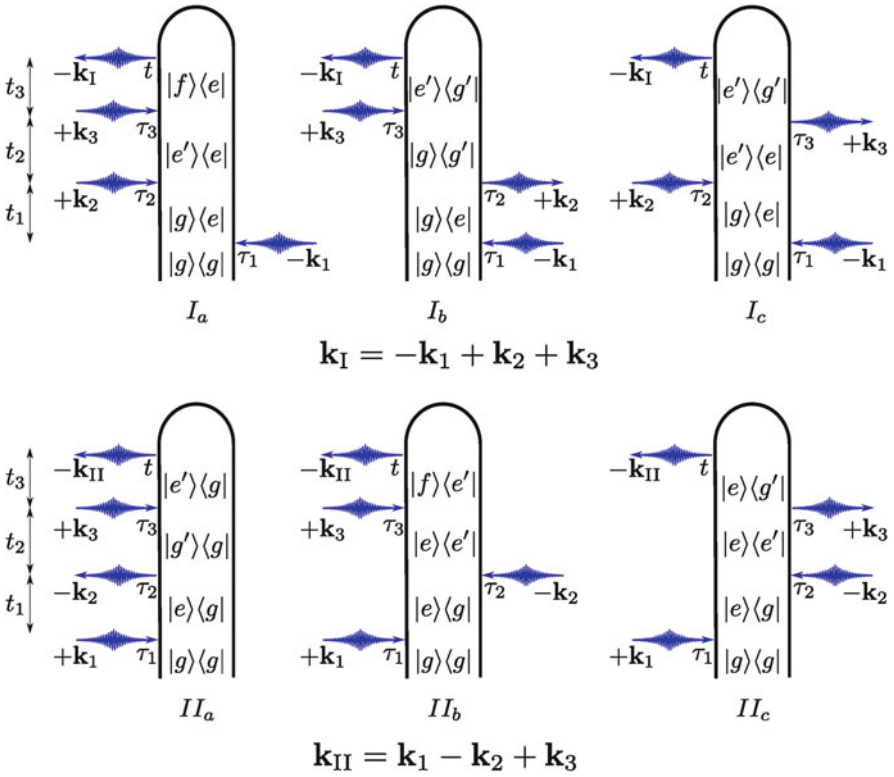

Fig. 2 Loop diagrams for the $\mathbf{k}_\mathrm{I}$ (*top row*) and $\mathbf{k}_\mathrm{II}$ (*bottom row*) signals. The system begins in the ground state (or more generally, a distribution of states as in (30)) and then interacts once with each of the four sequentially applied pulses. For diagram rules see [23]

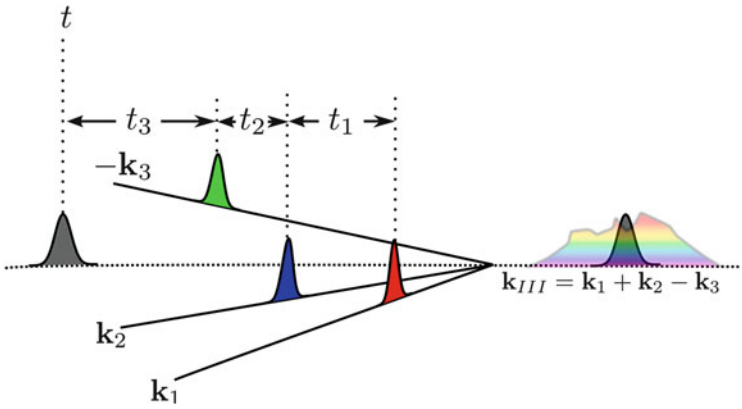

Fig. 3 Schematic depiction of the double quantum coherence technique. Four time-ordered pulses are shown impinging on the sample from different directions. The transmission of the final pulse is recorded as a function of the delay times or their conjugate frequencies. Figure taken from [24]

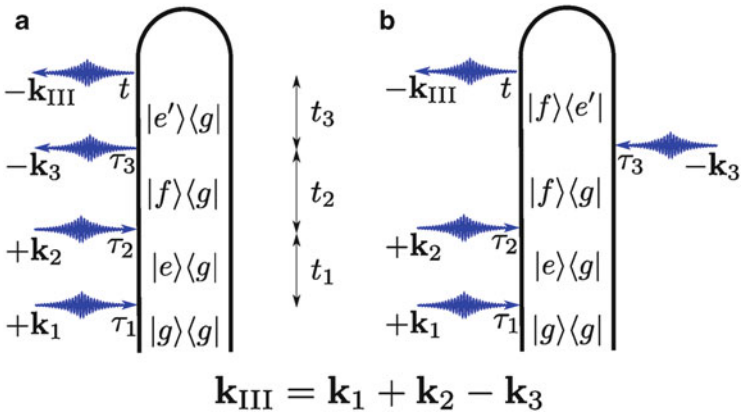

Fig. 4 The two loop diagrams contributing to the $\mathbf{k}_{\mathrm{III}}$ (DQC) signal. The system begins in the ground state (or more generally, a distribution of states as in (30)) and then interacts once with each of the four sequentially applied pulses. Note that the phase choice for this signal ($\mathbf{k}_{\mathrm{III}} = +\,\mathbf{k}_1 + \mathbf{k}_2 - \mathbf{k}_3$) guarantees that the second excitation manifold is reached and provides resonances between the ground state and this manifold

From the diagrams in Fig. 4, one can immediately obtain the time-domain signals:

$$\begin{aligned} S_{\mathbf{k}_{\mathrm{III}}}(\Lambda) = \; & \Im \int dt \int_0^\infty dt_3 dt_2 dt_1 \tilde{\mathcal{E}}_4(t-\bar{\tau}_4) e^{i\omega_4(t-\bar{\tau}_4)} \tilde{\mathcal{E}}_3(t-t_3-\bar{\tau}_3) e^{i\omega_3(t-t_3-\bar{\tau}_3)} \\ & \times \tilde{\mathcal{E}}_2(t-t_3-t_2-\bar{\tau}_2) e^{i\omega_2(t-t_3-t_2-\bar{\tau}_2)} \tilde{\mathcal{E}}_1(t-t_3-t_2-t_1-\bar{\tau}_1) \\ & \times e^{-i\omega_1(t-t_3-t_2-t_1-\bar{\tau}_1)} \left[\left\langle \psi_0 \middle| \hat{U}^\dagger(t_1+t_2+t_3) \hat{V}\, \hat{U}\,(t_3) \hat{V}\, \hat{U}\,(t_2) \hat{V}^\dagger \hat{U}\,(t_1) \hat{V}^\dagger \middle| \psi_0 \right\rangle \right. \\ & \left. - \left\langle \psi_0 \middle| \hat{U}^\dagger(t_1+t_2) \hat{V}\, \hat{U}^\dagger(t_3) \hat{V}\, \hat{U}\,(t_2+t_3) \hat{V}^\dagger \hat{U}\,(t_1) \hat{V}^\dagger \middle| \psi_0 \right\rangle \right] e^{i(\phi_1+\phi_2-\phi_3-\phi_4)} \end{aligned} \tag{10}$$

It is important to note that this signal carries a phase $\phi_1 + \phi_2 - \phi_3 - \phi_4$ which, when randomly averaged, causes the signal to vanish. Observing this signal therefore requires phase control of the pulses. For pulses of finite duration, the distinction between the actual interaction times and delays between successive interaction times (the τ_p and t_p, respectively) and the central times of the pulse envelopes and delays between successive central times (the $\bar{\tau}_p$ and $\bar{t}_p$, respectively) must be made. The former are dummy variables of integration whereas the latter are control parameters which determine the signal. It is common to perform such experiments with very short, well-separated pulses. The resulting impulsive signal is then well parameterized by the interpulse delay times ($\bar{t}_1$, $\bar{t}_2$, and $\bar{t}_3$).

To understand the impulsive signal better, we may replace all τ_p by $\bar{\tau}_p$ and t_p by $\bar{t}_p$ in Fig. 4. The signal may be Fourier transformed with respect to any or all of these delays. From the diagrams, we can see that transforming with respect to $\bar{t}_2$ ($\bar{t}_1$) reveals resonances at double (single) excitations from the ground state

whereas the t_3 resonances contain single excitations from the ground state or double excitations from the single-excitation manifold depending on the diagram. We can therefore fix one of $\bar{t}_1$ or $\bar{t}_3$ and transform with respect to the other two time arguments to obtain a two-dimensional frequency plot which reveals correlations between the double excitations and single excitations (either from the ground state or the single-excitation manifold). We denote this impulsive signal by a 0 superscript:

$$\begin{aligned} S^0_{\mathbf{k}_{\mathrm{III}}}(\bar{t}_3,\bar{t}_2,\bar{t}_1) = {} & \mathcal{E}_4\mathcal{E}_3\mathcal{E}_2\mathcal{E}_1 e^{-\mathrm{i}\omega_1\bar{t}_1-\mathrm{i}(\omega_1+\omega_2)\bar{t}_2-\mathrm{i}(\omega_1+\omega_2+\omega_3)\bar{t}_3}\delta(\omega_1+\omega_2-\omega_3-\omega_4) \\ & \times\left[\left\langle\psi_0\middle|\hat{U}^\dagger(\bar{t}_1+\bar{t}_2+\bar{t}_3)\hat{V}\,\hat{U}\,(\bar{t}_3)\hat{V}\,\hat{U}\,(\bar{t}_2)\hat{V}^\dagger\hat{U}\,(\bar{t}_1)\hat{V}^\dagger\middle|\psi_0\right\rangle\right. \\ & \left.-\left\langle\psi_0\middle|\hat{U}^\dagger(\bar{t}_1+\bar{t}_2)\hat{V}\,\hat{U}^\dagger(\bar{t}_3)\hat{V}\,\hat{U}\,(\bar{t}_2+\bar{t}_3)\hat{V}^\dagger\hat{U}\,(\bar{t}_1)\hat{V}^\dagger\middle|\psi_0\right\rangle\right]. \end{aligned} \tag{11}$$

The signal is then Fourier transformed:

$$S_{\mathbf{k}_{\mathrm{III}}}(\Omega_3,\Omega_2,\Omega_1) = \int d\bar{t}_3 d\bar{t}_2 d\bar{t}_1 S_{\mathbf{k}_{\mathrm{III}}}(\bar{t}_3,\bar{t}_2,\bar{t}_1)e^{\mathrm{i}(\Omega_3\bar{t}_3+\Omega_2\bar{t}_2+\Omega_1\bar{t}_1)}, \tag{12}$$

in order to reveal resonances better. Finite pulse envelopes may now be incorporated and, when the correlation functions are expanded in material eigenstates, we obtain

$$\begin{aligned} S_{\mathbf{k}_{\mathrm{III}},\mathrm{a}}(\Omega_3,\Omega_2,\Omega_1) = {} & \sum_{fe'e}\frac{\widetilde{\mathcal{E}}_4^*\left(\omega_4-\omega_{e'g}\right)V_{ge'}\widetilde{\mathcal{E}}_3^*\left(\omega_3-\omega_{fe'}\right)V_{e'f}\widetilde{\mathcal{E}}_2\left(\omega_3-\omega_{fe}\right)V_{fe}}{\left(\Omega_3-\omega_{e'g}+\mathrm{i}\gamma_{e'g}\right)\left(\Omega_2-\omega_{fg}-\mathrm{i}\gamma_{fg}\right)} \\ & \times\frac{\widetilde{\mathcal{E}}_1\left(\omega_1-\omega_{eg}\right)V_{eg}}{\left(\Omega_1-\omega_{eg}-\mathrm{i}\gamma_{eg}\right)}, \end{aligned} \tag{13}$$

$$\begin{aligned} S_{\mathbf{k}_{\mathrm{III}},\mathrm{b}}(\Omega_3,\Omega_2,\Omega_1) = {} & \sum_{fe'e}\frac{\widetilde{\mathcal{E}}_4^*\left(\omega_4-\omega_{fe'}\right)V_{e'f}\widetilde{\mathcal{E}}_3^*\left(\omega_3-\omega_{e'g}\right)V_{ge'}\widetilde{\mathcal{E}}_2\left(\omega_3-\omega_{fe}\right)V_{fe}^*}{\left(\Omega_3-\omega_{fe'}+\mathrm{i}\gamma_{fe'}\right)\left(\Omega_2-\omega_{fg}-\mathrm{i}\gamma_{fg}\right)} \\ & \times\frac{\widetilde{\mathcal{E}}_1\left(\omega_1-\omega_{eg}\right)V_{eg}^*}{\left(\Omega_1-\omega_{eg}-\mathrm{i}\gamma_{eg}\right)}, \end{aligned} \tag{14}$$

where $\omega_{ij}\equiv\varepsilon_i-\varepsilon_j$ and γ_{ij} are the frequency and the dephasing rate of the $i\rightarrow j$ transition, respectively. The contributions from diagrams a and b may be read directly from Fig. 4. The numerator contains all transition dipoles as well as the field-envelope factors which determine the material transitions permitted by the bandwidths. The denominators contain the resonance factors for these material transitions.

At the level of Hartree theory, which assumes *independent electrons,* the DQC signal vanishes because of interference. TDHF (or TDDFT) goes one step further and provides a picture of *independent transitions* (quasiparticles). Here the signal no longer vanishes, but shows a limited number of peaks. When correlation effects are fully incorporated, the many-electron wavefunctions become superpositions of states with different numbers and types of e-h pairs. The Ω_2 and Ω_3 axes then contain many more peaks corresponding to all many-body states (in the frequency range spanned by the pulse bandwidths), which project into the doubly-excited states. Thus, along Ω_2 the peaks are shifted, reflecting the level of theory used to describe electron correlations. Along Ω_3, the effect is even more dramatic and new peaks show up corresponding to splittings between various levels. We show the X-ray DQC signals of formamide as an example in Sect. 4.3. This highly-resolved two-dimensional spectrum provides an invaluable direct dynamical probe of electron correlations (both energies and wavefunctions) [25, 26].

2.3 Stimulated X-Ray Raman Spectroscopy

Linear techniques contain the single-excitation spectrum whereas we have just seen that the DQC ($\mathbf{k}_{\mathrm{III}}$) signal gives access to the double-excitation spectrum. Both of these spectra thus characterize the intermanifold structure of the material (the transitions between manifolds). We may obtain a window into the intramanifold structure (transitions within the same manifold) by using the stimulated Raman signal (SXRS in the X-ray regime) [2, 27, 28]. As with the DQC signal, this technique is third-order (involving four interactions with the electromagnetic field). However, rather than four sequential pulses, 1D-SXRS employs only two pulses, each of which interacts twice with the material. This process is shown diagramatically in Fig. 5. Note that, because the pair of interactions with each pulse are of opposite Hermiticity, the overall absolute phase is $\phi_1 - \phi_1 + \phi_4 - \phi_4 = 0$ and this technique therefore does not require phase control to obtain a finite signal.

The first pulse in the SXRS process creates a superposition of excited states in the ground state manifold. After a controlled delay period, the sample interacts with the second pulse which returns the system to the original state.

For calculating this signal, we find it more convenient to work with the actual interaction times τ rather than the time delays t_j $(j = 1, 2, 3)$. It is straightforward to write down a time-domain expression for the 1D-SXRS signal directly from the diagrams in Fig. 5. Its form is similar to (10):

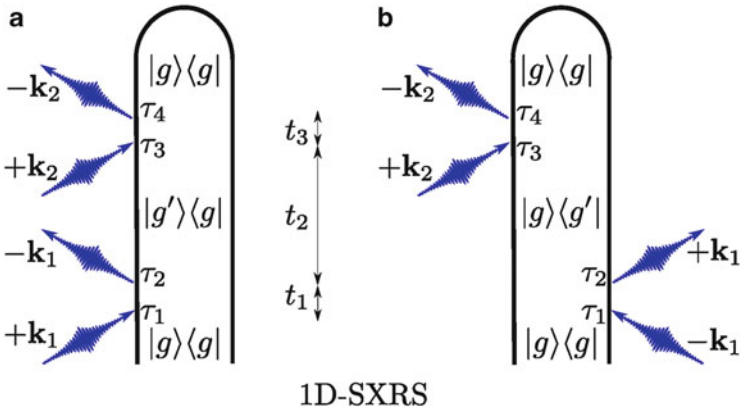

Fig. 5 Two contributing loop diagrams (labeled as a, b in the figure) for the 1D-SXRS technique. As before, the system begins in the ground state but this time interacts twice with each of the two sequentially applied pulses. Note that the phase for this signal ($\phi_1 - \phi_1 + \phi_2 - \phi_2$) automatically vanishes, making the signal incoherent. The first pulse prepares a wavepacket of valence excitations that evolves for the interpulse delay period before being probed with the second pulse

$$\begin{aligned} S_{\mathrm{SXRS}}(\Lambda) = \Im \int d\tau_4 \int_{-\infty}^{\tau_4} d\tau_3 \int_{-\infty}^{\tau_3} d\tau_2 \int_{-\infty}^{\tau_2} d\tau_1 (\mathrm{i})^3 \mathcal{E}_2^*(\tau_4)\mathcal{E}(\tau_3) \\ \times \Big[\mathcal{E}_1^*(\tau_2)\mathcal{E}_1(\tau_1)\big\langle \psi_0 \big| \hat{V}(\tau_4)\hat{V}^\dagger(\tau_3)\hat{V}(\tau_2)\hat{V}^\dagger(\tau_1)\big|\psi_0\big\rangle \\ + \mathcal{E}_1(\tau_2)\mathcal{E}_1^*(\tau_1)\big\langle \psi_0 \big| \hat{V}^\dagger(\tau_1)\hat{V}(\tau_2)\hat{V}(\tau_4)\hat{V}^\dagger(\tau_3)\big|\psi_0\big\rangle \Big] \end{aligned} . \tag{15}$$

Because the interactions are paired within a given pulse and the pulses are temporally well-separated, we may extend the upper limit for the τ_2 integration to infinity. This permits us to define formally the polarizability $\hat{\alpha}_p$ induced by the pth pulse:

$$\hat{\alpha}_p(\Lambda_p) \equiv \mathrm{i} \int_{-\infty}^{\infty} d\tau \int_{-\infty}^{\tau} d\tau' \hat{V}(\tau)\hat{V}^\dagger(\tau')\mathcal{E}_p^*(\tau)\mathcal{E}_p(\tau'), \tag{16}$$

which is both a material operator and a function of Λ_p, the parameters of the pth pulse. In the limit of ultrashort pulses, the primary Λ_p parameter is the central pulse time $\bar{\tau}_p$ and the principal control variable for the 1D-SXRS signal is the interpulse delay $T = \bar{\tau}_2 - \tau_1$ and the signal is recast as

$$S(T) = \Re\big[\langle \hat{\alpha}_2(T)\hat{\alpha}_1(0)\rangle + \big\langle \hat{\alpha}_1^*(0)\hat{\alpha}_2(T)\big\rangle\big], \tag{17}$$

where we have set $\bar{\tau}_1 = 0$ as the origin of time. Taking matrix elements in the Hamiltonian eigenbasis gives the sum-over-states expression

$$\alpha_{p,g'g''} \equiv \mathrm{i}\sum_e V_{g'e}V_{eg''}\int_{-\infty}^{\infty} d\tau_2 \int_{-\infty}^{\tau_2} d\tau_1 \mathcal{E}_p^*(\tau_2)\mathcal{E}_p(\tau_1) e^{\mathrm{i}\left(\omega_p-\omega_{eg'}+\mathrm{i}\gamma_e\right)\tau_2-\mathrm{i}\left(\omega_p-\omega_{eg''}+\mathrm{i}\gamma_e\right)\tau_1}. \tag{18}$$

Here, ω_{ev} is the frequency for the $v \to e$ transition, and γ_e is the inverse of the excitation lifetime. In some applications, it may be more convenient to work in the frequency domain where the spectral (rather than temporal) field envelopes are used. This can be accomplished by explicitly writing the propagators in (16) and replacing the temporal field envelopes by their Fourier transforms yielding

$$\begin{aligned}\hat{\alpha}_p = \int \frac{d\omega d\omega_p d\omega'_p}{(2\pi)^3} \mathcal{E}_p^*\left(\omega'_p\right)\mathcal{E}_p\left(\omega_p\right) \\ \frac{1}{\omega+\omega_p-\omega'_p-\hat{H}_0+\mathrm{i}\eta}\hat{V}\frac{1}{\omega+\omega_p-\hat{H}_0+\mathrm{i}\eta}\hat{V}^\dagger\frac{1}{\omega-\hat{H}_0+\mathrm{i}\eta}.\end{aligned} \tag{19}$$

Expanding in eigenstates then gives the matrix elements

$$\alpha_{p,g',g''} = \sum_e \frac{V_{g'e}V_{eg''}}{2\pi}\int d\omega \frac{\mathcal{E}_p^*(\omega)\mathcal{E}_p\left(\omega+\omega_{g'g''}\right)}{\omega+\omega_p-\omega_{eg'}+\mathrm{i}\gamma_e}. \tag{20}$$

Starting from (20), we may now write the frequency-domain 1D-SXRS signal as

$$\begin{aligned}S_{\mathrm{SXRS}}(\Omega) = & -\sum_{g'}\frac{\Re\left(\alpha_{2;gg'}\alpha_{1;g'g}\right)\left(\gamma_{g'}-\mathrm{i}\Omega\right)+\Im\left(\alpha_{2;gg'}\alpha_{1;g'g}\right)\omega_{g'g}}{\gamma_{g'}^2-2\mathrm{i}\gamma_{g'}\Omega-\Omega^2+\omega_{g'g}^2} \\ & +\frac{\Re\left(\alpha_{1;gg'}^*\alpha_{2;g'g}\right)\left(\gamma_{g'}-\mathrm{i}\Omega\right)+\Im\left(\alpha_{1;gg'}^*\alpha_{2;g'g}\right)\omega_{g'g}}{\gamma_{g'}^2-2\mathrm{i}\gamma_{g'}\Omega-\Omega^2+\omega_{g'g}^2},\end{aligned} \tag{21}$$

which is the Fourier transform of (15) with respect to the interpulse delay T. The first term in (17) and (21) can be viewed as a valence wavepacket $\alpha_1|\psi_0\rangle$, created by pulse 1, which propagates forward in time T and overlaps with a wavepacket $\langle\psi_0|\alpha_2$ created by pulse 2. The second term can be viewed as a wavepacket $\alpha_2|\psi_0\rangle$ created by pulse 2 propagating backward in time $-T$ to overlap with the wavepacket $\langle\psi_0|\alpha_1^\dagger$ created by pulse 1. The SXRS technique creates a wavepacket of valence excitations and, after a specified delay period T, probes this wavepacket so as to track its evolution. A 2D extension of this 1D-SXRS in which three successive pulses are employed is shown in Fig. 6. The resulting signal $S_{\mathrm{SXRS}}(\Omega_1, \Omega_2)$ requires expansion to fifth order in the field and carries information about correlations between dynamics during the two delay periods which would not be available in 1D-SXRS [29]. This technique can also be applied following a pump pulse which prepares the system by exciting a core hole. The subsequent SXRS process then

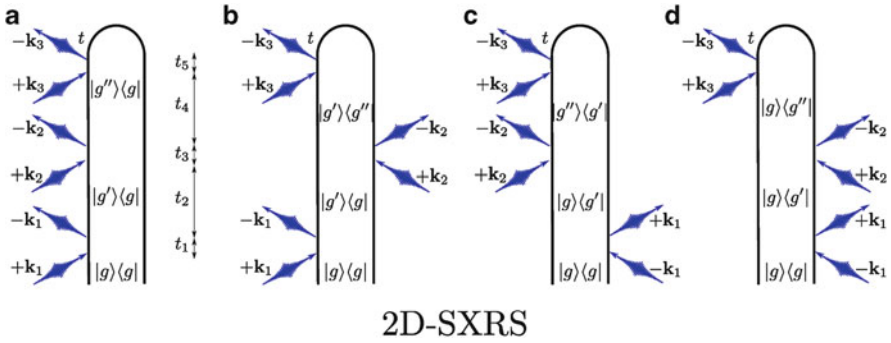

Fig. 6 Four contributing loop diagrams (labeled as a, b, c, d in the figure) for the 2D-SXRS technique. The system begins in the ground state then interacts twice with each of three sequentially applied pulses. As with 1D-SXRS, the phase vanishes and the signal is incoherent. The additional delay period allows information about couplings and correlations of valence excitations that are not available in 1D-SXRS to be extracted

creates a valence excitation and tracks its motion along the potential energy surface produced by the core hole [30].

2.4 Correlation Function Expressions for SXRS Signals

In the previous section, we defined $\hat{\alpha}_p$ by combining two time-dependent dipole interactions (excitation and de-excitation) as well as the pulse envelope (see (16)). All time-dependence is then encoded into the polarizability $\hat{\alpha}_p$ and the result (see (17)) is compact but too complicated. Although perfectly suited to an expansion in eigenstates, as shown in the previous section, this form of $\hat{\alpha}_p$ suffers from some drawbacks. Recalling the definition of operator time-dependence in the interaction picture (see (7)), we see that there are three time propagation periods. This definition for the polarizability therefore contains material propagation both for interpulse and intrapulse time periods. Because these occur on two different timescales, a separation permits different treatments. In particular, it is then possible to treat the intrapulse propagation perturbatively while preserving the full form of the longer-time interpulse propagator.

That the two impinging fields are temporally well-separated guarantees that there exist $\tilde{\tau}_{1i}$ and $\tilde{\tau}_{1f}$ ($\tilde{\tau}_{2i}$ and $\tilde{\tau}_{2f}$), the initial and final times of the first (second) pulse. The $\tilde{\tau}_{pi}$ and $\tilde{\tau}_{pf}$ are used to bound the possible interaction times with the pth pulse. They are a formal tool used to separate the interpulse propagation from the intrapulse propagation and can be unambiguously defined as

$$\begin{aligned}\tilde{\tau}_{pi} &\equiv \sup\{t : E_p(t') = 0 \forall t' < t\} \\ \tilde{\tau}_{pf} &\equiv \inf\{t : E_p(t') = 0 \forall t' > t\}\end{aligned}, \tag{22}$$

making the procedure unarbitrary. Explicitly writing the time propagators in an exponential form, we can recast the material correlation function pertaining to diagram a in Fig. 5 (diagram b in Fig. 5 follows similarly so we exclude it for the sake of brevity) as

$$\left\langle e^{i\hat{H}_0\tau_4}\hat{V}e^{-i\hat{\hat{H}}_0(\tau_4-\tau_3)}\hat{V}^\dagger e^{-i\hat{H}_0\tau_3}e^{i\hat{H}_0\tau_2}\hat{V}e^{-i\hat{\hat{H}}_0(\tau_2-\tau_1)}\hat{V}^\dagger e^{-i\hat{H}_0\tau_1}\right\rangle. \tag{23}$$

Inserting identities to separate the propagation at $\tilde{\tau}$ then gives

$$\begin{aligned}&\left\langle e^{i\hat{H}_0\tilde{\tau}_{2f}}e^{i\hat{H}_0(\tau_4-\tilde{\tau}_{2f})}\hat{V}e^{-i\hat{\hat{H}}_0}(\tau_4-\tau_3)\hat{V}^\dagger e^{-i\hat{H}_0(\tau_3-\tilde{\tau}_{2i})}e^{i\hat{H}_0(\tilde{\tau}_{2i}-\tilde{\tau}_{1f})}\right. \\ &\left.\times e^{i\hat{H}_0(\tau_2-\tilde{\tau}_{1f})}\hat{V}e^{-i\hat{\hat{H}}_0}(\tau_2-\tau_1)\hat{V}^\dagger e^{-i\hat{H}_0(\tau_1-\tilde{\tau}_{1i})}e^{-i\hat{H}_0\tilde{\tau}_{1i}}\right\rangle.\end{aligned} \tag{24}$$

We thus define the polarizability as

$$\hat{\alpha}_p(\tilde{\tau}_{pf},\tilde{\tau}_{pi}) \equiv i\int_{-\infty}^{\infty}d\tau\int_{-\infty}^{\tau}d\tau' e^{i\hat{H}_0(\tau-\tilde{\tau}_{pf})}\hat{V}e^{-i\hat{\hat{H}}_0(\tau-\tau')}\hat{V}^\dagger e^{-i\hat{H}_0(\tau'-\tilde{\tau}_{pi})}\mathcal{E}^*_p(\tau)\mathcal{E}_p(\tau'). \tag{25}$$

where the properties of the pulse and the choice of the $\tilde{\tau}$ guarantee the appropriate sign of the propagators. This is an operator in the valence excitation space. It may be recast in the frequency domain as before:

$$\begin{aligned}\hat{\alpha}_p(\tilde{\tau}_{pf},\tilde{\tau}_{pi}) \quad &= \int\frac{d\omega d\omega_p d\omega'_p}{(2\pi)^3}\mathcal{E}^*_p(\omega'_p)\mathcal{E}_p(\omega_p)e^{-i\omega(\tilde{\tau}_{pf}-\tilde{\tau}_{pi})}e^{-i(\omega_p-\omega'_p)\tilde{\tau}_{pf}} \\ &\times\frac{1}{\omega+\omega_p-\omega'_p-\hat{H}_0+i\eta}\hat{V}\frac{1}{\omega+\omega_p-\hat{H}_0+i\eta}\hat{V}^\dagger\frac{1}{\omega-\hat{H}_0+i\eta},\end{aligned} \tag{26}$$

and may differ from (19) in the appearance of $\tilde{\tau}_p$-dependent phase-factors. Note that, because the choice of the $\tilde{\tau}_p$ is set by the pulse shape, their appearance on the left hand side is not necessary and we merely include them for clarity. With this definition, the contribution to the signal from diagram a in Fig. 5 is

$$S_a = \Re\left[\left\langle e^{i\hat{H}_0\tilde{\tau}_{2f}}\hat{\alpha}_2(\tilde{\tau}_{2f},\tilde{\tau}_{2i})e^{-i\hat{H}_0(\tilde{\tau}_{2i}-\tilde{\tau}_{1f})}\hat{\alpha}_1(\tilde{\tau}_{1f},\tilde{\tau}_{1i})e^{-i\hat{H}_0\tilde{\tau}_{1i}}\right\rangle\right]. \tag{27}$$

Defining the duration of the pth pulse $t_p \equiv \tilde{\tau}_{pf} - \tilde{\tau}_{pi}$ and the interpulse delay $T \equiv \tilde{\tau}_{2i} - \tilde{\tau}_{1f}$ we have, in the limit of well-separated pulses, $T >> t_p\, p \in \{1,2\}$. Assuming that, having accounted for the finite pulse duration in the definition of α, we may take $t_p \to 0$ for the purposes of the free evolution in (27), the signal becomes

$$S_{\mathrm{a}}(T) = \Re\left[\left\langle e^{\mathrm{i}\hat{H}_0 T}\hat{\alpha}_2 e^{-\mathrm{i}\hat{H}_0 T}\hat{\alpha}_1\right\rangle\right] = \Re[\langle\hat{\alpha}_2(T)\hat{\alpha}_1(0)\rangle], \tag{28}$$

where we have set $\tilde{\tau}_{1i} = \tau_{1f}$ as the zero point of time and the last equality defines the interaction picture polarizability $\alpha_p(t)$. Note that this expression for $S_a(T)$ matches the first term in (17) (with the second term standing for $S_{\mathrm{b}}(T)$). Besides being necessary for certain applications, the separation of interpulse and intrapulse propagations prominently features the dependence on the key time parameter, the interpulse delay T. All other parameters defining the pulses are encoded in the definition of the $\hat{\alpha}_p$. We pause to recall that the only assumption necessary in reaching (28) (just as for (17)) is that the interpulse delay be much larger than the temporal pulse widths.

It is important to note that separating interpulse and intrapulse propagation periods yields a formally identical expression and may seem an unnecessary artifice, as indeed it is within an eigenstate representation. The utility then is manifest when the eigenstates are prohibitively expensive to calculate. For example, in the configuration interaction representation, states are expanded in a basis consisting of the many-body ground state (the orbitals being filled up to some maximum energy level) and excitations on this ground state obtained by successively higher orders of electron creation-annihilation operator pairs:

$$|\psi\rangle = |g\rangle + \sum_{ij} C_{ij}\hat{c}_i^{\dagger}\hat{c}_j|g\rangle + \ldots \tag{29}$$

Because the material may generally be taken to begin an experiment in the many-body ground state, perturbative treatment of nonlinear spectroscopies naturally produces such states. At low order, there are many fewer states in this treatment than in the full eigenbasis and a significant numerical speedup can be achieved. In order to exploit this form requires a similar recasting of the $\hat{\alpha}_p$ and this is explored in Sect. 4.2. Corresponding expressions for the 2D signal $s_{\mathrm{SXRS}}(T_2, T_1)$ (Fig. 6) are given in [29, 31].

2.5 *Discussion of Signals*

In the above sections we provided two different types of expressions for the DQC and SXRS signals. The first ((10) and (15)) are given in terms of time correlation functions of the dipole operator. This form is convenient for direct *ab initio* dynamic simulations of electrons and nuclei [31, 32]. It can take into account, e.g., in nonadiabatic dynamics, conical intersections, etc. Real-time time-dependent density functional theory can then be applied to calculate the signal. Alternatively, the second procedure ((13), and (17)–(20)) expands the correlation functions in molecular eigenstates. This is convenient for simpler models when only a few electronic states participate and for relatively small systems where the many-

body states can be computed. The sum-over-states expansions also facilitate interpretation of the resulting signal as the meaning of the various resonances is transparent in this form. Both the correlation function and sum-over-states forms may be displayed either in the time-domain (as a function of $\bar{t}_3, \bar{t}_2, \bar{t}_1$) or the frequency domain (as a function of the conjugate variables Ω_3, Ω_2, Ω_1). It is often useful to employ a mixed representation, e.g., $S(\Omega_1, t_2, \Omega_3)$, which is 2D in frequency and 1D in time so that correlations between resonances observed at the two frequencies can be observed and monitored as the time argument is allowed to vary. These techniques can therefore provide a high degree of selectivity and carry a rich abundance of information on the electronic and nuclear structure and dynamics.

Our correlation function expressions (10) and (15) are given by the expectation values with respect to $|\psi_0\rangle$. Alternatively, we may describe the system using the density matrix

$$\hat{\rho} = \sum_i P_i |\psi_i\rangle\langle\psi_i|, \tag{30}$$

whose dynamics is determined by the Liouville equation

$$\dot{\hat{\rho}} = -\mathrm{i}\big[\hat{H}, \hat{\rho}\big] - \mathrm{i}\big[\hat{H}_{\mathrm{int}}, \hat{\rho}\big]. \tag{31}$$

Here P_i is the probability that the system is found in state $|\psi_i\rangle$. When all degrees of freedom are treated at the Hamiltonian level, it is more convenient to remain in Hilbert space rather than recasting in Liouville space (as is done in [1]). This facilitates computations because Hilbert space has far fewer dimensions than the associated Liouville space. In these cases, the above equations may still be utilized formally with appropriate choice of the P_i. In terms of the density matrix, the expectation value of the dipole is given by

$$\langle\hat{\mu}(t)\rangle \equiv \mathrm{Tr}[\hat{\mu}(t)\hat{\rho}(t)], \tag{32}$$

and we may expand $\rho(t)$ perturbatively to arbitrary order in the interaction Hamiltonian

$$\begin{aligned}\hat{\rho}^{(n)}(t) = (\mathrm{i})^n \int d\mathbf{r}_n \ldots d\mathbf{r}_1 \int_{t_0}^{t} d\tau_n \ldots \int_{t_0}^{\tau_2} d\tau_1 E(\mathbf{r}_n, \tau_n) \ldots E(\mathbf{r}_1, \tau_1) \\ \times [\hat{\mu}(\tau_n), [\ldots, [\hat{\mu}(\tau_1), \hat{\rho}]] \ldots].\end{aligned} \tag{33}$$

One can then include the effects of coupling to a bath by introducing further terms to the equation of motion – see (30) – which represent the dissipation of system excitations into the bath. One numerically inexpensive strategy to implement this idea is the stochastic Liouville equation (SLE)

$$\dot{\hat{\rho}} = -\mathrm{i}\left[\hat{H}, \hat{\rho}\right] + \hat{L}_b\hat{\rho}\,, \tag{34}$$

where $\hat{L}_b$ represents the stochastic Markovian dynamics of the bath. The SLE is an equation for the field-free evolution of the joint system-bath density matrix and can be used to write a reduced equation of motion for the system density matrix which incorporates (perturbatively) the effects of the bath. This can, for example, be done at the level of the Lindblad equation [33, 34]. The model for the bath and system-bath coupling determines the form of $\hat{L}_b$. Examples are the n-state jump and Brownian oscillator models [1, 35].

Equations (32) and (33) give one procedure for obtaining the nth order signal and generates 2^n terms when the commutators with the initial density matrix are fully expanded. Equations (8) and (7) offer an alternative procedure which, upon expanding the time-ordered exponentials in the $\hat{U}^{(\dagger)}(t)$, generates $n+1$ terms at nth order. The latter procedure obviously involves less terms and it is often numerically preferable to propagate the wavefunction rather than the density matrix. On the other hand, only a density matrix based procedure can properly account for system-bath interactions and the dephasing-effects these cause. Moreover, the real-time interpulse delays appear more naturally in a density-matrix formulation. Equations (32) and (33) are therefore more expensive to implement but provide a more intuitive picture and are necessary when a proper account of system-bath dynamics is crucial [1].

As previously mentioned, the nth-order expansion of the density matrix as per (33) generates 2^n terms. Interpreting the resulting signal requires expanding the interaction Hamiltonian into its constituent terms (which are, in the rotating wave, ($\hat{\mathcal{E}}^\dagger\hat{V}$ and $\hat{\mathcal{E}}\hat{V}^\dagger$)). There are thus a total of 4^n terms which may be depicted diagrammatically (in the case of temporally overlapping fields, this is further complicated and leads to an additional factor of up to $(n+1)!$ representing permutations of the temporal order of field interactions). These diagrams represent different excitation and evolution pathways for the system density matrix and we refer to them as Liouville space pathways. This proliferation of terms (64 at 3rd order) with a variety of different resonances during different time periods makes the general problem of interpreting a signal quite difficult. Fortunately, the diagrams that contribute to an experimental signal can be reduced by various techniques (additionally, some diagrams vanish when the material begins the process in the ground state). Principally, experimentalists can exploit the phase-sensitivity of nonlinear signals to control the pathways taken by the system. Conceptually, the simplest method to accomplish this selectivity is to use a non-collinear beam geometry as depicted for the DQC technique in Fig. 3. In the large sample (relative to the light wavelength) limit, the spatial integrations give a delta function $\delta(-\mathbf{k}_4 \pm \mathbf{k}_3 \pm \mathbf{k}_2 \pm \mathbf{k}_1)$. This phase matching sets the directions along which a nonlinear signal may be detected and naturally separates the diagrams that contribute in particular directions [36]. Each wavevector $\mathbf{k}_4$ of the detected beam then selects a subset of diagrams as shown in Figs. 2 and 4. Alternatively, the same

degree of control can be achieved in a collinear beam geometry by controlling the phases of the various beams. A linear combination of measurements with different phases can then yield the desired signal with $\phi_4 = \pm\phi_3 \pm \phi_2 \pm \phi_1$ corresponding to the equivalent spatial-phase selection in the non-collinear arrangement [37, 38]. This technique is known as phase cycling [39] and is always employed in multidimensional NMR because the wavevectors are close to zero in radio frequencies [40]. In the infrared, visible, and X-ray regimes, both phase matching and phase cycling protocols for pathway selection are possible depending on experimental convenience.

So far, we have been concerned with processes in which the system is initially in the ground state. In the X-ray regime, techniques employed can then study resonances of core excitations in relation to this ground state as well as the evolution of valence excitations along the ground state potential surface. This procedure may be generalized to account for a more general initial density matrix as may be obtained from previous excitation or pumping of the system. A complete account of these more general techniques involves explicit incorporation of the pumping process and results in higher-order correlation functions [18, 30]. Although more complicated, these techniques open up the possibility of studying excited state resonances (as well their correlations) and tracking the motion of valence excitations in the presence of core holes.

The present formalism may be further utilized in electronic spectroscopies such as time-resolved photoelectron and Auger electron spectroscopy (TRPES and AES, respectively). These techniques provide an alternative toolbox that complements and supplements the optical techniques discussed here. In particular, TRPES has simplified selection rules compared to optical detection schemes (any orbital may be ionized and the transition dipole to the continuum states does not depend much on the precise continuum state and may be approximated as flat in certain regions). The probabilities for excitation to various continuum states still depend sensitively on the final molecular electronic state and one can therefore use knowledge of the continuum as a probe [41, 42]. On the other hand, AES has entirely different selection rules, being based on a Coulomb matrix element (rather than a transition dipole) and has been used to track the radiationless decay of photoexcited molecules [43]. Despite these differences, a very similar formalism can be applied, the only differences being in the operators in the correlation functions. This then allows the use of the array of simulation procedures discussed for electronic spectroscopies and, in particular, gives a straightforward way to incorporate bath dynamics and dissipation effects without explicitly including corresponding degrees of freedom at the Hamiltonian level [44].

3 Quantum Chemistry Methods

Signal expressions in Sect. 2 require the calculation of core excited states and transition dipole moments. Here we review the quantum chemistry methods that can be used in their simulation and present a few examples.

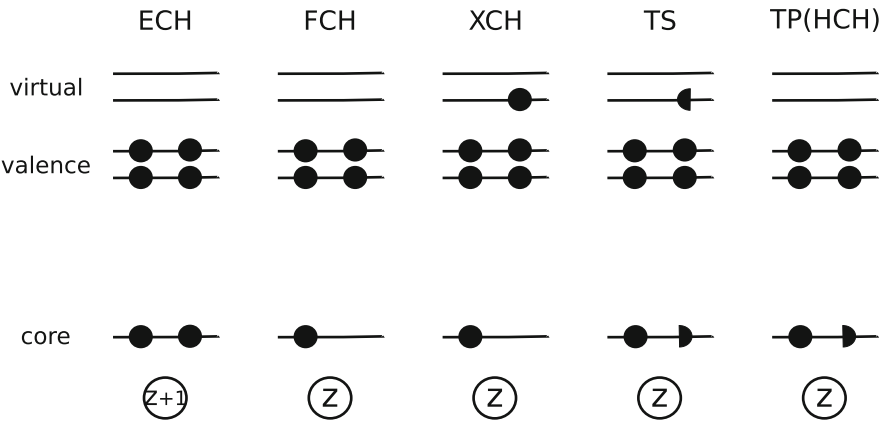

Fig. 7 Approximation schemes for core hole excitations. *ECH* equivalent core hole (Z+1) approximation, *FCH* full core hole approximation, *XCH* excited core hole approximation, *TS* transition state method, *TP*(*HCH*) transition potential method (half core hole approximation). *Full discs* represent electrons and *half discs* represent half electrons. *Numbers in circles* at the *bottom* represent nuclear charges, where Z is the number of electrons of the system

3.1 ΔSCF-Based Methods

3.1.1 Different Core Hole Approximations

An X-ray photon usually excites a core electron leaving a core hole in the system. Describing core holes properly is the primary task of resonant X-ray spectroscopy simulation. In Fig. 7 we show the most widely used approximation schemes for core holes [45]. The simplest is to represent a core hole as an additional nuclear charge.

This equivalent core hole (ECH) also known as (Z+1) approximation [46, 47] is adequate for deep core holes because for electrons in the exterior shells a deep core hole behaves as does a positive nuclear charge. It is simple to apply (no additional coding in standard quantum chemistry packages is necessary) and multiple core holes can also be easily represented by additional nuclear charges. However, it is a crude approximation which does not apply to shallow core holes. It further artificially changes the spin state of the system.

The ECH approximation was used in our early X-ray nonlinear spectroscopy simulations [48–52]. The photon echo signal $\mathbf{k}_\mathrm{I} = -\mathbf{k}_1 + \mathbf{k}_2 + \mathbf{k}_3$ of the para and ortho isomers of aminophenol was calculated in [48] (see Fig. 8). The second time delay t_2 is set to zero. The signals reveal the correlation between the O1s core excitations (Ω_1) and the N1s core excitations ($-\Omega_3$). The equivalent-core molecular orbitals corresponding to the three strong O1s XANES peaks (marked A, B, and C) are also shown. In a simple single orbital picture, orbital A is populated by the excited O1s electron in the lowest O1s excitation. The XANES signals are not sensitive to the corresponding core excited states, as can be seen from the top of Fig. 8. Although the orbitals corresponding to peak Bs of the two isomers look very

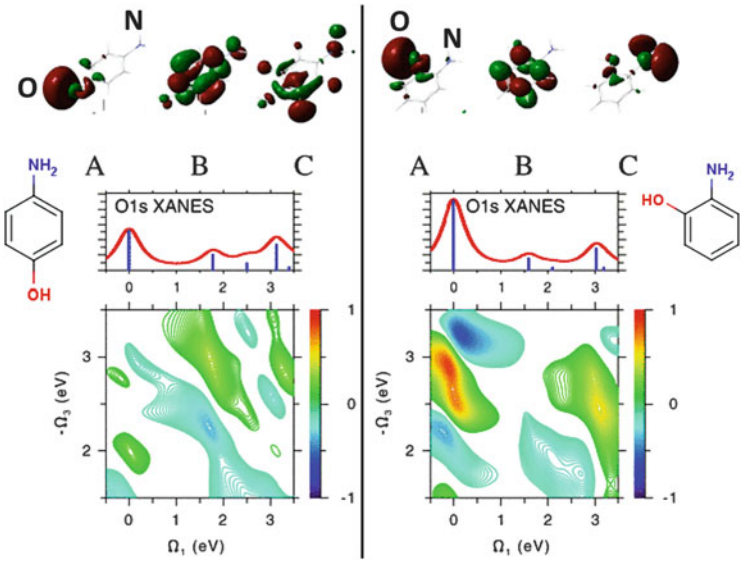

Fig. 8 Simulated O1s XANES and O1s/N1s photon echo crosspeak (at $t_2 = 0$) of para- (*left*) and ortho-aminophenol (*right*) with the ECH approximation. All single core excitation energies are shown as $\omega - \omega_j$, where ω_j is the lowest O1s or N1s excitation energy. Molecular orbitals populated by the promoted O1s electron for each of core-excited states contributing to the signal are show on the top. The positions of N and O atoms are labeled. Figure adapted from [48]

different, the two peak Bs are similar in energy and lineshape. This is because XANES only detects the local electronic structure of atoms. However, the photon echo signals show many differences. In the para isomer, the orbital corresponding to peak B is delocalized and extends from the O to N atom. So, the N1s and O1s core excitations corresponding to this orbital affect each other and generate a crosspeak (Fig. 8, left). However, in the ortho isomer, because the orbital corresponding to peak B vanishes in the surroundings of the N atom, the N1s and O1s core excitations corresponding to this orbital do not affect each other and thus we cannot see a crosspeak (Fig. 8, right). Although it is much stronger in O1s XANES of the para isomer, peak A contributes to a much weaker crosspeak than peak B. This is because the orbital corresponding to peak A in the para isomer is highly localized to the O atom and far away from the N atom. It is also understandable that peaks A and C produce much stronger crosspeaks of the ortho isomer than those of the para isomer because O and N atoms are closer in the ortho isomer. In all, photon echo signals carry detailed information about the wavefunctions of the core excited states involved in the experiment.

More than four decades ago Slater had proposed the transition state (TS) method for calculating core excitation energies. In this method the two orbitals involved in the transition are occupied by a half electron and solved self-consistently. The excitation energy is given by the difference between the two orbital energies [53, 54]. The excitation energy obtained in this way is accurate up to second

order in the occupation number changes of the transition orbitals. The transition state method is convenient and sufficiently accurate in many cases, but it is not suitable for calculating many excited states because of the nonorthogonality and self-consistent field (SCF) collapse of the excited states. An alternative is the transition potential method (TP) [55, 56], in which the potential corresponding to the transition hole state (a half electron on the hole orbital; see Fig. 7) is used to produce a set of orthogonal excited states. The excitation energy is determined by the differences between transition potential orbital energies. TP is widely used in X-ray absorption spectroscopy simulation [57].

Similar core hole approximations have been proposed in solid state physics. The half core hole approximation (HCH; see Fig. 7) is similar to the transition potential method, and the full core hole approximation (FCH; see Fig. 7) is similar to the direct exchange method (STEX) [58–60] in quantum chemistry (this is explained in detail in the next subsection). In FCH, the impact of the excited electron on the core hole is neglected. If it is included, we obtain the excited core hole approximation (XCH) [61]. We have used XCH combined with TDDFT to simulate X-ray double-quantum-coherence spectroscopy [24].

3.1.2 Static Exchange Method (STEX)

In Hartree–Fock theory, occupied orbitals often provide an adequate description for the ground state but virtual orbitals give a less satisfactory description of the excited states. Hunt and Goddard proposed to use the Hartree–Fock virtual orbitals of an (N−1)-electron system to represent the excited state orbitals of the corresponding N-electron system. This is known as the improved virtual orbital or N−1 approximation [58]. In STEX, the occupied orbitals of an N-electron core-excited system are also represented by the occupied orbitals of the (N−1)-electron ionic system with the corresponding core hole. A core electron is removed and a restricted open-shell Hartree–Fock (ROHF) calculation is carried out to obtain the occupied orbitals of the ionic system. A major difficulty is that the electrons often collapse to fill the core hole during the SCF calculation. This can be remedied by the maximum overlap method (MOM) [62], which is explained in detail in the following sections. However, even with MOM, the SCF iteration may converge to a wrong electronic state or even may not converge at all. To guide the SCF iteration towards the designated ionic state, a careful choice of the other SCF convergence parameters such as the damping and level-shifting factors [63–65] and many trial-and-error calculations with different initial guesses are usually necessary. New convergence schemes are required to improve the SCF calculations of such ionic states.

Once the occupied orbitals of the ionic state are obtained, a single electron is placed in a virtual orbital and the resulting open-shell singlet reads

$$\left|\Psi_{j,l}^{N}\right\rangle = \frac{1}{\sqrt{2}}\left(\hat{a}_{l\alpha}^{\dagger}\left|\Psi_{j\alpha}^{N-1}\right\rangle + \hat{a}_{l\beta}^{\dagger}\left|\Psi_{j\beta}^{N-1}\right\rangle\right), \tag{35}$$

where $\left|\Psi_{j\sigma}^{N-1}\right\rangle \equiv \hat{a}_{j\sigma}\left|\Psi_{\mathrm{ref}}^{N}\right\rangle$ and $\sigma = \alpha, \beta$ are spin states, j is the core orbital index, l is the virtual orbital index, $\left|\Psi_{\mathrm{ref}}^{N}\right\rangle$ is the N-electron neutral reference state, and $\hat{a}$ and $\hat{a}^{\dagger}$ are annihilation and creation operators, respectively. The excited orbitals within the N−1 approximation satisfy the eigenvalue equations:

$$\hat{F}_{\mathrm{STEX}}^{j}\psi_{l}^{j} = \varepsilon_{l}^{j}\psi_{l}^{j}, \tag{36}$$

where ψ_{l}^{j} is the exited orbital and ε_{l}^{j} is the corresponding orbital energy. The STEX Fock operator

$$\hat{F}_{\mathrm{STEX}}^{j} = \hat{h} + \sum_{i\neq j}^{\mathrm{occ}}\left(2\hat{J}_{i} - \hat{K}_{i}\right) + \hat{J}_{j} + \hat{K}_{j}, \tag{37}$$

is constructed using the orbitals of the (N−1)-electron ionic system. $\hat{h}$ is the single particle Hamiltonian (kinetic plus nuclear attraction part) and $\hat{J}_j$ and $\hat{K}_j$ are the Coulomb and exchange operators for the core orbital j, respectively:

$$\begin{aligned} \hat{J}_{j}(1) &= \int \mathrm{d}\mathbf{r}_{2}\psi_{j}^{*}(2)r_{12}^{-1}\psi_{j}(2), \\ \hat{K}_{j}(1)\psi_{l}(1) &= \left[\int \mathrm{d}\mathbf{r}_{2}\psi_{j}^{*}(2)r_{12}^{-1}\psi_{l}(2)\right]\psi_{j}(1). \end{aligned} \tag{38}$$

The eigenvectors of $\hat{F}_{\mathrm{STEX}}^{j}$ are not orthogonal to the occupied orbitals of the (N−1)-electron ionic system, and an orthogonalization procedure is necessary. We can use the projection operator

$$\hat{P}^{j} = \sum_{k\neq j}^{\mathrm{occ}}\left|\psi_{k}^{j}\right\rangle\left\langle\psi_{k}^{j}\right|, \tag{39}$$

to project out all occupied orbitals of the (N−1)-electron ionic system and solve the projected STEX equation

$$\left(\hat{1} - \hat{P}^{j}\right)\hat{F}_{\mathrm{STEX}}^{j}\left(\hat{1} - \hat{P}^{j}\right)\psi_{l}^{j} = \varepsilon_{l}^{j}\psi_{l}^{j}. \tag{40}$$

The solutions of this equation should serve as a good approximation to the excited orbitals. The core excitation energy is finally given by

$$\omega_{j,l} = \mathrm{IP}_j + \varepsilon_{j,l}, \tag{41}$$

where IP_j is the ionization potential of the core electron j (determined from the energy differences of the (N−1)-electron ionic system and the N-electron neutral system).

STEX is a single excitation theory in which particle and hole are independent. Channel interaction can be included by diagonalizing the configuration interaction matrix in the space of linear combinations of different single excitation channels. This extension is known as the STEX-CIS (configuration interaction singles) method. Double excitations can also be treated with a STEX Hamiltonian based on the (N−2)-electron ionic system, but the SCF convergence problem is more serious and the spin coupling schemes are complicated [66].

State-to-state transition dipoles are necessary in order to simulate the nonlinear X-ray spectroscopy signals. Because the STEX orbitals are not orthogonal to the MOs of the N-electron system, Löwdin's rule [67] may be used for calculating the transition dipoles between two states with nonorthogonal single particle orbitals. The transition dipoles for single excitations are

$$\left\langle \Psi_{\mathrm{A}} \middle| \hat{d} \middle| \Psi_{\mathrm{B}} \right\rangle = \sum_{m,n}^{N_{\mathrm{config.}}} a_m b_n \sum_{i,j} (-1)^{i+j} d_{ij}^{mn} \mathrm{Minor}(\mathbf{S}^{mn})_{ij}, \tag{42}$$

where $\Psi_{\mathrm{A,B}}$ are two excited states with nonorthogonal single particle orbitals, $\hat{d}$ is the transition dipole operator, and a_m and b_n are configuration interaction (CI) coefficients for different single excitation configurations (m and n) of state A and B, respectively.

$$d_{ij}^{mn} = \sum_{p,q} c_{ip,m,\mathrm{A}}^{*} c_{jq,n,\mathrm{B}} \int \phi_p^{*} \hat{d}\, \phi_q \mathrm{d}\tau, \tag{43}$$

is the transition dipole matrix between the single excitation configurations m and n, $c_{ip,m,\mathrm{A}}$ and $c_{j,q,n,\mathrm{B}}$ are MO coefficients for the configurations m and n of state A and B, respectively, and

$$S_{ij}^{mn} = \sum_{k,l} c_{ik,m,\mathrm{A}}^{*} c_{jl,n,\mathrm{B}} \int \phi_i^{*} \phi_j \mathrm{d}\tau, \tag{44}$$

is the overlap matrix between the MOs of the configurations m and n of state A and B, respectively. $\phi_{i,j}$ in (43) and (44) are basis functions and i, j, p, q, k, l are indices for these basis functions. Minor $(S^{mn})_{ij}$ denotes the (i, j) minor of the matrix $\mathbf{S}^{mn}$.

We next present 1D and 2D SXRS signals calculated using STEX [29, 68]. Figure 9 shows the 2D-SXRS spectrum of *N*-methylacetamide (NMA) with the OOO (O1s pump with two O1s probes) pulse sequence, together with 1D projections

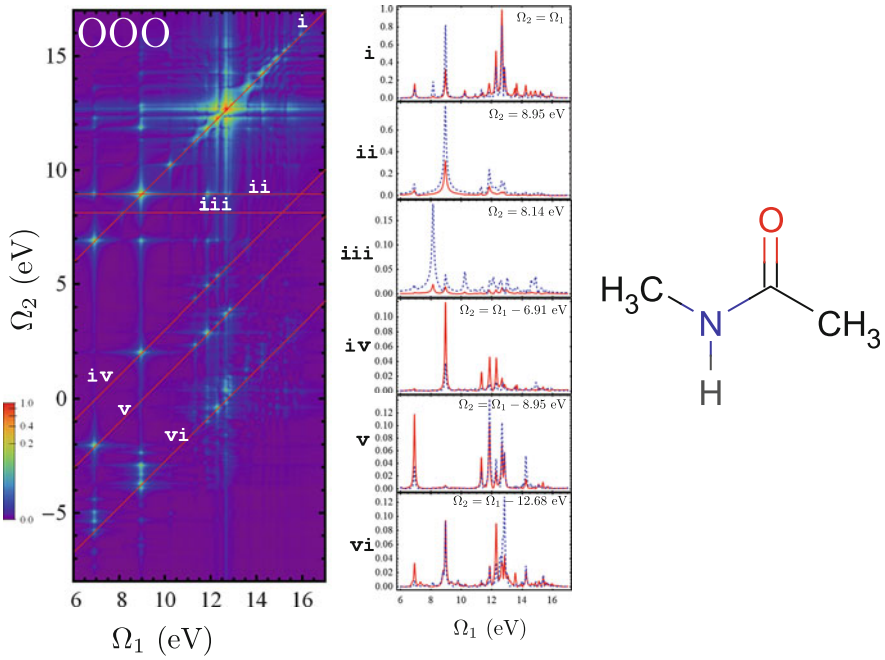

Fig. 9 The 2D-SXRS signal $S_{SXRS}(\Omega_1, \Omega_2)$ and its 1D traces of NMA (*right*) from STEX calculations. *Left*: the OOO spectrum. All these pulses are resonant with the O K-edge. *Middle*: *horizontal* and *diagonal slices* of the 2D spectrum on the *left* (*in red*) plotted together with the corresponding traces from the corresponding OON (*dashed*, *blue*) to highlight the effect of changing the probe pulse in the three-pulse sequence. Figure adapted from [29]

along several horizontal and diagonal traces. We also show the corresponding traces from the OON 2D-SXRS signal in blue dashed lines for comparison. The only difference between the two types of 1D signals are the third pulse. Peaks along the diagonal line ($\Omega_2 = \Omega_1$, **i** in Fig. 9) resemble those from the 1D-SXRS spectrum of the same molecule [29]. Peaks along the horizontal lines drawn at the representative valence excitation energies ($\Omega_2 = 8.95$, 8.14 eV, **ii** and **iii** in Fig. 9) reveal the interference of the two Liouville space quantum pathways represented by diagrams a and d in Fig. 6, and peaks along the diagonal lines shifted with representative valence excitation energies ($\Omega_2 = \Omega_1 - 6.91$, 8.95, 12.68 eV, **vi**, **v**, and **vi** in Fig. 9) reveal the interference of the other two quantum pathways represented by diagrams b and c in Fig. 6. Figure 9 illustrates that multidimensional SXRS signals reveal couplings of different valence excitations, and interferences of quantum pathways.

Comparison of STEX with another method for calculating core excited states, the restricted excitation window time-dependent density functional theory (REW-TDDFT), was given in [69]. Core excitation energies from both methods must be shifted to match experiment. Because of the inclusion of core orbital relaxation, the shifts of STEX core excitation energies (<10 eV) are usually smaller

than those of TDDFT (>10 eV). However, being an independent particle and hole theory, STEX cannot account for core hole mixing in X-ray spectroscopy, whereas REW-TDDFT can. The SCF calculation of a core ionized state is often tricky. Convergence is not guaranteed. In addition, because the STEX equation (40) is not solved self-consistently, the occupied and virtual STEX orbitals are not variational for the total energy. Evaluating core excited state properties, e.g., electron density, thus become complicated [70]. State-to-state transition dipole calculations are expensive.

3.1.3 ΔSCF-DFT Method

A straightforward extension of DFT to excited states (including core excitations) is achieved by employing non-Aufbau occupations of Kohn–Sham orbitals and running SCF calculations to obtain the target excited states as is done in ground state calculations [71–74]. This is known as the ΔSCF-DFT (or simply the ΔSCF) method. The biggest difficulty is the collapse to the lower energy states below the excited state during the SCF iterations. Special care must be taken to keep the electrons in the designated excited configuration. The maximum overlap method (MOM) [62] is widely used to avoid SCF collapse. Here, the new occupied orbitals in the current SCF cycle are chosen as the orbitals which have a maximum overlap with the occupied orbitals in the last cycle. The orbital overlap matrix is given by

$$\mathbf{O} = \left(\mathbf{C}^{n-1}\right)^{\dagger}\mathbf{S}\mathbf{C}^{n}, \tag{45}$$

where $\mathbf{C}^{n-1}$ and $\mathbf{C}^{n}$ are the molecular orbital coefficient matrices in the last and current SCF iteration, respectively, $\mathbf{S}$ is the overlap matrix of basis functions, and the matrix element O_{ij} represents the overlap between the ith old orbital and the jth new orbital. The projection of the jth new orbital onto the old occupied orbital space may be defined as

$$P_j = \sum_{i}^{\text{occ}} O_{ij} = \sum_{l}^{\text{occ}} \left[\sum_{k}^{\text{occ}} \left(\sum_{i}^{\text{occ}} C_{ik}^{n-1} \right) S_{kl} \right] C_{lj}^{n}. \tag{46}$$

The orbitals with the largest P_js are chosen as the new occupied orbitals. In some cases (46) is not robust when selecting new occupied orbitals. Alternative projections such as

$$P_j = \sum_{i}^{\text{occ}} \left| O_{ij} \right|, \tag{47}$$

and

$$P_j = \sum_i^{\text{occ}} |O_{ij}|^2, \tag{48}$$

have been implemented in the quantum chemistry packages Q-CHEM [75] and GAMESS [76]. The same projection scheme as in (48) was also proposed by other authors very recently [77]. When all O_{ij}s do not have the same sign, or a number of orbitals are nearly degenerate during the SCF iteration, (48) is believed to perform better than (47) [77].

Unlike STEX, a spin-unrestricted scheme is employed in ΔSCF-DFT. Thus for a system with a closed shell ground state, ΔSCF-DFT usually gives a broken-symmetry spin state which is a mixture of a singlet and a triplet state. The singlet excitation energy can be obtained through the spin-purification formula [72]

$$E_S = 2E_{BS} - E_T, \tag{49}$$

where E_S is the energy of the open shell singlet, E_{BS} is the spin broken-symmetry state energy, and E_T is the triplet energy from a separated ΔSCF-DFT calculation. Spin-purification is necessary in valence excitation calculations [78, 79] but is less important in core excitations, where $E_{BS} \approx E_T$ so that $E_S \approx E_{BS}$.

ΔSCF-DFT can be easily extended to calculate various excited state properties other than the excitation energy [79]. It also includes orbital relaxation upon excitation, which is neglected in TDDFT. Note that the (N−1) approximation in STEX may not be necessary for ΔSCF-DFT because the DFT virtual orbitals experience the same potential as do the occupied orbitals. However, it has some drawbacks. First, ΔSCF-DFT is a state-specific approach; one should calculate the excited states one by one. This makes it unsuitable for broadband spectroscopy simulations, where many excited states are needed. Second, it only gives excited states which can be well described by a single determinant. Excited states with strong configuration interactions are missed. Third, excited states from separated ΔSCF-DFT calculations are not orthogonal, and there is no unique way to enforce the orthogonality requirement. Finally, it is an open question how to run variational DFT calculations of excited states because there is no Hohenberg–Kohn theorem for a generic excited state [80]. Despite its drawbacks, ΔSCF-DFT has been revived recently in charge-transfer excitation [81], Rydberg excitation [82], and excited state potential energy surface calculations [83], and looks very promising in the X-ray regime.

3.2 TDDFT Techniques

As explained in the introduction section, the discussions in this section are based on adiabatic TDDFT. Although similar formulation for time-dependent Hartree-Fock (TDHF) theory had existed for more than two decades [84], the time-domain

extension of DFT was not possible until Runge and Gross established the one-to-one mapping of electron density and time-varying external potential [85]. There are two categories for applying TDDFT to calculate excited state properties: the response theory based on perturbation in the frequency domain and the direct real-time propagation methods in the time domain. The frequency-domain formalism of TDDFT, which is based on linear response theory, became popular after Casida proposed a density matrix response equation which is very similar to the renowned random phase approximation (RPA) equation [86]. The Casida equation can be derived by solving the equation of motion (EOM) of the single electron reduced density matrix to the first order of external perturbation in the frequency domain. Similar expressions have been obtained for TDHF in the collective electronic oscillator (CEO) method [87–89]. Nonlinear response functions of the system can be calculated in CEO by applying high order perturbation theory [89].

Another way to obtain excited state properties is to solve the EOM of single-electron reduced density matrix by direct propagation in the time domain. Time-dependent properties of the system induced by the time-dependent external perturbation can be calculated directly and Fourier transform can recover the excited state information in the frequency domain.

In this section, we start with the linear-response formalism of Casida, and then present a specific variant of linear-response TDDFT applied to core excited state (restricted excitation window time-dependent density functional theory, REW-TDDFT). Moreover, high order perturbation theory methods for nonlinear response properties of the system are introduced and finally the real-time propagation methods are discussed. It should be noted that the response and real-time propagation methods are very general and not restricted to DFT/TDDFT, but we focus on the DFT/TDDFT formalisms of these methods in this chapter.

3.2.1 Linear Response Theory

The Casida equation can be derived by calculating the linear response of the density matrix or through an EOM approach. One may start with the EOM of the one-particle transition density matrix $P_I = |I\rangle\langle 0|$:

$$\left[\hat{H}, P_I\right] = \mathrm{i}\frac{\partial P_I}{\partial t} = \omega P_I, \tag{50}$$

where $|I\rangle$ and $|0\rangle$ are the Ith excited state and ground state, respectively, $\hat{H}$ is the Hamiltonian of the system, and ω is the excitation energy. Considering the idempotency property of density matrix, the transition density matrix can be expanded as

$$P_I = \sum_{i,a} \left(X_{ia} \hat{a}^\dagger \hat{i} + Y_{ia} \hat{i}^\dagger \hat{a} \right), \tag{51}$$

where X_{ia} and Y_{ia} are one-particle/one-hole (1p1h) excitation and de-excitation amplitudes, respectively, and i, a represent an occupied and virtual orbital, respectively. Substituting (51) into (50), after some algebraic manipulations, one can obtain the Casida equation:

$$\begin{pmatrix} \mathbf{A} & \mathbf{B} \\ \mathbf{B}^* & \mathbf{A}^* \end{pmatrix} \begin{pmatrix} \mathbf{X} \\ \mathbf{Y} \end{pmatrix} = \omega \begin{pmatrix} \mathbf{1} & \mathbf{0} \\ \mathbf{0} & -\mathbf{1} \end{pmatrix} \begin{pmatrix} \mathbf{X} \\ \mathbf{Y} \end{pmatrix}, \tag{52}$$

where

$$\begin{aligned} A_{ia\sigma,\, jb\tau} &= \delta_{ij}\delta_{ab}\delta_{\sigma\tau}(\varepsilon_{a\sigma} - \varepsilon_{i\tau}) + K_{ia\sigma,\, jb\tau}, \\ B_{ia\sigma,\, jb\tau} &= K_{ia\sigma, b\, j\tau}, \\ K_{ia\sigma,\, jb\tau} &= \left(i_\sigma a_\sigma \middle| j_\tau b_\tau\right) + \left(i_\sigma a_\sigma \middle| f_{xc} \middle| j_\tau b_\tau\right), \end{aligned} \tag{53}$$

and

$$\begin{aligned} \left(i_\sigma a_\sigma \middle| j_\tau b_\tau\right) &= \int\int \psi_{i\sigma}(\mathbf{r})^* \psi_{a\sigma}(\mathbf{r}) \frac{1}{|\mathbf{r} - \mathbf{r}'|} \psi_{j\tau}(\mathbf{r}')^* \psi_{b\tau}(\mathbf{r}') \mathrm{d}\mathbf{r}\mathrm{d}\mathbf{r}', \\ \left(i_\sigma a_\sigma \middle| f_{xc} \middle| j_\tau b_\tau\right) &= \int\int \psi_{i\sigma}(\mathbf{r})^* \psi_{a\sigma}(\mathbf{r}) \frac{\delta^2 E_{\mathrm{XC}}}{\delta\rho_\sigma(\mathbf{r})\delta\rho_\tau(\mathbf{r}')} \psi_{j\tau}(\mathbf{r}')^* \psi_{b\tau}(\mathbf{r}') \mathrm{d}\mathbf{r}\mathrm{d}\mathbf{r}'. \end{aligned} \tag{54}$$

Here i, j and a, b represent occupied and virtual orbitals, respectively, σ, τ are spin indices, ε is the orbital energy, and f_{xc} is the exchange-correlation kernel which is expressed as the second-order functional derivative of the exchange-correlation energy with respect to electron density (54). In (52), $\mathbf{X}$ and $\mathbf{Y}$ should be considered as column vectors. Alternatively, it is possible to derive these equations for the reduced single electron density matrix. This has been done in the CEO method [87–89] for both TDHF [89] rather than TDDFT [90, 91].

Because of its balance of accuracy and computational cost, and its robustness and black-box character, linear-response TDDFT has become the method of choice for computing excited states, including core excited states. We have also based our nonlinear X-ray spectroscopy simulation work on TDDFT [24, 69, 92, 93]. Unlike ΔSCF-DFT, linear-response TDDFT does not target a single excited state. Only ground state orbitals are necessary in the calculation, so that a manifold of excited states is obtained in one shot. However, linear-response TDDFT also has its limitations. Usually based on a single-referenced Kohn–Sham state, linear-response TDDFT cannot handle excited states calculations for a ground state with a heavy multiconfigurational character. Orbital relaxation for different excited states is missed. Approximate energy functionals do not have proper long-range asymptotic behavior, and thus linear-response TDDFT has difficulties in handling charge-transfer excited states [94] and Rydberg states. The same limitation applies to

core excited states [14]. The long-range corrected density functionals are discussed in Sect. 4.1. In addition, within the adiabatic (frequency-independent) exchange-correlation kernels, linear-response TDDFT cannot properly describe double excitations [95]. This is a major obstacle for simulating nonlinear spectroscopy experiments, which directly access double or multiple excited states. Double excitations and frequency-dependent exchange-correlation kernels are discussed in Sect. 4.3.

3.2.2 Restricted Excitation Window TDDFT

Calculating core excited states directly using (52) is prohibitively expensive because there are numerous low energy excited states below the target high energy core excited state. Any bottom-up matrix eigenvalue numerical algorithm becomes very tedious. This difficulty can be circumvented by allowing electrons to move only between a certain set of relevant occupied and virtual orbitals. This is the basis for the restricted excitation window (REW) or restricted excitation channel approach. This method was proposed by Stener and co-workers [96], and followed by other authors [97–100]. One can select the orbitals in the restricted excitation window by their orbital indices or energies. In the first scheme all molecular orbitals (MO) are examined and then the relevant orbitals (e.g., the MOs dominated by the target oxygen 1s atomic orbitals) are selected out. Alternatively, an orbital energy or energy difference cutoff is used to filter out all relevant orbitals or transition orbital pairs. Orbital index selection is intuitive but becomes cumbersome if there are too many relevant orbitals. The orbital energy (energy difference) selection scheme is convenient for building a large REW. If there are multiple target atoms of the same type in the molecule, the target MOs would become degenerate or near-degenerate. The orbital index selection scheme can explore the contribution of a single target atom to the core excitation and the spectroscopy signal, whereas the orbital energy selection scheme can study hole-mixing effects. Another method with the same effect of building a REW is to shift the core excitation energy difference. This was proposed by Schmidt et al. [101] very recently and is very similar to Stener and co-workers' early implementation in the ADF package. After the REW is determined, trial excitation vectors are prepared in this REW and a Davidson-type iterative solver [102] is usually employed to find the relevant matrix eigenvalues and eigenvectors. REW-TDDFT has been implemented in standard quantum chemistry packages such as ADF [103], Q-Chem [104], ORCA [105], NWChem [106], and Gaussian [107].

Minimum inputs (relevant orbitals, number of excited states) are needed for running a REW-TDDFT calculation. It is almost black-box and robust and can handle all types of excited states with deep as well as shallow holes. It is a response method and avoids the state-specific SCF convergence problem. Hole-mixing can be observed, which is not possible with STEX or ΔSCF-DFT. Electron correlation can be considered in the exchange-correlation functional. Moreover, REW-TDDFT can easily calculate many core excited states. If unrelaxed CIS-type wave functions (Tamm–Dancoff approximation, TDA) are used to represent the excited states, the

state-to-state transition dipoles in REW-TDDFT reduce to sums of transition dipoles between certain MOs because all MOs are mutually orthogonal. This drastically reduces the computational cost compared to (42).

In order to calculate nonlinear X-ray spectroscopy signals, we developed a computational approach based on REW-TDDFT implemented in the quantum chemistry package NWChem. In a series of publications [6, 69, 108], we had extended the conventional optical Raman spectroscopy techniques into the X-ray regime. One- and two-dimensional stimulated X-ray Raman spectroscopy (1D- and 2D-SXRS) signals of the small amino acid cysteine were simulated and compared to the conventional resonant inelastic X-ray scattering (RIXS) signals. Compared to RIXS, which is a frequency domain technique, multi-color time domain SXRS provide a better window to the electronic coupling dynamics in a molecule. We also calculate the X-ray four-wave mixing $\mathbf{k}_{\mathrm{I}} = -\mathbf{k}_1 + \mathbf{k}_2 + \mathbf{k}_3$ and $\mathbf{k}_{\mathrm{II}} = \mathbf{k}_1 - \mathbf{k}_2 + \mathbf{k}_3$ signals. To compare these with the SXRS signals, we took the time delay t_2 between $\mathbf{k}_2$ and $\mathbf{k}_3$ longer than the lifetimes (<10 fs) of the core excited states in this system, so that only the ground-state-bleach (GSB) terms in the signals survive. $\mathbf{k}_{\mathrm{I,II}}$ signals have three frequency variables Ω_j ($j = 1, 2, 3$), where Ω_1 and Ω_3 correspond to core excitations and Ω_2 corresponds to valence excitations. We can cut some slices of these 3D signals to interpret them. In Fig. 10 we show slices of the two-color $\mathbf{k}_{\mathrm{II}}$ (OOSS) signal with constant Ω_2 at different peaks in the two-color integrated two-pulse SXRS signal. These plots show the correlation between core excitations at different places in the molecule. We can find both the valence excitations at $\Omega_2 = 6.6$ and 8.9 eV are coupled to the S1s core excitation at $\Omega_3 = 2475.5$ eV, but they are coupled to different O1s core excitations at $\Omega_1 = 532.2$ and 536.1 eV, respectively. The valence excitation at $\Omega_2 = 11.4$ is coupled to S1s core excitation with higher energies. Moreover, the frequency dispersed two-pulse SXRS signals can give the same information about electron correlation as do projected photon echo signals [108], whereas the SXRS experiment is much simpler than the photon echo. However, photo echo experiments have more control variables and can reveal the correlation between core excitations directly (see Fig. 10), although SXRS can only infer them through valence excitations.

The same simulation approach was applied to porphyrin dimers. Multiporphyrin systems are good candidates for artificial photosynthesis or molecular electronics applications, so understanding the detailed excitation energy transfer (EET) mechanisms in these systems becomes very important. Simulated SXRS signals of various porphyrin heterodimer systems were obtained [92, 93] using REW-TDDFT. In Fig. 11 we show the time-domain 1D SXRS signals and the corresponding evolving electron and hole densities in the Zn and Ni porphyrin heterodimer (structure shown on the top of Fig. 11). We found an almost constant $\pi/2$ phase difference between the one-color Zn2p pump and Zn2p probe (Zn2p/Zn2p) signal and the two-color Zn2p pump and Ni2p probe (Zn2p/Ni2p) signal ((c) at bottom left in Fig. 11). Because the SXRS signal can be considered as an overlap between the time-dependent doorway wavepacket created by the pump pulse and the time-independent window wavepacket created by the probe pulse [92], this phase difference corresponds to a back-and-forth motion of the doorway wavepacket.

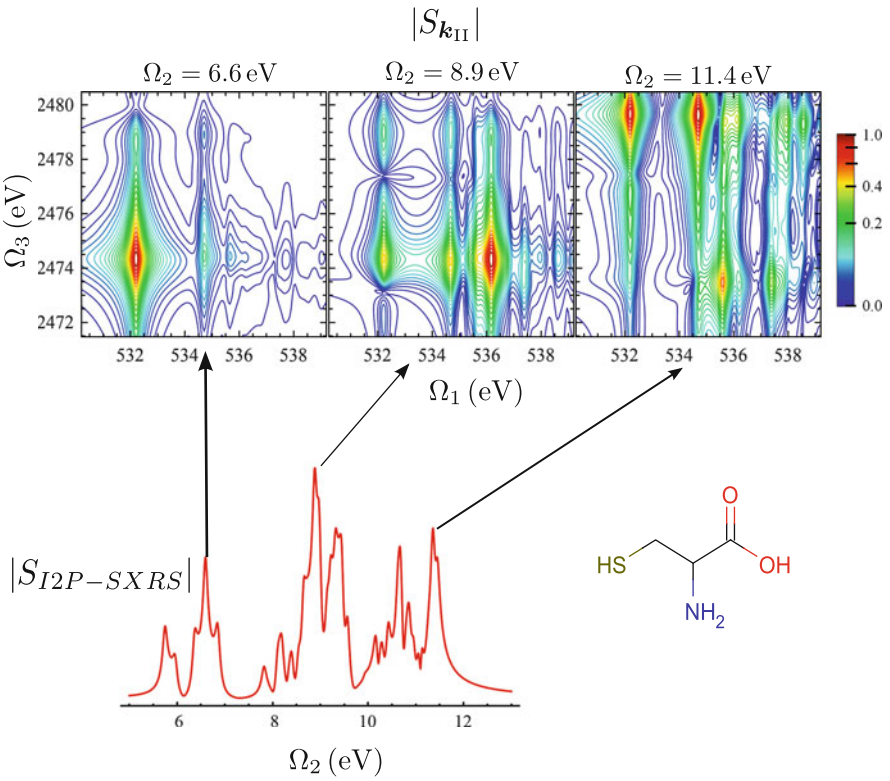

Fig. 10 Four-wave mixing and I2P-SXRS signals of cysteine (structure shown on the *bottom right*) from REW-TDDFT calculations. *Top*: constatnt-Ω_2 slices of the 3D $\mathbf{k}_{\rm II}$ signal $S_{\mathbf{k}_{\rm II}}$ (Ω_1, $\Omega_2 = 6.6$, 8.9, 11.4 eV, Ω_3) using an OOSS pulse sequence with *xxxx* polarization. *Bottom left*: the integrated two-pulse SXRS signal using an OS pulse sequence with *xx* polarization. Figure adapted from [108]

Correlation between the motion of the doorway wavepacket and the fluctuations of the SXRS signal profiles can be established. The time-domain signals provide a real-time image of EET in the system, which is not possible for time-resolved fluorescence anisotropy decay studies. SXRS could become a powerful tool in revealing EET mechanisms in molecular systems. Further geometrical and structural factors that control EET in a series of porphyrin heterodimer systems were studied in [93].

In another SXRS simulation study we investigated long-range electron transfer (ET) in the small redox protein azurin [109]. Borrowing the ET kinetic parameters from time-resolved infrared (IR) and optical measurements, time-resolved SXRS signals at the electron donor, hopping intermediate and electron acceptor were simulated with REW-TDDFT. We found that the SXRS signals depend sensitively on the local electronic structure changes around the excited atoms, and could serve as an excellent indicator for detecting electron transfer dynamics. The atomic

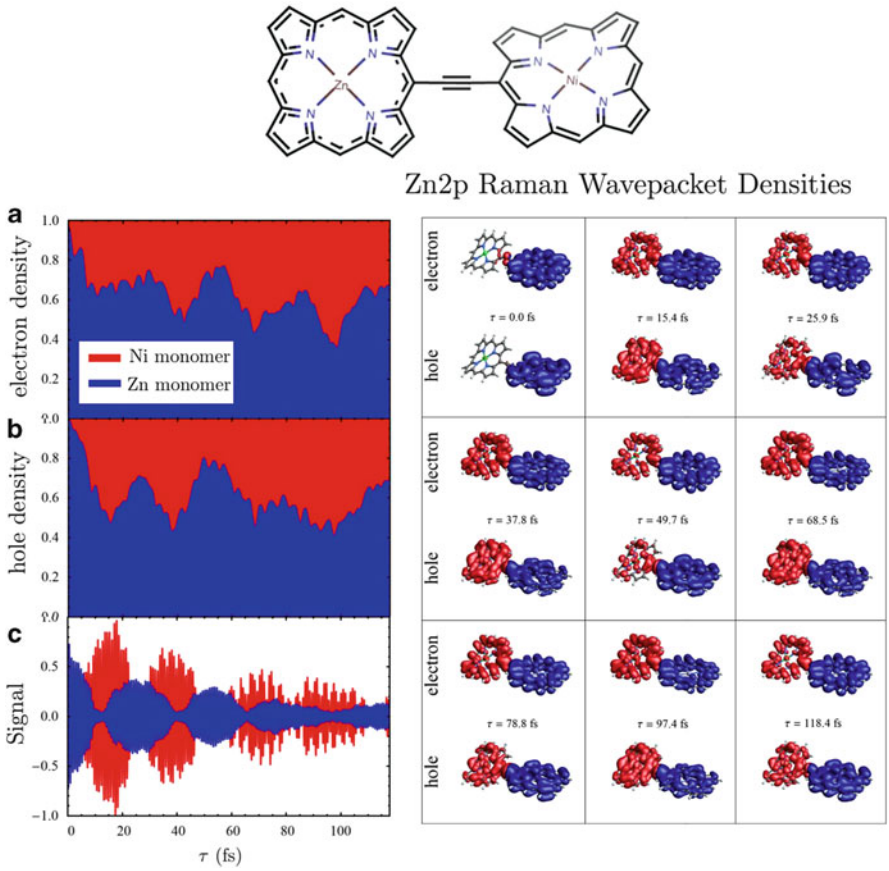

Fig. 11 Time-domain 1D SXRS signals that reveal excitation energy transfer in porphyrin heterodimers from REW-TDDFT calculations. *Top*: the molecular structure of the Zn-Ni porphyrin heterodimer studied. *Bottom left*: (**a**, **b**) Spatially integrated hole and electron densities on the Ni (*red*) and Zn monomer (*blue*). (**c**) The time-resolved integrated two-pulse SXRS signals of the porphyrin dimer between 0 and 120 fs. The single color Zn2p/Zn2p signal is in *blue* and the two-color Zn2p/Ni2p signal is in *red*. *Bottom right*: electron and hole densities of the Zn2p valence superposition state prepared by SXRS for various times after excitation. The isosurfaces are colored according to which monomer they reside on, *red* for Ni and *blue* for Zn. Figure adapted from [92]

pinpoint spatial accuracy also makes SXRS a convenient tool in studying different ET pathways. Such measurements are difficult for conventional IR or optical techniques. SXRS should complement linear transient X-ray absorption [110] in studying ultrafast ET molecular processes.

3.2.3 Perturbation Methods for High Order Responses

Nonlinear optical response properties can be obtained by going beyond the first order of perturbation in equations similar to (50). Response equation (Sternheimer equation) of wave functions instead of density matrix can also been considered [111]. Following the standard time-dependent perturbation theory, Orr and Ward derived the sum-over-state (SOS) expressions of the nonlinear optical polarizations four decades ago [112]. The SOS expressions are general and excited states from any level of theory could be used. Much TDDFT work has been done along these lines [91, 111, 113–121]. A weak time-dependent external electric field is introduced as a perturbation to the original Kohn–Sham system. Then the coupled-perturbed TDDFT equations, which are similar to the coupled-perturbed Kohn-Sham equations in DFT geometry optimization calculations, are solved at different orders of the perturbation and nonlinear response properties are evaluated by perturbed wave function or density matrix. Using the $2n+1$ rule [122], third order response properties can be obtained through the first perturbed wave function. These approaches can also be used to calculate the nonlinear response to X-ray pulses.

The complex polarization propagator (CPP) method for XANES simulation was proposed by Norman and coworkers [123–125]. They first parameterized the orbital rotation during time evolution, then started from an EOM of the state-transfer operators with external perturbations and a phenomenological damping term. With this damping term, decay of excited states can be considered in the now-complex response functions and resonance divergences are eliminated. With perturbation techniques, the EOM can be solved at different orders of perturbation and the corresponding response properties can be calculated. For the linear polarizability, one has

$$\alpha_{ij}(\omega) = -\mu_i^{[1]\dagger}\left[E^{[2]} - (\omega + \mathrm{i}\gamma)S^{[2]}\right]^{-1}\mu_j^{[1]}, \tag{55}$$

where $i, j = x, y, z$ are coordinate axis indices, $\mu_{i,j}^{[1]}$ is the electric-dipole property gradient along the coordinate axis i, j, respectively, $E^{[2]}$ is the electronic Hessian, γ is the phenomenological damping parameter, and $S^{[2]}$ is the overlap matrix [125]. The CPP method is general and when DFT orbitals are used, it gives excellent XANES spectra of large molecules such as copper phthalocyanine [126]. A constant shift (usually it is a blue shift) is still needed to match the calculated XANES to experiment. The constant shift depends on the system and functional used, e.g., for the water molecule the shifts are 15.15 and 4.0 eV for the CAM-B3LYP and LB94 functional, respectively [125]. Nevertheless, third order electronic Hessian is needed to calculate second-order response, making the calculation quite involved.

Coupled-perturbed TDDFT results in SOS expressions of nonlinear response functions [127], which become increasingly more complex for higher order

response. High order functional derivatives of the exchange-correlation energy functional are necessary [111, 121]. Because many excited states and orbitals, including virtual orbitals, are involved, high order perturbation methods are unsuitable for simulations of large systems because of their unfavorable computational scaling.

3.2.4 Real-Time Propagation Methods

In the frequency domain, each relevant excited state must be explicitly calculated when the SOS expressions of nonlinear X-ray spectroscopy signals are employed. The calculation becomes very expensive when many excited states contribute to the signals. In recent attosecond laser spectroscopy experiments [128–140], the orbital relaxation as well as the nonadiabatic dynamics with significant geometry changes involve many excited states. Real-time methods are then preferable.

In real-time time-dependent density functional theory (RT-TDDFT), rather than solving for eigenstates, the wave function or the one-electron reduced density matrix[1] is directly propagated in the time domain. Spectroscopic signals can be extracted from Fourier transform of time-dependent system properties such as the polarization of the molecule driven by the external electric field. The entire spectrum can be obtained at once and direct calculation of specific excited states is avoided.

The Liouville–von Neumann equation of motion of the reduced single electron density matrix $\boldsymbol{\sigma}(t)$ is [141]

$$\mathrm{i}\frac{\partial \boldsymbol{\sigma}(t)}{\partial t} = [\mathbf{F}(t), \boldsymbol{\sigma}(t)], \tag{56}$$

where $\mathbf{F}(t)$ is the Fock matrix in DFT. The time-dependent electric dipole moment $\mu(t)$, can be calculated by

$$\mu(t) = -\mathrm{Tr}[\boldsymbol{\mu}\boldsymbol{\sigma}(t)]. \tag{57}$$

Other time-dependent single electron molecular properties can be obtained in a similar way. The unitary time evolution operator $U(t_2, t_1)$ propagates the many-electron wave function $\psi(t_1)$ at time t_1 to the wave function $\psi(t_2)$ at time t_2:

$$\psi(t_2) = \hat{U}(t_2, t_1)\psi(t_1). \tag{58}$$

For the density matrix propagation, we have

[1] Throughout this chapter we mean one-electron reduced density matrix for density matrix unless explicitly explained with another meaning.

$$\boldsymbol{\sigma}(t+\Delta t) = \mathbf{U}(t+\Delta t, t)\boldsymbol{\sigma}(t)\mathbf{U}^{\dagger}(t+\Delta t, t), \tag{59}$$

where t is a time point and Δt is a time delay. Formally, the time evolution operator can be expanded in time-ordered products:

$$\begin{aligned}\mathbf{U}(t+\Delta t, t) &= \hat{T}\exp\left(-\mathrm{i}\int_t^{t+\Delta t}\hat{F}(\tau)\mathrm{d}\tau\right)\\ &= \sum_{n=0}^{\infty}\frac{(-\mathrm{i})^n}{n!}\int_t^{t+\Delta t}\mathrm{d}\tau_1\int_t^{t+\Delta t}\mathrm{d}\tau_2\cdots\int_t^{t+\Delta t}\mathrm{d}\tau_n\hat{T}\left\{\hat{F}(\tau_1)\hat{F}(\tau_2)\cdots\hat{F}(\tau_n)\right\},\end{aligned} \tag{60}$$

where $\hat{T}$ is the time-ordering operator [1] and $\hat{F}$ is the Fock operator.

There are excellent reviews on the numerical integrators in real-time propagation calculations [142, 143]. Here we only give a brief summary of the major methods.

Direct propagation of wavefunctions or density matrices using (58) and (59) requires evaluating the time-ordered exponential of the Fock operator. Generally the Fock operator is time-dependent, which complicates the problem. This time dependence can be handled by dividing the time interval $(t,\ t+\Delta t)$ into small segments and considering the Fock operator fixed within each such segment (short-time approximation). Then the task is to evaluate the exponential of the time-independent Fock operator for short time intervals.

The most straightforward method to calculate the exponential of an operator is to use the Taylor expansion of the exponential function. Practically, a truncation at order four of this expansion works well [143, 144]. Alternatively, one can also choose the Chebychev polynomial to approximate the exponential function [142, 145–147]. The Chebychev polynomial is optimal for approximating functions in the range $[-1, 1]$, but renormalization of the Fock operator is necessary.

Another popular approach to calculate the exponential of an operator is the Krylov subspace method, e.g., the Lanczos iteration method [148–151]. In these methods the operator is projected onto a subspace (Krylov subspace) generated by consecutively applying the operator on the target vector. Any function of the operator can be approximate within this subspace, whose dimension is much smaller than that of the original operator.

The Fock operator consists of the kinetic energy operator, which is diagonal in reciprocal space, and the potential energy operator, which is diagonal in real space. This leads to the split-operator approach to calculate the exponential of the Fock operator. The exponential of the Fock operator can be approximated as the product of exponentials of the kinetic and potential energy operators [152, 153], which can be calculated exactly. There are higher order extensions of this simple split-operator scheme [154].

For time-dependent Fock matrices, integrating (56) numerically is not easy because nonsymplectic integrators such as the common Runge–Kutta methods, are numerically unstable for large scale simulations. One way to avoid such

numerical difficulties is by using the Magnus (cumulant) expansion [1, 141, 155, 156]. The Magnus expansion of $\mathbf{U}(t+\Delta t, t)$ is

$$\mathbf{U}(t+\Delta t, t) = \hat{T}\exp\left(-\mathrm{i}\int_t^{t+\Delta t}\mathbf{F}(\tau)\mathrm{d}\tau\right) = \mathrm{e}^{\mathbf{\Omega}_1+\mathbf{\Omega}_2+\cdots}, \tag{61}$$

and

$$\mathbf{\Omega}_1(t+\Delta t, t) = -\mathrm{i}\int_t^{t+\Delta t}\mathbf{F}(\tau)\mathrm{d}\tau, \tag{62}$$

$$\mathbf{\Omega}_2(t+\Delta t, t) = -\frac{1}{2}\int_t^{t+\Delta t}\int_t^{\tau_1}[\mathbf{F}(\tau_1), \mathbf{F}(\tau_2)]\mathrm{d}\tau_2\mathrm{d}\tau_1. \tag{63}$$

The higher order $\mathbf{\Omega}$ terms can be expressed with nested commutators of $\mathbf{F}$ at different times [155]. If we truncate the exponential expansion at first order in (61) and use the midpoint value $\mathbf{F}(t+\Delta t/2)$ to represent all $\mathbf{F}$ values in the time interval t, $t+\Delta t$, we have

$$\mathbf{U}(t+\Delta t, t) = \mathrm{e}^{\mathbf{\Omega}_1}, \tag{64}$$

$$\mathbf{\Omega}_1(t+\Delta t, t) = -\mathrm{i}\mathbf{F}(t+\Delta t/2)\Delta t. \tag{65}$$

Equation (59) then becomes

$$\boldsymbol{\sigma}(t+\Delta t) = \mathrm{e}^{-\mathrm{i}\mathbf{F}(t+\Delta t/2)\Delta t}\boldsymbol{\sigma}(t)\mathrm{e}^{\mathrm{i}\mathbf{F}(t+\Delta t/2)\Delta t}. \tag{66}$$

One problem with using (66) in direct propagation is that $\mathbf{F}(t+\Delta t/2)$ is unknown at time t. $\mathbf{F}(\mathrm{t}+\Delta t/2)$ should be estimated by linearly extrapolating the $\mathbf{F}$ values at previous times, or through some predictor-corrector technique [157]. However, the latter breaks the time evolution symmetry. Alternatively, we can say backward time propagation with the predictor-corrector cannot reproduce the original state of the system at early time. The modified midpoint unitary transform method (MMUT) [158, 159] maintains this time-reversibility. In this method, $\mathbf{U}(t+\Delta t, t-\Delta t)$ is constructed from the eigenvectors $\mathbf{C}(\mathbf{t})$ and the eigenvalues $\boldsymbol{\varepsilon}(t)$ of $\mathbf{F}(t)$ at the time midpoint:

$$\mathbf{U}(t+\Delta t, t-\Delta t) = \exp[\mathrm{i}\cdot 2\Delta t\,\mathbf{F}(t)] = \mathbf{C}(t)\exp[\mathrm{i}\cdot 2\Delta t\,\boldsymbol{\varepsilon}(t)]\mathbf{C}^{\dagger}(t). \tag{67}$$

The corresponding density matrix time propagation equation is

$$\boldsymbol{\sigma}(t+\Delta t) = \mathbf{U}(t+\Delta t, t-\Delta t)\boldsymbol{\sigma}(t-\Delta t)\mathbf{U}^{\dagger}(t+\Delta t, t-\Delta t). \tag{68}$$

For other popular integrators such as the one combined split-operator with the enforced time-reversal symmetry method, see [143]. Implementations of

RT-TDDFT/TDHF are available in standard quantum chemistry packages such as Gaussian [158, 160], NWChem [156], and Octopus [161].

RT-TDDFT has been used to calculate X-ray linear absorption spectroscopy [100, 162]. The time-dependent perturbed Fock matrix is

$$\mathbf{F}(t) = \mathbf{F}(0) - \mathbf{D} \cdot \mathbf{E}(t), \tag{69}$$

where $\mathbf{D}$ is the dipole matrix and $\mathbf{E}(t)$ is the time-dependent external electric field. An impulsive external electric field is used in the calculation:

$$\mathbf{E}(t) = \hat{r} \cdot k\delta(t), \tag{70}$$

where $\hat{r} = x, y, z$, k is the perturbation strength, and $\delta(t)$ is the δ function. The density matrix is then propagated under this perturbation and the time-dependent dipole moment is calculated through (57). The molecular polarizability is proportional to the Fourier transform of $\mu(t)$:

$$\alpha_{ij}(\omega) = \frac{\tilde{\mu}_{ij}(\omega)}{k}, \tag{71}$$

where $i, j = x, y, z$. The linear absorption spectrum can be obtained from the imaginary part of the molecular polarizability:

$$S(\omega) = \frac{4\pi\omega}{c} \cdot \mathrm{Im}\frac{\mathrm{Tr}[\boldsymbol{\alpha}(\omega)]}{3}, \tag{72}$$

where c is the speed of light.

An impulsive perturbation can excite electrons over a broad energy range (e.g., 1,000 eV). So real-time methods have advantages if a large energy range is requested and many excited states are involved in the signal. Real-time methods avoid the diagonalization of a large matrix, but the numerical problem switches to sampling the time interval properly in the Fourier transform. Signal post-processing techniques such as window function are often necessary to obtain sharp core excitation peaks [100].

Suppose the vectorial external electric field has multiple frequency components along different coordinate axes:

$$E_i(t) = \sum_{\omega} E_i^{\omega} \mathrm{e}^{-\mathrm{i}\omega t}, \tag{73}$$

where $i = x, y, z$ is the coordinate axis index and the summation runs over negative and positive frequency domains to keep the external electric field real. Expansion of the time-dependent dipole under this external field gives

$$\begin{aligned}\mu_i(t) = \quad & \mu_i^0 + \sum_{\omega} \alpha_{ij}(-\omega;\omega) E_j^{\omega} \mathrm{e}^{-\mathrm{i}\omega t} + \\ & \frac{1}{2} \sum_{\omega_1,\omega_2} \beta_{ijk}(-\omega_s;\omega_1,\omega_2) E_j^{\omega_1} E_k^{\omega_2} \mathrm{e}^{-\mathrm{i}\omega_s t} + \\ & \frac{1}{6} \sum_{\omega_1,\omega_2,\omega_3} \gamma_{ijkl}(-\omega_s;\omega_1,\omega_2,\omega_3) E_j^{\omega_1} E_k^{\omega_2} E_l^{\omega_3} \mathrm{e}^{-\mathrm{i}\omega_s t} + \cdots,\end{aligned} \tag{74}$$

where μ^0 is the permanent dipole; $i, j, k, l = x, y, z$ are coordinate axis indices; and ω_s is the sum of frequencies: for β, $\omega_s = \omega_1 + \omega_2$; and for γ, $\omega_s = \omega_1 + \omega_2 + \omega_3$. In (74), $\alpha_{ij}(-\omega;\ \omega)$ is the linear polarizability in (71); $\beta_{ijk}(-\omega_s;\ \omega_1,\ \omega_2)$ is the first order nonlinear hyperpolarizability, and $\gamma_{ijkl}(-\omega_s;\ \omega_1,\ \omega_2,\ \omega_3)$ is the second-order nonlinear hyperpolarizability. β controls the second-order optical processes such as the electro-optical Pockels effect and second-harmonic generation; whereas γ determines third order optical processes such as the electro-optical Kerr effect, intensity-dependent refractive index, and electric-field-induced second-harmonic and third-harmonic generation. With the full knowledge of these nonlinear dynamical hyperpolarizabilities, in principle one can calculate the nonlinear response of the system under any sequence of laser pulses with different central frequencies and time delays, so that the corresponding nonlinear spectroscopy signals can be simulated. Thus calculating such nonlinear hyperpolarizabilities becomes the major task for quantum chemists in nonlinear spectroscopy simulation studies.

RT-TDDFT has been used to calculate dynamical hyperpolarizabilities. Wang et al. [121] adopted the filter diagonalization method [163–165] to extract components at specific frequencies (e.g., double or triple the input frequency) of the time-dependent dipole moment as a result of solving the EOM of (56). A careful choice of the perturbation field strength was necessary. The strength can neither be too weak nor too strong because a too weak perturbation field results in negligible second and third order response, and a too strong perturbation field makes even higher order response dominant. Moreover, the perturbation should be turned on slowly to avoid nonadiabatic response. They also derived the EOM for the first and second-order response of the density matrix, but evaluating dynamical hyperpolarizabilities using these equations is more costly than using (56). Takimoto et al. [166] used a Gaussian enveloped quasimonochromatic perturbation to approach a δ distribution in the frequency domain in their RT-TDDFT simulation. With this choice, the response equation connecting hyperpolarizabilities and density matrix response at different orders can be easily reverted and dynamical hyperpolarizabilities are determined. Recently, Li and coworkers [167] applied the finite field (numerical differential) method to obtain the time-dependent dipoles at different orders through RT-TDDFT calculations. The components with specific frequencies were extracted by numerical fitting to sinusoidal waves with these frequencies. This scheme avoids Fourier transform which requires a long time simulation.

Two types of time bookkeeping protocols may be used in calculating nonlinear spectroscopy signals. The first is based on the wavefunction. The signals can then

be represented by loop diagrams where the ket moves first forward and then backward to account for the bra [168]. The second protocol uses the density matrix and can be represented by ladder diagrams [1]. The first protocol does not maintain the bookkeeping of relative time ordering of bra and ket interactions and results in $n+1$ basic terms for the nth order response. The second protocol fully keeps track of time ordering. Both ket and bra move forward, yielding more 2^n terms [1, 23]. [2] Even though the Casida (or CEO) equations of motion represent the reduced single electron density matrix, this density matrix is simply used for parameterizing the many electron wavefunction given by a single Slater determinant. The response predicted by the equations of motion for the density matrix turns out to correspond to the many-electron wavefunction rather than the density matrix [86, 89].

RT-TDDFT should have many advantages in nonlinear X-ray spectroscopy simulation. Because it does not calculate individual states, it saves computing time when many excited states are involved, which is the case for ultrashort broadband X-ray pulse excitation. Direct propagation of the density matrix, only involves occupied orbitals, so the computational scaling of RT-TDDFT is much better than any SOS method [112], which involves a large number of virtual orbitals. There are already many linear scaling algorithms both in both time [169] and frequency domains [170] for RT-TDDFT in excited state calculations. Both methods rely on the diagonal dominance of single-electron density matrices or transition density matrices. The key issue is to calculate the highly nonlocal exchange components in the popular hybrid density functionals efficiently, which has only recently been addressed [171]. Unlike the perturbation method (to be discussed in the next section), high order functional derivatives are not necessary in RT-TDDFT calculations, so the well-behaved but complicated energy functionals, such as the orbital-dependent functionals or the optimized effective potential (OEP) functionals, can be readily used. In addition, RT-TDDFT has advantages for nonlinear response because the calculations are no more difficult than for linear response, whereas for the frequency domain methods such as SOS, they become increasingly more complex for higher order response. Nuclear motions can also be accounted for by Ehrenfest dynamics [159, 172]. RT-TDDFT offers a direct simulation of nonlinear spectroscopy experiments with short pulses. However, we still have some tradeoffs in using RT-TDDFT. Because individual excited states are not available in RT-TDDFT, it is hard to interpret the spectral features. So far, RT-TDDFT applications have been restricted to calculating standard dynamical hyperpolarizabilities. Simulations of the signals presented in Sect. 2 constitute challenges.

[2] Each electronic oscillator which parameterizes the evolution of a single-electron density matrix corresponds to a single electronic excited state appearing in the linear response regime. Nonlinear SOS response calculations are then reformulated as sum-over-oscillator expressions, where multiply excited oscillators appear in the higher order responses leading to 2^n terms. It is interesting that the expressions for the TDHF CEO [89] (or equivalently the Casida TDDFT [86]) response obtained from the equations of motion correspond to the wavefunction, not the density matrix.

3.3 MCSCF Method

The multiconfigurational self-consistent-field (MCSCF) method, particularly of the complete active space SCF (CASSCF) type, has become a practical tool for studying systems with near-degenerate states, e.g., molecules with open-shell character, conical intersections (CoIns), transition metal complexes, and bond breaking molecules (see [173] for a recent review). It describes static correlation in medium-sized molecules well with affordable computational cost, and serves as the basis for more accurate methods which consider the dynamical correlation better, such as MRPT, MRCI, or multireference coupled cluster (MRCC) methods. CASSCF [174–176], which allows full CI expansion in the pre-selected active orbital space, is the most common and successful MCSCF implementation. The concept was introduced in the 1970–1980s by Ruedenberg et al. [177–179] under the name full optimization reaction space (FORS) and it is now known as complete active space, as coined by Roos, Tayler, and Siegbahn [174]. The essential step is the choice of active orbitals. Starting orbitals include localized orbitals [180–183], natural orbitals [184, 185], or pair natural orbitals [186–188], and the corresponding guidance has been reviewed [189, 190]. As a variation to CASSCF, the restricted active space (RASSCF) method [191, 192] decomposes the active space into three subspaces (RAS1, RAS2, RAS3), which allows one to consider more orbitals. Full CI is only allowed in RAS2 while a maximum number of holes and electrons are enforced in RAS1 and RAS3, respectively. Many excellent reviews of the MCSCF method exist (see [173] and references therein), but these mainly focus on the ground and valence excited states. Below we discuss the calculation of core excited states.

3.3.1 Manipulation of the Core Hole

MCSCF core state calculations were first performed in the 1980s by Ågren et al. [193–196], who studied the state-specific low-lying single and double core hole (DCH) states of a series of small molecules, systematically investigated the influence of correlation and relaxation effects on energies, and computed the effective transition dipole moments (TDMs) between separately optimized MCSCF states. The method was rediscovered about 20 years later [197]. In recent years it was employed for work on DCH states and spectra of various small molecules by Tashiro et al. [198–201]. Odelius et al. [202] first employed the state-averaged RASSCF (SA-RASSCF) method [192] in conjunction with the state-interaction treatment of SO effects [203] for L-edge XANES and RIXS spectra of transition-metal-based complexes, and soon calculations were performed for various other similar systems [204–207]. Hua et al. applied it to study the O K-edge ASRS signals of furan conical intersections in the photo-induced ring-opening reaction [208].

Table 1 SCF and MCSCF core hole orbital relaxation energies (eV) for single and double core ionized states of formamide. Singlet energies are used although triplet energies are included in parenthesis if different. Rebuilt based on [196]

Core hole		SCF	MCSCF
Single	$O1s^{-1}$	0.90	0.87
	$N1s^{-1}$	0.88	0.86
	$C1s^{-1}$	0.85	0.83
One-site double	$O1s^{-2}$	−0.28	−0.38
	$N1s^{-2}$	−0.23	−0.35
	$C1s^{-2}$	−0.17	−0.34
Two-site double	$O1s^{-1}N1s^{-1}$	1.79	1.72 (1.73)
	$O1s^{-1}C1s^{-1}$	1.78 (1.76)	1.69
	$N1s^{-1}C1s^{-1}$	1.74	1.68 (1.67)

Core hole calculations require a RAS1 space for the core hole orbital with fixed occupation number. The RAS2 space (and RAS3 space, if necessary) is used for valence correlation. Optimization of the MCSCF wavefunction with core holes must avoid the variational collapse. A rigorous treatment of orbital relaxation can be realized by a two-step procedure [193, 196]. One first freezes the orbital with core hole (RAS1) and relaxes the rest; the frozen core orbital is relaxed in the second step. Different optimization algorithms may be used for the two steps, for example, combining the second-order norm-extended optimization (NEO) algorithm [209, 210] and a straight Newton–Raphson (NR) algorithm. The effect of the second step can be illustrated by the resulting energy change (i.e., the core orbital relaxation energy). Table 1 gives an example for single and double core hole ionization of formamide [196]. The core orbital relaxation energy is a few electronvolts. For a single core hole, it is almost 1 eV; for a one-site double core hole, it is even less; whereas for two-site double core hole, it reaches about 2 eV. This gives an estimate of the effect of freezing the core orbital.

The optimization in step two in practice is more difficult to implement, especially when a state-averaged MCSCF is used, because in this case the object function to optimize is more complicated. It is usually sufficient to skip step two. The underlying physics is that the core orbital is well separated in energy from the valence orbitals, so core orbital relaxation hardly influences the nature of the valence orbitals, but mainly leads to a few electronvolts red shift of transition energies. The calibration can be obtained by aligning the main peak in the calculated XANES spectrum to experiment (this also covers relativistic effects and basis set incompleteness). Because the relaxation energies are similar at the SCF and MCSCF levels (Table 1), one can also estimate the shift value at the simpler SCF level.

3.3.2 Verification of the Active Spaces

A practical way to perform the core hole calculations is to run a valence CASSCF calculation first. One chooses the most important orbitals (e.g., localized or natural orbitals around a breaking bond, 3d orbitals of an excited transition metal) which have flexible occupations in the active space. The converged wavefunction serves as the initial guess for the RASSCF calculation. The original active space is included in the RAS2 space, and the excited core orbital is placed in the RAS1 space. Overall, one extra orbital (the core orbital) and two additional electrons (two core electrons) are added to the active space for core hole calculations to achieve more consistency in valence and core excited states calculations. Including additional virtual orbitals in the RAS3 space can help get a broader energy range for easier comparison with experimental XANES spectra, especially when the ionic potential is relatively high. For example, while studying the metal $L_{2,3}$-edge spectra from the *n*p shell, the RAS2 space should be the 3d orbitals of the metal, and some ligand orbitals can be included in the RAS3 space to represent the ligand-to-metal or metal-to-ligand charge transfer effects [202].

Even though there are general guidelines for choosing the active space [189, 190], it is still necessary to verify by checking the convergence of energy and/or spectra with the active space size. Figure 12 gives an example for the "UV absorption" and "O1s XANES" spectra of a furan CoIn in the photo-induced ring-opening reaction, obtained from a non-adiabatic molecular dynamics trajectory [208]. Such spectra may not be directly observed (because the system is in a superposition of valence states instead of the ground electronic state), but serve as good tests for the active space. They also give an estimate of the accuracy of the calculated transition dipole moments (see next section) which are essential for simulation of the time-domain nonlinear X-ray signals. In Fig. 12a, 10-state-averaged CASSCF was used, and, as expected, a smaller active space expands a broader energy range. Increase of the active space introduces more states with smaller oscillator strengths, and 10 electrons in 10 orbitals (10, 10) is sufficient to obtain essentially converged UV spectra. The optimized valence state wavefunction serves as the initial guess for core hole calculations. In Fig. 12b, 50 states were calculated using SA-RASSCF. Because core states have a higher density of states than valence states, additional states are needed to get an energy range of several to 10 eV for spectral usage. The 10 valence orbitals (RAS2) plus 1 core orbital (RAS1) [labeled as "(12, 1/10/0)". Twelve electrons include the 10 valence electrons and 2 electrons originally in the O1s orbital; numbers separated by slashes refer to the sizes of RAS1, RAS2, and RAS3] can give converged O1s XANES. Such active space settings are enough to obtain accurate and consistent electronic structure for both the valence and core-excited state manifolds. Note that here the convergence is much faster than the valence level. A test that includes 20 more orbitals in the RAS3 space "(6, 1/4/20)" shows that it can generate more states in the higher-energy region (534–540 eV) and modify the fine structure of spectra.

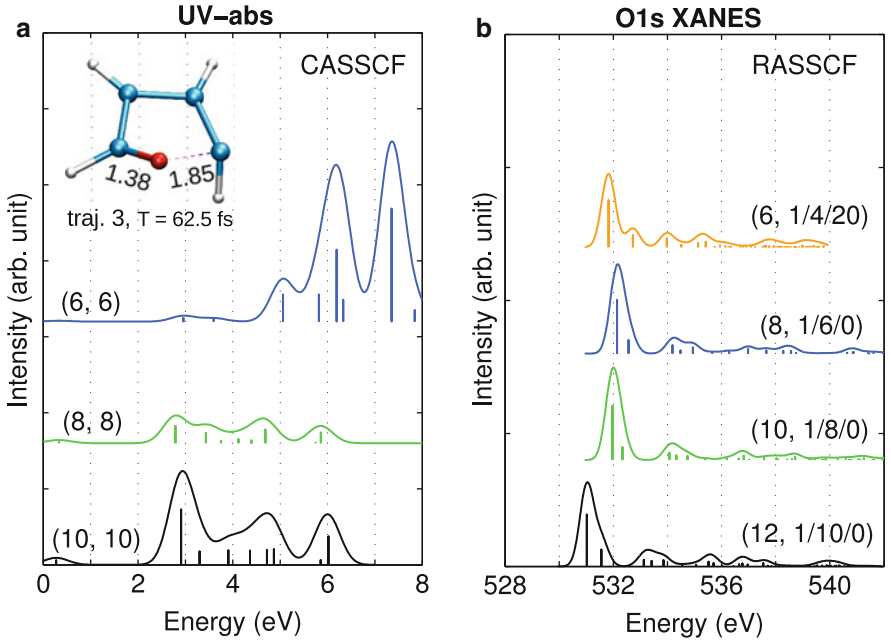

Fig. 12 Simulated (**a**) UV absorption and (**b**) O1s XANES spectra of a furan conical intersection (snapshot at $T = 62.5$ fs in trajectory 3 of the nonadiabatic MD simulation) at different active spaces by using the state-averaged CASSCF or RASSCF method. Active spaces are labeled by (n, m) in panel a or $(n, m_1/m_2/m_3)$ in panel b, where n, m are the number of electrons and orbitals in the active space, and m_1, m_2, and m_3 are the numbers of orbitals in the RAS1, RAS2, RAS3 spaces, respectively. All core hole energies have been uniformly shifted by −3.05 eV. *Inset* in a: geometry of the snapshot with C–O distances labeled in Å. Rebuilt based on [208]

3.3.3 Transition Dipole Moments Between Different Orbital Sets

Application of MCSCF to non-linear X-ray spectroscopy requires the computation of transition dipole moments between the valence, single-core, and double-core manifolds. This is more difficult than valence spectroscopy computations. In the latter case, the ground and the low-lying valence states can be generated in a single state-averaged MCSCF calculation using the same set of optimized orbitals, and the TDMs can be easily obtained by applying the Slater–Condon rule directly. The energies of states differ by one core hole are several tens to hundreds of electronvolts apart, and should be obtained in separate MCSCF calculations. The resulting orbitals are orthogonal within each set but non-orthogonal between different sets. MCSCF is an extension of the TDDFT/TDA or CIS method, so a similar simple solution can be applied. We denote the MCSCF wavefunctions of valence state m and core states e, respectively, as

$$\left|\Phi_m^{\mathrm{MCSCF}}\right\rangle = \sum_j \lambda_j^m \left|\phi_j^m\right\rangle, \tag{75}$$

$$\left|\Theta_e^{\mathrm{MCSCF}}\right\rangle = \sum_i \kappa_i^e \left|\theta_i^e\right\rangle, \tag{76}$$

where $|\phi_j^m\rangle$ and $|\theta_i^e\rangle$ are Slater determinants, and λ_j^m and κ_i^e are the CI coefficients. The corresponding transition dipole matrix is given by

$$\left\langle \Phi_m^{\mathrm{MCSCF}} \middle| \hat{\boldsymbol{\mu}} \middle| \Theta_e^{\mathrm{MCSCF}} \right\rangle = \sum_i \sum_j \left(\lambda_j^m\right)^* \kappa_i^e \left\langle \phi_j^m \middle| \hat{\boldsymbol{\mu}} \middle| \theta_i^e \right\rangle. \tag{77}$$

Because the MOs of the two manifolds are non-orthogonal, terms of $\left\langle \phi_j^m \middle| \hat{\boldsymbol{\mu}} \middle| \theta_i^e \right\rangle$ are calculated using the Löwdin rules [67, 211]. Because this method is based on the determinants, it has a lengthy expansion over configurations. The advantage is that it is easy for programming and parallelization. This algorithm was employed to compute the TDMs between the O1s core excited states and valence excited states of furan [208].

A more efficient approach is the CAS or RAS state interaction (CASSI/RASSI) method based on configuration state functions (CSFs) developed by Malmqvist and Roos [212, 213]. Because a many-electron wavefunction can be equivalently described in different sets of molecular orbitals, the orbitals are rotated (and the coefficients are changed correspondingly) to be biorthonormal. We can then simply use the Slater–Condon rule. Methods for including the spin-orbit (SO) coupling have been developed [203]. This algorithm was employed in early effective TDMs calculations between state-specific valence and core MCSCF states [195] and widely used in recent L-edge XANES and RIXS calculations [202, 204–207].

3.3.4 Example: ASRS Signals as a Probe of Conical Intersections in Furan

We use the furan ring-opening reaction as an example to illustrate the simulation of nonlinear time-domain X-ray signals at the MCSCF level. The ASRS signal provides a sensitive probe of the photo-induced reaction in the vicinity of a CoIn. CASSCF is employed to describe the near-degeneracy introduced by C–O bond-breaking. We first performed a non-adiabatic molecular dynamics simulation by using the trajectory surface hopping (TSH) method [214]; then representative snapshots are chosen for valence and O1s core-excited states calculations by using state-averaged CASSCF and RASSCF, respectively. TDMs were then determined and ASRS signals were calculated. Figure 13 displays the calculated ASRS signals of furan during the passage of a V_1/V_0 CoIn (V_0 and V_1 stand for the ground and lowest valence excited states, respectively) [208]. It is found that as time goes from 27.5 to 33.0 fs, the molecule gradually goes from V_1 to V_0 (Fig. 13b). The

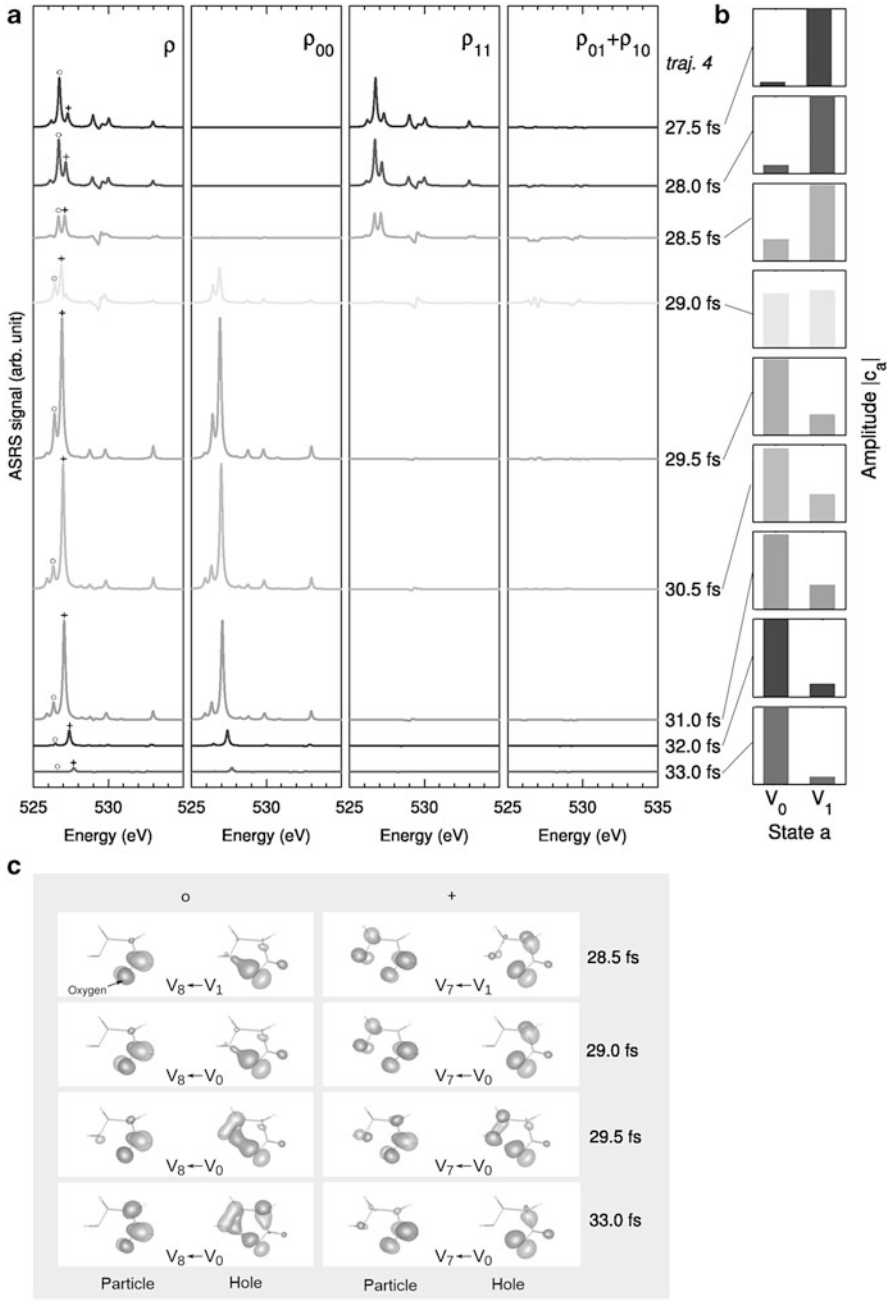

Fig. 13 (**a**) Simulated ASRS signals of for furan during the passage of V_1/V_0 conical intersection ($T = 27.5$–33.0 fs in MD trajectory 4) by using the MCSCF method. From *left to right*, total signals and contributions from ρ_{00} and ρ_{11} populations, and from $\rho_{01} + \rho_{10}$ coherence (0 and 1 refer to states V_0 and V_1). (**b**) Absolute amplitudes of the two constituting states. (**c**) NTOs [215–217] for the two main peaks in the ASRS signals (denoted by "o" and "+"). Dominant hole and particle orbitals are plotted with contour isovalue = 0.08. Rebuilt based on [208]

resulting signals are sensitive to the change in chemical and electronic structure (Fig. 13a, left). Moreover, the contributions from ρ_{00} and ρ_{11} populations and ρ_{01} and ρ_{10} coherences may be separated. Below 29.0 fs the signals mainly come from the V_1 state and after 29.0 fs from the V_0 state. At the transition point $T = 29.0$ fs both V_0 and V_1 populations have comparable contributions to the signals, and coherence terms have larger contributions than at any other time. We had further analyzed two major peaks in the total signals (denoted as "o" and "+", the former is always lower in energy) and found that they can be tracked by varying time-dependent strength: peak "o" is stronger before $T = 29.0$ fs, when peak "+" becomes stronger. Both peaks correspond to transitions from the oxygen p orbital to π^* transitions, as indicated by the dominant natural transition orbital (NTO) [215–217] pairs (Fig. 13c). As time increases, for peak "o" the hole orbital changes from localized on the C–O bond to delocalized. For peak "+", the particle orbital changes from delocalized to localized on the C–O bond.

3.4 Other Core Hole State Simulation Techniques

Unlike most of the practical implementations of DFT, which contain empirical parameters from numerical fitting to experimental data or results from higher level theories, the Green's function method based on many-body perturbation theory provides a systematic way to achieve higher accuracy. Quasiparticle orbital energies can be obtained by solving a set of coupled Hedin equations [218]. These orbital energies offer a much better estimation of the ionization potential and the electron affinity of the system than do Kohn–Sham orbital energies. In Hedin's equations, the one-particle Green's function is solved through a Dyson-like equation with a self-energy, which is complex and energy-dependent. Self-energy plays a similar role as does exchange-correlation energy in DFT. The most popular approximation of self-energy is the GW approximation, where the vertex operator is simplified as product of δ-function and self-energy becomes the product of single-particle Green's function (G) and the dynamically screened Coulomb interaction (W) [218, 219]. Moreover, particle-hole interaction, which is neglected in TDDFT, can be considered and another Dyson-like equation for the four-point polarization function (two-particle Green's function) can be derived [220]. This is the Bethe–Salpeter equation (BSE). GW/BSE equations have to be solved iteratively in a self-consistent way. DFT orbitals and their energies can be used as initial guesses, but the full self-consistent solutions are independent on the initial guesses [221]. BSE can be recast into a form similar to the Casida equation in linear response TDDFT (see (52)), but the kernel in BSE could be frequency-dependent [222–224], which offers a model for designing non-adiabatic exchange-correlation kernel in TDDFT. For a thorough comparison of GW/BSE and TDDFT, see

[219]. The GW/BSE approach has been successfully applied to XANES calculations of solids [225–231]. Until now, GW/BSE is still a theory of heavy solid state flavor. Adapting it to a molecular theory is currently in progress [232–234].

The many-body Green's function techniques with algebraic diagrammatic construction (ADC) [235] was also used to study core excited states [236] and the dynamics of core holes and particles [237, 238]. So far, most applications of the above many-body methods have been made to XANES, and their use to calculate core excited states is limited to small systems because of computational cost. Nonlinear X-ray spectroscopy simulation of large systems is an important future goal.

Other theoretical methods were designed primarily for metal L-edge calculations. These are more challenging than the ligand or metal K-edge calculations because of multiplet effects, spin-orbital coupling, and metal-to-ligand or ligand-to-metal charge transfer. Such transition metal-based systems have attracted broad interest because of the numerous applications in biology (e.g., metallic enzyme centers) and artificial light harvesting (e.g., dye-sensitized solar cells). Because the $2p \rightarrow 3d$ transitions are dipole-allowed, the metal $L_{2,3}$-edge spectra can better reflect the valence electron structure of the metal 3d orbitals which are more essential to the chemistry. For metal K-edge spectra, the $1s \rightarrow 3d$ transitions are dipole forbidden. These methods have mainly been applied to XANES and RIXS spectra. Nonlinear X-ray spectra require accurate transition dipole moments. To obtain these, both the valence and core-excited states must be treated with consistent accuracy.

Early theoretical efforts on transition metal L-edge X-ray spectra were based on semi-empirical methods developed by de Groot and coworkers [239, 240], namely the crystal field multiplet (CFM) and the charge transfer multiplet (CTM) models. These methods start with the SO-coupled multiplets of the excited metal atom and include the effect of ligands using ligand field theory (LFT). Adjustable parameters include the crystal field splitting and the charge transfer energy. In recent years, there are developments in *ab initio* theory including the *ab initio* CTM based on DFT-CI [241], *ab initio* multiplet ligand-field theory (MLFT) method with Wannier orbitals [242], and method employing the Russel–Saunders coupling [243]. These methods are usually computationally expensive and were employed for relatively small systems with high symmetry. Neese and co-workers [244, 245] proposed an efficient approach by combining DFT and the restricted-open-shell configuration interaction singles (DFT/ROCIS). It introduces global empirical parameters for the periodic table to scale the CI matrix and includes dynamic correlation and the SO coupling effects. Excellent agreement with experiment was obtained for most systems. Besides RASSCF, Odelius et al. [202] further tested the influence of dynamic correlations by using the multiconfigurational second-order perturbation theory (RASPT2) for a $[Ni^{II}(H_2O)_6]^{2+}$ complex. TDDFT has also been tested for this topic. Although it is widely believed that TDDFT is only valid for transition metal-based systems with closed-shell (e.g., the low spin form of Fe^{II}, $S = O$) but not to those open-shells (e.g., the high spin form of Fe^{II}, $S = 2$), it is still necessary to examine its performance because of its high efficiency. It was found [246] that,

for a SCO complex $[Fe^{II}(tren(py)_3)]^{2+}$, the TDDFT approach can predict the Fe L_3-edge XANES spectra of both the low-spin and high-spin complexes which agree well with experiment [247–249]. However, such agreement depends on the system. When the same procedure was applied to a variety of Fe^{II} and Fe^{III} complexes with different spin states, the accuracy did not always persist (Hua et al., submitted).

Other post-HF methods have been employed for simulating the K-edge XES, XAS, or RIXS spectra of very small molecules. The intentions are to examine the effect of electron correlation, to include the effect of shake-up/shake-off processes, and/or to consider the influence of bond breaking. Ågren and coworkers had reported early CI studies of XAS [250, 251] and XES [252, 253] spectra of CO and N_2. Recently, Neese et al. [254] studied the vibrationally-resolved RIXS spectra of CO_2 using the MRCI method. Coupled cluster (CC)-based methods have been developed for core state calculations, including single-reference equation-of-motion CC (EOM-CC) [255, 256], state-specific multireference CC (SS-MRCC) [257], and open-shell symmetry-adapted cluster configuration interaction (SAC-CI) methods [258, 259].

4 Other Computational Issues

4.1 Density Functionals for Core Excitations

Core excitation energies are often underestimated by TDDFT. It is often necessary to shift the TDDFT core excitation spectrum by tens of electronvolts for light atom excitations and hundreds of electronvolts for heavy atom core excitations to match experiment. The corresponding shifts for ΔSCF type methods are much smaller, with typical values < 2 eV [57] for light atom core excitations. Both ΔSCF and TDDFT have relativistic and basis set errors. The large differences between their shifts come from the self-interaction error of energy density functionals and the absence of orbital relaxation in TDDFT. A constant (even large) shift to a simulated linear X-ray absorption spectrum does not change the relative positions of spectroscopic features. This may not be the case for nonlinear X-ray spectroscopy spectra because core excitations may interact with each other, and those shifts cannot be considered as constants. Thus a proper choice of energy density functional is essential for a successful TDDFT simulation of nonlinear X-ray spectroscopy signals.

The failure of common generalized gradient approximation (GGA) or hybrid functionals to capture long-range charge transfer excited states was analyzed thoroughly [94], and is attributed to the self-interaction error in the functionals used. Surprisingly, a simple Perdew–Zunger self-interaction correction (SIC) scheme [260] applied to ΔSCF or TDDFT does not correct the core excitation energies in the right direction [261]. This SIC scheme has already been combined with the CPP method (explained in the previous section) to produce improved core

excitation energies [262]. Core excitations share many similarities with long-range charge transfer excitations, because the transition orbitals involved in these excitations have negligible overlaps. This suggests that a similar strategy may be used for designing energy functionals for core excitation as is done for long-range charge transfer excitations. The range-separated functionals [263–277] are good choices. In these functionals, the long-range part of the exchange energy is evaluated using Hartree–Fock theory, and in the short-range DFT exchange is used. The $1/r_{12}$ operator is partitioned to two parts:

$$\frac{1}{r_{12}} = \frac{\mathrm{erf}(\mu r_{12})}{r_{12}} + \frac{1 - \mathrm{erf}(\mu r_{12})}{r_{12}}, \tag{78}$$

where $\mathrm{erf}(r)$ is the error function and μ is a parameter to control the separation of the long- and short-ranges. We had employed this type of long-range corrected functionals in SXRS simulations [92, 109].

To improve the performance of these long-range corrected functionals, Hartree–Fock exchange should be introduced because core orbitals are very localized. This can be done by adding a Gaussian correction term in the $1/r_{12}$ operator partition scheme:

$$\frac{1}{r_{12}} = \frac{\mathrm{erf}(\mu r_{12})}{r_{12}} - k\frac{2\mu}{\sqrt{\pi}}\mathrm{e}^{-\frac{\mu^2}{a}}r_{12}^2 + \frac{1 - \mathrm{erf}(\mu r_{12})}{r_{12}} + k\frac{2\mu}{\sqrt{\pi}}\mathrm{e}^{-\frac{\mu^2}{a}}r_{12}^2, \tag{79}$$

where k, a are additional parameters for introducing Hartree-Fock exchange in the short-range. The above scheme can be used to obtain the LCgau-core-BOP functional [278]. For light atoms, it can predict their core excitation energies with less than 1 eV errors.

Similarly, Besley and coworkers had proposed the following partition scheme [279]:

$$\frac{1}{r_{12}} = \boxed{C_{\mathrm{SHF}}\frac{1 - \mathrm{erf}(\mu_{\mathrm{SR}} r_{12})}{r_{12}} + C_{\mathrm{LHF}}\frac{1 - \mathrm{erf}(\mu_{\mathrm{LR}} r_{12})}{r_{12}}} - \boxed{C_{\mathrm{SHF}}\frac{1 - \mathrm{erf}(\mu_{\mathrm{SR}} r_{12})}{r_{12}} + C_{\mathrm{LHF}}\frac{1 - \mathrm{erf}(\mu_{\mathrm{LR}} r_{12})}{r_{12}}} + \frac{1}{r_{12}}, \tag{80}$$

where the C_{SHF} and C_{LHF} parameters control the Hartree–Fock exchange contribution in the long- and short-range. In the above equation the terms in the first box are evaluated with Hartree–Fock exchange and the second with DFT exchange. The resulting SRC1 functional is

$$E_{\mathrm{xc}}^{\mathrm{SRC1}} = \boxed{C_{\mathrm{SHF}} E_{\mathrm{x}}^{\mathrm{SR\text{-}HF}}(\mu_{\mathrm{SR}}) + C_{\mathrm{LHF}} E_{\mathrm{x}}^{\mathrm{LR\text{-}HF}}(\mu_{\mathrm{LR}})} - \boxed{C_{\mathrm{SHF}} E_{\mathrm{x}}^{\mathrm{SR\text{-}DFT}}(\mu_{\mathrm{SR}}) + C_{\mathrm{LHF}} E_{\mathrm{x}}^{\mathrm{LR\text{-}DFT}}(\mu_{\mathrm{LR}})} + E_{\mathrm{xc}}^{\mathrm{DFT}}. \tag{81}$$

An alternative form of the short-range corrected functional (SRC2) is

$$E_{\mathrm{xc}}^{\mathrm{SRC1}} = \boxed{C_{\mathrm{SHF}} E_{\mathrm{x}}^{\mathrm{SR\text{-}HF}}(\mu_{\mathrm{SR}}) + C_{\mathrm{LHF}} E_{\mathrm{x}}^{\mathrm{LR\text{-}HF}}(\mu_{\mathrm{LR}})} - \boxed{(1 - C_{\mathrm{SHF}}) E_{\mathrm{x}}^{\mathrm{SR\text{-}DFT}}(\mu_{\mathrm{SR}}) + (1 - C_{\mathrm{LHF}}) E_{\mathrm{x}}^{\mathrm{LR\text{-}DFT}}(\mu_{\mathrm{LR}})} + E_{\mathrm{c}}^{\mathrm{DFT}}. \tag{82}$$

The two functionals coincide when $\mu_{\mathrm{SR}} = \mu_{\mathrm{LR}}$. Both functionals can predict light atom core excitation energies with sub-1 eV accuracy [279].

Instead of partitioning the Coulombic operator in real space, Nakai and coworkers had divided the electron density (orbitals) into the core and valence groups. They proposed to use hybrid functionals with large Hartree–Fock exchange components for core electrons and common hybrid functionals for valence electrons. In the total energy expression, the hybrid scheme varies in the core–core, core–valence, and valence–valence interaction terms. After numerical fitting of the hybrid parameters, the resulting core–valence-(CV) B3LYP functional [280] gives very good core excitation energies for light atoms (error less than 1 eV). In addition, this scheme can be extended to Rydberg states [281]. Despite their success in core excitation calculations, such orbital-specific functionals not only lead to a complicated TDDFT implementation, but also bring some conceptual difficulties such as the lack of a unique Fock operator.

In summary, exchange-correlation functionals specific for core excitations can be designed along the same lines for long-range charge transfer excitations. The key issue is that core excitation functionals cannot be too specific, because, in many nonlinear X-ray spectroscopy experiments, both core and valence excited states are involved and should be treated on the same footing. The core excitation functionals discussed above should be tested in future nonlinear X-ray spectroscopy simulations.

4.2 *Expansion of the Polarizability in Electron–Hole Operators*

In vibrational Raman spectroscopy the polarizability can be expanded perturbatively in the normal mode operators $\hat{Q}_i$ of the system,

$$\hat{\alpha}_v = \hat{\alpha}_{v0} + \sum_i \frac{\partial \hat{\alpha}_v}{\partial \hat{Q}_i}\hat{Q}_i + \sum_{ij} \frac{\partial^2 \hat{\alpha}_v}{\partial \hat{Q}_i \partial \hat{Q}_j}\hat{Q}_i\hat{Q}_j + \cdots, \tag{83}$$

where

$$\hat{Q}_i = \sqrt{\frac{\hbar}{2m_i\omega_i}}\left(\hat{a}_i^\dagger + \hat{a}_i\right). \tag{84}$$

Here α_{v0} is the polarizability at the equilibrium geometry, and $\hat{a}_i^\dagger$ ($\hat{a}_i$) is the ith phonon creation (annihilation) operator.

In analogy to this, the effective polarizability in electronic X-ray Raman scattering ((18) or (20)) can also be expanded as

$$\hat{\alpha}_p = \alpha_0^{(p)} + \sum_{i,\,j} K_{ij}^{(p)} \hat{c}_i^\dagger \hat{c}_j + \sum_{i,\,j,k,\,l} L_{ijkl}^{(p)} \hat{c}_i^\dagger \hat{c}_j \hat{c}_k^\dagger \hat{c}_l + \cdots, \tag{85}$$

where $\hat{c}_i^\dagger$ ($\hat{c}_i$) is the creation (annihilation) operator for an electron in the ith valence orbital and i, j, k, l are valence orbital indices. The super- and subscript ps indicate the pulse inducing the polarizability and appear on the right hand side as a superscript for typographical convenience. $\hat{\alpha}_0^{(p)}$ is the effective polarizability responsible for Rayleigh scattering. The electron–hole pairs created by $\hat{c}_i^\dagger \hat{c}_j$ play the same role in X-ray Raman scattering as do the vibrational normal modes $\hat{Q}_i$ in optical Raman scattering.

The direct use of the sum-over-state expression of the effective polarizability ((18) or (20)) would require calculation of large number of many-body states and the corresponding state-to-state transition dipoles, which is tedious for large systems. X-Ray Raman signals may be calculated alternatively by solving equations of motion for the reduced, single-electron density matrix in the valence space [87–89, 158]. The polarizability should then be expanded in valence electron creation and annihilation operators (see (85)) avoiding the eigenstate expansion. Core excitations can be included approximately in the calculation of the expansion coefficients, but then the X-ray response is calculated in the valence space. We can view the valence (occupied and unoccupied) orbitals as an open system that exchanges electrons with the core space. This is formally analogous to molecular junctions and the same methods can be applied to the X-ray signals [282–288].

In the following we show how to calculate the expansion coefficients of $\hat{\alpha}_p$, $K_{ij}^{(p)}$ and $L_{ijkls}^{(p)}$, starting with a model Hamiltonian. In solid state applications it is common to construct an electron-boson model Hamiltonian to represent all core and valence excitations [289–293]. Model Hamiltonians can be obtained semi-empirically by numerical fitting to experimental results, or from high level quantum chemistry calculations of model systems. The model Hamiltonian is written in terms of the creation and annihilation operators $\hat{c}_{i(\kappa)}^{(\dagger)}$ for single-particle valence

(core) orbitals $\phi_{i(\kappa)}$ (where the anticommutation relations $\left\{\hat{c}_i^\dagger, \hat{c}_j\right\} = \delta_{ij}$ are satisfied). The following model Hamiltonian describes the valence and core orbitals and their interaction:

$$H = \sum_i \varepsilon_i \hat{c}_i^\dagger \hat{c} + \sum_{ijkl} U_{ijkl} \hat{c}_i^\dagger \hat{c}_j^\dagger \hat{c}_k \hat{c}_l + \sum_\kappa \varepsilon_\kappa \hat{c}_\kappa^\dagger \hat{c}_\kappa + \sum_{ij\kappa} U_{ij\kappa} \hat{c}_i^\dagger \hat{c}_j \hat{c}_\kappa \hat{c}_\kappa^\dagger, \tag{86}$$

where ε_i is the energy of the orbital ϕ_i and U_{ijkl} is a nonlinear-interaction matrix element. This could, for example, be the coulomb interaction

$$U_{ijkl} = \int d\mathbf{r} d\mathbf{r}' \phi_i(\mathbf{r}) \phi_j(\mathbf{r}') \frac{1}{\mathbf{r} - \mathbf{r}'} \phi_k(\mathbf{r}') \phi_l(\mathbf{r}). \tag{87}$$

We thus write the Hamiltonian of the valence electrons in the absence of core holes

$$\hat{H}_0 = \sum_i \varepsilon_i \hat{c}_i^\dagger \hat{c}_i + \sum_{ijkl} U_{ijkl} \hat{c}_i^\dagger \hat{c}_j^\dagger \hat{c}_k \hat{c}_l. \tag{88}$$

The transition dipole operator in the core-excitation regime is written

$$\begin{pmatrix} \hat{V} \\ \hat{V}^\dagger \end{pmatrix} = \sum_{i\kappa} \begin{pmatrix} \mu_{i\kappa}^* \hat{c}_\kappa^\dagger \hat{c}_i \\ \mu_{i\kappa} \hat{c}_i^\dagger \hat{c}_\kappa \end{pmatrix}, \tag{89}$$

where κ labels core orbitals. We may now treat the core-valence interaction term in (86) perturbatively to obtain an effective Hamiltonian for the valence electrons in the presence of a single core hole or by recalculating the orbitals of the model in the presence of the core hole potential. In the latter case we must start on the basis of 1-hole orbitals (denoted by ϕ_a, etc.), in which the valence Hamiltonian is

$$\hat{\tilde{H}}_0 = \sum_a \varepsilon_a \hat{c}_a^\dagger \hat{c}_a + \sum_{abcd} U_{abcd} \hat{c}_a^\dagger \hat{c}_b^\dagger \hat{c}_c \hat{c}_d, \tag{90}$$

and then transform to the original orbitals with the overlap matrix **T:**

$$\hat{c}_a^{(\dagger)} = \sum_i t_{ai}^{(*)} \hat{c}_i^{(\dagger)}. \tag{91}$$

This immediately permits us to rewrite $\tilde{H}_0$ on the basis of 0-hole orbitals ϕ_i:

$$\hat{\tilde{H}}_0 = \sum_{ij} \tilde{\varepsilon}_{ij} \hat{c}_i^\dagger \hat{c}_j + \sum_{ijkl} \tilde{U}_{ijkl} \hat{c}_i^\dagger \hat{c}_j^\dagger \hat{c}_k \hat{c}_l, \tag{92}$$

where we have defined the auxiliary parameters

$$\tilde{\varepsilon}_{ij} \equiv \sum_a \varepsilon_a t_{ai}^* t_{aj} \quad \tilde{U}_{ijkl} \equiv \sum_{abcd} U_{abcd} t_{ai}^* t_{bj}^* t_{ck} t_{dl}. \tag{93}$$

These are the basic relations required to obtain an explicit second-quantized representation for the polarizability $\hat{\alpha}_p$. α has been expanded in creation/annihilation operators in (85). Although one may question the convergence of such a series in general, we can see that higher order terms are proportional to successively higher powers of the pulse duration and it is therefore useful in the limit of ultrashort pulses. To obtain explicit expressions for the coefficients (K_{ij}, etc.) in (85), we expand the exponentials in (25) order by order and adopt a consistent operator ordering. Although the ordering $\hat{c}^\dagger \hat{c} \hat{c}^\dagger \hat{c} \ldots$ is used here, normal ordering with all c to the right is also possible. Because the indices are unrestricted over valence orbitals (both occupied and virtual), there is not much reason to prefer one or the other for low-order expansion and many-electron systems (in particular, this holds because we are interested in a form for $\hat{\alpha}$ which is equally valid for arbitrary valence excited states and not simply polarizability of the ground state). This is important for nonlinear spectroscopies and monitoring of nonequilibrium processes. In expanding the exponentials in (85), various time factors are brought down as multiplicative constants. Integration over these factors with the field envelopes defines a set of auxiliary functions:

$$f_p^{(lmn)}(\Lambda) \equiv \int_{-\infty}^{\infty} d\tau \int_{-\infty}^{\tau} d\tau' \frac{\mathcal{E}_p^*(\tau)\mathcal{E}_p(\tau')}{l!m!n!} \left(\frac{\tau' - \tilde{\tau}_{pi}}{\mathrm{i}}\right)^l \left(\frac{\tau - \tau'}{\mathrm{i}}\right)^m \left(\frac{\tilde{\tau}_{pf} - \tau}{\mathrm{i}}\right)^n, \tag{94}$$

which encode all time dependence and depend on the pulse parameters (collectively denoted as Λ). This auxiliary function enters proportional to terms in (85) which result from lth order expansion in the first propagator, mth order in the second, and nth order in the third. Note that, because of the properties of the pulse and the definition of the $\tilde{\tau}$, the lower limits of integration may be truncated at $\tilde{\tau}_{pi}$ and the upper limit of the $d\tau$ integration may be truncated at $\tilde{\tau}_{pf}$. These auxiliary functions vanish in the limit of $t_p \to 0$ and, moreover, higher order auxiliary functions (resulting from higher-order terms in the exponential expansion) vanish progressively faster so that the ratio of successive functions also vanishes and the series converges for sufficiently short pulses (pulses shorter than the inverse of any relevant material energy scales). Further insight is gained by considering flat pulses, in which case $f_p^{(lmn)}$ is roughly proportional to a power of the pulse duration $(T_p)^N$ where $N = l + m + n$ (neglecting factors of i and factorials). Because this procedure naturally separates the parametric field dependence from the material operators, we can write the expansion coefficients (K_{ij}, etc.) generically without specifying a

pulse envelope. To simplify these expressions, we define $\mu_{ij} \equiv \sum_{\kappa} \mu^{*}_{i\kappa}\mu_{j\kappa}$. A straightforward but lengthy calculation then yields the first few terms in (85):

$$\alpha_0^{(p)} = \sum_i \mu_{ii} + f_p^{(010)}(\Lambda)\sum_i \mu_{ii}\tilde{\varepsilon}_{ii}, \tag{95}$$

$$\begin{aligned} K_{ij}^{(p)} = -\mu_{ij} + \left(f_p^{(100)} + f_p^{(001)}\right)\left(\sum_l \mu_{ll}\right)\left(\varepsilon_i\delta_{ij} + \sum_l U_{illj}\right) \\ -f_p^{(010)}\left(\sum_k \left(\mu_{jk}\tilde{\varepsilon}_{ik} + \mu_{ki}\tilde{\varepsilon}_{kj}\right) + \sum_{kl}\mu_{kl}\tilde{U}_{kijl}\right) \end{aligned}, \tag{96}$$

$$L_{ijkl}^{(p)} = -\sum_m \left\{ f_p^{(001)}\mu_{ij}U_{kmml} + f_p^{(010)}\left(\mu_{jm}\tilde{U}_{iklm} + \mu_{mk}\tilde{U}_{mijl}\right) + f_p^{(100)}\mu_{lk}U_{immj} \right\}, \tag{97}$$

where, in the first line, we have explicitly notated the dependence on the pulse parameters via the auxiliary function f (omitting this dependence in further expressions for brevity). Note that the above is an expansion up to first order roughly in the product $T_p\varepsilon$ where ε is the material energy scale and higher order expansions generate higher order terms in this quantity which contribute to every coefficient in (85). Because the order of the expansion is determined by the sum $l+m+n$, expanding to second-order adds terms proportional to $f_p^{(101)}, f_p^{(110)}, f_p^{(011)}, f_p^{(200)}$ etc.

4.3 Double Excitations and the X-Ray Double-Quantum-Coherence Signal

Double core excitations or double excitations with a core hole and a valence hole are directly probed by nonlinear X-ray four-wave mixing spectroscopy (e.g., photo echo [48] and double-quantum-coherence [24]) and multidimensional SXRS [108] experiments. Calculating double excitations is of essential importance in nonlinear X-ray spectroscopy simulation. Double core states studied in X-ray two-photon photoelectron spectroscopy can be considered as doubly core excited states of the system with two electrons removed. These double core states are more sensitive to the chemical environment and carry more pronounced electronic many-body effects compared to singly core excited states [201, 294–297]. Strong double excitations (shake-up) features can be found even in linear XANES signals [298].

A doubly excited state can be phenomenologically defined as an excited state with energy close to the sum of two single excitation energies. This definition may be misleading. First, near-degeneracy in energy does not mean the excited states share the same character, and, second, there exists double excitations lower in energy than any single excitation [299]. A proper definition for doubly excited states in quantum chemistry relies on a single Slater determinant reference state. If an excited state can

be well described by a multiple Slater determinant expansion based on this reference, and the CI coefficients of the double excitation configurations are dominant, we call it a doubly excited state. According to this definition, different reference states may lead to different double-excitation character [300, 301].

Double excitation remains one of the challenges in DFT and TDDFT [301]. Maitra et al. showed that a frequency-dependent exchange-correlation kernel, which is not available in the common implementation of adiabatic TDDFT, is essential for accessing double excitations [95]. In contrast to early expectations [302], quadratic response theory in adiabatic TDDFT only gives double excitation frequencies as sums of two single excitation frequencies [91, 301, 303]. Adiabatic TDDFT implicitly assumes that the double excited state wave functions are products of single excited state wave functions. This has been shown in [303]. These trivial double excitations behave as harmonic oscillators and result in vanishing double-quantum-coherence signals [24]. Originally dressed TDDFT was proposed to remedy this double excitation issue, but information about the relevant double excitation a priori hinders its practical application. Frequency-dependent exchange-correlation kernels based on the Bethe–Salpeter equation were proposed [224, 304–306], but they have only been tested in simple models or small molecular systems because of complexity. The matrix elements of unknown exchange-correlation kernel can also be extracted from the branching ratio of the experimental $L_{2,3}$-edge X-Ray absorption spectra of 3d transition metals [307]. Spin-flip TDDFT (SF-TDDFT) may access some doubly excited states through a triplet reference state [307–312]. Very recently, the constricted variational DFT (CV-DFT) [313–315] was developed to address double excitations [316]. Implementation and testing of this method is under way. We have also combined the ΔSCF method with REW-TDDFT to calculate doubly core excited state and apply it in X-ray double-quantum-coherence (XDQC) signal simulation [24]. The main difficulty with this approach is the unbalanced treatment of the two core holes: one core hole was obtained with ΔSCF and the other with REW-TDDFT. Althgough the two core holes are not symmetric, different calculation order (either ΔSCF first or REW-TDDFT first) would lead to different simulation results [24]. Other high level *ab initio* methods, such as CASSCF/CASPT2 [317], coupled cluster (CC) [318], MRCI [319, 320], symmetry-adapted cluster configuration interaction (SAC-CI) [321], algebraic diagrammatic construction (ADC) [299, 322, 323], and multireference Møller–Plesset perturbation theory (MRMP) [324, 325], can accurately capture double excitations, but their use is limited to small systems because of high computational cost.

The DQC signal probes doubly excited states and strongly depends on the coupling between single excitations. In the infrared regime, DQC signals detect the couplings between vibrational modes, which determine their anharmonicities [326]. In the optical regime, DQC signals were used to reveal quantitative information about electron–electron interactions, many-body wave functions, and electron correlation in excitons [327]. The X-ray variant of this technique (XDQC) is sensitive to correlation and exciton scattering in doubly core excited states, making it an attractive experimental test for electronic structure theories of strongly

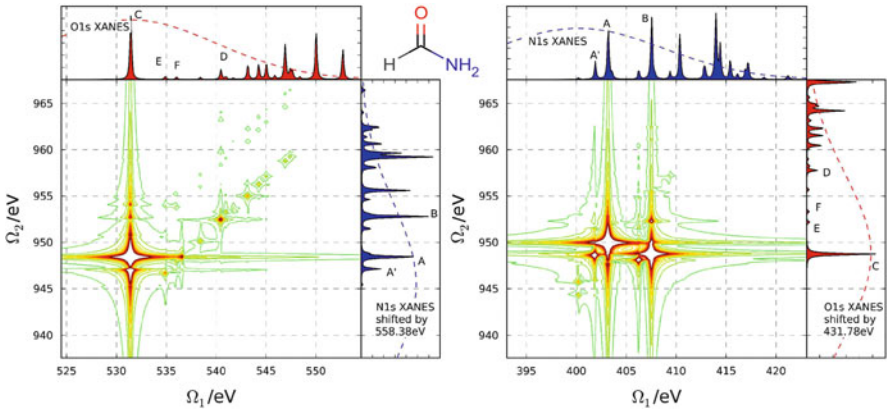

Fig. 14 Comparison of the absolute values of the ONNO (*left*) and NONO (*right*) S_{XDQC} ($t_3 = 5$ fs, Ω_2, Ω_1) signals of formamide (structure shown on the *top*) from calculations combined ΔSCF with REW-TDDFT. XANES spectra are shown in the *marginals*. Figure adapted from [24]

correlated systems [328]. XDQC signals exist only when single core excitations interact with each other and doubly core-excited states are not simply an outer product of two singly core-excited states. XDQC signals vanish for noninteracting single core excitations.

We have simulated the XDQC signals of formamide at the N and O K-edges [24]. In Fig. 14 we show the 2-D projections (we set the last time delay to 5 fs) of the XDQC signals for different pulse orders (ONNO and NONO). The Ω_1 axis represents the N1s or O1s single excitation energies and the Ω_2 axis represents the N and O1s double excitation energies. The intensity of the 2-D XDQC signal at the position (Ω_1, Ω_2) represents the correlation between the single excitation at Ω_1 and the double excitation at Ω_2. The (shifted) XANES spectra are also placed in the marginals to help the signal analysis. In the plot of the ONNO (O excitation first, and then N excitation; see the left column of Fig. 14) signal we can find features scattered along several diagonal straight lines, which indicates almost uniform interaction between the O1s and N1s single excitations, so that the double excitations are almost sums of the single excitations with constant shifts. This can also be confirmed by comparing the energy differences of spectroscopic features in the XANES and XDQC spectra. Take peak A and A′ in the N1s XANES spectrum (right marginal of the ONNO signal) for an example. The energy difference between these two peaks is 1.29 eV in XANES and 1.34 eV in the ONNO spectrum, which are very close to each other. This means the first O1s excitation shifts all N1s excitations in almost the same way, so the energy differences between peaks would not change too much. The same linear pattern is not observed in the NONO signal (the right column of Fig. 14). This tells us the second O1s excitations are affected very differently from each other by the first N1s excitations. From the ONNO signal we can also find that peak B in the N1s XANES only correlates weakly with peak C in the O1s XANES when the O1s electron is excited first, whereas if the N1s

electron is excited first, the N1s excitation which corresponds to peak B heavily affects the following O1s excitation which corresponds to peak C (a strong feature connecting peak B and C in the NONO spectrum). By comparing XDQC signals of different pulse orders, we can understand the subtle many-body correlations between core excitations. Generally, X-ray four-wave mixing signals including the XDQC signals can measure double core excited states directly, thus providing new experimental tests for the accuracy of the electronic structure methods and offering a way to visualize projections of the complicated many-electron wave functions [25, 26].

4.4 Ionization, Photoelectron Signals and Resonances

X-Ray photons with energies higher than the ionization threshold can excite the system to a metastable resonance state, and then this resonance decays to a cationic species and a leaving electron. In spectroscopy, either the cationic species or the leaving electron can be detected, both providing us with windows into the electronic structure of the parent neutral system.

In addition to excitation, molecular ionization is another way to trigger impulsively rich electronic and nuclear dynamics such as geometry relaxation, molecular dissociation [329], charge migration [330–334], and radiation emission [335]. Ionization has advantages over excitation in pumping the system because there is no selection rule to restrict which ionization is allowed, and there is usually a lower number of energetically accessible cationic states compared to the large number of high energy exited neutral states in excitation experiments. Moreover, after ionization, we have the freedom to detect the cationic states or the ejected electron, which can provide more information about the parent neutral species. X-Ray ionization and fragmentation have been used to probe transient molecular structures during a photoinduced chemical reaction process [336]. Recently we studied the cationic states of the amino acid glycine prepared by a sudden N1s core ionization produced by an attosecond X-ray pulse [337]. The created superposition of cationic states is probed by 2D transient X-ray absorption (TXAS) and 3D ASRS. Our simulated ASRS results reveal the complex coupling of the valence and core excited states of the cation.

X-Ray photoelectron spectroscopy (XPS) [338] is a powerful technique for probing the chemical compositions and electronic states of molecular systems and materials. By measuring the kinetic energy of the ejected photoelectrons, the electronic energy levels of the ionized species can be determined. The photoelectrons also carry momenta. Additional information about the initial and final electronic wavefunctions can be obtained by measuring photoelectron angular distributions (PAD) [339–341]. TRPES [342, 343] is also used to monitor the electronic structure changes during a chemical reaction.

The total TRPES signal $S_{\mathrm{TRPES}}(E_k, t)$ can be expressed as a sum of the probabilities of transitions from the neutral electronic state I to the cationic electronic state F and free electron state $\eta\big(P_{I\to F\eta}(E_k, t)\big)$:

$$S_{\mathrm{TRPES}}(E_k, t) = \sum_{I, F, \eta(E_k)} P_{I\to F\eta}(t), \tag{98}$$

where E_k is the kinetic energy of the ejected electron, and t is the observation time. For the probability of a single transition, we have

$$P_{I\to F\eta}(t) \propto \left|\boldsymbol{E}_{\mathrm{probe}} \cdot \left\langle \psi_{\mathrm{F}}\psi_\eta \middle| \hat{\boldsymbol{\mu}} \middle| \psi_{\mathrm{I}} \right\rangle\right|^2 \delta(\hbar\omega - E_k(\eta) - \Delta E_{\mathrm{IF}}), \tag{99}$$

where $\boldsymbol{E}_{\mathrm{probe}}$ and ω are the polarization vector and frequency of the probe light field, respectively, ψ_I, ψ_F, and ψ_η are the wavefunction of the neutral state I, the cationic state F, and the free electron state η, respectively, and $\Delta E_{\mathrm{IF}} = E_{\mathrm{F}} - E_{\mathrm{I}}$ is the ionization energy corresponding to the neutral state I and cationic state F. Here we employ the sudden ionization approximation [344, 345], in which the ionization process is very fast and the leaving electron does not interact with the cation, so the final state function can be written as a product of ψ_F and ψ_η. We can also assume that ψ_η is orthogonal with ψ_I, so (99) can be recast as

$$P_{I\to F\eta}(t) \propto \left|\left\langle \psi_\eta \middle| \boldsymbol{E}_{\mathrm{probe}} \cdot \hat{\boldsymbol{\mu}} \middle| \psi_{\mathrm{IF}}^{\mathrm{D}} \right\rangle\right|^2 \delta(\hbar\omega - E_k(\eta) - \Delta E_{\mathrm{IF}}). \tag{100}$$

Here we introduce a one-electron quantity called the Dyson orbital $\psi_{\mathrm{IF}}^{\mathrm{D}}$, defined as the generalized overlap amplitudes between the neutral state I and the cationic state F [345]:

$$\psi_{\mathrm{IF}}^{\mathrm{D}}(\mathbf{r}_N) = \sqrt{N}\int \psi_{\mathrm{F}}^{*}(\mathbf{r}_1, \mathbf{r}_2, \ldots, \mathbf{r}_{N-1})\psi_{\mathrm{I}}(\mathbf{r}_1, \mathbf{r}_2, \ldots, \mathbf{r}_N)\mathrm{d}\mathbf{r}_1\mathrm{d}\mathbf{r}_2 \ldots \mathrm{d}\mathbf{r}_{N-1}, \tag{101}$$

where N is the number of electrons in the system. If the polarization of the probe field and the angular distribution of the photoelectron is ignored, (100) can be simplified as [346, 347]

$$P_{I\to F\eta}(t) \propto \left|\psi_{\mathrm{IF}}^{\mathrm{D}}\right|^2 \bar{\mu}_\eta^2 \delta(\hbar\omega - E_k(\eta) - \Delta E_{\mathrm{IF}}), \tag{102}$$

where $\bar{\mu}_\eta$ is an appropriate average value for the transition dipole matrix element between the Dyson orbital $\psi_{\mathrm{IF}}^{\mathrm{D}}$ and free electron state ψ_η. If all free electron states η with a kinetic energy E_k are summed over in (100), we have

$$P_{I\to F}(E_k, t) \propto \left|\psi_{\mathrm{IF}}^{\mathrm{D}}\right|^2 \left[\bar{\mu}_\eta(E_k)\right]^2 \rho(E_k)\delta(\hbar\omega - E_k - \Delta E_{\mathrm{IF}}), \tag{103}$$

where $\bar{\mu}_\eta(E_k)$ represents an average transition dipole matrix element corresponding

to a kinetic energy E_k, and $\rho(E_k)$ is the density of the free electron state at the kinetic energy E_k. Photoelectron experiments tell us that usually in the low kinetic energy region, $\left[\bar{\mu}_l(E_k)\right]^2\rho(E_k) \approx$ const. [348], so (103) can be further simplified as

$$P_{I\to F}(E_k,t) \propto \left|\psi_{\mathrm{IF}}^{\mathrm{D}}\right|^2\delta(\hbar\omega - E_k - \Delta E_{\mathrm{IF}}), \tag{104}$$

and the total photoelectron signal is

$$S_{\mathrm{TRPES}}(E_k,t) = \sum_{I,F} w_{\mathrm{IF}} P_{I\to F}(E_k,t), \tag{105}$$

where w_{IF} is some weighting factor because different $P_{I\to F}(E_k,t)$ has different prefactors in (104). In a simplified treatment we can set all w_{IF}s to be equal [349], or treat them as adjustable parameters [347]. Accurate determination of those weighting factors requires complicated electron-molecule scattering calculations [350], which is beyond the scope of this chapter. Recently, we extended 2D TRPES technique (see (105)) to multidimension by adding more pump pulses before the probe ionization pulse [351]. The TRPES of thioflavin T in its photoisomerization has also been studied with *ab initio* molecular dynamics (AIMD) and TDDFT simulations [349].

The Dyson orbital defined in (101) can be considered as the diagonal element of the one-electron reduced transition density matrix between the neutral and the cationic states. Dyson orbitals are generally not normalized. Their norms reflect the one-electron character of the ionization process. In the simplest case when the neutral and cationic states are well described by Hartree–Fock orbitals and the Koopmans theorem applies, the Dyson orbitals reduce to the canonical Hartree–Fock orbitals and their norms are one. Dyson orbitals are solutions of an effective single-particle equation with ionization energies as their eigenvalues [352–354]. Dyson orbitals are widely used in calculating Compton profiles [355, 356] and electron momentum spectra [357], and interpreting orbital imaging experiments [358–360]. Krylov and coworkers [346] describe an implementation of Dyson orbital calculation at the coupled cluster singles and doubles (CCSD) or EOM-CCSD level of theory.

X-Ray photons often bring the molecule into a superexcited state (excitation above the ionization threshold, or resonance). These resonances are usually short-lived with strong coupling with the continuum leading to the final ionization or dissociation of the system. Generally, resonances can be divided into shape resonance and Feshbach type [361, 362]. Resonances are ubiquitous in radiation damage studies of biomolecules [363], molecular electronic device design [364], attosecond pulse generation [365], and X-ray ionization [13].

Resonances may not be captured by conventional quantum chemistry methods because of their unbound nature and lack of variational principle. To compute these unbound states with finite lifetimes, one must use a non-Hermitian Hamiltonian [366]. One approach for calculating resonance is the complex absorbing potential

(CAP) method [367, 368]. In the method, a complex potential is added to the exterior region of the metastable system to absorb the scattering electron and makes the wave function square-integrable, i.e.,

$$\hat{H}_\eta = \hat{H} - \mathrm{i}\eta W, \tag{106}$$

where $\hat{H}$ is the original molecular Hermitian Hamiltonian, W is a box potential which only exists in the exterior region of the system, and η is the parameter to control the strength of this absorbing potential. Ideally, the complex energy of the resonance can be calculated by letting $\eta \to 0^+$, whereas in practical calculations with finite basis sets, one has to find the optimal η to stabilize the complex energy, i.e., the trajectory calculation [367]. The CAP method was extensively used to calculate resonances [369, 370] and was recently combined with DFT [371]. The major problem of this method is that there are at least two parameters (strength and box size) of the CAP to be determined. In some systems the trajectory calculations cannot give certain results [371].

An alternative for resonance is the complex scaling method [372–375]. Other than adding an arbitrary potential to the original Hamiltonian, one transforms the Hamiltonian with a complex coordinate rotation:

$$\mathbf{r}' \to \mathbf{r}\mathrm{e}^{\mathrm{i}\theta}. \tag{107}$$

Here θ is the rotation angle. As in the CAP method, trajectory calculations are necessary to find an optimal θ value. However, because this is the only parameter to be determined, the degree of uncertainty is greatly reduced compared to the CAP calculations. A DFT combined with the complexed scaling method has been developed for resonances [376–379] and has been used to study Stark ionization of atoms and molecules [380]. The trajectory calculation becomes tedious when the system is large. Moreover, there are still some fundamental questions needs to be answered in extending DFT to resonance. For example, the complex version of the v-representability problem.

Quantum chemistry method development for resonance is still in its infancy. Most applications so far are for resonance energy and lifetime calculations of model or very small atomic and molecular systems. Recently, a non-Hermitian RT-TDDFT study of near and above ionization excitations of small molecules was reported [381]. In this study an absorption boundary condition was used to emulate the continuum. This scheme has a potential to be used in the future for X-ray ionization and photoelectron spectroscopy simulations.

4.5 Vibronic Coupling

In the Frank–Condon (FC) region, nuclear motion acts as a bath for electronic transitions. Including this effect introduces high-resolution fine structure to the recorded spectra. Theoretical simulations are usually under the Born–Oppenheimer (BO) and the harmonic oscillator approximations, which are usually good in the FC region. The potential energy surfaces (PESs) of the ground and excited states are well separated. The simplest approach to account for vibronic coupling is the linear coupling model (LCM). It assumes the mode-k PES of excited state has the same curvature as that of the ground state but only shifted by a displacement. This approach is efficient and can be applied to medium and large molecules. It has been well illustrated in various linear and nonlinear X-ray spectroscopy calculations including the XPS, XANES, RIXS, and SXRS spectra (see, e.g., [246, 382–388]). A more rigorous method is to include the Duschinsky rotation and/or the non-Condon effects. For time-domain nonlinear spectroscopy, the nuclear and electronic coordinates are mixed together. The response function can be evaluated via the cumulant expansion [1] till truncated order. The vibrationally resolved SXRS spectra were studied by Hua et al. [387] combining the LCM and cumulant expansion till the second-order. With the inclusion of vibronic coupling, a faster decay in the time domain signals, and new splitting and shoulder structures in the frequency-domain were observed.

5 Conclusions and Perspectives

In this chapter we have surveyed some typical nonlinear X-ray spectroscopy signals and the quantum chemistry methods used for their simulation. Because of their balance in accuracy and computational cost, DFT/TDDFT methods are commonly used in excited state calculations. With the fast development of new exchange-correlation functionals and linear scaling algorithms, these methods provide a most valuable quantum chemistry tool for nonlinear X-ray spectroscopy simulation. DFT/TDDFT often provides an adequate zero order electronic structure at reasonable cost, which paves the way for the application of high level methods. DFT/TDDFT-based semiempirical methods such as density functional tight binding (DFTB) [389–392] or time-dependent density functional tight binding (TDDFTB) [393, 394], and their linear scaling forms [395] have been shown useful in spectroscopy simulations of large systems.

DFT/TDDFT works well in many cases but fails for double excitations, long-range charge transfer excitations, and conical intersections. Much effort has been made to address these difficulties by designing more elaborate functionals and schemes. We believe that rather than putting the burden on the functionals, it makes more sense to use DFT/TDDFT results as fast zero-order inputs to high level wave-function approaches and many-body techniques. The recent

developments of *ab initio* [396, 397] and many-body perturbation theory [398–401] follow this route. The density matrix renormalization group (DMRG) method should allow one to calculate core or doubly excited state properties with large active spaces [402]. In addition, high-level methods for handling correlation-driven hole delocalization dynamics are still restricted to small systems [403]. Ehrenfest dynamics simulations for most of the systems, which can include nuclear motion, are still formidably expensive [404]. Highly efficient real-time propagation algorithms for large systems are needed to meet the demands of upcoming nonlinear X-ray spectroscopy measurements.

Acknowledgements This work was supported by the U.S. Department of Energy, Office of Science, Basic Energy Sciences under Award #DE-FG02-04ER15571. Yu Zhang and Weijie Hua acknowledge a postdoctoral fellowship by the Department of Energy grant. We also gratefully acknowledge the support of the National Science Foundation (Grant CHE-1361516), and the National Institutes of Health (Grant GM-59230). Helpful comments from Dr. Sergei Tretiak, Dr. Niri Govind and Prof. Kieron Burke are greatly appreciated.

References

1. Mukamel S (1995) Principles of nonlinear optical spectroscopy. Oxford University Press, New York
2. Zewail AH (2000) J Phys Chem A 104(24):5660
3. Krausz F, Ivanov M (2009) Rev Mod Phys 81(1):163
4. Cho M (2008) Chem Rev 108(4):1331
5. Kim H, Cho M (2013) Chem Rev 113(8):5817
6. Mukamel S, Healion D, Zhang Y, Biggs JD (2013) Annu Rev Phys Chem 64:101
7. Beye M, Schreck S, Sorgenfrei F, Trabant C, Pontius N, Schüßler-Langeheine C, Wurth W, Föhlisch A (2013) Nature 501:191
8. Lutman A, Coffee R, Ding Y, Huang Z, Krzywinski J, Maxwell T, Messerschmidt M, Nuhn HD (2013) Phys Rev Lett 110(13):134801
9. Weninger C, Purvis M, Ryan D, London RA, Bozek JD, Bostedt C, Graf A, Brown G, Rocca JJ, Rohringer N (2013) Phys Rev Lett 111(23):233902
10. Marcus G, Penn G, Zholents A (2014) Phys Rev Lett 113(2):024801
11. Bennett K, Biggs JD, Zhang Y, Dorfman KE, Mukamel S (2014) J Chem Phys 140(20): 204311
12. Biggs JD, Bennett K, Zhang Y, Mukamel S (2014) J Phys B At Mol Opt Phys 47(12):124037
13. Carravetta V, Ågren H (2011) In: Barone V (ed) Computational strategies for spectroscopy: from small molecules to nano systems. Wiley, Hoboken, pp 137–205
14. Besley NA, Asmuruf FA (2010) Phys Chem Chem Phys 12:12024
15. Milne C, Penfold T, Chergui M (2014) Coord Chem Rev 277–278:44
16. Salam A (2010) Molecular quantum electrodynamics: long-range intermolecular interactions. Wiley, Hoboken, NJ
17. Dorfman KE, Mukamel S (2012) Phys Rev A 86(1):013810
18. Dorfman KE, Bennett K, Zhang Y, Mukamel S (2013) Phys Rev A 87(5):053826
19. Stöhr J (1992) NEXAFS spectroscopy. Springer, Berlin Heidelberg New York
20. De Groot F, Kotani A (2008) Core level spectroscopy of solids. CRC, Boca Raton
21. Bressler C, Chergui M (2004) Chem Rev 104(4):1781

22. Abramavicius D, Palmieri B, Voronine DV, Sanda F, Mukamel S (2009) Chem Rev 109(6): 2350
23. Mukamel S, Rahav S (2010) In: Berman P, Arimondo E, Lin C (eds) Advances in atomic, molecular, and optical physics, vol 59. Elsevier, Amsterdam, pp 223–263
24. Zhang Y, Healion D, Biggs JD, Mukamel S (2013) J Chem Phys 138(14):144301
25. Mukamel S, Oszwaldowski R, Yang L (2007) J Chem Phys 127(22):221105
26. Li Z, Abramavicius D, Mukamel S (2008) J Am Chem Soc 130(11):3509
27. Weiner AM, Silvestri SD, Ippen EP (1985) J Opt Soc Am B 2(4):654
28. Tanaka S, Mukamel S (2002) Phys Rev Lett 89(4):043001
29. Biggs JD, Zhang Y, Healion D, Mukamel S (2012) J Chem Phys 136(17):174117
30. Dorfman KE, Fingerhut BP, Mukamel S (2013) J Chem Phys 139(12):124113
31. Dorfman KE, Fingerhut BP, Mukamel S (2013) Phys Chem Chem Phys 15(29):12348
32. Fingerhut BP, Dorfman KE, Mukamel S (2014) J Chem Theory Comput 10(3):1172
33. Kossakowski A (1972) Rep Math Phys 3(4):247
34. Lindblad G (1976) Commun Math Phys 48(2):119
35. Ando H, Fingerhut BP, Dorfman KE, Biggs JD, Mukamel S (2014) J Am Chem Soc 136(42): 14801
36. Brixner T, Stiopkin IV, Fleming GR (2004) Opt Lett 29(8):884
37. Scheurer C, Mukamel S (2001) J Chem Phys 115(11):4989
38. Tian P, Keusters D, Suzaki Y, Warren WS (2003) Science 300(5625):1553
39. Turner DL (2007) Encyclopedia of magnetic resonance. Wiley, New York
40. Ernst RR, Bodenhausen G, Wokaun A (1990) Principles of nuclear magnetic resonance in one and two dimensions. Oxford University Press, New York
41. Stolow A, Bragg AE, Neumark DM (2004) Chem Rev 104(4):1719
42. Seel M, Domcke W (1991) J Chem Phys 95(11):7806
43. McFarland B, Farrell J, Miyabe S, Tarantelli F, Aguilar A, Berrah N, Bostedt C, Bozek J, Bucksbaum P, Castagna J, Coffee RN, Cryan JP, Fang L, Feifel R, Gaffney KJ, Glownia JM, Martinez TJ, Mucke M, Murphy B, Natan A, Osipov T, Petrović VS, Schorb S, Schultz T, Spector LS, Swiggers M, Tenney I, Wang S, White JL, White W, Gühr M (2014) Nat Commun 5:4235
44. Bennett K, Kowalewski M, Mukamel S (2014) Faraday Discuss. doi:10.1039/C4FD00178H
45. Hua W, Gao B, Luo Y (2012) Prog Chem 24(06):964
46. Nozières P, De Dominicis CT (1969) Phys Rev 178:1097
47. Schwarz WHE, Buenker RJ (1976) Chem Phys 13:153
48. Schweigert IV, Mukamel S (2007) Phys Rev Lett 99:163001
49. Schweigert IV, Mukamel S (2007) Phys Rev A 76:012504
50. Schweigert IV, Mukamel S (2008) J Chem Phys 128:184307
51. Schweigert IV, Mukamel S (2008) Phys Rev A 78:052509
52. Healion DM, Schweigert IV, Mukamel S (2008) J Phys Chem A 112:11449
53. Slater JC (1972) Adv Quantum Chem 6:1
54. Slater JC, Johnsson KH (1972) Phys Rev B 5:844
55. Stener A, Lisini M, Decleva P (1995) Chem Phys 191:141
56. Triguero L, Pettersson LGM, Ågren H (1998) Phys Rev B 58:8097
57. Brena B, Siegbahn PE, Ågren H (2012) J Am Chem Soc 134(41):17157
58. Hunt WJ, Goddard WA III (1969) Chem Phys Lett 3:414
59. Ågren H, Carravetta V, Vahtras O, Pettersson LGM (1994) Chem Phys Lett 222:75
60. Ågren H, Carravetta V, Vahtras O, Pettersson LGM (1997) Theor Chem Acc 97:14
61. Prendergast D, Galli G (2006) Phys Rev Lett 96:215502
62. Gilbert ATB, Besley NA, Gill PMW (2008) J Phys Chem A 112:13164
63. Sleeman DH (1968) Theor Chim Acta 11(2):135
64. Saunders V, Hillier I (1973) Int J Quantum Chem 7(4):699
65. Guest M, Saunders V (1974) Mol Phys 28(3):819
66. Ågren H, Carravetta V, Pettersson LG, Vahtras O (1996) Phys Rev B 53(23):16074

67. Löwdin PO (1955) Phys Rev 97:1474
68. Healion D, Wang H, Mukamel S (2011) J Chem Phys 134(12):124101
69. Zhang Y, Biggs JD, Healion D, Govind N, Mukamel S (2012) J Chem Phys 137:194306
70. Wiberg KB, Hadad CM, LePage TJ, Breneman CM, Frisch MJ (1992) J Phys Chem 96(2): 671
71. Slater JC, Wood JH (1970) Int J Quantum Chem 5(S4):3
72. Ziegler T, Rauk A, Baerends EJ (1977) Theor Chim Acta 43(3):261
73. Levy M, Perdew J (1985) Phys Rev A 32(4):2010
74. Levy M, Nagy Á (1999) Phys Rev Lett 83(21):4361
75. Q-Chem Version 4.2 User's Manual (2014) Q-Chem, Inc.
76. GAMESS Documentation, Input Description, P56, Department of Chemistry, Iowa State University, May 2013 www.msg.ameslab.gov/gamess/GAMESS_Manual/input.pdf, accessed on 3/27/2015
77. Liu J, Zhang Y, Liu W (2014) J Chem Theory Comput 10(6):2436
78. Kowalczyk T, Yost SR, Voorhis TV (2011) J Chem Phys 134(5):054128
79. Hanson-Heine MWD, George MW, Besley NA (2013) J Chem Phys 138(6):064101
80. Gaudoin R, Burke K (2004) Phys Rev Lett 93(17):173001
81. Baruah T, Olguin M, Zope RR (2012) J Chem Phys 137(8):084316
82. Yang K, Peverati R, Truhlar DG, Valero R (2011) J Chem Phys 135(4):044118
83. Gavnholt J, Olsen T, Engelund M (2008) J Schiøtz Phys Rev B 78(7)
84. Thouless DJ (1972) The quantum mechanics of many-body systems. Academic, New York
85. Runge E, Gross EK (1984) Phys Rev Lett 52(12):997
86. Casida ME (1995) In: Chong DP (ed) Recent advances in density functional methods, part I, chap. V. World Scientific, Singapore, pp 155–192
87. Tretiak S, Chernyak V, Mukamel S (1996) Chem Phys Lett 259(1):55
88. Tretiak S, Chernyak V, Mukamel S (1997) J Am Chem Soc 119(47):11408
89. Tretiak S, Mukamel S (2002) Chem Rev 102:3171
90. Berman O, Mukamel S (2003) Phys Rev A 67(4):042503
91. Tretiak S, Chernyak V (2003) J Chem Phys 119(17):8809
92. Biggs JD, Zhang Y, Healion D, Mukamel S (2013) Proc Natl Acad Sci 110(39):15597
93. Zhang Y, Biggs JD, Mukamel S (2014) J Mod Opt 61(7):558
94. Dreuw A, Head-Gordon M (2004) J Am Chem Soc 126(12):4007
95. Maitra NT, Zhang F, Cave RJ, Burke K (2004) J Chem Phys 120:5932
96. Stener M, Fronzoni G, de Simone M (2003) Chem Phys Lett 373:115
97. Besley NA, Noble A (2007) J Phys Chem C 111:3333
98. DeBeer-George S, Petrenko T, Neese F (2008) Inorg Chim Acta 361:965
99. Liang W, Fischer SA, Frisch MJ, Li X (2011) J Chem Theory Comput 7(11):3540
100. Lopata K, Kuiken BEV, Khalil M, Govind N (2012) J Chem Theory Comput 8:3284
101. Schmidt N, Fink R, Hieringer W (2010) J Chem Phys 133:054703
102. Davidson ER (1975) J Comput Phys 17:84
103. ADF2013, SCM, Theoretical chemistry. Vrije Universiteit, Amsterdam, The Netherlands. http://www.scm.com
104. Shao Y, Gan Z, Epifanovsky E, Gilbert AT, Wormit M, Kussmann J, Lange AW, Behn A, Deng J, Feng X et al. (2014) Mol Phys 113(2):184
105. Neese F (2011) Wiley Interdiscip Rev Comput Mol Sci 2(1):73
106. Valiev M, Bylaska E, Govind N, Kowalski K, Straatsma T, van Dam H, Wang D, Nieplocha J, Apra E, Windus T, de Jong W (2010) Comput Phys Commun 181:1477
107. Frisch MJ, Trucks GW, Schlegel HB, Scuseria GE, Robb MA, Cheeseman JR, Scalmani G, Barone V, Mennucci B, Petersson GA, Nakatsuji H, Caricato M, Li X, Hratchian HP, Izmaylov AF, Bloino J, Zheng G, Sonnenberg JL, Hada M, Ehara M, Toyota K, Fukuda R, Hasegawa J, Ishida M, Nakajima T, Honda Y, Kitao O, Nakai H, Vreven T, Montgomery JJA, Peralta JE, Ogliaro F, Bearpark M, Heyd JJ, Brothers E, Kudin KN, Staroverov VN, Kobayashi R, Normand J, Raghavachari K, Rendell A, Burant JC, Iyengar SS, Tomasi J,

Cossi M, Rega N, Millam JM, Klene M, Knox JE, Cross JB, Bakken V, Adamo C, Jaramillo J, Gomperts R, Stratmann RE, Yazyev O, Austin AJ, Cammi R, Pomelli C, Ochterski JW, Martin RL, Morokuma K, Zakrzewski VG, Voth GA, Salvador P, Dannenberg JJ, Dapprich S, Daniels AD, Farkas Ö, Foresman JB, Ortiz JV, Cioslowski J, Fox DJ (2009) Gaussian 09. Gaussian Inc, Wallingford CT
108. Biggs JD, Zhang Y, Healion D, Mukamel S (2013) J Chem Phys 138(14):144303
109. Zhang Y, Biggs JD, Govind N, Mukamel S (2014) J Phys Chem Lett 5:3656
110. Chen LX, Zhang X (2013) J Phys Chem Lett 4(22):4000
111. Andrade X, Botti S, Marques MAL, Rubio A (2007) J Chem Phys 126(18):184106
112. Orr B, Ward J (1971) Mol Phys 20(3):513
113. van Gisbergen SJA, Snijders JG, Baerends EJ (1998) J Chem Phys 109(24):10644
114. Larsen H, Jørgensen P, Olsen J, Helgaker T (2000) J Chem Phys 113(20):8908
115. Iwata JI, Yabana K, Bertsch GF (2001) J Chem Phys 115(19):8773
116. Furche F (2001) J Chem Phys 114(14):5982
117. Hait Heinze H, Della Sala F, Gorling A (2002) J Chem Phys 116(22):9624
118. Salek P, Vahtras O, Helgaker T, Ågren H (2002) J Chem Phys 117(21):9630
119. Ye A, Autschbach J (2006) J Chem Phys 125(23):234101
120. Ye A, Patchkovskii S, Autschbach J (2007) J Chem Phys 127(7):074104
121. Wang F, Yam CY, Chen G (2007) J Chem Phys 126(24):244102
122. Shavitt I, Bartlett RJ (2009) Many-body methods in chemistry and physics: MBPT and coupled-cluster theory. Cambridge University Press, Cambridge
123. Norman P, Bishop DM, Jensen HJA, Oddershede J (2001) J Chem Phys 115(22):10323
124. Norman P, Bishop DM, Jensen HJA, Oddershede J (2005) J Chem Phys 123(19):194103
125. Ekström U, Norman P, Carravetta V, Ågren H (2006) Phys Rev Lett 97(14)
126. Linares M, Stafström S, Rinkevicius Z, Ågren H, Norman P (2011) J Phys Chem B 115(18):5096
127. Norman P, Ruud K (2006) In: Leszczynski J (ed) Challenges and advances in computational chemistry and physics, vol 1. Springer, Dordrecht, pp 1–49
128. Bertrand JB, Wörner HJ, Bandulet HC, Bisson É, Spanner M, Kieffer JC, Villeneuve DM, Corkum PB (2011) Phys Rev Lett 106(2):023001
129. Niikura H, Wörner HJ, Villeneuve DM, Corkum PB (2011) Phys Rev Lett 107(9):093004
130. Wörner HJ, Bertrand JB, Fabre B, Higuet J, Ruf H, Dubrouil A, Patchkovskii S, Spanner M, Mairesse Y, Blanchet V, Mével E, Constant E, Corkum PB, Villeneuve DM (2011) Science 334(6053):208
131. Ranitovic P, Hogle CW, Riviere P, Palacios A, Tong XM, Toshima N, Gonzalez-Castrillo A, Martin L, Martin F, Murnane MM et al (2014) Proc Natl Acad Sci 111(3):912
132. Bergues B, Kübel M, Johnson NG, Fischer B, Camus N, Betsch KJ, Herrwerth O, Senftleben A, Sayler AM, Rathje T et al (2012) Nat Commun 3:813
133. Neppl S, Ernstorfer R, Bothschafter EM, Cavalieri AL, Menzel D, Barth JV, Krausz F, Kienberger R, Feulner P (2012) Phys Rev Lett 109(8):087401
134. Krausz F, Stockman MI (2014) Nat Photonics 8(3):205
135. Mikosch J, Boguslavskiy A, Wilkinson I, Spanner M, Patchkovskii S, Stolow A (2013) Phys Rev Lett 110(2):023004
136. Leone SR, McCurdy CW, Burgdörfer J, Cederbaum LS, Chang Z, Dudovich N, Feist J, Greene CH, Ivanov M, Kienberger R et al (2014) Nat Photonics 8(3):162
137. Frumker E, Kajumba N, Bertrand JB, Wörner HJ, Hebeisen CT, Hockett P, Spanner M, Patchkovskii S, Paulus GG, Villeneuve DM et al (2012) Phys Rev Lett 109(23):233904
138. Ivanov M, Smirnova O (2011) Phys Rev Lett 107(21):213605
139. Shafir D, Soifer H, Bruner BD, Dagan M, Mairesse Y, Patchkovskii S, Ivanov MY, Smirnova O, Dudovich N (2012) Nature 485(7398):343
140. Mairesse Y, Higuet J, Dudovich N, Shafir D, Fabre B, Mével E, Constant E, Patchkovskii S, Walters Z, Ivanov MY et al (2010) Phys Rev Lett 104(21):213601
141. Jakowski J, Morokuma K (2009) J Chem Phys 130(22):224106
142. Kosloff R (1988) J Phys Chem 92(8):2087

143. Castro A, Marques MAL, Rubio A (2004) J Chem Phys 121(8):3425
144. Yabana K, Bertsch G (1996) Phys Rev B 54(7):4484
145. Tal-Ezer H, Kosloff R (1984) J Chem Phys 81(9):3967
146. Chen R, Guo H (1999) Comput Phys Commun 119(1):19
147. Baer R, Gould R (2001) J Chem Phys 114(8):3385
148. Lanczos C (1950) J Res Natl Bur Stand 45:225
149. Park TJ, Light JC (1986) J Chem Phys 85(10):5870
150. Saad Y (2011) Numerical methods for large eigenvalue problems. SIAM, Philadelphia
151. Hochbruck M, Lubich C (1997) SIAM J Numer Anal 34(5):1911
152. Feit M, Fleck J, Steiger A (1982) J Comput Phys 47(3):412
153. Feit MD (1983) J Chem Phys 78(1):301
154. Sugino O, Miyamoto Y (1999) Phys Rev B 59(4):2579
155. Blanes S, Casas F, Oteo J, Ros J (2009) Phys Rep 470(5–6):151
156. Lopata K, Govind N (2011) J Chem Theory Comput 7(5):1344
157. Cheng CL, Evans JS, Van Voorhis T (2006) Phys Rev B 74(15)
158. Li X, Smith SM, Markevitch AN, Romanov DA, Levis RJ, Schlegel HB (2005) Phys Chem Chem Phys 7(2):233
159. Isborn CM, Li X, Tully JC (2007) J Chem Phys 126(13):134307
160. Liang W, Chapman CT, Li X (2011) J Chem Phys 134(18):184102
161. Andrade X, Alberdi-Rodriguez J, Strubbe DA, Oliveira MJT, Nogueira F, Castro A, Muguerza J, Arruabarrena A, Louie SG, Aspuru-Guzik A, Rubio A, Marques MAL (2012) J Phys Condens Matter 24(23):233202
162. Akama T, Imamura Y, Nakai H (2010) Chem Lett 39(4):407
163. Wall MR, Neuhauser D (1995) J Chem Phys 102(20):8011
164. Mandelshtam VA, Taylor HS (1997) J Chem Phys 106(12):5085
165. Pang JW, Dieckmann T, Feigon J, Neuhauser D (1998) J Chem Phys 108(20):8360
166. Takimoto Y, Vila FD, Rehr JJ (2007) J Chem Phys 127(15):154114
167. Ding F, Van Kuiken BE, Eichinger BE, Li X (2013) J Chem Phys 138(6):064104
168. Biggs JD, Voll JA, Mukamel S (2012) Phil Trans R Soc A 370(1972):3709
169. Yam C, Zhang Q, Wang F, Chen G (2012) Chem Soc Rev 41(10):3821
170. Challacombe M (2014) Computation 2(1):1
171. Challacombe M, Bock N (2014) J Chem Phys 140(11):111101
172. Li X, Tully JC, Schlegel HB, Frisch MJ (2005) J Chem Phys 123(8):084106
173. Szalay PG, Müller T, Gidofalvi G, Lischka H, Shepard R (2012) Chem Rev 112:108
174. Roos BO, Taylor PR, Siegbahn PEM (1980) Chem Phys 48:157
175. Siegbahn PEM, Heiberg A, Roos BO, Levy B (1980) Phys Scr 21:323
176. Siegbahn PEM, Almlöf J, Heiberg A, Roos BO (1981) J Chem Phys 74:2384
177. Ruedenberg K, Sundberg KR (1976) In: Calais JL, Goscinski O, Linderberg J, Öhrn Y (eds) Quantum science. Plenum, New York, pp 505–515
178. Ruedenberg K, Schmidt MW, Gilbert MM, Elbert ST (1982) Chem Phys 71:41
179. Ruedenberg K, Schmidt MW, Gilbert MM (1982) Chem Phys 71:51
180. Pipek J, Mezey PG (1989) J Chem Phys 90:4916
181. Boys SF (1960) Rev Mod Phys 32:296
182. Edmiston C, Ruedenberg K (1963) Rev Mod Phys 35:457
183. Aquilante F, Pedersen TB, de Merás AS, Koch H (2006) J Chem Phys 125:174101
184. Pulay P, Hamilton TP (1988) J Chem Phys 88:4926
185. Bofill JM, Pulay P (1989) J Chem Phys 90:3637
186. Kutzelnigg W (1963) Theor Chim Acta 1:327
187. Ahlrichs R, Driessler F (1975) Theor Chim Acta 36:275
188. Taylor PR (1981) J Chem Phys 74:1256
189. Veryazov V, Malmqvist PÅ, Roos BO (2011) Int J Quantum Chem 111:3329
190. Schmidt MW, Gordon MS (1998) Annu Rev Phys Chem 49:233
191. Olsen J, Roos BO, Jørgensen P, Jensen HJA (1988) J Chem Phys 89:2185

192. Malmqvist PÅ, Rendell A, Roos BO (1990) J Phys Chem 94:5477
193. Jensen HJA, Jørgensen P, Ågren H (1987) J Chem Phys 87:451
194. Ågren H, Jensen HJÅ (1987) Chem Phys Lett 137:431
195. Ågren H, Flores-Riveros A, Jensen HJÅ (1989) Phys Scr 40:745
196. Ågren H, Jensen HJÅ (1993) Chem Phys 172:45
197. Rocha AB (2011) J Chem Phys 134:024107
198. Tashiro M, Ehara M, Fukuzawa H, Ueda K, Buth C, Kryzhevoi NV, Cederbaum LS (2010) J Chem Phys 132:184302-1
199. Eland JHD, Tashiro M, Linusson P, Ehara M, Ueda K, Feifel R (2010) Phys Rev Lett 105: 213005
200. Takahashi O, Tashiro M, Ehara M, Yamasaki K, Ueda K (2011) Chem Phys 384:28
201. Tashiro M, Ueda K, Ehara M (2012) Chem Phys Lett 521:45
202. Josefsson I, Kunnus K, Schreck S, Föhlisch A, de Groot F, Wernet P, Odelius M (2012) J Phys Chem Lett 3:3565
203. Malmqvist PA, Roos BO, Schimmelpfennig B (2002) Chem Phys Lett 357:230
204. Wernet P, Kunnus K, Schreck S, Quevedo W, Kurian R, Techert S, de Groot FMF, Odelius M, Föhlisch A (2012) J Phys Chem Lett 3:3448
205. Suljoti E, Garcia-Diez R, Bokarev SI, Lange KM, Schoch R, Dierker B, Dantz M, Yamamoto K, Engel N, Atak K, Kühn O, Bauer M, Rubensson JE, Aziz EF (2013) Angew Chem Int Ed 52:9841
206. Bokarev SI, Dantz M, Suljoti E, Kühn O, Aziz EF (2013) Phys Rev Lett 111:083002
207. Atak K, Bokarev SI, Gotz M, Golnak R, Lange KM, Engel N, Dantz M, Suljoti E, Kühn O, Aziz EF (2013) J Phys Chem B 117:12613
208. Hua W, Oesterling S, Biggs JD, Zhang Y, Ando H, de Vivie-Riedle R, Fingerhut BP, Mukamel S (submitted)
209. Jensen HJÅ, Jørgensen P (1984) J Chem Phys 80(3):1204
210. Jensen HJÅ, Ågren H (1984) Chem Phys Lett 110:140
211. Cook DB (2005) Handbook of computational quantum chemistry. Dover, Mineola, New York
212. Malmqvist PÅ (1986) Int J Quantum Chem 30:479
213. Malmqvist PÅ, Roos BO (1989) Chem Phys Lett 155:189
214. Tully JC (1990) J Chem Phys 93:1061
215. Martin R (2003) J Chem Phys 118:4775
216. Mayer I (2007) Chem Phys Lett 443:420
217. Malmqvist PÅ, Veryazov V (2012) Mol Phys 110:2455
218. Hedin L (1965) Phys Rev 139(3A):A796
219. Onida G, Rubio A (2002) Rev Mod Phys 74(2):601
220. Salpeter E, Bethe H (1951) Phys Rev 84(6):1232
221. Caruso F, Rinke P, Ren X, Scheffler M, Rubio A (2012) Phys Rev B 86(8):081102(R)
222. Myöhanen P, Stan A, Stefanucci G, van Leeuwen R (2008) Europhys Lett 84(6):67001
223. Säkkinen N, Manninen M, van Leeuwen R (2012) New J Phys 14(1):013032
224. Zhang D, Steinmann SN, Yang W (2013) J Chem Phys 139(15):154109
225. Shirley EL (1998) Phys Rev Lett 80:794
226. Soininen JA, Shirley EL (2001) Phys Rev B 54:165112
227. Shirley EL (2004) J Electron Spectrosc Relat Phenom 136(1):77
228. Rehr JJ, Kas JJ, Prange MP, Sorini AP, Takimoto Y, Vila F (2009) C R Phys 10(6):548
229. Olovsson W, Tanaka I, Puschnig P, Ambrosch-Draxl C (2009) J Phys Condens Matter 21 (10):104205
230. Vinson J, Rehr J, Kas J, Shirley E (2011) Phys Rev B 83(11):115106
231. Vinson J, Rehr J (2012) Phys Rev B 86(19):195135
232. Baumeier B, Andrienko D, Ma Y, Rohlfing M (2012) J Chem Theory Comput 8(3):997
233. Baumeier B, Andrienko D, Rohlfing M (2012) J Chem Theory Comput 8(8):2790
234. van Setten MJ, Weigend F, Evers F (2013) J Chem Theory Comput 9(1):232

235. Schirmer J, Trofimov AB, Stelter G (1998) J Chem Phys 109:4734
236. Wenzel J, Wormit M, Dreuw A (2014) J Comput Chem 35(26):1900
237. Kuleff AI, Cederbaum LS (2007) Phys Rev Lett 98:083201
238. Dutoi AD, Cederbaum LS, Wormit M, Starcke JH, Dreuw A (2010) J Chem Phys 132:144302
239. de Groot FMF, Fuggle JC, Thole BT, Sawatzky GA (1990) Phys Rev B 42:5459
240. Stavitski E, de Groot FM (2010) Micron 41:687
241. Ikeno H, Mizoguchi T, Tanaka I (2011) Phys Rev B 83:155107-1
242. Haverkort MW, Zwierzycki M, Andersen OK (2012) Phys Rev B 85:165113
243. Bagus PS, Freund H, Kuhlenbeck H, Ilton ES (2008) Chem Phys Lett 455:331
244. Moemelt M, Maganas D, DeBeer S, Neese F (2013) J Chem Phys 138:204101
245. Maganas D, Roemelt M, Weyhermüller T, Blume R, Hävecker M, Knop-Gericke A, DeBeer S, Schlögl R, Neese F (2014) Phys Chem Chem Phys 16(1):264
246. Hua W, Tian G, Fronzoni G, Li X, Stener M, Luo Y (2013) J Phys Chem A 117:14075
247. Huse N, Kim TK, Jamula L, McCusker JK, de Groot FMF, Schoenlein RW (2010) J Am Chem Soc 132:6809
248. Huse N, Cho H, Hong K, Jamula L, de Groot FMF, Kim TK, McCusker JK, Schoenlein RW (2011) J Phys Chem Lett 2:880
249. Cho H, Strader ML, Hong K, Jamula L, Gullikson EM, Kim TK, de Groot FMF, McCusker JK, Schoenlein RW, Huse N (2012) Faraday Discuss 157:463
250. Arneberg R, Ågren H, Müller J, Manne R (1982) Chem Phys Lett 91:362
251. Ågren H, Arneberg R (1984) Phys Scr 30:55
252. Ågren H, Arneberg R (1983) Phys Scr 28:80
253. Ågren H, Arneberg R, Müller J, Manne R (1984) Chem Phys 83:53
254. Maganas D, Kristiansen P, Duda LC, Knop-Gericke A, DeBeer S, Schlögl R, Neese F (2014) J Phys Chem C 118:20163
255. Nooijen M, Bartlett RJ (1995) J Chem Phys 102(17):6735
256. Besley NA (2012) Chem Phys 542:42
257. Brabec J, Bhaskaran-Nair K, Govind N, Pittner J, Kowalski K (2012) J Chem Phys 137(17): 171101
258. Kuramoto K, Ehara M, Nakatsuji H (2005) J Chem Phys 122(1):014304
259. Ohtsuka Y, Nakatsuji H (2006) J Chem Phys 124(5):054110
260. Perdew JP (1981) Phys Rev B 23(10):5048
261. Imamura Y, Nakai H (2006) Int J Quantum Chem 107(1):23
262. Tu G, Rinkevicius Z, Vahtras O, Ågren H, Ekström U, Norman P, Carravetta V (2007) Phys Rev A 76(2):022506
263. Tawada Y, Tsuneda T, Yanagisawa S, Yanai T, Hirao K (2004) J Chem Phys 120(18):8425
264. Yanai T, Tew DP, Handy NC (2004) Chem Phys Lett 393(1–3):51
265. Peach MJG, Cohen AJ, Tozer DJ (2006) Phys Chem Chem Phys 8(39):4543
266. Chai JD, Head-Gordon M (2008) J Chem Phys 128(8):084106
267. Chai JD, Head-Gordon M (2008) Chem Phys Lett 467(1–3):176
268. Rohrdanz MA, Martins KM, Herbert JM (2009) J Chem Phys 130(5):054112
269. Toulouse J, Zhu W, Ángyán JG, Savin A (2010) Phys Rev A 82(3)
270. Irelan RM, Henderson TM, Scuseria GE (2011) J Chem Phys 135(9):094105
271. Song JW, Peng D, Hirao K (2011) J Comput Chem 32(15):3269
272. Hermet J, Cortona P, Adamo C (2012) Chem Phys Lett 519–520:145
273. Refaely-Abramson S, Sharifzadeh S, Govind N, Autschbach J, Neaton JB, Baer R, Kronik L (2012) Phys Rev Lett 109(22)
274. Seth M, Ziegler T (2012) J Chem Theory Comput 8(3):901
275. Modrzejewski M, Chałasński G, Szczęńiak MM (2014) J Chem Theory Comput 10(10):4297
276. Mardirossian N, Head-Gordon M (2014) Phys Chem Chem Phys 16(21):9904
277. Tsuneda T, Hirao K (2014) Wiley Interdiscip Rev Comput Mol Sci 4(4):375
278. Song JW, Watson MA, Nakata A, Hirao K (2008) J Chem Phys 129(18):184113
279. Besley NA, Peach MJG, Tozer DJ (2009) Phys Chem Chem Phys 11(44):10350

280. Nakata A, Imamura Y, Otsuka T, Nakai H (2006) J Chem Phys 124(9):094105
281. Nakata A, Imamura Y, Nakai H (2006) J Chem Phys 125(6):064109
282. Nitzan A, Ratner MA (2003) Science 300(5624):1384
283. Galperin M, Ratner MA, Nitzan A, Troisi A (2008) Science 319(5866):1056
284. Niehaus TA, Chen G (2012) In: Zeng J, Zhang RQ, Treutlein HR (eds) Quantum simulations of materials and biological systems. Springer, Dordrecht, Netherlands, pp 17–32
285. Xie H, Jiang F, Tian H, Zheng X, Kwok Y, Chen S, Yam C, Yan Y, Chen G (2012) J Chem Phys 137(4):044113
286. Zhang Y, Chen S, Chen G (2013) Phys Rev B 87(8):085110
287. Zhang Y, Yam CY, Chen G (2013) J Chem Phys 138(16):164121
288. Kwok Y, Zhang Y, Chen G (2013) Front Phys 9(6):698
289. Lundqvist BI (1967) Phys kondens Materie 6(3):193
290. Langreth D (1970) Phys Rev B 1(2):471
291. Overhauser A (1971) Phys Rev B 3(6):1888
292. Hedin L (1999) J Phys Condens Matter 11(42):R489
293. Mukamel S (2005) Phys Rev B 72(23):235110
294. Santra R, Kryzhevoi NV, Cederbaum LS (2009) Phys Rev Lett 103:013002
295. Ueda K, Takahashi O (2012) J Electron Spectrosc Relat Phenom 185(8–9):301
296. Kryzhevoi NV, Santra R, Cederbaum LS (2011) J Chem Phys 135:084302
297. Salén P, van der Meulen P, Schmidt HT, Thomas RD, Larsson M, Feifel R, Piancastelli MN, Fang L, Murphy B, Osipov T, Berrah N, Kukk E, Ueda K, Bozek JD, Bostedt C, Wada S, Richter R, Feyer V, Prince KC (2012) Phys Rev Lett 108(15):153003
298. Otero E, Kosugi N, Urguhart SG (2009) J Chem Phys 131:114313
299. Starcke JH, Wormit M, Schirmer J, Dreuw A (2006) Chem Phys 329:39
300. Casida M, Ipatov A, Cordova F (2006) In: Marques MA, Ullrich CA, Nogueira F, Rubio A, Burke K, Gross EKU (eds) Time-dependent density functional theory, chap. 16, vol 706, Lecture notes in physics. Spinger, Berlin Heidelberg, pp 243–257
301. Elliott P, Goldson S, Canahui C, Maitra NT (2011) Chem Phys 391:110
302. Gross EKU, Dobson JF, Petersilka M (1996) In: Nalewajski RF (ed) *Density-functional theory II, topics in current chemistry*, vol 181. Spinger, Berlin, pp 81–172
303. Tretiak S, Chernyak V, Mukamel S (1998) Int J Quantum Chem 70:711
304. Casida ME (2005) J Chem Phys 122:054111
305. Romaniello P, Sangalli D, Berger JA, Sottile F, Molinari LG, Reining L, Onida G (2009) J Chem Phys 130:044108
306. Sangalli D, Romaniello P, Onida G, Marini A (2011) J Chem Phys 134:034115
307. Scherz A, Gross EKU, Appel H, Sorg C, Baberschke K, Wende H, Burke K (2005) Phys Rev Lett 95(25):253006
308. Krylov AI (2001) Chem Phys Lett 338:375
309. Krylov AI (2001) Chem Phys Lett 350:522
310. Krylov AI, Sherrill CD (2002) J Chem Phys 116:3194
311. Slipchenko LV, Krylov AI (2002) J Chem Phys 117:3694
312. Shao Y, Head-Gordon M, Krylov AI (2003) J Chem Phys 118:4807
313. Wang F, Ziegler T (2004) J Chem Phys 121:12191
314. Ziegler T, Seth M, Krykunov M, Autschbach J, Wang F (2009) J Chem Phys 130(15):154102
315. Cullen J, Krykunov M, Ziegler T (2011) Chem Phys 391(1):11
316. Ziegler T, Krykunov M, Cullen J (2012) J Chem Phys 136(12):124107
317. Seidu I, Krykunov M, Ziegler T (2013) Mol Phys 112(5–6):661
318. Angeli C, Pastore M (2011) J Chem Phys 134:184302
319. Lehtonen O, Sundholm D, Send R, Johansson MP (2009) J Chem Phys 131:024301
320. Marian CM, Gilka N (2008) J Chem Theory Comput 4:1501
321. Schmidt M, Tavan P (2012) J Chem Phys 136:124309
322. Mikhailov IA, Tafur S, Masunov AE (2008) Phys Rev A 77:012510
323. Starcke JH, Wormit M, Dreuw A (2009) J Chem Phys 131:144311

324. Knippenberg S, Starcke JH, Wormit M, Dreuw A (2010) Mol Phys 108:2801
325. Nakayama K, Nakano H, Hirao K (1998) Int J Quantum Chem 66:157
326. Kurashige Y, Nakano H, Nakao Y, Hirao K (2004) Chem Phys Lett 400:425
327. Zhuang W, Abramavicius D, Mukamel S (2005) Proc Natl Acad Sci 102(21):7443
328. Kim J, Mukamel S, Scholes GD (2009) Acc Chem Res 42(9):1375
329. Fausti D, Tobey RI, Dean N, Kaiser S, Dienst A, Hoffmann MC, Pyon S, Takayama T, Takagi H, Cavalleri A (2011) Science 331:189
330. Schinke R (1993) Photodissociation dynamics: spectroscopy and fragmentation of small polyatomic molecules. Cambridge University Press, Cambridge
331. Weinkauf R, Schanen P, Metsala A, Schlag EW, Bürgle M, Kessler H (1996) J Phys Chem 100(47):18567
332. Cederbaum L, Zobeley J (1999) Chem Phys Lett 307(3–4):205
333. Breidbach J, Cederbaum LS (2005) Phys Rev Lett 94(3):033901
334. Remacle F, Levine RD (2006) Proc Natl Acad Sci U S A 103(18):6793
335. Breidbach J, Cederbaum LS (2007) J Chem Phys 126(3):034101
336. Kuleff AI, Cederbaum LS (2011) Phys Rev Lett 106(5):053001
337. Petrović VS, Siano M, White JL, Berrah N, Bostedt C, Bozek JD, Broege D, Chalfin M, Coffee RN, Cryan J, Fang L, Farrell JP, Frasinski LJ, Glownia JM, Guhr M, Hoener M, Holland DMP, Kim J, Marangos JP, Martinez T, McFarland BK, Minns RS, Miyabe S, Schorb S, Sension RJ, Spector LS, Squibb R, Tao H, Underwood JG, Bucks-baum PH (2012) Phys Rev Lett 108(25):253006
338. Zhang Y, Biggs JD, Hua W, Mukamel S, Dorfman KE (2014) Phys Chem Chem Phys 16: 24323
339. van der Heide P (2012) X-Ray photoelectron spectroscopy. Wiley, Hoboken, NJ
340. Wang K, McKoy V (1995) Annu Rev Phys Chem 46(1):275
341. Reid KL (2003) Annu Rev Phys Chem 54(1):397
342. Sanov A (2014) Annu Rev Phys Chem 65(1):341
343. Wu G, Hockett P, Stolow A (2011) Phys Chem Chem Phys 13(41):18447
344. Suzuki T (2012) Int Rev Phys Chem 31(2):265
345. Pickup B, Goscinski O (1973) Mol Phys 26(4):1013
346. Pickup BT (1977) Chem Phys 19(2):193
347. Melania Oana C, Krylov AI (2007) J Chem Phys 127(23):234106
348. Thompson AL, Martínez TJ (2011) Faraday Discuss 150:293
349. Rabalais JW (1977) Principles of ultraviolet photoelectron spectroscopy. Wiley, New York
350. Ren H, Fingerhut BP, Mukamel S (2013) J Phys Chem A 117(29):6096
351. Lucchese R, Raseev G, McKoy V (1982) Phys Rev A 25(5):2572
352. Rahav S, Mukamel S (2010) Phys Rev A 81(6):063810
353. Cederbaum LS, Domcke W (1977) Adv Chem Phys 36:205
354. Ortiz J (1999) Adv Quantum Chem 35:33
355. Linderberg J, Öhrn Y (2004) Propagators in quantum chemistry, 2nd edn. Wiley, Hoboken
356. Kaplan I, Barbiellini B, Bansil A (2003) Phys Rev B 68(23):235104
357. Barbiellini B, Bansil A (2004) J Phys Chem Solids 65(12):2031
358. Miao YR, Ning CG, Liu K, Deng JK (2011) J Chem Phys 134(20):204304
359. Murray R, Spanner M, Patchkovskii S, Ivanov MY (2011) Phys Rev Lett 106(17):173001
360. Saliéres P, Maquet A, Haessler S, Caillat J, Taïeb R (2012) Rep Prog Phys 75(6):062401
361. Mignolet B, Kus T, Remacle F (2013) In: Grill L, Joachim C (eds) Imaging and manipulating molecular orbitals. Springer, Berlin, pp 41–54
362. Schulz G (1973) Rev Mod Phys 45(3):378
363. Simons J (1984) In: Truhlar DG (ed) Resonances in electron-molecule scattering van der Waals complexes, and reactive chemical dynamics. American Chemical Society, Washington, DC, pp 3–16
364. Sanche L (2009) Nature 461(7262):358
365. Goyer F, Ernzerhof M, Zhuang M (2007) J Chem Phys 126(14):144104

366. Strelkov V (2010) Phys Rev Lett 104(12):123901
367. Moiseyev N (2011) Non-Hermitian quantum mechanics. Cambridge University Press, Cambridge
368. Riss U, Meyer HD (1993) J Phys B At Mol Opt Phys 26(23):4503
369. Muga JG, Palao J, Navarro B, Egusquiza I (2004) Phys Rep 395(6):357
370. Santra R, Cederbaum LS (2002) Phys Rep 368(1):1
371. Santra R, Cederbaum LS (2002) J Chem Phys 117(12):5511
372. Zhou Y, Ernzerhof M (2012) J Phys Chem Lett 3(14):1916
373. Aguilar J, Combes JM (1971) Commun Math Phys 22(4):269
374. Balslev E, Combes JM (1971) Commun Math Phys 22(4):280
375. Simon B (1979) Phys Lett A 71(2):211
376. Moiseyev N (1998) Phys Rep 302(5):212
377. Wasserman A, Moiseyev N (2007) Phys Rev Lett 98(9):093003
378. Whitenack DL, Wasserman A (2009) J Phys Chem Lett 1(1):407
379. Whitenack DL, Wasserman A (2011) Phys Rev Lett 107(16):163002
380. Whitenack DL, Wasserman A (2012) J Chem Phys 136(16):164106
381. Larsen AH, De Giovannini U, Whitenack DL, Wasserman A, Rubio A (2013) J Phys Chem Lett 4(16):2734
382. Lopata K, Govind N (2013) J Chem Theory Comput 9(11):4939
383. Hergenhahn U (2004) J Phys B At Mol Opt Phys 37:R89
384. Minkov I, Gel'Mukhanov F, Friedlein R, Osikowicz W, Suess C, Öhrwall G, Sorensen SL, Braun S, Murdey R, Salaneck WR, Ågren H (2004) J Chem Phys 121:5733
385. Minkov I, Gel'mukhanov F, Ågren H, Friedlein R, Suess C, Salaneck WR (2005) J Phys Chem A 109:1330
386. Svensson S (2005) J Phys B At Mol Opt Phys 38:S821
387. Gel'mukhanov F, Ågen H (1999) Phys Rep 312:87
388. Hua W, Biggs JD, Zhang Y, Healion D, Ren H, Mukamel S (2013) J Chem Theory Comput 9:5479
389. Fronzoni G, Baseggio O, Stener M, Hua W, Tian G, Luo Y, Apicella B, Alfé M, de Simone M, Kivimäki A, Coreno M (2014) J Chem Phys 141:044313
390. Porezag D, Frauenheim T, Köhler T, Seifert G, Kaschner R (1995) Phys Rev B 51(19):12947
391. Seifert G, Porezag D, Frauenheim T (1996) Int J Quantum Chem 58(2):185
392. Elstner M, Porezag D, Jungnickel G, Elsner J, Haugk M, Frauenheim T, Suhai S, Seifert G (1998) Phys Rev B 58(11):7260
393. Zheng G, Lundberg M, Jakowski J, Vreven T, Frisch MJ, Morokuma K (2009) Int J Quantum Chem 109(9):1841
394. Niehaus T, Suhai S, Della Sala F, Lugli P, Elstner M, Seifert G, Frauenheim T (2001) Phys Rev B 63(8):085108
395. Trani F, Scalmani G, Zheng G, Carnimeo I, Frisch MJ, Barone V (2011) J Chem Theory Comput 7(10):3304
396. Wang F, Yam C, Chen G, Wang X, Fan K, Niehaus T, Frauenheim T (2007) Phys Rev B 76 (4):045114
397. Thom AJ, Head-Gordon M (2009) J Chem Phys 131(12):124113
398. Sundstrom EJ, Head-Gordon M (2014) J Chem Phys 140(11):114103
399. van Aggelen H, Yang Y, Yang W (2013) Phys Rev A 88(3):030501
400. Yang Y, van Aggelen H, Steinmann SN, Peng D, Yang W (2013) J Chem Phys 139 (17):174110
401. Peng D, Steinmann SN, van Aggelen H, Yang W (2013) J Chem Phys 139(10):104112
402. Scuseria GE, Henderson TM, Bulik IW (2013) J Chem Phys 139(10):104113
403. Chan GKL, Sharma S (2011) Annu Rev Phys Chem 62(1):465
404. Kuleff AI, Cederbaum LS (2014) J Phys B At Mol Opt Phys 47(12):124002
405. Ding F, Chapman CT, Liang W, Li X (2012) J Chem Phys 137(22):22A512

Top Curr Chem (2016) 368: 347–376
DOI: 10.1007/128_2015_638

Published online: 24 May 2015

Computational Molecular Electronic Spectroscopy with TD-DFT

Denis Jacquemin and Carlo Adamo

Abstract In this chapter we present applications of TD-DFT aiming at reproducing and rationalizing the optical signatures of molecules, and, more precisely, the absorption and fluorescence spectra of conjugated compounds belonging to both organic and inorganic families. We particularly focus on the computations going beyond the vertical approximation, i.e., on the calculation of 0–0 energies and vibronic spectra with TD-DFT, and on large applications performed for "real-life" structures (organic and inorganic dyes, optimization of charge-transfer structures, rationalization of excited-state proton transfer, etc.). We present a series of recent applications of TD-DFT methodology for these different aspects. The main conclusions of TD-DFT benchmarks aiming at pinpointing the most suited exchange-correlation functionals are also discussed.

Contents

D. Jacquemin (✉)
CEISAM, UMR CNRS 6230, Université de Nantes, 2, rue de la Houssinière, 44322 Nantes, France

Institut Universitaire de France, 103, blvd Saint-Michel, 75005 Paris, France
e-mail: Denis.Jacquemin@univ-nantes.fr

C. Adamo
IRCP UMR CNRS 8247, ENSCP-Chimie ParisTech, 11, rue Pierre et Marie Curie, 75005 Paris, France

Institut Universitaire de France, 103, blvd Saint-Michel, 75005 Paris, France

1 Introduction

By analyzing the continuously increasing number of quantum chemistry works relying on Time-Dependent Density Functional Theory (TD-DFT) [1–5], it appears that the vast majority of TD-DFT's applications are devoted to the modeling of the most widely available excited-state (ES) properties, namely optical spectra. One can roughly split these works into two major categories. In the first, which contains the majority of the TD-DFT investigations, the so-called vertical approximation is applied, i.e., a frozen ground-state (GS) geometry is considered and transition energies are determined without accounting for vibrational couplings [6]. This approach is computationally very efficient, allows one to characterize the nature of the relevant excited-states, and has been successfully used to design dyes or to understand environmental effects, albeit the vertical energies cannot be experimentally measured in most cases. However, more and more works of the second category, looking for well-grounded theory-measurement comparisons, have recently appeared. These studies, which imply higher computational efforts than their vertical counterparts, aimed at determining the 0–0 energies and/or vibrationally-resolved spectra [7–17]. Indeed, on the one hand, the 0–0 energies can be directly measured in the gas-phase for small molecules, or taken as the crossing point between absorption and emission curves (AFCP: absorption/fluorescence crossing point) in the experimental spectra of large solvates species [13], whereas, on the other hand, vibronic couplings give access to both band shapes and absolute intensities, which can also be directly correlated with measurements. The calculation of these properties implies the determination of the ES Hessian. Thanks to the development and implementation of analytic first and second derivatives [18–22], TD-DFT has indeed become an efficient approach to explore the potential energy surfaces (PES) of the ES in large compounds, the accuracy obtained being in most cases reasonable, at least close to the Franck–Condon point [23]. TD-DFT can therefore not only be used to probe the nature of the ES responsible for the absorption and fluorescence spectra but also provide many other properties, e.g., ES geometries and dipole moments, which are difficult (or costly) to measure

experimentally. Nevertheless, the application of TD-DFT to spectroscopic problems generally implies two major approximations: the use of the adiabatic approximation (i.e., only a frequency-independent exchange and correlation kernel is applied) and the selection of an adequate exchange-correlation functional (XCF). These two drawbacks limit the final accuracy of the results obtained and numerous works have been devoted to the appraisal of the most suited XCF [24], as well as to schemes going beyond linear-response TD-DFT [5, 25] in the framework of the simulation of optical spectra. Despite these limits, TD-DFT clearly remains the most applied theory for evaluating the spectral properties of "real-life" structures and this popularity can be ascribed to the simplicity and speed of use of this single-reference approach and also to the modeling of environmental effects which can be achieved with several theories [26, 27]. This general statement is particularly true for solvation effects for which a panel of refined models is now accessible [28–32].

In this chapter we summarize several recent advances in the TD-DFT spectroscopy field with a focus on recent works dealing with 0–0 energies, for which a protocol is detailed in Sect. 2. We next present the results of several benchmarks performed for these 0–0 energies (Sect. 3) before going through a series of examples obtained in the dye chemistry field (Sect. 4).

2 Protocol to Determine the 0–0 Energies

In this section we present a popular approach to compute the 0–0 energies with TD-DFT. This also allows us to define a series of different energies which are subsequently used, and to propose an easy-to-follow protocol to obtain all the relevant parameters which are represented in Fig. 1, in which R^{GS} and R^{ES} stand for the optimal geometries of the ground- and excited-states, respectively, whereas E^{GS} and E^{ES} are the total energies of these two states. Following [15], we first explain the more straightforward gas-phase situation before extending the protocol to the condensed phase.

2.1 Gas Phase

In the gas phase, the vertical absorption can simply be defined as the difference between the ES and GS energies at the optimal ground-state geometry,

$$E^{\text{vert}-\text{a}} = E^{\text{ES}}\left(R^{\text{GS}}\right) - E^{\text{GS}}\left(R^{\text{GS}}\right), \tag{1}$$

whereas the vertical fluorescence is the corresponding data estimated at the optimal geometry of the relevant excited-state,

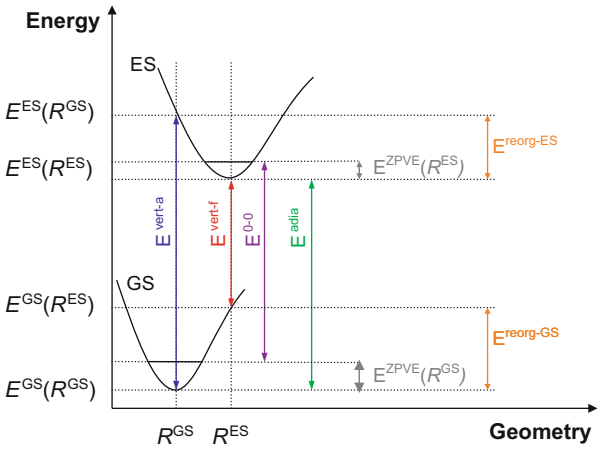

Fig. 1 Simplified energy diagram representing only two singlet states without intersections and describing key theoretical parameters. Reproduced with permissions from Jacquemin et al. [15]. Copyright 2012, American Chemical Society

$$E^{\text{vert}-\text{f}} = E^{\text{ES}}\left(R^{\text{ES}}\right) - E^{\text{GS}}\left(R^{\text{ES}}\right). \tag{2}$$

We note that the second quantity implies a force minimization process performed at the ES to define R^{ES}, and can be obtained efficiently with a wide panel of quantum chemistry codes which include analytical TD-DFT gradients (e.g., Gaussian, Turbomole, Q-Chem, and NWChem to cite a few) [18–20]. The adiabatic energy can be obtained as a simple by-product of the two previous equations,

$$E^{\text{adia}} = E^{\text{ES}}\left(R^{\text{ES}}\right) - E^{\text{GS}}\left(R^{\text{GS}}\right), \tag{3}$$

or, alternatively by combining vertical transition energies with the geometrical reorganization energies,

$$E^{\text{adia}} = \frac{1}{2}\left[E^{\text{vert}-\text{f}} + E^{\text{vert}-\text{a}}\right] + \frac{1}{2}\left[E^{\text{reorg}-\text{GS}} - E^{\text{reorg}-\text{ES}}\right]. \tag{4}$$

In this latter equation the first term tends to be dominant, and, in a first crude approximation the second term can be neglected. Indeed, the second term is the difference of reorganization energies between the two considered states, which is significant only when there is a strong difference between R^{GS} and R^{ES}. Next, one needs to determine the difference of zero-point vibrational energy (ZPVE) between the ES and GS,

$$\Delta E^{\text{ZPVE}} = E^{\text{ZPVE}}\left(R^{\text{ES}}\right) - E^{\text{ZPVE}}\left(R^{\text{GS}}\right), \tag{5}$$

a computationally demanding term, as second derivatives (Hessian) of the ES PES need to be computed, either analytically [21, 22] or numerically. For small molecules, at least, comparisons with the results obtained using wavefunction

approaches, demonstrated that TD-DFT generally provides accurate ΔE^{ZPVE} [17]. To reach the 0–0 energies, one adds the two previous terms:

$$E^{0-0} = E^{\mathrm{adia}} + \Delta E^{\mathrm{ZPVE}}. \tag{6}$$

We note that ΔE^{ZPVE} is almost systematically negative, as the PES of the ES tends to be flatter than its GS counterpart and, consequently, E^{0-0} is generally smaller than E^{adia}. As stated above, E^{0-0} can be directly compared to the absorption-fluorescence crossing point for solvated molecules, and it subsequently offers a much more solid basis for theory–experiment comparisons than $E^{\mathrm{vert-a}}$, which often has no straightforward experimental counterpart.

2.2 Condensed Phase

When considering an environment surrounding the molecule of interest (the compound undergoing the electronic transition), it is crucial to determine how the medium reacts to the change of electronic state of the photo-active compound. Irrespective of the nature of the environment, one distinguishes the equilibrium (eq) and non-equilibrium (neq) regimes [26]. In the former, a full (electrons and nuclei) medium relaxation takes place, and such a regime is adapted to determine "slow properties", e.g., both R^{ES} and $E^{\mathrm{ZPVE}}(R^{\mathrm{ES}})$. Essentially, it implies that the dye-environment interactions can be accounted for in a similar way as in the GS. In the latter neq limit, only the electronic cloud of the medium can adapt to the new electronic configuration of the chromophore, and this scheme is useful to model rapid phenomena, typically transition energies. Indeed, the vertical transition energies now read

$$E^{\mathrm{vert-a}}(\mathrm{neq}) = E^{\mathrm{ES}}\left(R^{\mathrm{GS}}, \mathrm{neq}\right) - E^{\mathrm{GS}}\left(R^{\mathrm{GS}}, \mathrm{eq}\right), \tag{7}$$

for absorption, and

$$E^{\mathrm{vert-f}}(\mathrm{neq}) = E^{\mathrm{ES}}\left(R^{\mathrm{ES}}, \mathrm{eq}\right) - E^{\mathrm{GS}}\left(R^{\mathrm{ES}}, \mathrm{neq}\right), \tag{8}$$

for emission. For the former phenomenon, one starts from an eq GS and goes to a neq ES, whereas for the latter phenomenon, the ES is in equilibrium whereas the GS is in non-equilibrium, and a proper modeling of the latter process requires quite advanced computational approaches [30–32]. Differences between eq and neq vertical transition energies can be significant in polar solvents [26]. By definition, both the adiabatic and 0–0 energies are equilibrium properties as they correspond to a transition between two states at their respective minima:

$$E^{0-0}(\text{eq}) = E^{\text{adia}}(\text{eq}) + \Delta E^{\text{ZPVE}}(\text{eq}). \tag{9}$$

However, this raises a difficulty, because the experimental absorption-fluorescence crossing point corresponds to the intersection of two curves in the experimental spectra, each being associated with a neq phenomenon. This cannot be properly modeled by the use of (9). To resolve this inconsistency, it has been proposed to correct the $E^{0-0}(\text{eq})$ in the following way [33]:

$$E^{\text{AFCP}}(\text{neq}) = E^{0-0}(\text{eq}) + \frac{1}{2}\left[\Delta E^{\text{vert}-\text{a}} + \Delta E^{\text{vert}-\text{f}}\right], \tag{10}$$

where the correcting terms are

$$\Delta E^{\text{vert}-\text{a}} = E^{\text{vert}-\text{a}}(\text{neq}) - E^{\text{vert}-\text{a}}(\text{eq}), \tag{11}$$

$$\Delta E^{\text{vert}-\text{f}} = E^{\text{vert}-\text{f}}(\text{neq}) - E^{\text{vert}-\text{f}}(\text{eq}). \tag{12}$$

The rationale for this correction can be obtained by examining (4). Indeed, in (10), the only approximations are the neglect of the difference between non-equilibrium and equilibrium environmental effects on the difference between the reorganization energies of the two states, a very small contribution, and the consideration of equilibrium limit during the computation of ΔE^{ZPVE}, but the eq–neq variations for this average term are generally trifling.

2.3 Further Comments

2.3.1 Calculations with the Polarizable Continuum Model

The most popular approach for modeling solvent effects is the Polarizable Continuum Model (PCM) which treats the environment as a structureless material presenting the macroscopic properties of the actual solvent. The solute is embedded in a cavity inside this solvent, and charges located on the surface of this cavity are determined self-consistently to account for the electrostatic interactions between the solute and the solvent [26]. We briefly describe here the different variations of the PCM model which have been developed for ES. In the (simplest) linear response (LR) model [28, 29], the GS-to-ES transition densities are used to determine the variations of the charges localized on the cavity when the solute changes its electronic configuration. In the corrected linear response (cLR) [30], the one-particle TD-DFT density matrix (the actual density of the ES within the selected approximation) is used in a perturbative approach, to evaluate the changes of the charges of the cavity when the solute changes electronic state [30]. The use of the one-particle TD-DFT density, rather than the transition density, advantageously allows one to account for orbital relaxation, and this density is also used in the two

self-consistent approaches, namely the state specific (SS) [31] and the vertical excitation model (VEM) [32] approaches. One of the principal differences between the two approaches is that the former implies a modification of the GS reference during the self-consistent process, whereas the latter does not. When the change of polarity of the chromophore between the GS and ES is large, e.g., for charge-transfer (CT) transitions, going beyond the LR-PCM approximation is recommended, though the most adequate model in that case remains a matter of debate [34, 35].

We underline that, although all these approaches can be used to determine E^{ES} analytically, analytic gradients (and hence efficient access to R^{ES}) are only available with the LR approach [20]. Subsequently, a popular approach is to determine $E^{\mathrm{vert-a}}$, $E^{\mathrm{vert-f}}$, and E^{adia} with one of the three refined PCM approaches (cLR, SS, and VEM) on geometries computed within the LR-PCM model. Likewise, ΔE^{ZPVE} is often calculated at the LR-PCM level, so that the results of (10) are generally obtained with mixed environmental models, the energy (geometry and vibrations) being obtained with a refined (simpler) PCM level of theory [33].

2.3.2 0–0 Energies with Mixed DFT/Wavefunction Approaches

Besides TD-DFT, there is a wide panel of alternative and (very) accurate ab initio methods with, on the one hand, multi-reference approaches, e.g., Complete Active Space second-order Perturbation Theory (CAS-PT2) [36] and Multi-Reference Configuration Interaction (MR-CI) [37], and, on the other hand, single-reference (highly-)correlated schemes, e.g., Equation-of-Motion Coupled Cluster (EOM-CC) [38–41], Symmetry Adapted Cluster CI (SAC-CI) [42], Algebraic Diagrammatic Construction (ADC) [43], and Configuration Interaction singles with a perturbative correction for double excitations [CIS(D)] [44, 45]. Despite the rapid developments of these approaches and the implementations of efficient protocols (e.g., the resolution of identity scheme), their less favorable scalings with system size than TD-DFT generally limit their applications to vertical calculations but for rather small molecules. Therefore, it has been proposed to combine TD-DFT's ES geometries and vibrations to $E^{\mathrm{vert-a}}$ and $E^{\mathrm{vert-f}}$ obtained with these more advanced approaches. In the protocol proposed by Goerigk and Grimme [13], the experimental 0–0 energies are first transformed into "experimental" vertical energies by applying successive corrections for solvation, vibration, and geometrical reorganization effects determined with TD-DFT. Alternatively, one can determine AFCP energies through (10) and next correct them through wavefunction (Ψ) vertical calculations performed on the DFT GS and TD-DFT ES geometries [46, 47]. For approaches that can only be used for gas-phase vertical transition energies, the corrected AFCP energy simply becomes

$$E_{\mathrm{BE}}^{\mathrm{AFCP}}(\mathrm{neq}) = E_{\mathrm{TD-DFT}}^{\mathrm{AFCP}}(\mathrm{neq}) + \left[E_{\Psi}^{\mathrm{adia}}(\mathrm{gas}) - E_{\mathrm{TD-DFT}}^{\mathrm{adia}}(\mathrm{gas})\right], \qquad (13)$$

where BE stands for best estimates. Compared to (10), (13) only requires, for the TD-DFT part, two additional vertical gas-phase calculations (one for each optimal geometry) and the time-limiting step generally remains the wavefunction computation. The accuracy of the results obtained with (13) of course depends not only on the quality of the wavefunction model but also partly on the "starting" accuracy obtained with TD-DFT. When TD-DFT strongly underestimates the transition energies, using (13) could be less efficient.

2.3.3 Band Shapes

Once the GS and ES vibrational signatures have been determined, for instance in the course of computing the ΔE^{ZPVE} contribution to E^{0-0}, it is possible to obtain vibronic couplings and hence to estimate absorption and emission band shapes. This requires the calculation of the coupling factors between the different vibrational states of the GS and the ES, a task often achieved by the Franck–Condon (for strongly dipole allowed transitions) and/or Herzberg–Teller (for forbidden or weakly allowed transitions) approaches [7, 9, 12, 48–51]. Such schemes are now implemented in several codes, and can also be used to gain access to absolute intensities, i.e., the molar absorptivity (generally noted ε in the well-known Beer–Lambert's law). This offers additional direct comparisons with experimental data.

2.3.4 Choice of an Exchange-Correlation Functional

Though this topic is discussed in more detail in Sect. 3, is it probably worth giving some general comments regarding the selection of an appropriate XCF. First, one can select a hybrid functional, incorporating a fraction of the so-called *exact* exchange: they generally yield much more accurate results than the typical LDA or GGA approaches which tend to provide much too low transition energies in most compounds. If valence ES are investigated, one should distinguish the localized ES, typically resulting for $n \rightarrow \pi^{\star}$ and $\pi \rightarrow \pi^{\star}$ transitions, for which standard global hybrids such as B3LYP [52] or PBE0 [53] are well suited from charge-transfer excited-states, for which the selection of range-separated hybrids which present an amount of *exact* exchange increasing with the interelectronic distance, e.g., CAM-B3LYP [54] of ωB97X-D [55], generally provide more accurate transition energies. Eventually, range-separated hybrids are also often a better choice for Rydberg ES [56].

2.3.5 Choice of an Atomic Basis Set

Similar to DFT, TD-DFT is relatively less sensitive to the size of the atomic basis set than the corresponding highly-correlated wavefunction theories, though exceptions have been reported [57]. Irrespective of the agreement with experimental data, reaching ES data which are converged with respect to the extension of the basis set generally requires the selection of larger atomic basis sets than for GS properties. For electronic transitions to low-lying excited-states in conjugated molecules, a double-ζ (or, better, triple-ζ) polarized atomic basis set augmented with diffuse orbitals appears to be a judicious choice. In other words, 6-31+G(d) or *aug*-cc-pVDZ could be advised as reasonable compromises between computational cost and accuracy for both $E^{\text{vert}-\text{a}}$ and $E^{\text{vert}-\text{f}}$. Of course, for Rydberg ES, a much larger basis set may be necessary, e.g., *aug*-cc-pVTZ. When optimizing the geometry of a given ES, one should also be cautious as the PES are often quite flat and diffusionless basis sets could yield rather poor results but in strongly constrained fluorophores. The interested reader can find elsewhere longer discussions regarding basis set effects for both small [58] and large [15] molecules in the context of TD-DFT spectroscopic investigations.

3 Benchmarks

In this section we present the results obtained in several benchmarks aiming to pinpoint the most adequate XCF. Both 0–0 energies and band topologies, obtained through the calculation of vibronic couplings, are discussed. A general statement, at least applicable to low-lying ES of organic molecules, is that pure XCF which do not include exact exchange (e.g., BLYP [59, 60] or PBE [61]) tend to provide much poorer results than hybrid XCF. In global hybrid functionals (e.g., B3LYP [52], PBE0 [53, 62], and M06-2X [63, 64]) the main parameter affecting the computed E^{AFCP} is the mixing between the exact and DFT exchange, whereas in range-separated hybrids (e.g., CAM-B3LYP [54] and ωB97X-D [55]), the attenuation parameter which defines the rate at which one goes from DFT to exact exchange is the key parameter. We redirect the interested readers to [24] for a longer and more general review of existing TD-DFT benchmarks.

3.1 AFCP Energies

In this section we focus on investigations treating the E^{AFCP} of large molecules [7, 13, 15, 65], though there are several works dealing with small gas-phase compounds for which the 0–0 band can be accurately measured [17, 19, 66–69]. First, as ΔE^{ZPVE} is the most computationally expensive term, let us discuss its magnitude

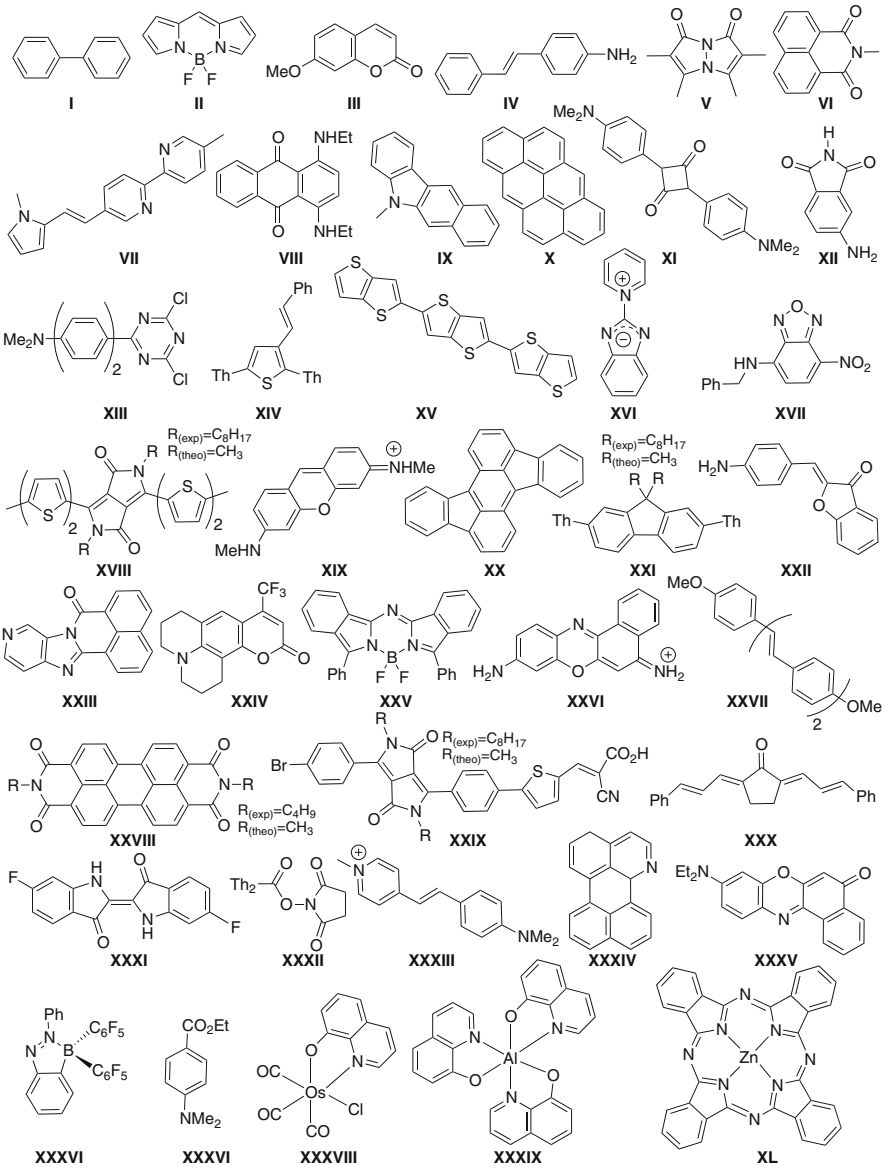

Fig. 2 Set of 40 test molecules used in several benchmarks of AFCP energies [15, 70, 71]. Reproduced with permissions from Jacquemin et al. [70]. Copyright 2014, American Chemical Society

and XCF dependence. For the 40 molecules displayed in Fig. 2, it has been found that the variations when changing the XCF are weak (ca. ± 0.02 eV) [15], a conclusion also reached in other studies on smaller systems [17, 66], indicating that ΔE^{ZPVE} can, in general, be evaluated with any XCF. In addition, this term was

Table 1 MSE and MAE obtained during benchmarks of E^{AFCP} of large structures. All data in eV. LC-PBE* and LC-PBE0* are optimally-tuned range-separated hybrid functionals

XCF	Molecular set	MSE	MAE	References
BP86	41 conjugated molecules	−0.56	0.57	[7]
BLYP	12 large dyes	−0.49	0.51	[13]
B3LYP	41 conjugated molecules	−0.33	0.34	[7]
	12 large dyes	−0.22	0.31	[13]
	40 dyes (Fig. 2)	−0.14	0.27	[15]
APF-D	40 dyes (Fig. 2)	−0.06	0.27	[71]
PBE0	40 dyes (Fig. 2)	−0.03	0.22	[15]
M06	40 dyes (Fig. 2)	0.05	0.23	[15]
PBE0-1/3	40 dyes (Fig. 2)	0.14	0.22	[71]
BMK	12 large dyes	0.07	0.19	[13]
SOGGA11-X	40 dyes (Fig. 2)	0.21	0.24	[70]
M06-2X	40 dyes (Fig. 2)	0.25	0.26	[15]
BHHLYP	41 conjugated molecules	−0.01	0.18	[7]
CAM-B3LYP	12 large dyes	0.11	0.18	[13]
	40 dyes (Fig. 2)	0.24	0.25	[15]
ωB97X-D	40 dyes (Fig. 2)	0.30	0.30	[70]
LC-PBE	40 dyes (Fig. 2)	0.56	0.57	[15]
LC-PBE*	40 dyes (Fig. 2)	0.12	0.20	[70]
LC-PBE0*	40 dyes (Fig. 2)	0.25	0.26	[71]
B2PLYP	12 large dyes	−0.11	0.20	[13]
B2GPPLYP	12 large dyes	−0.01	0.16	[13]

found to be non-negligible, e.g., it is −0.08 eV on average for the set of molecules shown in Fig. 2 [15]. Similar values have been obtained with other sets of molecules [13, 66].

With coworkers, we have investigated the E^{AFCP} of the compounds displayed in Fig. 2 using (10) and 12 XCF [15, 70, 71]. More precisely, we have used the LR-PCM model combined to the 6-31+G(d) atomic basis set for the geometrical and (harmonic) vibrational parameters whereas the electronic energies were computed at the cLR-PCM level with the 6-311++G(2df,2p) atomic basis set. The results of these works are summarized in Table 1 together with other works. In Table 1, the mean signed (MSE) and mean absolute (MAE) errors are given. Overall, one finds a general correlation between the amount of exact exchange included in the XCF and the MSE. Indeed, although PBE0 (25% exact exchange) [53, 62] is on average on the experimental spot (MSE close to 0), XCF including a larger fraction of exact exchange tend to yield positive MSE, i.e., they overestimate the experimental E^{AFCP}. This trend is quite general for low-lying ES: the larger the fraction of exact exchange included in the XCF, the larger the transition energies. However, the MAE tend to be quite similar for all approaches (ca. 0.25 eV), but for the LC-PBE range-separate hybrid [72] this is obviously not the most adequate approach in the present case. It should be noted that functionals such as M06-2X

[63, 64] and CAM-B3LYP [54] provide more consistent values, i.e., larger correlation coefficients with respect to experimental results (than B3LYP [52] or PBE0 [53, 62]) and can therefore be valued if design is sought: they overshoot the transition energies in a rather systematic way. The best results for the set of molecules of Fig. 2 are obtained with the optimally-tuned LC-PBE*, but at the cost of a systematic (non-empirical) optimization of the attenuation parameter.

Grimme and coworkers also performed a series of benchmarks [7, 13, 65] with a similar focus on "real-life" structures, and the results are collected in Table 1. In their first contribution, they evaluated 3 XCF (BP86 [59, 73], B3LYP [52], and BHLYP [74]) on 30 singlet–singlet and 13 doublet–doublet transitions in aromatic and radical dyes, respectively. Solvent effects were empirically accounted for by applying a standard correction to the experimental 0–0 energies. These authors concluded that global hybrids with 30–40% exact exchange emerged the best compromises [7]. More recently, the same group treated 12 molecules, transforming the measured energies in reference vertical values thanks to TD-DFT calculations. With this model, they could obtain deviations smaller than 0.2 eV with a recent global hybrid (BMK [75]), a range-separated hybrid (CAM-B3LYP [54]), and their double hybrid (B2GPPLYP [65]).

In short, the typical TD-DFT errors for E^{AFCP} are of the order of 0.2–0.3 eV, when hybrid XCF are used. It should also be noted that XCF including a large share of exact exchange (ca. 50%) deliver too large transition energies but tend to yield a good consistency (large correlation coefficient) with experiment. The most accurate results are obtained with double-hybrids or optimally-tuned range-separated XCF but for an increased computational effort.

3.2 Band Shapes

The accuracy of the band topologies obtained with several XCF has been evaluated by several groups [7, 16, 27, 71]. For the sake of consistency with the E^{AFCP} works presented above, we discuss here the two latter investigations which relied on a set of 20 conjugated molecules belonging to the same families as the one shown in Fig. 1. The selected protocol also relied on the 6-31+G(d) atomic basis set and included environmental effects thanks to the PCM approach. Selected key statistical data are given in Table 2. As all vibronic calculations have been performed on the basis of GS and ES vibrations obtained in the harmonic approximation, the clear trend is to overestimate the separation between the different vibronic peaks, irrespective of the selected XCF, an error which could be reduced by including anharmonic effects [16, 76, 77]. It is also obvious that the average absolute errors are smaller for absorption (ca. 100 cm^{-1}) than for emission (ca. 250 cm^{-1}). All XCF, apart from LC-PBE, provide rather similar deviations, and it is therefore difficult to select an unambiguously more accurate hybrid functional. Nevertheless, it should be noted that the obtained accuracy is significantly system dependent, e.g., most XCF are able to reproduce accurately the characteristic multi-peak structure of

Table 2 MSE and MAE obtained during benchmarks of the band shapes of absorption and emission spectra. The errors are given in cm^{-1} and correspond to difference of separation with the 0–0 peak which has been set to 0 cm^{-1} in both the theoretical and experimental spectra. All data have been taken in [16, 71]

	Absorption		Fluorescence	
XCF	MSE	MAE	MSE	MAE
B3LYP	51	80	80	225
APF-D	57	112	12	194
PBE0	63	117	115	263
M06	83	95	110	244
PBE0-1/3	89	134	47	227
SOGGA11-X	75	117	60	229
M06-2X	83	106	106	262
CAM-B3LYP	88	108	129	242
ωB97X-D	57	107	60	211
LC-PBE*	93	121	104	240
LC-PBE0*	120	139	87	235
LC-PBE	172	182	229	351

fused aromatics but they fail to provide the correct height of the shoulder in cyanines (see below for a discussion on the latter derivatives) [16]. For the relative intensities (setting the intensity of the most intense peak to 1), the typical TD-DFT error attains 10–15% for both absorption and emission, an average discrepancy which is again rather independent of the selected XCF. Eventually, as for E^{AFCP}, optimally-tuned approaches vastly improve the original LC-PBE results, though they do not outperform other XCF for band shapes. In other words, optimal tuning improves the transition energies without deteriorating the accuracy of the computed band shapes [71].

3.3 Challenging Cases

In this last part of this section, we consider a limited number of known TD-DFT problems for low-lying singlet ES. In these cases, the accuracy of TD-DFT is either worse than expected (cyanines) or can only be maintained with the selection of a specific XCF (charge-transfer). It should also be noted that triplet ES and, consequently, singlet-triplet splittings may be challenging for conventional TD-DFT [78–81] but this particular error is beyond our scope here.

3.3.1 Cyanine Excited-States

Cyanine derivatives are (positively or negatively) charged π-conjugated derivatives containing a linker possessing an odd number of sp^2 carbon atoms capped by two electronegative centers (typically, nitrogen, oxygen, or sulfur atoms). Both the canonical streptocyanines and the fluoroborate dyes (e.g., boron-dipyrromethene, BODIPY) belong to that class and it has been shown that they can hardly be

modeled with adiabatic TD-DFT [33, 82–93]. Indeed, the TD-DFT transition energies are too large (by ca. 0.3–1.0 eV) in cyanines, and this conclusion has been reached through comparisons of both TD-DFT's $E^{\text{vert}-\text{a}}$ with their highly-correlated wavefunction counterparts [82, 87] and TD-DFT's E^{AFCP} with experimental references for fluoroborate emitters [88, 89]. More puzzling is the fact that the errors seem to be almost independent of the selected XCF and that this error is not related to a multi-determinant nature. The fundamental reasons explaining this failure of TD-DFT have been given in [90–92, 94, 95] and summarized in a recent account [93]. A pragmatic approach to obtain accurate E^{AFCP} is to apply (13) selecting an appropriate variant of the CIS(D), ADC(2) or CC2 approaches as the wavefunction method [47, 96]. Examples of applications of such mixed approach are given in Sect. 4.

3.3.2 Energy and Geometry of Charge-Transfer States

One generally denotes as CT states, states in which the photon absorption or emission induces a strong displacement of the electronic density, i.e., when the electron and the hole are spatially separated. For those CT ES, it is now well recognized that both pure and global hybrid XCF including a small fraction of exact exchange tend to deliver (much) too small $E^{\text{vert}-\text{a}}$, $E^{\text{vert}-\text{f}}$, and E^{AFCP} [97–100]. For instance, Dreuw and Head-Gordon have shown that LDA [101], BLYP [59, 60], and B3LYP [52] XCF yield errors of 1 eV or more for the bacteriochlorophyll-spheroidene dyad. Within the adiabatic TD-DFT approximation, this error can be strongly reduced by using a range-separated hybrid XCF, e.g., CAM-3LYP [54], LC-BOP [102], or ωB97-X [103] which restores a correct interaction between the electron and the hole [104–107] and therefore provides an efficient answer to the CT challenge.

Additionally, the TD-DFT determination of the R^{ES} can be problematic for CT ES. Tozer was the first to unravel the qualitatively incorrect PES obtained for 4-(dimethylamino)-benzonitrile with B3LYP [108]. Indeed, this popular XCF predicts that the twisted ES, in which the NMe_2 terminal group becomes perpendicular to the central phenyl ring, is more stable than the corresponding planar geometry, whereas accurate wavefunction theories yield the opposite conclusion (more stable planar structure). As for the transition energies, the use of range-separated hybrid XCF restores a physically correct behavior. Similar conclusions to that of Tozer have been obtained for several other compounds [15, 109, 110] and it indicates that one should be particularly cautious when interpreting dual-fluorescence originating from an equilibrium between planar and twisted intramolecular CT.

In short, for CT states, both the structures and transition energies are more accurately evaluated using range-separated hybrid XCF.

4 Illustrations

4.1 Organic Electronic Chromophores

As stated previously, one of the advantages of computing vibrationally-resolved spectra is the access to both band topologies and absolute intensities, both data being unreachable with vertical calculations. We recently illustrated these aspects for a series of small organic chromophores used in organic electronics [111]. For three compounds proposed by Bäuerle and collaborators, a dramatic effect of the end groups was noted experimentally [112]. Indeed, adding terminal electro-accepting groups induces strong variations of the position, intensity, and shape of the optical curves. As illustrated in Fig. 3, the selected TD-DFT approach perfectly restores: (1) the auxochromic displacements related to substitution for both absorption and emission; (2) the relative intensities which are in a 1.0:1.9:3.4 ratio (see Fig. 3) for the black:blue:red spectra, matching the experimental values of 1.0:1.8:3.1; (3) the band shapes, especially the marked vibronic progression in the unsubstituted dye and the presence of strong shoulders for the substituted structures. In [111], 8 additional compounds have been studied for a total of 11 dyes, and the agreement between TD-DFT's band topologies and experimental data was found to be excellent in all cases but one. This is a remarkable result as the measured spectra often result from the overlapping contributions of several ES.

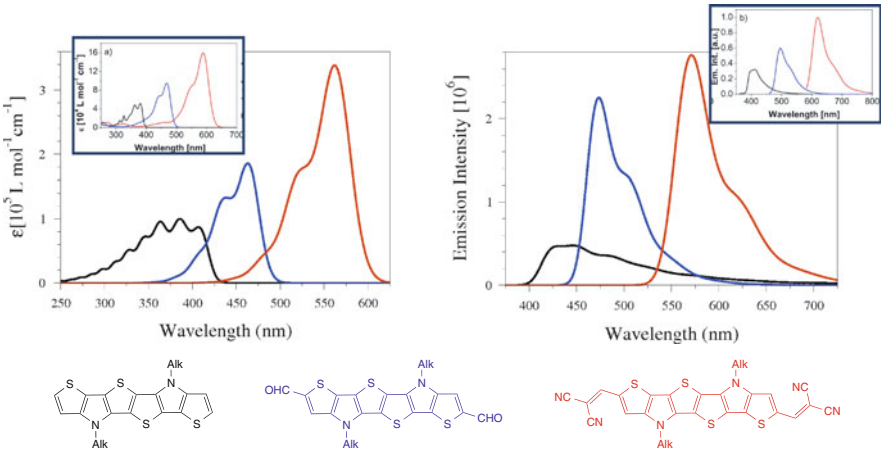

Fig. 3 Theoretical [cLR-PCM-M06/6-31+G(d)] absorption (*left*) and emission (*right*) band shapes obtained for three dyes (*bottom*). The experimental graphs are shown as *insets*. Adapted from [111] with permission from the Royal Society of Chemistry. No offset nor normalization was applied to the theoretical data. Experimental spectra adapted, with permission from Wetzel et al. [112]. Copyright 2014, American Chemical Society

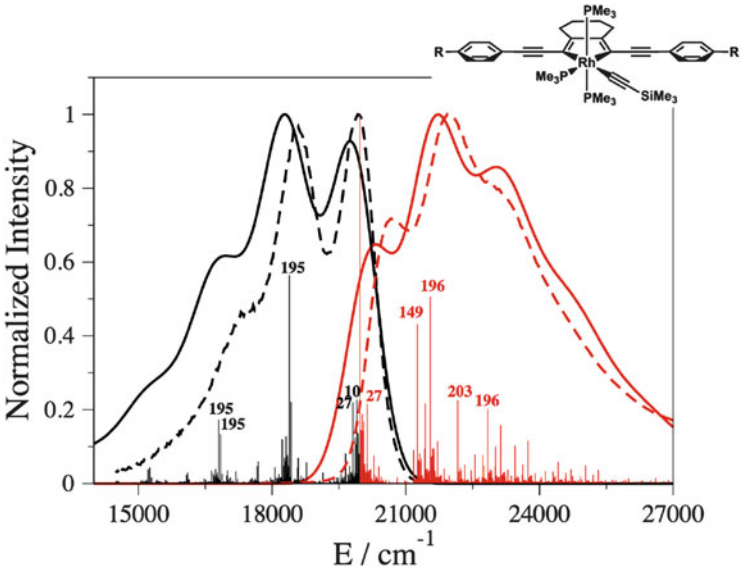

Fig. 4 Comparison between theoretical (*full lines*) and measured (*dashed lines*) absorption (*red*) and emission (*black*) band shapes of an inorganic complex. No shifting of the AFCP energies was applied. For the theoretical absorption and emission spectra, both the convoluted and stick spectra are displayed with numbering for the most contributing modes. Reproduced with permission from, Steffen et al. [115]. Copyright 2014, American Chemical Society

4.2 Inorganic Dyes

Although to date most applications of TD-DFT vibronic calculations have been performed for organic structures, there have also been several simulations for inorganic dyes [113–115]. An example of such successful work is given in Figure 4 that presents a direct comparison between measured and TD-DFT absorption and emission spectra for a rhodacyclopentadiene chromophore [115]. The good agreement is obvious: the AFCP energies are almost perfectly equal and the band topologies are also very close. Indeed, for emission, there are two peaks of nearly equivalent intensity followed by a shoulder whereas for the absorption, the 0–0 band is significantly less intense than the second peak. This good match confirmed that the complex experimental shapes originate from vibronic couplings and not from several energetically close electronic states. This finding was helpful to interpret several experimental outcomes [115]. For absorption (which is mostly influenced by ES vibrations), modes 27, 149, 196, and 203 appear at 160, 1290, 1578 and 2191 cm^{-1}, respectively. The second and third modes are mainly responsible for the most intense band at ca. 22000 cm^{-1}. These two vibrations correspond to stretchings of the double and single CC bonds of the rhodacycle.

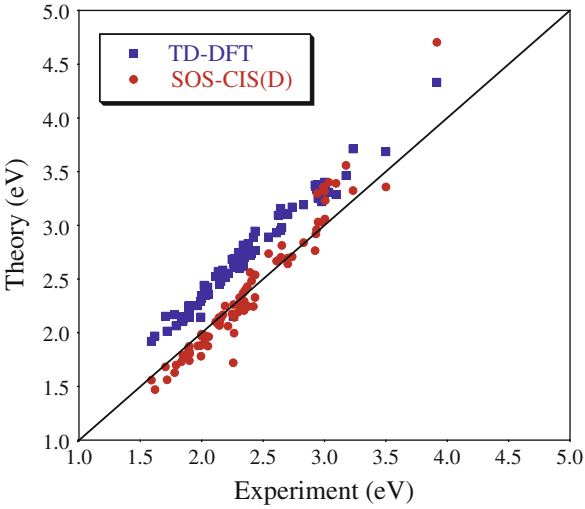

Fig. 5 Comparison between TD-DFT, SOS-CIS (D) and experimental 0–0 energies (eV) for a set of 83 fluoroborates. All TD-DFT calculations have been performed at the PCM-TD-M06-2X/6-311+G(2d,p)//PCM-M06-2X/6-31G(d) level, using either the cLR or the SS PCM approach for the transition energies. The *central line* indicates a perfect match between theory and experiment

4.3 Fluoroborate Derivatives

BODIPY and other similar derivatives relying on a fluoroborate group to ensure the chemical stability of the dyes constitute one of the most important classes of organic emitters [116–118]. Indeed, they present sharp fluorescence emission bands and large quantum yields. A large panel of chemical groups can be added around the central chromogens so as to modify the absorption and emission energies. These fluorophores present ES of cyanine nature, which is known to be challenging for TD-DFT (see above). Figure 5 displays the E^{AFCP} obtained with TD-DFT for a set of 83 fluoroborates using (10). This large set was obtained by putting together the panel of molecules considered in [47, 89, 96, 119] and was modeled using the M06-2X XCF. It is obvious that TD-DFT overestimates the E^{AFCP} in an almost systematic way (TD-DFT underestimates this energy in only 1 out of 83 cases), and this error is significant, as the MAE attains 0.354 eV. However, the variations of E^{AFCP} with the chemical structures is well reproduced by TD-DFT, and this can be seen by computing the linear determination coefficient, R^2, which attains 0.965 eV. This indicates that this protocol misses only 3.5% of the total variability of the experimental energies. To obtain values in better absolute agreement with experiment, it has been shown that applying a scaled opposite spin (SOS) variant of the CIS(D) model [45], that is using (13) with $\Psi = \mathrm{SOS\text{-}CIS(D)}$, is a very effective approach. Indeed, it allows the MAE to decrease by a factor of 3 (0.115 eV), at the same time inducing only a slight decrease of the R^2 (0.949). This is well illustrated in Fig. 5

Despite the systematic overestimation of the transition energy, it has been shown that TD-DFT allows reproduction of the band shapes of both the absorption and emission of fluoroborates with good to excellent accuracy [34, 35, 47, 88, 89, 120]. In other words, the PES provided by TD-DFT are reasonably accurate for

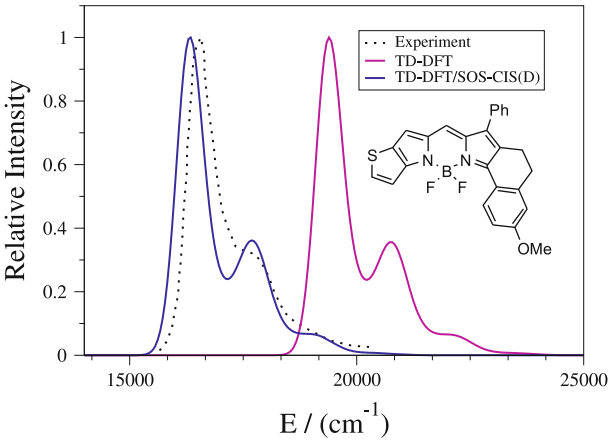

Fig. 6 Comparison between theoretical and experimental band topologies for a typical BODIPY derivative. The impact of the SOS-CIS(D) correction which shifts the E^{AFCP} is shown. Reproduced with permissions from Chibani et al. [47]. Copyright 2014, American Chemical Society

this class of dyes. This is illustrated in Fig. 6 for a strongly conjugated BODIPY designed to redshift the optical spectra. In Fig. 6 the band shape – which of course remains unchanged when applying the SOS-CIS(D) correction to the energy – clearly fits the experimental reference, with a marked shoulder displaced by ca. 1,500 cm^{-1} from the 0–0 band. The accuracy of TD-DFT's vibronic coupling has also been confirmed by computing the Huang–Rhys factors which were used to provide an estimation of the non-radiative deactivation vibrational pathways in selected BODIPY [89]. These factors correlated well with the measured quantum yields of emission: the larger the Huang–Rhys factors, the more efficient the non-radiative pathways, and the smaller the emission quantum yields.

4.4 ESIPT and Dual Emitters

Excited-state intramolecular proton transfer (ESIPT) is an extremely fast tautomerization process induced by photon absorption. ESIPT can take place in dyes presenting a strong intramolecular hydrogen bond, when the most stable isomer differs at the GS and ES. As illustrated in Fig. 7 for the typical enol/keto tautomerism, the structures of the absorbing and emitting species are strongly different, which advantageously yields very large Stokes shifts [121, 122]. Additionally, if the ES reaction is not quantitative, one can obtain emissions from both tautomers and hence reach dual fluorescence with a single compound [123]. This can be further optimized to design single-molecule white light emitting units [124], as ESIPT quantum yield tends to increase when going from solution to solid state.

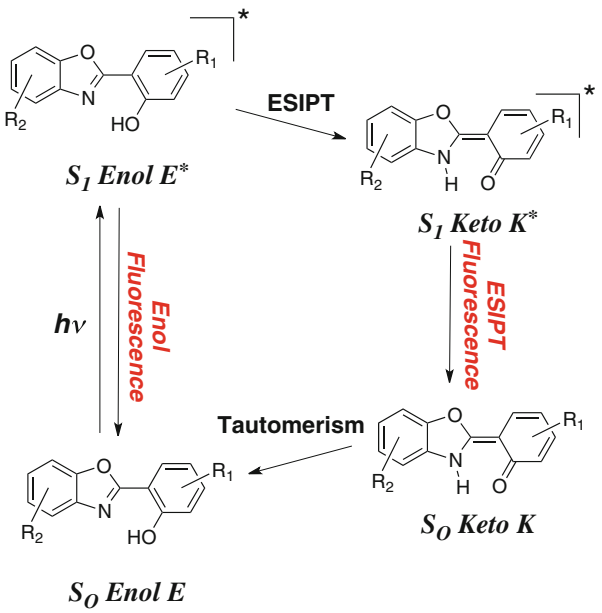

Fig. 7 Schematic representation of an ESIPT system containing an enol and a keto isomer. Adapted with permissions from Benelhadj et al. [124]. Copyright 2014, Wiley

There are numerous applications of TD-DFT and wavefunction approaches to rationalizing excited-state proton transfer [124–144] and, for the sake of consistency, we summarize here some of the works that have been performed with an approach similar to that used in the previous section, i.e., cLR-PCM/TD-M06-2X [124, 139–141]. Houari et al. explored the GS and ES PES of two hydroxyphenylbenzoxazole (HBO) dyes, differing only by their end groups [123, 139]. The alkyl-substituted system only shows emission from the keto tautomer experimentally, whereas the amino-substituted compound displays (dual-)emission from both enol and keto tautomers [123]. Houari et al. obtained the PES of both the GS and the ES (see Fig. 8) which helped to rationalize the experimental trends. Indeed, for the dye presenting sole ESIPT emission, the PES of the ES presents only a small transition state which disappears when vibrational corrections are included. In other words, after photon absorption there is a downhill slope for the ESIPT reaction on the free energy scale and only the keto isomer corresponds to a true minimum and can emit light. For the second dye (right panel in Fig. 8), the transition state is higher in energy and the enol minimum on the ES surface applies once vibrational corrections are included, indicating that dual emission is feasible. These conclusions fit the corresponding experimental data perfectly [123]. Figure 8 also shows that the transition states for the proton transfer are located at very different geometries for the GS and the ES, e.g., at respective O–H distances of 1.410 and 1.185 Å, for the first dye, indicating that a simple vertical TD-DFT calculation performed on the GS transition state would fail to deliver valuable insights. In the same work [139], the computed vibrationally-resolved emission spectra were compared to experiment to allow an approximate determination of the relative quantum yields of enol and keto

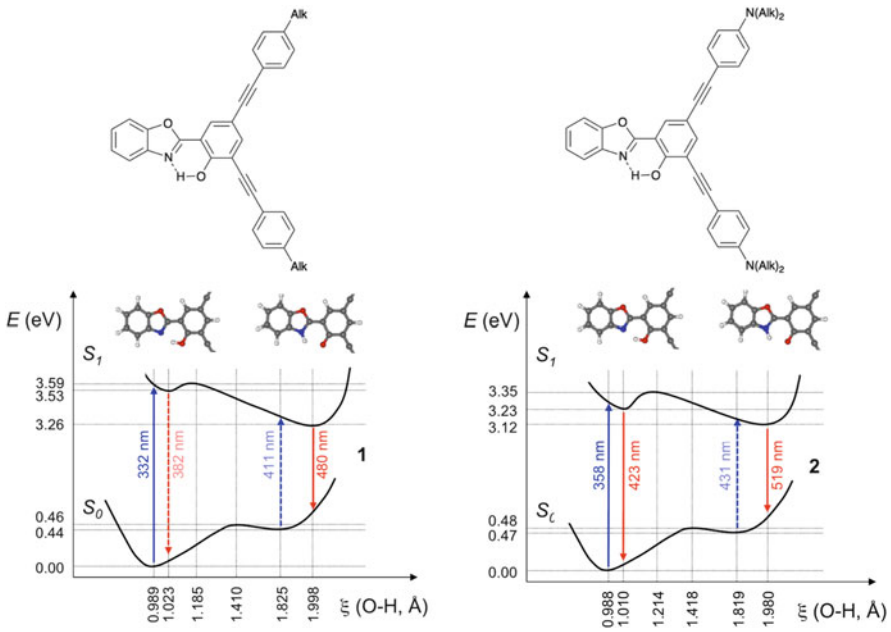

Fig. 8 Potential energy surfaces obtained for two HBO dyes. *Left*: alkyl substituted structure presenting only ESIPT emission experimentally. *Right*: amino-substituted structure displaying dual fluorescence in several solvents. For both dyes, the PES go from the enol (small O–H distance) to the keto (large O–H distance). Adapted from Houari et al. [139] with permission from the Royal Society of Chemistry

emission for a solvent in which the measured fluorescence bands for these two tautomers overlap.

In a subsequent investigation [124], TD-DFT was used to rationalize the properties of seven large hydroxybenzofuranbenzoxazole (HBBO) derivatives differing by their substitution patterns. A comparison between the experimental ratio of ESIPT and normal emissions (I^{keto}/I^{enol}) with the theoretical relative stabilities of the two tautomers determined for the ES (ΔG^{ES}) is given in Fig. 9. When the ΔG^{ES} are smaller than −0.1 eV, the driving force is sufficient to yield a quantitative proton transfer and only ESIPT emission is observed. Between −0.1 and 0.0 eV, there is an equilibrium between the two forms which emit and dual emission can only be obtained in this narrow energetic window. The correlation between the measured relative fluorescence intensities and the computed driving force for ESIPT is obvious in Fig. 9. This study led to the development of single-molecule white organic light emitting diodes [124].

4.5 Caging Effects

As stated above, TD-DFT can be coupled with several models to reproduce the impact of the environment on the spectral properties of a chromophore. Besides the

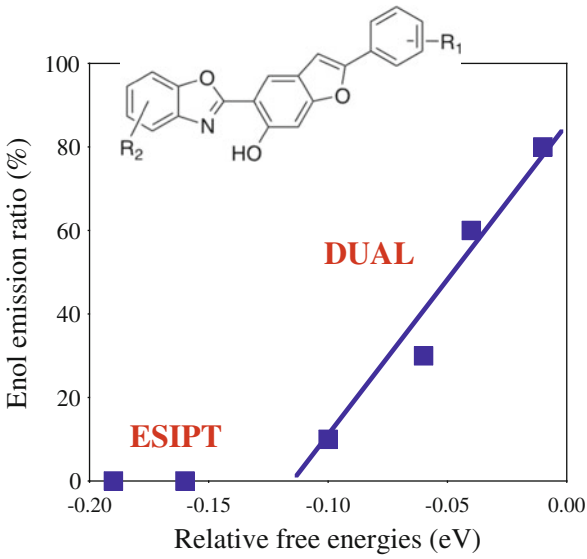

Fig. 9 Comparison between the theoretical relative free energies of the enol and keto isomers determined at the ES and the experimentally observed ratio of enol emission. See Benelhadj et al. [124]

most widely treated case of organic solvents, such an environment can involve a biomolecule [145–148], a cage [149, 150] a metal [151–153], an inorganic solid [154–156], or a molecular crystal [157] to cite a few examples. Depending on the exact nature of the environment, one needs to set up a specific computational protocol, but the general idea is to split the total system into two parts: the chromophore where the electronic excitation takes place and which is treated with TD-DFT whereas the surroundings are modeled with a simpler theoretical model, typically Molecular Mechanics (MM). We illustrate here such a procedure for an organic cage and redirect interested readers to a previous review on the topic for other examples and references [27]. The selected system consists of a squaraine dye encapsulated in a tetralactam macrocycle (see Fig. 10). Such an assembly was experimentally investigated by Smith and coworkers [158] and later modeled [149]. The macrocyclic cage aims to protect the dye from (bio-)chemical degradations and was not designed to tune the observed color. Indeed, the hallmark absorption band of the dye is shifted after complexation by −0.06 eV only [158], a bathochromic effect which can be almost perfectly reproduced by TD-DFT calculations considering the full system quantum mechanically (−0.07 eV). However, such a brute force approach implies a large computational cost. As the excitation is clearly localized on the squaraine, using a hybrid TD-DFT/MM is justified. The first approach proposed in [149] was to account self-consistently for the ground-state polarization by determining atomic point charges of the cage equilibrated with the density of the dye. Such a procedure yields a qualitatively incorrect hypsochromic shift of +0.10 eV. In a second approach, the response of the cage density to the change of electronic state of the dye was modeled through a

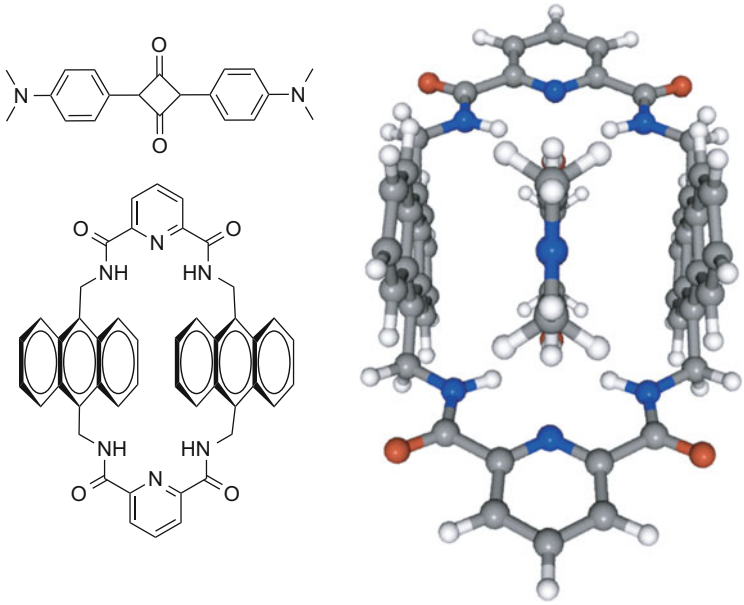

Fig. 10 Representation of the squaraine dye (*top left*) and cage (*bottom left*) used by Smith and coworkers [158]. On the right hand side, a side view of the DFT (PBE0) optimized complex is given [149]

polarizable continuum model inspired from PCM. This second scheme, denoted Electronic Response of the Surroundings, yields, for a negligible computational cost, a shift of −0.09 eV, in good agreement with both experiment and full TD-DFT calculation.

4.6 Charge-Transfer Optimization

Photoinduced charge-transfer excited states play a key role in several applications, notably in dye sensitized solar cells (DSSC) [159–163]. In DSSC, the absorption of light by a dye anchored on a semi-conducting surface, typically a metallic oxide, induces a CT on the dye which eventually leads to charge separation, the electron (or the hole) being injected into the semi-conductor. Charge transfer is therefore the key step initiating the light-to-electricity conversion process [164]. To quantify CT, several schemes have been proposed [56, 165–168] and we present here the d^{CT} index [165, 166]. This approach uses the ground- and excited-states electronic densities (ρ^{GS} and ρ^{ES}) to provide a CT distance (d^{CT}), the amount of charge transferred (q^{CT}), and CT dipole (μ^{CT}). First one computes the difference of densities between the excited and ground states:

$$\Delta\rho(\mathbf{r}) = \rho^{\mathrm{ES}}(\mathbf{r}) - \rho^{\mathrm{GS}}(\mathbf{r}). \tag{14}$$

Subsequently, one divides $\Delta\rho(\mathbf{r})$ into two parts according to the increase/decrease of the density resulting from the electronic transition. For the former, this reads

$$\rho^{+}(\mathbf{r}) = \begin{cases} \Delta\rho(\mathbf{r}) & \text{if} \quad \Delta\rho(\mathbf{r}) > 0 \\ 0 & \text{if} \quad \Delta\rho(\mathbf{r}) < 0\,, \end{cases} \tag{15}$$

and similarly for $\rho^{-}(\mathbf{r})$. The amount of charge transferred is obtained by integration

$$q^{\mathrm{CT}} = \int \rho^{+}(\mathbf{r}) d\mathbf{r}, \tag{16}$$

and an equivalent result is obtained by integrating $\rho^{-}(\mathbf{r})$. One next computes the barycenters corresponding to the $\rho^{+}(\mathbf{r})$ and $\rho^{-}(\mathbf{r})$ functions

$$r^{+} = (x^{+}, y^{+}, z^{+}) = \frac{1}{q^{\mathrm{CT}}} \int \mathbf{r}\rho^{+}(\mathbf{r}) d\mathbf{r}, \tag{17}$$

$$r^{-} = (x^{-}, y^{-}, z^{-}) = \frac{1}{q^{\mathrm{CT}}} \int \mathbf{r}\rho^{-}(\mathbf{r}) d\mathbf{r}. \tag{18}$$

The distance separating these two points is the CT distance

$$d^{\mathrm{CT}} = \sqrt{(x^{+} - x^{-})^2 + (y^{+} - y^{-})^2 + (z^{+} - z^{-})^2}, \tag{19}$$

whereas the CT dipole is

$$\left|\left|\mu^{\mathrm{CT}}\right|\right| = d^{\mathrm{CT}} q^{\mathrm{CT}}. \tag{20}$$

μ^{CT} is also equal to the difference of dipoles computed from the total GS and ES densities. This procedure was applied to design rod-like dyes with a maximal CT distance, using densities obtained with TD-DFT and more precisely with the CAM-B3LYP functional [169]. The compounds considered in [169] consist of an electron-donor group and an electron-acceptor moiety separated by a π-conjugated linker. All parameters were investigated (nature of the donor, size and nature of the linker, strength of the acceptor. . .). An illustration of the results obtained is given in Fig. 11 for three typical push–pull systems. For the shortest system, one indeed notices a typical CT state, the nitro (amino) group gaining (losing) density upon electronic excitation and d^{CT} is large. When the π-conjugated chain gets longer, one observes, contrary to expectations, that d^{CT} decreases. This can be qualitatively understood from Fig. 11: as the chain gets longer the excited-state starts to be

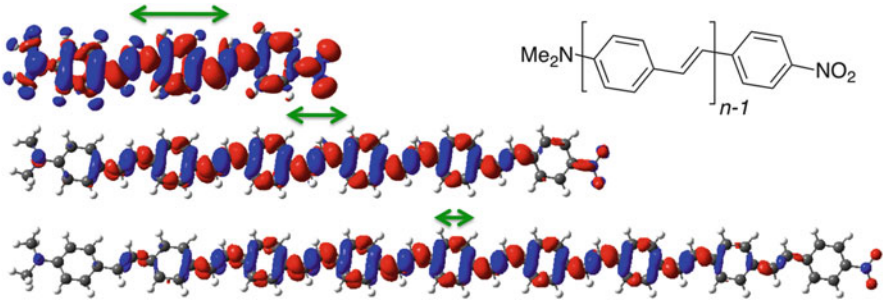

Fig. 11 Representation of $\Delta\rho(\mathbf{r})$ for three oligomers (trimer, hexamer, and nonamer). The *green vector* indicates the CT distance. The *blue* (*red*) regions indicate decrease (increase) of density after photon absorption. Adapted with permission from Ciofini et al. [169]. Copyright 2012, American Chemical Society

localized on the central part of the dye, with a minimal involvement of the terminal groups and the CT character is lost, because the excited-state eventually corresponds to a delocalized but symmetric $\pi \rightarrow \pi^\star$ transition. This means that, to maximize CT, there is an optimal linker length. For α,ω-NMe_2,NO_2 oligomers, this maximal CT is obtained for an oligomeric length of ca. 3–5 connecting rings, smaller (larger) systems being limited by the lack of efficient delocalization (the ineffective communication between the end groups). In [169] it was therefore concluded that *there is a systematic fine balance between the three elements of the rod-like compounds, and simply increasing the strength of the terminal electro-active groups or improving the delocalizability by adding more π-electrons in the bridge does not necessarily mean improvement of the CT properties.*

5 Conclusions

Theoretical spectroscopy in general, and Time-Dependent Density Functional Theory in particular, have now become mature tools to reproduce, predict, and interpret both absorption and emission spectra of a wide range of "real-life" molecules in "real-life" environments. TD-DFT is regularly applied as a black-box model to complement experimental measurements. As illustrated in this review, TD-DFT is now used not only to probe the nature of excited states within the vertical approximation, but also to determine 0–0 energies and band shapes for compounds containing up to ca. 150 atoms. These more demanding, but more insightful, simulations will undoubtedly become increasingly popular in the near future. Another key advantage of TD-DFT is that it can be coupled to several models for describing several kinds of environmental effects (solvents, cages, metals, surfaces…). Although some wavefunction approaches can be more accurate for specific systems, their less favorable scaling with system size remains an important limitation to their applicability to extended systems. The main weakness

of the adiabatic approximation to TD-DFT is its exacerbated dependency on the selected XCF. Nevertheless, the know-how is actually so great in this field that one can often easily select an adequate functional for the molecule and state considered. In the following years, it should become a common approach to combine TD-DFT geometries and vibrational frequencies to wavefunction vertical excitation energies so as to improve the accuracy of the final results and decrease the functional dependency. At the same time, the focus moves from the "static" spectral properties to "dynamic" excited-state reactions (proton-transfer, energy transfer photochromism. . .).

Acknowledgements D.J. acknowledges the European Research Council (ERC) and the *Région des Pays de la Loire* for financial support in the framework of a Starting Grant (Marches – 278845) and a *recrutement sur poste stratégique*, respectively. The COST-CMTS Action CM1002: COnvergent Distributed Environment for Computational Spectroscopy (CODECS) and its members are acknowledged for many fruitful discussions.

References

1. Runge E, Gross EKU (1984) Phys Rev Lett 52:997
2. Casida ME (1995) Time-dependent density-functional response theory for molecules. In: Recent advances in density functional methods, vol 1. World Scientific, Singapore, pp 155–192
3. Dreuw A, Head-Gordon M (2005) Chem Rev 105:4009
4. Ullrich C (2012) Time-dependent density-functional theory: concepts and applications. Oxford Graduate Texts (Oxford University Press), New York
5. Casida ME, Huix-Rotllant M (2012) Annu Rev Phys Chem 63:287
6. Laurent AD, Adamo C, Jacquemin D (2014) Phys Chem Chem Phys 16(28):14334
7. Dierksen M, Grimme S (2004) J Phys Chem A 108:10225
8. Fortrie R, Chermette H (2007) J Chem Theory Comput 3:852
9. Santoro F, Lami A, Improta R, Bloino J, Barone V (2008) J Chem Phys 128:224311
10. Guthmuller J, Zutterman F, Champagne B (2008) J Chem Theory Comput 4(2):2094
11. Peltier C, Laine PP, Scalmani G, Frisch MJ, Adamo C, Ciofini I (2009) J Mol Struct (THEOCHEM) 914:94
12. Improta R, Santoro F, Barone V, Lami A (2009) J Phys Chem A 113(52):15346
13. Goerigk L, Grimme S (2010) J Chem Phys 132:184103
14. Lopez GV, Chang CH, Johnson PM, Hall GE, Sears TJ, Markiewicz B, Milan M, Teslja A (2012) J Phys Chem A 116(25):6750
15. Jacquemin D, Planchat A, Adamo C, Mennucci B (2012) J Chem Theory Comput 8:2359
16. Charaf-Eddin A, Planchat A, Mennucci B, Adamo C, Jacquemin D (2013) J Chem Theory Comput 9:2749
17. Winter NOC, Graf NK, Leutwyler S, Hattig C (2013) Phys Chem Chem Phys 15:6623
18. van Caillie C, Amos RD (1999) Chem Phys Lett 308:249
19. Furche F, Ahlrichs R (2002) J Chem Phys 117:7433
20. Scalmani G, Frisch MJ, Mennucci B, Tomasi J, Cammi R, Barone V (2006) J Chem Phys 124:094107
21. Liu F, Gan Z, Shao Y, Hsu CP, Dreuw A, Head-Gordon M, Miller BT, Brooks BR, Yu JG, Furlani TR, Kong J (2010) Mol Phys 108(19–20):2791
22. Liu J, Liang WZ (2011) J Chem Phys 135(18):184111

23. Barbatti M, Crespo-Otero R (2015) Density-functional methods for excited states. In: Ferré N, Filatov M, Huix-Rotllant M (eds) Topics in current chemistry. Springer, Berlin/Heidelberg, pp 1–30. doi:10.1007/128_2014_605
24. Laurent AD, Jacquemin D (2013) Int J Quantum Chem 113:2019
25. Ziegler T, Krykunov M, Cullen J (2012) J Chem Phys 136:124107
26. Tomasi J, Mennucci B, Cammi R (2005) Chem Rev 105:2999
27. Jacquemin D, Mennucci B, Adamo C (2011) Phys Chem Chem Phys 13:16987
28. Cammi R, Mennucci B (1999) J Chem Phys 110:9877
29. Cossi M, Barone V (2001) J Chem Phys 115:4708
30. Caricato M, Mennucci B, Tomasi J, Ingrosso F, Cammi R, Corni S, Scalmani G (2006) J Chem Phys 124:124520
31. Improta R, Scalmani G, Frisch MJ, Barone V (2007) J Chem Phys 127:074504
32. Marenich AV, Cramer CJ, Truhlar DG, Guido CG, Mennucci B, Scalmani G, Frisch MJ (2011) Chem Sci 2:2143
33. Jacquemin D, Zhao Y, Valero R, Adamo C, Ciofini I, Truhlar DG (2012) J Chem Theory Comput 8:1255
34. Chibani S, Charaf-Eddin A, Le Guennic B, Jacquemin D (2013) J Chem Theory Comput 9:3127
35. Chibani S, Charaf-Eddin A, Mennucci B, Le Guennic B, Jacquemin D (2014) J Chem Theory Comput 10(2):805
36. Andersson K, Malmqvist P, Roos BO (1992) J Chem Phys 96(2):1218 http://scitation.aip.org/content/aip/journal/jcp/96/2/10.1063/1.462209
37. Buenker RJ, Peyerimhoff SD (1968) Theor Chim Acta 12(3):183
38. Stanton JF, Bartlett RJ (1993) J Chem Phys 98(9):7029
39. Christiansen O, Koch H, Jørgensen P (1995) Chem Phys Lett 243:409
40. Kállay M, Gauss J (2004) J Chem Phys 121(19):9257
41. Hättig C, Weigend F (2000) J Chem Phys 113:5154
42. Nakatsuji H, Ehara M (1993) J Chem Phys 98:7179
43. Schirmer J, Trofimov AB (2004) J Chem Phys 120:11449
44. Head-Gordon M, Maurice D, Oumi M (1995) Chem Phys Lett 246:114
45. Rhee YM, Head-Gordon M (2007) J Phys Chem A 111(24):5314
46. Boulanger P, Chibani S, Le Guennic B, Duchemin I, Blase X, Jacquemin D (2014) J Chem Theory Comput 10(10):4548
47. Chibani S, Laurent AD, Le Guennic B, Jacquemin D (2014) J Chem Theory Comput 10:4574
48. Guthmuller J, Zutterman F, Champagne B (2009) J Chem Phys 131:154302
49. Improta R, Barone V (2009) J Mol Struct (THEOCHEM) 914(1–3):87
50. Avila Ferrer FJ, Improta R, Santoro F, Barone V (2011) Phys Chem Chem Phys 13(38):17007
51. Avila Ferrer FJ, Santoro F (2012) Phys Chem Chem Phys 14(39):13549
52. Becke AD (1993) J Chem Phys 98:5648
53. Adamo C, Barone V (1999) J Chem Phys 110:6158
54. Yanai T, Tew DP, Handy NC (2004) Chem Phys Lett 393:51
55. Chai JD, Head-Gordon M (2008) Phys Chem Chem Phys 10:6615
56. Peach MJG, Benfield P, Helgaker T, Tozer DJ (2008) J Chem Phys 128:044118
57. Picconi D, Avila Ferrer FJ, Improta R, Lami A, Santoro F (2013) Faraday Discuss 163:223
58. Ciofini I, Adamo C (2007) J Phys Chem A 111:5549
59. Becke AD (1988) Phys Rev A 38:3098
60. Lee C, Yang W, Parr RG (1988) Phys Rev B 37:785
61. Perdew JP, Burke K, Ernzerhof M (1996) Phys Rev Lett 77:3865
62. Ernzerhof M, Scuseria GE (1999) J Chem Phys 110:5029
63. Zhao Y, Truhlar DG (2008) Acc Chem Res 41:157
64. Zhao Y, Truhlar DG (2008) Theor Chem Accounts 120:215
65. Goerigk L, Moellmann J, Grimme S (2009) Phys Chem Chem Phys 11:4611
66. Send R, Kühn M, Furche F (2011) J Chem Theory Comput 7(8):2376

67. Bates JEE, Furche F (2012) J Chem Phys 137:164105
68. Barnes L, Abdul-Al S, Allouche AR (2014) J Phys Chem A 118(46):11033, PMID: 25350349
69. Fang C, Oruganti B, Durbeej B (2014) J Phys Chem A 118:4157
70. Jacquemin D, Moore B, Planchat A, Adamo C, Autschbach J (2014) J Chem Theory Comput 10(4):1677
71. Moore B, Charaf-Eddin A, Planchat A, Adamo C, Autschbach J, Jacquemin D (2014) J Chem Theory Comput 10(10):4599
72. Song JW, Hirosawa T, Tsuneda T, Hirao K (2007) J Chem Phys 126:154105
73. Perdew JP (1986) Phys Rev B 33:8822
74. Becke AD (1993) J Chem Phys 98:1372
75. Boese AD, Martin JML (2004) J Chem Phys 121:3405
76. Biczysko M, Bloino J, Brancato G, Cacelli I, Cappelli C, Ferretti A, Lami A, Monti S, Pedone A, Prampolini G, Puzzarini C, Santoro F, Trani F, Villani G (2012) Theor Chem Accounts 131(4):1201
77. Stendardo E, Ferrer FA, Santoro F, Improta R (2012) J Chem Theory Comput 8(11):4483
78. Jacquemin D, Perpète EA, Ciofini I, Adamo C (2010) J Chem Theory Comput 6:1532
79. Peach MJG, Williamson MJ, Tozer DJ (2011) J Chem Theory Comput 7(11):3578
80. Sears JS, Koerzdoerfer T, Zhang CR, Brédas JL (2011) J Chem Phys 135:151103
81. Peach MJG, Tozer DJ (2012) J Phys Chem A 116(39):9783
82. Fabian J (2001) Theor Chem Accounts 106:199
83. Schreiber M, Bub V, Fülscher MP (2001) Phys Chem Chem Phys 3:3906
84. Grimme S, Neese F (2007) J Chem Phys 127:154116
85. Jacquemin D, Perpète EA, Scalmani G, Frisch MJ, Kobayashi R, Adamo C (2007) J Chem Phys 126:144105
86. Fabian J (2010) Dyes Pigm 84:36
87. Send R, Valsson O, Filippi C (2011) J Chem Theory Comput 7(2):444
88. Chibani S, Le Guennic B, Charaf-Eddin A, Maury O, Andraud C, Jacquemin D (2012) J Chem Theory Comput 8:3303
89. Chibani S, Le Guennic B, Charaf-Eddin A, Laurent AD, Jacquemin D (2013) Chem Sci 4:1950
90. Moore B II, Autschbach J (2013) J Chem Theory Comput 9:4991
91. Filatov M, Huix-Rotllant M (2014) J Chem Phys 141(2):024112
92. Zhekova H, Krykunov M, Autschbach J, Ziegler T (2014) J Chem Theory Comput 10:3299
93. Le Guennic B, Jacquemin D (2015) Acc Chem Res 48:530
94. Ziegler T, Krykunov M, Seidu I, Park Y (2015) Density-functional methods for excited states. In: Ferré N, Filatov M, Huix-Rotllant M (eds) Topics in current chemistry. Springer, Berlin/Heidelberg, pp 1–35. doi:10.1007/128_2014_611
95. Filatov M (2015) Density-functional methods for excited states. In: Ferré N, Filatov M, Huix-Rotllant M (eds) Topics in current chemistry. Springer, Berlin/Heidelberg. doi:10.1007/128_2014_630
96. Charaf-Eddin A, Le Guennic B, Jacquemin D (2014) RSC Adv 4:49449
97. Tozer DJ, Amos RD, Handy NC, Roos BO, Serrano-Andrès L (1999) Mol Phys 97:859
98. Cai ZL, Sendt K, Remiers R (2002) J Chem Phys 117:5543
99. Gritsenko OV, Baerends EJ (2004) J Chem Phys 121:655
100. Dreuw A, Head-Gordon M (2004) J Am Chem Soc 126:4007
101. Vosko SJ, Wilk L, Nusair M (1980) Can J Phys 58:1200
102. Iikura H, Tsuneda T, Yanai T, Hirao K (2001) J Chem Phys 115:3540
103. Chai JD, Head-Gordon M (2008) J Chem Phys 128:084106
104. Tawada T, Tsuneda T, Yanagisawa S, Yanai T, Hirao K (2004) J Chem Phys 120:8425
105. Rudberg E, Salek P, Helgaker T, Agren H (2005) J Chem Phys 123:184108
106. Cai ZL, Crossley MJ, Reimers JR, Kobayashi R, Amos RD (2006) J Phys Chem B 110:15624
107. Lange AW, Rohrdanz MA, Herbert JM (2008) J Phys Chem B 112:6304
108. Wiggins P, Gareth Williams JA, Tozer DJ (2009) J Chem Phys 131:091101

109. Plötner J, Tozer DJ, Dreuw A (2010) J Chem Theory Comput 6(8):2315
110. Guido CA, Mennucci B, Jacquemin D, Adamo C (2010) Phys Chem Chem Phys 12:8016
111. Charaf-Eddin A, Cauchy T, Felpin FX, Jacquemin D (2014) RSC Adv 4:55466
112. Wetzel C, Mishra A, Mena-Osteritz E, Liess A, Stolte M, Würthner F, Bäuerle P (2014) Org Lett 16(2):362. doi:10.1021/ol403153z. http://pubs.acs.org/doi/abs/10.1021/ol403153z
113. Lanthier E, Reber C, Carrington T Jr (2006) Chem Phys 329(1–3):90, Electron correlation and multimode dynamics in molecules (in honour of Lorenz S. Cederbaum)
114. Latouche C, Baiardi A, Barone V (2015) J Phys Chem B (in press)
115. Steffen A, Costuas K, Boucekkine A, Thibault MH, Beeby A, Batsanov AS, Charaf-Eddin A, Jacquemin D, Halet JF, Marder TB (2014) Inorg Chem 53(13):7055
116. Loudet A, Burgess K (2007) Chem Rev 107:4891
117. Ulrich G, Ziessel R, Harriman A (2008) Angew Chem Int Ed 47:1184
118. Nepomnyashchii AB, Bard AJ (2012) Acc Chem Res 45(11):1844
119. Chibani S, Laurent AD, Le Guennic B, Jacquemin D (2015) J Phys Chem A. PMID:25522826
120. Zakrzewska A, Zalesny R, Kolehmainen E, Osmialowski B, Jedrzejewska B, Agren H, Pietrzak M (2013) Dyes Pigm 99(3):957
121. Henary MM, Wu Y, Fahrni CJ (2004) Chem Eur J 10(12):3015
122. Wu Y, Peng X, Fan J, Gao S, Tian M, Zhao J, Sun S (2007) J Org Chem 72(1):62
123. Massue J, Ulrich G, Ziessel R (2013) Eur J Org Chem 2013(25):5701
124. Benelhadj K, Muzuzu W, Massue J, Retailleau P, Charaf-Eddin A, Laurent AD, Jacquemin D, Ulrich G, Ziessel R (2014) Chem Eur J 20:12843
125. Sobolewski AL, Domcke W (1999) Phys Chem Chem Phys 1:3065
126. Aquino AJA, Lischka H, Hattig C (2005) J Phys Chem A 109:3201
127. Aquino AJA, Plasser F, Barbatti M, Lischka H (2009) Croat Chem Acta 82:105
128. Barbatti M, Aquino AJA, Lischka H, Schriever C, Lochbrunner S, Riedle E (2009) Phys Chem Chem Phys 11:1406
129. Plasser F, Barbatti M, Aquino AJA, Lischka H (2009) J Phys Chem A 113(30):8490
130. Randino C, Ziolek M, Gelabert R, Organero JA, Gil M, Moreno M, Lluch JM, Douhal A (2011) Phys Chem Chem Phys 13:14960
131. Cui G, Lan Z, Thiel W (2012) J Am Chem Soc 134(3):1662
132. Xie L, Chen Y, Wu W, Guo H, Zhao J, Yu X (2012) Dyes Pigm 92(3):1361
133. Hayaki S, Kimura Y, Sato H (2013) J Phys Chem B 117(22):6759
134. Moreno M, Ortiz-Sanchez JM, Gelabert R, Lluch JM (2013) Phys Chem Chem Phys 15:20236
135. Padalkar VS, Ramasami P, Sekar N (2013) J Fluoresc 23(5):839
136. Phatangare KR, Gupta VD, Tathe AB, Padalkar VS, Patil VS, Ramasami P, Sekar N (2013) Tetrahedron 69(6):1767
137. Savarese M, Netti PA, Adamo C, Rega N, Ciofini I (2013) J Phys Chem B 117(50):16165
138. Savarese M, Netti PA, Rega N, Adamo C, Ciofini I (2014) Phys Chem Chem Phys 16:8661
139. Houari Y, Charaf-Eddin A, Laurent AD, Massue J, Ziessel R, Ulrich G, Jacquemin D (2014) Phys Chem Chem Phys 16:1319
140. Laurent AD, Houari Y, Carvalho PHPR, Neto BAD, Jacquemin D (2014) RSC Adv 4:14189
141. Hubin PO, Laurent AD, Vercauteren DP, Jacquemin D (2014) Phys Chem Chem Phys 16:25288
142. Wilbraham L, Savarese M, Rega N, Adamo C, Ciofini I (2015) J Phys Chem B 119:2459
143. Raucci U, Savarese M, Adamo C, Ciofini I, Rega N (2015) J Phys Chem B 119:2650
144. Houari Y, Chibani S, Jacquemin D, Laurent AD (2015) J Phys Chem B 119:2180
145. Riccardi D, Schaefer P, Yang Y, Yu H, Ghosh N, Prat-Resina X, Konig P, Li G, Xu D, Guo H, Elstner M, Cui Q (2006) J Phys Chem B 110(13):6458
146. Wanko M, Hoffmann M, Frähmcke J, Frauenheim T, Elstner M (2008) J Phys Chem B 112 (37):11468
147. Konig C, Neugebauer J (2011) Phys Chem Chem Phys 13:10475

148. Curutchet C, Kongsted J, Munoz-Losa A, Hossein-Nejad H, Scholes GD, Mennucci B (2011) J Am Chem Soc 133:3078
149. Jacquemin D, Perpète EA, Laurent AD, Assfeld X, Adamo C (2009) Phys Chem Chem Phys 11:1258
150. Garcia G, Ciofini I, Fernández-Gómez M, Adamo C (2013) J Phys Chem Lett 4(8):1239
151. Masiello DJ, Schatz GC (2010) J Chem Phys 132:064102
152. Morton SM, Jensen L (2010) J Chem Phys 133:074103
153. Sanchez-Gonzalez A, Corni S, Mennucci B (2011) J Phys Chem C 115(13):5450
154. Onida G, Reining L, Rubio A (2002) Rev Mod Phys 74:601
155. Tilocca A, Fois E (2009) J Phys Chem C 113(20):8683
156. Labat F, Le Bahers T, Ciofini I, Adamo C (2012) Acc Chem Res 45(8):1268
157. Presti D, Labat F, Pedone A, Frisch MJ, Hratchian HP, Ciofini I, Menziani MC, Adamo C (2014) J Chem Theory Comput 10:5577
158. Gassensmith JJ, Arunkumar E, Barr L, Baumes JM, DiVittorio KM, Johnson JR, Noll BC, Smith BD (2007) J Am Chem Soc 129:15054
159. Odobel F, Le Pleux L, Pellegrin Y, Blart E (2010) Acc Chem Res 43:1063
160. Lin HC, Jin BY (2010) Materials 3(8):4214
161. Planells M, Pelleja L, Clifford JN, Pastore M, De Angelis F, Lopez N, Marder SR, Palomares E (2011) Energy Environ Sci 4:1820
162. Zhao Y, Liang W (2012) Chem Soc Rev 41:1075
163. Le Bahers T, Pauporté T, Lainé PP, Labat F, Adamo C, Ciofini I (2013) J Phys Chem Lett 4 (6):1044
164. Kalyanasundaram K, Grätzel M (1998) Coord Chem Rev 177:347
165. Le Bahers T, Adamo C, Ciofini I (2011) J Chem Theory Comput 8:2498. Code available at Chimie Paristech, www.chimie-paristech.fr/labos/LECA/Research/site_msc/
166. Jacquemin D, Le Bahers T, Adamo C, Ciofini I (2012) Phys Chem Chem Phys 14:5383. Code available at Université de Nantes, http://www.sciences.univ-nantes.fr/CEISAM/erc/marches/ . Accessed 1 May 2014
167. Guido CA, Cortona P, Mennucci B, Adamo C (2013) J Chem Theory Comput 9(7):3118
168. Etienne T, Assfeld X, Monari A (2014) J Chem Theory Comput 10(9):3906
169. Ciofini I, Le Bahers T, Adamo C, Odobel F, Jacquemin D (2012) J Phys Chem C 116:11946, erratum: *ibidem* 14736–14736

Top Curr Chem (2016) 368: 377–414
DOI: 10.1007/128_2015_635

Published online: 1 July 2015

Absorption Spectroscopy, Emissive Properties, and Ultrafast Intersystem Crossing Processes in Transition Metal Complexes: TD-DFT and Spin-Orbit Coupling

Chantal Daniel

Abstract Absorption spectroscopy, emissive properties, and ultrafast intersystem crossing processes in transition metal complexes are discussed in the light of recent developments in time-dependent density functional theory (TD-DFT) , spin-orbit coupling (SOC) effects, and non-adiabatic excited states dynamics. Methodological highlights focus on spin-orbit and vibronic couplings and on the recent strategies available for simulating ultra-fast intersystem crossings (ISC).

The role of SOC in the absorption spectroscopy of third-row transition metal complexes is illustrated by two cases studies, namely Ir(III) phenyl pyridine and Re (I) carbonyl bipyridine complexes.

The problem of luminescence decay in third-row transition metal complexes handled by TD-DFT linear and quadratic response theories including SOC is exemplified by three studies: (1) the phosphorescence of Ir(III) complexes from the lowest triplet state; (2) the emissive properties of square planar Pt(II) complexes with bidentate and terdentate ligands characterized by low-lying metal-to-ligand-charge-transfer (MLCT) and metal-centered (MC) states; and (3) the ultra-fast luminescence decay of Re(I) carbonyl bipyridine halides via low-lying singlet and triplet charge transfer states delocalized over the bipyridine and the halide ligands.

Ultrafast ISC occurring in spin crossover $[Fe\ (bpy)_3]^{2+}$, in $[Ru\ (bpy)_3]^{2+}$, and $[Re\ (Br)(CO)_3(bpy]$ complexes are deciphered thanks to recent developments based on various approaches, namely non-radiative rate theory within the Condon approximation, non-adiabatic surface hopping molecular dynamics, and quantum wave packet dynamics propagation.

C. Daniel (✉)
Laboratoire de Chimie Quantique, Institut de Chimie UMR 7177 CNRS/Université de Strasbourg, 1 Rue Blaise Pascal BP 296/R8, F-67008 Strasbourg Cedex, France
e-mail: c.daniel@unistra.fr

Keywords Absorption/emission spectroscopies • Excited states dynamics • Intersystem crossings • Quantum chemistry • Spin-orbit coupling • Transition metal complexes • Vibronic coupling

Contents

Abbreviations

AMFI	Atomic mean field approximation
B3LYP	Becke-3-parameter-Lee-Yang-Parr
BO	Born–Oppenheimer
BP	Breit–Pauli
CASPT2	Complete active space perturbation theory second order
CASSCF	Complete active space self consistent field
COSMO	Conductor-like screening model
DK	Douglas Kroll
ECP	Effective core potential
FC	Franck Condon
GGA	Generalized gradient approximation
HF	Hartree–Fock
IL	Intra-ligand
ISC	Intersystem crossing
JT	Jahn–Teller
KS	Kohn–Sham
LC	Ligand-centered
LLCT	Ligand-to-ligand-charge-transfer
LVC	Linear vibronic coupling

MC	Metal-centered
MCQDPT	Multiconfiguration quasi-degenerate perturbation theory
MCTDH	Multiconfiguration time-dependent Hartree
MLCT	Metal-to-ligand-charge-transfer
MS-CASPT2	Multi-state CASPT2
PBE0	Perdew–Burke–Ernzerhof
PCM	Polarized continuum model
PES	Potential energy surfaces
PW91	Perdew–Wang 1991
RASSI	Restricted active space state interaction
SOC	Spin-orbit coupling
XANES	X-Ray absorption near-edge structure
ZFS	Zero field splitting
ZORA	Zeroth order regular approximation

1 Introduction

Triplet electronic excited states play a central role in the spectroscopy, photochemistry, and photophysics of transition metal complexes. They perturb the fine structure of absorption spectra and are responsible for long-lived emission via low-lying metal-to-ligand-charge-transfer (MLCT) states over a wide range of energy domains [1–12]. They can quench emission by triggering electron transfer processes via charge-separated (CS) states [13–15] or by inducing competitive dissociation via metal-centered (MC) states [16–20]. Triplet sigma-bond charge transfer states induce metal–alkyl bond homolysis [21, 22] sigma-bond sigma-bond excited states are precursors of metal–metal bond homolysis [23] whereas intra-ligand (IL) localized triplet states conduct isomerization pathways under visible irradiation [24–26].

The kinetics of intersystem crossing (ISC) processes entirely control the population of the low-lying triplet states after UV/visible absorption and strongly influence the branching ratio between radiative and non-radiative decays. The development of time-resolved spectroscopy, within femtosecond (fs)/picosecond (ps) time scales, has opened the route to new experimental investigations in the field of first-, second-, and third-row transition metal complexes photophysics supporting evidence of ultra-fast ISC [27–32]. In order to understand the role of the high spin states and to interpret these experimental findings, quantum chemistry needs powerful methods able to describe correctly the excited states properties: (1) electronic and geometrical structures; (2) transition energies; (3) spin-orbit interaction between states of different multiplicities; and (4) multiplet spin-orbit splitting. The electronic structure calculations should also figure out the shape of the potential energy surfaces (PES) underlying the non-adiabatic excited states dynamics. A direct correlation between the experimental data and the outcome of

theory, namely branching ratio, time scales, or luminescence quantum yields, needs simulation of the dynamics in real time. Obviously, whereas a complete quantum treatment is possible for small molecules involving 5 or 6 atoms [33, 34] other strategies have to be employed for large transition metal complexes with ~50–100 atoms and a metal center.

The purpose of this chapter is to review density functional theory (DFT)-based methods for computing with reasonable accuracy excited states properties, including spin-orbit coupling (SOC) in transition metal complexes, and to point to pioneering strategies to simulate ultra-fast ISC processes in this class of molecules. Whenever possible, the time-dependent DFT (TD-DFT) excited states properties are compared either to the results obtained by more accurate ab initio methods or to experimental data. The first section is devoted to methodological highlights oriented to the computation of SOC and its interplay with vibronic coupling, and to the simulation of ISC. The two next sections are dedicated to SOC effects on the absorption and emission spectroscopies exemplified by recent theoretical studies performed on third-row Ir(III), Re(I), and Pt(II) complexes. The last section reports on recent pioneering simulations of ultra-fast ISC processes in various complexes from first to third row on the basis of different approaches.

2 Methodological Highlights

Transition metal complexes cumulate most of the complexities inherent to theoretical studies: size, electronic delocalization, near-degeneracy, high density of electronic states of various characters, multi-configurational electronic structures, long-range charge transfer states, relativistic effects, especially spin-orbit coupling, dissociative states, states mixing, and vibronic couplings.

Recent reviews and articles give the reader an idea of the latest developments and applications related to excited states in large molecules and/or transition metal complexes [18, 19, 35–43].

In spite of well-known drawbacks, the long-range charge transfer problem being particularly pertinent in the case of transition metal complexes [35] (and references therein), the TD-DFT approach remains a computationally simple and efficient method. This approach, thanks to recent developments [44], can treat practical problems in a reasonable time scale at low cost as compared to highly correlated ab initio methods [45–54]. This section focuses on three issues, especially relevant for transition metal complexes excited states: (1) the spin-orbit coupling (SOC) problem; (2) the vibronic coupling problem; (3) the simulation of ISC processes.

2.1 Spin-Orbit Coupling

Molecules that contain heavy elements (in particular 5d transition metals) play an important role in the photochemistry and photophysics of coordination compounds with regard to their luminescent properties and their implication in catalysis and energy/electron transfer processes. Whereas molecular properties and electronic spectroscopy of light molecules can be studied in a non-relativistic quantum chemical framework, one has to consider the theory of relativity when dealing with elements that belong to the lower region of the periodic table. As far as transition metal complexes are concerned, one has to distinguish between different manifestations of relativity. Important but not directly observable manifestations of relativity are the mass velocity correction and the Darwin correction. These terms lead to the so-called *relativistic contraction* of the *s*- and *p*-shells and to the *relativistic expansion* of the *d*- and *f*-shells. A chemical consequence of this is, for instance, a destabilization of the 5d shells with respect to the 3d shells in transition metals.

Other important evidence of relativity in electronic spectroscopy, photophysics, and photochemistry is the spin-orbit coupling between states of different multiplicities. Indeed, most light-induced processes in transition metal complexes involve a change of spin state and are not allowed in non-relativistic quantum formalism. A fully relativistic treatment based on the Dirac equation [55] and a four-component Hamiltonian including scalar and spin-orbit contributions for many electrons systems is unrealistic and beyond the scope of the systems and problems of interest in this review. The reduction of the Dirac equation and its extension to many-electron problems has opened the route to several relativistic approaches based on approximate Hamiltonians applied with success to chemistry [56]. The spin-orbit coupling terms arise from one- and two-electron operators developed within the two-component formalism of the relativistic theory obtained by transformation of the four-component equation. The Douglas–Kroll (DK) [57, 58] and Breit–Pauli (BP) [59–62] forms are the most popular relativistic two-component operators.

In most of today's applications the SOC effects in large transition metal complexes are included by means of two approaches: (1) the restricted active space state interaction (RASSI) including SOC [63] developed on the basis of a one-electron Fock-type spin-orbit Hamiltonian [64] within the atomic mean field approximation (AMFI) [65]; and (2) the zeroth-order regular approximation (ZORA) to the full relativistic Hamiltonian based on a one effective two-component regular Hamiltonian developed at the zeroth-order [66–68]. Both methods are derived from the BP spin-orbit Hamiltonian and are a good approximation to the BP theory. Whereas RASSI-SOC formalism has been developed for correlated wave functions, the ZORA operator is better adapted to perturbation and Kohn–Sham (KS) theories. Most ZORA applications are performed within the framework of DFT despite some limitations [35, 69]. SOC has recently been evaluated by means of a full BP Hamiltonian applied to multi-reference CI wave functions or combined with

multiconfiguration quasi-degenerate perturbation theory (MCQDPT) and used with success for transition metal complexes [70, 71].

Whereas in nonrelativistic theory the eigenstates form a basis for an irreducible representation of the molecular point group, the eigenstates of the spin-orbit operator form a basis for an irreducible representation of the molecular point double group [72].

When introducing spin-orbit interaction, spin eigenfunctions are affected by symmetry operations and cannot be described in general by any of the symmetry operations permitted by the point group of the molecule. The extension of molecular point group to molecular point double group representation by additional symmetry elements associated with spin eigenfunctions allows the description of multiplet non-degenerate eigenstates, so-called fine structure, generated by spin-orbit splitting. For a discussion on the calculation of spin-orbit splitting in transition metal atoms at various levels of approximation, one can refer to [73, 74].

Two ingredients are particularly important when discussing transition metal complexes' optical properties, namely the SOC terms and the spin-orbit splitting of the triplet states. Whereas splitting is usually small and can appear as a perturbation, the SOC values may vary from a few tens of cm^{-1} to 1,000 cm^{-1}. However, the heavy atom effect is not always operating simply because of the molecular character of the electronic states that are delocalized over the ligands. This has important consequences on the absorption spectroscopy and photophysics of transition metal complexes as illustrated in recent applications [26, 75–83] and examples discussed in Sects. 3–5.

2.2 *Vibronic Couplings*

An additional difficulty in transition metal complexes is the simultaneous treatment of vibronic and spin-orbit couplings, sometimes together with Jahn–Teller (JT) effects. Indeed, the interplay between these effects contributes to the structural characteristics of the electronic spectra and cannot be neglected for a meaningful comparison between experimental and computed absorption spectra [84, 85]. Of course this is true for all kind of molecules but more crucial for transition metal complexes as shown by the vibronic structure of the well-resolved experimental spectrum of the permanganate anion MnO_4^- already available in the 1960s, but hardly assigned by the most accurate methods of quantum chemistry [86]. Another illustration is given by the combined effects of Jahn–Teller (JT) and SOC on the adiabatic PES and electronic spectra of a series of first-row transition metal halides MF_3 (M = Mn, Co, Ti, Cr, and Ni) recently investigated from first-principles methods based on the derivation of a Hamiltonian expanded up to linear, quadratic, and higher order in normal modes displacements active for JT distortions and including spin-orbits up to first order in these modes [87]. This original work has put in evidence spin-orbit-induced JT distortions not detectable by the standard

model in which SOC is considered as a static property independent of the nuclear motion.

Spin-orbit and vibronic couplings directly influence the probability of elementary processes such as internal conversions and ISC. The interpretation of ultrafast structural changes, time-resolved spectra, quantum yields, and time scales of elementary processes or transient lifetimes not only needs robust theoretical tools in quantum chemistry but developments in quantum dynamics for solving electronic and nuclear problems. Quantum dynamics has to treat dynamical processes which are not confined to a single electronic PES and which violate the Born–Oppenheimer (BO) separation of electronic and nuclear motions, taking into account nonadiabatic coupling between two or more electronic states via several vibrational modes [84].

In the applications discussed in the present contribution, running quantum nuclear dynamics by wavepacket propagation on a set of adiabatic potential energy hypersurfaces associated with excited states of different multiplicities coupled both vibronically and by SOC is out of reach. The alternative is to construct a spin-vibronic coupling model Hamiltonian based on selected relevant normal modes which includes the electronic states of interest at the early stage of the dynamical process, namely between 0 fs and 1 ps.

The Hamiltonian is expanded as a Taylor series in normal modes displacements:

$$\hat{H} = \hat{H}_0 + \hat{W}^{(0)} + \hat{W}^{(1)} + \hat{W}^{(2)} + \cdots \quad (1)$$

where the first term includes the kinetic energy operator and a harmonic term representing the ground state Hamiltonian and $\hat{W}^{(0)}$ is the zero-order diagonal coupling matrix which contains the vertical excited state energies calculated at the FC geometry. The first-order term $\hat{W}^{(1)}$ contains the linear coupling elements and the second-order non-adiabatic coupling term $\hat{W}^{(2)}$ is included to take into account the change of frequency in the electronic excited states. The truncation of the Taylor expansion has to be adapted to the problematic and to the size of the molecule.

The multi-state spin-vibronic interactions within a set of n electronic excited states are deduced from the diabatic electronic representation including all pertinent coupling terms. Explicitly, the intrastate κ^{n} and interstate $\lambda^{n,m}$ vibronic coupling constants between the n and m electronic states are derived from the gradient and Hessian of the potential energy with respect to the nuclear coordinates. The $\delta^{n,m}$ SOC and the necessary ingredients, potential energy and its derivatives, are extracted from the electronic structure data obtained by means of wave function or DFT approaches. Not all coupling elements survive to the integration because of group symmetry constraints. For instance, within the linear vibronic coupling (LVC) approximation the non-vanishing intrastate κ^{n} and interstate, $\lambda^{n,m}$ coupling constants are those for which the product of the irreducible representations of states n and m and of the nuclear normal mode coordinate Q_i contain the totally symmetric representation. Recent applications to vibronic spectra of first-row transition

metal trifluorides [88] and to ultra-fast excited states dynamics in Cu (I) phenanthroline complexes [89] illustrate the potential of the (spin)-vibronic coupling multimode quantum dynamics in this field of research.

2.3 Intersystem Crossings

Ultrafast intersystem crossing (ISC) processes coupled to nuclear relaxation and solvation dynamics play a central role in the photophysics and photochemistry of a wide range of transition metal complexes [27–32, 89–97]. These phenomena are investigated experimentally by ultrafast picosecond (ps) and femtosecond (fs) transient absorption or luminescence spectroscopies, and optical laser pump-X-ray probe techniques using ps and fs X-ray pulses. Again, we are facing the determination of multi-dimensional PES associated with various multiplet electronic excited states and with simultaneous treatment of vibronic and spin-orbit couplings which control ultrafast intramolecular relaxation and photophysical decays.

The qualitative rules such as El-Sayed [98] or energy gap law [99, 100] are of no help for the determination of the kinetics of ISC in this context. The golden rule approximation is adapted to organic systems with a limited number of interacting states, typically S_1/T_1 where the SOC is small compared to their adiabatic energy difference [56] (and references therein). Alternatively, ISC rates can be determined assuming direct spin-orbit coupling with separation of electronic and vibrational contributions within the Condon approximation based on harmonic potentials. In contrast to the time-independent approach which requires the computation of the Franck–Condon integrals, the recently developed time-dependent formalism [101, 102] is especially adapted to the treatment of ISC in large molecules with a high number of degrees of freedom and large adiabatic electronic energy differences. This is illustrated by recent applications, both in organic and inorganic systems [90, 103].

The determination of ultra-fast ISC kinetics by means of direct quantum dynamical simulation of a cascade of transitions via several electronic states of different multiplicities is based on wavepacket propagations on spin-vibronic coupled multi-dimensional PES. Various methods of electronic structure theory available for transition metal complexes, among them the most popular TD-DFT approach, are able to compute electronic excited states and associated nuclear forces with reasonable accuracy. The bottleneck is the computation of accurate multi-dimensional PES, seat of the ultra-fast dynamics observed in time-resolved experiments. To bypass these difficulties two strategies can be considered: (1) ab initio molecular dynamics where efficient electronic structure methods are coupled to classical trajectory-based approaches [104] (and reference therein); and (2) quantum dynamics where both electronic and nuclear wave functions are treated exactly within a given level of approximation [84, 105–107].

Molecular dynamics, usually coupled with DFT methods and extended recently to the non-adiabatic regime [104, 108, 109] is adapted to large systems involving a

restricted number of active electronic excited states in the dynamical process. The lack of coherence and phase of the nuclei and the total time per trajectory are the limiting factors of semi-classical trajectory surface hopping. The advantages are the inclusion of all nuclear degrees of freedom, the use of on-the-fly calculated potentials, and the ease of improving accuracy by including more trajectories.

The applicability of the full quantum approach is limited by the nuclear dimensionality and requires very robust electronic structure methods for excited states [70, 110]. The drawbacks of wavepacket dynamics are the complexity of setting up an appropriate effective Hamiltonian, the use of approximate fitted potentials, and the choice of selected vibrational modes.

The pioneering dynamical simulations performed on transition metal complexes are far from being routine and need specific developments to be applicable to a wide range of systems and ultra-fast phenomena circumscribed by spin-vibronic coupling [111]. Recent applications to first-, second-, and third-row transition metal complexes based on various approaches are developed in section 5 dedicated to ultra-fast ISC processes.

3 Absorption Spectroscopy

The purpose of the next sections devoted to the absorption spectroscopy of third-row transition metal complexes is to illustrate by recent examples the importance of SOC in the computation of TD-DFT vertical electronic spectra using ZORA approach. Whenever possible, the SOC-TD-DFT approach is compared to the SOC-CASSCF/MS-CASPT2 method based on RASSI. In these examples the electronic SOC effect is treated independent of any nuclear relaxation that could influence its contribution to the absorption spectra.

3.1 Electronic Spectroscopy of Ir(III) Complexes

In this application the absorption spectra of [Ir $(ppy)_3$] **1** and [Ir $(ppy)_2(CO)Cl$)] **2** (ppy = tris(2-phenylpyridine) (Scheme 1) have been calculated by means of TD-DFT methods based on optimized structures in vacuum and including spin-orbit coupling [80].

Both TD-DFT/B3LYP and TD-DFT/PW91 "spin-free" absorption spectra have been computed. The TD-DFT/B3LYP results shift the theoretical spectrum of [Ir $(ppy)_3$] **1** to the blue, as compared to the PW91 results, by 0.75 eV, with a first transition calculated at 25,080 cm^{-1} of significant oscillator strength ($f = 0.023$). Moreover, this overestimated transition is characterized by an important unrealistic ligand-to-ligand-charge-transfer (LLCT) character which is only minor in the TD-DFT/PW91.

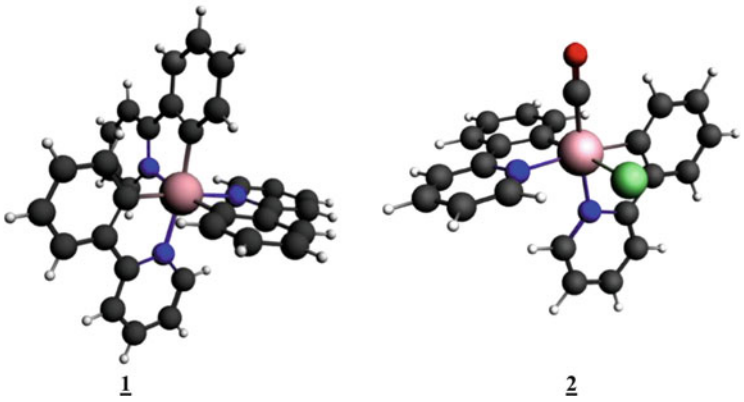

Scheme 1 Optimized structures of *fac*-[Ir (ppy)$_3$] **1** and *cis*-[Ir (ppy)$_2$(CO)(Cl)] **2** (data from [80])

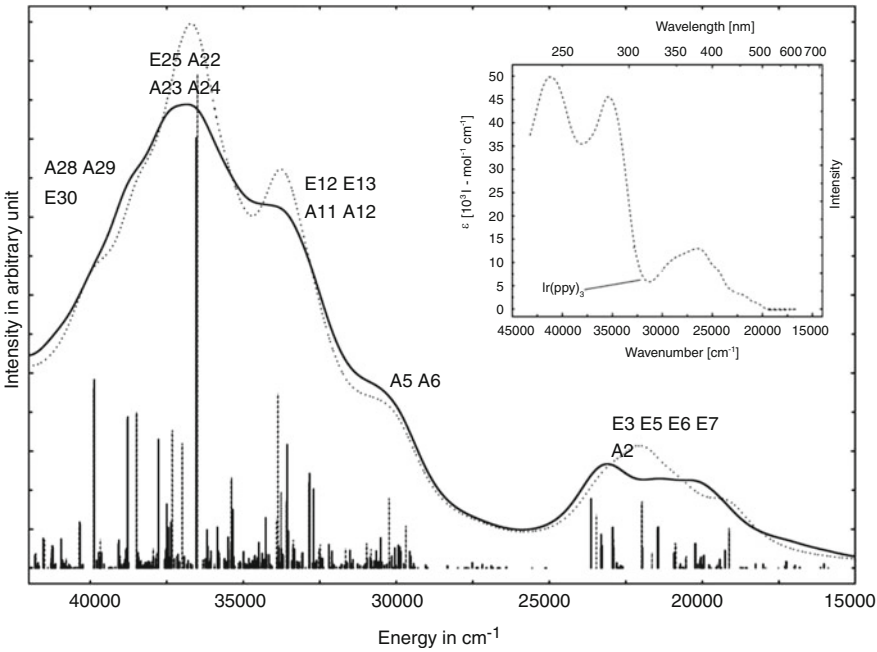

Fig. 1 TD-DFT/PW91 "spin-orbit" absorption spectrum of *fac*-[Ir (ppy)$_3$] **1** compared to the experimental one (in *inset*). The "spin-free" spectrum is represented by *dotted line* and the main bands are assigned according to the A$_n$ and E$_n$ "spin-orbit" states generated by the splitting of the lowest triplet states T$_n$ and their mixing with the singlet S$_n$ states (Table 2) (reprinted with permission from Brahim and Daniel [80] Copyright 2014 Elsevier)

Whereas spin-orbit effects modify the spectrum of the tri-substituted phenylpyridine reference complex **1** (Fig. 1), they do not change significantly the absorption properties of the carbonyl/halide substituted complex **2** which is not discussed in this contribution.

The experimental absorption spectrum of *fac*-[Ir (ppy)$_3$] **1** has been recorded in various media such as neat film, THF, toluene, and CH_2Cl_2 [112]. Whatever the medium, the absorption starts at about 17,500 cm^{-1} and is characterized by several shoulders at 20,410, 21,740, and 24,390 cm^{-1}, one peak at 26,315 cm^{-1}, a shoulder at 28,170 cm^{-1}, and two intense bands centered at 34,840 and 40,820 cm^{-1}, respectively. This insensitivity to the media as well as the small effect on the optimized geometry of *fac*-[Ir (ppy)$_3$] [80] justifies the neglect of solvent corrections in the theoretical approach.

The TD-DFT absorption spectrum of *fac*-[Ir (ppy)$_3$] **1** depicted in Fig. 1 has been assigned on the basis of the spin-orbit states and the emissive properties of the complexes have been interpreted from the singlet/triplet mixing and spin-orbit splitting of the lowest S_n singlet and T_n triplet states (Tables 1 and 2).

The theoretical absorption spectrum obtained in vacuum starts at about 17,360 cm^{-1} (Fig. 1) with states of low intensity not reported in Table 1 and is

Table 1 TD-DFT/PW91 "spin-free" states (in cm^{-1}) of *fac*-[Ir (ppy)$_3$] **1** and associated oscillator strengths (adapted from Brahim and Daniel [80])

State	Label	Character	Transition energy in cm^{-1}	Transition energy in eV	f[a]
^{1}A	S_2	MLCT	18,560	2.32	7×10^{-3}
^{1}E	S_5	MLCT	20,720	2.59	0.015
^{1}E	S_7	MLCT	21,760	2.72	0.041
^{3}E	T_5	MLCT	22,080	2.76	
^{1}E	S_8	MLCT	22,720	2.84	0.013
^{1}A	S_9	MLCT	23,280	2.91	0.033
^{3}E	T_7	LC	27,440	3.43	
^{3}E	T_{12}	LC/MLCT	29,920	3.74	
^{1}A	S_{12}	LC	30,000	3.75	0.042
^{1}A	S_{17}	LC	32,240	4.03	2×10^{-3}
^{1}A	S_{18}	LC/MLCT	32,560	4.07	0.05
^{1}E	S_{21}	LC/MLCT	33,280	4.16	0.040
^{1}A	S_{22}	MLCT	33,440	4.18	0.046
^{1}E	S_{23}	LC/MLCT	33,520	4.19	0.015
^{1}A	S_{24}	MLCT	33,600	4.20	0.106
^{1}E	S_{33}	MLCT	36,720	4.59	0.075
^{1}A	S_{34}	MLCT	37,040	4.63	0.083
^{1}A	S_{35}	MLCT	37,280	4.66	5×10^{-3}
^{3}A	T_{34}	LC/MLCT	37,360	4.67	
^{3}A	T_{36}	LC	37,520	4.69	
^{1}A	S_{36}	LC/MLCT	37,600	4.70	0.012
^{1}A	S_{44}	LC	39,520	4.94	0.109
^{3}E	T_{43}	MLCT	39,920	4.99	
^{1}E	S_{45}	LC	40,000	5.00	0.023

[a]Only the "spin-free" states of interest entering in the composition of the "spin-orbit" states described in Table 2 are reported

Table 2 TD-DFT/PW91 "spin-orbit" states (in cm^{-1}) of *fac*-[Ir $(ppy)_3$] and associated oscillator strengths ($f > 0.005$) (adapted from Brahim and Daniel [80])

State	Composition[a]	Transition energy in cm^{-1}	Transition energy in eV	f
E3	23% S_5 12% S_2 12% T_5	20,080	2.51	0.011
E5	54% S_5 22% S_7	21,280	2.66	0.017
E6	41% S_7 32% T_7	22,720	2.84	0.017
E7	68% S_8	23,120	2.89	0.014
A2	90% S_9	23,440	2.93	0.030
A5	25% S_{17} 20% T_{12} 17% S_{12}	29,680	3.71	0.010
A6	66% S_{17} 16% S_{12}	29,840	3.73	0.009
A11	38% S_{22} 13% S_{24} 10% T_{28}	32,400	4.05	0.030
A12	74% S_{18}	32,560	4.07	0.040
E12	27% S_{21} 8% S_{23}	33,280	4.16	0.015
E13	38% S_{24} 20% S_{22}	33,280	4.16	0.053
E25	25% S_{33} 12% T_{36}	37,040	4.63	0.019
A22	16% S_{36} 14% T_{34} 10% T_{36}	37,120	4.64	0.017
A23	18% T_{36} 15% S_{36} 11% S_{35}	37,200	4.65	0.027
A24	65% S_{34}	37,440	4.68	0.054
A28	73% S_{44}	39,520	4.94	0.080
E30	82% S_{45}	40,000	5.00	0.019
A29	31% T_{43} 10% S_{44}	40,640	5.08	0.012

[a]The label of the singlet (S_n) and triplet (T_n) states refer to Table 1

characterized by a series of low-lying MLCT states between 18,480 cm^{-1} (S_1) and 23,280 cm^{-1} (S_9). Above 30,000 cm^{-1} the ligand-centered LC state's contributions become more important with two intense peaks calculated at 33,600 cm^{-1} (S_{24}) and 39,520 cm^{-1} (S_{44}). These LC states and the peripheral transitions calculated above 33,360 cm^{-1} contribute to the two intense experimental UV bands centered at 34,840 and 40,820 cm^{-1}. Whereas the maximum observed at 34,840 cm^{-1} is well reproduced by the theoretical "spin-free" spectrum, the maximum at 40,820 cm^{-1} is red shifted by 0.5 eV by the calculation. Moreover, the theoretical maximum at 36,160 cm^{-1}, not observed in the experimental spectrum, corresponds to a metal-centered transition corresponding mainly to a $d_{Ir} \rightarrow 6$ s excitation with a diffuse Rydberg character. Knowing that TD-DFT is not the method of choice for describing the Rydberg excited states [113], this assignment has to be taken with care. The quality of the upper part of TD-DFT spectrum could certainly be improved by requesting more roots (actually 200).

The experimental and theoretical maxima of the first band observed between 20,000 and 25,000 cm^{-1} do not coincide exactly, the theoretical band being slightly shifted to the red. However, several MLCT states with rather large oscillator strengths are calculated in this region (Table 1). The accuracy of the calculations performed in vacuum does not allow further comparison. The data reported in Table 1 illustrate the high density of singlet and triplet excited states within

3.4 eV specific to this class of molecules representative of highly luminescent transition metal complexes.

From the results reported above for the reference molecule, namely the complex *fac*-[Ir (ppy)$_3$] **1**, we can conclude that the chosen computational strategy is reasonable, leading to realistic structural and spectroscopic properties. The quality of the PW91 based on generalized gradient approximation (GGA) functional must be pointed out for this class of compact nearly spherical molecules with bulky ligands. This surprisingly good agreement between the TD-DFT/PW91 absorption spectrum in vacuum and the experimental one could also be due of compensation of errors. Solvent corrections could induce red shift whatever the functional is, and could improve the TD-DFT/B3LYP spectrum as well [114]. However, the presence of LLCT states in the lowest part of the TD-DFT/B3LYP theoretical spectrum indicates a particular problem of charge transfer description in this class of molecules with the hybrid functional. This failure of the B3LYP functional for this class of molecules is not surprising and has already been observed for other Ir(III) complexes with phenylisoquinoline phenylpyridine ligands [81].

When taking into account SOC, the density of states does increase drastically by the splitting of the triplet states. The A and E "spin-orbit" states in C_3 point group reported in Table 2 are generated by the "spin-free" ^{1,3}A and ^{1,3}E states according to the zero-field splitting. Each ^{3}A state is split into A + E, each ^{3}E state into E + E + A. ^{1}A remains A and ^{1}E remains E in the so-called double group representation.

As already observed in other theoretical studies [75–79] the singlet/triplet mixing induces a decrease of the intensities and a red shift (1,600 cm^{-1}) of the visible part of the spectrum because triplet states gain weak oscillator strengths ($<10^{-3}$). Whereas a few states remain nearly pure singlet or triplet, most of the "spin-orbit" excited states reported in Table 2 present mixed character. Another consequence of the SOC effects on the absorption spectrum of *fac*-[Ir (ppy)$_3$] **1a** is an increase of the MLCT/LC mixing in the lowest part of the spectrum.

Whereas the "spin-orbit" states A and E calculated between 19,120 cm^{-1} and 21,760 cm^{-1} remain essentially MLCT, the ^{1}E (S_7, f = 0.041), for instance, gains 32% of LC contribution by coupling with the ^{3}E (T_7) leading to the E6 "spin-orbit" state calculated at 22,720 cm^{-1} of decreasing intensity ($f = 0.0017$). The visible band calculated between 17,000 and 25,000 cm^{-1} (Fig. 1) is enlarged and decreases in intensity compared to the one calculated in the "spin-free" spectrum. This band is composed essentially of MLCT states (E1–E7, A1, A2). Whereas the global energetics and the shape of the absorption spectrum of *fac*-[Ir (ppy)$_3$] **1** is only slightly modified by SOC effects, the character of the transitions is affected. The main consequence is an increase of mixed LC/MLCT character of the excited states above 30,000 cm^{-1}. The two intense LC peaks S_{24} ($f = 0.106$) and S_{44} ($f = 0.109$) (Table 1) decrease in intensity, either by coupling with MLCT states or by coupling with triplet states. The S_{44} state ($f = 0.109$) is not affected energetically, remains LC in character, but decreases in intensity by coupling with several triplet states, leading to the "spin-orbit" state A28 ($f = 0.080$).

From the SOC/TD-DFT theoretical study of the absorption spectra of the reference [Ir $(ppy)_3$] **1** and CO/Cl substituted [Ir $(ppy)_2(CO)(Cl)$] **2** complexes, several conclusions have been reached.

Whereas the spin-orbit effects are significant for [Ir $(ppy)_3$] **1**, they do not modify drastically the absorption spectrum of [Ir $(ppy)_2(CO)(Cl)$] **2**. The negligible spin-orbit effects, especially the minor splitting of the lowest T_1 state of mixed XLCT/MLCT character in the CO/Cl substituted complexes, is responsible for distinct emission properties which differ from those of the reference complex [Ir $(ppy)_3$] characterized by low-lying MLCT states.

This investigation of two molecules representative of Ir(III) phenyl pyridine complexes with specific emissive properties confirms the experimental trends and brings a detailed assignment of the absorption spectra including spin-orbit effects by adding new elements to the recent theoretical studies performed on the reference [$Ir(ppy)_3$] complex [115–119]. Introduction of spin-orbit interactions highlights the complexity of the absorption spectroscopy in third-row transition metal complexes and gives a new interpretation of the emissive properties in this class of molecules. This last point is emphasized in Sect. 4 dedicated to emission spectroscopy.

3.2 *Electronic Spectroscopy of Re(I) Complexes*

In this joined experimental/theoretical study, the lowest lying spectral transitions in [$ReX(CO)_3(bpy)$] (X = Cl, Br, I; bpy = 2,2′-bipyridine) complexes (Scheme 2) were calculated by means of SOC-TD-DFT in solvent and SOC multi-state complete active space second order perturbation theory SOC-MS-CASPT2 in vacuum, and compared with absorption spectra measured in different solvents [79].

This study is part of a more ambitious theoretical project dedicated to the understanding and simulation of ultra-fast electronic-vibrational relaxation dynamics that characterizes these complexes upon excitation at 400 nm [120–122].

Whereas both spin-free and spin-orbit quantum chemical calculations (MS-CASPT2, TD-DFT) simulate UV–vis electronic spectra of [$Re(X)(CO)_3(bpy)$] complexes (Fig. 2) in reasonable agreement with experiment

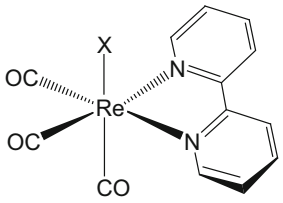

Scheme 2 Schematic representation of the complexes [$ReX(CO)_3(bpy)$] (X = Cl, Br, I; bpy = 2,2′-bipyridine)

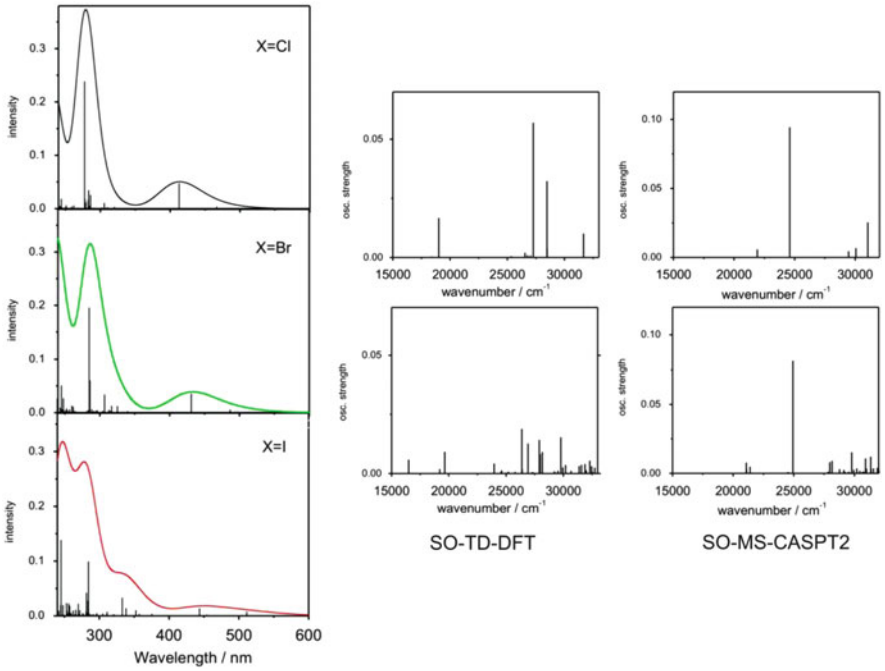

Fig. 2 "Spin-orbit" TD-DFT/PBE0/COSMO-CH_2Cl_2 absorption spectra of [Re(X)$(CO)_3$(bpy)] (X = Cl, Br, I] (*left*) and comparison between "spin-free" (*right*, *top*) and "spin-orbit" (*right*, *bottom*) TD-DFT and MS-CASPT2 transitions of [Re(I)$(CO)_3$(bpy)] (reprinted with permission from Heydova et al. [79] Copyright 2012 American Chemical Society)

(Fig. 3), they give a very different interpretation of the absorption bands and only the SO treatment can account for all the observed spectral features, namely the low-energy shoulders.

SO-TD-DFT transitions are spread over a broader energy range and have more similar relative intensities than the SO-MS-CASPT2 ones. The SO-TD-DFT theoretical spectrum thus accounts better for the large widths and shoulders observed experimentally. The SO-MS-CASPT2 and solvent corrected SO-TD-DFT transition energies calculated for the lowest states of [Re(I)$(CO)_3$(bpy)] are reported in Table 3. In contrast to the experiment, SO-MS-CASPT2 predicts an increase of the lowest absorption band intensity on going from Cl to Br and I, with increasing oscillator strengths of the strongest contributing transition in the order Cl ($f = 0.038$) < Br (0.068) < I (0.082). On the other hand, SO-TD-DFT predicts decreasing molar absorptivity of the lowest band Cl ($f = 0.047$) > Br (0.036) > I (0.013), in qualitative agreement with the experimental trend (Fig. 3). This difference between the two computational techniques is probably caused by a limited active space, smaller MLCT-XLCT delocalization, and the neglect of solvent effects in SO-MS-CASPT2.

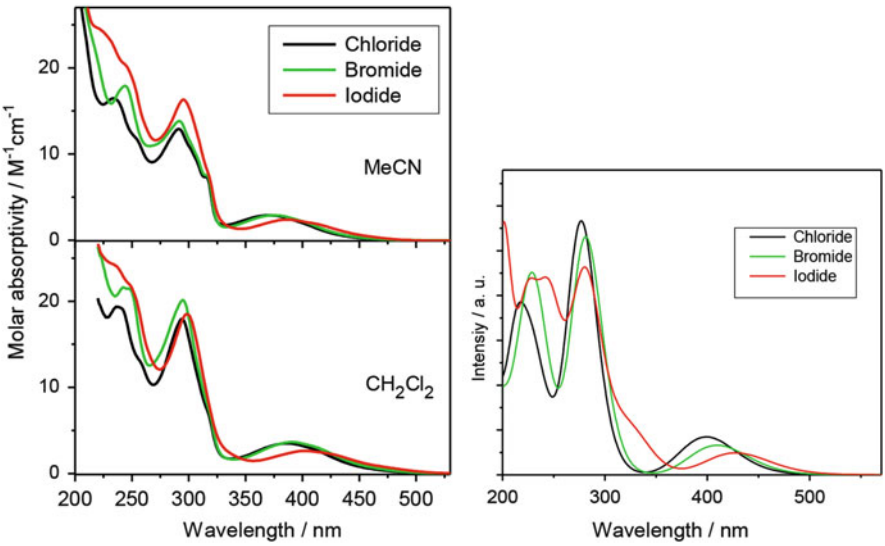

Fig. 3 Comparison between experimental UV–vis spectra in different solvents (*left*) and "spin-free" TD-DFT/PBE0/COSMO-CH_2Cl_2 absorption spectra (*right*) of [$ReX(CO)_3(bpy)$] (X = Cl, Br, I) (reprinted with permission from Heydova et al. [79] Copyright 2012 American Chemical Society)

Within the TD-DFT spin-free model, the lowest absorption band originates from a single strong transition and two satellites occurring at higher and lower energy, respectively. The spin-orbit analysis interprets the lowest band as resulting from a whole series of weaker transitions and assigns the two lowest lying shoulders as transitions to spin-mixed states. Notably, even the strongest transition contributing to the lowest band possesses only partial singlet character which decreases in the order Cl (88%) > Br(81%) >> I(58%) at the SO-TD-DFT level (Table 3).

A correlation diagram between "spin-free" and "spin-orbit" states of [ReI $(CO)_3(bpy)$] is shown in Fig. 4. Left and right columns show "spin-free" singlet and triplet states, respectively, and the SO states are presented in the middle, with dashed lines indicating the principal contributions. Figure 4 illustrates the spin-orbit interactions of "spin free" singlet and triplet states in the formation of two sets of "spin orbit" states. Transition to the fourth and sixth "spin orbit" excited states cA′ and dA′ have an oscillator strength of 0.0061 and 0.0018, respectively, explaining the occurrence and relative intensities of the two low-energy bands in the experimental spectrum of [$ReI(CO)_3(bpy)$] and the presence of shoulders for the other two complexes. These features cannot be accounted for by the "spin-free" calculations, where the lowest transitions to $^{1,3}A''$ and $^{3}A'$ states are forbidden.

Including SOC explicitly not only improves the quantitative correspondence with the experimental spectra but also provides a physically more correct insight into the nature of the excited-states involved and their deactivation pathways.

Table 3 "Spin orbit" MS-CASPT2 and solvent corrected (CH_2Cl_2) SO-TD-DFT transition energies to the lowest excited states of [Re(I)$(CO)_3$(bpy)], associated wavelengths, in nm and oscillator strengths *f*

SO state	Composition of the SO-states in terms of spin-free states	Transition energies in cm^{-1}	Wavelength in nm	*f*
MS-CASPT2				
2A′	a^3A'' (87%) + b^1A' (9%)	21,085	474	0.0078
1A″	a^3A'' (86%) + a^3A' (12%)	21,100	474	
3A′	a^3A'' (87%) + a^3A' (9%)	21,110	474	0.0031
2A″	a^1A'' (84%) + a^3A' (14%)	21,400	467	0.0048
3A″	a^3A' (86%) + a^3A'' (9%)	24,460	409	0.0002
4A′	a^3A' (86%) + a^3A'' (12%)	24,500	408	0.0009
4A″	a^3A' (85%) + a^1A'' (11%)	24,570	407	0.0008
5A′	b^1A' (86%) + a^3A'' (12%)	24,930	401	0.082
6A′	b^3A'' (90%) + c^3A' (7%)	27,800	360	0.0001
5A″	b^3A'' (90%) + c^3A' (8%)	27,800	360	
7A′	b^3A'' (93%)	27,825	359	0.0011
TD-DFT				
1A″	a^3A'' (51%) + a^3A' (47%)	19,160	522	
2A′	a^3A'' (52%) + a^3A' (47%)	19,170	521	0.0001
2A″	a^3A' (55%) + a^1A''(44%)	19,410	515	0.0003
3A′	a^3A'' (65%) + a^1A' (31%)	19,560	511	0.0073
3A″	a^3A' (48%) + a^3A'' (44%)	21,920	456	
4A′	a^3A' (47%) + a^3A'' (45%)	22,010	454	0.0019
4A″	a^1A'' (51%) + a^3A' (44%)	22,200	450	0.0003
5A′	b^1A' (58%) + a^3A''(30%)	22,535	444	0.013
5A″	b^3A' (84%)	24,960	400	
6A′	b^3A'' (84%)	24,970	400	
7A′	b^3A'' (94%)	25,120	398	0.0015
6A″	b^3A'' (49%)	26,040	384	0.0001
7A″	b^3A'' (95%)	26,205	382	
8A′	b^3A' (30%) + c^1A' (26%) + c^3A' (14%)	26,320	380	0.0006
9A′	c^3A' (40%) + b^3A' (36%) + d^1A' (6%)	26,630	375	0.0036

Only the contributions of the "spin-free" states ≥5% are given (the "spin-free" and "spin orbit" electronic ground state are labeled a^1A' and 1A′, respectively) (adapted with permission from Heydova et al. [79] Copyright 2012 American Chemical Society)

Similar SOC effects have been put in evidence on the electronic spectroscopy of [Re(imidazole)$(CO)_3$(phen)]$^+$ [76] for which correlation diagrams between "spin-free" and "spin-orbit" states become very complicated as illustrated in Fig. 5.

The lowest parts of the two correlation diagrams (Fig. 5) are qualitatively similar with little differences because of solvent corrections not being included in the MS-CASPT2 calculations. The lowest MLCT states (a^3A'', a^3A', b^3A'') remain predominantly triplets but contribute to the "spin-orbit" spectrum by admixture of singlets.

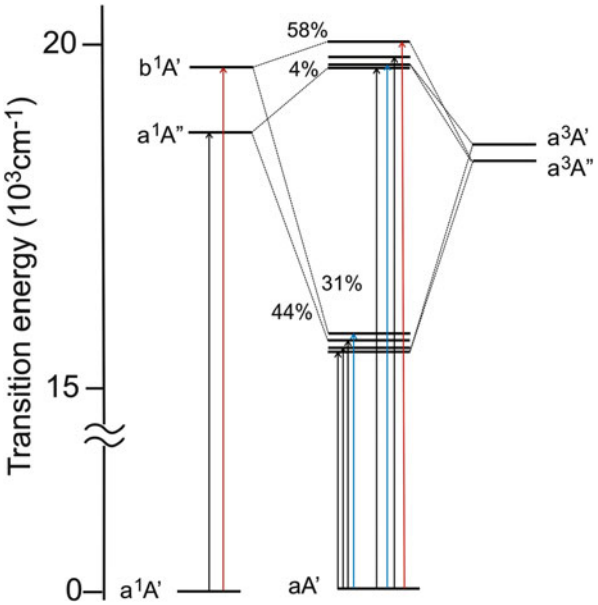

Fig. 4 Correlation of SO-TD-DFT/PBE0 lowest singlet (*left*) and triplet (*right*) "spin-free" states with "spin-orbit" states (*middle*) of $[Re(I)(CO)_3(bpy)]$ in solvent. *Red*, *blue*, and *black arrows* indicate transitions with oscillator strengths larger than 0.01, 0.001–0.01, and 0.0005–0.001, respectively (reprinted with permission from Heydova et al. [79]. Copyright 2012 American Chemical Society)

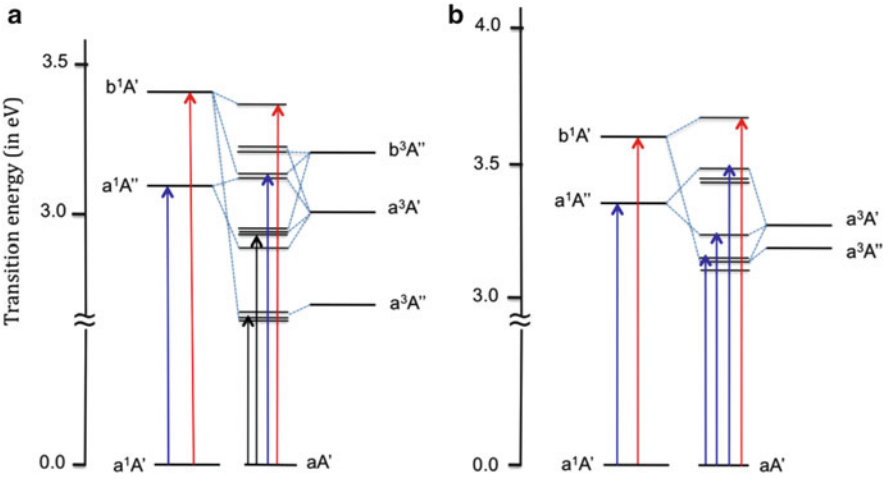

Fig. 5 Correlation of (**a**) SO-MS-CASPT2 and (**b**) SO-TD-DFT between singlet (*left*) and triplet (*right*) "spin-free" states and "spin-orbit" states (*middle*) of $[Re(imidazole)(CO)_3(phen)]^+$. *Red*, *blue*, and *black arrows* indicate transitions with oscillator strengths larger than 0.01, 0.001–0.01, and 0.0005–0.001, respectively (adapted from Bakova et al. [76])

4 Emission Spectroscopy

This chapter is dedicated to the emissive properties of third-row transition metal complexes determined on the basis of optimized structures of the low-lying singlet and triplet states. Whereas the $S_0 \rightarrow S_n$ electronic absorption spectra are easily obtained by means of TD-DFT with or without solvent corrections, the emissive properties originating from S_n, $T_n \rightarrow S_0$ transitions have been difficult to analyze until now because the determination of the degree of mixing between the singlet and triplet states by SOC and the systematic search for nuclear distortions in several close-lying excited states is still a challenge for computational chemistry. We may distinguish between two categories of complexes, the first represented by Ir(III) complexes seats of long-lived luminescence, most of the time attributed to the lowest triplet T_1 state. The second class of molecules represented by Re (I) complexes is characterized by shorter lived signals following a cascade of ultra-fast luminescence processes attributed to S_n as well as T_n states. Obviously all in-between luminescent behaviors may occur in transition metal complexes. The Pt(II) square planar complexes are a pertinent example. The purpose of this section is to present three case studies illustrating the contribution of TD-DFT and linear and quadratic response theories including SOC to the problematic of luminescent processes in third-row transition metal complexes.

4.1 Phosphorescence of Ir(III) Complexes

The dipole moment of $T_1 \rightarrow S_0$ spin-forbidden phosphorescent transition in Ir(III) complexes with large π-conjugated ligands may acquire some non-negligible strength by means of strong SOC. In a series of theoretical studies based on TD-DFT and using linear and quadratic response theory, Minaev et al. [42, 81, 123] investigated the SOC effects and radiative lifetimes to elucidate and compare the mechanism of phosphorescence in *fac*-[Ir(ppy$_3$)] (Scheme 1, **1**) and *fac*-[Ir(piq)$_x$(ppy)$_{3-x}$] (ppy = 2-phenlypyridine; piq = 1-phenylisoquinoline; $n = 3,4$) complexes **3**, **4**, and **5** (Scheme 3).

In this study a semi-empirical effective single electron SOC operator [73, 74] combined with effective core potentials (ECP) is used, whereas the τ_k phosphorescence lifetime from the three spin-orbit sub-levels of T_1, $|T_1^k\rangle$ ($k = 1,2,3$) is calculated from

$$\frac{1}{\tau_k} = \frac{4}{3t_0}\alpha_0^3\left(\Delta E^k\right)^3 \sum_{\alpha\in\{x,y,z\}} \left|M_\alpha^k\right|^2, \tag{2}$$

where $t_0 = (4\pi\varepsilon_0)^2\hbar^3/m_e e^4$, α_0 is the fine-structure constant, ΔE^k is the transition energy from S_0 to $|T_1^k\rangle$, and M_α^k is the α-axis projection of the electric dipole

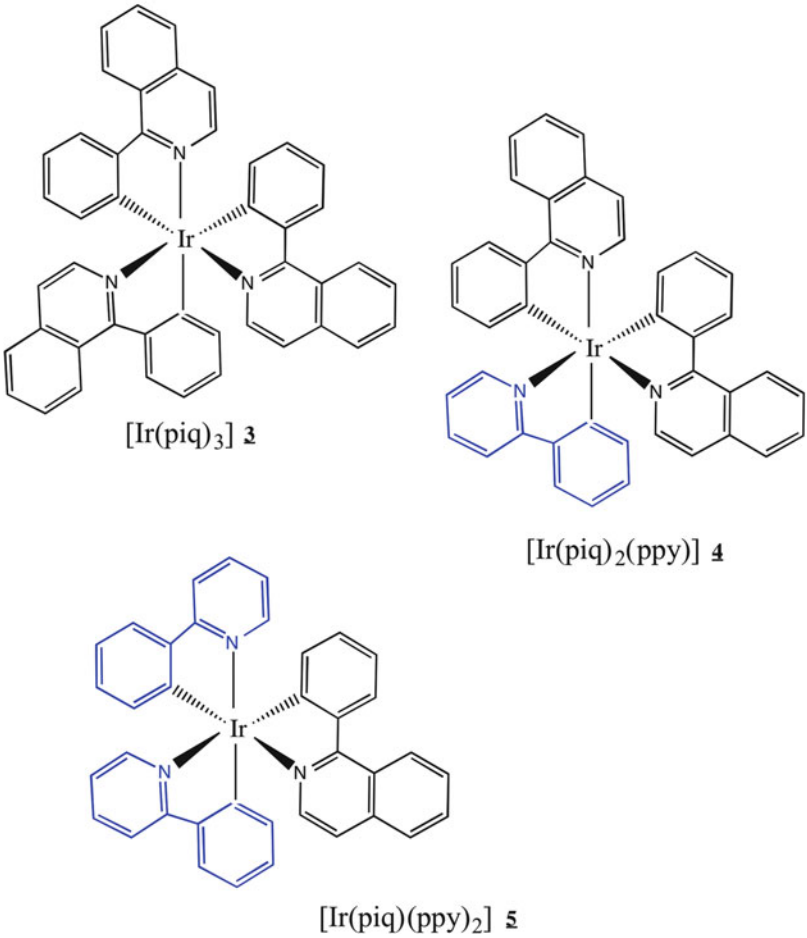

Scheme 3 Structure of the [Ir $(piq)_x(ppy)_{3-x}$] complexes

moment between the ground state and the k-spin sub-levels of the triplet T_1. Both the S_0 electronic ground state and triplet T_1 states were fully optimized at the DFT/B3LYP level.

In the pioneering study performed on the reference complex [Ir $(ppy)_3$], and the piq-substituted complexes depicted in Scheme 3, neither solvent nor vibronic coupling effects have been included. The electric dipole moments associated with the transitions between T_1 and the ten lowest T_n triplets and between S_0 and the ten lowest S_n singlets, as well as SOC matrix elements between T_1, S_0, and the ten lowest S_n singlet states have been computed [123].

From this detailed investigation it has been shown that at vertical $S_0 \rightarrow T_1$ transition the T_1 state is highly delocalized over the three ligands with a mixed LC/MLCT character. When relaxed to its minimum potential energy, T_1 becomes

Table 4 ZFS sub-levels (in cm^{-1}) of T_1 state of [Ir $(ppy)_3$] at the DFT/B3LYP/6-311G*/SDD level (reprinted with permission Jansson et al. [123] Copyright 2007 Elsevier)

T_1 spin-orbit sub-levels	S_0-geom	T_1-geom
T_1^z	19,989.06	16,609.87
T_1^y	20,021.79	16,663.47
T_1^x	20,092.98	16,678.48

localized on a single ligand. The zero-field splitting (ZFS) spin sub-levels and their spontaneous emission characteristics have been obtained at some intermediate geometry between S_0 and T_1 structures because of the anharmonicity of the potential associated with T_1. The large SOC between T_1 and the S_5 singlet MLCT state together with large dipole interactions between S_5 and S_0 are responsible for the intense phosphorescence of the reference complex [Ir $(ppy)_3$]. The ZFS sub-levels of T_1 calculated at S_0 and T_1 geometries are reported in Table 4

The values reported in Table 4 and the lowest position of the T_1^z sub-level, as well as the calculated lifetimes originated from these spin-orbit sub-levels agree rather well with the data obtained by temperature-dependent refined spectroscopic experiments [124]. Moreover, the theoretical model, despite the neglect of vibronic coupling effects, recovers the overall phosphorescence experimental lifetime of ~2 μs in the high temperature limit as soon as the S_0 geometry is chosen in the phosphorescence rate calculation.

On the basis of the same computational strategy, the photophysical properties of [Ir $(piq(ppy)_2$] **5**, [Ir $(piq)_2(ppy)$] **4**, and [Ir$(piq)_3$] **3** have been elucidated and successfully compared to the accurate experimental data available for this class of molecules [81]. It has been shown that increasing the number of piq ligands shifts the emission maximum to the red by about 10 nm and enhances radiative rate constants by 60% within the range of the experimental trends. Interestingly, the SOC strength and the radiative rate constant are diminished by the presence of fluorine atoms in [Ir$(F_n ppy)_3$] complexes [42] resulting from the inverse heavy-atom effect also observed in the [Re $(X)(CO)_3(bpy)$] complexes discussed in Heydova et al. [79], Cannizzo et al. [120], and Gourlaouen et al. [121].

4.2 Emissive Properties of Square Planar Pt(II) Complexes

A recent systematic study of the optical properties of a series of five Pt(II) planar complexes with bidentate ligands, namely [Pt $(bpy)Cl_2$] (bpy = 2,2′-bipyridine) **6** and [Pt $(ppy)Cl_2]^-$ (ppy = 2-phenylpyridine) **7** and terdentate ligands, namely [Pt $(tpy)Cl]^+$ (tpy = 2,2′:6′,2″-terpyridine) **8**, [Pt (phbpyR)Cl] (phbpy = 6-phenyl-2,2′-bipyridine; R = H) **9**, and [Pt (dpybR)Cl] (dpyb = 2,6-di(2-pyridyl)benzene; R = CH_3) **10** (Scheme 4) by means of TD-DFT including solvent correction has allowed us to rationalize the puzzling emissive behavior of this class of molecules [75].

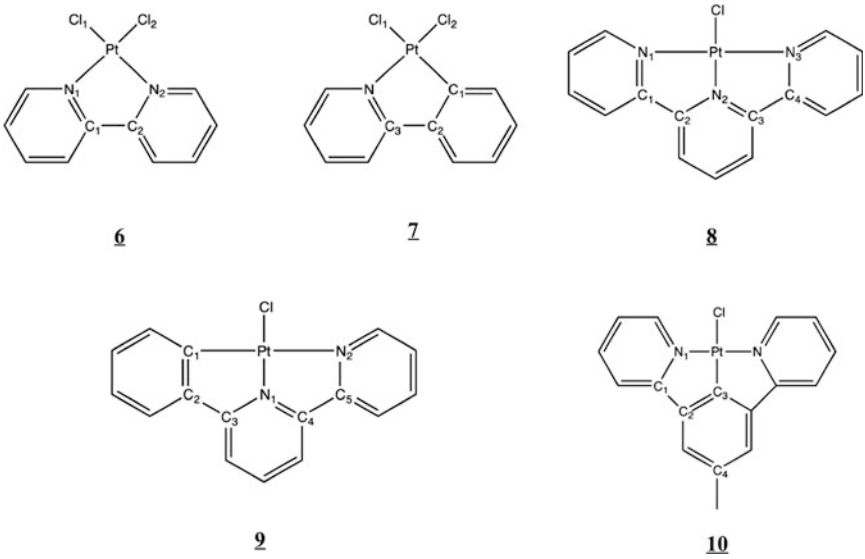

Scheme 4 Structures of [Pt (bpy)Cl_2] **6**, [Pt (ppy)Cl_2]$^-$ **7**, [Pt (tpy)Cl]$^+$ **8**, [Pt (phbpyR)Cl] **9**, and [Pt (dpybR)Cl] **10**

In this example, SOC has been included only for the computation of the absorption spectra and has been neglected for the determination of the emission wavelengths reported in Table 5. The nearly pure triplet character of the "spin-orbit" states and the negligible singlet/triplet mixing in these molecules justify this choice [75].

On the basis of fully optimized structures and energetics, we have shown that the structures remain nearly planar in the low-lying singlet and triplet excited states of charge transfer character, namely MLCT and XLCT, whereas a significant distortion corresponding to the out-of-plane-bending of the Pt–Cl bond characterizes the geometry of the metal-centered (MC) states. The presence of these strongly distorted non-radiative MC states minima, situated well below the charge transfer states minima ($\Delta E = -0.3$ to -0.8 eV) and easily accessible upon irradiation in the visible, explains the poor luminescence of the bipyridine and terpyridine non-cyclometalated complexes **6** and **8** at room temperature.

In contrast, the minima of the emissive states of mixed MLCT/XLCT/LC character are efficiently populated in **7**, **9**, and **10**, especially in the terdentate complexes. The luminescence of complex **10**, cyclometalated in axial position, is particularly efficient because the minimum of the lowest emissive state is well separated from those of the MC states ($\Delta E = +0.23$ eV) in contrast to its analog, complex **9**, cyclometalated in lateral position where the emissive MLCT/LC state minimum is nearly degenerate with the lowest MC state minimum ($\Delta = +0.01$ eV). Whereas SOC correction probably overstabilizes the MC states with respect to the charge transfer states, it should not overturn the relative order of the minima

Table 5 TD-DFT/B3LYP vertical $T_n \rightarrow S_0$ transition energies (in eV) and corresponding emission wavelengths (in nm) of complexes **6** to **10** depicted in Scheme 4 (adapted with permission from Gourlaouen and Daniel [75] Copyright 2014 Royal Society of Chemistry)

	State	Vertical $T_n \rightarrow S_0$ transition energy (eV)	Emission wavelength (nm)
[Pt (bpy)Cl_2] **6**	T_1 MC	−0.36	–
	T_2 MC/XLCT	0.92	1,355
[Pt (tpy)Cl]$^+$ **8**	T_1 MC	0.41	3,012
	T_2 MLCT/LC	1.92	645
[Pt (ppy)Cl_2]$^-$ **7**	T_1 MLCT/XLCT/LC	2.34	530
	T_2 MC/LC	2.28	544
	T_3 MC	2.33	531
	T_4 MC/LMCT/MLCT	2.41	515
[Pt (phbpyH)Cl] **9**	T_1 MLCT/LC	2.02	613
	T_2 MC	0.43	2,852
	S_1 MLCT/LC	2.35	527
	T_3 MLCT/XLCT/LC	2.71	458
[Pt (dpybR)Cl] **10** (R = CH_3)	T_1 MLCT/LC/XLCT	2.42	513
	T_2 MLCT/LC/XLCT	2.48	500
	T_3 MC	0.98	1,271
	T_4 MC	1.47	846

reported in Table 5. Indeed, when calculating the triplet spin-orbit sub-levels by applying SOC correction at their optimized geometries the stabilization of the minima never exceeds 0.1 eV as illustrated by the results obtained for Re(I) carbonyl α-diimine complexes discussed in the next section.

The presence of MC states situated well above the MLCT/XLCT/LC emissive states, needing strong structural stabilizing out-of-plane deformation for being populated, ensures the effectiveness of luminescence in this class of Pt (II) molecules. This study has shown that the usual oversimplified picture of a single T_1 triplet state for explaining luminescent properties of the Pt(II) square planar complexes is far from realistic.

4.3 Luminescence of Re(I) Complexes

In the following example, emissive properties of [ReX$(CO)_3$(bpy)] (X = Cl, Br, I; bpy = 2,2′-bipyridine) complexes (Scheme 2) have been interpreted on the basis of TD-DFT $T_n \rightarrow S_0$ transition energies calculated at the fully optimized geometries of the six low-lying singlet and triplet excited states and corrected by SOC (Table 6) [121].

The "spin-free" and "spin-orbit" excited states reported in Table 6 are of mixed either MLCT/XLCT (X = Cl and Br; complexes **11** and **12**) or XLCT/MLCT (X = I; complex **13**) character and potentially emissive after absorption at

Table 6 SOC-TD-DFT vertical S_n, $T_n \rightarrow S_0$ transition energies (in eV) and corresponding emission wavelengths (in nm) of the lowest relaxed singlet and triplet states of [Re(Cl)$(CO)_3$(bpy)] **11**, [Re(Br)$(CO)_3$(bpy)] **12**, and [Re(I)$(CO)_3$(bpy)] **13** calculated in CH_3CN (adapted from Gourlaouen et al. [121])

State	Vertical S_n, $T_n \rightarrow S_0$ transition energy (in eV)	Emission wavelength (in nm) with SOC
X = Cl **11**		
a^3A''	2.048	610 (A″)
	2.049	610 (A′)
	2.060	607 (A′)
a^3A'	2.171	575 (A″)
	2.172	576 (A′)
	2.191	570 (A″)
a^1A''	2.173	575 (A″)
b^1A'	2.521	496 (A′)
b^3A''	2.593	482 (A′)
	2.648	472 (A″)
	2.681	466 (A″)
X = Br[a] **12**		
T_1 a^3A''	2.054	609 (A″)
	2.055	608 (A′)
	2.069	604 (A′)
T_2 a^3A'	2.130	587 (A″)
	2.130	587 (A′)
	2.145	583 (A″)
S_1 a^1A''	2.169	576 (A″)
S_2 b^1A'	2.475	505 (A′)
T_3 b^3A''	2.565	487 (A′)
	2.675	467 (A″)
	2.675	467 (A′)
X = I **13**		
a^3A''	2.017	620 (A″)
	2.018	619 (A′)
	2.043	612 (A′)
a^3A'	2.016	620 (A″)
	2.017	620 (A′)
	2.027	617 (A″)
a^1A''	2.102	595 (A″)
b^1A'	2.164	577 (A′)
b^3A''	2.443	512 (A′)
	2.589	483 (A′)
	2.609	479 (A″)

[a]The labels S_n and T_n are used in Sect. 5.3 dedicated to the ultra-fast luminescence decay of [Re (Br)$(CO)_3$bpy]

400 nm. We may notice a very small spin-orbit splitting of the triplets. The structural deformations when going from the electronic ground state to the relaxed low-lying excited states are quite small. After nuclear relaxation into the potential wells of the excited states, the Re–X shortening does not exceed 0.097 Å in the singlet states and 0.043 Å in the triplet states. This deformation is accompanied by an elongation of the Re–C_{ax} bonds (<3%) together with a minor shortening of the Re–N bonds in all excited states.

According to the calculations, the luminescence should start from the b^1A' state calculated at 505 nm (or 496 nm with SOC) and 522 nm (or 505 nm with SOC) for the chloride **11** and bromide **12** complexes, respectively. These values lead to theoretical Stokes shifts of 5,640 (5,200) cm^{-1} and 5,880 (5,640) cm^{-1}, respectively, in agreement with the experimental data (~6,000 cm^{-1}). Accordingly, the two complexes behave similarly and the small calculated red shift is also observed on the experimental luminescence spectra when going from Cl to Br [120].

The emission wavelengths reported in Table 6 correlate nicely with the three domains of luminescence detected by ultra-fast resolved spectroscopy [120], namely in the ranges 500–550, 550–600, and 600–620 nm for the three molecules. It is noteworthy that both b^3A'' and b^1A' states participate in the early short-lived emission whereas both a^1A'' and a^3A' contribute to the intermediate band. The only purely phosphorescent process is the long-lived emission generated by a^3A'' in the chloride and bromide complexes and by both a^3A' and a^3A'' in the iodide complex, these states keeping a nearly pure triplet character.

5 Ultra-Fast Intersystem Crossings

This chapter is devoted to the simulation of ultra-fast ISC processes in first-, second- and third-row transition metal complexes by means of various approaches, namely the time-dependent formalism within the Condon approximation, the non-adiabatic surface-hopping semi-classical method, and the quantum wavepacket dynamics propagation.

5.1 Excited States Dynamics in Spin Crossover Fe $(bpy)_3]^{2+}$ Complex

A recent promising approach, applied to the spin crossover complex $[Fe(bpy)_3]^{2+}$ [90] has been developed by C. M. Marian et al. [101, 102]. This method is based on time-dependent calculations of ISC rates in the multi-mode harmonic oscillator and Condon approximations and beyond, where the electronic spin-orbit matrix elements depend linearly on the nuclear coordinates within a spin-vibronic coupling scheme. The ISC rate can be decomposed into three contributions, namely direct, mixed direct vibronic, and vibronic.

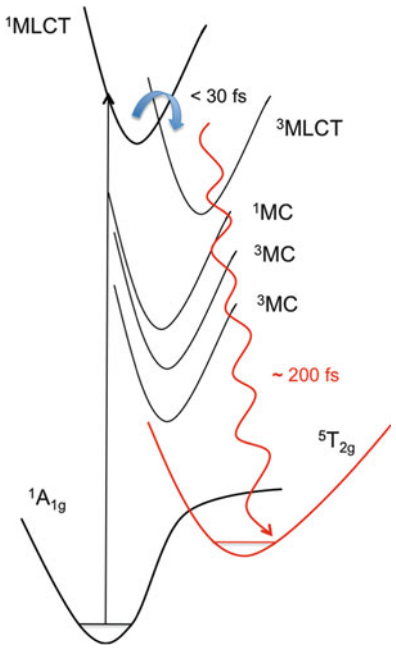

Scheme 5 Schematic diagram of the $^1\text{MLCT} \rightarrow {}^5T_{2g}$ deactivation channel in $[\text{Fe (bpy)}_3]^{2+}$ (adapted from Bressler et al. [95, 96])

The deactivation mechanism of light-induced spin crossover of $[\text{Fe (bpy)}_3]^{2+}$ from the ^{1}MLCT state to the metastable high spin $^5T_{2g}$ state has been the subject of a number of various experimental and theoretical studies [90] (and references therein). Ultra-fast optical and X-ray spectroscopy in solution [95, 96] pointed to the population of the high spin state within 200 fs, starting with an ultra-fast $^1\text{MLCT} \rightarrow {}^3$MLCT ISC occurring in less than 30 fs (Scheme 5). Moreover, X-ray absorption near-edge structure (XANES) measurements put in evidence intermediate ^{3}MC states the role of which in the mechanism is still uncertain. The life time of the high spin state is relatively short, being of the order of 650 ps.

The purpose of this recent theoretical investigation [90] based on previous quantum chemical studies by the same authors [125] is to focus on the role of SOC and ultra-fast ISC in the deactivation mechanism of $[\text{Fe (bpy)}_3]^{2+}$. Geometries and vibrational frequencies obtained from TD-DFT calculations combined with CASPT2 relative energies of the different spin states and SOC matrix elements calculated at the RASSI level are used in a subsequent investigation of the excited states dynamics. The ISC rate constants are computed from Fermi's golden rules in the Condon approximation within a time-dependent approach [101, 102]:

$$k_{\text{ISC}} = \left|\langle \phi_i | \hat{H}_{\text{SO}} | \phi_f \rangle\right|^2 \int_{-\infty}^{\infty} dt G(t) \mathrm{e}^{it\left(\Delta E_{if} + \frac{1}{2} Tr\Omega i\right)} \tag{3}$$

where ϕ_i and ϕ_f are the initial and final electronic states, respectively, Ω_i is a matrix that contains vibrational frequencies of the initial state, and $G(t)$ is a time-dependent correlation function which contains information about the vibrational frequencies and normal coordinates of the initial and final states.

The SOC matrix of 144×144 dimension generated by the 16 lowest electronic states in each multiplicity contains nearly 4,500 non-zero elements. This illustrates the complexity of the spin-orbit interactions in transition metal complexes characterized by a high density of various electronic states. The ^{1}MLCT/^{3}MLCT and ^{1}MLCT/^{3}MC SOC do not exceed 200 cm^{-1} and the ^{3}MLCT/$^5T_{2g}$ is very small (~6 cm^{-1}). In contrast, the ^{3}MC/$^5T_{2g}$ and ^{3}MC/$^1A_{1g}$ are characterized by large values (~500 cm^{-1}). The calculated ^{1}MLCT $\rightarrow$ ^{3}MLCT and ^{1}MLCT $\rightarrow$ ^{3}MC ISC rates are reported in Table 7.

The ^{3}MLCT $\rightarrow$ $^5T_{2g}$ ISC rate has been estimated to be greater than 10 ps, whereas the ^{3}MC $\rightarrow$ $^5T_{2g}$ ISC process is fast with a rate estimated to be 62 fs. This gives an overall time scale qualitatively comparable to the experimental one [95].

This theoretical study has pointed to a step-by-step mechanism showing that the ^{3}MC states play a key role in the deactivation process from the initially populated ^{1}MLCT state.

The interest of the method is that spin-orbit and vibrational contributions to the ISC rates can be easily extracted. However, some drawbacks should be pointed out. In this approach the vibrational relaxation at Franck–Condon and the variation of SOC as a function of the normal modes are not considered. The validity of the Fermi golden rule approximation is questionable because we are facing ultra-fast non-BO processes which need to be described by spin-vibronic coupling model Hamiltonians [84, 87, 88]. An alternative is to run semi-classical trajectories on PES computed on the fly, coupled non-adiabatically and by SOC. Such a tentative proposal, under some approximation, is presented in the next example dedicated to the ^{1}MLCT $\rightarrow$ ^{3}MLCT ISC in $[Ru(bpy)_3]^{2+}$ [126]. This type of simulation is based on TD-DFT calculations of the energies valid for second- and third-row transition metal complexes but hardly applicable to first-row transition metal complexes such as $[Fe(bpy)_3]^{2+}$ because of electron correlation and multireference electronic configurations.

Table 7 Calculated ^{1}MLCT $\rightarrow$ ^{3}MLCT and ^{1}MLCT $\rightarrow$ ^{3}MC intersystem-crossing rates in $[Fe(bpy)_3]^{2+}$

ϕ_i	ϕ_f	k_{ISC} (s^{-1})	τ (fs)
^{1}MLCT	^{3}MLCT	3.31×10^8	28
^{1}MLCT	^{3}MC	2.28×10^8	23
^{1}MLCT	^{3}MC[a]	2.26×10^7	718

Reprinted with permission from Sousa et al. [90] Copyright 2013 Wiley
[a]This ^{3}MC state is the lowest one in Scheme 5

5.2 *Ultra-Fast Relaxation Processes in $[Ru(bpy)_3]^{2+}$ Complex*

The first simulation based on TD-DFT energies and forces (gradient and Hessian) computed on-the-fly and introducing both vibronic and SO coupling effects has been able to reproduce semi-quantitatively the ultra-fast relaxation of the photo excited ^{1}MLCT state of $[Ru(bpy)_3]^{2+}$ (bpy = 2,2′-bipyridine) followed by ISC to the lowest ^{3}MLCT state [126].

This study focuses on the ultra-fast excited states dynamics of $[Ru(bpy]^{2+}$ in water with emphasis on the ISC processes through the seven low-lying singlet and triplet states. Time-resolved spectroscopy [127, 128] has shown a fast decay within less than 100 fs after absorption leading to a long-lived ^{3}MLCT state during a few hundreds of ps.

The non-adiabatic dynamics of the early events (50 fs) is simulated on the fly by means of linear response TD-DFT-based trajectories surface hopping according to the Tully algorithm [129]. SOC between qualitatively selected singlet and triplet states is obtained from a perturbative approach [130].

In order to take into account the solvent effects, the initial system constituted of the Ru(II) complex surrounded by 3,298 water molecules and the counter ions Cl^- is heated at 300 K. The non-BO dynamics represented by the panels in Fig. 6 show that the internal conversion processes through the individual singlet states manifold occur within a few to 10 fs, showing strong singlet triplet SOC occurring within the

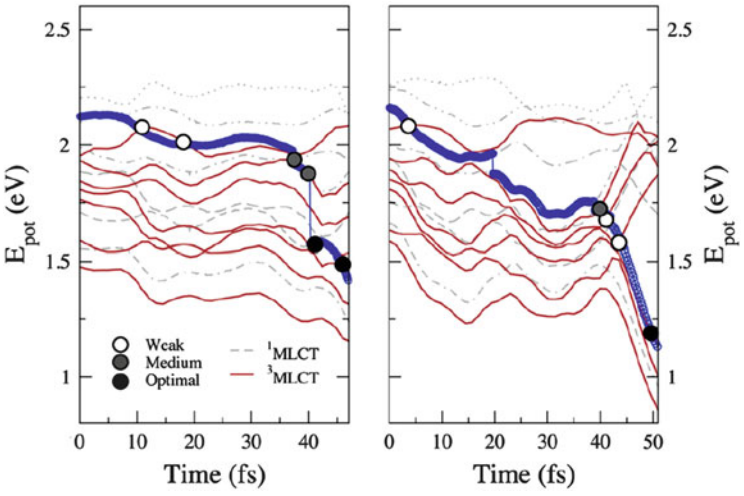

Fig. 6 Non-adiabatic molecular dynamics of $[Ru(bpy)_3]^{2+}$ in water represented by the population of the low-lying seven singlet (in *gray*) and seven triplet states (in *red*) as function of time. The SOC at states crossing are represented by *white* (weak SOC), *gray* (medium SOC), and *black* (strong SOC) *filled circles* (reprinted with permission from Tavernelli et al. [126] Copyright 2011 Elsevier)

first 40–50 fs. The largest SOC is predicted between the lowest ^{1}MLCT and its associated triplet state. The importance of solvation dynamics is also emphasized.

The drawback of this pioneering promising approach is the limited number of trajectories and the qualitative estimation of the SOC, the value of which should be determined quantitatively on the fly as well. However, this strategy opens the route to new applications in large transition metal complexes as soon as the electronic structure can be described correctly by means of TD-DFT.

5.3 *Ultra-Fast Luminescence Decay in [Re (Br)(CO)$_3$(bpy)] Complexes*

In this very recent application we focus on the excited states decay of [Re (Br)(CO)$_3$(bpy)] within the first 500 fs by means of non-adiabatic quantum dynamics including spin vibronic couplings within the linear approach and based on TD-DFT energies and frequencies [122]. For this purpose we have constructed a model Hamiltonian including five electronic states, namely S_2 which absorbs at 400 nm, S_1 and the three lowest triplet states T_3, T_2, and T_1 (Scheme 6) and up to six vibrational normal modes. The five states are coupled by SOC and vibronically. The SOC values are assumed to be constant as functions of the nuclear displacements. This is justified in a first approximation, for the bromide-substituted complex in which the calculated SOC remain nearly constant as function of the Re–Br stretching bond [121]. The calculated emission wavelengths of these five excited states, including SOC, are reported in Table 6 (Sect. 4.3). To validate the PES generated within the LVC harmonic model starting from Franck–Condon geometry, we have computed the TD-DFT PES as function of the mass and frequency weighted Re–Br stretching normal mode [121].

Scheme 6 proposes a qualitative correlation between the experimental data obtained from time-resolved luminescence spectroscopy and the state diagram built on the basis of the calculated emission wavelengths reported in Table 6 (Sect. 4.3).

The purpose of the simulation based on wave packet propagations with multi-configuration time-dependent Hartree MCTDH [131, 132] is to recover the populations of the involved electronic states as function of time within the first 500 fs and to interpret the ultra-fast luminescent decay observed experimentally [120].

The interplay between SOC and vibronic coupling, based on symmetry rules, controlled entirely the ISC process. Indeed, when including SOC matrix elements together with four normal modes of symmetry a′, namely two modes associated with the Re–Br stretching and two modes associated with the Re–CO stretching, we

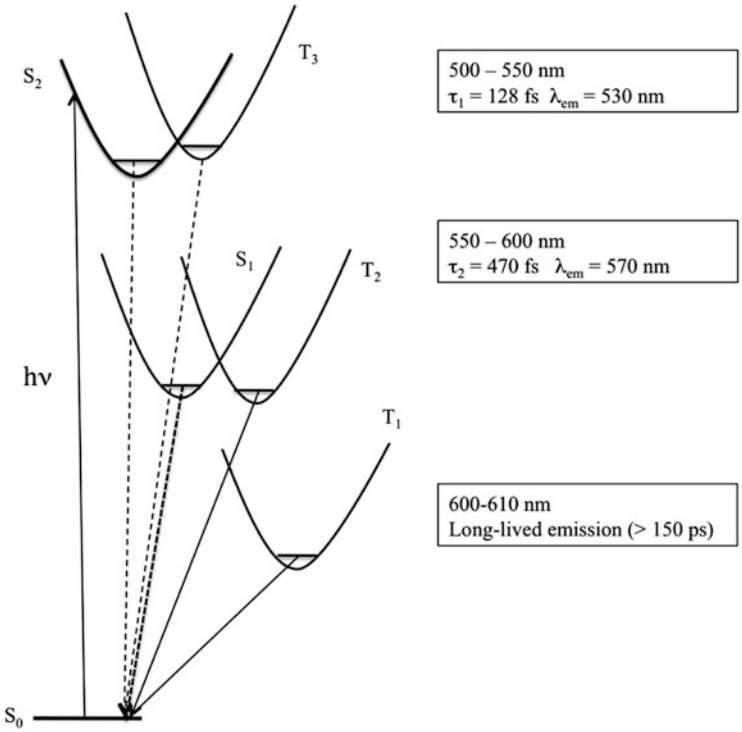

Scheme 6 State diagram representing the low-lying potentially emissive singlet and triplet states of [Re (Br)$(CO)_3$(bpy]. Experimental data are reported on the left side (adapted from Cannizzo et al. [120])

observe a fast and efficient population of T_1 and T_3 (Fig. 7, top) with a rapid decay of the S_2 population to less than 40% within 20 fs. The nearly instantaneous population of T_1 is because of a large value of SOC between this state and S_2 (600 cm^{-1}), whereas the population of T_3 is controlled by the significant degree of spin-orbit mixing and the small energy gap between this state and S_2.

When two additional normal modes of symmetry a″ corresponding to out-of-plane bending of the bpy ligand are taken into account (Scheme 7), the population of T_1 and T_3, controlled mainly by SOC, is not modified but we observe a modest population of S_1 and T_2 starting after a few tens of fs and increasing until a maximum of 20% at 350 fs (Fig. 7, bottom, black dashed and red). Interestingly, the population of T_3 optimum within 25 fs decays rapidly to less than 20%. This confirms the participation of T_3 together with S_2 to the early signal observed in the 500–550 nm domain of energy (Scheme 6).

The increase in population of S_1 and T_2 coupled by spin-orbit (>600 cm^{-1}) and activated by vibronic coupling follows the decay of S_2 until about 300 fs, but most of the triplet population is trapped into T_1 which remains stable around 20%. As expected from the luminescent static properties analyzed in Sect. 4.3, both S_1 and T_2 should contribute to the intermediate signal observed within a few hundred of fs

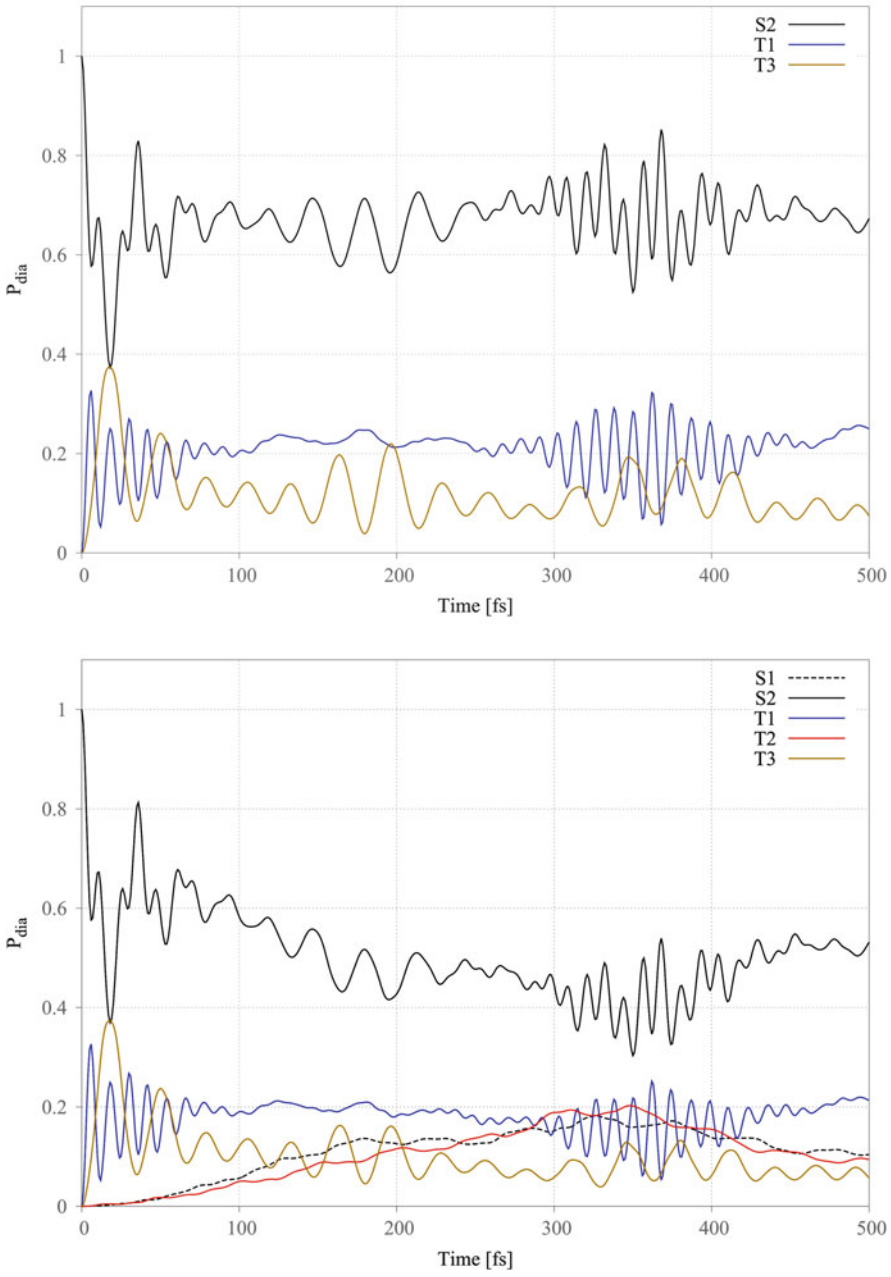

Fig. 7 Non-adiabatic quantum dynamics of [Re (Br)$(CO)_3$(bpy)] including SOC with four normal modes associated to Re-Br and Re-CO a′ stretching modes (*top*) and SOC with six modes including two normal modes associated to bpy a″ out-of-plane-bending modes (*bottom*). The population of S_2 (in *black*), S_1 (*dashed line*), T_1 (in *blue*), T_2 (in *red*), and T_3 (in *sienna*) are represented as function of time

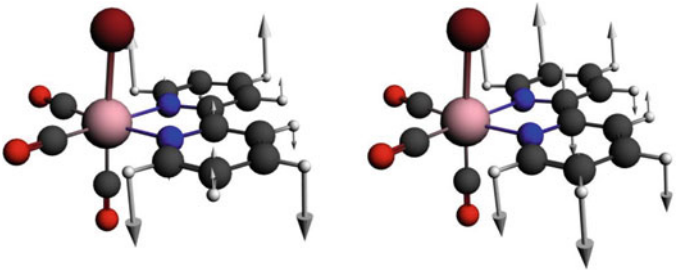

Scheme 7 Out-of-plane bending normal modes displacements of the bpy ligand of symmetry a″ calculated at 557 cm^{-1} (*left*) and 820 cm^{-1} (*right*)

between 550 and 600 nm (Scheme 6). The states population analysis at longer time scale is meaningful because of the restricted number of active normal modes included in the simulation. After 300 fs we observe an exchange of population, mainly between S_2 and T_1 strongly coupled with SOC.

This study, which does not take into account the anharmonicity of the excited states potentials and keeps constant the SOC values as function of the nuclear displacements, points to the importance of spin vibronic effects in describing ISC processes. The interplay between geometry distortion and SOC has also been shown in the phosphorescence decay of [Ir $(ppy)_3$] complexes described in Sect. 4.1 and in the excited states dynamics of spin crossover complex $[Fe(bpy)_3]^{2+}$ in Sect. 5.1 of the present contribution, as well as in the pioneering work by Domcke et al. [87].

6 Concluding Remarks

Whereas the simulation of vertical electronic absorption spectra of transition metal complexes by TD-DFT including solvent effects via polarized continuum models (PCM) has been consistently performed with success since the beginning of the 2000s, the coverage of spin orbit and vibronic coupling effects in this field is far from being routine. This contribution reviews the methods available within the TD-DFT framework for taking into account with reasonable accuracy these important effects. Indeed, they modify the shape of the theoretical spectra and, more importantly, revise the interpretation of the experimental features.

Whereas the absorption spectra are easily obtained by means of TD-DFT, the emissive properties originating from S_n, $T_n \rightarrow S_0$ transitions have been difficult to analyze until now because the determination of the degree of mixing between the singlet and triplet states by SOC and the systematic search for nuclear distortions in several close-lying excited states is still a challenge for computational chemistry. The applications reported in this chapter have shown three cases for which different computation strategies have to be developed. The first class of molecules is represented by Ir(III) complexes, seats of long-lived luminescence, most of the

time attributed to the lowest triplet T_1 state. In this case, a detailed study of spin-induced ZFS and vibronic effects may result in a direct comparison with accurate experimental findings. The second category of molecules represented by Re (I) complexes is characterized by shorter lived signals following a cascade of ultra-fast luminescence decays attributed to S_n and T_n states. The interpretation of the processes underlying emissive properties has to be based on non-adiabatic excited states dynamics, either within a full quantum method from first principle or following surface hopping trajectories within a semi-classical approach. Nevertheless, a TD-DFT static approach based on the optimized structures of the key emissive states is very useful for deciphering the mechanism as preamble to the dynamical study. The in-between luminescent behaviors exemplified by flexible Pt (II) square planar complexes have to be treated with care, some basic approximation such as Kasha rules being meaningless in that case as illustrated by the applications reported in the present contribution.

The simulation of ISC processes by means of wave packet propagations on spin-vibronic coupled multi-dimensional PES is out of reach for large transition metal complexes. Pioneering studies based on recent methodological developments have been able to reproduce with reasonable accuracy ultrafast luminescent time scales observed in first-, second- and third-row transition metal complexes. Counterintuitive heavy atom effects on ISC kinetics observed experimentally have found explanations in detailed theoretical analysis.

Whereas TD-DFT absorption spectra have been validated by a number of joined experimental/theoretical studies or by comparison with accurate ab initio methods in the past decade, we do not have the benefit of hindsight as far as the emissive properties are concerned.

The interpretation of ultra-fast time-resolved spectroscopy outcomes is especially challenging because both spin-orbit and vibronic coupling effects have to be considered. In the systems investigated so far involving mostly singlet and triplet states, the standard level of approximation used for SOC assessment seems realistic. For higher multiplicities or situations with large mixing between electronic states of different multiplicities, a more refined treatment of spin-orbit interactions could be mandatory. The newly developed perturbational treatment for generally applicable high-level multireference methods is one useful approach [133].

The simulation and computation of ISC rates in pioneering applications are based on different strategies: (1) non-adiabatic molecular dynamics where TD-DFT is coupled to classical trajectory-based methods; (2) quantum dynamics where both electronic and nuclear wave functions are treated exactly within a given level of approximation; and (3) time-dependent non-radiative rate theory in the multi-mode harmonic oscillator and Condon approximations, where the electronic spin-orbit matrix elements depend linearly on the nuclear coordinates within a spin-vibronic coupling scheme. As illustrated by the examples developed above for first-, second- and third-row transition metal complexes, each approach has its strengths and weaknesses. Several important aspects have to be considered in this expanding field, namely the solvation dynamics, the variation of spin-vibronic couplings with nuclear relaxation, the construction of realistic model Hamiltonians, and the

anharmonicity of excited states potentials. One additional difficulty is the selection of appropriate active normal modes in large complexes with metal atoms, the nuclear flexibility of which cannot be inferred from experience gained from organic molecules.

References

1. Crosby GA (1975) Acc Chem Res 8(7):231
2. Hipps KW, Crosby GA (1974) Inorg Chem 13(6):1543
3. Hager GD, Crosby GA (1975) J Am Chem Soc 97(24):7031
4. Crosby GA, Hipps KN, Elfing WH Jr (1974) J Am Chem Soc 96(2):629
5. Striplin DR, Crosby GA (1995) J Phys Chem 99(20):7977
6. Striplin DR, Crosby GA (1994) Chem Phys Lett 221(5–6):426
7. Rausch AF, Thompson ME, Yersin H (2009) J Phys Chem A 113(20):5927
8. Mak CSK, Pentlehner D, Stich M, Wolfseis OS, Chan WK, Yersin H (2009) Chem Mater 21 (11):2173
9. Rausch AF, Homeier HHH, Yersin H (2010) Topic Organomet Chem 29:193
10. Fischer T, Czerwieniec R, Hofbeck T, Osminina MM, Yersin H (2010) Chem Phys Lett 486 (1–3):53
11. Hofbeck T, Yersin H (2010) Inorg Chem 49(20):9290
12. Yersin H, Rausch AF, Czerwieniec R, Hofbeck T, Fischer T (2011) Coord Chem Rev 255 (21–22):2622
13. Blanco-Rodríguez AM, Di Bilio AJ, Shih C, Museth AK, Clark IP, Towrie M, Cannizzo A, Sudhamsu JJ, Crane BR, Sykora J, Winkler JR, Gray HB, Záliš S, Vlček A Jr (2011) Chem A Eur J 17:5350
14. Blanco-Rodriguez AM, Towrie M, Sykora J, Záliš S, Vlček A Jr (2011) Inorg Chem 50:6122
15. Blanco-Rodríguez AM, Busby M, Grädinaru C, Crane BR, Di Bilio AJ, Matousek P, Towrie M, Leigh BS, Richards JH, Vlček A Jr, Gray HB (2006) J Am Chem Soc 128:4365
16. Kalinowski J, Fattori V, Cocchi M, Gareth Williams JA (2011) Coord Chem Rev 255 (21–22):2401
17. Gareth Williams JA (2007) Topic Curr Chem 281:205
18. Heully JL, Alary F, Boggio-Pasqua M (2009) J Chem Phys 131:184308
19. Alary F, Boggio-Pasqua M, Heully JL, Marsden CJ, Vicendo P (2008) Inorg Chem 47 (12):5259
20. Camilo MR, Cardoso CR, Carlos RM, Lever ABP (2014) Inorg Chem 53(7):3694
21. Nieuwenhuis HA, van de Ven MCE, Stufkens DJ, Oskam A, Goubitz K (1995) Organometallics 14(2):780
22. Rossenaar BD, Kleverlaan CJ, Stufkens DJ, Oskam A (1994) J Chem Soc Commun 63
23. Wegman RW, Olsen RJ, Gard DR, Faulkner LR, Brown TL (1981) J Am Chem Soc 103:6089
24. Vlček A Jr, Busby M (2006) Coord Chem Rev 250:1755
25. Busby M, Hartl F, Matousek P, Towrie M, Vlček A Jr (2008) Chem Eur J 14:6912
26. Kayanuma M, Gindensperger E, Daniel C (2012) Dalton Trans 41:13191
27. Juban EA, Smeigh AL, Monat JE, McCusker JK (2006) Coord Chem Rev 250:1783
28. McCusker JK (2003) Acc Chem Res 36:876
29. Chergui M (2012) Dalton Trans 41:13022
30. Bräm O, Messina F, Baranoff E, Cannizzo A, Nazeeruddin MK, Chergui M (2013) J Phys Chem C 117:15958
31. El Nahhas A, Consani C, Blanco-Rodríguez AM, Lancaster KM, Braem O, Cannizzo A, Towrie M, Clark IP, Záliš S, Chergui M, Vlček A Jr (2011) Inorg Chem 50:2932

32. Renske M, van der Veen RM, Cannizzo A, van Mourik F, Vlček A Jr, Chergui M (2011) J Am Chem Soc 133:305
33. Schinke R (1995) Photodissociation dynamics spectroscopy and fragmentation of small polyatomic molecules, Cambridge monograph on atomic, molecular and chemical physics. Cambridge University Press, Cambridge
34. Hochlaf M (2013) Spectroscopy and dynamics of medium sized molecules and clusters. Phys Chem Chem Phys 15:9967
35. Daniel C (2015) Coord Chem Rev 282–283:19
36. Neese F (2009) Coord Chem Rev 253:526
37. González L, Escudero D, Serrano-Andres L (2012) Chem Phys Chem 13:28
38. Vancoillie S, Zhao H, van Tran T, Hendrickx MFA, Pierloot K (2011) J Chem Theor Comp 7:3961
39. Dreuw A, Head-Gordon M (2005) Chem Rev 105:4009
40. Adamo C, Jacquemin D (2013) Chem Soc Rev 42:845
41. Labat F, Le Bahers J, Ciofini I, Adamo C (2012) Acc Chem Res 45(8):1268
42. Li X, Minaev B, Ågren H, Tian H (2011) Eur J Inorg Chem 2517
43. Zhekova HR, Seth M, Ziegler T (2014) Int J Quantum Chem 114:1019
44. Casida ME, Huix-Rotlant M (2012) Annu Rev Phys Chem 63:287, Johnson MA, Martinez TJ (eds)
45. Rosa A, Baerends EJ, Gisbergen SJA, van Lenthe E, Groeneveld JA, Snijders JG (1999) J Am Chem Soc 121:10356
46. Wakamatsu K, Nishimito K, Shibahara T (2000) Inorg Chem Commun 3:677
47. Van Gisbergen SJA, Groeneveld JA, Rosa A, Snijders JG, Baerends EJ (1999) J Phys Chem A 103:6835
48. Ricciardi G, Rosa A, van Gisbergen SJA, Baerends EJ (2000) J Phys Chem A 104:635
49. Rosa A, Ricciardi G, Baerends EJ, van Gisbergen SJA (2001) J Phys Chem A 105:3311
50. Ricciardi G, Rosa A, Baerends EJ (2001) J Phys Chem A 105:5242
51. Turki M, Daniel C, Záliš S, Vlček A Jr, van Slageren J, Stufkens DJ (2001) J Am Chem Soc 123:11431
52. Full J, González L, Daniel C (2001) J Phys Chem A 105:184
53. Daniel C (2006) Photochemistry of transition metal complexes. In: Crabtree RH (ed) Encyclopedia of inorganic chemistry. Wiley, Chichester. doi:10.1002/9781119951438.eibc0175
54. Daniel C (2005) In: Yersin H (ed) Topics in current chemistry, vol 241. Springer, Heidelberg, p 119
55. Dirac PAM (1928) Proc Roy Soc Lond A 117:610
56. Marian CM (2012) WIREs Comput Mol Sci 2:187
57. Douglas N, Korll NM (1974) Ann Phys 82:89
58. Hess BA (1986) Phys Rev A 33:3742
59. Breit G (1929) Phys Rev 34:553
60. Bethe H, Salpeter E (1957) Quantum mechanics of one- and two-electron atoms. Springer, Berlin
61. Breit G (1930) Phys Rev 36:363
62. Breit G (1932) Phys Rev 39:616
63. Malmqvist PÅ, Roos BO, Schimmelpfennig B (2002) Chem Phys Lett 357:230
64. Hess BA, Marian C, Wahlgren U, Gropen O (1996) Chem Phys Lett 251:365
65. Christiansen O, Gauss J, Schimmelpfennig B (2000) Phys Chem Chem Phys 2:965
66. van Lenthe E, Baerends EJ, Snijders JG (1993) J Chem Phys 99:4597
67. van Wüllen C (1998) J Chem Phys 109(2):392
68. van Lenthe E, Baerends EJ, Snijders JG (1994) J Chem Phys 101:9783
69. Neese F (2003) J Chem Phys 118:3939
70. Ando H, Iuchi S, Sato H (2012) Chem Phys Lett 535:177
71. Zeng T, Fedorov DG, Schmidt MW, Klobukowski MJ (2012) Chem Theor Comput 8:3061

72. Herzberg G (1966) Molecular spectra and molecular structure III. Electronic spectra and electronic structure of polyatomic molecules. van Nostrand, New York
73. Koseki S, Schmidt MW, Gordon MS (1998) J Phys Chem A 102(50):10430
74. Koseki S, Fedorov DG, Schmidt MW, Gordon MS (2001) J Phys Chem A 105(35):8262
75. Gourlaouen C, Daniel C (2014) Dalton Trans 43(47):17806
76. Bakova R, Chergui M, Daniel C, Vlček A Jr, Záliš S (2011) Coord Chem Rev 255:975
77. Brahim H, Daniel C, Rahmouni A (2012) Int J Quantum Chem 112:2085
78. Vallet V, Strich A, Daniel C (2005) Chem Phys 311:13
79. Heydova R, Gindensperger E, Romano R, Sykora J, Vlček A Jr, Záliš S, Daniel C (2012) J Phys Chem A 116:11319
80. Brahim H, Daniel C (2014) Comp Theor Chem 1040/104:219
81. Li X, Minaev B, Ågren H, Tian H (2011) J Phys Chem C 115:20724
82. Ronca E, De Anglis F, Fantucci S (2014) J Phys Chem C 118:17067
83. Fantacci S, Ronca E, De Angelis F (2014) J Phys Chem Lett 5:375
84. Köppel H, Domcke W, Cederbaum LS (1984) Adv Chem Phys 57:59
85. Hazra A, Nooijen M (2005) Phys Chem Chem Phys 7:1759
86. Neugebauer J, Baerends EJ, Nooijen M (2005) J Phys Chem A 109:1168
87. Mondal P, Opalka D, Poluyanov LV, Domcke W (2012) J Chem Phys 136:084308
88. Mondal P, Opalka D, Poluyanov LV, Domcke W (2011) Chem Phys 387:56
89. Capano G, Penfold TJ, Röthlisberger U, Tavernelli I (2014) CHIMIA 68(4):227
90. Sousa C, de Graaf C, Rudavskyi A, Broer R, Tatchen J, Etinski M, Marian CM (2013) Chem Eur J 19:17541
91. El Nahhas A, Cannizzo A, van Mourik F, Blanco-Rodríguez AB, Zalis S, Vlček A Jr, Chergui M (2010) J Phys Chem A 114:6361
92. Kuimova MK, Alsindi WZ, Blake AJ, Davies ES, Lampus DJ, Matousek P, McMaster J, Parker AW, Towrie M, Sun X-Z, Wilson C, George MW (2008) Inorg Chem 47:9857
93. Huse N, Kim TK, Jamula L, McCusker JK, de Groot FMF, Schoenlein RW (2010) J Am Chem Soc 132:6809
94. Huse N, Cho H, Hong K, Jamula L, de Groot FMF, Kim TK, McCusker JK, Schoenlein RW (2011) J Phys Chem Lett 2:880
95. Bressler CH, Milne C, Pham V-T, El Nahhas A, van der Veen RM, Gawelda W, Johnson S, Beaud P, Grolimund D, Kaiser M, Borca CN, Ingold G, Abela R, Chergui M (2009) Science 323:489
96. Zhang W, Alonso-Mori R, Bergmann U, Bressler C, Chollet M, Galler A, Gawelda W, Hadt RC, Hartsock RW, Kroll T, Kjær KS, Kubiček K, Lemke HT, Liang HW, Meyer DA, Nielsen MM, Purser C, Robinson JS, Solomon EI, Sun Z, Sokaras D, van Driel TB, Vankó G, Weng T-C, Zhu D, Gaffney KJ (2014) Nat Lett 509:345
97. Blanco-Rodríguez AM, Kvapilová H, Sýkora J, Towrie M, Nervi C, Volpi G, Záliš S, Vlček A Jr (2014) J Am Chem Soc 136:5963
98. El-Sayed MA (1963) J Chem Phys 38:2834
99. Englman R, Jortner J (1970) Mol Phys 18:145
100. Freed KF, Jortner J (1970) J Chem Phys 52:6272
101. Etinski M, Tatchen J, Marian CM (2011) J Chem Phys 134:154105
102. Etinski M, Rai-Constapel V, Marian CM (2014) J Chem Phys 140:114104
103. Tatchen J, Gilka N, Marian CM (2007) Phys Chem Chem Phys 9:5209
104. Curchod BFE, Rothlisberger U, Tavernelli I (2013) Chem Phys Chem 14:1314
105. Köppel H, Domcke W (1998) In: von Ragué Schleyer P (ed) Encyclopedia in computational chemistry. Wiley, New York, p 3166
106. Domcke W, Yarkony DR, Köppel H (eds) (2004) Conical intersections – electronic structure, dynamics and spectroscopy, vol 15, Advanced series in physical chemistry. World Scientific, Singapore
107. Baer M (2006) Beyond Born-Oppenheimer electronic nonadiabatic coupling terms and conical intersection. Wiley-Interscience, Hoboken

108. Curchod BFE, Penfold TJ, Rothlisberger U, Tavernelli I (2013) Cent Eur J Phys 11:1059
109. de Carvalho FF, Bouduban MEF, Curchod BFE, Tavernelli I (2014) Entropy 16:62
110. Worth GA, Welch G, Paterson MJ (2006) Mol Phys 104:1095
111. McKinlay RG, Zurek JM, Paterson MJ (2010) Advances in inorganic chemistry, vol 62. Academic, p 351
112. Holzer W, Penzkofer A, Tsuboi T (2005) 308:93
113. Ciofini I, Adamo C (2007) J Phys Chem A 111:5549
114. Vlček A Jr, Záliš S (2007) Coord Chem Rev 25:258
115. Hay PJ (2002) Phys Chem A 106:1634
116. Nozaki KJ (2006) Chin Chem Soc 53:101
117. Jansson E, Minaev B, Schrader S, Ågren H (2007) Chem Phys 110:1849
118. Fine J, Diri K, Krylov AI, Nemirow C, Lu Z, Wittig C (2012) Mol Phys 110:1849
119. Nemirow C, Fine J, Lu Z, Diri K, Krylov AI, Wittig C (2012) Mol Phys 110:1893
120. Cannizzo A, Blanco-Rodríguez AM, El Nahhas A, Sebera J, Záliš S, Vlček A Jr, Chergui M (2008) J Am Chem Soc 130:8967
121. Gourlaouen C, Otsuka M, Gindensperger E, Daniel C (2015) J Chem Theory Comp 11(1):99
122. Eng J, Gourlaouen C, Gindensperger E, Daniel C (2015) Acc Chem Res 48(3):809
123. Jansson E, Minaev B, Schrader S, Ågren H (2007) Chem Phys 333:157
124. Finkenzeller WJ, Yersin H (2003) Chem Phys Lett 377:299
125. de Graaf C, Sousa C (2011) Int J Quantum Chem 111:3385
126. Tavernelli I, Curchod BFE, Rothlisberger U (2011) Chem Phys 391:101
127. Yeh AT, Shank CV, McCusker JK (2000) Science 289(5481):935
128. Cannizzo A, van Mourik F, Gawelda W, Zgrablic G, Bressler C, Chergui M (2006) Angew Chem Int Ed 3174
129. Tully JC (1990) J Chem Phys 93:1061
130. Wang F, Ziegler T (2005) J Chem Phys 123(15):154102
131. Manthe U, Meyer H-D, Cederbaum LS (1992) J Chem Phys 97:3199
132. Meyer H-D, Manthe U, Cederbaum LS (1990) Chem Phys Lett 165:73
133. Mai S, Müller T, Plasser F, Marquetand P, Lischka H, González L (2014) J Chem Phys 141:074105

Top Curr Chem (2016) 368: 415–444
DOI: 10.1007/128_2014_605

Published online: 24 February 2015

Surface Hopping Dynamics with DFT Excited States

Mario Barbatti and Rachel Crespo-Otero

Abstract Nonadiabatic dynamics simulation of electronically-excited states has been a research area of fundamental importance, providing support for spectroscopy, explaining photoinduced processes, and predicting new phenomena in a variety of specialties, from basic physical-chemistry, through molecular biology, to materials engineering. The demands in the field, however, are quickly growing, and the development of surface hopping based on density functional theory (SH/DFT) has been a major advance in the field. In this contribution, the surface hopping approach, the methods for computation of excited states based on DFT, the connection between these methodologies, and their diverse implementations are reviewed. The shortcomings of the methods are critically addressed and a number of case studies from diverse fields are surveyed.

Keywords Density functional theory • Excited states • Nonadiabatic dynamics • Photochemistry • Surface hopping

Contents

M. Barbatti (✉)
Max-Planck-Institut für Kohlenforschung, Kaiser-Wilhelm-Platz 1, 45470 Mülheim an der Ruhr, Germany
e-mail: barbatti@kofo.mpg.de

R. Crespo-Otero
School of Biological and Chemical Sciences, Queen Mary University of London, Mile End Road, London E1 4NS, UK

Abbreviations

ADC	Algebraic diagrammatic construction
ALDA	Adiabatic local density approximation
CASSCF	Complete active space self-consistent field
CC	Coupled cluster
CI	Configuration interaction
CIS	CI with single excitations
CPA	Classical path approximation
DFT	Density functional theory
DFTB	Density functional based tight binding
DISH	Decoherence-induced surface hopping
GFSH	Global-flux surface hopping
LR	Linear response
KS	Kohn–Sham
MCSCF	Multiconfigurational self-consistent field
MRCI	Multireference CI
MR-CISD	MRCI with singles and doubles
MRPT	Multireference perturbation theory
REKS	Spin-restricted ensemble-referenced KS
ROKS	Restricted open-shell KS
RPA	Random phase approximation
SDKS	Single determinant KS
SH	Surface hopping
SH/DFT	Surface hopping with DFT excited states
TD	Time-dependent
TDA	Tamm–Dancoff approximation
TDHF	Time-dependent Hartree–Fock
UBS	Spin-unrestricted broken symmetry

1 Introduction

Motivated by the advances in computational capabilities and algorithms, computational research on dynamics simulations of electronically-excited molecular systems has been quickly developing in the last decade. Larger and more complex systems are reported from groups all over the world on a daily basis, providing fundamental information to interpret excited-state phenomena revealed by advanced spectroscopic techniques, to explain the photochemical process occurring

in different fields, and to predict new properties with potential technological applications.

There are a relatively large number of methods for excited-state calculations available. They include wavefunction-based and density-functional-based methods derived from different approaches, such as configuration interaction, perturbation theory, and coupled cluster; and providing different approximation levels, from semiempirical to fully first principles, from single-reference to multireference, from short truncated spaces to complete configurational expansions. Each of these methods and their hybrid combinations has its own domain of applicability depending on the nature and size of the molecular system. For this very reason, none of them can be expected to perform equally well for every problem without exception.

Extensive benchmarks of excitation energies have shown that most of methods present mean deviation errors of about 0.2–0.3 eV for vertical excitation energies [1–5]. Not only are such values of the order of magnitude of many reaction barriers, but also these errors are unevenly distributed among several states for the same method and tend to grow bigger out of the Franck–Condon region. Well known examples are the relatively large errors of the energy of ionic states predicted by truncated ab initio configuration interaction [6] or of the energy of charge-transfer states of time-dependent density functional theory with conventional functionals [7].

The root of this problem rests on the very nature of electronic excitations. Electronically-excited states lie close to each other in the energy spectrum and relatively small variations in the molecular geometry may lead to their reordering. Moreover, the characters of these states may be extremely different: from diffuse Rydberg, through charge-transfer, to spatially localized densities.

Given these features, a basic requirement for a proper computational description of an excited-state phenomenon is that the theoretical model should describe different types of states for different nuclear geometries on the same footing. At this moment, this is a requirement that no single method can fully and affordably satisfy. The consequence is that the simulations often deliver an unbalanced description of the electronic states, with deep implications on the reliability of predictions.

This problem is under relative control in static simulation of reaction pathways, where only a few degrees of freedom are considered. In dynamics simulations, however, it may grow out of control because of the much greater number of degrees of freedom and variables (now, time among them) to tackle.

Besides the question of the accuracy of the potential energy surfaces, dynamics simulations add two new layers of potential complications to the simulations: first, nonadiabatic phenomena [8, 9], originated by the coupling of nuclear and electronic degrees of freedom during the dynamics propagation, must be taken into account; second, the dynamics propagation itself multiplies the computational costs.

Again, several methods are available for nonadiabatic excited-state dynamics simulations, from full propagation of the electronic wavefunctions [10], which requires predefinition of multidimensional potential energy surfaces, to

semiclassical approximations, which reduce the wavefunction propagation to ensembles of independent trajectories based only on local properties [11]. In particular, the independent-trajectory approximation, essential to the surface hopping approach, cannot predict nonlocal quantum effects, such as tunneling, quantum phases, or decoherence [8, 12, 13]. Moreover, the statistical ensembles are often of too reduced size to comply with the computational capabilities, leading to high statistical uncertainties [14]. (For recent discussions on nonadiabatic dynamics beyond the independent-trajectories approach, see [15–17].)

From the point of view of semiclassical nonadiabatic excited-state dynamics simulations, the ideal method for electronic structure calculations should satisfy the following criteria:

1. Be computationally fast
2. Provide energies for excited states of different natures with similar accuracy
3. Provide reliable (preferentially analytical) gradients for excited states
4. Allow the computation of electronic structures near intersection seams with the ground state
5. Allow the computation of electronic structures near intersection seams between excited states
6. Be independent of human intervention for running large ensembles of different geometries

With different accuracies, methods for excited-states computation based on DFT comply with most of these criteria, especially computational efficiency. These methods, however, usually fail criterion 4, the description of the crossing seam with the ground state. Nevertheless, still considering the *pros* and *cons*, surface hopping based on DFT excitations (SH/DFT) is a good alternative for nonadiabatic simulations, on condition that it is applied critically, bearing in mind all these restrictions and limitations.

In this contribution, we examine the current situation of the SH/DFT methods, starting with a review of surface hopping in Sect. 2. In Sect. 3 we address the methods for computing the excited state in the DFT framework, especially focusing on the linear-response time-dependent methodology and its relation to lower-level methods (Sect. 3.1). In Sect. 3.2 we review the computation of nonadiabatic couplings in DFT. In Sect. 3.3 the limitations of the method in the context of dynamics simulations are critically addressed. In Sect. 4 the elements from Sects. 2 and 3 are put together to discuss the different SH/DFT implementations. Finally, in Sect. 5 we present a series of case studies showing the potentials and limitations of using SH/DFT in diverse fields.

2 Surface Hopping Overview

In surface hopping, the time propagation of the quantum wavepacket is approximated by a swarm of semiclassical trajectories evolving on Born–Oppenheimer surfaces of multiple electronic states. Nonadiabatic events (wavepacket density transfer between states; see [8] for an excellent review on this topic) are simulated by a stochastic algorithm which allows each trajectory to jump to other states during the propagation. Thus, the statistics over the ensemble of trajectories in terms of fraction of trajectories in each electronic state in each time step is expected to be an approximated representation of the wavepacket density distribution among the excited states as a function of time. The method was conceptually proposed by Nikitin [18] and was used first by Tully and Preston [19]. It has been recently reviewed in [11, 20–22].

In the most common surface hopping approach, all nuclear coordinates are driven by Newton's equations of motion on a single adiabatic electronic state K. For the coordinates $\mathbf{R}_m$ with the associated nuclear mass M_m, they are given by

$$\frac{d^2\mathbf{R}_m}{dt^2} = -\frac{1}{M_m}\frac{\partial E_K}{\partial \mathbf{R}_m}, \tag{1}$$

where E_K is the adiabatic potential energy of the current state K. Given a set of initial positions and velocities, (1) is numerically integrated.

Along with the Newton's equations, the probability for the system to hop to another state L is evaluated. Diverse schemes for the evaluation of such probabilities have been developed [19, 23–30]. The most successful and popular approach has been the fewest switches proposed by Tully in the early 1990s [28].

In the fewest switches, the number of hopping events within one time step Δt is minimized. Under this condition, the hopping probability between states K and L is

$$P_{K\to L} = \frac{\text{Population increment in } L \text{ due to flux from } K \text{ during } \Delta t}{\text{Population of } K}. \tag{2}$$

The population of each electronic state L is given in terms of the coefficients $c_L(t)$ of the time-dependent wavefunction written as a linear combination of electronic time-independent electronic wavefunctions Ψ_L:

$$\varphi(\mathbf{r}, \mathbf{R}, t) = \sum_J c_J(t)\,\Psi_J(\mathbf{r}; \mathbf{R}(t)). \tag{3}$$

The coefficients c_J are obtained by solving a local approximation for the time-dependent electronic Schrödinger equation, given in the adiabatic representation by [28]

$$\frac{dc_L}{dt} + \frac{i}{\hbar} E_L c_L + \sum_J \sigma_{LJ} \; c_J = 0. \tag{4}$$

In this equation, the coupling terms between any pair of states L and M are

$$\sigma_{LM} \equiv \left\langle \Psi_L \middle| \frac{\partial}{\partial t} \Psi_M \right\rangle = \boldsymbol{\tau}_{LM} \cdot \mathbf{v}, \tag{5}$$

where $\boldsymbol{\tau}_{LM}$ is the first-order nonadiabatic coupling vector

$$\boldsymbol{\tau}_{LM} \equiv \langle \Psi_L | \nabla_{\mathbf{R}} \Psi_M \rangle. \tag{6}$$

and $\mathbf{v}$ is a vector collecting the nuclear velocities.

When explicit nonadiabatic coupling vectors $\boldsymbol{\tau}_{LM}$ are not available (and this is often the case for excited states based on DFT), the coupling terms σ_{LM} can be computed by finite differences as [31]

$$\begin{aligned} \sigma_{LM}(t) &\approx \frac{1}{2\Delta t}\left[\left\langle \Psi_L\left(t - \frac{\Delta t}{2}\right) \middle| \Psi_M\left(t + \frac{\Delta t}{2}\right) \right\rangle - \left\langle \Psi_L\left(t + \frac{\Delta t}{2}\right) \middle| \Psi_M\left(t - \frac{\Delta t}{2}\right) \right\rangle \right] \\ &\approx \frac{1}{4\Delta t}[3S_{LM}(t) - 3S_{ML}(t) - S_{LM}(t - \Delta t) + S_{ML}(t - \Delta t)], \end{aligned} \tag{7}$$

where $S_{LM}(t) \equiv \langle \Psi_L(t - \Delta t) | \Psi_M(t) \rangle$ are wavefunction overlaps between different time steps. This method can be generally used for any electronic-structure method, provided that a configuration interaction representation of the electronic wavefunction can be worked out [32–35]. In the last part of (7), the coupling is conveniently written in terms of full time steps (t, $t - \Delta t$, $t - 2\Delta t$) rather than in terms of midpoints ($t + \Delta t/2$, $t - \Delta t/2$) as in the original model. This shift is explained in [33]. Comparisons between couplings computed with the finite-difference approach and with analytical derivatives are made in [33, 35, 36].

Alternatively, c_L can still be obtained by the local diabatization approach [37]. In this case, instead of integrating (4), the array of coefficients after one time step is given by

$$\mathbf{c}(t + \Delta t) = \mathbf{T}^{-1} \exp\left(-\mathrm{i}\hbar^{-1} \frac{\mathbf{E}(t) + \mathbf{T}\mathbf{E}(t + \Delta t)\mathbf{T}^{-1}}{2} \Delta t \right) \mathbf{c}(t), \tag{8}$$

where $\mathbf{E}$ is a diagonal matrix containing the adiabatic energies and $\mathbf{T}$ is an adiabatic-to-diabatic transformation constructed by a Löwdin orthogonalization of the $\mathbf{S}(t)$ wavefunction overlap matrix:

$$S_{LM}(t) = \sum_J \left\langle \eta_L(t - \Delta t) \middle| \eta_J(t) \right\rangle T_{JM}(t). \tag{9}$$

In this equation, $\{|\eta\rangle\}$ represents the diabatic basis, which is obtained along the trajectory as explained in [37]. It has been shown that this method is more stable in the presence of weak nonadiabatic couplings than conventional algorithms [38]. An alternative surface-hopping diabatization method is discussed in [39].

Either via (4) or (8), as soon as the coefficients c_L are obtained, the hopping probability can be computed and within the fewest switches approach in the adiabatic representation it is given by

$$P_{K\to L} = \max\left[0, \ \frac{-2\Delta t}{|c_K|^2}\mathrm{Re}\left(c_K c_L^*\right) \ \sigma_{LK}\right]. \tag{10}$$

In the most recent implementations of the fewest switches, the coefficients c_L are corrected for decoherence effects [8, 40–42] before probabilities are computed [43, 44].

Jaeger, Fischer, and Prezhdo recently proposed the decoherence-induced surface hopping (DISH) method, a hopping algorithm which relies entirely on the decoherence times of each adiabatic state to determine the state branching [30]. Another recently proposed alternative to the fewest switches is global-flux surface hopping (GFSH) [23], which computes the hopping probability between groups of states with reduced or increased population. In this way, hops can occur even between indirectly coupled states (super-exchange).

With hopping probabilities at a time t, a stochastic algorithm is invoked to decide in which state the dynamics continue to be in the next time step. A hopping from state K to state L occurs if a uniformly selected random number r_t in the [0, 1] interval is such that

$$\sum_{J=1}^{L-1} P_{K\to J}(t) < r_t \le \sum_{J=1}^{L} P_{K\to J}(t), \tag{11}$$

and the energy gap between the final and initial states satisfies [22]

$$E_L(\mathbf{R}) - E_K(\mathbf{R}) \le E_{\mathrm{kin}}. \tag{12}$$

Equation (12) ensures that, if the nuclear kinetic energy (E_{kin}) cannot compensate the variation of potential energy, the hop is rejected ("frustrated hop"). If the state changes, the momentum is changed accordingly to ensure conservation of total energy. Normally, the momentum adjustment is carried out in the direction of the nonadiabatic coupling vector. When the vector direction is not available, as in the case of computation of the coupling terms via (7), then the adjustment may be carried out in the linear momentum direction.

Surface hopping is not restricted to internal conversion, and other types of nonadiabatic transitions may be considered, such as those induced by spin-orbit couplings (intersystem crossing) [45, 46] or electromagnetic fields [47–50]. From a general standpoint, to consider these effects it is sufficient to redefine the coupling term in (5). For instance, a σ_{KL} including simultaneously internal conversion, intersystem crossing, and an electromagnetic field may appear as

$$\sigma_{LM} \equiv \left\langle \Psi_L \left| \frac{\partial}{\partial t} \Psi_M \right. \right\rangle - \frac{i}{\hbar} H_{LM}^{SO} - \frac{E_M - E_L}{\hbar^2 c} \boldsymbol{\mu}_{ML} \cdot \mathbf{A}_0 e^{-i\omega t}, \tag{13}$$

where H_{LM}^{SO} are the spin-orbit couplings [46] and the last term accounts for the dipole interaction of the molecule with the field ($\boldsymbol{\mu}_{ML}$ is the transition dipole moment between the L and M and $\mathbf{A}_0$ is the vector potential) [49]. In Sect. 3.2, we discuss how these couplings can be computed within the DFT framework.

3 Excited States in DFT

3.1 Excitation Energies in DFT

In this section, different approximations for the computation of excited states based on DFT are analyzed. We start from a general description of the popular linear-response (LR) TDDFT. A number of other methods for computing excitation energies based on DFT have been used for surface hopping as well. They are also described here, highlighting the hierarchic relations between them. Methods other than linear response – such as real-time TDDFT [51, 52] – or beyond linear response [53] can also be used to study excited states, but discussion of these is beyond of the scope of this chapter as these methods have not yet been generally applied for surface hopping. Multiconfigurational DFT is briefly addressed in Sect. 3.3.

The excitation energies ω_L in the LR-TDDFT are given by [54]

$$\boldsymbol{\Omega} \vec{F}_L = \omega_L^2 \vec{F}_L, \tag{14}$$

where

$$\boldsymbol{\Omega} = (\mathbf{A} - \mathbf{B})^{1/2} (\mathbf{A} + \mathbf{B}) (\mathbf{A} - \mathbf{B})^{1/2}, \tag{15}$$

and the elements of $\mathbf{A}$ and $\mathbf{B}$ are

$$A_{ia,jb} = \delta_{ij} \delta_{ab} \Delta\varepsilon_{jb} + K_{ia,jb}, \tag{16}$$

$$B_{ia,jb} = K_{ia,bj}. \tag{17}$$

In these equations, i and j denote occupied orbitals and a and b denote virtual orbitals. **A** and **B** are defined here for a restricted approach, single excitation, and a functional without any fraction of Hartree–Fock exchange. For more general expressions, see Eq. (4.33) of [54]. For hybrid functionals, see Eqs. (95) and (96) of [55].

In (16) and (17),

$$\Delta\varepsilon_{jb} = \varepsilon_b - \varepsilon_j, \tag{18}$$

is the difference between the KS energies of the orbitals and

$$K_{ia,jb} = (ia|jb) + (ia|f_{\mathrm{XC}}|jb), \tag{19}$$

is given in terms of the two-electron integrals

$$(ia|jb) = \int\int d\mathbf{r}d\mathbf{r}'\psi_i(\mathbf{r})\psi_a(\mathbf{r})(\mathbf{r}-\mathbf{r}')^{-1}\psi_j(\mathbf{r}')\psi_b(\mathbf{r}'), \tag{20}$$

$$(ia|f_{\mathrm{XC}}|jb) = \int\int d\mathbf{r}d\mathbf{r}'\psi_i(\mathbf{r})\psi_a(\mathbf{r})f_{\mathrm{XC}}\psi_j(\mathbf{r}')\psi_b(\mathbf{r}'), \tag{21}$$

for real KS orbitals ψ_k and within the adiabatic local density approximation (ALDA) [54]:

$$f_{\mathrm{XC}} = \frac{\delta^2 E_{\mathrm{XC}}}{\delta\rho(\mathbf{r})\delta\rho(\mathbf{r}')}, \tag{22}$$

where E_{XC} is the exchange-correlation energy.

If f_{XC} is neglected, the time-dependent Hartree–Fock (also known as the random phase approximation, RPA) is recovered [55]. If $\mathbf{B} = 0$, we have the Tamm–Dancoff approximation (TDA) [55], which has often been used for surface hopping (see Sect. 4). Another approximation also often used in SH/DFT is the time-dependent density-functional-based tight binding (TD-DFTB) [56]. TD-DFTB is based on a second-order expansion of the KS total energy with respect to charge-density fluctuations, followed by a time-dependent linear-response procedure, where the transition densities $\psi_i\psi_a$ in the coupling matrix $K_{ia,jb}$ (see (19)–(21)) are approximated by atom-centered contributions [57].

To understand the next DFT methods for computing excitation energies and to have a better insight of the meaning of the TDDFT solutions, we may explicitly check the structure of the TDDFT energies for a simple case of one occupied orbital p and two virtual orbitals r and s (Fig. 1). For this minimal system, the eigenvalue problem in (14) can be written as

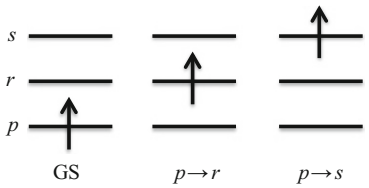

Fig. 1 Schematic illustration of a reduced system with one occupied and two virtual orbitals. The ground state (GS) determinant can give an origin to two single excitations

$$\begin{bmatrix} \Omega_{pr,pr} & \Omega_{pr,ps} \\ \Omega_{ps,pr} & \Omega_{ps,ps} \end{bmatrix} \begin{bmatrix} F_1 \\ F_2 \end{bmatrix} = \omega^2 \begin{bmatrix} F_1 \\ F_2 \end{bmatrix}. \tag{23}$$

The eigenvalues of this Hermitian problem are

$$\omega_{2,1}^2 = \left(\frac{\Omega_{pr,pr} + \Omega_{ps,ps}}{2} \right) \pm \sqrt{\left(\frac{\Omega_{pr,pr} - \Omega_{ps,ps}}{2} \right)^2 + \Omega_{pr,ps}^2}. \tag{24}$$

If the nondiagonal terms of $\mathbf{\Omega}$ are null (which occurs when $K_{pr,ps} = K_{ps,pr} = 0$, see (26)), the excitations energies are simply

$$\omega_1 = \Omega_{pr,pr}^{1/2} \quad \omega_2 = \Omega_{ps,ps}^{1/2}, \tag{25}$$

implying that the energy of each state is associated with a unique singly-excited determinant (for instance, $p \rightarrow r$) and independent from the remaining determinants.

The matrix elements of $\mathbf{\Omega}$ can be explicitly written as (see Eq. (4.33) of [54])

$$\Omega_{ia,jb} = \delta_{ij}\delta_{ab}\Delta\varepsilon_{jb}^2 + 2\sqrt{\Delta\varepsilon_{ia}} K_{ia,jb} \sqrt{\Delta\varepsilon_{jb}}. \tag{26}$$

With (26), the lowest excitation energy in (25) becomes

$$\omega_1 = \sqrt{\Delta\varepsilon_{pr}^2 + 2\Delta\varepsilon_{pr} K_{pr,pr}}. \tag{27}$$

An equivalent equation holds for ω_2 caused by $p \rightarrow s$ excitation. If $K_{pr,pr} \ll \Delta\varepsilon_{pr}$, the excitation energy can be approximated by

$$\omega_1 \simeq \Delta\varepsilon_{pr} + K_{pr,pr}. \tag{28}$$

This result corresponds to the excitation energy computed with density functional perturbation theory to the first order [58] and it is also directly obtained with TDA ($\mathbf{B} = 0$).

If $K_{pr,pr}$ is completely neglected, the excitation energy is given simply by the bare energy gap between orbitals

$$\omega_1 \simeq \Delta\varepsilon_{pr} = \varepsilon_r - \varepsilon_p. \tag{29}$$

corresponding to the zeroth order of the perturbative expansion [59].

One realistic situation where $K_{pr,pr}$ is near zero occurs in charge-transfer states. In such cases, ψ_p and ψ_r are localized in different parts of the molecules with little overlap. The excitation energy reduces to (29), which does not have the expected 1/R Coulomb attraction term, rendering the well known underestimation of the charge-transfer excitation energies [55].

The LR-TDDFT excitation energies given by (14) are derived by an analytic treatment of the poles of the dynamic polarizability of KS orbitals dynamically perturbed by an external field [54, 55]. We have seen that LR-TDDFT improves the bare KS energy gap, (29), through two kinds of corrections: first, with diagonal terms which shift the energy of the uncoupled single excitation, (28), and, second, with nondiagonal terms, which bring contributions from all other single excitations in the KS orbital space, (24) [60].

A series of methods based on independent propagation of non-interacting orbitals through the time-dependent KS equation have been proposed to be used in connection with surface hopping [61–64]. In such methods, derived aiming at large systems with high density of states, the excited states are computed from single determinants or spin-adapted single configurations using KS orbitals, with energies given by the bare KS gaps. Equation (29) is a particular case for an excited state represented by a singly-excited determinant. For more general cases, see Eq. (20) of [61]. Throughout this chapter we refer to this class of methods for determining DFT excitation energies as single-determinant Kohn–Sham (SDKS).

A two-determinant DFT excitation method, the restricted open-shell Kohn–Sham (ROKS) by Frank and co-authors [65], was often employed in the earliest investigations of SH/DFT [66–68]. In that approximation, the ground state is taken as the usual closed-shell KS determinant, while the first excited state is represented by a spin-adapted singly-excited singlet configuration. The two determinants forming the configuration are formed from excited-state KS orbitals, which are obtained by optimizing an ad hoc energy functional designed to represent the singlet-triplet split in a two-electron/two-orbital configuration. Other formulations of restricted open-shell Kohn–Sham formalism have also been proposed in [69–71], but, as far as we know, they have not been used in surface hopping simulations.

3.2 Nonadiabatic Couplings in DFT

Nonadiabatic couplings between different electronic states are needed for propagation of surface hopping dynamics. While analytical energy gradients for excited states computed with TDDFT are well established [72] and implemented in diverse computational-chemistry programs, analytical nonadiabatic couplings are still mostly unavailable.

The theoretical background for computation of these couplings has been established by Chernyak and Mukamel [73] and, alternatively, by Baer [51]. Hu and co-workers have further developed the Chernyak–Mukamel approach for computation of first-order nonadiabatic coupling vectors between the ground state and the first excited state [74–76]. Send and Furche have shown that the previous result neglects molecular orbitals derivatives [77]. Their own derivation, including such terms but still limited to couplings between the ground and the first excited states, is implemented in Turbomole [78].

Because of the lack of analytical couplings between excited states in standard quantum-chemistry programs, finite-difference couplings have been largely used in surface hopping [32–34]. They are usually based on the approach proposed by Hammes-Schiffer and Tully [31], who showed that the couplings can be written in terms of wavefunction overlaps between sequential time steps during the dynamics – see (7).

A particular problem with using TDDFT in this approach is the lack of an explicit wavefunction for the electronic states. A common solution has been to take the Casida's ansatz for the state assignment [54] as an approximation to the wavefunctions. In this case, the ground- and excited-state wavefunctions are given (for a local functional) by

$$\Psi_0 = |\mathrm{KS}\rangle, \tag{30}$$

$$\Psi_L = \sum_{j,b} \sqrt{\frac{\Delta\varepsilon_{jb}}{\omega_L}} F_L^{jb} |jb\rangle, \tag{31}$$

where $|\mathrm{KS}\rangle$ is the ground-state KS determinant and $|jb\rangle$ is the determinant with a single excitation from j to b. With these wavefunctions, which are analogous to a CIS expansion, the coupling terms σ_{LM} can be evaluated according to (7) in terms of atomic orbital overlap integrals [33]. Although the validity of Casida's ansatz for computation of couplings approach still needs to be extensively tested, it has been shown that TDDFT dynamics computed with these couplings compares well with dynamics based on CASSCF [79] and MRCI [80].

Equation (31) forms a non-orthogonal set, which can have consequences for the evaluation of the couplings. Werner et al. [81] recommended the use the linear-response coefficients without the square-root term in (31) as the CIS coefficients, which forms an orthogonal set within TDA. An alternative solution is to orthogonalize the approximate wavefunctions given by (31) before computing the couplings. In practical terms, far from conical intersections with the ground state, either of these approximations provides similar dynamical pictures. In some cases, negative excitation energies are obtained (see Sect. 3.3), and consequently the wavefunctions are complex and imaginary couplings may be obtained. In such situations, as we discuss later, it is not recommended to continue the SH/TDDFT propagation.

The Casida wavefunctions given in (30) and (31) have been employed by Tavernelli and co-workers to derive analytical nonadiabatic coupling vectors

between the ground and the first excited states [82] and also between excited states [83]. They are given by

$$\boldsymbol{\tau}_{0L} = \sum_{ia} \sqrt{\frac{\Delta\varepsilon_{ia}}{\omega_L}} F_L^{ia} \langle \psi_i | \nabla_{\mathbf{R}} H_{\mathrm{KS}} | \psi_a \rangle, \tag{32}$$

$$\begin{aligned} \boldsymbol{\tau}_{LM} = & \sum_{iab} \sqrt{\frac{\Delta\varepsilon_{ia}}{\omega_L}} \sqrt{\frac{\Delta\varepsilon_{ib}}{\omega_M}} F_L^{ia\dagger} F_M^{ib} \langle \psi_a | \nabla_{\mathbf{R}} H_{\mathrm{KS}} | \psi_b \rangle \\ & - \sum_{ija} \sqrt{\frac{\Delta\varepsilon_{ia}}{\omega_L}} \sqrt{\frac{\Delta\varepsilon_{ja}}{\omega_M}} F_L^{ia\dagger} F_M^{ja} \langle \psi_i | \nabla_{\mathbf{R}} H_{\mathrm{KS}} | \psi_j \rangle. \end{aligned} \tag{33}$$

(As in the previous section, ψ_k corresponds to the molecular orbitals, i, j run over occupied orbitals, and a, b over virtual orbitals.)

In [84] it is shown that $\boldsymbol{\tau}_{0L}$ in (32) is equivalent to the analytical coupling vector derived by Hu et al. in [74], but, also as the Hu et al.'s result, it does not fully agree with Chernyak–Mukamel [73]. Ou et al. [36] have pointed out that in the formalism leading to (32) and (33), only the KS Fock matrix is differentiated, omitting the full coupling induced by the second derivative of the exchange-correlation functionals. Still working with a CIS expansion based on TDA amplitudes, these authors have derived nonadiabatic coupling vectors (including excited-excited terms) fully consistent with Chernyak–Mukamel [36].

Apart from their limitations, (32) and (33) are general results, which are still valid by replacing the operator $\nabla_{\mathbf{R}} H_{\mathrm{KS}}$ by any single-body operator $\hat{O}$ [83], such as, for example, the electronic dipole operator, to obtain the transition dipole moment $\boldsymbol{\mu}_{LM}$.

Recently, spin-orbit coupling elements [85] were also derived based on the Casida wavefunctions, opening the possibility of performing surface hopping between surfaces with different multiplicities within the TDDFT approach. The coupling between singlet and triplet states, for instance, is given by

$$H_{ST}^{SO} = \sum_{ia\rho, jb\rho'} \sqrt{\frac{\Delta\varepsilon_{ia\rho}}{\omega_S}} F_S^{ia\rho} \sqrt{\frac{\Delta\varepsilon_{jb\rho'}}{\omega_T}} F_T^{jb\rho'} \langle ia_S | H^{SO} | jb_T \rangle, \tag{34}$$

where ρ and ρ' are spin indexes. In [85], H^{SO} is approximated by the one-electron Breit–Pauli operator [86]. The computation of the two-electron operator is discussed by Chiodo and Russo in [87, 88].

In [89], the computation of Dyson orbitals based on Casida wavefunctions is discussed. These Dyson orbitals were used to evaluate photoionization cross-sections during the dynamics and to simulate time-dependent photoelectron imaging spectra.

In SDKS methods, the computation of the couplings is largely simplified by the singe-determinant approximation. As shown in (21) of [61], the couplings in such

cases are reduced to derivatives of KS orbitals, which can be inexpensively computed by finite differences during dynamics propagation.

For a discussion about the computation of the nonadiabatic couplings with ROKS, see [90]. For a discussion about computation of these couplings with REKS, see [91].

3.3 *Critical Appraisal*

One of the main challenges in excited-state dynamics simulations is that trajectories span large regions of the configuration space. Thus, the electronic structure method used to compute energies, energy gradients, couplings, and other properties should be able to deal with the large variety of electronic densities induced by different conformations.

A good deal of the problem arises from a bad description of the ground state (see Fig. 2). Strictly speaking, DFT should be valid even at the crossing seam between the ground and the first excited state, as the Hohenberg–Kohn theorems [92] can be generalized to degenerate ground states [93, 94]. However, the KS formulation of DFT needs to fulfill two basic conditions [95]: (1) the reference state should be a single-determinant state to compute exchange energy and (2) the correlation hole should be reasonably described by homogenous (or weakly inhomogeneous) electron gas to compute the correlation energy. In diverse cases, for instance in biradicals species, where nondynamic electron correlation plays a strong role, one or both conditions are not satisfied, rendering a bad description of the ground state

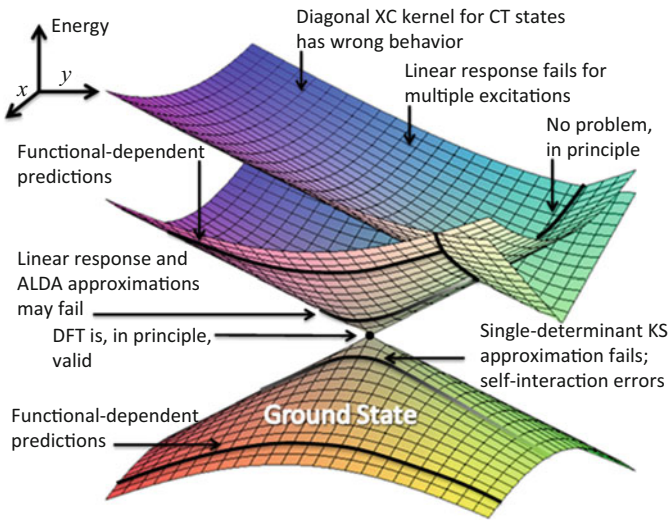

Fig. 2 Illustration of the main problems with DFT and TDDFT occurring in different regions of the ground- and excited-state surfaces

and, consequently, of the excited-states based upon. In particular, the methods for computing excitation energies discussed in Sect. 3.1 have in common the assumption that the ground state can be described by a single KS determinant. (For a conceptual discussion of nondynamic electron correlation in DFT, see [95]. For a discussion about conical intersection in DFT, see [96]).

The development of a density functional theory including nondynamic (or "strong") electron correlation – which Becke designated as the "last frontier" in DFT [97] – has been pursued by many groups following different approaches. Among these approaches, we may cite the use of restricted open-shell ground-state representations [98], configuration ensembles with fractional occupations [91, 99–101], configuration interaction [102, 103], multiconfigurational DFT [104], hybrid multiconfiguration/(TD)DFT [105, 106], and spin-unrestricted broken-symmetry (UBS) [107] approaches. Unfortunately, analytical energy gradients are not available for most of these methods, which rules out their use in surface hopping dynamics.

All the troubles caused by nondynamic electron correlation are rather restricted to the crossing between the ground and the first excited state. In the case of crossing between excited states, however, if each of these states is well represented by single excitations from a well-behaved ground state, the description of the crossing does not present further problems.

SH/DFT has other potential problems (Fig. 2) besides nondynamical electron correlation. First, the results are deeply dependent on the functional. Second, double and higher excitations are not properly described by LR-TDDFT. Third, diffuse and charge-transfer states may be poorly described by conventional functionals. All these problems, though, are not exclusive of dynamics simulations and are part of routine investigations of excited states based on DFT. As such, they are addressed in the same way, by systematic test of functionals, methodological comparisons, and use of range-separated functionals.

To illustrate the current situation of excited state description for SH/DFT, we show in Fig. 3 the potential-energy surfaces for the S_1 state and for the S_1/S_0 gap of ethylene along two important reaction coordinates, H_2CCH_2-torsion (θ) and CCH_2-pyramidalization (φ). All other coordinates are kept at their ground-state values optimized at the same level as used for energy calculations. These surfaces were computed with several different DFT-based methods and with ab initio MR-CISD, which is taken as the reference method. With the exception of the DFT-MRCI [102], computed with the SV(P) basis set [108], all other DFT-based surfaces were computed with the 6-31G* basis set [109]. LC-BLYP [110–112] was computed with $\mu = 0.2\ a_0^{-1}$ [113]. TD-DFTB was based on analytic expressions for the matrix elements [114]. MR-CISD was based on a small (two electron, two orbital)-space [115] with the aug-cc-pVTZ basis set [116] assigned to C and cc-pVDZ assigned to H.

Ethylene S_1 surface is a specially challenging problem, starting from (i) the adequate computation of the excitation into the V state [6], then (ii) the description of the right topography of the state, which includes a crossing with the Z state near the twisted structure and a conical intersection at twisted-pyramidalized geometries

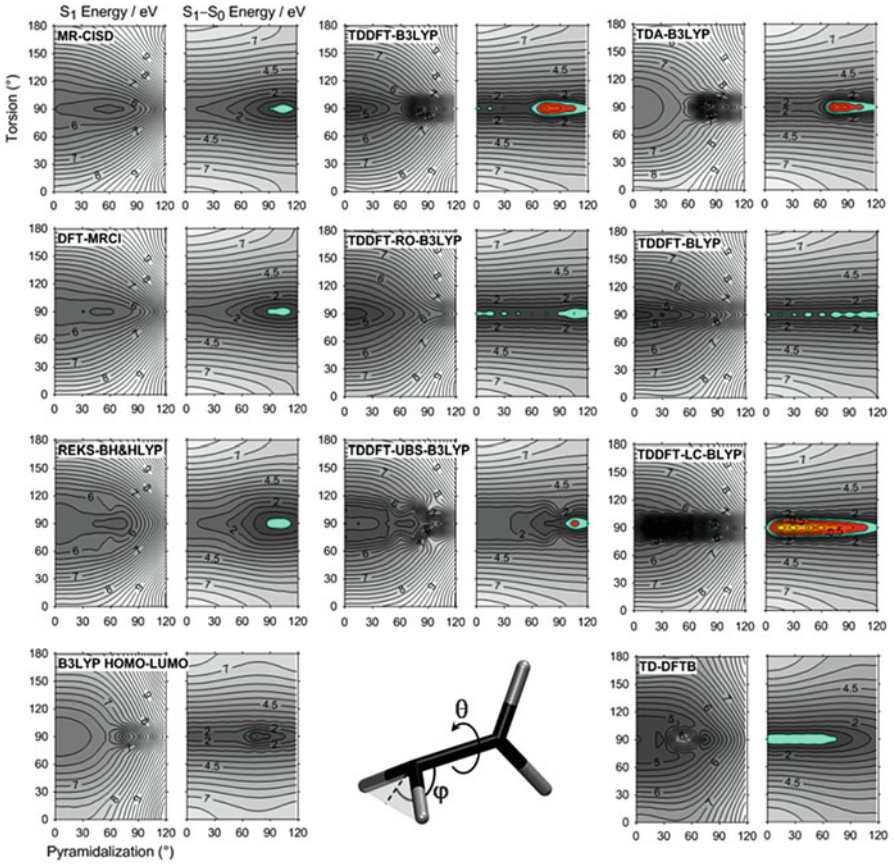

Fig. 3 S_1 and S_1/S_0 potential-energy surfaces of ethylene computed with diverse methods. *Green regions* indicate the crossing seam. *Red/orange regions* are negative energy gaps. In the illustration, ethylene has $\theta = 90°$ and $\varphi = 45°$

[115], to finally (iii) the dynamics evolution itself, which has motivated a long debate between theorists and experimentalists [117–119]. In fact, Levine et al. [120] have used maps similar to those in Fig. 3 (but computed for stretched CC distances) to discuss the qualitative deficiencies in the excited-state description provided by TDDFT.

The MR-CISD result in Fig. 3 has two main features which dominate the topography and the dynamics in the S_1 state: (a) there is an S_1 minimum near $\theta = 90°$ and $\varphi = 60°$ and (b) there is a conical intersection at $\theta = 90°$ and $\varphi = 110°$. Among all tested methods, the only ones able to reproduce both features are the DFT-MRCI [102] and REKS [91, 99, 101], which makes clear the importance of having a multiconfigurational description of the ground state. TDDFT-UBS, which is usually considered a good alternative for qualitatively recovering nondynamic electron correlation near a degeneracy [71], can describe reasonably well the

conical intersection, but the topography along the $\theta = 90°$ line shows diverse spurious minima.

Spurious minima were also observed in TDDFT and TDA with B3LYP [121, 122]. The minimum is at a qualitatively wrong position at TDDFT-B3LYP with restricted open shell (TDDFT-RO). The same happens for TDDFT-BLYP. TDA can qualitatively predict the conical intersection ($\theta = 90°$, $\varphi > 70°$). Somewhat surprisingly, the simple HOMO–LUMO gap is the only other method predicting a twisted-pyramidalized conical intersection (at $\theta = 90°$, $\varphi = 70°$). All other methods wrongly predict an extended S_1/S_0 seam along the $\theta = 90°$ line, starting from $\varphi = 0°$.

A disturbing feature which can be observed in TDDFT-B3LYP, TDDFT-UBS-B3LYP, TDA-B3LYP, and TDDFT-LC-BLYP is that the excitation may become negative near the crossing seam. This is not an exclusive problem with DFT-based methods; it can be observed in other single-reference methods as well, such as coupled cluster with either equation-of-motion or linear-response approaches.

As discussed in [123], near the degeneracy, self-interaction errors may cause the HOMO to be less stable than the LUMO, leading to imaginary excitation energies in TDDFT – see (27). This does not happen at TDA because the excitation energy is given by terms such as those in (28). This feature has been said to represent an improved stability of the TDA-based dynamics in comparison to that based on TDDFT [123]. Nevertheless, as we can see in the negative gap regions in Fig. 3, both methods are still unstable near the degeneracy. These negative excitations are clearly caused by the mixing with the other singly-excited determinants, which cannot be avoided either in TDDFT or in TDA.

In SDKS methods, the excitation energies are given by the bare KS gaps [61]. In the case of the ethylene, we can see in Fig. 3 that the bare KS energy (given by the HOMO–LUMO gap and neglecting double excitations near the twisted structure) gives an adequate representation of the S_1 state and of the S_1/S_0 gap. This good behavior, however, should not be taken for granted. Maitra [60], in a critical discussion of these approximation in the context of surface hopping, showed that the bare KS energies may be far from adiabatic and closer to diabatic energies.

Ethylene is admittedly too harsh a case for DFT-based methods, as its dynamics is deeply controlled by coordinates involved in the nonadiabatic events. SH/DFT methods have been developed to deal with large molecular systems and in these cases the dynamics may evolve in the configurational space spanning regions relatively far from any muticonfigurational ground state. Under such situation, the excited-state dynamics involving a large manifold of excited states can be well simulated with DFT-based methods.

Take, for instance, the schematic dynamics illustrated in Fig. 4 (top). The dynamics starts at a high excited state (here, the second state to simplify the picture). Using a multireference method such as MRCI, we would observe a relaxation to the first excited state (a), then oscillation around the minimum of this state (b). From this minimum, the molecule can eventually fluoresce to the ground state (c) or cross a barrier (d) to reach a conical intersection, from where it relaxes to the ground state minimum (e).

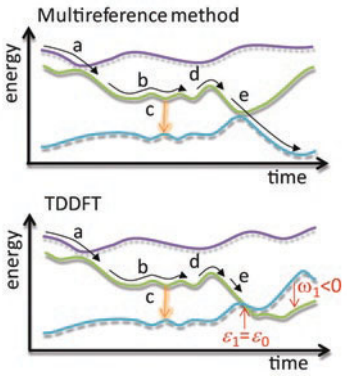

Fig. 4 Schematic comparison of a trajectory computed with surface hopping based on multireference method (*top*) and on TDDFT (*bottom*)

In principle, SH/TDDFT can adequately describe most of this process (Fig. 4, bottom). The relaxation through the manifold of excited states (a) can be described if these states are dominated by single excitations from a well-behaved ground state and if the functional allows the description of special features such as charge-transfer states. The oscillation around the excited minimum (b) is also not a problem, at least if this minimum is not on the top of a multiconfigurational ground state. Neither the radiative process (c) nor the barrier crossing (d) presents any special problems, apart from functional dependencies. Even the relaxation until near the crossing with the ground state (e) can in principle be described. In fact, this whole process may be better described with TDDFT and other correlated single-reference methods such as the algebraic diagrammatic construction to the second order (ADC(2) [124, 125]), than with an uncorrelated multiconfigurational method such as CASSCF [35]. The real problem starts very close to the state crossing (usually for energy gaps smaller than 0.1 eV), where the convergence of the KS equations tends to fail and, even if convergence is achieved, regions with negative excitation energies may be reached. Besides that, as discussed by Levine et al.[120], the lack of nonadiabatic interactions between the ground and the excited states may lead in some cases to the wrong dimensionality of the intersection seam with the ground state. (See [126] for a comparative discussion of the shape of the crossing seam computed with different methods.)

Although diverse groups working with SH/DFT choose to compute hops to the ground state, it is our opinion that the results obtained from this procedure are not reliable. We have adopted a strategy to stop the dynamics simulations as soon as a certain energy-gap threshold is reached, usually 0.15 eV (see, for instance, [127]). This last time step is then taken as an estimate of the time for internal conversion to the ground state. This strategy, which we apply not only for TDDFT, but also for ADC(2) [35, 128], allows the computation of excited-state lifetimes and the early split of population between different reaction channels, but unfortunately it does not provide enough information for computation of reaction yields in the ground state.

4 Surface-Hopping/DFT Implementations

One of the reasons for the popularity of the surface hopping method is that its implementation is straightforward. This has given rise to several home-made private codes to simulate SH/DFT [62, 63, 81, 129]. There are also a few general programs of public access (either commercial or non-commercial) with SH/DFT capability, including Newton-X [130, 131], PYXAID [61, 132], Turbomole [78], and CPMD (www.cpmd.org).

The main difference between the several implementations of SH/DFT is exactly which DFT method is being used for computing the electronic-structure quantities. The main features of the most common implementations are summarized in Table 1.

The most computationally efficient implementation of SH/DFT available is based on SDKS approximations [134], such as that implemented in the PYXAID program using plane waves. Variants of this method have also been developed by Fischer, Handt, and Schmidt [50, 62, 135] using Gaussian functions, by Gao and co-workers using DFTB KS orbitals [63], and by Shenvi, Roy, and Tully based on a model Hamiltonian parameterized by DFT data [64, 136]. SDKS has been used to investigate diverse problems, especially in condensed matter (see Sect. 5). Besides the computational efficiency granted by the single-determinant approximation, Shenvi and co-workers [64] have pointed out that, while in TDDFT the electronic Hilbert space must be truncated to include only a relatively small number of states, this restriction does not apply to SDKS, being a big advantage for the treatment of systems with large density of states. Moreover, SDKS also allows the inclusion of double and higher excitations [61]. On the down side, the bare KS energy gaps may

Table 1 Survey of diverse implementations of SH/DFT. Excited states can be computed with linear response time-dependent (LR-TD) theory, single determinant KS (SDKS), or restricted open shell KS (ROKS); single (SS) or multiple (MS) excited states can be included; states can be restricted to single (SE) or multiple (ME) excitations; propagation can be done in terms of Gaussian functions (GF) or plane waves (PW)

DFT excitations	Number of states	Excitation level	Basis type	Refs.	Public implementation
LR-TDDFT	MS	SE	GF	[32]	Newton-X
LR-TDDFT	SS	SE	GF	[77]	Turbomole
LR-TD-DFTB	MS	SE	GF	[133]	
TDA	MS	SE	GF	[38]	Newton-X
TDA	MS	SE	PW	[34, 83]	CPMD
ROKS	SS	SE	PW	[68]	CPMD
SDKS	MS	ME	GF	[63]	
SDKS	MS	ME	GF	[62]	
SDKS	MS	ME	PW	[61, 134]	PYXAID

not only deviate strongly from the exact energies, but also provide a poor approximation for adiabatic surfaces [60].

Still aiming at maximum computational optimization, Prezhdo and co-workers have also introduced the so-called "classical path approximation" (CPA) in PYXAID [61]. The CPA implies that the nuclear dynamics is supposed to evolve independently of the electrons, driven by kinetic effects. In practical terms, it means that the nuclear dynamics is propagated in the ground state and then is used to compute the nonadiabatic electronic events in the excited states using either the fewest switches surface hopping or one of the other surface hopping algorithms developed by the Prezhdo group [132]. The CPA may be especially inadequate for systems undergoing significant chemical changes such as photofragmentation and chemical reactions.

Another efficient implementation of SH/DFT is based on ROKS and was developed by Doltsinis and Marx [137]. The spin-adapted wavefunctions and the KS orbitals optimized for the excited-state density should in principle be an improvement over the SDKS. SH/ROKS, however, is limited to a single excited state, which is a very strong limitation for most realistic problems. Such an approach is implemented in the CPMD program.

SH/LR-TDDFT has been pioneered by Tavernelli and Rothlisberger [34] and by Mitrić and Bonačić-Koutecký [81]. Linear response should provide a better description of the excited-state surfaces than single determinant and ROKS approaches, at higher computational costs naturally (see Sect. 3.1). TDDFT is also not limited to a single surface as ROKS, but it cannot describe multiple excitations. In the framework of linear response, surface hopping dynamics has been investigated with TDDFT, TDA, and TD-DFTB (see Sect. 5). In the CPMD program, this approach is implemented based on plane waves, while in Newton-X, it is implemented on a localized basis. It is also implemented in Turbomole, but limited to couplings between the ground state and the first excited state. Ehrenfest dynamics [138], another related semiclassical nonadiabatic dynamics method, can be performed with TDDFT using the Octopus program [139].

In the case of Newton-X, the coefficients c_L to compute the hopping probabilities (10) can be obtained either by integrating (4) or by using the local diabatization method (8). The program also allows the computation of surface hopping through interfaces with different programs (Turbomole, Gaussian [140], Columbus [141, 142], Gamess [143]) and using different methods (TDA, TDDFT, ADC(2), CC2, CASSCF, MRCI), making it particularly convenient for comparative analysis.

5 Case Studies

There are a large number of molecular systems which have been investigated with SH/DFT. This section does not aim at providing a comprehensive review of them, but instead at pointing out the main classes of problems in different fields, from where the reader can search for more information.

SH/DFT has been developed mainly for the treatment of large systems, for which wavefunction-based methods are computationally too expensive. It is possible, however, to find a series of investigations for photoreactions of small molecules (see Table 2), which has been useful to gauge the quality of these simulations.

Table 2 Survey of case studies with SH/DFT

System	Method	Refs.	System	Method	Refs.
Basic processes in small molecules			*Systems of biological interest*		
Pyrrole, imidazole, furan	TDDFT	[80, 89, 144]	Diphenyldibenzofulvene	SDKS	[63]
Pyrazine	TDDFT	[81, 145]	Riboflavin	TDDFT	[146]
Pyrrole	ROKS	[147]	Kynurenine	TDDFT	[129]
CH_2=NH	ROKS	[68]	Adenine	TDDFT	[35, 148]
CH_2=NH_2^+	TDA, SDKS	[79, 149]	Adenine gas and in water	TDDFTB	[133]
CH_2Cl–CF_3	TDDFT	[150]	Guanine, cytosine, uracil,	ROKS	[66, 151–153]
Oxyrane	TDA	[123]	Guanine-cytosine pairs	ROKS	[154]
Indole in water	TDDFT	[155]	Protonated tryptophan	TDA	[156]
$O(^3P) + C_2H_2$ (ISC)	ΔUDFT	[157]	Acetylphenylalaninylamide	TDDFT	[158]
Photoinduced proton transfer, isomerization			*Systems of interest for materials sciences, surfaces*		
Hydroxyquinoline-NH_3	TDA	[159]	Carbon nanotubes	SDKS	[160, 161]
Methylformamide dimer	TDDFT	[127]	Graphene	SDKS	[162]
Bridged azobenzene	ROKS	[163]	$Cd_{33}Se_{33}$, $Si_{29}H_{24}$ (quantum dot)	SDKS	[23, 149]
Azobenzene gas and in water	ROKS	[164]	NO/Au(111)	SDKS	[64, 136]
Azobenzene, stilbene	SDKS	[165]	Pentacene crystal	SDKS	[61]
Diphenydibenzofulvene	SDKS	[63]	Pentacene/C_{60}	SDKS	[166]
Catalysis			*Reviews*		
$Cr(CO)_6$	TDDFT	[167]	Nonadiabatic phenomena		[8, 126, 168]
Ru (II) trisbipyridine in water	TDA	[169]	Surface hopping		[11, 138, 170]
Chromophore-TiO_2	SDKS	[134]	Dynamics/TDDFT		[20, 171]
Water splitting on GaN	SDKS	[172]	DFT excited states		[54, 55, 173]

$CH_2NH_2^+$, for instance, has been used as a test case of SH/TDA [34, 79] and SH/SDKS [149]. In both cases, qualitative agreement with surface SH/CASSCF [174] is observed. We should note, however, that this agreement may be accidental, as $CH_2NH_2^+$ is a very small system with only two relevant excited states, a single dominant reaction path, and a lifetime shorter than 100 fs. More impressive is the semi-quantitative agreement observed between SH/TDDFT [80] and SH/MRCI [175] for pyrrole. In this case, TDDFT dynamics with ten excited states has successfully predicted the excited-state lifetime and the split of population among several reaction paths.

A more applied class of systems investigated with SH/DFT excitations involves photoinduced proton transfer and photoinduced isomerization in medium-sized molecules. A typical example of such a class is azobenzene, which has been studied with SH/ROKS [164] and SH/SDKS [165]. Dynamics based on both provides a good description of the *cis-trans* isomerization of azobenzene in the gas phase in comparison to other semiempirical and ab initio wavefunction-based surface hopping simulations [176–180]. Azobenzene has been chosen by a number of groups, including ours, as a standard test case for methods. We should consider, however, that this molecule may not be challenging enough to be a good test case. After S_1 excitation, azobenzene evolves adiabatically until finding the intersection to the ground state, approaching the crossing seam along torsional coordinates. These features imply that neither nonadiabatic effects between excited states nor the dimensionality of the crossing seam can be really tested with this system. On the other hand, azobenzene is an excellent system to probe the topography of S_1 and the S_1/S_0 coupling strength, which can be done through simulations of excited-state lifetime and isomerization yield.

One of the main problems with SH/DFT is the deep dependence on the chosen functional. This can be illustrated with an example we have recently investigated, the excited-state dynamics of *N*-methylformamide dimer (NMF) [127]. These simulations showed that NMF dimers are protected against photodissociation by a proton-transfer mechanism. The excited-state proton transfer occurs according the Sobolewski–Domcke mechanism [181], where an electron is transferred first, followed by the proton (see Fig. 5). For properly describing the charge-transfer state, SH/TDDFT was done with the range-separated LC-BLYP functional [110–112]. The range-separation parameter was fixed at $\mu = 0.2\ a_0^{-1}$, a value based on a non-empirical parameterization [113]. Our tests with diverse other values of μ showed that the ratio between dissociation and proton transfer was deeply dependent on this parameter. Not surprisingly, larger values favored dissociation by under-stabilizing the charge-transfer state. (In the Gaussian program [140], for instance, the default value of μ is $0.47\ a_0^{-1}$.) Lower values favored proton transfer for the opposite reason.

Diverse systems of biological interest have also been investigated with SH/DFT (see Table 2). In this class, a challenging case has been the description of purine nucleobases. An indication of the problem was already in the earliest simulations of 9Me-keto guanine with SH/ROKS [151, 152], whose trajectories did not reveal any conical intersection with the ground state. At that point, the internal conversion of

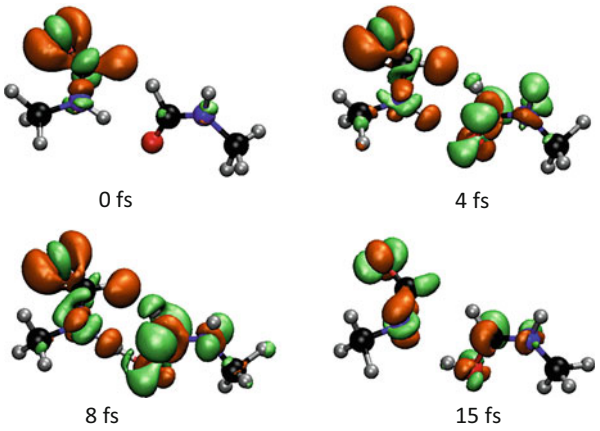

Fig. 5 Evolution of the (S_1-S_0) electron density difference during a single surface-hopping trajectory of *N*-methylformamide dimer computed with TDDFT with LC-BLYP ($\mu = 0.2\ a_0^{-1}$). *Green* (*orange*) indicates electron acceptor (donor) regions (Based on data from [127])

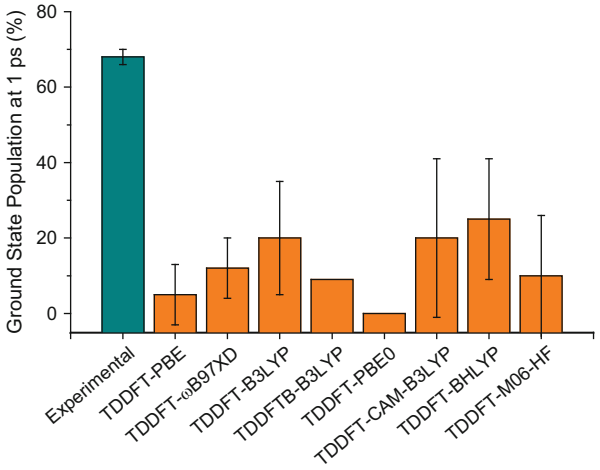

Fig. 6 Ground-state population of adenine gas 1 ps after photoexcitation according to the experiment [182] and surface hopping based on diverse LR-TDDFT simulations. TDDFT data from [35, 148]. TDDFTB from [133] (supposing simple exponential decay). Sampling error of the simulations for 90% confidence level

guanine was attributed to an enhanced nonadiabatic coupling promoted by out-of-plane vibrations. Later, SH/TD-DFTB [133] predicted an excited-state lifetime of 11 ps for adenine gas, ten times longer than the experimental result. The deviation was then attributed to the distribution of initial energies. More recently, systematic investigations of adenine gas with SH/TDDFT with several functionals once more led to very long excited-state lifetimes [35, 148]. These results are conveniently plotted in Fig. 6 in terms of the S_0 population 1 ps after photoexcitation. Even the most optimistic SH/TDDFT simulation at the limit of the error bar is inferior to 40%, while the experimental result reaches 68%. The root of the problem seems to be connected to an overstabilization of the ground state energy along planar distortions in comparison to nonplanar distortions. This unbalanced ground state profile leads to a wrong description of the excited-state minimum [148].

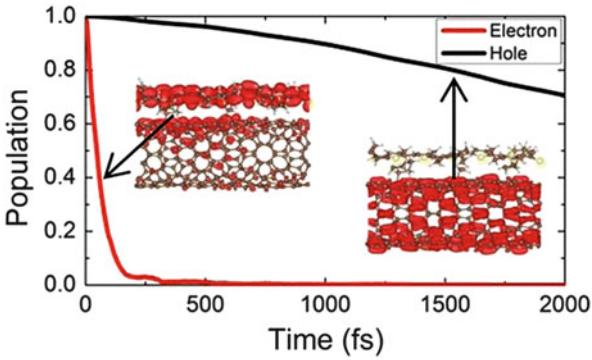

Fig. 7 Decay of the population of the electron and hole donor states in a P3HT (donor) – nanotube (acceptor) interface. (Reprinted with permission from [161]. Copyright 2014 American Chemical Society)

SH/SDKS has allowed the limits of the simulations to be stretched much beyond what can currently be done with TDDFT or wavefunction-based methods. In particular, it has allowed one to investigate large organic chromophores [63], adsorbance of molecules on metal [64, 136] and semiconductor [134, 172] surfaces, Auger dynamics in quantum dots [23], carbon nanostructures [160, 162], and organic crystals [61, 166].

An interesting example in this class of systems related to condensed matter and materials science is the recently published simulations for a P3HT/carbon-nanotube heterojunction [161]. Organic heterojunctions have been intensively explored for the development of organic photovoltaics based on photoinduced electron transfer [183, 184]. P3HT (poly(3-hexylthiophene)) is a standard organic polymer used as chromophore and electron donor [185], while carbon nanotubes (CNT) are electron-acceptor materials with enhanced charge-transport properties [186]. Notwithstanding the limitations of DFT to approach this type of system [187], dynamics with SH/SDKS predicts that there is a strong asymmetry between the electron and hole transports in P3HT/CNT interface (Fig. 7). While photoexcitation of P3HT leads to an electron transfer within 100 fs, the hole transfer takes much longer, occurring on the few picoseconds scale.

6 Conclusions

In the last decade, surface hopping dynamics has become an essential tool for the investigation of nonadiabatic processes in diverse fields, providing fundamental information to interpret data from time-resolved spectroscopy, to explain photochemical processes, and to predict new properties with potential technological applications. Motivated by the advances in computational capabilities and algorithms, such simulations are under constant pressure to address ever larger and more complex systems. The development of SH/DFT has opened possibilities to go far beyond where wavefunction ab initio methods could achieve.

In most implementations reported in the literature so far, DFT excitations used for surface hopping are obtained either from linear-response time-dependent theory or from bare KS gaps. Currently, we observe great effort from different research groups to generalize the methods for different kinds of nonadiabatic interactions, to provide better theoretical foundations, and to improve the hopping algorithms. The availability of SH/DFT in a small amount of public computational-chemistry software has also helped to popularize the method.

SH/DFT very successfully expanded the range of systems which can be approached for nonadiabatic dynamics investigations. We should, however, be aware that many methodological restrictions remain and must still be properly addressed. Such restrictions involve intrinsic limitations in the semi-classical local approach for nonadiabatic dynamics, in the sampling of statistical ensembles, and, more fundamentally, in the quality of the DFT excited-state predictions. In particular, the multireference character of regions of energy crossing between the excited and the ground states is still a challenge waiting for better solutions than those so far available.

Acknowledgments We would like to thank Dr. Michael Filatov for kindly providing the REKS data for Fig. 3 and also Dr. W. Arbelo-González, Dr. Fazzi, Dr. G. Rodrigues, and Dr. T. Very for helpful discussions.

References

1. Winter NOC, Graf NK, Leutwyler S, Hattig C (2013) Phys Chem Chem Phys 15:6623
2. Silva-Junior MR, Thiel W (2010) J Chem Theory Comput 6:1546
3. Silva-Junior MR, Schreiber M, Sauer SPA, Thiel W (2010) J Chem Phys 133:174318
4. Schreiber M, Silva-Junior MR, Sauer SPA, Thiel W (2008) J Chem Phys 128:134110
5. Silva-Junior MR, Schreiber M, Sauer SPA, Thiel W (2008) J Chem Phys 129:104103
6. Wu W, Zhang H, Braïda B, Shaik S, Hiberty P (2014) Theor Chem Acc 133:1
7. Dreuw A, Weisman JL, Head-Gordon M (2003) J Chem Phys 119:2943
8. Yonehara T, Hanasaki K, Takatsuka K (2011) Chem Rev 112:499
9. Yarkony DR (2011) Chem Rev 112:481
10. Worth GA, Cederbaum LS (2004) Annu Rev Phys Chem 55:127
11. Barbatti M (2011) WIREs Comput Mol Sci 1:620
12. Nelson T, Fernandez-Alberti S, Roitberg AE, Tretiak S (2013) J Chem Phys 138:224111
13. Zheng J, Meana-Pañeda R, Truhlar DG (2014) J Phys Chem Lett 5:2039
14. Nelson T, Fernandez-Alberti S, Chernyak V, Roitberg AE, Tretiak S (2012) J Chem Phys 136:054108
15. Akimov AV, Prezhdo OV (2014) Phys Rev Lett 113:153003
16. Gorshkov VN, Tretiak S, Mozyrsky D (2013) Nat Commun 4:2144
17. Kelly A, van Zon R, Schofield J, Kapral R (2012) J Chem Phys 136:084101
18. Nikitin EE (1968) In: Hartmann H, Heidberg J, Heydtmann H, Kohlmaier GH (eds) Chemische Elementarprozesse. Springer, Berlin
19. Tully JC, Preston RK (1971) J Chem Phys 55:562
20. Curchod BFE, Rothlisberger U, Tavernelli I (2013) ChemPhysChem 14:1314
21. Akimov AV, Neukirch AJ, Prezhdo OV (2013) Chem Rev 113:4496
22. Fabiano E, Keal TW, Thiel W (2008) Chem Phys 349:334

23. Wang L, Trivedi D, Prezhdo OV (2014) J Chem Theory Comput 10:3598
24. Fabiano E, Groenhof G, Thiel W (2008) Chem Phys 351:111
25. Kammerer CF, Lasser C (2008) J Chem Phys 128:144102
26. Lasser C, Swart T (2008) J Chem Phys 129:034302
27. Zhu C, Nakamura H, Nobusada K (2000) Phys Chem Chem Phys 2:557
28. Tully JC (1990) J Chem Phys 93:1061
29. Blais NC, Truhlar DG (1983) J Chem Phys 79:1334
30. Jaeger HM, Fischer S, Prezhdo OV (2012) J Chem Phys 137:22A545
31. Hammes-Schiffer S, Tully JC (1994) J Chem Phys 101:4657
32. Mitrić R, Werner U, Bonačić-Koutecký V (2008) J Chem Phys 129:164118
33. Pittner J, Lischka H, Barbatti M (2009) Chem Phys 356:147
34. Tapavicza E, Tavernelli I, Rothlisberger U (2007) Phys Rev Lett 98:023001
35. Plasser F, Crespo-Otero R, Pederzoli M, Pittner J, Lischka H, Barbatti M (2014) J Chem Theory Comput 10:1395
36. Ou Q, Fatehi S, Alguire E, Shao Y, Subotnik JE (2014) J Chem Phys 141:024114
37. Granucci G, Persico M, Toniolo A (2001) J Chem Phys 114:10608
38. Plasser F, Granucci G, Pittner J, Barbatti M, Persico M, Lischka H (2012) J Chem Phys 137:22A514
39. Wang L, Prezhdo OV (2014) J Phys Chem Lett 5:713
40. Schwartz BJ, Bittner ER, Prezhdo OV, Rossky PJ (1996) J Chem Phys 104:5942
41. Zhu CY, Nangia S, Jasper AW, Truhlar DG (2004) J Chem Phys 121:7658
42. Akimov AV, Long R, Prezhdo OV (2014) J Chem Phys 140:194107
43. Granucci G, Persico M (2007) J Chem Phys 126:134114
44. Granucci G, Persico M, Zoccante A (2010) J Chem Phys 133:134111
45. Bajo JJ, González-Vázquez J, Sola IR, Santamaria J, Richter M, Marquetand P, González L (2011) J Phys Chem A 116:2800
46. Granucci G, Persico M, Spighi G (2012) J Chem Phys 137:22A501
47. Jones GA, Acocella A, Zerbetto F (2008) J Phys Chem A 112:9650
48. Mitric R, Petersen J, Bonacic-Koutecky V (2009) Phys Rev A 79:053416
49. Tavernelli I, Curchod BFE, Rothlisberger U (2010) Phys Rev A 81:052508
50. Fischer M, Handt J, Schmidt R (2014) Phys Rev A 90:012527
51. Baer R (2002) Chem Phys Lett 364:75
52. Lopata K, Govind N (2011) J Chem Theory Comput 7:1344
53. Dobson JF, Bunner MJ, Gross EKU (1997) Phys Rev Lett 79:1905
54. Casida M (1995) In: Chong D (ed) Recent advances in density functional methods, part I. World Scientific, Singapore, p 155
55. Dreuw A, Head-Gordon M (2005) Chem Rev 105:4009
56. Elstner M, Porezag D, Jungnickel G, Elsner J, Haugk M, Frauenheim T, Suhai S, Seifert G (1998) Phys Rev B 58:7260
57. Niehaus TA, Suhai S, Della Sala F, Lugli P, Elstner M, Seifert G, Frauenheim T (2001) Phys Rev B 63:085108
58. Gonze X, Scheffler M (1999) Phys Rev Lett 82:4416
59. Görling A (1996) Phys Rev A 54:3912
60. Maitra NT (2006) J Chem Phys 125:014110
61. Akimov AV, Prezhdo OV (2013) J Chem Theory Comput 9:4959
62. Fischer M, Handt J, Schmidt R (2014) Phys Rev A 90:012525
63. Gao X, Peng Q, Niu Y, Wang D, Shuai Z (2012) Phys Chem Chem Phys 14:14207
64. Shenvi N, Roy S, Tully JC (2009) J Chem Phys 130:174107
65. Frank I, Hutter J, Marx D, Parrinello M (1998) J Chem Phys 108:4060
66. Doltsinis NL, Markwick PRL, Nieber H, Langer H (2008) In: Shukla MK, Leszczynski J (eds) Radiation induced molecular phenomena in nucleic acids. Springer, The Netherlands, p 265
67. Röhrig UF, Guidoni L, Laio A, Frank I, Rothlisberger U (2004) J Am Chem Soc 126:15328

68. Doltsinis NL, Marx D (2002) Phys Rev Lett 88:166402
69. Filatov M, Shaik S (1998) Chem Phys Lett 288:689
70. Okazaki I, Sato F, Yoshihiro T, Ueno T, Kashiwagi H (1998) J Mol Struct (THEOCHEM) 451:109
71. Gräfenstein J, Kraka E, Cremer D (1998) Chem Phys Lett 288:593
72. Furche F, Ahlrichs R (2002) J Chem Phys 117:7433
73. Chernyak V, Mukamel S (2000) J Chem Phys 112:3572
74. Hu C, Hirai H, Sugino O (2007) J Chem Phys 127:064103
75. Hu C, Sugino O, Tateyama Y (2009) J Chem Phys 131:114101
76. Hu C, Sugino O, Watanabe K (2014) J Chem Phys 140:054106
77. Send R, Furche F (2010) J Chem Phys 132:044107
78. Ahlrichs R, Bär M, Häser M, Horn H, Kölmel C (1989) Chem Phys Lett 162:165
79. Tavernelli I, Tapavicza E, Rothlisberger U (2009) J Mol Struct (THEOCHEM) 914:22
80. Barbatti M, Pittner J, Pederzoli M, Werner U, Mitrić R, Bonačić-Koutecký V, Lischka H (2010) Chem Phys 375:26
81. Werner U, Mitrić R, Suzuki T, Bonačić-Koutecký V (2008) Chem Phys 349:319
82. Tavernelli I, Tapavicza E, Rothlisberger U (2009) J Chem Phys 130:124107
83. Tavernelli I, Curchod BFE, Laktionov A, Rothlisberger U (2010) J Chem Phys 133:194104
84. Tavernelli I, Curchod BFE, Rothlisberger U (2009) J Chem Phys 131:196101
85. Franco de Carvalho F, Curchod BFE, Penfold TJ, Tavernelli I (2014) J Chem Phys 140:144103
86. Marian CM (2012) Wiley Interdiscip Rev Comput Mol Sci 2:187
87. Chiodo S, Russo N (2008) J Comput Chem 29:912
88. Chiodo SG, Russo N (2010) Chem Phys Lett 490:90
89. Humeniuk A, Wohlgemuth M, Suzuki T, Mitrić R (2013) J Chem Phys 139:134104
90. Billeter SR, Curioni A (2005) J Chem Phys 122:034105
91. Filatov M (2015) Top Curr Chem (in press)
92. Hohenberg P, Kohn W (1964) Phys Rev 136:B864
93. Gross EKU, Oliveira LN, Kohn W (1988) Phys Rev A 37:2805
94. Katriel J, Zahariev F, Burke K (2001) Int J Quantum Chem 85:432
95. Cremer D (2001) Mol Phys 99:1899
96. Huix-Rotllant M, Nikiforov A, Thiel W, Filatov M (2015) Top Curr Chem (in press)
97. Becke AD (2014) J Chem Phys 140:18A301
98. Cremer D (2013) WIREs Comput Mol Sci 3:482
99. Filatov M, Shaik S (1999) Chem Phys Lett 304:429
100. Gross EKU, Oliveira LN, Kohn W (1988) Phys Rev A 37:2809
101. Filatov M (2015) WIREs Comput Mol Sci 5:146
102. Grimme S, Waletzke M (1999) J Chem Phys 111:5645
103. Beck EV, Stahlberg EA, Burggraf LW, Blaudeau J-P (2008) Chem Phys 349:158
104. Kurzweil Y, Lawler KV, Head-Gordon M (2009) Mol Phys 107:2103
105. Sharkas K, Savin A, Jensen HJA, Toulouse J (2012) J Chem Phys 137:044104
106. Fromager E, Knecht S, Jensen HJA (2013) J Chem Phys 138:084101
107. Gräfenstein J, Kraka E, Filatov M, Cremer D (2002) Int J Mol Sci 3:360
108. Weigend F, Ahlrichs R (2005) Phys Chem Chem Phys 7:3297
109. Hehre WJ, Ditchfield R, Pople JA (1972) J Chem Phys 56:2257
110. Iikura H, Tsuneda T, Yanai T, Hirao K (2001) J Chem Phys 115:3540
111. Becke AD (1988) Phys Rev A 38:3098
112. Lee C, Yang W, Parr RG (1988) Phys Rev B 37:785
113. Minami T, Nakano M, Castet F (2011) J Phys Chem Lett 2:1725
114. Zheng G, Witek HA, Bobadova-Parvanova P, Irle S, Musaev DG, Prabhakar R, Morokuma K, Lundberg M, Elstner M, Köhler C, Frauenheim T (2007) J Chem Theory Comput 3:1349
115. Barbatti M, Paier J, Lischka H (2004) J Chem Phys 121:11614

116. Dunning TH (1989) J Chem Phys 90:1007
117. Sellner B, Barbatti M, Müller T, Domcke W, Lischka H (2013) Mol Phys 111:2439
118. Mori T, Glover WJ, Schuurman MS, Martinez TJ (2012) J Phys Chem A 116:2808
119. Kosma K, Trushin SA, Fuss W, Schmid WE (2008) J Phys Chem A 112:7514
120. Levine BG, Ko C, Quenneville J, Martínez TJ (2006) Mol Phys 104:1039
121. Becke AD (1993) J Chem Phys 98:5648
122. Stephens PJ, Devlin FJ, Chabalowski CF, Frisch MJ (1994) J Phys Chem 98:11623
123. Tapavicza E, Tavernelli I, Rothlisberger U, Filippi C, Casida ME (2008) J Chem Phys 129:124108
124. Hättig C (2005) Adv Quantum Chem 50:37
125. Schirmer J (1982) Phys Rev A 26:2395
126. Gozem S, Melaccio F, Valentini A, Filatov M, Huix-Rotllant M, Ferré N, Frutos LM, Angeli C, Krylov AI, Granovsky AA, Lindh R, Olivucci M (2014) J Chem Theory Comput 10:3074
127. Crespo-Otero R, Mardykov A, Sanchez-Garcia E, Sander W, Barbatti M (2014) Phys Chem Chem Phys 16:18877
128. Barbatti M (2014) J Am Chem Soc 136:10246
129. Tuna D, Došlić N, Mališ M, Sobolewski AL, Domcke W (2014) J Phys Chem B 119:2112
130. Barbatti M, Granucci G, Ruckenbauer M, Plasser F, Crespo-Otero R, Pittner J, Persico M, Lischka H (2013) NEWTON-X: a package for Newtonian dynamics close to the crossing seam: www.newtonx.org
131. Barbatti M, Ruckenbauer M, Plasser F, Pittner J, Granucci G, Persico M, Lischka H (2014) WIREs Comput Mol Sci 4:26
132. Akimov AV, Prezhdo OV (2014) J Chem Theory Comput 10:789
133. Mitrić R, Werner U, Wohlgemuth M, Seifert G, Bonačić-Koutecký V (2009) J Phys Chem A 113:12700
134. Craig CF, Duncan WR, Prezhdo OV (2005) Phys Rev Lett 95:163001
135. Fischer M, Handt J, Schmidt R (2014) Phys Rev A 90:012526
136. Shenvi N, Tully JC (2012) Faraday Discuss 157:325
137. Doltsinis NL (2002) In: Grotendorst J, Marx D, Muramatsu A (eds) Quantum simulations of complex many-body systems: from theory to algorithms. John von Neumann Institute for Computing, Julich
138. Tully JC (1998) Faraday Discuss 110:407
139. Castro A, Appel H, Oliveira M, Rozzi CA, Andrade X, Lorenzen F, Marques MAL, Gross EKU, Rubio A (2006) Phys Status Solidi B 243:2465
140. Frisch MJ, Trucks GW, Schlegel HB, Scuseria GE, Robb MA, Cheeseman JR, Scalmani G, Barone V, Mennucci B, Petersson GA, Nakatsuji H, Caricato M, Li X, Hratchian HP, Izmaylov AF, Bloino J, Zheng G, Sonnenberg JL, Hada M, Ehara M, Toyota K, Fukuda R, Hasegawa J, Ishida M, Nakajima T, Honda Y, Kitao O, Nakai H, Vreven T, Montgomery JA Jr, Peralta JE, Ogliaro F, Bearpark M, Heyd JJ, Brothers E, Kudin KN, Staroverov VN, Kobayashi R, Normand J, Raghavachari K, Rendell A, Burant JC, Iyengar SS, Tomasi J, Cossi M, Rega N, Millam NJ, Klene M, Knox JE, Cross JB, Bakken V, Adamo C, Jaramillo J, Gomperts R, Stratmann RE, Yazyev O, Austin AJ, Cammi R, Pomelli C, Ochterski JW, Martin RL, Morokuma K, Zakrzewski VG, Voth GA, Salvador P, Dannenberg JJ, Dapprich S, Daniels AD, Farkas Ö, Foresman JB, Ortiz JV, Cioslowski J, Fox DJ (2013) Gaussian 09, revision D.01. Gaussian, Inc., Wallingford
141. Lischka H, Müller T, Szalay PG, Shavitt I, Pitzer RM, Shepard R (2011) WIREs Comput Mol Sci 1:191
142. Lischka H, Shepard R, Shavitt I, Pitzer RM, Dallos M, Müller T, Szalay PG, Brown FB, Ahlrichs R, Böhm HJ, Chang A, Comeau DC, Gdanitz R, Dachsel H, Ehrhardt C, Ernzerhof M, Höchtl P, Irle S, Kedziora G, Kovar T, Parasuk V, Pepper MJM, Scharf P, Schiffer H, Schindler M, Schüler M, Seth M, Stahlberg EA, Zhao J-G, Yabushita S, Zhang Z,

Barbatti M, Matsika S, Schuurmann M, Yarkony DR, Brozell SR, Beck EV, Blaudeau J-P, Ruckenbauer M, Sellner B, Plasser F, Szymczak JJ (2012) COLUMBUS, an ab initio electronic structure program, release 7.0: www.univie.ac.at/columbus
143. Gordon MS, Schmidt MW (2005) In: Dykstra CE, Frenking G, Kim KS, Scuseria GE (eds) Theory and applications of computational chemistry the first forty years. Elsevier, Amsterdam, p 1167
144. Crespo-Otero R, Barbatti M, Yu H, Evans NL, Ullrich S (2011) ChemPhysChem 12:3365
145. Tomasello G, Humeniuk A, Mitrić R (2014) J Phys Chem A 118:8437
146. Klaumunzer B, Kroner D, Lischka H, Saalfrank P (2012) Phys Chem Chem Phys 14:8693
147. Frank I, Damianos K (2007) J Chem Phys 126:125105
148. Barbatti M, Lan Z, Crespo-Otero R, Szymczak JJ, Lischka H, Thiel W (2012) J Chem Phys 137:22A503
149. Fischer SA, Habenicht BF, Madrid AB, Duncan WR, Prezhdo OV (2011) J Chem Phys 134:024102
150. Rodrigues GP, Ventura E, do Monte SA, Barbatti M (2014) J Phys Chem A 118:12041
151. Langer H, Doltsinis NL (2004) Phys Chem Chem Phys 6:2742
152. Langer H, Doltsinis NL, Marx D (2005) ChemPhysChem 6:1734
153. Nieber H, Doltsinis NL (2008) Chem Phys 347:405
154. Markwick PRL, Doltsinis NL, Schlitter J (2007) J Chem Phys 126:045104
155. Wohlgemuth M, Bonačić-Koutecký V, Mitrić R (2011) J Chem Phys 135:054105
156. Mercier SR, Boyarkin OV, Kamariotis A, Guglielmi M, Tavernelli I, Cascella M, Rothlisberger U, Rizzo TR (2006) J Am Chem Soc 128:16938
157. Hu W, Lendvay G, Maiti B, Schatz GC (2008) J Phys Chem A 112:2093
158. Mališ M, Loquais Y, Gloaguen E, Biswal HS, Piuzzi F, Tardivel B, Brenner V, Broquier M, Jouvet C, Mons M, Došlić N, Ljubić I (2012) J Am Chem Soc 134:20340
159. Guglielmi M, Tavernelli I, Rothlisberger U (2009) Phys Chem Chem Phys 11:4549
160. Habenicht BF, Prezhdo OV (2008) Phys Rev Lett 100:197402
161. Long R, Prezhdo OV (2014) Nano Lett 14:3335
162. Habenicht BF, Prezhdo OV (2009) J Phys Chem C 113:14067
163. Böckmann M, Doltsinis NL, Marx D (2010) Angew Chem 122:3454
164. Bockmann M, Doltsinis NL, Marx D (2010) J Phys Chem A 114:745
165. Neukirch AJ, Shamberger LC, Abad E, Haycock BJ, Wang H, Ortega J, Prezhdo OV, Lewis JP (2013) J Chem Theory Comput 10:14
166. Akimov AV, Prezhdo OV (2014) J Am Chem Soc 136:1599
167. Crespo-Otero R, Barbatti M (2011) J Chem Phys 134:164305
168. Garavelli M (2006) Theor Chem Acc 116:87
169. Tavernelli I, Curchod BFE, Rothlisberger U (2011) Chem Phys 391:101
170. Jasper AW, Zhu CY, Nangia S, Truhlar DG (2004) Faraday Discuss 127:1
171. Casida M, Natarajan B, Deutsch T (2012) In: Marques MAL, Maitra NT, Nogueira FMS, Gross EKU, Rubio A (eds) Fundamentals of time-dependent density functional theory. Springer, Berlin/Heidelberg, p 279
172. Akimov AV, Muckerman JT, Prezhdo OV (2013) J Am Chem Soc 135:8682
173. Casida ME, Huix-Rotllant M (2012) Annu Rev Phys Chem 63:287
174. Barbatti M, Aquino AJA, Lischka H (2006) Mol Phys 104:1053
175. Vazdar M, Eckert-Maksic M, Barbatti M, Lischka H (2009) Mol Phys 107:845
176. Weingart O, Lan Z, Koslowski A, Thiel W (2011) J Phys Chem Lett 2:1506
177. Pederzoli M, Pittner J, Barbatti M, Lischka H (2011) J Phys Chem A 115:11136
178. Carstensen O, Sielk J, Schonborn JB, Granucci G, Hartke B (2010) J Chem Phys 133:124305
179. Ootani Y, Satoh K, Nakayama A, Noro T, Taketsugu T (2009) J Chem Phys 131:194306
180. Gao A-H, Li B, Zhang P-Y, Liu J (2014) Comput Theor Chem 1031:13
181. Sobolewski AL, Domcke WG (2007) J Phys Chem A 111:11725
182. Evans NL, Ullrich S (2010) J Phys Chem A 114:11225

183. Mishra A, Bäuerle P (2012) Angew Chem Int Ed 51:2020
184. Ameri T, Khoram P, Min J, Brabec CJ (2013) Adv Mater 25:4245
185. Grancini G, Polli D, Fazzi D, Cabanillas-Gonzalez J, Cerullo G, Lanzani G (2011) J Phys Chem Lett 2:1099
186. Veera S, Nismy NA, Adikaari AADT, Simon JH, Maxim S, Silva SRP (2011) Nanotechnology 22:265607
187. Sen K, Crespo-Otero R, Weingart O, Thiel W, Barbatti M (2013) J Chem Theory Comput 9:533

Top Curr Chem (2016) 368: 445–476
DOI: 10.1007/128_2015_631

Published online: 21 April 2015

Description of Conical Intersections with Density Functional Methods

Miquel Huix-Rotllant, Alexander Nikiforov, Walter Thiel, and Michael Filatov

Abstract Conical intersections are perhaps the most significant mechanistic features of chemical reactions occurring through excited states. By providing funnels for efficient non-adiabatic population transfer, conical intersections govern the branching ratio of products of such reactions, similar to what the transition states do for ground-state reactivity. In this regard, intersections between the ground and the lowest excited states play a special role, and the correct description of the potential energy surfaces in their vicinity is crucial for understanding the mechanism and dynamics of excited-state reactions. The methods of density functional theory, such as time-dependent density functional theory, are widely used to describe the excited states of large molecules. However, are these methods suitable for describing the conical intersections or do they lead to artifacts and, consequently, to erroneous description of reaction dynamics? Here we address the first part of this question and analyze the ability of several density functional approaches, including the linear-response time-dependent approach as well as the spin-flip and ensemble formalisms, to provide the correct description of conical intersections and the potential energy surfaces in their vicinity. It is demonstrated that the commonly used linear-response time-dependent theory does not yield a proper description of these features and that one should instead use alternative computational approaches.

M. Huix-Rotllant
Institute of Physical and Theoretical Chemistry, Goethe University Frankfurt, Max-von-Laue-Str. 7, 60438 Frankfurt am Main, Germany

A. Nikiforov and W. Thiel
Max-Planck-Institut für Kohlenforschung, Kaiser-Wilhelm-Platz 1, 45470 Mülheim an der Ruhr, Germany

M. Filatov (✉)
Institut für Physikalische und Theoretische Chemie, Universität Bonn, Beringstr. 4, 53115 Bonn, Germany
e-mail: mike.filatov@gmail.com

Keywords conical intersections • ensemble DFT • excited states • spin-flip TD-DFT • TD-DFT

Contents

1 Introduction

The molecular potential energy surface (PES) is perhaps one of the most significant concepts in molecular physics which enables one to model molecular structure in terms of specific spatial arrangements of atoms (molecular geometries) [1]. Defining (meta)stable molecular conformations (local minima) and transient species (saddle points or transition states) in terms of the molecular electronic energy–molecular geometry relationship [2], the PES concept is a basis for theories of molecular structure and reactivity and serves as a starting point for even more approximate models, such as force-field molecular mechanics [3]. Rooted in the Born–Oppenheimer approximation [4], the PES concept is naturally valid in situations where the coupling between the motion of the nuclei and electrons is negligibly weak, that is, when the separation between the electronic states is much greater than the characteristic energy of nuclear motion [5]. This assumption breaks down in the vicinity of points where two (or more) PESs corresponding to distinct electronic states become degenerate, the surface crossing points [5–8]. Near these points, the non-adiabatic coupling between the electronic and nuclear degrees of freedom becomes decisive for the dynamics of transformations occurring in the excited states [9–12] as well as in the ground state [13, 14] of molecules.

Especially interesting and at the same time especially challenging for their accurate theoretical description are situations of accidental (that is, not symmetry-imposed) crossing of PESs of states of the same spatial and spin symmetry, the conical intersections (CIs) [6, 15–19]. Such crossings occur in the subspace of $M-2$ internal molecular degrees of freedom (for a nonlinear molecule, $M = 3N - 6$, N – the number of atoms). The degeneracy between the electronic states is lifted along the two remaining directions, which span the branching plane

(BP) of the CI [6]. At a CI, the non-adiabatic coupling between the nuclear and electronic degrees of freedom becomes divergent [6, 9]; hence, the manifold of CI points, the CI seam, plays a decisive role for the dynamics of the electronic states by providing funnels for the efficient population transfer [9–12, 20]. As the BP defines all possible directions of exiting the strong non-adiabatic coupling region [6], it becomes a very important descriptor of the CI which, very similar to the transition vector in transition state theory [21, 22], determines the branching of possible products of the reaction occurring through the CI [23].

The correct theoretical description of CIs requires the use of computational methods capable of describing various electron correlation effects in the ground and the excited states with high and unbiased accuracy [10, 12, 24]. Naturally, since the first realization of the importance of CIs for the dynamics of excited states [9, 10], the computational investigation of CIs has been the realm of multi-reference (MR) methods of wavefunction theory (WFT), such as the complete active space self-consistent field (CASSCF) [25–28], the CAS-based second-order perturbation theory (CASPT2) [29], and the MR configuration interaction (MRCI) [30] methods. Although capable of delivering highly accurate results, these methods are computationally demanding and can be used routinely to calculate small molecular systems limited to just a handful of atoms. To go beyond this limitation and to match the challenges presented by the rapidly expanding use of ultrafast spectroscopy in photochemistry and photobiology [31, 32] one needs to employ computational methods capable of realistically describing large molecules. As the methods of density functional theory (DFT) [33, 34] offer a reasonably accurate description of electron correlation effects (which are vital for molecular bonding and structure) at a typical mean-field computational cost, these methods seem to represent a viable alternative to MR-WFT approaches.

However, there is a caveat. Originally [33], DFT was formulated for ground states only, and it was deemed inappropriate to apply it to variational calculation of individual excited states [35–37]. A way around this problem is offered by the response formalism implemented in the currently widely used linear-response (LR) time-dependent DFT (TD-DFT) approach [38, 39]. LR-TD-DFT (or TD-DFT for brevity) enables one to obtain the excitation energies from the poles of the ground-state density-density response function [38, 39], thus enabling the use of ground-state theory for obtaining excited states. Although capable of describing crossings between excited states correctly, TD-DFT may experience difficulties with the S_0/S_1 Cls as the ground electronic state (S_0) is the variationally optimized reference state for the response calculation and is thus described on a different footing than the excited state (S_1), which is a response state. In particular, there is no coupling between the ground and excited states in most approximate LR-TD-DFT methods, which results in a wrong dimensionality of the S_0/S_1 crossing seam, $M-1$ instead of $M-2$ [40–43].

An interesting modification of the original LR-TD-DFT formalism is implemented in the spin-flip (SF) TD-DFT method which employs a variationally optimized high-spin open-shell reference state (e.g., triplet state) to access lower spin states (e.g., singlets) by allowing one-electron transitions with simultaneous

inversion of the spin (spin-flip transitions) [44–47]. In SF-TD-DFT, the ground singlet state and the excited singlet states are obtained on the same footing as response states. This enables some interaction between these states and reinstates the correct dimensionality of the S_0/S_1 conical intersection [40, 43, 48]. However, the downside of SF-TD-DFT is a substantial spin-contamination of the so-obtained singlet state, which may lead to the occurrence of mixed spin-symmetry states, thus complicating the identification of physically meaningful excited states [48].

An alternative to the response formalism, for obtaining excited states in the context of DFT, is offered by the ensemble DFT approaches [39, 49–52]. Ensemble DFT, formulated in the seminal works of Lieb [53] (ground-state ensembles) and of Gross, Oliveira, and Kohn [49] (ensembles of ground and excited states) enables one to obtain excitation energies from the variational calculation, as contrasted with the response states of LR-TD-DFT and SF-TD-DFT. A practical implementation of ensemble DFT in the form of a generally applicable computational scheme was achieved in the spin-restricted ensemble-referenced Kohn–Sham (REKS) method [54–56] and its state-averaged (SA) extensions, SA-REKS [57] and SI-SA-REKS [42, 58] (SI: state-interaction). In particular, the SI-SA-REKS method has proved its ability to describe properly the S_0/S_1 CIs by yielding the correct dimensionality of the CI, $M-2$ [43, 58, 59]. Being a spin-restricted method which employs the same spatial orbitals for electrons with opposite spins, REKS is free from the spin-contamination which infests the SF-TD-DFT description, and yields a spin and space (if present) symmetry adapted description of ground and excited states.

The aforementioned computational approaches (LR-TD-DFT, SF-TD-DFT, and REKS) cover all the practically accessible implementations of DFT for describing the ground and excited states of molecules. In this chapter, the ability of these computational methods to describe CIs, and particularly S_0/S_1 CIs, of molecules is assessed in relation to probably the best description that the MR-WFT world can offer, namely MRCISD (MRCI with single and double excitations). When using approximate density functionals, LR-TD-DFT often yields good results for the energies of one-electron valence transitions and it seems tempting to believe that TD-DFT should be capable of yielding PES crossings as well. Although its inability to do so was clearly spelled out in the past [40, 41], the use of TD-DFT for modeling photodynamics and the underlying mechanistic features, such as CIs, seems to be gaining ground [60–73]. The consequences of using TD-DFT for photodynamics are reviewed in another chapter of this book;[1] here, we focus on the ability (or, more precisely, the inability) of this formalism to provide a proper description of CI topography while yielding seemingly reasonable geometries and relative energies of the minimum-energy crossing points.

As an alternative to TD-DFT, we investigate the performance of SF-TD-DFT and REKS methodologies which are known to yield the proper dimensionality of the CI seam [43]. Besides the molecular geometry at the minimum-energy CI

[1] See the chapter “Surface Hopping Dynamics with DFT Excited States” by M. Barbatti and R. Crespo-Otero.

(MECI) and its relative energy, we focus on the BP of the intersection and compare the BP vectors obtained in the DFT calculations with the corresponding MRCISD-derived vectors [59]. When benchmarking the DFT methods, we address a set of CIs of diverse topography occurring in unsaturated molecules during double-bond torsion; however, the conclusions drawn from these benchmarks should remain valid for other CIs as well, such as those in cyclic molecules or in nucleobases. The reason why we focus on relatively small molecules is that it would be extremely difficult to carry out MRCISD calculations with good-quality basis sets for larger molecules.

2 Conical Intersections

CIs are manifolds of points at which there is a real crossing (degeneracy) between two (or more) adiabatic Born–Oppenheimer PESs of electronic states of the same spatial and spin symmetry. The fundamental conditions for the occurrence of such intersections have been known since the early days of quantum mechanics [15, 17]. For two adiabatic electronic states Ψ_m and Ψ_n, which can be represented by the solutions of a 2×2 secular problem

$$\begin{pmatrix} H_{mm} & H_{mn} \\ H_{nm} & H_{nn} \end{pmatrix} \begin{pmatrix} C_{mm} & C_{mn} \\ C_{nm} & C_{nn} \end{pmatrix} = \begin{pmatrix} E_m & 0 \\ 0 & E_n \end{pmatrix} \begin{pmatrix} C_{mm} & C_{mn} \\ C_{nm} & C_{nn} \end{pmatrix}, \tag{1}$$

formulated in terms of (in general, arbitrary) diabatic orthogonal states Φ_m and Φ_n as $\Psi_m = C_{mm}\Phi_m + C_{nm}\Phi_n$ and $\Psi_n = C_{mn}\Phi_m + C_{nn}\Phi_n$, the crossing occurs whenever the two conditions

$$H_{mm} - H_{nn} = E_m - E_n = 0, \tag{2a}$$

$$H_{mn} = H_{nm} = 0, \tag{2b}$$

are fulfilled [6, 9, 11, 17–19, 74]. In the above equations, H_{mn} are the matrix elements, $H_{mn} = \langle \Phi_m | \hat{H} | \Phi_n \rangle$, of the Hamiltonian $\hat{H}$ in Born–Oppenheimer approximation evaluated with respect to the diabatic states. As was pointed out in the Introduction, these conditions can be fulfilled in the space of $M-2$ internal molecular coordinates; thus, the CIs may occur in molecules with three or more atoms.

2.1 Branching Plane Vectors

The degeneracy of the two electronic states is lifted in the subspace of the two coordinates which can be found expanding the Hamiltonian in (1) around the point of degeneracy through the first order in internal nuclear coordinates $\mathbf{Q}$,

$$\begin{pmatrix} H_{mm} & H_{mn} \\ H_{nm} & H_{nn} \end{pmatrix} \approx \mathbf{I}_2 \nabla_{\mathbf{Q}} \overline{H}.\delta\mathbf{Q} + \begin{pmatrix} \frac{1}{2}\nabla_{\mathbf{Q}}(H_{mm} - H_{nn}) & \nabla_{\mathbf{Q}} H_{nm} \\ \nabla_{\mathbf{Q}} H_{mn} & -\frac{1}{2}\nabla_{\mathbf{Q}}(H_{mm} - H_{nn}) \end{pmatrix} \cdot \delta\mathbf{Q}, \quad (3a)$$

$$= \mathbf{I}_2 \mathbf{s} \cdot \delta\mathbf{Q} + \begin{pmatrix} \mathbf{g} & \mathbf{h} \\ \mathbf{h} & -\mathbf{g} \end{pmatrix} \cdot \delta\mathbf{Q}, \quad (3b)$$

where $\overline{H} = (H_{mm} + H_{nn})/2$ is the average diagonal element, $\delta\mathbf{Q}$ is the nuclear displacement vector, $\nabla_{\mathbf{Q}}$ denotes differentiation with respect to nuclear coordinates, and $\mathbf{I}_2$ is a 2×2 unit matrix. The normalized vectors

$$\mathbf{x}_1 = \frac{\mathbf{g}}{\|g\|}, \quad (4a)$$

$$\mathbf{x}_2 = \frac{\mathbf{h}}{\|h\|}, \quad (4b)$$

span the branching plane of the CI which contains all the nuclear displacements lifting the degeneracy of the electronic states Ψ_m and Ψ_n. In the vicinity of a CI, the adiabatic PESs depend linearly on the nuclear displacements and have the topography of a double cone [6, 17]; hence the name.

The definition of the BP vectors of a CI given in (3) and (4) is not unique [74]; the vectors spanning *the same* plane can be defined via the adiabatic states Ψ_{m} and Ψ_{n}, which leads to the following definition:

$$\mathbf{x}_1^{'} = \frac{\mathbf{g}^{'}}{\|g^{'}\|}; \quad \mathbf{g}^{'} = \nabla_Q (E_m - E_n), \quad (5a)$$

$$\mathbf{x}_2^{'} = \frac{\mathbf{h}^{'}}{\|h^{'}\|}; \quad \mathbf{h}^{'} = \langle \Psi_m | \nabla_Q \hat{H} | \Psi_n \rangle. \quad (5b)$$

Although the planes spanned by the $(\mathbf{x}_1, \mathbf{x}_2)$ and $(\mathbf{x}_1^{'}, \mathbf{x}_2^{'})$ vector pairs are the same, the individual vectors are not necessarily aligned with each other. Furthermore, as was first demonstrated by Ruedenberg et al. [6], the vectors $(\mathbf{x}_1^{'}, \mathbf{x}_2^{'})$ are rigidly rotated within the plane when traveling along a loop around a CI. This leads to a certain arbitrariness in the directions of the $(\mathbf{x}_1^{'}, \mathbf{x}_2^{'})$ vectors obtained from CI optimization carried out with finite numerical accuracy. As the crossing point at which the optimization stops may be infinitesimally close to the CI, but not exactly at the CI, the BP vectors $(\mathbf{x}_1^{'}, \mathbf{x}_2^{'})$ obtained in a series of CI optimizations utilizing

the same computational method but started from different initial conditions may not coincide with each other.[2]

When comparing BP vectors $(\mathbf{x}_1', \mathbf{x}_2')$ obtained using different computational schemes, the arbitrariness in their orientation within the BP can be bypassed by aligning the vector pairs such as to maximize the projection of one of the vectors, e.g., $\mathbf{x}_1'$, obtained using computational method A onto the matching vector ($\mathbf{x}_1'$ or $\mathbf{x}_1$) obtained using method B [59, 76]. As proposed recently [59], such an alignment can be carried out by a similarity transformation $\mathbf{SRS}^{-1}$ that spans a 2D orthogonal rotation $\mathbf{R}$ and a shear transformation $\mathbf{S}$. The latter transformation is necessary because the BP vectors are not, in general, orthogonal with respect to one another, i.e., the inner products $\left(\mathbf{x}_1' \cdot \mathbf{x}_2'\right)$ and $(\mathbf{x}_1 \cdot \mathbf{x}_2)$ are not zero. The shear transformation leaves the inner product invariant upon rotation within the plane. The same publication [59] also introduced a number of useful measures to compare the BPs obtained using different computational methods. Thus, projections $p_B\left(\mathbf{x}_k^A\right)$, $k = 1, 2$ of the vectors $\mathbf{x}_k$ (or $\mathbf{x}_k'$) obtained using method A onto the BP obtained by method B and the projection r_{AB} of a rectangle spanned by the vector pair $(\mathbf{x}_1^A, \mathbf{x}_2^A)$ onto the $(\mathbf{x}_1^B, \mathbf{x}_2^B)$ rectangle were introduced to quantify the similarity (or discrepancy) between the BP vectors produced by different computational methods [59]. These measures are used in the following, when comparing the computational methods addressed in this chapter.

The use of the alignment procedure and the numerical measures described above for comparing BP vectors become especially useful when addressing computational schemes for which the BP vectors cannot be obtained using definitions (4) or (5), such as the TD-DFT or SF-TD-DFT methods. For these methods, only the $\mathbf{x}_1'$ vector can be determined explicitly by differentiation of the respective electronic energies. The $\mathbf{x}_2'$ vector is obtained during optimization for a CI using the branching space update method of Maeda et al. [77] as an orthogonal complement to $\mathbf{x}_1'$ in a plane that iteratively converges to the BP of the CI. The $(\mathbf{x}_1', \mathbf{x}_2')$ vector pairs so obtained have been shown to approximate sufficiently accurately the true BPs of the optimized CIs [77]. However, the resulting vectors are strictly orthogonal, a property not shared by the explicitly calculated vectors. In the context of the REKS method, the BP vectors are defined by (4), which uses diabatic states and, therefore, yields a unique orientation of the vectors. This feature becomes especially important when analyzing the Cls and their BPs in chemical terms.

[2] As shown by Yarkony [74, 75], a rotation of the crossing states which orthogonalizes the BP vectors brings the vectors to a unique orientation, especially when symmetry is present. Application of such a prescription, however, modifies the BP vectors, while leaving the BP unchanged.

2.2 Double Bond Torsion and Conical Intersections

In this chapter, we focus on the CIs arising during double-bond torsion in unsaturated molecules; thus, let us look more closely at this situation. The origin of CIs for double-bond torsion can be traced back to a crossing between the electronic states caused by homolytic and heterolytic breaking of the π-component of the double bond [78]. The homolytic bond breaking results in a diradicaloid electronic configuration, whereas the heterolytic bond breaking leads to an ionic (or zwitterionic) electronic configuration. According to the sign-change theorem of Longuet-Higgins [19], a CI should be present inside a loop connecting the conformations that correspond to the two bond-breaking mechanisms [12, 79–81]; see Fig. 1.

Let us now assume a nuclear movement in the direction of the $\mathbf{x}_1$ vector while keeping the interstate coupling element H_{mn} at zero. When passing through the CI, the S_0 wavefunction experiences a sudden switch from ionic to diradical (or vice versa) and the S_1 wavefunction does precisely the opposite. It is therefore natural to associate with the $\mathbf{x}_1$ vector a direction that corresponds to the transition between the uncoupled ionic and diradical states; it is these two electronic states that are included into the ensemble averaging in the SI-SA-REKS method; see Sect. 3.1. Conversely, a displacement along the $\mathbf{x}_2$ vector while keeping the energy difference H_{mm}–H_{nn} at zero should correspond to increasing (decreasing) the coupling between the states; hence, this motion should contain the torsion about the double bond axis. Indeed, when the two fragments connected by the double bond attain an

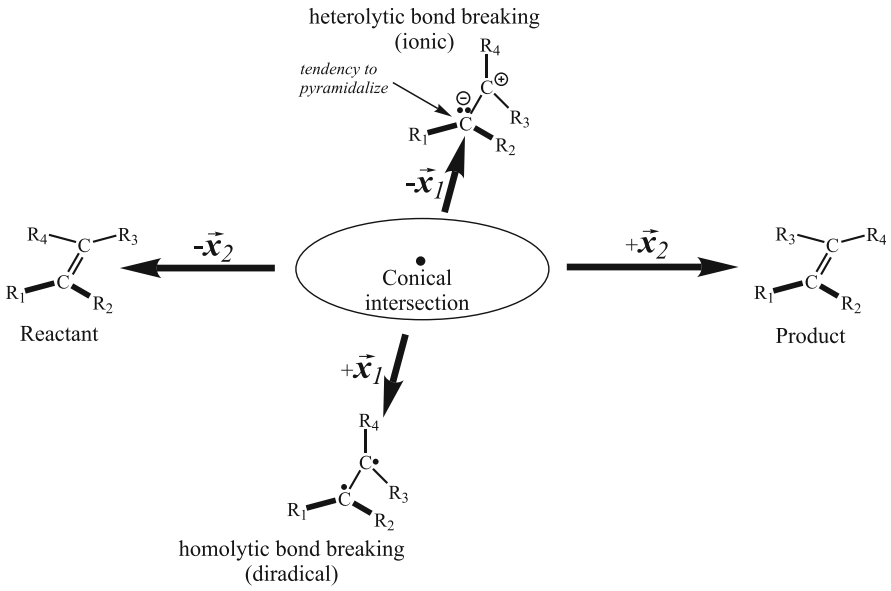

Fig. 1 Schematic representation of conical intersection for double bond isomerization. Reproduced with permission from [81]. Copyright © (2014) American Chemical Society

approximately orthogonal orientation during the torsion, the interaction between the fragment wavefunctions vanishes and this results in a vanishing H_{mn} element. Thus, the gradient of the interstate coupling element in the SI-SA-REKS method (see Sect. 3.1) can be conveniently associated with the $\mathbf{x}_2$ vector.

From this brief discussion, the advantage of the specific orientation of the BP vectors as in Fig. 1 is that it offers a simple chemical interpretation of the CI and the factors influencing its occurrence. In particular, the relative electronegativity of the fragments connected by the double bond and, consequently, the relative preference for one of the bond breaking mechanisms define the molecular geometry at a CI [58, 81]. For example, in alkenes, the homolytic π-bond breaking is energetically preferred over the heterolytic bond breaking, and this results in a pronounced pyramidalization at a CI which is needed to stabilize the ionic structure and (along with the torsion) to reach the point of surface crossing. By contrast, in organic molecules with strongly electron-withdrawing (or electron-donating) functional groups, the two bond breaking mechanisms may become nearly isoenergetic and a CI can be reached without requiring pyramidalization; in this case, the molecular geometry at the CI corresponds to double bond torsion combined with stretching/compression of the other single and double bonds, hence a bond length alternation (BLA) distortion [81]. Because the BP vectors obtained in the SI-SA-REKS calculations have a unique orientation and a transparent chemical interpretation, the vectors obtained by other methods, TD-DFT, SF-TD-DFT, and MRCISD, are aligned with them by using the recently introduced similarity transformation [59].

3 Computational Methods

In the following, we give a brief overview of the computational methods used to study the CIs in this chapter. A complete description of these computational schemes can be found in other chapters of this book, and so we recapitulate only those features most relevant for PES crossings. The interested reader is advised to consult the other chapters in this book and the literature references cited therein for more detail on the computational methodologies.

3.1 REKS Method

The REKS method [54–56] employs the ideas behind ensemble DFT to describe the non-dynamic correlation in the ground and excited states of molecules and to access the excited states through the application of the variational principle [42, 57, 58]. Perhaps the most important realization in ensemble DFT that was rigorously proved by Lieb [53] and computationally verified by Schipper et al. [82, 83] and by Morrison [84] is that the density and the ground-state energy of a strongly

correlated fermionic system is to be exactly represented by a weighted sum (ensemble) of the densities (and energies) of several electronic configurations (ensemble components). In the REKS method, the ensemble representation of the non-interacting Kohn–Sham reference system is used to describe the non-dynamic correlation arising because of near degeneracy of several electronic configurations; such as in situations with dissociating chemical bonds, near transition states of symmetry-forbidden reactions, biradicaloid species, etc. The ensemble representation leads to fractional occupation numbers (FONs) of several frontier Kohn–Sham orbitals, which are obtained simultaneously with the orbitals from the variational optimization of the total ground-state energy.

The excited states are accessed within the REKS methodology by applying the ensemble variational principle proved by Gross et al. [49]:

$$\sum_{K=1}^{M}\lambda_K\left\langle\Phi_K\left|\hat{H}\right|\Phi_K\right\rangle \geq\sum_{K=1}^{M}\lambda_K E_K;\quad 0\leq\lambda_K\leq 1;\quad \sum_{K=1}^{M}\lambda_K=1\,, \tag{6}$$

which states that the energy of an ensemble of trial wavefunctions Φ_K representing several *lowest* states of the many-body Hamiltonian $\hat{H}$ is always bounded from below by the weighted sum of the *exact* eigenenergies of this Hamiltonian taken with the same (positive definite) weighting factors λ_K. Restricting the ensemble averaging to two states, S_0 and S_1, the ground and the lowest excited states of an atom or a molecule, one obtains the excitation energy from the variational optimization of an ensemble

$$E_\omega=(1-\omega)E_0+\omega E_1, \tag{7}$$

of the two states by taking the energy difference

$$\Delta E=E_1-E_0=\frac{E_\omega-E_0}{\omega}, \tag{8}$$

where $0\leq\omega\leq 1$ is a fixed (that is, not variationally optimized) weighting factor.

For a system with two strongly correlated electrons in two orbitals (e.g., a biradical or a dissociating bond), the ground state as described by the REKS(2,2) method corresponds to a two-configurational model wavefunction [85],

$$\Phi_0=\sqrt{\frac{n_a}{2}}\left|\ldots\phi_a\overline{\phi}_a\right\rangle-\sqrt{\frac{n_b}{2}}\left|\ldots\phi_b\overline{\phi}_b\right\rangle, \tag{9}$$

where ϕ_a and ϕ_b are the fractionally occupied frontier orbitals, n_a and n_b are the respective FONs, and the unbarred and barred orbitals are occupied with α- and β-spin electrons, respectively. When the two active orbitals belong to two different irreducible representations of the molecular symmetry group (e.g., a homosymmetric biradical, H_2 with stretched bond, double bond torsion in C_2H_4,

etc.), the lowest singlet excited state arising from a one-electron excitation in the space of the two orbitals ϕ_a and ϕ_b can be approximated by an open-shell singlet (OSS) wavefunction [85],

$$\Phi_1 = \frac{1}{\sqrt{2}}|\ldots\phi_a\overline{\phi}_b\rangle + \frac{1}{\sqrt{2}}|\ldots\phi_b\overline{\phi}_a\rangle.. \tag{10}$$

The OSS state can be described by the spin-restricted open-shell Kohn–Sham (ROKS) method [86, 87].

Combining the two energies, $E^{\mathrm{REKS(2,2)}}$ and E^{ROKS} in an ensemble as in (7) and variationally optimizing the KS orbitals and the FONs of the active orbitals in REKS, one obtains the state-averaged energy E_ω from which the excitation energy is obtained by (8). In the SA-REKS method described, the same set of KS orbitals is used to construct the two energies, $E^{\mathrm{REKS(2,2)}}$ and E^{ROKS}. Typically, the weighting factor ω is set to 1/2, which corresponds to an equi-ensemble of the S_0 and S_1 states.

The SA-REKS method [57] treats S_0 and S_1 as uncoupled states, e.g., as in a homosymmetric biradical where the interaction between the states is prevented by symmetry. When the two states belong to the same symmetry species, e.g., as in a heterosymmetric biradical, the states approximated by the wavefunctions in (9) and (10) interact with each other and this interaction should be taken into account when calculating the energies of the individual ensemble components in (7) and (8). Within the REKS formalism, the uncoupled S_0 and S_1 states can be obtained by diagonalizing a 2×2 secular matrix

$$\begin{pmatrix} E^{\mathrm{REKS(2,2)}} & H_{01} \\ H_{01} & E^{\mathrm{ROKS}} \end{pmatrix}, \tag{11}$$

where the coupling matrix element H_{01}:

$$H_{01} = \sqrt{n_a}\langle\phi_a|n_a\hat{F}_a|\phi_a\rangle - \sqrt{n_b}\langle\phi_a|n_b\hat{F}_b|\phi_b\rangle = (\sqrt{n_a} - \sqrt{n_b})\varepsilon_{ab}, \tag{12}$$

is obtained by the application of Slater–Condon rules and the variational condition for the SA-REKS orbitals. In (12), $\hat{F}_a$ and $\hat{F}_b$ are the Fock operators for the open-shell orbitals and ε_{ab} is the off-diagonal Lagrange multiplier in the open-shell Lagrangian [54]. Equations (11) and (12) constitute the state-interaction SI-SA-REKS method [42, 58]. Provided that the weighting factor ω in (7) is set to 1/2, the state-averaged energy E_ω in the SA-REKS and SI-SA-REKS methods remains the same and the SA-REKS orbitals can be used in the SI-SA-REKS method. Note that (11) and (12) can also be obtained by using the adiabatic connection argument for an ensemble of two states [52].[3]

[3] See also the chapter "Ensemble DFT approach to excited states of strongly correlated molecular systems" by M. Filatov.

In the framework of the SI-SA-REKS method, a CI occurs when the two energies $E^{\mathrm{REKS(2,2)}}$ and E^{ROKS} become equal and the coupling matrix element H_{01} vanishes. Hence, the BP vectors $\mathbf{x}_1$ and $\mathbf{x}_2$ of the CI can be obtained by the differentiation of the respective energy differences and matrix elements as in (4), where the **g** and **h** vectors are given by (13) [59, 81]:

$$\mathbf{g} = \nabla_Q \left(E^{\mathrm{REKS(2,2)}} - E^{\mathrm{ROKS}} \right), \tag{13a}$$

$$\mathbf{h} = \nabla_Q H_{01}. \tag{13b}$$

The BP vectors as defined in the SI-SA-REKS method are in accord with the chemical interpretation presented in Sect. 2 [81]. Indeed, the $\mathbf{x}_1$ (or **g**) vector points in the direction of the difference of the gradients of the energies of the *non-interacting* states S_0 and S_1, exactly as it should be when moving along the $\mathbf{x}_1$ vector in Fig. 1. The same is true for the $\mathbf{x}_2$ vector as well. As the SI-SA-REKS energy formula can be obtained by the adiabatic connection argument, and hence within the domain of DFT, the BP vectors given in (13) can be regarded as approximations to the true DFT BP vectors, had these vectors been known from the exact theory.

Thus, when using the SI-SA-REKS method, the excited states are obtained from a variational calculation in strict correspondence with the ensemble variational principle of DFT [49]. The variational calculation of excited states is also implemented in constricted variational DFT (CV-DFT) [88, 89] reviewed in another chapter of this book. The use of the SI-SA-REKS method offers markedly improved accuracy when describing certain types of excitations, particularly excitations of extended π-conjugated molecular systems [90], charge-transfer excitations in donor-acceptor systems [91], and excitations of strongly correlated ground-state systems (biradicals, molecules with broken bonds, etc.) [90]. With regard to CIs, the SI-SA-REKS method yields the correct dimensionality ($M-2$) of the CI seam and the correct shape of the S_0 and S_1 PESs in its vicinity [43, 59]. This follows not only from the numerical tests presented below in this chapter but also from the general theoretical argument that the coupling between the S_0 and S_1 states is consistently taken into account in the SI-SA-REKS method.

3.2 Linear-Response Methods

In linear-response methods with local potentials, the excitation energies are obtained from the residues of the exact Fourier-transformed density-density response function χ [38],

$$\delta\rho(\mathbf{r},\omega) = \int \chi\left(\mathbf{r},\mathbf{r}',\omega\right) \delta v_{\mathrm{ext}}\left(\mathbf{r}',\omega\right) d\mathbf{r}', \tag{14}$$

where $v_{\mathrm{ext}}(\mathbf{r}, \omega)$ corresponds to the Fourier-transformed time-dependent external potential. Separating the time-dependent Hamiltonian into time-independent (zeroth-order) and time-dependent (first-order) parts, one arrives, after a few steps, at the linear-response equation

$$\chi^{LR}\left(\mathbf{r}, \mathbf{r}', \omega\right) = \chi_s\left(\mathbf{r}, \mathbf{r}', \omega\right) + \int\int \chi_s(\mathbf{r}, \mathbf{r}_1, \omega) f_{\mathrm{Hxc}}(\mathbf{r}_1, \mathbf{r}_2, \omega) \chi^{LR}\left(\mathbf{r}_2, \mathbf{r}', \omega\right) d\mathbf{r}_1 d\mathbf{r}_2, \tag{15}$$

where $\chi^{LR}(\mathbf{r},\mathbf{r}',\omega)$ is the LR function, $\chi_s(\mathbf{r},\mathbf{r}',\omega)$ is the zeroth-order response function, and $f_{\mathrm{Hxc}}(\mathbf{r}_1,\mathbf{r}_2,\omega) = |\mathbf{r}_1 - \mathbf{r}_2|^{-1} + f_{\mathrm{xc}}(\mathbf{r}_1,\mathbf{r}_2,\omega)$ is the Hartree plus the exchange-correlation (xc) kernel. All LR approaches extract the poles of some form of (15), differing mainly in the choice of the zeroth-order density used to construct the non-interacting response function and the xc kernel.

3.2.1 LR-TD-DFT

In LR-TD-DFT, the poles of the LR function (15) are cast in matrix form

$$\begin{bmatrix} \mathbf{A}(\omega) & \mathbf{B}(\omega) \\ \mathbf{B}^*(\omega) & \mathbf{A}^*(\omega) \end{bmatrix} \begin{bmatrix} \mathbf{X} \\ \mathbf{Y} \end{bmatrix} = \omega \begin{bmatrix} \mathbf{1} & \mathbf{0} \\ \mathbf{0} & -\mathbf{1} \end{bmatrix} \begin{bmatrix} \mathbf{X} \\ \mathbf{Y} \end{bmatrix}, \tag{16}$$

where the matrices $\mathbf{A}(\omega)$ and $\mathbf{B}(\omega)$ are defined as

$$[A(\omega)]_{ai,bj} = \left(\varepsilon_a^{KS} - \varepsilon_i^{KS}\right)\delta_{ij}\delta_{ab} + \left(ai\middle|f_{\mathrm{Hxc}}(\omega)\middle|bj\right), \tag{17a}$$

$$[B(\omega)]_{ai,bj} = \left(ia\middle|f_{\mathrm{Hxc}}(\omega)\middle|bj\right). \tag{17b}$$

In (17), $i, j, \ldots, a, b, \ldots$ and $p, q, \ldots$ are the indices for occupied, virtual, and general (occupied or virtual) spin-orbitals, and ε_p^{KS} are the eigenvalues of the KS Hamiltonian.

Adiabatic LR-TD-DFT based on a KS initial density employs the XC kernel taken in the adiabatic approximation (i.e., implying locality of the exchange-correlation (XC) kernel in the time domain),

$$f_{\mathrm{xc}}^{AA}\left(\mathbf{r}, \mathbf{r}'\right) = \frac{\delta^2 E_{\mathrm{xc}}[\rho]}{\delta\rho(\mathbf{r})\delta\rho(\mathbf{r}')}. \tag{18}$$

The fact that the xc kernel is frequency independent makes it impossible to account properly for doubly excited states within the adiabatic approximation [92, 93]. These reasons are believed to be the major causes of the failure of LR-TD-DFT methods to describe correctly the low-lying excited states in

highly-conjugated systems [94]. Recent advances in LR-TD-DFT beyond the adiabatic approximation are surveyed in another chapter of this book.[4]

When using the conventional closed-shell KS reference state, the LR-TD-DFT description in the adiabatic approximation breaks down near an S_0/S_1 conical intersection. Indeed, the assumption of pure-state v-representability employed in the traditional KS theory fails near the surface crossing points where the two electronic states become (nearly) degenerate. This is usually reflected in severe convergence problems of the KS self-consistent field iterations, which can be alleviated by either allowing holes below the Fermi level [82] or using a more general density *Ansatz,* such as in ensemble DFT [53, 82]. Furthermore, the interaction between the ground and the excited states is missing in adiabatic LR-TD-DFT, which results in a linear crossing instead of a conical intersection [40]. Surprisingly, it was observed by Levine et al. [40] and by Cordova et al. [95] that, even though the PESs are defective, the geometries and branching planes of minimal energy crossing points may look reasonable in comparison with other, theoretically justified, methods. The topography of conical intersections between different excited states is expected to be correct even at the adiabatic LR-TD-DFT level; however because of the missing effect of doubly-excited configurations its geometry and energy level may be incorrect [40].

3.2.2 Spin-Flip TD-DFT

Several schemes have been developed that attempt to ameliorate some of the problems arising in the adiabatic LR-TD-DFT description of S_0/S_1 conical intersections. Among them, one of the most successful is the spin-flip time-dependent DFT, SF-TD-DFT. In SF-TD-DFT, electronic configurations arising from the excitation operators with $\Delta M_s = \pm 1$ are coupled, unlike the usual formulation of TD-DFT in which only spin-preserving excitation operators with $\Delta M_s = 0$ are allowed. Several formulations of SF-TD-DFT appear in the literature [44–47]. Ziegler and Wang's formulation of SF-TD-DFT [45] relies on the non-collinear spin DFT framework, which operates with the KS spinors, rather than spin-free orbitals. In this formulation, the xc kernel is given by

$$f_{\mathrm{xc}}^{SF}\left(\mathbf{r},\mathbf{r}'\right) = \frac{\nu_{\mathrm{xc}}^{\alpha}(\mathbf{r}) - \nu_{\mathrm{xc}}^{\beta}(\mathbf{r})}{\rho^{\alpha}(\mathbf{r}') - \rho^{\beta}(\mathbf{r}')}, \tag{19}$$

where $\nu_{\mathrm{xc}}^{\sigma}$ and $\rho^{\sigma}(\mathbf{r}')$ are the xc potential and the electronic density of spin σ, respectively.

The configurations arising from the spin-flip $\alpha\beta$ and $\beta\alpha$ excitations are decoupled. Starting from an open-shell triplet reference in a two-electron

[4] See the chapter "Current status and recent developments in linear response time-dependent density-functional theory" by Mark E. Casida and Miquel Huix-Rotllant.

two-orbital model, this gives rise to two closed-shell configurations (a double excitation and a ground state) and two open-shell configurations which can be coupled to a singlet or a triplet configuration (see Fig. 2). Beyond this model, open-shell spin-uncompensated configurations are present so that spin-contaminated excitation energies are obtained, which can be partially purified by an a posteriori correction scheme [96].

The SF-TD-DFT approach has several advantages over adiabatic LR-TD-DFT, especially when describing a conical intersection region involving the ground state. First, the reference state is a triplet, which satisfies more easily the KS condition of non-interacting pure state v-representability. Second, SF-TD-DFT includes some extra double-excitation character in the excited states because of the configuration arising from the $a_\beta^\dagger i_\alpha$ excitation. Thus, ground and excited states are coupled in SF-TD-DFT, and this yields the correct dimensionality of the conical intersection region. This is a clear advantage over the usual spin-preserving TDDFT, in which the ground state and the excited states are decoupled [40].

SF-TD-DFT is able to introduce the ground and excited state coupling correctly, albeit only within the restricted configuration space represented in Fig. 2. In general, most CIs are well represented by SF-TD-DFT, but more complicated intersections are described only approximately [48]. One of the most important problems is that SF-TD-DFT states are frequently spin-mixed. In order to correct this problem, an a posteriori spin purification scheme has been proposed [96]. However, when using this scheme, the correct dimensionality of the CI seam is lost [43].

Within the two LR approaches, TD-DFT and SF-TD-DFT, CIs can be located using the branching space update method of Maeda et al. [77] which employs a projected gradient algorithm for optimizing the branching plane. The $\mathbf{x}_1'$-vector is calculated by (5) and the $\mathbf{x}_2'$-vector is approximated by an iterative update scheme. Note that in this approach the $\mathbf{x}_1'$ and $\mathbf{x}_2'$ vectors are strictly orthogonal, although the exact BP vectors need not necessarily have this property [6].

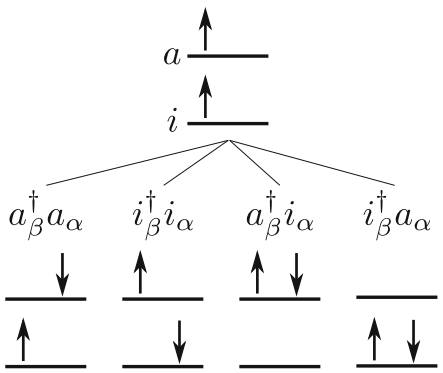

Fig. 2 Spin-flip excitations from an open-shell triplet reference

4 Application of DFT Methods to Conical Intersections

In this section we discuss the application of the computational methods described above to study CIs in a number of organic molecules and organic and biological chromophores [59]. The geometries of the MECIs optimized using the SI-SA-REKS (denoted for brevity as SSR), SF-TD-DFT (abbreviated to SF), and LR-TD-DFT (abbreviated to TD) methods are superimposed with the MRCISD geometries in Fig. 3. All the calculations reported here employed the 6-31+G** basis set and the BH&HLYP density functional (DFT calculations), with the exception of stilbene and anionic HBI, for which the MRCISD calculations employed a smaller 6-31G** basis set. The results of the MRCISD, SSR, and SF calculations are taken from [59] and the TD calculations were carried out using the same settings as in the SF calculations. In particular, the Tamm–Dancoff approximation (TDA) was used in the SF and TD calculations and both methods applied the algorithm by Maeda et al. [77] to locate the MECI points.

The majority of CIs arising in the molecules in Fig. 3 originate from a crossing between diradical and ionic electronic configurations along the reaction coordinate which corresponds to double bond torsion [12, 78, 79]. As discussed in Sect. 2, these CIs can be classified as twist-pyramidalization CIs (tw-pyr, for brevity), for

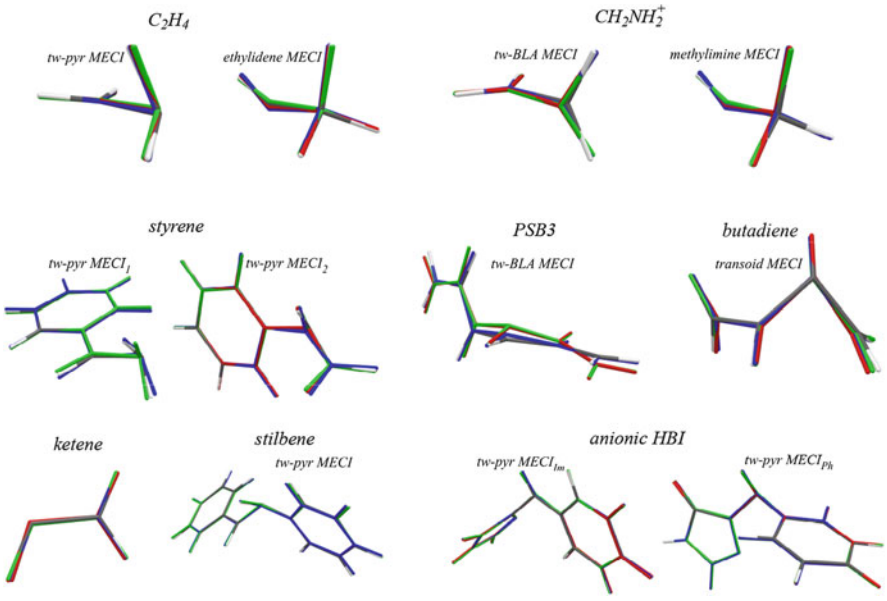

Fig. 3 Superimposed geometries at the respective MECI points optimized using MRCISD/6-31 + G** (*standard colors*), SSR-BH&HLYP/6-31 + G** (*solid blue*), SF-TD-DFT-BH&HLYP/6-31 + G** (*solid green*), LR-TD-DFT-BH&HLYP/6-31 + G** (*solid red*). MRCISD calculations employed the 6-31G** basis set for stilbene and anionic HBI. The MRCISD, SSR, and SF geometries are taken from [59]

situations where the homolytic breaking of the π-bond is energetically preferred, and as twist-bond_length_alternation (tw-BLA) CIs, for cases when the two π-bond breaking mechanisms, homolytic and heterolytic, either become nearly isoenergetic or the latter mechanism is preferred [81]. An accurate description of this type of CI requires a balanced description of the relative stability of diradical and ionic electronic configurations; thus the ability of computational methods to deliver such a description is probed by this type of CI.

Another type of CI shown in Fig. 3 can be described as n/π^* CIs that originate from the crossing between an electron configuration with a doubly occupied lone pair orbital ($n^2\pi^{*0}$) and a singly excited configuration ($n^1\pi^{*1}$) [97]. These CIs occur in ketene, ethylene (ethylidene or methylcarbene CI), and methyliminium cation (methylimine CI) as shown in Fig. 3. This type of CI probes the accuracy of description of lone-pair excitations by the tested theoretical methods.

The set of CIs shown in Fig. 3 misses some other types, in particular those found in cyclic molecules, such as nucleobases; however, good-quality reference MRCISD data for these CIs would be extremely difficult to obtain because of the large size of these molecules. We therefore omit these CIs from comparisons and focus instead on the ability of the DFT computational schemes to reproduce the molecular geometry and relative energy of the MECI points and the shape of the S_0 and S_1 PESs in their vicinity. To this end, we compare the BP vectors obtained using the DFT approaches with the respective MRCISD vectors, and we investigate the S_0 and S_1 PESs around the optimized MECI points by scanning the PESs (1) in the direction of the BP vectors and (2) along a closed path around the MECI point [98]. The latter scans enable us to evaluate the ability of the respective theoretical methods to describe the correct dimensionality of the CI seam [43, 98].

As is evident from Table 1, all the DFT methods are capable of describing the vertical excitations at the Franck–Condon (FC) point sufficiently accurately as compared to the best estimates of these energies. The accuracy of the MRCISD description is sometimes inferior to the DFT methods, probably because of certain restrictions with regard to the primary active space and the basis set employed [59]. The TD method tends to overestimate the vertical excitation energies as compared to the other two DFT methods. The relative energies of the MECI points obtained in the DFT calculations are in semi-quantitative agreement with the MRCISD energies; deviations of ca. 0.5 eV or slightly more (e.g., for ketene or PSB3) are observed in Table 1. However, the MRCISD energies in Table 1 cannot be regarded as highly accurate benchmark reference data because of the aforementioned basis set and active space restrictions; these data illustrate what is currently achievable at the computationally affordable MR-WFT level of calculation [59].

The accuracy of the optimized molecular geometries at the MECI points is characterized in Fig. 3 in graphical form and in Table 2 in terms of root-mean-square-deviations (RMSDs) between the optimized Cartesian coordinates. With the exception of the PSB3 cation, for which the SF and TD methods predict a much too strong pyramidalization of the C_3 atom, there are no conspicuous differences between the DFT and MRCISD geometries. This is reflected in the DFT vs

Table 1 Relative energies ΔE (in eV) with respect to the lowest ground-state minimum. Energies at the Franck–Condon (FC) point are vertical excitation energies of the lowest singlet $\pi \rightarrow \pi^*$ transition (best estimates given boldface in parentheses). Energies of optimized MECI structures refer to conical intersections between the S_1 and S_0 states. The MRCISD, SSR, and SF data are taken from [59]

Geometry		MRCI[a]	SSR[b]	SF[c]	TD[d]	Geometry		MRCI	SSR	SF	TD
Ethylene						Methyliminium					
FC point[e]	(**7.80**) [99]	8.11	7.55	7.70	7.53	FC point		9.52	8.62	9.22	8.32
tw-pyr MECI		4.79	4.96	4.82	4.73	tw-BLA MECI		3.82	3.83	4.27	4.14
eth MECI[f]		4.69	3.96	4.52	4.26	meth MECI[g]		5.63	4.54	5.46	5.22
Styrene						Penta-2,4-dieniminium cation, PSB3					
FC point	(**4.88**) [100]	5.76	5.10	5.29	5.25	*trans*-FC point[k]		4.47	4.18	4.43	4.97
tw-pyr CI_1[h]		4.68	4.29	4.01	n.a.[i]	$\Delta E^{S_0\ 1}_{cis-trans}$		0.16	0.15	0.13	0.14
tw-pyr CI_2[j]		5.28	4.97	4.83	4.72	*cis*-FC point[m]	(**4.20**) [101]	4.24	4.08	4.28	4.93
						tw-BLA MECI		2.38	3.00	3.08	2.82
Butadiene						Ketene					
trans-FC point[n]	(**6.18**) [99]	6.89	5.76	5.94	6.43	FC point	(**3.84**) [102]	4.01	3.93	4.01	4.06
$\Delta E^{S_0\ 1}_{cis-trans}$		0.07	0.14	0.11	0.14	MECI		2.43	3.00	2.82	3.27
cis-FC point[m,o]		6.68	5.54	5.96	6.05						
transoid MECI		4.89	5.58	5.19	5.40						
Stilbene						Anionic HBI					
trans-FC point[k]	(**4.1**) [103]	(5.35)[q]	4.18	4.35	4.42	FC point	(**3.06**) [104]	(3.88)[p]	3.00	3.14	3.56
$\Delta E^{S_0\ 1}_{cis-trans}$		(0.13)	0.18	0.35	0.33	tw-pyr $MECI_{Im}$[q]		(2.87)	2.97	2.84	2.60
cis-FC point[m]	(**4.6**) [103]	(5.74)	4.54	4.49	4.86	tw-pyr $MECI_{ph}$[r]		(3.20)	3.24	3.20	2.81
tw-pyr MECI		(4.50)	4.26	4.20	n.a.[i]						

[a]MRCISD/6-31+G** method
[b]SI-SA-REKS-BH&HLYP/6-31+G** method
[c]SF-TD-DFT-BH&HLYP/6-31+G** method
[d]LR-TD-DFT-BH&NLYP/6-31+G** method
[e]Franck–Condon point corresponding to the So minimum
[f]Ethylidene MECI
[g]Methylimine MECI
[h]Twisted-pyramidalized MECI1
[i]LR-TD-DFT energy is not available because of lack of convergence
[j]Twisted-pyramidalized MECI2
[k]*trans*-conformation
[l]Energy difference between *cis*- and *trans*-conformations in the ground state
[m]*cis*-conformation
[n]*trans*-conformation, transition to the bright B_u state
[o]Transition to the B1 state
[p]6-31G** basis set
[q]Twisted-pyramidalized MECI with twisted imidazole ring
[r]Twisted-pyramidalized MECI with twisted phenyl ring

Table 2 Root-mean-square deviations (RMSDs) between the MECI geometries and branching plane projections averaged over all molecules in Fig. 3. The MRCISD, SSR, and SF data are taken from [59]

RMSD (Å)[a]					BP projection[b]				
	MRCI	SSR	SF	TD	MRCI	SSR	SF	TD	
MRCI	0.0000	0.0609	0.0698	0.0658	MRCI	1.0000	0.8059	0.9027	0.6307
SSR	0.0609	0.0000	0.0712	0.0420	SSR	0.7845	1.0000	0.8089	0.6459
SF	0.0698	0.0712	0.0000	0.0304	SF	0.8996	0.8064	1.0000	0.6721
TD	0.0789	0.0504	0.0365	0.0000	TD	0.7378	0.7677	0.8111	1.0000

[a]RMSDs are given as a matrix with the off-diagonal elements corresponding to the values for methods *A* and *B*

[b]BP projections are given as a matrix with the off-diagonal elements r_{AB} representing the projection of the BP obtained using method *A* onto the BP obtained using method *B*

MRCISD RMSDs in Table 2, which vary in the range between 0.061 Å (SSR) and 0.079 Å (TD). An even better agreement is seen between the geometries obtained by the different DFT methods, especially for the SF and TD methods (0.030 Å). The BP projections in Table 2 indicate that all methods produce nearly the same BP vectors at the MECI geometries. The very good agreement between the DFT methods and MRCISD seems to indicate that these much simpler methods can be confidently used in lieu of MRCISD for locating CIs and analyzing the S_0 and S_1 PESs in their vicinity. However, there is a caveat: despite the seemingly good agreement with the high-level MR-WFT approach, not all the DFT methods produce the correct dimensionality of the CI seam. In the following, we focus on three molecules and their respective CIs, ethylene and its tw-pyr MECI, cationic PSB3 and its tw-BLA MECI, as well as ketene molecule and its n/π^* MECI, as representatives of the specific types of CIs discussed above.

4.1 Ethylene

On the S_0/S_1 CI seam in ethylene there are two distinct MECI points that correspond to a tw-pyr MECI (the major photorelaxation funnel) and to a MECI point with partial transfer of a hydrogen atom; see the tw-pyr and ethylidene MECIs of C_2H_4 in Fig. 3 [105–108]. The tw-pyr MECI originates from a crossing between the PESs for homolytic and heterolytic π-bond breaking along the double bond torsion mode. As the heterolytic π-bond breaking is strongly disfavored in ethylene, the tw-pyr MECI features a strong pyramidalization of one of the carbon atoms to stabilize the ionic electronic configuration.

All the DFT methods employed here predict the vertical excitation energy at the FC point in a good agreement with the best theoretical estimate of 7.8 eV. The energy level of the tw-pyr MECI is much lower than the FC point. The DFT methods yield tw-pyr MECI energies varying between 4.96 eV (SSR) and 4.73 eV (TD), in good agreement with the MRCISD value 4.79 eV; see Table 1. The BP vectors predicted by the DFT methods are in very good agreement with the MRCISD BP vectors, as can be seen from a visual comparison of the vectors in Fig. 4 and from the BP projections (see Sect. 2) which lie in the range 0.99–0.97 in each case.

From these results it seems that all the DFT methods are capable of describing the tw-pyr MECI in ethylene correctly. However, a closer look at the S_0 and S_1 PESs near the MECI point reveals that the surface crossing predicted by adiabatic LR-TD-DFT is not actually a conical intersection but is rather a linear crossing. As seen in Fig. 5, the S_1 PES produced by adiabatic LR-TD-DFT falls below the S_0 PES when moving along the $\mathbf{x}_1$ direction.[5] Furthermore, the shape of the S_0 and S_1 PESs

[5] The conventional KS DFT/LR-TD-DFT calculations experienced severe convergence problems in the vicinity of the MECI point, which are reflected in the shape of the S_1 PES in the upper right panel of Fig. 5.

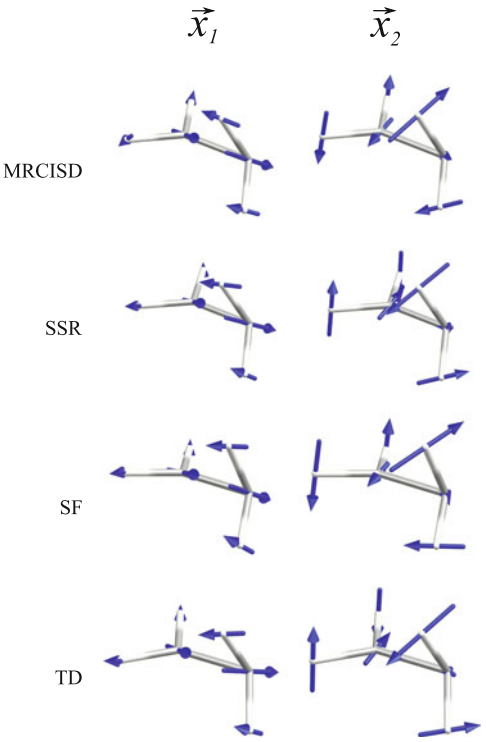

Fig. 4 BP vectors of twisted-pyramidalized MECI of ethylene calculated using MRCISD, SSR-BH&HLYP, SF-TD-BH&HLYP, and LR-TD-BH&HLYP methods

along the $\mathbf{x}_2$ direction as predicted by adiabatic LR-TD-DFT is inconsistent with the SSR and SF PESs. It appears as though the S_0 state is unaware of the proximity to the S_1 state. The SSR and SF methods yield some interaction between these states which is reflected in the shapes of the S_0 and S_1 PESs; the latter appear to be (approximately) symmetrically split around some median level, whereas no such (quasi) symmetric splitting can be seen in the adiabatic LR-TD-DFT PESs; see the lower right panel of Fig. 5. Thus, adiabatic LR-TD-DFT predicts a linear S_0/S_1 PES crossing, as expected from the vanishing off-diagonal matrix element in (1); hence, only one degree of freedom is sufficient to make the PESs cross, which leads to the $M-1$ dimensionality of the crossing seam in adiabatic LR-TD-DFT [40, 41, 43].

These observations are corroborated by the plot in Fig. 6, which shows the S_0–S_1 energy difference along a loop with a radius of 0.002 Å around the MECI point. The SSR and SF energy differences always remain finite which means that there is a finite gap at all geometries which lift the degeneracy of the S_0 and S_1 states at the MECI point. By contrast, the adiabatic LR-TD-DFT energy difference curve crosses the zero level twice when going around the loop. It is also noteworthy that the shape of the energy difference curve as produced by adiabatic LR-TD-DFT is markedly different from those of the other two methods. The angle θ that parameterizes the loop is taken from the direction of the $\mathbf{x}_1$ vector. This implies that the coupling between the S_0 and S_1 states should vanish at the points $\theta = 0°$ and

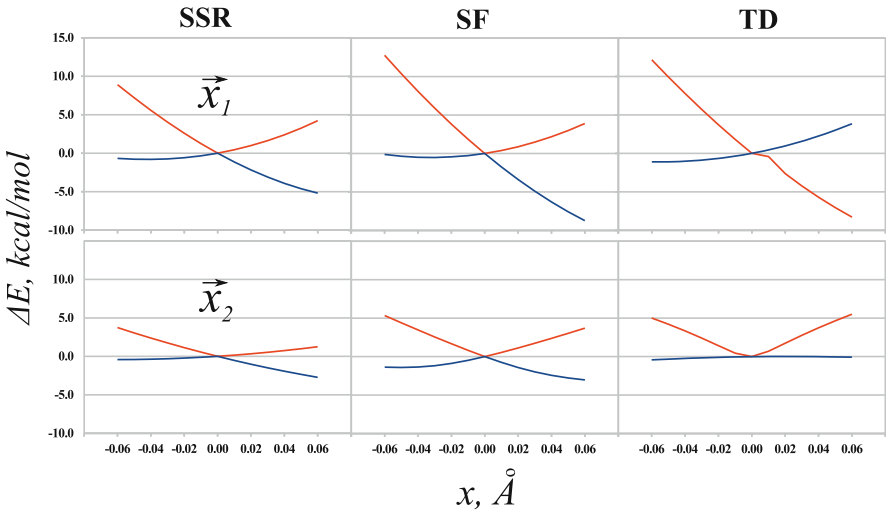

Fig. 5 S_0 (*blue*) and S_1 (*red*) PES profiles near the tw-pyr MECI of ethylene. *Upper panels* – profiles along the $\mathbf{x}_1$ BP vector, *lower panels* – along the $\mathbf{x}_2$ BP vector. *Leftmost panels* – profiles obtained using the SSR-BH&HLYP/6-31 + G** method, *middle panels* – obtained by the SF-TD-BH&HLYP/6-31 + G** method, *rightmost panels* – using the TD-BH&HLYP/6-31 + G** method. For each computational method, the MECI energy level is taken as the origin of the energy scale (in kcal/mol). The variable x corresponds to displacement (in Å) from the MECI geometry in the direction of the $\mathbf{x}_1$ or $\mathbf{x}_2$ vector, respectively

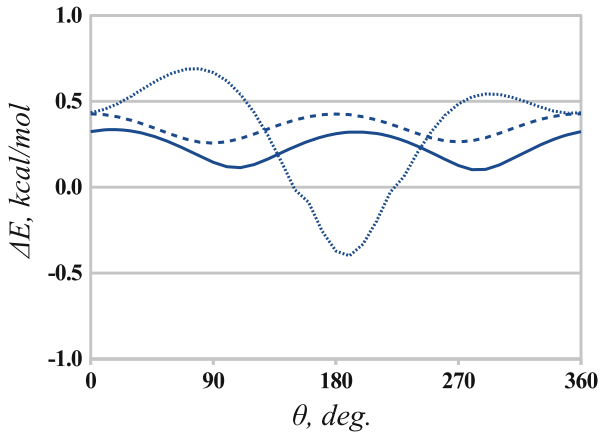

Fig. 6 The S_0–S_1 energy difference (in kcal/mol) along a loop around the MECI point of ethylene. The *solid line* corresponds to the SSR-BH&HLYP/6-31 + G** method, the *dashed line* to the SF-TD-BH&HLYP/6-31 + G** method, and the *dotted line* to the TD-BH&HLYP/6-31 + G** method. The loop radius is 0.002 Å. For each method, the angle θ (in deg) is taken from the direction of the $\mathbf{x}_1$ vector

$\theta = 180°$; note that the off-diagonal element H_{mn} in (1) is supposed to zero out when moving along the $\mathbf{x}_1$ direction. The SSR and SF methods predict the maximum S_0–S_1 splitting in the $\mathbf{x}_1$ direction, whereas adiabatic LR-TD-DFT yields the maximum splitting approximately in the $\mathbf{x}_2$ direction ($\theta \approx 0°$).

As found by Gozem et al. [43, 98] for the example of PSB3, the multi-state CASPT2 and MRCISD methods yield energy difference curves around a MECI which are similar in shape to those predicted by SSR and SF and dissimilar to TD-DFT. Therefore, in spite of its seemingly good predictions for the geometry and energy of the tw-pyr MECI of ethylene, TD-DFT fails to give the correct conical topography of the crossing and yields the wrong shape of the two PESs in the vicinity of the crossing point. As discussed by Barbatti and Crespo-Otero (see Footnote 1) this has severe consequences for the description of the dynamics near the crossing points, rendering TD-DFT practically useless for modeling non-adiabatic population transfer through PES crossings.

4.2 Penta-2,4-Dieniminium Cation, PSB3

In the protonated Schiff base PSB3 (penta-2,4-dieniminium), which is often used as the simplest model of the Schiff base retinal chromophore, the presence of a strong electron-withdrawing substituent, the cationic nitrogen, leads to the occurrence of a tw-BLA MECI which originates from a crossing between the diradical and ionic electronic configurations obtained by homolytic and heterolytic breaking of the central π-bond along the torsion mode [42, 43, 81, 109, 110]. The ionic configuration is stabilized by the presence of the electron-withdrawing group and no pyramidalization is needed to reach the crossing point with the diradical configuration.

The SSR and SF methods predict the vertical excitation energy at the FC point in good agreement with the available theoretical best estimate, the quantum Monte–Carlo excitation energy of 4.2 eV for the *cis*-conformation. The TD-DFT FC excitation energy is in error by more than 0.7 eV, which is typical of this method when applied to extended π-conjugated systems, such as, e.g., cyanine dyes [90]. Despite the discrepancy at the FC point, the tw-BLA MECI of PSB3 is predicted by all the DFT methods to lie at approximately the same energy level of ca. 3 eV; see Table 1. The BP vectors of PSB3 correspond to the BLA distortion (the $\mathbf{x}_1$ vector) and to the torsion mode (the $\mathbf{x}_2$ vector) in good agreement with the MRCISD vectors; see Fig. 7.

The shape of the S_0 and S_1 PESs in the vicinity of the MECI point (see Fig. 8) exhibits the same trend as for ethylene; the SSR and SF methods yield a sole crossing point at the MECI and the surfaces are (approximately) symmetrically split when moving along the $\mathbf{x}_2$ direction within the branching plane. The adiabatic LR-TD-DFT surfaces do not show any interaction between the S_0 and S_1 states along the $\mathbf{x}_2$ direction (see right lower panel of Fig. 8) and there are several crossing points between the states when moving along the $\mathbf{x}_1$ direction, which indicates that the

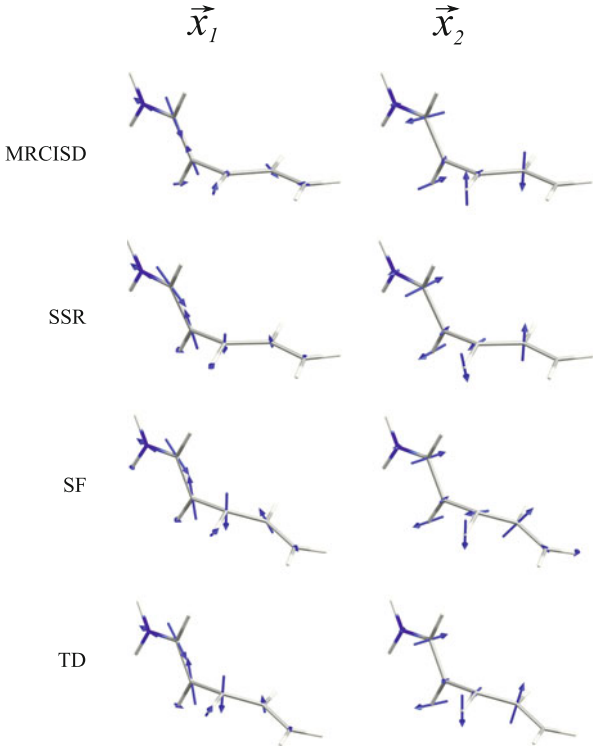

Fig. 7 BP vectors of the twisted-BLA MECI of PSB3 calculated using MRCISD, SSR-BH&HLYP, SF-TD-BH&HLYP, and LR-TD-BH&HLYP methods

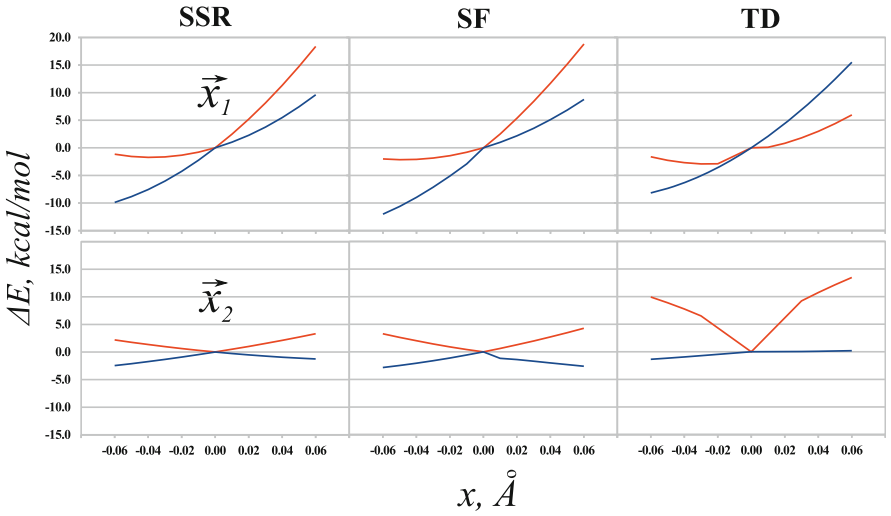

Fig. 8 S_0 (*blue*) and S_1 (*red*) PES profiles near the tw-BLA MECI of PSB3. See caption of Fig. 5 for the legend

surface crossing has a linear rather than conical character. Furthermore, the adiabatic LR-TD-DFT method experiences severe convergence problems in the vicinity of the crossing point which prevented us from obtaining a reasonable S_0–S_1 energy difference plot along a loop around the MECI. Nevertheless, the curves in Fig. 8 corroborate the fact that the adiabatic LR-TD-DFT method is incapable of yielding the correct topography of the S_0/S_1 crossing point and that the other two DFT methods, SSR and SF, are thus preferred for studying the non-adiabatic dynamics of the excited state of PSB3 and related molecules.

4.3 Ketene

Ketene displays an S_0/S_1 CI along the C–C–O bending mode which, as first analyzed by Yarkony [97], originates from a crossing between the ^{1}A' and ^{1}A" electronic states. This crossing is linear under the C_s symmetry constraint; however, it becomes conical when the symmetry restriction is lifted, as there emerges another direction which lifts the degeneracy between these states. Hence, the BP vectors of this CI correspond to the a'-symmetric C–C–O bending mode ($\mathbf{x}_1$) and the out-of-plane H–C–C–O torsional mode ($\mathbf{x}_2$).

As shown in Fig. 9, the DFT methods yield BP vectors in very good agreement with the MRCISD vectors. However, all the DFT methods predict the MECI point

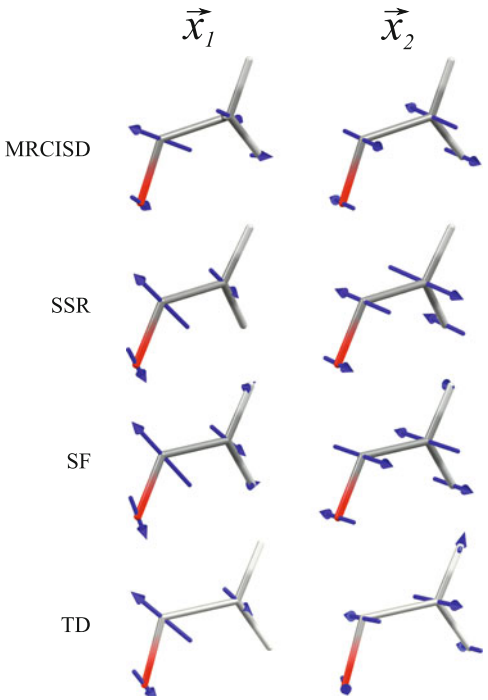

Fig. 9 BP vectors of twisted MECI of ketene calculated using MRCISD, SSR-BH&HLYP, SF-TD-BH&HLYP, and LR-TD-BH&HLYP methods

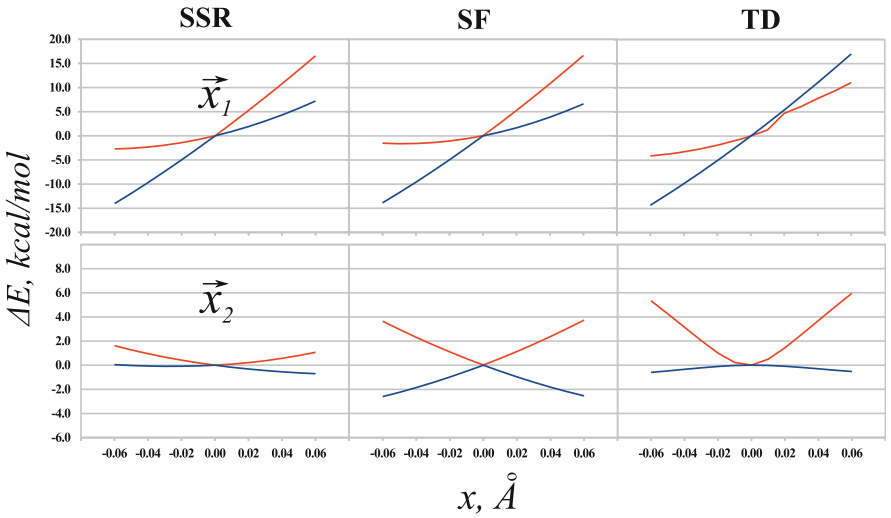

Fig. 10 S_0 (*blue*) and S_1 (*red*) PES profiles near the MECI of ketene. See caption of Fig. 5 for the legend

at a somewhat higher, by ca. 0.4–0.8 eV, energy level than MRCISD. This difference may likely be caused by a somewhat stiffer C–C bond predicted by the DFT calculations. This can be asserted from the $\mathbf{x}_1$ vectors in Fig. 9, which describes a C–C bond stretching combined with the C–C–O bending motion: there is a notably greater degree of bond stretching in the MRCISD vector. As can be seen from Fig. 10, which shows the S_0 and S_1 PES profiles along the BP vectors, this motion noticeably destabilizes the S_0 (^{1}A′) state in which the C–C π-bonding orbital is doubly occupied. It is therefore plausible that MRCISD somewhat underestimates the strength of the C–C bond in ketene because of the rather small basis set and the limited active space employed in the calculations [59].

Although the DFT methods agree with one another on the strength of the C–C bond in ketene, the TD-DFT method differs from the other two methods as to the character of the S_0/S_1 crossing; whereas SSR and SF predict it to be conical, TD yields a linear crossing. This is confirmed by the plots of the S_0–S_1 energy difference along a loop around the minimal energy crossing point in Fig. 11. In this plot, a loop with a greater radius, 0.02 Å, was chosen to bypass certain SCF convergence problems in the DFT calculations with a smaller radius (0.002 Å was used in Fig. 6). The adiabatic LR-TD-DFT energy difference in Fig. 11 (dotted curve) again crosses the zero line twice which indicates a linear crossing. The same linear character of the S_0/S_1 PES crossing can be seen in the rightmost plots in Fig. 10, which show the PES profiles along the BP vectors. Similar to the cases of ethylene and PSB3, there is no coupling between the crossing states in the adiabatic LR-TD-DFT curves. By contrast, the SSR and SF methods correctly predict (nearly) the symmetric splitting of the states which indicates a proper description of the coupling and therefore a correct conical character of the PES crossing point.

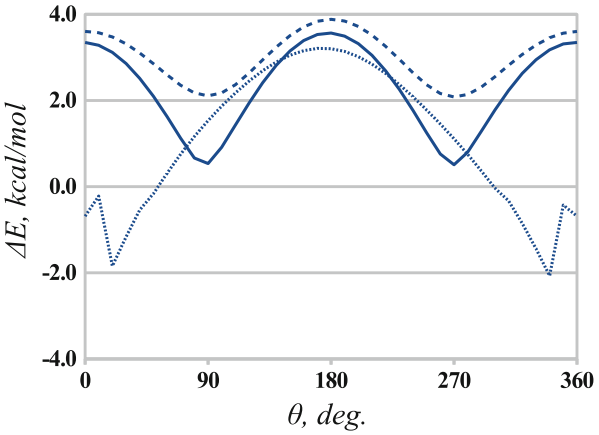

Fig. 11 The S_0–S_1 energy difference (in kcal/mol) along a loop around the MECI point of ketene. See text for details of the loop. See caption of Fig. 6 for the legend

5 Conclusions and Outlook

In this chapter we have analyzed the ability of practically available computational schemes based on density functional theory to describe conical intersections and the ground- and excited-state potential energy surfaces in their vicinity. We have investigated three DFT-based methods, namely the popular LR-TD-DFT approach as well as the less common SF-TD-DFT and SI-SA-REKS methods, and have evaluated their performance by comparing with reference results from standard MRCISD-WFT calculations.

In accord with previous analysis from the literature [40, 41, 43], we find that the LR-TD-DFT method is incapable of properly describing the topography of the S_0/S_1 crossing point, yielding a linear instead of a conical intersection seam (i.e., $M-1$ rather than $M-2$ dimensionality). In LR-TD-DFT, the excited states are obtained as the response states and thus do not couple with the ground state (the reference state), which leads to the observed linear character of the intersection. In addition, there are generally serious SCF convergence problems near the crossing point in the conventional DFT calculation, which often result in aborted TD-DFT calculations. These shortcomings render the LR-TD-DFT method largely useless for modeling non-adiabatic relaxation processes.

The other two methods considered here, SF-TD-DFT and SI-SA-REKS, do not suffer from the erratic SCF convergence near the crossing point and yield the correct dimensionality of the CI seam and the correct shape of the S_0 and S_1 PESs in its vicinity. Being based on ensemble DFT, the SI-SA-REKS method is capable of correctly treating the multi-reference character of the nearly degenerate crossing states. This method has the further advantage of not suffering from the erroneous spin-contamination which plagues the SF-TD-DFT states. Although the use of the high-spin (triplet) state as the reference state in SF-TD-DFT removes the SCF convergence issues near the surface crossing points, the spin contamination inherent in this approach often complicates the identification of proper excited

configurations and results in the occurrence of unphysical mixed-spin states. The use of ad hoc spin-purification procedures [96] should be discouraged as it destroys the correct dimensionality of the CI seam [43].

In view of the widespread availability of the LR-TD-DFT method in quantum chemical codes, we would like to raise concerns about using this method for investigating the dynamics of excited states. It is our hope that the arguments presented in this chapter can help researchers in this area to make reasonable choices when selecting the computational methodology for applications.

References

1. McNaught AD, Wilkinson A (1997) IUPAC. Compendium of chemical terminology, 2nd edn. (The "Gold Book"). Blackwell, Oxford
2. Mezey PO (1987) Potential energy hypersurfaces. Elsevier, New York
3. Allinger NL (1976) In: Gold V, Bethell D (eds) Advances in physical organic chemistry, vol 13. Academic, London, pp 1–82
4. Born M, Oppenheimer R (1927) Ann Phys 84:457
5. Baer M (2006) Beyond Born–Oppenheimer: electronic nonadiabatic coupling terms and conical intersections. Wiley, Hoboken
6. Atchity GJ, Xantheas SS, Ruedenberg K (1991) J Chem Phys 95:1862
7. Domcke W, Yarkony DR, Köppel H (eds) (2004) Conical intersections. Electronic structure, dynamics and spectroscopy. Advanced series in physical chemistry, vol 15. World Scientific, Singapore
8. Domcke W, Yarkony DR, Köppel H (eds) (2011) Conical intersections. Theory, computation and experiment. Advanced series in physical chemistry, vol. 17 World Scientific, Singapore
9. Yarkony DR (1996) Rev Mod Phys 68:985
10. Bernardi F, Olivucci M, Robb MA (1996) Chem Soc Rev 25:321
11. Yarkony DR (2004) In: Domcke W, Yarkony DR, Köppel H (eds) Conical intersections. electronic structure, dynamics and spectroscopy. Advanced series in physical chemistry, vol 15. World Scientific, Singapore, pp 41–127
12. Migani A, Olivucci M (2004) In: Domcke W, Yarkony DR, Köppel H (eds) Conical intersections. electronic structure, dynamics and spectroscopy. Advanced series in physical chemistry, vol 15. World Scientific, Singapore, pp 271–320
13. Butler LJ (1998) Annu Rev Phys Chem 49:125
14. Soto J, Arenas JF, Otero JC, Pelez D (2006) J Phys Chem A 110:8221
15. Hund F (1927) Z Phys 40:742
16. von Neumann J, Wigner E (1929) Physik Z 30:467
17. Teller E (1937) J Phys Chem 41:109
18. Herzberg G, Longuet-Higgins HC (1963) Discuss Faraday Soc 35:77
19. Longuet-Higgins HC (1975) Proc R Soc Lond Ser A 344:147
20. Truhlar DG, Mead CA (2003) Phys Rev A 68:032501
21. Polanyi JC (1972) Acc Chem Res 5:161
22. Polanyi JC (1987) Science 236:680
23. Sellner B, Barbatti M, Lischka H (2009) J Chem Phys 131:024312
24. Robb MA (2011) In: Domcke W, Yarkony DR, Köppel H (eds) Conical intersections. Theory, computation and experiment. Advanced series in physical chemistry, vol 17. World Scientific, Singapore, pp 3–50

25. Docken KK, Hinze J (1972) J Chem Phys 57:4928
26. Ruedenberg K (1976) K.R. Sundberg. In: Calais JL, Goscinski O, Linderberg J, Öhrn J (eds) Quantum science. Plenum, New York, pp 505–515
27. Ruedenberg K (1979) In: Report on the NRCC 1978 workshop on post-Hartree–Fock quantum chemistry. Lawrence Berkeley Laboratory, Univ. of California, Report LBL 8233, UC4, CONF 780883, pp 46–64
28. Roos BO (1987) In: Lawley KP (ed) Ab initio methods in quantum chemistry II. Wiley, New York, pp 399–446
29. Andersson K, Malmqvist P, Roos BO (1992) J Chem Phys 96:1218
30. Shavitt I (1977) In: Schaefer HF III (ed) Modern theoretical chemistry, vol 3. Methods of electronic structure theory. Plenum, New York, pp 189–275
31. Zewail AH (2000) J Phys Chem A 104:5660
32. Zewail AH (2010) Chem Phys 378:1
33. Hohenberg P, Kohn W (1964) Phys Rev 136:B864
34. Kohn W, Sham LJ (1965) Phys Rev 140:A1133
35. Gaudoin R, Burke K (2004) Phys Rev Lett 93:173001
36. Gaudoin R, Burke K (2005) Phys Rev Lett 94:029901
37. Ziegler T, Krykunov M, Autschbach J (2014) J Chem Theory Comput 10:3980
38. Casida ME, Jamorski C, Bohr F, Guan JO, Salahub DR (1994) In: Karna SP, Yeates AT (ed) Nonlinear optical materials: theory and modeling, ACS symposium series, vol 628, Div Comp Chem, 1996. Symposium on nonlinear optical materials – theory and modeling, at the 208th national meeting of the American-Chemical-Society, Washington, DC, Aug 21–25, 1994, pp 145–163
39. Marques MAL, Gross EKU (2003) In: Fiolhais C, Nogueira F, Marques MAL (eds) A primer in density-functional theory. Lecture notes in physics, vol 620. Springer, Berlin, pp 144–184
40. Levine BG, Ko C, Quenneville J, Martínez TJ (2006) Mol Phys 104:1039
41. Yang S, Martínez TJ (2011) In: Domcke W, Yarkony DR, Köppel H (eds) Conical intersections. Theory, computation and experiment, advanced series in physical chemistry, vol 17. World Scientific, Singapore, pp 347–374
42. Huix-Rotllant M, Filatov M, Gozem S, Schapiro I, Olivucci M, Ferré N (2013) J Chem Theory Comput 9:3917
43. Gozem S, Melaccio F, Valentini A, Filatov M, Huix-Rotllant M, Ferré N, Frutos LM, Angeli C, Krylov AI, Granovsky AA, Lindh R, Olivucci M (2014) J Chem Theory Comput 10:3074
44. Shao Y, Head-Gordon M, Krylov AI (2003) J Chem Phys 118:4807
45. Wang F, Ziegler T (2004) J Chem Phys 121:12191
46. Rinkevicius Z, Vahtras O, Ågren H (2010) J Chem Phys 133:114104
47. Bernard YA, Shao Y, Krylov AI (2012) J Chem Phys 136:204103
48. Huix-Rotllant M, Natarajan B, Ipatov A, Wawire CM, Deutsch T, Casida ME (2010) Phys Chem Chem Phys 12:12811
49. Gross EKU, Oliveira LN, Kohn W (1988) Phys Rev A 37:2805
50. Gross EKU, Oliveira LN, Kohn W (1988) Phys Rev A 37:2809
51. Oliveira LN, Gross EKU, Kohn W (1988) Phys Rev A 37:2821
52. Franck O, Fromager E (2014) Mol Phys 112:1684
53. Lieb EH (1983) Int J Quant Chem 24:243
54. Filatov M, Shaik S (1999) Chem Phys Lett 304:429
55. Filatov M, Shaik S (2000) J Phys Chem A 104:6628
56. Moreira IDPR, Costa R, Filatov M, Illas F (2007) J Chem Theory Comput 3:764
57. Kazaryan A, Heuver J, Filatov M (2008) J Phys Chem A 112:12980
58. Filatov M (2013) J Chem Theory Comput 9:4526
59. Nikiforov A, Gamez JA, Thiel W, Huix-Rotllant M, Filatov M (2014) J Chem Phys 141:124122

60. Send R, Sundholm D (2007) J Phys Chem A 111:8766
61. Tapavicza EE, Tavernelli I, Röthlisberger U, Filippi C, Casida ME (2008) J Chem Phys 129:124108
62. Baranovskii VI, Sizova OV (2008) J Struct Chem 49:803
63. Delchev VB, Ivanova IP (2012) Monatshefte Chem 143:1141
64. Mališ M, Loquais Y, Gloaguen E, Biswal HS, Piuzzi F, Tardivel B, Brenner V, Broquier M, Jouvet C, Mons M, Došlić N, Ljubić I (2012) J Am Chem Soc 134:20340
65. Baranovskii VI, Mal'tsev DA, Sizova OV (2013) Russ Chem Bull 61:973
66. Kumar A, Sevilla MD (2013) Photochem Photobiol Sci 12:1328
67. Zwijnenburg MA (2013) Phys Chem Chem Phys 15:11119
68. Moreno M, Ortiz-Sanchez JM, Gelabert R, Lluch JM (2013) Phys Chem Chem Phys 15:20236
69. Kobayashi R, Amos RD (2013) Mol Phys 111:1574
70. Talhi O, Lopes GR, Santos SM, Pinto DCGA, Silva AMS (2014) J Phys Org Chem 27:756
71. Wiebeler C, Bader CA, Meier C, Schumacher S (2014) Phys Chem Chem Phys 16:14531
72. Belfon KAA, Gough JD (2014) Chem Phys Lett 593:174
73. Baranovskii VI, Maltsev DA (2014) Comp Theor Chem 1043:71
74. Yarkony DR (2001) J Phys Chem A 105:6277
75. Yarkony DR (2000) J Chem Phys 112:2111
76. Toniolo A, Ben-Nun M, Martínez TJ (2002) J Phys Chem A 106:4679
77. Maeda S, Ohno K, Morokuma K (2010) J Chem Theory Comput 6:1538
78. Bonačić-Koutecký V, Koutecký J, Michl J (1987) Angew Chem Int Ed 26:170
79. Haas Y, Cogan S, Zilberg S (2005) Int J Quant Chem 102:961
80. Dick B, Haas Y, Zilberg S (2008) Chem Phys 347:65
81. Filatov M, Olivucci M (2014) J Org Chem 79:3587
82. Schipper PRT, Gritsenko OV, Baerends EJ (1998) Theor Chem Acc 99:329
83. Schipper PRT, Gritsenko OV, Baerends EJ (1999) J Chem Phys 111:4056
84. Morrison RC (2002) J Chem Phys 117:10506
85. Salem L, Rowland C (1972) Angew Chem Int Ed 11:92
86. Ziegler T, Rauk A, Baerends EJ (1977) Theor Chim Acta 43:261
87. Filatov M, Shaik S (1998) Chem Phys Lett 288:689
88. Krykunov M, Ziegler T (2013) J Chem Theory Comput 9:2761
89. Krykunov M, Seth M, Ziegler T (2014) J Chem Phys 140:18A502
90. Filatov M, Huix-Rotllant M (2014) J Chem Phys 141:024112
91. Filatov M (2014) J Chem Phys 141:124123
92. Maitra NT, Zhang F, Cave R, Burke K (2004) J Chem Phys 120:5932
93. Cave RJ, Zhang F, Maitra NT, Burke K (2004) Chem Phys Lett 389:39
94. Huix-Rotllant M, Ipatov A, Rubio A, Casida ME (2011) Chem Phys 391:120
95. Cordova F, Doriol LJ, Ipatov A, Casida ME, Filippi C, Vela A (2007) J Chem Phys 127:164111
96. Xu X, Gozem S, Olivucci M, Truhlar DG (2013) J Phys Chem Lett 4:253
97. Yarkony DR (1999) J Phys Chem A 103:6658
98. Gozem S, Schapiro I, Ferré N, Olivucci M (2012) Science 337:1225
99. Schreiber M, Silva-Junior MR, Sauer SPA, Thiel W (2008) J Chem Phys 128:134110
100. Leopold DG, Hemley RJ, Vaida V, Roebber JL (1981) J Chem Phys 75:4758
101. Valsson O, Angeli C, Filippi C (2012) Phys Chem Chem Phys 14:11015
102. Chiang SY, Bahou M, Wu YJ, Lee YP (2002) J Chem Phys 117:4306
103. Rice JK, Baronavski AP (1992) J Phys Chem 96:3359
104. Filippi C, Zaccheddu M, Buda F (2009) J Chem Theory Comput 5:2074
105. Ben-Nun M, Martínez TJ (2000) Chem Phys 259:237
106. Quenneville J, Martínez TJ (2003) J Phys Chem A 107:829

107. Barbatti M, Paier J, Lischka H (2004) J Chem Phys 121:11614
108. Virshup AM, Chen J, Martínez TJ (2012) J Chem Phys 137:22A519
109. Gozem S, Huntress M, Schapiro I, Lindh R, Granovsky AA, Angeli C, Olivucci M (2012) J Chem Theory Comput 8:4069
110. Gozem S, Krylov AI, Olivucci M (2013) J Chem Theory Comput 9:284

Index